[illegible]

VOLUME 78 JULY 18, 1974 NUMBER 15

JPCHAx

# THE JOURNAL OF PHYSICAL CHEMISTRY

ห้องสมุด กรมวิทยาศาสตร์

PUBLISHED BIWEEKLY BY THE AMERICAN CHEMICAL SOCIETY

THE JOURNAL OF

# PHYSICAL CHEMISTRY

**BRYCE CRAWFORD, Jr.**, *Editor*
WILMER G. MILLER, *Associate Editor*
ROBERT W. CARR, Jr., FREDERIC A. VAN-CATLEDGE, *Assistant Editors*

**EDITORIAL BOARD:** A. O. ALLEN (1970-1974), C. A. ANGELL (1973-1977), F. C. ANSON (1974-1978), V. A. BLOOMFIELD (1974-1978), J. R. BOLTON (1971-1975), L. M. DORFMAN (1974-1978), M. FIXMAN (1970-1974), H. S. FRANK (1970-1974), R. R. HENTZ (1972-1976), W. J. KAUZMANN (1974-1978), R. L. KAY (1972-1976), D. W. McCLURE (1974-1978), R. M. NOYES (1973-1977), J. A. POPLE (1971-1975), B. S. RABINOVITCH (1971-1975), H. REISS (1970-1974), S. A. RICE (1969-1975), F. S. ROWLAND (1973-1977), R. L. SCOTT (1973-1977), A. SILBERBERG (1971-1975), J. B. STOTHERS (1974-1978), W. A. ZISMAN (1972-1976)

**AMERICAN CHEMICAL SOCIETY**, *1155 Sixteenth St., N.W., Washington, D. C. 20036*

**Books and Journals Division**

JOHN K CRUM *Director*
RUTH REYNARD *Assistant to the Director*

CHARLES R. BERTSCH *Head, Editorial Processing Department*
D. H. MICHAEL BOWEN *Head, Journals Department*
BACIL GUILEY *Head, Graphics and Production Department*
SELDON W. TERRANT *Head, Research and Development Department*

©Copyright, 1974, by the American Chemical Society. Published biweekly by the American Chemical Society at 20th and Northampton Sts., Easton, Pa. 18042. Second-class postage paid at Washington, D. C., and at additional mailing offices.

All manuscripts should be sent to *The Journal of Physical Chemistry*, Department of Chemistry, University of Minnesota, Minneapolis, Minn. 55455.

*Additions and Corrections* are published once yearly in the final issue. See Volume 77, Number 26 for the proper form.

*Extensive or unusual alterations in an article after it has been set in type are made at the author's expense*, and it is understood that by requesting such alterations the author agrees to defray the cost thereof.

The American Chemical Society and the Editor of *The Journal of Physical Chemistry* assume no responsibility for the statements and opinions advanced by contributors.

Correspondence regarding accepted copy, proofs, and reprints should be directed to Editorial Processing Department, American Chemical Society, 20th and Northampton Sts., Easton, Pa. 18042. Department Head: CHARLES R. BERTSCH. Assistant Department Head: MARIANNE C. BROGAN. Assistant Editor: CELIA B. MCFARLAND. Editorial Assistant: JOSEPH E. YURVATI.

Advertising Office: Centcom, Ltd., 50 W. State St., Westport, Conn. 06880.

## Business and Subscription Information

Send all new and renewal subscriptions *with payment* to: Office of the Controller, 1155 16th Street, N.W., Washington, D. C. 20036. Subscriptions should be renewed promptly to avoid a break in your series. All correspondence and telephone calls regarding changes of address, claims for missing issues, subscription service, the status of records, and accounts should be directed to Manager, Membership and Subscription Services, American Chemical Society, P.O. Box 3337, Columbus, Ohio 43210. Telephone (614) 421-7230.

On changes of address, include both old and new addresses with ZIP code numbers, accompanied by mailing label from a recent issue. Allow four weeks for change to become effective.

Claims for missing numbers will not be allowed (1) if loss was due to failure of notice of change in address to be received before the date specified, (2) if received more than sixty days from date of issue plus time normally required for postal delivery of journal and claim, or (3) if the reason for the claim is "issue missing from files."

Subscription rates (1974): members of the American Chemical Society, $20.00 for 1 year; to nonmembers, $60.00 for 1 year. Those interested in becoming members should write to the Admissions Department, American Chemical Society, 1155 Sixteenth St., N.W., Washington, D. C. 20036. Postage to Canada and countries in the Pan-American Union, $5.00; all other countries, $6.00. Air freight rates available on request. Single copies for current year: $3.00. Rates for back issues from Volume 56 to date are available from the Special Issues Sales Department, 1155 Sixteenth St., N.W., Washington, D. C. 20036.

Subscriptions to this and the other ACS periodical publications are available on microfilm. Supplementary material not printed in this journal is now available in microfiche form on a current subscription basis. For information on microfilm or microfiche subscriptions, write Special Issues Sales Department at the address above.

**Notice to Authors last printed in the issue of June 6, 1974**

THE JOURNAL OF
# PHYSICAL CHEMISTRY

*Volume 78, Number 15 July 18, 1974*

JPCHAx 78(15) 1447–1572 (1974)
ISSN 0022-3654

Temperature Dependence of the Reactions of OH and $HO_2$ with $O_3$
**W. B. DeMore* and E. Tschuikow-Roux** 1447

Chemical Lasers Produced from $O(^3P)$ Atom Reactions. IV. CO Laser Emission from the O + CN Reaction . . . . . . . . . . . . . . . . . . . . . . . . . . . **R. G. Shortridge and M. C. Lin*** 1451

Relative Rates of the Reactions of $O(^1D_2)$ Atoms with Alkanes and Cycloalkanes
. . . **P. Michaud, G. Paraskevopoulos, and R. J. Cvetanović*** 1457

Condensed-Phase Photochemistry of Cyclobutanone
**Samuel G. Thomas, Jr., and William A. Guillory*** 1461

Shock Tube Cis–Trans Isomerization Studies. III. . . . . . . . . . . . . . . **Peter M. Jeffers** 1469

Low-Temperature Pulse Radiolysis. II. Time-Dependent Spectra of Anions of Aromatic Ketones
. . . **Mikio Hoshino,* Shigeyoshi Arai, and Masashi Imamura** 1473

Enthalpies of Mixing in Liquid Alkaline Earth Fluoride–Alkali Fluoride Mixtures. II. Calcium Fluoride with Lithium, Sodium, and Potassium Fluorides . **O. J. Kleppa* and K. C. Hong** 1478

Studies in High-Pressure Mass Spectrometry. V. Thermodynamics of Solvation Reactions. $NH_4^+$–$NH_3$ . . . . . . . . . . . . . . . . . . . . . . **M. R. Arshadi and Jean H. Futrell*** 1482

Thermodynamics of Polycarboxylate Aqueous Solutions. II. Dilatometry and Calorimetry of Nickel and Barium Binding . . . . . . . . . . . . . . . . . . **F. Delben* and S. Paoletti** 1486 ■

Micellar Effects on the Ionization of Carboxylic Acids and Interactions between Quaternary Ammonium Ions and Aromatic Compounds . . . . **Clifford A. Bunton* and M. J. Minch** 1490

Raman Spectra of Molten Mixtures Containing Aluminum Fluoride. I. The LiF–$Li_3AlF_6$ Eutectic Mixture . . . . . . . . . . . . . . **Signe Kjelstrup Ratkje and Erling Rytter*** 1499

Spectra and Structure of Boron–Nitrogen Compounds. II. Infrared and Raman Spectra of Trimethylamine–Borane . **J. D. Odom, J. A. Barnes, B. A. Hudgens, and J. R. Durig*** 1503 ■

Transition State Enthalpies of Transfer in Aqueous Dimethyl Sulfoxide Solutions. The Alkaline Hydrolysis of Ethyl Acetate
. . . **Richard Fuchs,* C. Patrick Hagan, and Randolph F. Rodewald** 1509

A Spectroscopic Study of Carbazole by Photoselection . . . . . . . . . . . . **G. E. Johnson** 1512

Electron Spin Resonance Spectra of Some Hydroxycyclohexadienyl Radicals Derived from Aromatic Carboxylic Acid Anions . . . . . . . . **Gordon Filby* and Kirsten Günther** 1521

Effect of Urea on Magnetic Relaxation in Aqueous Solutions of Poly(ethylene oxide)
. . . **A. A. Jones and W. H. Stockmayer*** 1528

Structure of Liquid Water. II. Improved Statistical Thermodynamic Treatment and Implications of a Cluster Model
. . . **Barry R. Lentz, Arnold T. Hagler, and Harold A. Scheraga*** 1531

Crystal Structure of a Dealuminated Y-Type Zeolite
. . . **P. Gallezot,* R. Beaumont, and D. Barthomeuf** 1550 ■

ห้องสมุด กรมวิทยาศาสตร์
24 ก.ย. 2517

Sequence and Shape of the Molecular Orbitals of the Disulfide HSSH . . . . **Donald B. Boyd** 1554 ■

Diffusion and Thermal Diffusion in Binary Dense Gas Mixtures of Loaded Spheres and Rough Spheres . . . . . . . . . . . . . . . . . . . **Marc O. Baleiko and H. Ted Davis*** 1564 ■

■ Supplementary and/or miniprint material for this paper is available separately, in photocopy or microfiche form. Ordering information is given in the paper.

* In papers with more than one author, the asterisk indicates the name of the author to whom inquiries about the paper should be addressed.

## AUTHOR INDEX

Arai, S., 1473
Arshadi, M. R., 1482

Baleiko, M. O., 1564
Barnes, J. A., 1503
Barthomeuf, D., 1550
Beaumont, R., 1550
Boyd, D. B., 1554
Bunton, C. A., 1490

Cvetanović, R. J., 1457

Davis, H. T., 1564
Delben, F., 1486
DeMore, W. B., 1447
Durig, J. R., 1503

Filby, G., 1521
Fuchs, R., 1509
Futrell, J. H., 1482

Gallezot, P., 1550
Guillory, W. A., 1461
Günther, K., 1521

Hagan, C. P., 1509
Hagler, A. T., 1531
Hong, K. C., 1478
Hoshino, M., 1473
Hudgens, B. A., 1503
Imamura, M., 1473

Jeffers, P. M., 1469
Johnson, G. E., 1512
Jones, A. A., 1528

Kleppa, O. J., 1478

Lentz, B. R., 1531
Lin, M. C., 1451

Michaud, P., 1457
Minch, M. J., 1490

Odom, J. D., 1503
Paoletti, S., 1486
Paraskevopoulos, G., 1457

Ratjke, S. K., 1499
Rodewald, R. F., 1509
Rytter, E., 1499

Scheraga, H. A., 1531
Shortridge, R. G., 1451
Stockmayer, W. H., 1528

Thomas, S. G., Jr., 1461
Tschuikow-Roux, E., 1447

THE JOURNAL OF

PHYSICAL CHEMISTRY

*Registered in U. S. Patent Office* *© Copyright, 1974, by the American Chemical Society*

VOLUME 78, NUMBER 15 JULY 18, 1974

# Temperature Dependence of the Reactions of OH and $HO_2$ with $O_3$[1]

**W. B. DeMore***

*Jet Propulsion Laboratory, Pasadena, California 91103*

**and E. Tschuikow-Roux**

*Department of Chemistry, University of Calgary, Calgary, Canada T2N 1N4* *(Received December 12, 1973)*

*Publication costs assisted by the Jet Propulsion Laboratory*

Chain destruction of $O_3$ by $HO_x$ radicals has been studied in the range 0–69° by the technique of steady-state photolysis of $O_2$–$H_2O$ and $O_2$–$H_2O$–CO mixtures at 1849 Å. The chain propagation and termination reactions are $OH + O_3 \rightarrow HO_2 + O_2$ (1), $HO_2 + O_3 \rightarrow OH + 2O_2$ (2), $OH + HO_2 \rightarrow H_2O + O_2$ (8), $HO_2 + HO_2 \rightarrow H_2O_2 + O_2$ (9). The results yield the rate constant ratios $k_2/k_9^{1/2} = 1.1 \times 10^{-7} \exp(-3100 \pm 500/RT)$ cm$^{3/2}$ sec$^{-1/2}$ and $k_8k_2/k_9k_1 = 12 \exp(-1600 \pm 500/RT)$. Hence, $E_2$(kcal mol$^{-1}$) = $3.1 \pm 0.5 + \frac{1}{2}E_9$ and $E_1$ (kcal mol$^{-1}$) = $1.5 \pm 0.7 + E_8 - \frac{1}{2}E_9$. Based on the result of Paukert and Johnston that $k_9 = 3.6 \times 10^{-12}$ cm$^3$ sec$^{-1}$, and assuming $E_9 \simeq 0$, then $k_2 = 2 \times 10^{-13} \exp[-(3100 \pm 500)/RT]$ cm$^3$ sec$^{-1}$, with an (estimated) uncertainty of a factor of 2 in the $A$ factor. If it is further assumed that $E_8 = 0$, then $E_1 = 1.5 \pm 0.7$ kcal mol$^{-1}$, which is in good agreement with Anderson and Kaufman who found $E_1 = 1.9$ kcal mol$^{-1}$. Our results give $k_8$(298°K) = $1.6 \times 10^{-10}$ cm$^3$ sec$^{-1}$, based on literature values of $k_1$ and the above quoted $k_9$. This result for $k_8$ is believed to be accurate to within a factor of 3. As a test of mechanism, the $O_3$ steady states were found to obey the predicted inverse square root dependence on water pressure over a wide range.

## Introduction

The effect of water on ozone photolysis has been of interest to photochemists for many years, and has received increased attention recently in connection with possible effects of exhaust from high-flying aircraft on stratospheric ozone.[2] Much of the literature on the effect of water on ozone photolysis stems from the early work of Heidt and Forbes[3] and Norrish and coworkers.[4] Catalytic destruction of ozone was discussed in 1935 by Weiss[5] in studies of the decomposition of ozone in aqueous solution, the cycle being as follows

$$OH + O_3 \longrightarrow HO_2 + O_2 \qquad (1)$$

$$HO_2 + O_3 \longrightarrow OH + 2O_2 \qquad (2)$$

Complete elucidation of the mechanism of wet ozone photolysis has been difficult, however, due in part to the complexity of pure ozone photolysis.

Recent steady-state experiments involving photolysis of $O_2$–$H_2O$ mixtures at 1849 Å[6] have provided direct evidence for the catalytic cycle represented by reactions 1 and 2, and rate constants for these reactions were measured at room temperature. In the present report we have extended the measurements to the temperature range 0–69° in order to measure temperature dependences of reactions 1 and 2. Additional experimental results confirming the reaction mechanism are also reported.

## Experimental Section

*Apparatus.* Figure 1 shows a schematic diagram of the cell and associated equipment. The light source was a spiral low-pressure mercury lamp. An $O_2$–$O_3$ filter, described previously,[6] was incorporated to remove the 2537-Å radiation which would otherwise have been absorbed strongly by $O_3$ in the cell proper. Ozone concentrations were monitored photometrically using a separate, relatively weak source of 2537-Å light which could be diverted either through or around the cell by means of appropriate mirrors and shutters.

The temperature of the cell was controlled by circulation of water from a constant temperature bath through a jacket surrounding the cell. Temperature inside the cell was monitored by means of a thermocouple probe which could be positioned at different points parallel to the cell axis to test for temperature gradients. Temperature variations were less than 1° except near the windows where differences up to 2° were noted.

Pressure measurements were made with a quartz spiral manometer (Texas Instruments Co.) and a calibrated

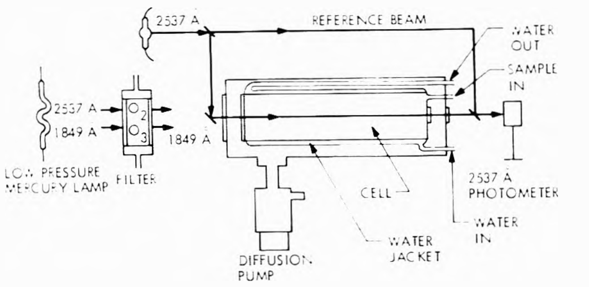

**Figure 1.** Schematic diagram of apparatus. The cell diameter (not including water jacket) is 15 cm and the length is 92 cm.

Wallace and Tiernan gauge. Water vapor measurements were made with the former instrument, and as a test these readings were compared with the known vapor pressure of water at 0°. The results indicated that accurate water pressure measurements could be obtained provided that sufficient time (about 10 min) was allowed for equilibrium. Tests also showed that the water pressure remained constant in the cell after equilibrium.

The experimental procedure for mixture preparation was to first equilibrate the water vapor pressure in the evacuated cell. Oxygen was then added, followed by nitrogen to bring the total pressure to 700 Torr.

*Chemicals.* The $O_2$ was Matheson "ultra-high purity" grade, containing less than 2 ppm of $H_2O$. The nitrogen was Air Products "extra-high purity" grade containing less than 10 ppm of $H_2O$. Carbon monoxide (Matheson Research Grade) was purified immediately before use by passage through a packed U-tube at −196°, and then compressively injected into the cell by means of a plunger.

## Mechanism

Photolysis of $O_2$-$H_2O$ mixtures at 1849 Å produces both ozone and $HO_x$ radicals as follows

$$O_2 + 1849\ \text{Å} \xrightarrow{I_a^{O_2}} O + O \tag{3}$$

$$O + O_2 + M \longrightarrow O_3 + M \tag{4}$$

$$H_2O + 1849\ \text{Å} \xrightarrow{I_a^{H_2O}} H + OH \tag{5}$$

$$H + O_2 + M \longrightarrow HO_2 + M \tag{6}$$

The $O_3$ concentration rises until a steady state is reached, at which point the rate of $O_3$ destruction by the chain reactions 1 and 2 exactly balances the rate of $O_3$ production by $O_2$ photolysis according to reactions 3 and 4. The occurrence of chain decomposition is proven by the fact that $O_3$ steady states are reached despite the fact that $I_a^{O_2} > I_a^{H_2O}$; that is, each $HO_x$ radical must account for the destruction of more than one $O_3$. An important feature of this method is that photolysis of $O_3$ does not occur to an appreciable extent because the 2537-Å line, which would be strongly absorbed by $O_3$, is filtered out (see Apparatus section). Attack on $O_3$ by H atoms

$$H + O_3 \longrightarrow OH + O_2 \tag{7}$$

is suppressed to a negligible extent by reaction 6, which is much more rapid than reaction 7 at the high $O_2/O_3$ ratios which are characteristic of this experiment.

The radical termination steps are

$$OH + HO_2 \longrightarrow H_2O + O_2 \tag{8}$$

$$HO_2 + HO_2 \longrightarrow H_2O_2 + O_2 \tag{9}$$

The reaction $OH + OH \rightarrow H_2O + O$, which has a rate constant about one-half that of reaction 9,[7] does not contribute appreciably to the radical termination rate because, as shown later, the ratio $OH/HO_2$ is small. Reaction 9, which produces $H_2O_2$, is always followed by

$$OH + H_2O_2 \longrightarrow H_2O + HO_2 \tag{10}$$

The net reaction, adding (9) and (10), is therefore equivalent to reaction 8, with the exception that the rate-determining factor is $k_9$. The fact that OH and $HO_2$ always disappear in pairs, combined with their production in pairs by the $H_2O$ photolysis, requires that the chain reactions 1 and 2 obey the relation

$$k_1[OH] = k_2[HO_2] \tag{11}$$

Equation 11, which can be verified by a steady-state treatment of the mechanism, shows that the ratio of radical concentrations $[OH]/[HO_2]$ is determined by the rates of the chain steps and is equal to $k_2/k_1$.

Addition of CO to the mixture has the effect of converting OH to $HO_2$, by the following reaction sequence

$$OH + CO \longrightarrow H + CO_2 \tag{12}$$

$$H + O_2 + M \longrightarrow HO_2 + M \tag{6}$$

Small concentrations of CO, of the order of 5 Torr, are sufficient to scavenge all OH and thereby suppress reaction 1.

The $O_3$ steady states are given by the following expressions, where $[O_3]_{ss}^0$ refers to the $O_3$ steady-state concentration in the absence of CO, and $[O_3]_{ss}^{CO}$ is the $O_3$ steady state in the presence of sufficient CO so that $k_{12}[CO] \gg k_1[OH]$.

$$[O_3]_{ss}^0 = \frac{2I_a^{O_2}}{k_1[OH]_{ss}^0 + k_2[HO_2]_{ss}^0} = \frac{I_a^{O_2}}{k_1[OH]_{ss}^0} = \frac{I_a^{O_2}}{k_2[HO_2]_{ss}^0} \tag{13}$$

$$[O_3]_{ss}^{CO} = 2I_a^{O_2}/k_2[HO_2]_{ss}^{CO} \tag{14}$$

Expressions for the $HO_2$ steady-state concentrations can be derived as follows

$$I_a^{H_2O} = k_8[OH]_{ss}^0[HO_2]_{ss}^0 + k_9([HO_2]_{ss}^0)^2 \tag{15}$$

Making use of the relation $k_1[OH]_{ss}^0 = k_2[HO_2]_{ss}^0$, we have

$$[HO_2]_{ss}^0 = (I_a^{H_2O})^{1/2}\Big/\left(\frac{k_8k_2}{k_1} - k_9\right)^{1/2} \tag{16}$$

When CO is present in excess, the only termination step of importance is reaction 9. Thus

$$I_a^{H_2O} = k_9([HO_2]_{ss}^{CO})^2 \tag{17}$$

$$[HO_2]_{ss}^{CO} = (I_a^{H_2O})^{1/2}/k_9^{1/2} \tag{18}$$

Substitution of these expressions for the $HO_2$ concentrations in (13) and (14) gives

$$[O_3]_{ss}^0 = \frac{\left(\frac{k_8k_2}{k_1} - k_9\right)^{1/2}}{k_2}\,\frac{I_a^{O_2}}{(I_a^{H_2O})^{1/2}} \tag{19}$$

$$[O_3]_{ss}^{CO} = \frac{2k_9^{1/2}I_a^{O_2}}{k_2(I_a^{H_2O})^{1/2}} \tag{20}$$

Taking the ratio of eq 19 and 20 gives

$$k_8k_2/k_9k_1 = 4([O_3]_{ss}^{O}/[O_3]_{ss}^{CO})^2 - 1 = 4\alpha^2 - 1 \qquad (21)$$

where $\alpha = [O_3]_{ss}^{O}/[O_3]_{ss}^{CO}$.

Equation 21 thus provides a simple relationship between the experimentally determined quantity $\alpha$ and the rate constants for chain propagation and termination.

The ratio $k_2/k_9^{1/2}$ can be obtained from eq 20. To make this calculation, it is necessary to express the ratio $I_a^{O_2}/(I_a^{H_2O})^{1/2}$ in terms of the total light absorbed by the mixture, $I_a^T$. Defining the quantities $f_{O_2}$ and $f_{H_2O}$ as the respective fractions of 1849-Å light absorbed by $O_2$ and $H_2O$ in a given mixture, we have

$$\frac{I_a^{O_2}}{(I_a^{H_2O})^{1/2}} = \frac{f_{O_2}I_a^T}{(f_{H_2O}I_a^T)^{1/2}} = \frac{f_{O_2}(I_a^T)^{1/2}}{(f_{H_2O})^{1/2}} \qquad (22)$$

Also

$$f_{O_2} = \frac{k_\lambda^{O_2}p^{O_2}}{k_\lambda^{O_2}p^{O_2} + k_\lambda^{H_2O}p^{H_2O}} \qquad (23)$$

The quantity $k_\lambda^{O_2}$ is the $O_2$ extinction coefficient at 1849 Å, and $p^{O_2}$ is the $O_2$ partial pressure. A similar expression holds for $f_{H_2O}$. The values used in this work are $k_\lambda^{O_2} = 0.29$ cm$^{-1}$ (atm STP)$^{-1}$ and $k_\lambda^{H_2O} = 2.1$ cm$^{-1}$ (atm STP)$^{-1}$. Actinometric measurements of $I_a^T$ were based on rates of $O_3$ production in the photolysis of pure $O_2$ at absorbances closely matching those of the $O_2$-$H_2O$ mixtures.

The final result for $k_2/k_9^{1/2}$ is

$$\frac{k_2}{k_9^{1/2}} = \frac{2}{[O_3]_{ss}^{CO}}\,\frac{k_\lambda^{O_2}p^{O_2}}{(k_\lambda^{H_2O})^{1/2}(k_\lambda^{O_2}p^{O_2} + k_\lambda^{H_2O}p^{H_2O})^{1/2}}\,\frac{(I_a^T)^{1/2}}{(p^{H_2O})^{1/2}} \qquad (24)$$

Useful tests of the mechanism can be made by examining the dependences of the $O_3$ steady states on light intensity and partial pressure of water. From eq 24, it can be seen that $[O_3]_{ss}^{CO}$ should be proportional to the square root of light intensity and inversely proportional to the square root of $p^{H_2O}$. The same dependences hold for $[O_3]_{ss}^{O}$, as can be seen by comparison of eq 19 and 20. In the previous report[6] it was shown that $[O_3]_{ss}^{O}$ shows the predicted dependence on light intensity when the latter was varied by a factor of 2. Larger variations in light intensity are not practical because of constraints arising from the amount of light available and the fact that excessively long times are required to reach steady state at very low light intensities. For these reasons emphasis was placed on varying the partial pressure of water rather than the light intensity.

## Results and Discussion

At all temperatures in the range 0-69° the ozone concentration *vs.* time behavior was qualitatively similar to that observed at room temperature. A steady state was reached in approximately 8-10 hr which then remained constant. For convenience, most of the steady-state determinations were made by allowing the irradiation to proceed overnight, first with no added CO, and then with excess CO. The excess CO was added either to the same mixture or to a fresh mixture. No difference in final steady states was noted in the latter types of CO additions. With the lamp turned off no appreciable $O_3$ decay occurred even at the higher temperatures.

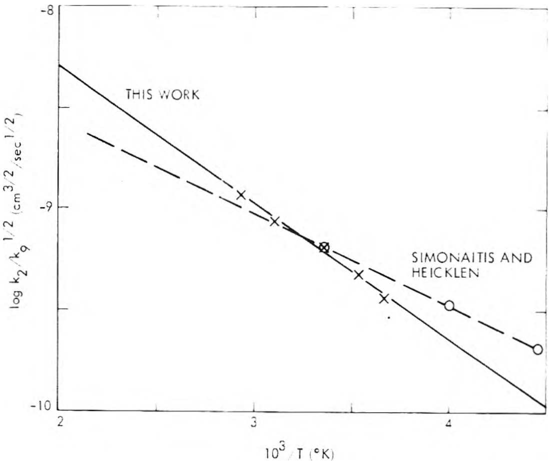

**Figure 2.** Arrhenius plot of $k_2/k_9^{1/2}$. Points represent average values of data for each temperature in Table I. Only those experiments in which the $O_2$ pressure was 200 Torr were used in computing the averages.

Table I shows the ozone steady states obtained in the presence and absence of excess CO. With allowance for effects of light intensity, a definite negative temperature dependence of the $O_3$ steady states is observed. Also, the quantity $\alpha$ shows a small but definite increase with temperature.

*The Rate Constant* $k_2$. Table I includes the values of $k_2/k_9^{1/2}$ calculated for each experiment from eq 24. These data are plotted in Arrhenius form in Figure 2. This gives

$$k_2/k_9^{1/2} = 1.1 \times 10^{-7} \exp(-3100 \pm 500/RT) \text{ cm}^{3/2} \text{ sec}^{-1/2} \qquad (25)$$

If we use the Paukert and Johnston[8] result that $k_9 = 3.6 \times 10^{-12}$ cm$^3$ sec$^{-1}$, and assume zero temperature dependence for $k_9$, then the resulting Arrhenius expression for $k_2$ is

$$k_2 = 2 \times 10^{-13} \exp(-3100 \pm 500/RT) \qquad (26)$$

The uncertainty of 0.5 kcal mol$^{-1}$ in $E_2$ is based on experimental scatter, and does not include any uncertainty in the temperature dependence of $k_9$. If $k_9$ has a nonzero activation energy, then

$$E_2(\text{corrected}) = 3.1 = 0.5 + \tfrac{1}{2}E_9 \text{ kcal mol}^{-1} \qquad (27)$$

The principal uncertainty in the absolute values of $k_2$ is associated with the calculation of $HO_2$ concentrations. These errors arise from uncertainty in $k_9$ and also from effects of nonuniform light absorption. As shown in the previous work, and as can be seen in Table I, there is an increase in the calculated $k_2$ at lower $O_2$ pressures (which gives more uniform light absorption). The error from this source is not greater than a factor of 1.5. Combined with an uncertainty of a factor of 2 in $k_9$ (which enters as the square root in the $k_2$ determination) the overall uncertainty in $k_2$ at a given temperature is about a factor of 2.

It should be pointed out that the value $k_2 = 1.2 \times 10^{-5}$ cm$^3$ sec$^{-1}$ is lower than the previously reported[6] value $k_2$ (25°) = $3 \times 10^{-15}$ cm$^3$ sec$^{-1}$, primarily because a higher value of $k_9$ was used in the previous work ($k_9 = 9.5 \times 10^{-12}$ cm$^3$ sec$^{-1}$),[9] and partly because of the above-mentioned dependence of $k_2$ on $O_2$ pressure.

**TABLE I: Summary of Experimental Data**

| $T$, °C | Mixture $H_2O$–$O_2$–$N_2$, Torr | $I_a10^3$, mTorr/sec | $(P_{O_3})_{ss}{}^{O}$, mTorr | $(P_{O_3})_{ss}{}^{CO}$, mTorr | $k_8k_2/k_9k_1$ | $k_2/k_9{}^{1/2} \times 10^9$, $cm^{3/2}$ $sec^{-1/2}$ |
|---|---|---|---|---|---|---|
| 0 | 2–200–500 | 2.33 | 81.1 | 127 | 0.631 | 0.35 |
| 0 | 3–200–500 | 9.10 | 114 | 180 | 0.604 | 0.38 |
| 0 | 2–200–500 | 7.55 | 136 | 216 | 0.586 | 0.36 |
| 10 | 2–200–500 | 4.44 | 75.7 | 121 | 0.566 | 0.50 |
| 10 | 2–100–600 | 3.66 | 42.3 | 64.4 | 0.726 | 0.58 |
| 10 | 2–200–500 | 7.10 | 105 | 162 | 0.680 | 0.47 |
| 10 | 3–200–500 | 8.78 | 93 | 140 | 0.765 | 0.48 |
| 25 | 3–200–500 | 9.10 | 73.7 | 109 | 0.829 | 0.64 |
| 50 | 2–200–500 | 6.34 | 58.3 | 81.4 | 1.05 | 0.90 |
| 50 | 2–200–500 | 5.22 | 51.0 | 73.5 | 0.926 | 0.90 |
| 50 | 1–200–500 | 6.67 | 87.1 | 129 | 0.824 | 0.83 |
| 50 | 3–200–500 | 6.00 | 46.3 | 65.0 | 1.03 | 0.87 |
| 50 | 1–200–500 | 6.39 | 88.2 | 125 | 0.991 | 0.83 |
| 69 | 3–300–400 | 4.44 | 44.9 | 60.3 | 1.22 | 1.00 |
| 69 | 2–200–500 | 5.23 | 38.9 | 54.9 | 1.01 | 1.20 |
| 69 | 1–100–600 | 3.66 | 30.2 | 41.6 | 1.11 | 1.32 |

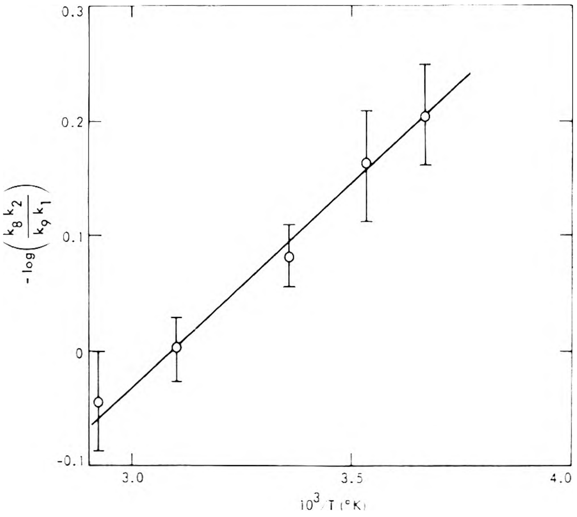

Figure 3. Arrhenius plot of data according to eq 21.

Figure 2 also includes for comparison the results of Simonaitis and Heicklen,[10] who measured the ratio $k_2/k_9{}^{1/2}$ by a method involving photolysis of $O_3$-$O_2$-$H_2$ mixtures at 2537 Å. The agreement is very good, although their Arrhenius expression $k_2/k_9{}^{1/2} = 1.9 \times 10^{-8} \exp(-2000/RT)$ is slightly different from ours.

*Activation Energy for $k_1$.* Figure 3 is a plot based on eq 21, taking average values of $\alpha$ at each temperature. The Arrhenius expression is

$$k_8k_2/k_9k_1 = 12 \exp(-1600 \pm 500/RT) \qquad (28)$$

Thus

$$(E_2 - E_1) + (E_8 - E_9) = 1.6 \pm 0.5 \text{ kcal mol}^{-1} \qquad (29)$$

Substitution of eq 27 in 29 then leads to

$$E_1 = 1.5 \pm 0.7 + E_8 - {}^1\!/_2E_9 \text{ kcal mol}^{-1} \qquad (30)$$

If, for the purpose of this discussion the radical-radical reactions 8 and 9 are assumed to have zero activation energies, then

$$E_1 = 1.5 \pm 0.7 \text{ kcal mol}^{-1} \qquad (31)$$

This result is in good agreement with the Anderson and Kaufman[11] value $E_1$ = 1.9 kcal mol$^{-1}$, suggesting that the quantity $E_8 - {}^1\!/_2E_9$ is in fact small. Reaction 8 is very rapid (see next section) and probably has a near-zero $E_a$.

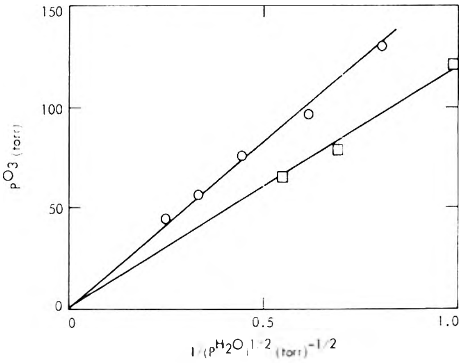

Figure 4. Dependence of $O_3$ steady states on partial pressure of water.

The foregoing results therefore suggest that reaction 9 also has a low or zero $E_a$.

*The Rate Constant $k_8$.* The data of Table I could be used to derive the complete Arrhenius expression for $k_1$, if both $k_8$ and $k_9$ were known precisely. In the preceding discussion, we employed the assumption that $E_8$ = 0 to derive $E_1$, but we did not use any absolute value of $k_8$. Since there are now four measurements of $k_1$,[6,11-13] all of which fall in the limits $k_1$(298°K) = 6 ± 2 × $10^{-14}$ cm$^3$ sec$^{-1}$, but only one measurement of $k_8$,[9] we have chosen to take $k_1$(298°K) as a known and to use our data to calculate $k_8$ at 298°K.

The experimental results are in the form

$$k_2/k_9{}^{1/2} = f(T) \qquad (25')$$

$$k_8k_2/k_9k_1 = f'(T) \qquad (28')$$

Solving for $k_8$, we have

$$k_8 = \frac{f'(T)}{f(T)}k_1k_9{}^{1/2} \qquad (32)$$

If we take $k_1$(298°K) = 6 × $10^{-14}$ cm$^3$ sec$^{-1}$ and $k_9$(298°K) = 3.6 × $10^{-12}$ cm$^3$ sec$^{-1}$,[8] then

$$k_8(298°\text{K}) = 1.6 \times 10^{-10} \text{ cm}^3 \text{ sec}^{-1} \qquad (33)$$

This value of $k_8$, which is believed to be accurate to within a factor of 3, supports the finding of ref 9 that reaction 8 is very fast. Further confirmation of this important rate constant is needed.

*Tests of Mechanism.* The reliability of the foregoing results depends on the accuracy and completeness of the proposed mechanism. This mechanism has the advantage of being very simple and apparently free of complicating side reactions, with the result that the $O_3$ steady states depend only on the rates of the chain-propagation and termination reactions, which are the quantities to be measured. One method which we have used to test for the presence of unknown mechanistic complications has been to examine the dependence of the $O_3$ steady states on pressure of water vapor over a wide range. Figure 4 shows a plot of $[O_3]_{ss}^{O}$ and $[O_3]_{ss}^{CO}$ *vs.* the inverse square root of water pressure (*cf.* eq 22). To simplify the plot, the following normalization procedure was followed in order to account for the effect of added water in decreasing the fraction of light absorbed by $O_2$

$$\left[\frac{1}{(p^{H_2O})^{1/2}}\right]^{corr} = \left[\frac{1}{(p^{H_2O})^{1/2}}\right]\left[\frac{(k_\lambda p^{O_2})^{1/2}}{(k_\lambda^{O_2}p^{O_2} + k_\lambda^{H_2O}p^{H_2O})^{1/2}}\right] \quad (34)$$

The results show that the $O_3$ steady states adhere closely to the predicted dependence on $p^{H_2O}$ over a wide range of water vapor pressures (in the $[O_3]_{ss}^{O}$ plot, $p^{H_2O}$ was varied from 1.5 to 12.64 Torr, and in the $[O_3]_{ss}^{CO}$ plot, $p^{H_2O}$ was varied from 1 to 3 Torr). This supports the proposed mechanism involving second-order termination reactions, and also demonstrates that both water pressures and $O_3$ steady states can be reproducibly and accurately measured. In addition, the results show that there is no indication of any dependence on the equilibrium $O_3$ concentrations, as might be expected to arise if there were any contribution to $O_3$ destruction due to reactions not accounted for.

*Acknowledgment.* The authors are grateful for helpful conversations concerning this work with Professor D. Volman, University of California, Davis, and Dr. D. Garvin, National Bureau of Standards.

### References and Notes

(1) This paper presents the results of one phase of research carried out at the Jet Propulsion Laboratory, California Institute of Technology, under Contract No. NAS7-100, sponsored by the National Aeronautics and Space Administration.
(2) "Proceedings of the Survey Conference," A. E. Barrington, Ed., Climatic Impact Assessment Program, Department of Transportation, Washington, D. C., 1972.
(3) L. J. Heidt and G. S. Forbes, *J. Amer. Chem. Soc.*, **56**, 1671 (1934).
(4) R. G. W. Norrish and R. P. Wayne, *Proc. Roy. Soc., Ser. A*, **288**, 361 (1965), and earlier references therein.
(5) J. Weiss, *Trans. Faraday Soc.*, **31**, 668 (1935).
(6) W. B. DeMore, *Science*, **180**, 735 (1973).
(7) "Chemical Kinetics Data Survey IV," D. Garvin, Ed., National Bureau of Standards, Washington, D. C., 1973.
(8) T. T. Paukert and H. S. Johnston, *J. Chem. Phys.*, **56**, 2824 (1972).
(9) C. J. Hochanadel, J. A. Ghormley, and P. J. Ogren, *J. Chem. Phys.*, **56**, 4426 (1972).
(10) C. J. Simonaitis and J. Heicklen, *J. Phys. Chem.*, **77**, 1932 (1973).
(11) J. Anderson and F. Kaufman, *Chem. Phys. Lett.*, **19**, 483 (1973).
(12) D. D. Davis, private communication.
(13) M. J. Kurylo, *Chem. Phys. Lett.*, submitted for publication.

---

# Chemical Lasers Produced from O($^3$P) Atom Reactions. IV. CO Laser Emission from the O + CN Reaction

**R. G. Shortridge**[1] **and M. C. Lin***

*Physical Chemistry Branch, Chemistry Division, Naval Research Laboratory, Washington, D. C. 20375*

*(Received February 21, 1974)*

*Publication costs assisted by the Naval Research Laboratory*

CO infrared stimulated emission has been observed from flash-initiated $SO_2$ + XCN (X = Br, Cl, and CN) mixtures. About 36 P(J) lines of vibrational-rotational transitions are present between $\Delta v$ (13-12) and $\Delta v$ (5-4). Dilution in $SF_6$ greatly enhances the laser emission, whereas only slight enhancement is obtained from such diluents as Ar and He. Mass spectrometric analysis shows that about 20% conversion of XCN occurs per five flashes at 2.1 kJ and that CO, NO, $CO_2$, and probably some $N_2$ are produced. The reaction, $O(^3P) + CN(X^2\Sigma) \rightarrow CO^\dagger + N(^4S)$, $\Delta H_1^\circ = -74$ kcal/mol, was confirmed to be the major pumping reaction of this system, and $O(^3P) + CN \rightarrow N(^2D) + CO^\dagger$, $\Delta H_2^\circ = -19$ kcal/mol, seemed to be unimportant on the basis of our laser emission measurements.

## Introduction

In the recently studied chemical laser producing reaction,[2a] $O(^1D) + CN \rightarrow CO + N$, it was shown on the basis of laser emission measurements, that the N atom was formed in its ($^2$D) state only, due probably to the spin conservation principle forbidding N($^4$S) production. However, in the corresponding reaction involving O($^3$P), production of both N($^4$S) and N($^2$D) are allowed processes

$$O(^3P) + CN(X^2\Sigma) \longrightarrow N(^4S) + CO^\dagger \qquad \Delta H_1^\circ = -73.8 \text{ kcal/mol} \quad (1)$$

$$O(^3P) + CN(X^2\Sigma) \longrightarrow N(^2D) + CO^\dagger \qquad \Delta H_2^\circ = -18.8 \text{ kcal/mol} \quad (2)$$

This system has recently been included in the preliminary investigation of several chemical laser-producing reactions, involving the O($^3$P) atomic species generated by the vacuum ultraviolet ($\lambda \geq 165$ nm) flash photolysis of $SO_2$.[2b] The present work is a more detailed study of this reaction which included a complete frequency analysis of the many vibrational-rotational lines comprising the observed stimulated emission, a study of the pressure as well as flash energy dependence of the laser emission intensity, and a mass spectrometric product analysis, in order to elucidate the reaction mechanism especially as regards the principal laser pumping reactions.

## Experimental Section

The flash-initiated laser apparatus has been previously described.[2b] Briefly, a Suprasil laser tube (1-m long, 2.2-cm i.d.), fitted with replaceable high-transmission ir windows at the Brewster angle, was positioned in an optical cavity formed by gold-coated mirrors at a separation of about 1.2 m. One of the mirrors has a 1-mm coupling hole at its center. Two 40-cm long quartz flash lamps were concentrically sealed, at about 2 cm apart, to the laser tube. The laser tube was directly connected, *via* the space between the two flash lamps to the all-glass, greaseless vacuum system. Frequency analysis was accomplished by passing the coupled laser output through a half-meter Minuteman Model 305M13 monochromator fitted with a kinematically mounted 150-line/mm grating blazed at 6 $\mu$m, and the lines were observed with a gold-doped germanium detector maintained at 77°K, in conjunction with a Tektronix 545A oscilloscope.

The BrCN used in this study was obtained from Aldrich, the $C_2N_2$ from Baker, and the ClCN from American Cyanimid Co., while the remainder of the gases used in this study were from the Matheson Gas Products Co. The noncondensable gases were delivered under high pressure after repeated purging and were used without further purification. The condensables were always degassed at 77°K prior to use and the $SO_2$ was further purified by trap-to-trap distillation using various slush baths. All experiments were conducted at room temperature 22 ± 2°.

## Results and Discussion

*(I) Pressure Dependence.* Figure 1 shows the total stimulated emission pulses observed from 20 Torr of a 3:1:20 BrCN:$SO_2$:$SF_6$ mixture, that from 14 Torr of a 3:1:20 $C_2N_2$:$SO_2$:$SF_6$ mixture, and that from 10 Torr of a 3:1:20 ClCN:$SO_2$:$SF_6$ mixture, all flashed at 2.06 kJ of energy. The flash pulse has about a 15-$\mu$sec rise time and a 45-$\mu$sec half-width. The emission begins at ~7-8 $\mu$sec and continues until ~45 $\mu$sec in the BrCN case and ~62 $\mu$sec in the $C_2N_2$ case, although it is much less intense during the $t > 20$ $\mu$sec period. Hence these systems seem to be intermediate between the $O(^1D)$ + CN and $O(^1D)$ + $C_3O_2$ systems.[2b,3] The emission from the ClCN system is much weaker due to its lower absorption coefficient; and like the $O(^1D)$ + CN case,[2b] extends only from ~8 to 20 $\mu$sec.

It should also be noted here, that laser emission on three previously observed lines of CN[4] was observed in the present system. When $SO_2$ was absent, weak to moderate emission was observed from 10 Torr of a 1:10 $C_2N_2$:$SF_6$ mixture on the CN ($X^2\Sigma$), $\Delta v(4-3)$, P(9), P(10), and P(11) lines. In the presence of $SO_2$, rather weak emission was observed from 10 Torr of a 3:1:20 $C_2N_2$:$SO_2$:$SF_6$ mixture on the P(9) line only.

Figure 2 shows the dependence of peak laser pulse power with total pressure for 1:1:20 and 1:2:20 mixtures of BrCN:$SO_2$:$SF_6$ flashed at 1.60 kJ. For both mixtures, the maximum occurs at a total pressure of ~60 Torr.

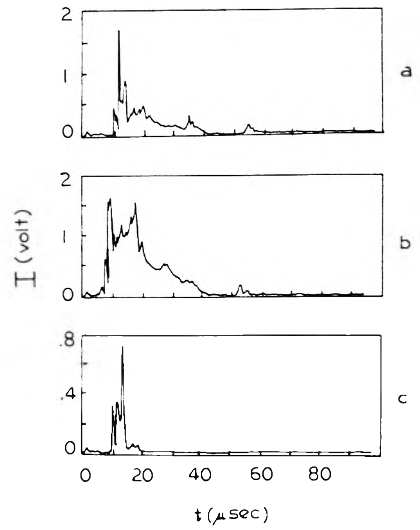

**Figure 1.** Total CO laser emission traces as a function of time: (a) from 20 Torr of a 3:1:20 BrCN:$SO_2$:$SF_6$ mixture; (b) from 14 Torr of a 3:1:20 $C_2N_2$:$SO_2$:$SF_6$ mixture; (c) from 10 Torr of a 3:1:20 ClCN:$SO_2$:$SF_6$ mixture; in all cases flash energy = 2.06 kJ.

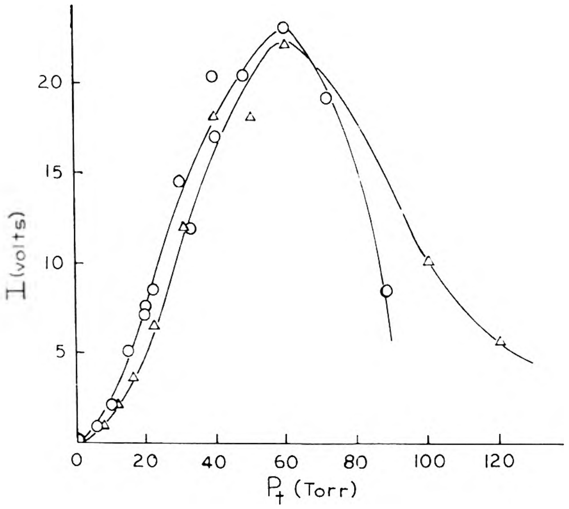

**Figure 2.** Relative laser peak pulse power as a function of total pressure at a flash energy of 1.6 kJ: (○) 1:1:20 $SO_2$:BrCN:$SF_6$ mixture used; (△) 2:1:20 $SO_2$:BrCN:$SF_6$ mixture used.

Similarly, Figure 3 shows the dependence of the peak laser pulse power upon the BrCN/$SO_2$ ratio. Varying pressures of BrCN were added to 20 Torr of a 1:20 $SO_2$:$SF_6$ mixture. It can be seen that BrCN/$SO_2$ ratios of 3 or greater produce significantly higher laser output than those in which the ratio is lower.

*(II) Flash Energy Dependence.* Figure 4 illustrates the dependence of the peak laser pulse intensity upon the *square* of the flash energy employed. The observed linear fit is consistent with the earlier proposed mechanism,[2b] in which both the reactant species which produce $CO^\dagger$ are generated flash photolytically. The reaction mechanism of this system will be discussed in section VI.

*(III) Effect and Role of Added Gas Diluents.* $SF_6$ was by far the most efficient diluent in enhancing the laser output intensity in the BrCN-$SO_2$ system. However, mixtures containing only $SO_2$ + BrCN were observed to lase weakly. Furthermore, He and Ar diluents were also found to enhance the laser output, though much less efficiently than $SF_6$. This enhancement is due to the lowering

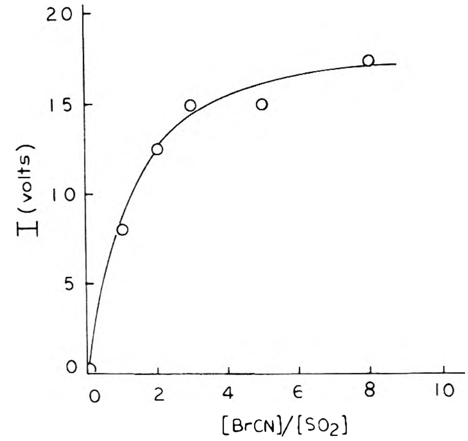

**Figure 3.** Relative laser peak pulse power as a function of the BrCN/SO$_2$ ratio. Varying BrCN pressures added to 20 Torr of a 1:20 SO$_2$:SF$_6$ mixture. Flash energy was 1.6 kJ.

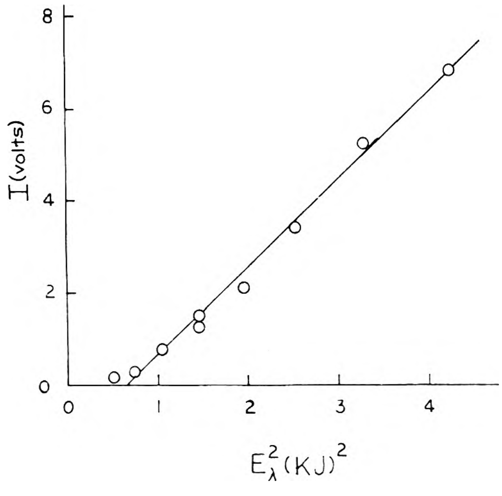

**Figure 4.** Relative laser peak pulse power as a function of flash energy for 30 Torr of a 1:1:20 SO$_2$:BrCN:SF$_6$ mixture.

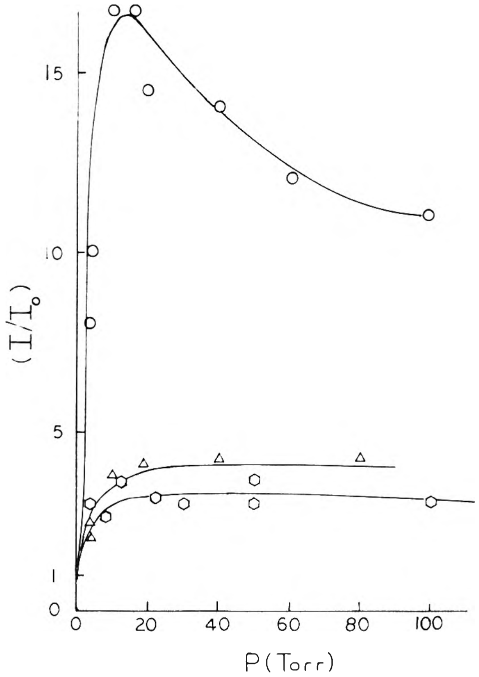

**Figure 5.** Relative laser peak pulse intensity as a function of the pressure of various inert gas diluents added to 20 Torr of a 1:1 BrCN:SO$_2$ mixture: (O) SF$_6$; (Δ) Ar; (○) He. Flash energy was 1.6 kJ.

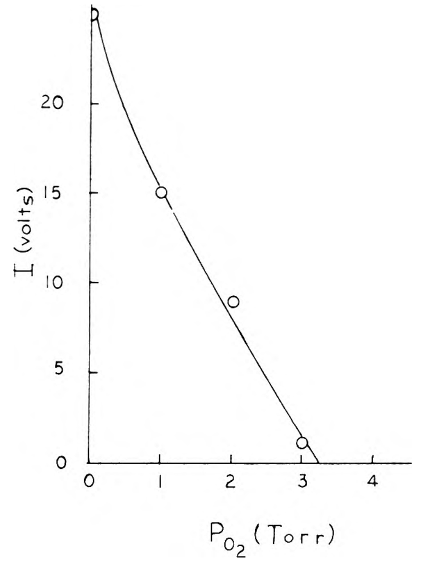

**Figure 6.** Relative laser peak pulse power as a function of the pressure of O$_2$. O$_2$ was added to 30 Torr of a 1:1 SO$_2$:BrCN mixture; flash energy was 1.6 kJ.

of the rotational temperature, and has been observed previously in such systems as O($^3$P) + CH,[5] O($^3$P) + CH$_2$,[6] and COS + $h\nu$.[7]

Conversely, addition of even small amounts of O$_2$ efficiently quenched the CO laser emission, presumably due to the chemical scavenging reaction, CN + O$_2$ → OCN + O, which is known to be as efficient as reaction 1.[8,9]

The results of all of these pressure studies are summarized in Figures 5 and 6. From Figure 5, it is noted that addition of 20 Torr of SF$_6$ diluent to 4 Torr of a 3:1 BrCN:SO$_2$ mixture yielded the maximum laser pulse intensity. Addition of SF$_6$ in excess of this optimum pressure resulted in a gradual decrease in laser intensity due probably to the occurrence of V-V relaxation.[10]

*(IV) Identification of Transitions.* Having thus determined the optimum 3:1:20 BrCN:SO$_2$:SF$_6$ lasing mixture, the individual rotational-vibrational transitions were identified employing the 0.5-m monochromator. A similar study was conducted for a 3:1:20 C$_2$N$_2$:SO$_2$:SF$_6$ mixture. The individual transitions observed with both mixtures are listed in Table I. In addition, there appeared to be a trace emission signal having its origin in the Δv (14-13) band, but it was too weak to resolve into specific P(J) assignments.

The absent and unexpectedly weak lines in Table I may be the result of absorption of these particular frequencies by BrCN and C$_2$N$_2$ both of which have infrared absorption bands in the 2150-cm$^{-1}$ region. This effect was also noted in the analogous O($^1$D) study.[2a] However, while 60 transitions were identified in that study, only 36 were found in this work.

*(V) Mass Spectrometric Analysis.* Gas mixtures were analyzed using a CEC-620 mass spectrometer. Both unflashed mixtures of 3:20:40 Ar:SO$_2$:BrCN and mixtures that had each been subjected to five consecutive flashes in the laser tube at a given flash energy ranging from 1.40 to 2.06 kJ were analyzed in this manner.

Five flashes at 1.40 kJ decreased the BrCN concentration by only ~10%, whereas about 20% depletion was ob-

**TABLE I: Observed Vibration–Rotation Transitions from Both the $C_2N_2$ and BrCN Systems**

| CO transition | | $C_2N_2/SO_2$[a] | $BrCN/SO_2$[b] |
|---|---|---|---|
| $\Delta v$ (13–12) | P(13) | w | t |
| | P(12) | | w |
| (12–11) | P(13) | w | |
| | P(12) | t | |
| | P(10) | t | |
| | P(14) | s | |
| (11–10) | P(13) | | m |
| | P(11) | w | m |
| (10–9) | P(14) | | t |
| | P(13) | m | w |
| | P(12) | s | m |
| (9–8) | P(14) | | t |
| | P(13) | s | m |
| | P(12) | t | |
| | P(11) | m | w |
| (8–7) | P(15) | | t |
| | P(14) | m | m |
| | P(13) | s | w |
| | P(12) | vs | m |
| | P(11) | t | w |
| | P(10) | m | |
| | P(9) | w | |
| | P(8) | t | |
| (7–6) | P(14) | m | |
| | P(13) | s | m |
| | P(12) | s | m |
| | P(11) | m | w |
| | P(10) | m | w |
| | P(9) | w | |
| (6–5) | P(16) | | w |
| | P(15) | | w |
| | P(14) | t | m |
| | P(13) | m | t |
| | P(12) | m | m |
| | P(11) | m | w |
| (5–4) | P(15) | t | t |
| | P(13) | | w |
| | P(12) | | m |

[a] 1:3:20 $SO_2$:$C_2N_2$:$SF_6$, total pressure 20 Torr. [b] 1:3:20 $SO_2$:BrCN:$SF_6$, total pressure 10 Torr. 2.06-kJ flash energy in both cases. No entry indicates that a transition is absent. vs = very strong, s = strong, m = medium, w = weak, and t = trace or very weak.

served from five flashes at 2.06 kJ. This is less than the observed 20% depletion for only one flash in the $O_3$:BrCN:$SF_6$ system, in which conversion was primarily due to the O($^1$D) + BrCN reaction.[2a] The analogous reaction with the O($^3$P) atom does not occur as readily.

Product peaks were identified at *m/e* 28, 30, 42 (trace yields only), and 44, and were attributed chiefly to $CO^+$, $NO^+$, probably traces of $OCN^+$, and $CO_2^+$, although $N_2^+$ formation may have contributed somewhat to the *m/e* 28 peak. These relative product yields, using the *m/e* 40 peak of Ar as the internal standard, are plotted against energy in Figure 7 and are observed to vary *linearly*, unlike the laser emission intensity which varied with the *square* of the flash energy. These apparently contradicting observations, as will be shown later, are likely due to the occurrence of various side reactions which take place at the later stage of a flash. Possible reactions responsible for the occurrence of these side products will be discussed in the next section.

(*VI*) *Reaction Mechanism.* As alluded to earlier, the observed dependence of the overall laser emission intensity upon the square of the flash energy is consistent with the following reactions occurring in the flash

$$XCN + h\nu \longrightarrow CN(X^2\Sigma) + X \quad X = Br, Cl, \text{ or } CN \quad (A)$$

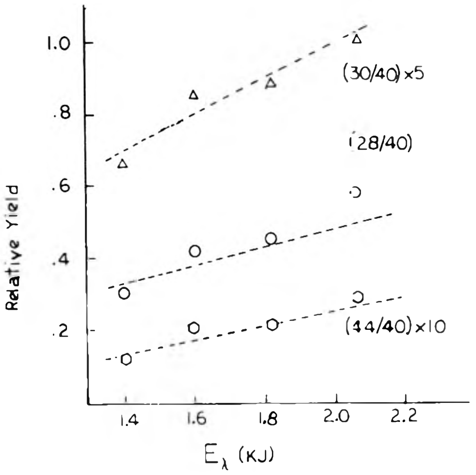

**Figure 7.** Results of the product analysis. Net relative product yields as a function of flash energy for 20 Torr of a 3:20:40 Ar:$SO_2$:BrCN mixture. Each sample was subjected to a series of five consecutive flashes at a given flash energy and subsequently analyzed with a CEC-620 mass spectrometer. The smooth dotted lines represent the corresponding theoretical yields at *t* = 1 msec (see text).

$$SO_2 + h\nu \longrightarrow SO(^3\Sigma^-) + O(^3P) \quad (B)$$

followed by the laser pumping reactions possible for this system

$$O(^3P) + CN(X^2\Sigma) \longrightarrow CO^\dagger + N(^4S) \qquad \Delta H_1^\circ = -73.8 \text{ kcal/mol} \quad (1)$$

$$O(^3P) + CN(X^2\Sigma) \longrightarrow CO^\dagger + N(^2D) \qquad \Delta H_2^\circ = -18.8 \text{ kcal/mol} \quad (2)$$

Both N($^2$D) and N($^4$S) production are permitted in terms of both spin and orbital angular momentum correlation rules,[11] whereas only N($^2$D) production was allowed in the O($^1$D) + CN reaction.[2a]

The exothermicity of reaction 2 is sufficient to populate CO up to the $v$ = 3 level. On the other hand, production of CO as high as $v$ = 13 is energetically feasible for reaction 1. From Table I, we observe individual transitions between $\Delta v$ (5–4) and $\Delta v$ (13–12). In addition, very weak emission around 5.69 $\mu$m was detected with the entrance and exit slits of the monochromator wide open. While the exact P(J) assignment could not be made with such low resolution, it is probable that this emission has its origin in the $\Delta v$ (14–13) band. These observations indicate that reaction 1 is the primary laser pumping process in this system.

However, it is not possible to conclusively rule out N($^2$D) production as a minor step in light of the following arguments. First, laser transitions from these lower vibrational levels obviously require at least a partial population inversion, and it is conceivable that the $v$ = 4 through $v$ = 1 CO bands are produced with a population distribution such that this inversion condition is not satisfied either originally or as the CO molecules subsequently undergo vibrational relaxation processes. Second, the originally produced CN(X$^2\Sigma$) radicals may themselves be vibrationally or electronically excited in the flash as suggested previously,[2a] and this excitation may be carried over into the CO product at much higher $v$ levels. The electronic excitation of the CN radical produced in the vacuum uv flash photolysis of $C_2N_2$ has recently been observed by West and Berry.[12] Furthermore, our observation of the laser

**TABLE II: Rate Constants Used in the Calculations for the Flash-Initiated BrCN–SO$_2$ Chemical Laser System**

| Reaction | Rate constant[a] | Ref |
|---|---|---|
| A | $\alpha t e^{-t/\tau}$ | See text |
| B | $\beta t e^{-t/\tau}$ | See text |
| 1 + 2 | $5.3 \times 10^{13} e^{-2.4/RT}$ | *b* |
| 3 | $1.0 \times 10^{13} e^{-7.5/RT}$ | *c* |
| 4 | $2.8 \times 10^{13} e^{-0.6/RT}$ | *b* |
| 5 | $5.5 \times 10^{12}$ | *c* |
| 6 | $2.2 \times 10^{12}$ | *b* |
| 7 | $10^{13}$ | Assumed |
| 8 | $10^{13}$ | Assumed |
| 9 | $10^{12}$ | Assumed |
| 10 | $3.2 \times 10^{17}$ | *b* |
| 11 | $5.9 \times 10^{15} e^{-4.1/RT}$ | *d* |
| 12 | $9.1 \times 10^{15}$ | *b* |

[a] Rate constants are in units of cc, mol, and sec, and activation energies in kcal/mol. [b] Data taken from the compilation of V. N. Kondratiev, "Rate Constants of Gas Phase Reactions," translated by L. J. Holtschlag and Edited by R. M. Fristrom, U. S. Department of Commerce, 1972. [c] Rate constants for N + SO and CN + SO are assumed to be the same as those for N + O$_2$ and CN + O$_2$ respectively. The values for the O$_2$ reactions are obtained from ref *b*. [d] R. Simonaitis and J. Heicklen, *J. Chem. Phys.*, **56**, 2004 (1972).

emission from the ($X^2\Sigma$), $\Delta v$ (4–3), P(9) transition of CN shows the existence of vibrationally hot CN in the present system, which should lead to the production of correspondingly more highly vibrationally excited CO.[2a] The appearance of the weak 14 → 13 transition may be due to this reactant excitation effect. It should be mentioned that the reaction of vibrationally excited CN($X^2\Sigma^+$, $v \leq 7$) with O($^3P$) and O$_2$ has recently been studied by Wolfrum and coworkers.[13]

In order to account for the apparently contradicting observations in the dependence of CO laser intensity and CO(+N$_2$) production on flash energy shown in Figures 4 and 7, respectively, we introduce the following additional reactions into our reaction scheme.

$$N + SO \longrightarrow NO + S \qquad (3)$$

$$N + NO \longrightarrow N_2 + O \qquad (4)$$

$$CN + SO \longrightarrow OCN + S \qquad (5)$$

$$CN + NO \longrightarrow N_2 + CO \qquad (6)$$

$$O + OCN \longrightarrow CO + NO \qquad (7)$$

$$N + OCN \longrightarrow CO + N_2 \qquad (8)$$

$$OCN + OCN \longrightarrow N_2 + 2CO \qquad (9)$$

$$O + SO + M \longrightarrow SO_2 + M \qquad (10)$$

$$O + CO + M \longrightarrow CO_2 + M \qquad (11)$$

$$O + SO_2 + M \longrightarrow SO_3 + M \qquad (12)$$

In this scheme, other reactions involving BrCN and SO$_2$ with atoms or free radicals are not included; they are probably slow and unimportant.

The concentration profiles of all species involved in the above reaction scheme were calculated on the basis of the rate constants given in Table II. Unfortunately, the rate constants for most of these reactions are not known. In those cases, we assign what we believe "reasonable values," in accordance with the available rates for analogous reactions as explained in the footnotes of the Table.

The rate constants for both flash-initiation reactions A and B were evaluated according to the measured conversions of both reactants, using the following expression;[7] taking BrCN, for example

$$k_A = \alpha t e^{-t/\tau} \qquad (I)$$

where $\alpha = \ln([BrCN]_{t=\infty}/[BrCN]_{t=0})/\tau^2$ and $\tau$ = the time at which flash intensity reaches its maximum value; it is $1.5 \times 10^{-5}$ sec for the present case.

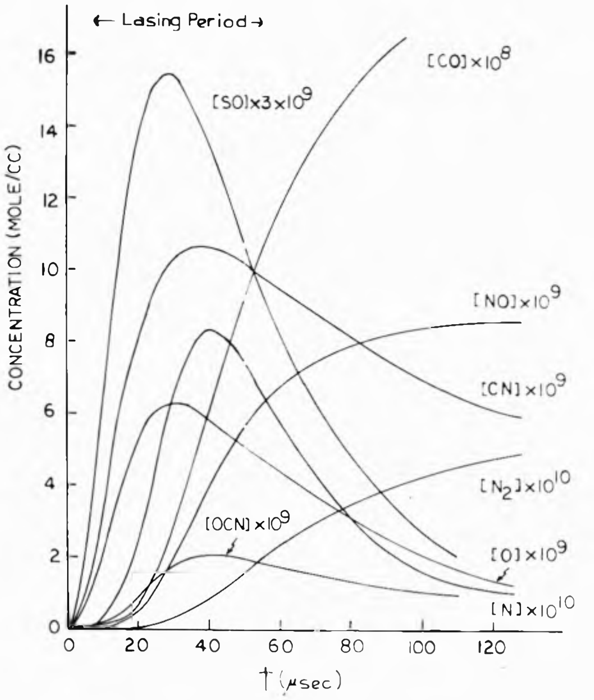

**Figure 8.** A plot of calculated concentration *vs.* time for several reactive species produced in a flash. 20 Torr of a 2:1 BrCN:SO$_2$ mixture was flashed at 2.1 kJ.

The concentration of each species as a function of time, *t*, was calculated by numerically integrating the coupled differential rate equations using a fourth-order Runge-Kutta method modified by Treanor.[14] A typical concentration *vs.* time plot for a 20 Torr 2:1 BrCN:SO$_2$ mixture, flashed with 2.1 kJ energy, at an earlier stage of reaction is shown in Figure 8. These results show that the concentrations of most reactive species such as O, N, and SO decrease significantly within 120 μsec after flash initiation. CO is the only major final product formed during the lasing period, ~10–50 μsec after the flash. The CO$_2$ yield is $10^6$ times less than that of CO at $t$ = 120 μsec; it plays no role at all in the chemistry of laser action because of its slow third-order formation rate.

The calculations were extended up to 1 msec after flash initiation. The concentrations of reactive species (O, N, CN, SO, and OCN) at $t$ = 1 msec are too low to be important. Figure 9 presents the calculated concentrations of CO and CO + N$_2$ (*i.e.*, the total *m/e* 28 yield) at 10 μsec and 1 msec ($t = \infty$), respectively, as functions of flash energy. The results show that at $t$ = 10 μsec, the approximate time at which the total laser output peaks, the concentration of CO increases linearly with the *second* power of flash energy, whereas the total yields of CO and N$_2$ at the end of a flash ($t = \infty$) vary linearly with the *first* power of flash energy. These results are in agreement with the experimental data given in Figures 4 and 7. According to these calculations, the final N$_2$ yield constitutes only ~28% of mass 28 in the whole range of flash energy studied.

In order to account for the observed gas analysis results

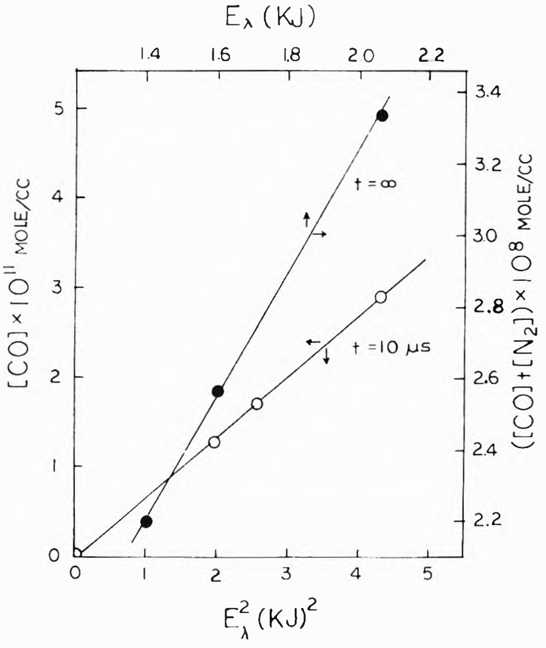

**Figure 9.** The theoretically calculated concentration of $[CO] + [N_2]$ at $t$ = 10 $\mu$sec and $t$ = 1 msec as a function of flash energy.

shown in Figure 7, computations were made for five consecutive flashes. For each flash the calculation was extended up to 1 msec after flash initiation. The theoretical yields of $m/e$ 28, 30 (NO), and 44 ($CO_2$) as functions of flash energy are compared with experimental results in Figure 7. The calculated yields given by dotted lines were normalized to the smoothed experimental values at 1.6 kJ because these values were measured only on a relative basis. The agreement is satisfactory considering the uncertainties involved in the assumed rates. It should be noted that the temperature of the system was assumed constant at 300°K for all calculations. This is probably not a problem in view of the small conversions of BrCN (~4%) and $SO_2$ (~3.5%) generated by a single flash at 2.1 kJ, the highest flash energy employed in these experiments. Because of the low conversions, the calculated relative yields of the three products ($m/e$ 28, 30, and 44) from a single flash differ only slightly from those given in Figure 7 for five flashes.

The trace yield at $m/e$ 42, presumably due to $OCN^+$, may result from the cracking peak of the products of combination reactions such as Br + OCN, NO + OCN, or SO + OCN.

## Conclusion

The results of the present study of the $O(^3P)$ + CN reaction tend to confirm that the production of CO + $N(^4S)$ *via* reaction 1 is the principal laser pumping reaction of the system and that the corresponding reaction 2 producing the $N(^2D)$ atom is not an important process in this system. Detailed calculations have been made to account for the observed $I \propto E_\lambda^2$ and yield $\propto E_\lambda$ relationships. We plan to study this system further using a laser-probing technique to obtain the complete vibrational population distribution of the CO molecule in order to more conclusively answer the question regarding the involvement of reaction 2.

## References and Notes

(1) NRC/NRL Postdoctoral Research Associate, Aug 1973–present. Aug 1973.
(2) (a) L. E. Brus and M. C. Lin, *J. Phys. Chem.*, **76**, 1429 (1972); (b) M. C. Lin, *Int. J. Chem. Kinet.*, **6**, 173 (1973).
(3) M. C. Lin and L. E. Brus, *J. Chem. Phys.*, **54**, 5423 (1971).
(4) M. A. Pollack, *Appl. Phys. Lett.*, 9, 230 (1966).
(5) M. C. Lin, *Int. J. Chem. Kinet.*, **6**, 1 (1974).
(6) M. C. Lin, "Chemiluminescence and Bioluminescence," M. J. Cormier, D. M. Hercules, and J. Lee, Ed., Plenum Press, New York, N.Y., 1973, p 61.
(7) M. C. Lin, manuscript in preparation.
(8) N. Basco, *Proc. Roy. Soc., Ser. A*, **283**, 302 (1965).
(9) J. C. Boden and B. A. Thrush, *Proc. Roy. Soc., Ser. A*, **305**, 107 (1968).
(10) S. Rosenwaks and I. W. M. Smith, *J. Chem. Soc., Faraday Trans. 2*, **69**, 1 (1973).
(11) K. J. Laidler, "The Chemical Kinetics of Excited States," Oxford University Press, London, 1955.
(12) G. A. West and M. J. Berry, presented at the 166th National Meeting of the American Chemical Society, Chicago, Ill., Aug 1973, Physical Chemistry Paper No. 100.
(13) H. Schacke, K. J. Schmatjzko, and J. Wolfrum, *Ber. Bunsenges. Phys. Chem.*, **77**, 248 (1973).
(14) C. E. Treanor, *Math. Computation*, **20**, 39 (1966).

# Relative Rates of the Reactions of O($^1D_2$) Atoms with Alkanes and Cycloalkanes[1a]

**P. Michaud,[1b] G. Paraskevopoulos, and R. J. Cvetanović***

*Division of Chemistry, National Research Council of Canada, Ottawa, Canada K1A OR9*

*(Received December 27, 1973)*

*Publication costs assisted by the National Research Council of Canada*

Rate constants relative to that of neopentane have been measured for the reactions of O($^1D_2$) atoms with $C_2H_6$, $C_3H_8$, $n$-$C_4H_{10}$, $n$-$C_5H_{12}$, 2,2,4-trimethylpentane, $c$-$C_3H_6$, $c$-$C_4H_8$, $c$-$C_5H_{10}$, and $c$-$C_6H_{12}$. The relative rate constant for $CH_4$, determined in the same manner earlier in this laboratory, is combined with the literature value of the absolute rate constant to convert the relative rate constants for the alkanes studied to absolute values. The rate constants were found to be proportional to the number of CH bonds but independent of their type or strength for alkanes with up to 12 CH bonds. For larger alkanes the average reactivity per CH bond appears to decrease.

## Introduction

The reactions of the electronically excited singlet oxygen atoms O($^1D_2$) with paraffins in the gas phase have been studied extensively in recent years.[2] The main features of the reactions are now well established although there are some minor details which are not as yet clear. The mechanism consists mainly of two reaction paths: (a) insertion of O($^1$D) atoms into the CH bonds to form vibrationally excited alcohols, which decompose if not stabilized by collisions, and (b) hydrogen abstraction from the paraffin to form OH and alkyl radicals. A third reaction path, molecular elimination of $H_2$, occurs to a much smaller extent. The reaction occurs without discrimination between the various CH bonds giving the statistical ratio of products.[2a,b]

A competitive technique has been developed in this laboratory to measure relative rates of reactions of O($^1$D) atoms.[3] This technique is based on the measurement of the decrease in the yield of neopentanol, the main product of the reaction of O($^1$D) with neopentane,[2c] when another gas competes with neopentane for the O($^1$D) atoms. The technique has been used successfully to measure relative rates for a number of O($^1$D) reactions.[3,4] In the present work we have extended these measurements to include relative rate constants of O($^1$D) reactions with a number of paraffins and cycloparaffins. The relative values so obtained were combined with the absolute rate constant of the reaction O($^1$D) + $CH_4$ to calculate absolute rate constants of the reactions studied.

## Method

Excited oxygen atoms, O($^1D_2$), were generated by photolysis of $N_2O$ at 2139 Å. At this wavelength the decomposition of $N_2O$ to $N_2$ + O($^1$D) is the only important primary photolytic step in the photolysis of $N_2O$.[5] In addition, there is enough energy to generate O($^1$D) but not the more highly excited O($^1$S) atoms.[2a,6] The relevant reactions are

$$N_2O + h\nu \longrightarrow N_2 + O(^1D) \quad (1)$$

$$O(^1D) + \text{neopentane} \longrightarrow \alpha(\text{ROH}) + (1-\alpha)(\text{R} + \text{OH}) \quad (2)$$

$$O(^1D) + \text{reactant} \longrightarrow \text{products} \quad (3)$$

where ROH is neopentanol. It is convenient to express the neopentanol yield relative to $N_2$, which is generated simultaneously with O($^1$D) in reaction 1 and serves as an internal actinometer when the ratio neopentane/$N_2O$ or (neopentane + reactant)/$N_2O$ is sufficiently large so that virtually no O($^1$D) reacts with $N_2O$. The vibrationally excited neopentanol formed in reaction 2 is completely stabilized and its yield becomes constant at a pressure of about 150 Torr.[2c] Under the above conditions the decrease in neopentanol yield, in experiments in which another gas has been added to compete with neopentane for O($^1$D), gives a measure of the reactivity toward O($^1$D) of the added gas relative to that of neopentane.

## Experimental Section

The 2139-Å light was provided by two Philips 93106 E zinc lamps and was focussed by two Ultrasil lenses. The cylindrical photolysis cell had a volume of 195.6 ml and Suprasil quartz windows 5 cm in diameter. The mercury free and mercury containing vacuum systems used and the experimental and analytical techniques have been described before.[2b] In the present experiments a solid nitrogen trap (−220°), capable of trapping ethylene, was added before the Toepler pump.

The $N_2$ formed in the photolysis of $N_2O$ (reaction 1) was measured in all experiments by gas-solid chromatography on an 18 ft, 13X molecular sieve column. Neopentanol was separated from the excess reactants and measured on a 300 ft long, 0.015 in. i.d. stainless steel capillary column coated with $\beta,\beta'$-thiodipropionitrile and equipped with a flame ionization detector.

The materials used were Phillips 66 research grade neopentane (99.97%), ethane (99.93%), propane (99.95%), $n$-butane (99.90%), and 2,2,5-trimethylpentane (99.98%); Matheson nitrous oxide (98.8%), cyclopropane (98.0%), and sulfur hexafluoride (98.0%); American Petroleum Institute cyclopentane (99.997%) and cyclohexane (99.995%); Matheson Coleman and Bell spectroquality $n$-pentane (99.0%); and Merck Sharp and Dohme cyclobutane. The reagents which are gases at standard temperature and pressure were subjected to three bulb-to-bulb distillations *in vacuo*, the last from a Dry Ice-acetone bath, and those which are liquids at standard temperature and pressure were degassed at −196°. All the reagents were further degassed at −196° before each experiment. Cyclobutane was passed through concentrated $H_2SO_4$ and

**TABLE I: Pressures of Reactants and Yields of $N_2$ and Neopentanol in the Experiments Used for the**

| $N_2O$, Torr | Reactant, Torr | Neopentane, Torr | Pressure, Torr | Reactant/ neopentane | $N_2$, μmol | Neopentanol/$N_2$ | $R_0/R$ |
|---|---|---|---|---|---|---|---|
| Data for neopentane alone (average of 12 experiments) | | | | | | | |
| ~50.0 | | ~200 | ~250 | | 2.0–9.0 | 0.620 | |
| Reactant = Ethane | | | | | | | |
| 49.7 | 103 | 152 | 305 | 0.68 | 2.46 | 0.451 | 1.38 |
| 36.7 | 186 | 112 | 335 | 1.66 | 9.47 | 0.341 | 1.82 |
| 29.8 | 292 | 125 | 447 | 2.34 | 2.73 | 0.286 | 2.17 |
| 37.0 | 287 | 71.4 | 395 | 4.02 | 9.82 | 0.209 | 2.97 |
| 37.0 | 316 | 57.7 | 411 | 5.48 | 9.22 | 0.164 | 3.78 |
| 36.7 | 200 | 28.7 | 265 | 6.99 | 9.89 | 0.135 | 4.59 |
| 53.0 | 218 | 29.7 | 301 | 7.35 | 3.14 | 0.131 | 4.77 |
| 36.8 | 358 | 42.8 | 438 | 8.36 | 9.24 | 0.118 | 5.25 |
| $k_{C_2H_6}/k_{neop}$ = 0.512 ± 0.005, Intercept = 0.982 ± 0.028 | | | | | | | |
| Reactant = Propane | | | | | | | |
| 37.0 | 201 | 127 | 365 | 1.58 | 2.88 | 0.300 | 2.07 |
| 36.5 | 261 | 100 | 397 | 2.61 | 8.15 | 0.230 | 2.69 |
| 36.3 | 328 | 80.6 | 445 | 4.07 | 9.27 | 0.170 | 3.65 |
| 36.0 | 330 | 57.5 | 423 | 5.74 | 10.3 | 0.131 | 4.73 |
| 36.7 | 385 | 58.5 | 480 | 6.58 | 11.1 | 0.111 | 5.59 |
| 37.0 | 390 | 46.7 | 474 | 8.35 | 7.84 | 0.098 | 6.33 |
| $k_{C_3H_8}/k_{neop}$ = 0.652 ± 0.027, Intercept = 1.03 ± 0.147 | | | | | | | |
| Reactant = *n*-Butane | | | | | | | |
| 36.5 | 122 | 79.6 | 238 | 1.53 | 11.2 | 0.269 | 2.30 |
| 37.9 | 165 | 54.6 | 257 | 3.02 | 20.9 | 0.159 | 3.90 |
| 36.6 | 179 | 45.2 | 261 | 3.96 | 11.2 | 0.140 | 4.43 |
| 37.5 | 200 | 40.3 | 278 | 4.96 | 9.85 | 0.120 | 5.17 |
| 36.8 | 202 | 33.4 | 272 | 6.05 | 10.8 | 0.096 | 6.46 |
| 36.5 | 252 | 39.1 | 328 | 6.44 | 18.5 | $0.095_4$ | 6.50 |
| 36.8 | 210 | 27.9 | 275 | 7.53 | 7.13 | $0.081_6$ | 7.60 |
| $k_{n\text{-}C_4H_{10}}/k_{neop}$ = 0.863 ± 0.033, Intercept = 1.06 ± 0.168 | | | | | | | |
| Reactant = *n*-Pentane | | | | | | | |
| 36.9 | 107 | 115 | 259 | 0.93 | 4.57 | 0.295 | 2.10 |
| 37.6 | 160 | 55.3 | 253 | 2.89 | 5.22 | 0.162 | 3.83 |
| 37.2 | 188 | 40.8 | 266 | 4.61 | 7.69 | 0.111 | 5.59 |
| 36.5 | 221 | 37.3 | 295 | 5.92 | 8.14 | 0.091 | 6.81 |
| 37.1 | 235 | 35.2 | 307 | 6.68 | 6.54 | 0.079 | 7.85 |
| $k_{n\text{-}C_5H_{12}}/k_{neop}$ = 0.988 ± 0.032, Intercept = 1.08 ± 0.150 | | | | | | | |
| Reactant = 2,2,4-Trimethylpentane | | | | | | | |
| 28.9 | 41.9 | 53.5 | $347^a$ | 0.78 | 2.87 | 0.319 | 1.94 |
| 18.1 | 43.4 | 23.1 | $317^a$ | 1.88 | 2.40 | 0.178 | 3.48 |
| 20.9 | 41.2 | 16.3 | $346^a$ | 2.53 | 2.32 | 0.154 | 4.03 |
| 14.5 | 41.9 | 10.9 | $332^a$ | 3.84 | 2.04 | 0.109 | 5.69 |
| 9.06 | 39.9 | 7.93 | $259^a$ | 5.03 | 5.63 | 0.084 | 7.38 |
| $k_{i\text{-}C_8H_{18}}/k_{neop}$ = 1.257 ± 0.041, Intercept = 0.969 ± 0.130 | | | | | | | |
| Reactant = Cyclopropane | | | | | | | |
| 23.8 | 53.1 | 53.5 | $331^a$ | 0.99 | 3.52 | 0.431 | 1.44 |
| 61.4 | 262 | 128 | 451 | 2.05 | 5.01 | 0.280 | 2.21 |
| 60.7 | 253 | 86.7 | 400 | 2.92 | 1.96 | 0.248 | 2.49 |
| 61.4 | 288 | 73.0 | 422 | 3.94 | 3.41 | 0.198 | 3.13 |
| 57.8 | 376 | 74.4 | 508 | 5.05 | 2.80 | 0.169 | 3.67 |
| $k_{c\text{-}C_3H_6}/k_{neop}$ = 0.538 ± 0.030, Intercept = 0.978 ± 0.099 | | | | | | | |
| Reactant = Cyclobutane | | | | | | | |
| 54.9 | 109 | 205 | 369 | 0.53 | 3.74 | 0.440 | 1.41 |
| 54.9 | 125 | 107 | 287 | 1.17 | 3.13 | 0.332 | 1.87 |
| 56.4 | 212 | 110 | 378 | 1.93 | 3.65 | 0.264 | 2.35 |
| 58.5 | 216 | 84.5 | 359 | 2.56 | 3.56 | 0.214 | 2.90 |
| 57.8 | 213 | 72.3 | 343 | 2.95 | 3.84 | 0.194 | 3.20 |
| 58.5 | 337 | 88.9 | 484 | 3.79 | 3.48 | 0.159 | 3.90 |
| $k_{c\text{-}C_4H_8}/k_{neop}$ = 0.762 ± 0.020, Intercept = 0.963 ± 0.049 | | | | | | | |
| Reactant = Cyclopentane | | | | | | | |
| 62.1 | 60.7 | 205 | 328 | 0.30 | 4.31 | 0.484 | 1.28 |
| 50.6 | 121 | 204 | 376 | 0.59 | 5.51 | 0.395 | 1.57 |
| 53.5 | 182 | 207 | 442 | 0.88 | 3.18 | 0.340 | 1.82 |
| 48.4 | 227 | 202 | 477 | 1.12 | 5.15 | 0.291 | 2.13 |
| 51.3 | 258 | 206 | 515 | 1.25 | 3.87 | 0.284 | 2.18 |
| 52.0 | 247 | 152 | 451 | 1.63 | 3.95 | 0.247 | 2.51 |
| 54.3 | 250 | 119 | 423 | 2.10 | 4.15 | 0.211 | 2.94 |
| $k_{c\text{-}C_5H_{10}}/k_{neop}$ = 0.918 ± 0.024, Intercept = 1.03 ± 0.030 | | | | | | | |

**Determination of Relative Rate Constants**

| $N_2O$, Torr | Reactant, Torr | Neopentane, Torr | Pressure, Torr | Reactant/neopentane | $N_2$, μmol | Neopentanol/$N_2$ | $R_0/R$ |
|---|---|---|---|---|---|---|---|
| | | | Reactant = Cyclohexane | | | | |
| 50.6 | 50.6 | 206 | 307 | 0.24 | 2.70 | 0.488 | 1.27 |
| 52.0 | 89.6 | 181 | 439[a] | 0.50 | 2.80 | 0.407 | 1.52 |
| 43.3 | 86.7 | 88.1 | 321[a] | 0.98 | 2.89 | 0.307 | 2.01 |
| 31.8 | 87.4 | 58.5 | 354[a] | 1.49 | 3.89 | 0.241 | 2.57 |
| 18.1 | 83.1 | 42.6 | 308[a] | 1.95 | 2.57 | 0.200 | 3.10 |
| | | $k_{c\text{-}C_6H_{12}}/k_{neop}$ = 1.07 ± 0.019, Intercept = 0.989 ± 0.023 | | | | | |

[a] Total pressure made up by addition of $SF_6$.

KOH pellets to remove traces of reactive impurities present, followed by preparative gas chromatographic separation.

## Results

Experiments were made at 300 ± 2°K. The pressures of $N_2O$, neopentane, and reactants are given in Table I. The total pressure was 240 to 500 Torr, *i.e.*, well above the pressure at which the neopentanol is completely stabilized.[2c] In cases of reactants with low vapor pressure (2,2,5-trimethylpentane and cyclohexane) the total pressure was made up with $SF_6$, which does not interact with $O(^1D)$ in any way.[3-6] At the ratios of (neopentane + reactant)/$N_2O$ used virtually all the $O(^1D)$ reacted with neopentane and the reactant; under such conditions $N_2$ provides a quantitative measure of $O(^1D)$ produced.[2c,3,4c] The amount of $N_2$ formed and the relative yields of neopentanol (expressed as neopentanol/$N_2$, *i.e.*, the yield per $O(^1D)$ atom) are also given in Table I. The average yield of neopentanol in experiments without added reactant is given as the first entry in Table I: it agrees with previous determinations[2c,3,4c] and represents the reaction of neopentane alone. When another reactant is added, the neopentanol yield decreases as a result of competition of the other reactant for $O(^1D)$. For reactions 1-3, with the usual steady-state approximation, the following expression is obtained

$$\frac{R_0}{R} = 1 + \frac{k_3}{k_2}\frac{[\text{reactant}]}{[\text{neopentane}]}$$

where $R_0$ is the rate of production of neopentanol in the absence of reactant, *i.e.*, when neopentane alone reacts with $O(^1D)$; $R$ is the rate of production of neopentanol when a reactant is added. The ratio $R_0/R$ is the ratio of the relative yields of neopentanol given in the last column of Table I. A plot of $R_0/R$ against [reactant]/[neopentane] should give a straight line with a slope of $k_3/k_2$ and an intercept of one. Such plots are shown in Figures 1 and 2 for paraffins and cycloparaffins, respectively. The least-squares values of $k_3/k_2$ and intercepts are given in Table I. The errors quoted are standard deviations. A possible nonrandom error in these measurements may be caused by interference of small peaks of products that were not separated well from the peaks of neopentanol or the internal standard in the gas chromatographic analysis. Although care was taken to avoid such interference by operating the column at 0° or by using different internal standards when necessary, an overall uncertainty of about 5-10% is perhaps more realistic than the very small standard deviations of measurements shown in Table I.

Attempts to determine relative rates for *n*-hexane and isobutane resulted in large errors due to the gas chromatographic interferences mentioned above; the value for the latter paraffin was estimated to be ~0.83 ± 10% from data in ref 2b and 3.

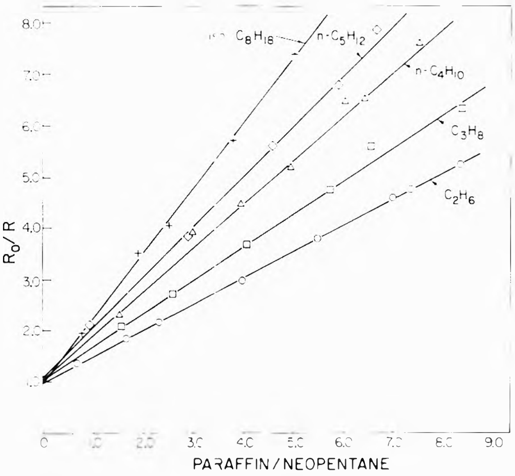

**Figure 1.** Plot of $R_0/R$ *vs.* the paraffin/neopentane ratio.

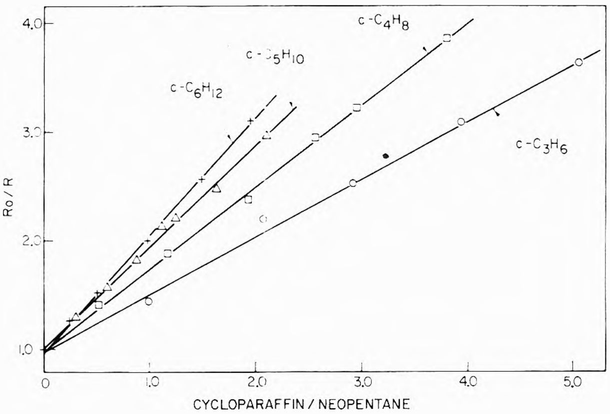

**Figure 2.** Plot of $R_0/R$ *vs.* the cycloparaffin/neopentane ratio.

## Discussion

Where comparison is possible, *i.e.*, for the present data for $C_2H_6$ and $C_3H_8$ and our earlier data for $H_2$ and $CH_4$,[3] agreement with existing data in the literature is very good. The latter include the relative rates (relative to the rate of $O(^1D)$ reaction with ozone) of DeMore[7] for the reactions of $H_2$, $CH_4$, $C_2H_6$, and $C_3H_8$ with $O(^1D)$ formed by photolysis of ozone in liquid argon and the absolute rates of Heidner and Husain[8] for the reactions of $H_2$ and $CH_4$ with $O(^1D)$ formed by flash photolysis of ozone and monitored by atomic absorption spectroscopy in the vacuum ultraviolet. The comparison is shown in Table II, where all the rates are expressed relative to that of $H_2$

**TABLE II: Comparison of Relative Rates from Different Sources[a]**

| Reactant | This work (300°K) | Ref 7[b] (87°K) | Ref 8[c] (300°K) |
|---|---|---|---|
| $H_2$ | 1.00 | 1.00 | 1.00 |
| $CH_4$ | 1.24 | 1.15 | 1.15 |
| $C_2H_6$ | 2.02 | 1.92 | |
| $C_3H_8$ | 2.57 | 2.46 | |

[a] All rate constants expressed relative to that of $H_2$ taken as unity. [b] $O(^1D)$ generated by photolysis of ozone in liquid argon. [c] $O(^1D)$ generated by flash photolysis of ozone.

**TABLE III: Relative and Absolute Rate Constants for the Reactions of $O(^1D)$ with Paraffins and Cycloparaffins at 300 ± 2°K**

| Reactant (r) | $k_r/k_{neop}$ | $k_r \times 10^{-14}$, $cm^3\ mol^{-1}\ sec^{-1}$ | $Z_{AB} \times 10^{-14}$,[a] $cm^3\ mol^{-1}\ sec^{-1}$ |
|---|---|---|---|
| Hydrogen | 0.254[b] | 1.63[c] | 2.82 |
| Methane | 0.315[b] | 1.87[c] | 1.79 |
| Ethane | 0.512 ± 0.005 | 3.03 | 1.87 |
| Propane | 0.652 ± 0.027 | 3.86 | 2.10 |
| *n*-Butane | 0.863 ± 0.033 | 5.11 | 2.11 |
| Isobutane | ~0.83[d] | 4.91 | 2.07 |
| *n*-Pentane | 0.988 ± 0.032 | 5.85 | 2.36 |
| Neopentane | 1.00 | 5.91 | 2.22 |
| 2,2,4-Trimethylpentane | 1.26 ± 0.041 | 7.46 | 3.24 |
| Cyclopropane | 0.538 ± 0.030 | 3.19 | 1.97 |
| Cyclobutane | 0.762 ± 0.020 | 4.51 | |
| Cyclopentane | 0.918 ± 0.024 | 5.44 | |
| Cyclohexane | 1.07 ± 0.019 | 6.34 | 2.28 |

[a] Molecular collision diameters, taken from ref 9, as discussed in the text. [b] Relative rates from ref 3, obtained by the same technique as the present values. [c] Absolute values of Heidner and Husain (ref 8). [d] Approximate value calculated from the data of ref 2b and 3.

taken as the common basis. The data for these compounds and for other compounds studied are summarized in Table III. Using the value of Heidner and Husain[8] for the absolute rate of the reaction of $O(^1D)$ with methane, absolute rates for the reactions of $O(^1D)$ with the other paraffins were calculated and are also listed in Table III, together with estimates for most of the reactants of the corresponding hard-sphere collision frequencies. The molecular collision diameters used in these estimates were taken from the work of Rabinovitch and coworkers,[9] which appears to provide a self-consistent set. The collision diameter for $O(^1D)$, $\sigma$ = 2.7 Å, was taken to be between that of He and Ne; for 2,2,4-trimethylpentane it was taken to be equal to that of *n*-octane. The estimates of the absolute values of collision frequency are only approximate but they do indicate that all the paraffins react with $O(^1D)$ very fast. This, combined with the evidence that these reactions occur to an appreciable extent at liquid argon temperature,[7] suggests that they should have negligible or very small activation energies.

With regard to the factors which determine the reactivities of the paraffins toward $O(^1D)$, expressed either as relative or absolute rate constants, the following observations may be made: (a) the reactivity is independent of the type or strength of CH bonds, in agreement with conclusions from earlier studies with propane[2a,7] and isobutane[2b,7] in which the isomeric alcohols were formed in their statistical ratios by indiscriminate insertion of $O(^1D)$ into the different CH bonds; (b) the reactivity increases with the size of the alkane and should depend therefore on a parameter related to the size of the alkane molecule. DeMore[7] has determined the relative rates of the reactions of $CH_4$, $C_2H_6$, $C_3H_8$, $C_2F_4$, and $C_2H_4$ in liquid argon. He found that the reactivities of these compounds could be represented adequately as sums of the average reactivities per CH and C=C bonds. Thus, for example, the relative reactivity of $C_2H_4$ could be represented as the sum of the reactivities of four CH bonds and one C=C double bond. A question that arises in this connection is whether this relationship is valid in the gas phase and whether it remains valid for increasingly large paraffins. A plot of the relative and absolute rates *vs.* the number of CH bonds is shown in Figure 3. A straight line may be drawn through the points up to the pentanes and cyclohexane. The reactivities of cycloalkanes appear to be slightly higher than those of the corresponding open chain alkanes with the same number of CH bonds but the differences border on the likely experimental errors. On the other hand, the value for 2,2,4-trimethylpentane lies well below the value expected from the additivity of the specific rate constants per bond. If we neglect the value for 2,2,4-trimethylpentane, a linear least-squares fit of the data for the other alkanes and cycloalkanes gives the relative reactivity per CH of 0.086 ± 0.0013 and the absolute reactivity per CH bond of 5.10 ± 0.08 × $10^{13}$ $cm^3\ mol^{-1}\ sec^{-1}$, where the quoted errors are the standard deviations.

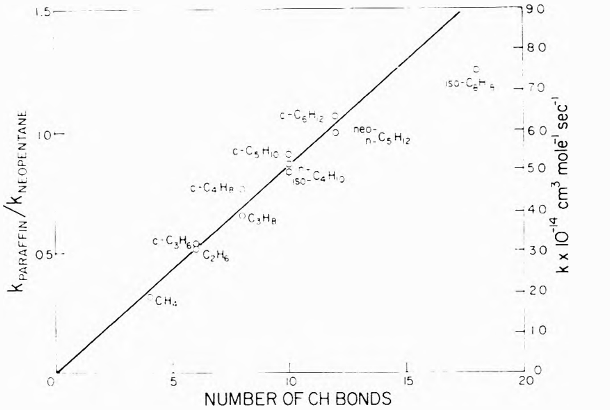

**Figure 3.** Plot of the relative and absolute values of the rate constants *vs.* the number of CH bonds.

The value of the rate constant obtained for 2,2,4-trimethylpentane appears to indicate that although the molecular reactivity of the alkanes increases with the number of CH bonds, *i.e.*, with the size of the molecule, there is a molecular size beyond which further increase in the chain length of the alkane does not result in a corresponding increase in reactivity, *i.e.*, the average reactivity per CH bond begins to decrease. This indicates that with larger alkanes steric considerations may become important. It appears reasonable that larger alkane molecules may assume configurations in which some CH bonds are no longer readily accessible to $O(^1D)$ atoms. It would be desirable to verify this effect with still larger alkanes but experiments with such compounds become difficult and unreliable under conditions used in the present study because of interferences in the gas chromatographic analysis, mentioned earlier in the text, and because they do not have sufficient vapor pressures.

*Acknowledgment.* The authors are grateful to Mr. R. G. Elder for assistance with a part of the experimental work reported.

## References and Notes

(1) (a) Issued as N.R.C.C. No. 14091. (b) National Research Council of Canada Postdoctorate Fellow 1969–1971.

(2) (a) H. Yamazaki and R. J. Cvetanović, *J. Chem. Phys.*, **41**, 3703 (1964); (b) G. Paraskevopoulos and R. J. Cvetanović, *ibid.*, **50**, 590 (1969); (c) *ibid.*, **52**, 5821 (1970); (d) P. Michaud and R. J. Cvetanović, *J. Phys. Chem.*, **76**, 1375 (1972); (e) C. L. Lin and W. B. DeMore, *ibid.*, **77**, 863 (1973).

(3) G. Paraskevopoulos and R. J. Cvetanović, *J. Amer. Chem. Soc.*, **91**, 7572 (1969).

(4) (a) G. Paraskevopoulos, K. F. Preston, and R. J. Cvetanović, *J. Chem. Phys.*, **54**, 3907 (1971); (b) G. Paraskevopoulos and R. J. Cvetanović, *Chem. Phys. Lett.*, **9**, 603 (1971); (c) G. Paraskevopoulos, V. B. Symonds, and R. J. Cvetanović, *Can. J. Chem.*, **50**, 1838 (1972).

(5) K. F. Preston and R. F. Barr, *J. Chem. Phys.*, **54**, 3347 (1971).

(6) K. F. Preston and R. J. Cvetanović, *J. Chem. Phys.*, **45**, 2888 (1966).

(7) W. B. DeMore, *J. Phys. Chem.*, **73**, 391 (1969).

(8) R. F. Heidner III and D. Husain, *Int. J. Chem. Kinet.*, **5**, 819 (1973).

(9) S. C. Chan, B. S. Rabinovitch, J. T. Bryant, L. D. Spicer, T. Fujimoto, Y. N. Lin, and S. P. Pavlou, *J. Phys. Chem.*, **74**, 3160 (1970).

# Condensed-Phase Photochemistry of Cyclobutanone

**Samuel G. Thomas, Jr., and William A. Guillory***[1]

*Department of Chemistry, Drexel University, Philadelphia, Pennsylvania 19104*

*(Received February 4, 1974)*

*Publication costs assisted by the National Science Foundation*

The ultraviolet and vacuum-ultraviolet photolyses of cyclobutanone ($c$-$C_3H_6CO$) in argon, carbon monoxide, and nitrogen matrices have been performed between 8 and 10 K. The results of these experiments suggest that the photodecomposition mechanism of cyclobutanone is a function of photon energy. The major products of photolysis observed are CO, $c$-$C_3H_6$, $CH_2CO$, $C_2H_4$, and $C_3H_6$. These products result from at least two and possibly three primary photolysis processes: $c\text{-}C_3H_6CO + h\nu \rightarrow C_2H_4 + CH_2CO$ (1); $c\text{-}C_3H_6CO + h\nu \rightarrow c\text{-}C_3H_6 + CO$ (2), and possibly $c\text{-}C_3H_6CO + h\nu \rightarrow C_3H_6 + CO$ (3). In process 2, propylene may also result from the isomerization of vibrationally excited cyclopropane, $c\text{-}C_3H_6^* \rightarrow C_3H_6$ (2c), if it is not first quenched by the matrix, $c\text{-}C_3H_6^* + M \rightarrow c\text{-}C_3H_6 + M$ (2b); where M is the matrix. No infrared detectable products were observed as a result of photolysis with a medium-pressure Hg lamp from exciting wavelengths above ~3100 Å. Photolysis into the predissociative region of the $n \rightarrow \pi^*$ (3350–2632 Å) band with the 3022-Å Hg line produced CO and $c$-$C_3H_6$ only, while exposure to the full Hg arc with major lines at 3022, 2967, 2894, and 2804 Å resulted in infrared detectable products of CO, $c$-$C_3H_6$, $CH_2CO$, and $C_3H_6$. Processes 1, 2, and possibly 3 are also the major reactions resulting from photolysis at 1745, 1634, 1580, and 1495 Å with various vacuum-ultraviolet resonance lamps, while no net photodecomposition or photoionization resulted at 1215 Å with a hydrogen resonance lamp. Based on relative intensities, the combination of processes 2 and 3 > 1 at all wavelengths employed in this study and (2c) and (3) are indistinguishable sources of $C_3H_6$. Although we obtained no direct evidence for the occurrence of (3) in this study nor have we been able to find any, we include its consideration because it is energically possible. Additional products obtained, due to secondary vacuum-ultraviolet photolysis below 1500 Å are methane, methylacetylene, allene, and $C_2O$. The results from experiments using the CO matrix as a triplet quencher suggest that (2) may also proceed through ISC from the $^1B_2$ state as observed for the first excited singlet, $^1A_2$. A discussion of the photophysical and photochemical processes occurring as a function of specific electronic absorptions is presented. Some tentative vibrational assignments for the infrared frequencies of matrix-isolated cyclobutanone have also been made.

## I. Introduction

The photochemistry of cyclobutanone ($c$-$C_3H_6CO$) in the gas phase has been studied by many workers and its photodecomposition has been interpreted in terms of two primary processes

$$\underline{CH_2CH_2CH_2C}{=}O + h\nu \longrightarrow CH_2{=}CH_2 + CH_2C{=}O \quad (1)$$

$$\underline{CH_2CH_2CH_2C}{=}O + h\nu \longrightarrow \Delta^* + CO \quad (2a)$$

where $\Delta^*$ which symbolizes excited cyclopropane is either collisionally stabilized (2b) or isomerizes to propylene (2c). The thermal decomposition from the vibrationally

$$\Delta^* + M \longrightarrow \Delta + M \quad (2b)$$

$$\Delta^* \longrightarrow C_3H_6 \quad (2c)$$

excited ground electronic state of $c$-$C_3H_6CO$ ($^1A_1^*$) leads almost exclusively to the formation of ethylene and ketene (99.5%), while only 0.5% is converted according to process 2.[2a,b] On the other hand, photodecomposition of $c$-$C_3H_6CO$ from its first excited triplet state ($^3A_2^*$) leads solely to the formation of CO and excited cyclopropane (2a),[2c] which subsequently isomerizes to propylene (2c) or is vibrationally relaxed (2b), depending on the extent of collisional stabilization.[3] Photodecomposition from the vibrationally excited first electronic singlet ($^1A_2^*$) leads to the occurrence of both processes 1 and 2. The product ratio, ($c$-$C_3H_6$ + $C_3H_6$)/($CH_2{=}CH_2$), varied from 0.4 to 0.8, when exciting wavelengths in the range of 3130 to 2654 Å were used,[3] indicating that process 1 > 2, and that the $C_3/C_2$ ratio increased as the photolyzing wavelength decreased. Fluorescence was also observed from the first excited singlet state of cyclobutanone in the gas phase with exciting wavelengths between 3050 and 3350 Å. The fluorescence emission quantum yield was $\sim$0.002 at $\lambda$ >3190 Å but decreased sharply below this wavelength due to the onset of molecular predissociation. Although there is still some question concerning the possible mechanism, the predissociation supposedly leads to the formation of $C_2$ products (1) favored relative to the $C_3$ products (2).[4] In the "nonpredissociative" region of $\lambda_{ex} \geq 3194$ Å, the $C_3/C_2$ ratio has been interpreted as the ratio of $k_{isc}/k_{ic}$. These results were based upon studies of the benzene photosensitization of cyclobutanone revealing that process 1 occurred *via* a singlet mechanism and process 2 *via* a triplet mechanism.[2c] With excitation wavelengths between 3130 and 3263 Å, the ratios of $C_3/C_2$ varied from 0.4 to 1.2,[4,5] suggesting that $C_3$ products were favored at long wavelengths (process 2 > 1).

The photodecomposition of cyclobutanone from the first excited singlet ($^1A_2^*$) leading to $C_3$ products was recently suggested to occur by the combination of three possible mechanisms: (1) $^1A_2^* \rightarrow {}^3A_2 \rightarrow C_3$; (2) $^1A_2^* \rightarrow C_3$; (3) $^1A_2^* \rightarrow {}^1A_1^* \rightarrow C_3$.[4] Since the total $C_3$ yield was approximately constant at two significantly different total pressures ($\sim$2 and 1200 Torr), the individual contributions were assumed to be varied. In this case, the constancy of the total $C_3$ yield as a function of pressure was apparently due to the fortuitous canceling of the three pressure-dependent contributions.[4] These results suggest that collision-induced energy transfer plays an important role in the photodissociative processes involving cyclobutanone in the gas phase. This effect has been recently shown to be a significant one, even down to a few torr total pressure by the laser-induced photochemical dissociation of formaldehyde by Yeung and Moore.[6]

As a result, it appeared to us that the matrix photolysis technique might provide an excellent means of practically eliminating intermolecular energy transfer processes and minimizing those with a rare gas matrix. This technique offers the advantage of surrounding the active molecule with an inert environment, thereby essentially preventing electronic state coupling due to an intermolecular effect. To the extent that these assumptions are accomplished, we are provided in essence the opportunity to study *intrinsic* photophysical and photochemical properties of a molecule. An additional advantage of the matrix photolysis technique lies in its natural ability to prevent photochemical fragmented diffusion of all but relatively light atoms. However, its most significant shortcoming involves the secondary photolysis of primary dissociation products. This problem can be minimized by using monochromatic or band pass filtered sources. In this particular study, the primary photodecomposition products, ketene, cyclopropane, and CO, are all stable molecular products and were easily identified from their known infrared spectra. Based on the infrared spectrum of matrix isolated propylene recorded in this laboratory, propylene was also identified as a primary and/or secondary product of photolysis along with other minor secondary products. The infrared spectra of these species provided a direct means, based on ratios of optical densities, to compare the relative importance of processes 1 and 2 as a function of exciting energy. A comparison of the ratios of optical densities of propylene and cyclopropane also provided a direct means to establish the relative importance of vibrational relaxation of hot cyclopropane *vs.* chemical and/or photochemical processes leading to propylene as a function of photon energy.

In addition to these photolysis experiments, tentative vibrational assignments for some of the infrared frequencies observed in this study for cyclobutanone in argon and nitrogen matrices are made. These assignments are based on comparisons with prior vibrational assignments of cyclobutane along with a previous normal coordinate calculation for cyclobutanone.

## II. Experimental Section

The cyclobutanone ($c$-$C_3H_6CO$) was obtained from the Aldrich Chemical Co. In order to remove traces of $CO_2$ impurities the gaseous cyclobutanone was passed through ascarite. The propylene used in this study was obtained from Air Products and Chemicals Inc. and used without further purification.

The matrix gases argon, carbon monoxide, and nitrogen (99.99% purity) were used without further purification. The ratios of the matrix to active materials (M:A) were either 400:1 or 800:1. Sample mixtures were prepared in a 2-l. bulb and delivered through a Granville-Phillips leak valve, generally at a rate of 1 mm/min or less. These mixtures were condensed on a cold CsI window, below 10 K. The cryogenic instrument used was an Air Products closed-cycle helium Displex refrigerator.

The photolysis of the matrix isolated species was accomplished by subjecting the samples on the cold CsI window to direct radiation through $CaF_2$, LiF, or Suprasil II vacuum-ultraviolet windows. A medium-pressure Hg lamp (Hanovia No. 30620) and microwave powered hydrogen, bromine, and nitrogen flow discharge lamps were used as photolysis sources.[7] The spectral characteristics of the Hg lamp and the hydrogen, bromine, and nitrogen discharge lamps have been discussed in previous publications.[8-10] The vacuum uv lamps have intensities of the order of $10^{15}$ quanta for the resonance line(s), while the Hg lamp is a multiline 150-W medium-pressure arc. The emission spectrum of each of the diatomic discharge lamps are observed to have a strong broad band which essentially spans the visible region. The nitrogen discharge lamp was used in conjunction with the Suprasil II window in order to isolate the nitrogen doublet (1743 and 1745 Å). The various wavelength regions of the Hg lamp were isolated by attaching calibrated glass filters (Esco Products) directly to the LiF window. The wavelength regions transmitted by these filters were the following: $\lambda$ >3000, 3100–4500, and 3100–4000 Å.[8]

The identification of the photochemically produced species was obtained from the infrared spectra after photolysis. A Perkin-Elmer 621 spectrophotometer was used for this purpose.

## III. Results

The infrared spectrum of a film of Ar:$c$-$C_3H_6CO$ = 800:1 before photolysis is shown in the solid trace of Figure 1 and summarized in the first column of Table I. The spectrum of the unphotolyzed sample agrees well with the gas-phase spectrum reported by Sadtler Research Laboratories, Inc.,[11] with consideration given for the usual slight

**TABLE I: Summary of Absorptions ($cm^{-1}$) in the $c$-$C_3H_6CO$ in Argon Experiments**

| Before photolysis | Vibrational[a] assignment | After photolysis[b] |  | Molecular assignment |
|---|---|---|---|---|
|  |  | 1 | 2 |  |
| 3524 vw |  |  |  | $c$-$C_3H_6CO$ |
|  |  | 3105 w<br>3090 w | 3090 w | $c$-$C_3H_6$ |
|  |  | 3073 vw<br>3059 m | 3059 w | $CH_2CO$ |
| 3010 m | $CH_2$ stretch |  |  | $c$-$C_3H_6CO$ |
| 2980 m | $CH_2$ stretch |  |  | $c$-$C_3H_6CO$ |
| 2933 m | $CH_2$ stretch |  |  | $c$-$C_3H_6CO$ |
|  |  | 2138 vs | 2138 vs<br>2123 m | CO |
|  |  | 2083 m | 2083 vw | $CH_2CO$ |
|  |  | 1975 w | 1975 vw | $C_2O$ |
|  |  |  | 1953 vw | $C_3H_4$ |
| 1804 vs<br>1799 vs<br>1795 vs<br>1778 s | CO stretch |  |  | $c$-$C_3H_6CO$ |
| 1751 m |  |  |  | $c$-$C_3H_6CO$ |
|  |  |  | 1647 w | $C_3H_6$ |
| 1452 m | $CH_2$ scis | 1452 w | 1452 m | $c$-$C_3H_6CO$, $C_3H_6$ |
|  |  | 1439 m | 1439 m | $c$-$C_3H_6$,$C_3H_6$ |
| 1395 s<br>1389 w | $CH_2$ scis |  |  | $c$-$C_3H_6CO$ |
|  |  | 1376 m | 1376 w | $CH_2CO$ |
| 1332 m |  |  |  | $c$-$C_3H_6CO$ |
|  |  |  | 1302 vw | $CH_4$ |
| 1240 m |  |  |  | $c$-$C_3H_6CO$ |
| 1206 s |  |  |  | $c$-$C_3H_6CO$ |
| 1161 m<br>1157 m |  |  |  | $c$-$C_3H_6CO$ |
| 1123 m |  |  |  | $c$-$C_3H_6CO$ |
|  |  |  | 1117 vw | $CH_2CO$ |
| 1084 w | Ring vibration |  |  | $c$-$C_3H_6CO$ |
| 1069 vs<br>1066 vs | Ring vibration |  |  | $c$-$C_3H_6CO$ |
| 1042 w | Ring vibration | 1042 w | 1042 w | $c$-$C_3H_6CO$, $C_3H_6$ |
|  |  | 1024 ms | 1024 m | $c$-$C_3H_6$ |
|  |  | 998 vw | 998 w | $C_3H_6$ |
|  |  | 988 vw | 988 w | $C_3H_6$ |
|  |  | 972 vw | 972 vw | $CH_2CO$ |
| 958 w<br>954 ms | Ring vibration |  |  | $c$-$C_3H_6CO$ |
|  |  | 940 vw<br>936 w | 936 vw | ? |
|  |  | 909 m | 909 ms | $C_3H_6$ |
|  |  | 866 m<br>863 ms | 871 w<br>866 m<br>863 m | $c$-$C_3H_6$ |
|  |  | 853 w | 853 w | $c$-$C_3H_6$ |
|  |  |  | 837 w | $C_3H_4$ |
| 823 m | Ring vibration |  |  | $c$-$C_3H_6CO$ |
| 737 m | $CH_2$ rock |  |  | $c$-$C_3H_6CO$ |
| 726 m | $CH_2$ rock |  |  | $c$-$C_3H_6CO$ |
| 665 m<br>662 m | $CH_2$ rock |  |  | $c$-$C_3H_6CO$ |
|  |  |  | 627 m | $C_2H_4$ |
|  |  | 593 w | 593 w | $CH_2CO$ |
|  |  |  | 577 w | $C_3H_6$ |
|  |  | 523 m | 523 w | $CH_2CO$ |
| 455 m | <CCO def in plane |  |  | $c$-$C_3H_6CO$ |

[a] Designates uncertainty in the vibrational assignment. [b] After photolysis with (1) a medium-pressure Hg lamp of an Ar:$c$-$C_3H_6CO$ = 400:1 film and (2) a nitrogen discharge lamp through (LiF) of an Ar:$c$-$C_3H_6CO$ = 800:1 film.

matrix shifts. Weak absorptions in some of these experiments due to slight $H_2O$ impurity introduced during deposition of the sample onto the cold window or previously present in the argon matrix gas have been omitted in Table I and Figure 1. The splittings observed in some of the features are probably due to multiple trapping sites in the matrix. Some new tentative vibrational assignments for the infrared absorption frequencies of cyclobutanone isolated in argon are shown in the second column of Table I. These assignments are based on comparisons with previous vibrational assignments for infrared frequencies of cyclobutane[12] and a normal coordinate analysis[13] which

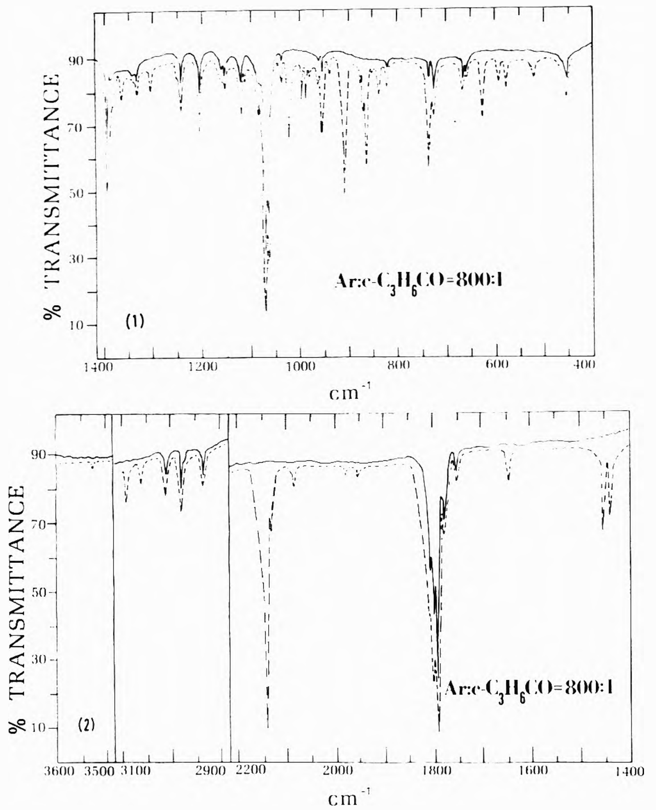

**Figure 1.** Infrared spectra of Ar:c-$C_3H_6CO$ = 800:1: (——) deposition at 8 K, 1 mm/min for 72 min from a 2.5-l. volume; (- - - - -) simultaneous deposition and photolysis for 5 hr with a nitrogen discharge lamp (LiF): (1) 1400–400 $cm^{-1}$; (2) 3600–3500, 3100–2900, 2200–1400 $cm^{-1}$.

assumes from microwave measurements that cyclobutanone has a planar ring skeleton and transforms according to symmetry group $C_{2v}$. It is assumed that the presence of the C=O group in cyclobutanone produces a small perturbation in its $CH_2$ and ring vibrational frequencies relative to those observed in cyclobutane. Therefore, the infrared features observed at 3010, 2980, and 2933 $cm^{-1}$ in cyclobutanone appear to be due to the $CH_2$ stretching vibrations; based on comparisons with these stretching vibrations of cyclobutane in the range of 2987–2878 $cm^{-1}$. The normal coordinate analysis predicts a value of 1816 $cm^{-1}$ for the CO stretch for cyclobutanone and this result suggests that the features observed in this study between 1804 and 1778 $cm^{-1}$ are due to this vibration. These calculations also predict five planar ring vibrations, mixed CC stretching and CCC bending, between 1100 and 650 $cm^{-1}$. Based on these calculations, the infrared features between 1084 and 823 $cm^{-1}$ have been assigned to planar ring vibrations. However no attempt is made here to distinguish between a CC stretch and a CCC angle deformation (in plane), since both types of vibrations are of the order of 1000 $cm^{-1}$ in cyclobutane and a large amount of mixing is expected. The assignment of the infrared features at 1452, 1395, and 1389 $cm^{-1}$ and 737, 726, 665, and 662 $cm^{-1}$ to the $CH_2$ bending vibrations are based on the observed infrared frequencies of cyclobutane at 1447 $cm^{-1}$ due to its $CH_2$ scissors and at 749 and 627 $cm^{-1}$ due to its $CH_2$ rocking vibrations. A calculated value for the planar CCO angle deformation of 450 $cm^{-1}$ appears to agree with the infrared feature observed to occur in this study at 455 $cm^{-1}$.

When an Ar:c-$C_3H_6CO$ = 400:1 film was subjected to radiation from an unfiltered medium-pressure Hg lamp, new absorptions appeared at 2138 $cm^{-1}$, due to CO,[14] and 3105, 3090, 1439, 1024, 866, 863, and 853 $cm^{-1}$, due to cyclopropane (c-$C_3H_6$). The assignment of the cyclopropane absorption frequencies agrees with the gas-phase work reported by previous workers,[15] taking into account the usual frequency shifts in going from the gas to the condensed phase. In addition to these absorptions, new features were observed at 1452, 998, 988, and 909 $cm^{-1}$, due to propylene ($C_3H_6$). The propylene absorption frequencies resulting from the Hg lamp photolysis agree well with the infrared spectrum (1648, 1452, 997, 987, and 909 $cm^{-1}$) of an Ar:$C_3H_6$ = 400:1 film recorded in this laboratory.[16] The complete infrared spectrum and photolysis of propylene in the condensed phase will be the subject of a future publication. Additional new features observed at 3073, 3059, 2083, 1376, 972, 593, and 523 $cm^{-1}$ are due to ketene ($CH_2CO$).[17] Although we have been unable to assign a new weak split feature at 940–936 $cm^{-1}$, the weak absorption observed at 1975 $cm^{-1}$ is possibly due to the free radical $C_2O$.[18] These results are summarized in Table I, column 1. Although the dashed trace of Figure 1 represents the results of 5 hr of simultaneous deposition and photolysis of an Ar:c-$C_3H_6CO$ = 800:1 film with a nitrogen discharge lamp, the results with the Hg lamp are similar except for the absence of some features due to secondary photolysis. In order to estimate where the onset of photodissociation occurred with our particular multiline source, the photolysis of a film of Ar:c-$C_3H_6CO$ = 800:1 was performed by passing the Hg radiation through a series of ultraviolet filters. The transmission characteristics of each of the filters were matched to excite specific portions of the n → $\pi^*$ transition (3350–2632 Å), both in the bound and predissociative regions.[19] The n′ → $\pi^*$ band (2060–1820 Å) corresponding to excitation of one of the second lone-pair electrons about oxygen is probably not excited to any significant extent because of relatively low intensity in this region. The results of simultaneous deposition and photolysis with the filtered Hg lamp (Table II, column 2), transmitting $\lambda$ >3000 Å, indicated new features at 2138, 1439, 1024, 866, and 863 $cm^{-1}$; the first due to CO and the others due to cyclopropane. When this film was subjected to radiation from filtered Hg lamps, transmitting between 3100–4500 and 3100–4000 Å, respectively, no new features were observed. These results suggest that major lines less than 3100 Å were primarily responsible for photodecomposition and the particular line at 3022 Å appeared to exclusively produce process 2. In Table II, the optical densities of several absorptions of the major products are shown, normalized relative to the 1069-$cm^{-1}$ parent absorption. Columns 1 and 2 summarize the results of the filtered and unfiltered Hg lamp experiments.

The next lowest electronic absorption of cyclobutanone is the continuous n → $\sigma_{(c)}^*$ 1802–1681-Å band.[19] For this system, photolysis was performed with the 1743-, 1745-, and 1495-Å resonance lines of a microwave powered nitrogen resonance lamp through the LiF transmitting window. In Figure 1 the results of the nitrogen discharge lamp photolysis of the Ar:c-$C_3H_6CO$ = 800:1 film are presented (dashed trace) along with the absorptions of the unphotolyzed sample (solid trace). The new features resulting in these experiments (Table I, column 2 and Table II, column 3) were similar to those obtained with a Hg lamp with the exception of additional features due to secondary photolysis. These additional features were observed to occur at 1953, 837, 627, 1647, 577, and 1302 $cm^{-1}$; the first

**TABLE II: Optical Densities of Product Absorptions Normalized to the Parent 1069-$cm^{-1}$ Absorption**[a]

| Photolysis product | Absorptions, $x$ $cm^{-1}$ | Ratios of optical densities[b,c] | | | | |
|---|---|---|---|---|---|---|
| | | Hg (unfiltered) (1) | λ 3000 (2) | $N_2$(LiF) (3) | $N_2$(SII) (4) | $Br_2$ (5) |
| CO | 2138 | 0.65 | 0.16 | 0.91 | 0.76 | 1.2 |
| $c$-$C_3H_6$ | 863 | 0.32 | 0.070 | 0.26 | 0.16 | 0.23 |
| $c$-$C_3H_6$ | 1024 | 0.18 | 0.049 | 0.18 | 0.12 | 0.13 |
| $c$-$C_3H_6$ | 1439 | 0.083 | 0.0055 | 0.16 | 0.074 | 0.13 |
| $CH_2CO$ | 523 | 0.057 | | 0.067 | 0.036 | 0.047 |
| $CH_2CO$ | 593 | 0.038 | | 0.040 | 0.018 | 0.029 |
| $CH_2CO$ | 1376 | 0.050 | | 0.071 | 0.041 | 0.073 |
| $C_3H_6$ | 577 | | | 0.077 | 0.048 | 0.049 |
| $C_3H_6$ | 909 | 0.042 | | 0.46 | 0.098 | 0.30 |
| $C_3H_6$ | 998 | 0.0066 | | 0.071 | 0.017 | 0.051 |

[a] Photolysis product at $x$ $cm^{-1}$/parent at 1069 $cm^{-1}$. [b] Computed from optical densities of products resulting from photolysis with the following lamps: (1) a medium-pressure Hg lamp; (2) a filtered medium-pressure Hg lamp (λ >3000 Å); (3) a nitrogen discharge lamp (LiF); (4) a nitrogen discharge lamp (Suprasil II); (5) a bromine discharge lamp (LiF). [c] Designates the absence of an infrared absorption for the photolysis product at $x$ $cm^{-1}$.

two due to allene ($C_3H_4$), the next due to methylacetylene ($C_3H_4$), the next two due to propylene ($C_3H_6$), and the last possibly due to methane ($CH_4$). These tentative assignments are based on preliminary work in progress in this laboratory involving the infrared spectrum and the vacuum-ultraviolet photolysis of matrix isolated propylene, where methylacetylene, methane, and allene are products of secondary photolysis. This study will be the subject of a separate publication.[16] Another new weak feature at 1117 $cm^{-1}$ due to ketene ($CH_2CO$) was also observed upon photolysis of cyclobutanone.[17] In order to exclusively excite into the 1802–1681-Å system, the nitrogen discharge lamp was used in conjunction with a Suprasil II window (cutoff at ~1650 Å); isolating the 1743-, 1745-Å nitrogen doublet and removing the 1495-Å line. The results of these filtered experiments (Table II, column 4) were similar to those of the unfiltered nitrogen discharge lamp except for the absence of features occurring at 1953, 1302, 1117, 837, and 627 $cm^{-1}$, corresponding to $CH_4$, allene, methylacetylene, and ketene.

Excitation into the broad banded region of the $\pi \rightarrow \pi^*$ (1601–1480 Å) electronic absorption band[19] and the superimposed ns Rydberg series[19] (1668–1367 Å) were also performed with radiation from a bromine discharge lamp (1634 and 1580 Å). After 5 hr of simultaneous deposition and photolysis of this sample (Table II, column 5) new absorptions similar to those obtained with the unfiltered nitrogen discharge lamp were observed with the exception of a small production of $C_2O$ *via* (10).

The hydrogen discharge lamp was also used to excite $c$-$C_3H_6CO$ into the ionization continuum beyond its onset at approximately 9.35 eV.[19] After 5 hr of deposition and photolysis of an Ar:$c$-$C_3H_6CO$ = 400:1 film with the 1215-Å line, no new features attributable to it were observed. In order to effectively produce ionic species in these condensed phase situations, it is presumably as important to efficiently photoionize the species under study as it is to have an efficient electron acceptor.

The ultraviolet and vacuum-ultraviolet photolysis experiments of cyclobutanone isolated in argon matrices in several cases produced new absorptions which were superimposed on absorptions of the parent. Two examples are shown in Table I; the 1452- and 1042-$cm^{-1}$ features each due to a superposition of cyclobutanone and propylene absorptions,[16] while the 1439-$cm^{-1}$ feature may be a superposition of two features due to cyclopropane[15] and propylene.[16]

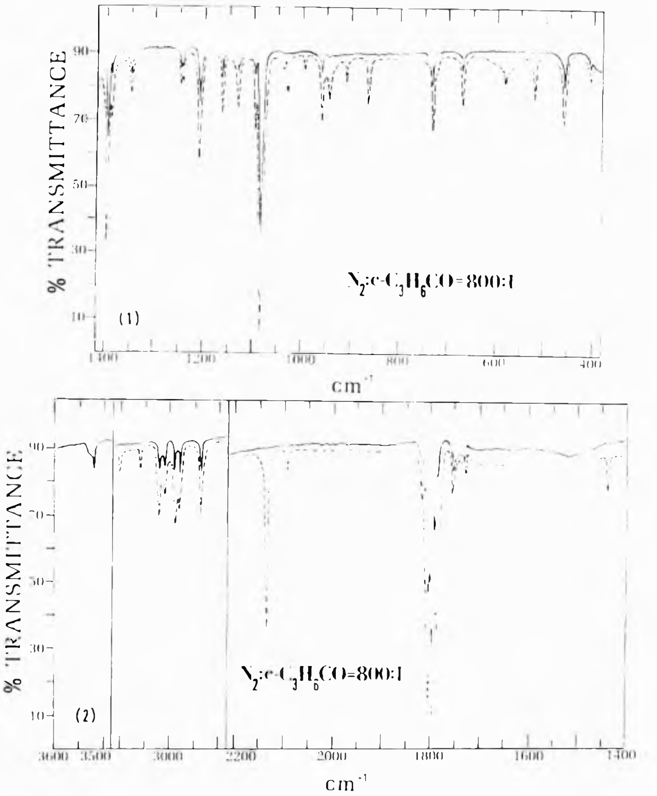

**Figure 2.** Infrared spectra of $N_2$:$c$-$C_3H_6CO$ = 800:1: (——) deposition at 8 K, 1 mm/min for 63 min from a 2.5-l. volume; (– – – –) simultaneous deposition and photolysis for 5 hr with a nitrogen discharge lamp ($CaF_2$): (1) 1400–400 $cm^{-1}$; (2) 3600–3500, 3100–2900, 2200–1400 $cm^{-1}$.

The infrared spectrum of cyclobutanone isolated in nitrogen before photolysis is shown in the solid trace of Figure 2 and the first column of Table III along with the vibrational assignments which are shown in the second column. These assignments are based on comparisons with vibrational assignments for cyclobutane[12] and the previously mentioned normal coordinate analysis[13] for cyclobutanone. Weak absorptions at 3725, 3689, and 1597 $cm^{-1}$ due to $H_2O$ impurity in the nitrogen matrix gas have been omitted in Table III and Figure 2.

After 5 hr of simultaneous deposition and photolysis of cyclobutanone in nitrogen with the nitrogen discharge lamp, the following new features were observed: 2139 $cm^{-1}$ due to CO;[14] 3101, 1438, 1029, 1026, and 867 $cm^{-1}$ due to cyclopropane;[15] 1041, 993, and 911 $cm^{-1}$ due to propylene;[16] 3062, 586, and 522 $cm^{-1}$ due to ketene;[17] 2096 $cm^{-1}$ due to diazomethane ($CH_2N_2$),[20] establishing

**TABLE III: Summary of Absorptions (cm$^{-1}$) in the $N_2$:c-$C_3H_6CO$ = 800:1 Experiments**

| Before photolysis | Vibrational assignment[a] | After photolysis[b] | Molecular assignment |
|---|---|---|---|
| 3519 m | | | c-$C_3H_6CO$ |
| | | 3101 w | c-$C_3H_6$ |
| | | 3062 w | $CH_2CO$ |
| 3022 m<br>3008 m | $CH_2$ stretch | | c-$C_3H_6CO$ |
| 2990 m<br>2980 m | $CH_2$ stretch | | c-$C_3H_6CO$ |
| 2939 m | $CH_2$ stretch | | c-$C_3H_6CO$ |
| | | 2139 vs | CO |
| | | 2096 w | $CH_2N_2$ |
| 1803 vs<br>1798 vs<br>1782 s | CO stretch | | c-$C_3H_6CO$ |
| 1755 m | | | c-$C_3H_6CO$ |
| 1734 w | | | c-$C_3H_6CO$ |
| | | 1438 m | c-$C_3H_6$ |
| 1397 s<br>1391 m | $CH_2$ scis | | c-$C_3H_6CO$ |
| 1350 m | | | c-$C_3H_6CO$ |
| 1248 w<br>1243 w | | | c-$C_3H_6CO$ |
| 1211 s | | | c-$C_3H_6CO$ |
| 1167 m | | | c-$C_3H_6CO$ |
| 1133 m | | | c-$C_3H_6CO$ |
| 1095 m | Ring vibration | | c-$C_3H_6CO$ |
| 1082 vs | Ring vibration | | c-$C_3H_6CO$ |
| 1041 vw | Ring vibration | 1041 vw | c-$C_3H_6CO$ |
| | | 1029 m<br>1026 m | c-$C_3H_6$ |
| | | 993 vw | $C_3H_6$ |
| 960 m<br>946 w | Ring vibration | | c-$C_3H_6CO$ |
| | | 911 w | $C_3H_6$ |
| | | 867 m | c-$C_3H_6$ |
| 729 m | $CH_2$ rock | | c-$C_3H_6CO$ |
| 669 w | $CH_2$ rock | | c-$C_3H_6CO$ |
| | | 586 w | $CH_2CO$ |
| | | 522 m | $CH_2CO$ |
| 462 m | <CCO def in plane | | c-$C_3H_6CO$ |
| 404 vw | CO out of plane def | | c-$C_3H_6CO$ |

[a] Designates uncertainty in the vibrational assignment. [b] After photolysis with a nitrogen discharge lamp ($CaF_2$).

the presence of a small amount of methylene ($CH_2$). These results are presented in the last two columns of Table III.

In order to further clarify the photophysical processes leading to dissociation, the 1745-, 1743-Å nitrogen line was used to photolyze a CO:c-$C_3H_6CO$ = 400:1 film. After 5 hr of deposition and photolysis, the resulting spectrum revealed new features due *only* to $CH_2CO$ and $C_2H_4$ and none due to either CO, $\triangle$, or $C_3H_6$. These results are particularly significant since the latter products are the most intensely absorbing species obtained in $N_2$ and Ar matrices under all conditions.

## IV. Discussion

The sources used here to photolyze matrix isolated cyclobutanone were a medium-pressure Hg lamp (5788 Å, 2.1-eV air cutoff), a nitrogen discharge lamp (1743 and 1495 Å, 7.1 and 8.3 eV), a bromine discharge lamp (1634 Å, 7.6 eV), and a hydrogen discharge lamp (1215 Å, 10.2 eV). Since the ionization potential of cyclobutanone is estimated to be 9.35 eV,[19] it is safe to assume that ion production is unimportant in these systems except in the case of the hydrogen discharge lamp, which will be discussed in detail later. From gas-phase work, cyclobutanone has been shown to thermally decompose ($E_{\mathrm{act}} \simeq 52$ kcal/mol, 2.3 eV) from its vibrationally excited ground electronic state to yield primarily ethylene and ketene (99.5%) and to a minor extent cyclopropane and CO (0.5%), as in (1) and (2).[2a,b] However, decomposition from the first excited triplet state has been shown to proceed almost exclusively *via* (2a).[2c] If the vibrationally excited cyclopropane is not collisionally stabilized, it can isomerize to propylene, as in (2c). However, in a matrix environment, vibrational relaxation is assumed to be very rapid[21] and will be competitive with the isomerization process. Although the critical energy for isomerization (2c) has been estimated to be ~63 kcal/mol (2.7 eV), the heat of reaction for cyclobutanone going to cyclopropane and CO, as in (2a) and (2b), is only ~6.7 kcal/mol (0.7 eV).[22] If it is assumed that all initial excitation energy, except that lost as the energy of reaction, is available for vibrational excitation, then process 2c can occur with all the light sources used in this study. From gas-phase work, the pressure and wavelength dependence of the total $C_3$ yield (c-$C_3H_6$ + $C_3H_6$) was presented as evidence that propylene was the result of a secondary (isomerization of hot cyclopropane) process rather than a primary photolysis process, as in (3).[22] Since the thermodynamic conversion of (3) is

$$\underline{\mathrm{CH_2CH_2CH_2CO}} + h\nu \longrightarrow \triangle + \mathrm{CO} \qquad (3)$$

endothermic by only 14-20 kcal, this direct formation of propylene is also possible with all the exciting sources used in this study.

The results of photolysis with the full intensity of a medium-pressure Hg lamp of cyclobutanone isolated in argon showed new features in the infrared due to carbon monoxide (CO), cyclopropane (c-$C_3H_6$), propylene ($C_3H_6$), and ketene ($CH_2CO$); as shown in Table I, column 1. Performing the same experiment with nitrogen, bromine, and hydrogen discharge lamps yielded the same new features as obtained with the Hg lamp with the addition of some new features probably due to allene ($C_3H_4$), methane ($CH_4$), methylacetylene ($C_3H_4$), and the free radical $C_2O$. Thus the secondary reactions which could be important in this system and serve as a basis of discussion, in addition to processes 1-3 are the following

$$\Delta + h\nu \longrightarrow CH_3CH{=}CH_2 \tag{4}$$

$$\Delta + h\nu \longrightarrow CH_2 + CH_2{=}CH_2 \tag{5}$$

$$\Delta + h\nu \longrightarrow H_2 + CH_2{=}C{=}CH_2 \tag{6}$$

$$\Delta + h\nu \longrightarrow H_2 + HC{\equiv}CCH_3 \tag{7}$$

$$CH_2{=}CO + h\nu \longrightarrow CH_2 + CO \tag{8}$$

$$CH_2 + CO \longrightarrow CH_2{=}CO \tag{9}$$

$$CH_2{=}CO + h\nu \longrightarrow H_2 + C_2O \tag{10}$$

$$CH_2{=}CH_2 + h\nu \longrightarrow H_2 + HC{\equiv}CH \tag{11}$$

$$CH_3CH{=}CH_2 + h\nu \longrightarrow CH_4 + HC{\equiv}CH \tag{12}$$

$$CH_3CH{=}CH_2 + h\nu \longrightarrow H_2 + CH_2{=}C{=}CH_2 \tag{13}$$

$$CH_3CH{=}CH_2 + h\nu \longrightarrow H_2 + HC{\equiv}CCH_3 \tag{14}$$

From prior work in this laboratory, the only observable infrared absorption frequencies of a film of Ar:$C_2H_4$ = 800:1 were at 946 and 1439 cm$^{-1}$; the first of very strong intensity and the other of medium intensity.[23] Based on previous gas-phase photolyses of cyclobutanone, we assume that ethylene is a primary product of photolysis (1) in this study and that the 946-cm$^{-1}$ feature is apparently masked by the strong 954-cm$^{-1}$ feature of the parent, cyclobutanone, in $N_2$ and Ar matrices. Since the 946-cm$^{-1}$ feature of ethylene was not observed after photolysis in these matrices, we assumed from relative intensity considerations that the 1439-cm$^{-1}$ feature of ethylene is sufficiently weak to be masked by new features due to cyclopropane (Table I, Figure 1) at the same frequency. Although no infrared features due to ethylene were observed in $N_2$ and Ar matrices, new features due to ketene and $C_2H_4$ (1) were observed in the CO matrix experiments, where the perturbation caused by the CO matrix was presumably sufficient to separate the $C_2H_4$ and c-$C_3H_6CO$ features.

The Hg photolysis experiments using the various ultraviolet filters indicated observable photodecomposition below 3100 Å. These results were obtained by exciting into the 3350-2632-Å band of cyclobutanone having an oscillator strength of ~5 × $10^{-4}$. This band is a superposition of about 75 individual peaks on a continuum which has several broad maxima. From gas-phase work, excitation into the first excited singlet state of cyclobutanone with exciting wavelengths in the range 3050-3350 Å resulted in fluorescence emission. However, this fluorescence emission disappeared below the exciting wavelength of 3100 Å due to the onset of molecular predissociation,[4,5] which has its onset at approximately 3190 Å. As in the previous condensed phase study of formaldehyde, no infrared detectable decomposition of c-$C_3H_6CO$ occurs above the threshold predissociative wavelength. Filtered Hg lamp photolysis experiments with the major line at 3022 Å between 3000 and 3100 Å resulted in new absorptions due to CO and cyclopropane only, as in processes 2a and 2b. These observations are consistent with a recent study in EPA glass at 77 K with exciting wavelengths at ~3000 Å,[24] where the time-dependent emission spectrum indicated possible photodissociation.

In addition to the 3022-Å line, exposure of matrix-isolated c-$C_3H_6CO$ to the unfiltered Hg arc with major lines at 3022, 2967, 2894, and 2804 Å, resulted in products indicative of processes 1, 2, and possibly 3. Although there is gas-phase evidence for the formation of propylene principally *via* (2c),[4] both (2c) and (3) are indistinguishable sources in these experiments. In addition, gas-phase energy-transfer studies involving exclusive excitation into the vibrationally excited ground state ($^1A_1$*) and the first triplet ($^3A_2$) have been identified with the photophysical conversions leading to (1) and (2) (and possibly (3)), respectively.[2c] Although, we were not able to test this mechanism in the exciting region under study here, results from the n → $\sigma_{CO}$* band do agree with this mechanism in that case. As the exciting wavelength decreases the relative propylene yield increases gradually. Although our experiments cannot distinguish between (2c) and (3), this behavior would appear to suggest isomerization as the more probable source of propylene.

In addition to the major products of photodissociation, a weak feature observed at 1975 cm$^{-1}$ tentatively assigned to $C_2O$ is probably a product of secondary photolysis. Of the primary products formed, only ketene has electronic absorptions[25] that could be excited by the Hg arc. One occurring at 3850-2600 Å which dissociates *via* (8) and recombines in the matrix cage according to (9) with no net reaction; the other occurs at 2130-1930 Å and is probably the source of $C_2O$ *via* (10).

Upon photolysis of matrix-isolated c-$C_3H_6CO$ with the various vacuum-ultraviolet sources (1743, 1745, 1634, 1580, 1495, and 1215 Å), new absorptions are observed in the infrared due to CO, cyclopropane, ketene, propylene, and possibly allene, methane, $C_2O$, and methylacetylene. These photodecomposition products are the result of excitation into the continuous n → $\sigma_{CO}$* 1802-1681-Å band with $f \simeq 7 \times 10^{-3}$ and into the $\pi \rightarrow \pi$* 1670-1480-Å band with $f \simeq 2 \times 10^{-1}$.[19] The $\pi \rightarrow \pi$* band has a maximum of intensity at 1587 Å and extends to 1480 Å, whereupon diffuseness sets in accompanied by considerable underlying continuous absorption.

The photolysis of c-$C_3H_6CO$ with the unfiltered $N_2$ discharge resulted in the generation of all the primary and secondary products cited above (Table I, column 2). Performing the same experiment through a Suprasil II window and isolating on the 1743-, 1745-Å doublet resulted in the elimination of all the products of secondary photolysis with the exception of a small production of $C_2O$ *via* (10). These observations would tend to confirm the major processes 1, 2, and possibly 3. Upon comparing the relative ratios of the normalized optical densities of the various products at a given wavelength with those at another, we are provided a *semiquantitative* measure of a reaction as a function of exciting frequency. In going from the unfiltered Hg arc to the 1743-, 1745-doublet, the ratios CO/ketene and c-$C_3H_6$/$C_3H_6$ increase and decreases, respectively; indicating the increased efficiency of (2) and possi-

ห้องสมุด กรมวิทยาศาสตร์

bly (3) *vs.* (1). The latter ratio denotes more efficient propylene formation relative to $c$-$C_3H_6$ from (2c) and/or (3). Conversion *via* (4) does not occur at these wavelengths since $c$-$C_3H_6$ absorbs below 1600 Å.[26] As mentioned above, no secondary photolysis of $C_3H_6$ occurs in this case. The 1495-Å line is apparently effective in producing all of the secondary products, and upon examination of the electronic absorption spectra of the various products, ∆, $CH_2CO$, and $C_3H_6$, this is indeed found to be the case.[25,26] The secondary photolysis of ketene *via* (8) was confirmed using a nitrogen matrix experiment. The results of an unfiltered nitrogen discharge lamp photolysis ($CaF_2$ window, ~1250-Å cutoff) of $c$-$C_3H_6CO$ in a nitrogen matrix (Figure 2 and Table III) verified the presence of a trace of methylene with the appearance of a new weak feature at 2096 $cm^{-1}$, due to diazomethane ($CH_2N_2$).[20]

Excitation into the broad banded region of the $\pi \rightarrow \pi^*$ transition (1670–1480 Å) and the Rydberg series (1668–1367 Å) with the bromine resonance doublet at 1634 and 1580 Å results in the same product absorptions as the unfiltered nitrogen lamp (Table I, column 2), with the exception of $C_2O$. In addition to the major processes 1, 2, and possibly 3, secondary photolysis of the major products gives rise to the other observed species. It should however be emphasized that these secondary products are extremely weakly absorbing, indicating that their production and presence plays a minimal role in the interpretation of the photophysical and photochemical processes. Using the data of Table II, the $CO/CH_2CO$ ratio of column 1 increases significantly in column 5, indicating that the combination of (2) and (3) are greater than (1) at the bromine wavelengths by roughly a factor of 2. In addition, the $c$-$C_3H_6/C_3H_6$ ratios indicate more efficient propylene production relative to cyclopropane. If indeed (3) is a negligible propylene contributor, then the increased energy sources simply provide a greater amount of vibrational energy for the cyclopropane fragment, leading to more efficient ring opening.

## V. Photophysical Processes

In a previous study in this laboratory[10] involving the photochemistry of the difluoroethylenes, we were rather surprised to observe that the CO matrix was not only useful as an atom quencher but also as a triplet quencher. If a photodissociative process were to proceed *via* a triplet state which happens to be in near resonance with a CO triplet, then quenching the triplet prior to dissociation in essence quenches the reaction. This technique can thus be used as means of identifying photodissociative processes proceeding *via* a triplet state. Carbon monoxide is particularly useful in this respect, since it has three triplet states which exist below the onset of its first excited single state $^1\Pi$, at 1546 Å. Assuming the triplet state corresponding to an observed singlet is in the near proximity below it, then the probability of quenching will depend on the near resonance of one of the CO triplets. In order to ensure that CO does not play an energy transfer role through its allowed singlet–singlet transition, the excitation source should be monochromatic and $\lambda > 1546$ Å. In this study, we note that the $n \rightarrow \sigma_{CO}^*$ transition (1802–1681 Å) is in near resonance with the $^3\Sigma$ CO band at approximately 1800 Å. The results of this experiment led to the complete quenching of (2) and possibly (3), but indicated the normal yield of (1). We conclude then that the former photodecompositions probably proceed through ISC and the latter through IC as observed from the $n \rightarrow \pi^*$ transition.

If we might be allowed to speculate concerning the mode of decomposition *via* the triplet, it would be that ISC occurs into a bound state, rather than directly into the triplet continuum; since a vibrational period would be insufficient time to quench the triplet. Thus, in the absence of CO, the triplet would be rapidly quenched to the ground vibrational state and phosphoresce. However, we noted earlier that all of these resonance sources have a broad emission which spans the visible and is greater by a factor of 10 than the resonance line. This source could produce a triplet–triplet transition from the $v = 0$ triplet lower state where there is a steady-state buildup as a result of the long triplet lifetime. In summary, process 2 and 3 might be proceeding *via* a biphotonic mechanism. A recent study involving the biphotonic chemistry of durene has recently been reported by Schwarz and Albrecht.[27]

## VI. Conclusions

The photodecomposition mechanism of matrix-isolated cyclobutanone has been shown to be a function of exciting energy. Exciting into the continuum of the $n \rightarrow \pi^*$ (3350–2632-Å) band below the onset of the predissociating wavelength, appears to indicate a predominance of process 2 and possibly 3 *vs.* 1. Exciting between 3000–3100 Å with the 3022-Å line appears to result in the exclusive production of (2).

Excitation into the diffuse or continuous electronic absorption bands corresponding to the $n \rightarrow \sigma_{CO}^*$ (1802–1680 Å) and the $\pi \rightarrow \pi^*$ (1670–1480 Å) with $N_2$ and $Br_2$ resonance lamps resulted in the same major primary photodecomposition modes 1, 2, and possibly 3, in addition to weak absorptions due to secondary photolysis.

The $n \rightarrow \pi^*$ conversions appear to be the same as the gas-phase observations where (1) and (2)–(3) proceed through $^1A_1{}^*$ and $^3A_2$, respectively. Experiments performed in this study using CO triplet state quenching of the $n \rightarrow \sigma_{CO}^*$ $^3B_2$ state indicate the possibility of a biphotonic mechanism giving rise to (2) and possibly (3).

In addition to the photochemical results, some tentative vibrational assignments for the vibrational frequencies of matrix-isolated cyclobutanone have been made. These assignments are based on a prior normal coordinate calculation,[13] which assumed a planar ring skeleton structure with $C_{2v}$ symmetry from microwave measurements, and comparisons with previous vibrational assignments for cyclobutane.[12]

*Acknowledgment.* We gratefully acknowledge support of this work by the National Science Foundation through Grant No. GP-34141 X.

## References and Notes

(1) Alfred P. Sloan Foundation Fellow. Address correspondence to the Department of Chemistry, University of Utah, Salt Lake City, Utah 84112.

(2) (a) M. N. Das, T. D. Coyle, and W. D. Walters, *J. Amer. Chem. Soc.*, **76**, 6271 (1954); (b) A. T. Blades, *Can. J. Chem.*, **47**, 615 (1969); (c) H. O. Denschlag and E. K. C. Lee, *J. Amer. Chem. Soc.*, **90**, 3628 (1968).

(3) (a) G. B. Kistiakowsky and S. W. Benson, *J. Amer. Chem. Soc.*, **64**, 80 (1942); (b) N. E. Lee and E. K. C. Lee, *J. Chem. Phys.*, **50**, 2094 (1969), and references therein.

(4) J. C. Hemminger and E. K. C. Lee, *J. Chem. Phys.*, **56**, 5284 (1972).

(5) J. C. Hemminger and E. K. C. Lee, *J. Chem. Phys.*, **54**, 1405 (1971).

(6) E. S. Yeung and C. B. Moore, *J. Chem. Phys.*, **58**, 3938 (1973).

(7) D. Davis and W. Braun, *Appl. Opt.*, 7, 2071 (1968).

(8) S. G. Thomas, Jr., and W. A. Guillory, *J. Phys. Chem.*, **77**, 2469 (1973).
(9) R. Isabel and W. A. Guillory, *J. Chem. Phys.*, **55**, 1197 (1971).
(10) G. H. Andrews, Jr., and W. A. Guillory, *J. Chem. Phys.*, submitted for publication.
(11) Sadtler Research Laboratories, Inc., IR 19106, 1966 Philadelphia, Pa.
(12) T. Shimanouchi, "Tables of Molecular Vibrational Frequencies Consolidated Volume I," U. S. Government Printing Office, Washington, D. C., 1972, p 145, and references therein.
(13) K. Frei, *Proc. Int. Meet. Mol. Spectrosc., 4th, 1959*, **2**, 783 (1962).
(14) G. E. Leroi, G. E. Ewing, and G. C. Pimentel, *J. Chem. Phys.*, **40**, 2298 (1964).
(15) See ref 12, p 120, and references therein.
(16) S. G. Thomas, Jr., and W. A. Guillory, unpublished data.
(17) C. B. Moore and G. C. Pimentel, *J. Chem. Phys.*, **38**, 2816 (1963).
(18) M. E. Jacox, D. E. Milligan, N. G. Moll, and W. E. Thompson, *J. Chem. Phys.*, **43**, 3734 (1965).
(19) R. F. Whitlock and A. B. F. Duncan, *J. Chem. Phys.*, **55**, 218 (1971).
(20) C. B. Moore and G. C. Pimentel, *J. Chem. Phys.*, **41**, 3504 (1964).
(21) B. Meyer, "Low Temperature Spectroscopy," American Elsevier, New York, N. Y., 1971, p 93.
(22) R. J. Campbell, E. W. Schlag, and B. W. Ristow, *J. Amer. Chem. Soc.*, **89**, 5098 (1967); R. J. Campbell and E. W. Schlag, *ibid.*, **89**, 5103 (1967).
(23) G. H. Andrews, Jr., and W. A. Guillory, unpublished data.
(24) W. D. Chandler and L. Goodman, *J. Mol. Spectrosc.*, **35**, 232 (1970).
(25) G. Herzberg, "Molecular Spectra and Molecular Structure. III. Electronic Spectra and Electronic Structure of Polyatomic Molecules," Van Nostrand, Princeton, N. J., 1966, p 530.
(26) J. G. Calvert and J. N. Pitts, "Photochemistry," Wiley, New York, N. Y., 1966, pp 502 and 505.
(27) F. P. Schwarz and A. C. Albrecht, *J. Phys. Chem.*, **77**, 2808 (1973).

# Shock Tube Cis–Trans Isomerization Studies. III

**Peter M. Jeffers**

*Department of Chemistry, State University College, Cortland, New York 13045* *(Received February 14, 1974)*

Single pulse shock tube relative rate measurements are reported for cis–trans isomerization of 2-butene, difluoroethylene, fluorodichloroethylene, fluorochloroethylene, and 2,3-dichlorohexafluoro-2-butene. The isomerizations all appear to be homogeneous and unimolecular, and the experiments were performed above the unimolecular falloff region. For the butenes, log $A^\infty$ = 14.4 ± 0.2, while for the ethylenes, log $A^\infty$ = 13.3 ± 0.1. The activation energy for 2-butene was $E_a$ = 66.2 kcal/mol (277 kJ/mol), while all the halogenated olefins had $E_a$ = 58.5 ± 2.5 kcal/mol (245 ± 10.5 kJ/mol).

Previous parts of this series[1,2] presented kinetic parameters for the thermal cis–trans isomerization of 2-butene, perfluoro-2-butene, 1,2-difluoroethylene, and 1,2-dichloroethylene. All of the reaction rates were determined using a single pulse shock tube relative rate technique. The starting point for these studies was the measurement of 2-butene isomerization *vs.* *tert*-butyl alcohol dehydration, with the other isomerization rates found relative to 2-butene. But, Lewis[3] has recently reevaluated the dehydration of *tert*-butyl alcohol and found substantially different Arrhenius parameters than the ones reported by Tsang[4] which were used as a basis for the values we reported for the isomerization.

The present paper contains the results of new relative rate measurements on *cis*-2-butene *vs.* cyclohexene decomposition, done to substantiate Lewis's findings, new data on *cis*-1,2-difluoroethylene *vs.* *cis*-2-butene, reports of *cis*-$CFCl{=}CHCl$, *cis*-$CHCl{=}CHF$, and *cis*-$CF_3CCl{=}CClCF_3$ isomerization which have not previously been studied, and revised parameters for the dichloroethylene and perfluoro-2-butene isomerizations in view of the revised *cis*-2-butene rate constant.

## Experimental Section

The shock tube and general procedures have been described.[1,2] Shocked gas samples (0.5–2 cc at 200–350 Torr) were transferred from the shock tube to the gas chromatograph with a Precision Sampling Co. syringe.

*Materials.* The *cis*-2-butene was Phillips research grade and contained 0.05% of the trans isomer. Baker, "Baker Grade," cyclohexene was used as supplied, after thorough degassing. The halogenated ethylenes and butene were obtained from Peninsular Chem Research. Separation of liquid 1,2-dichloro-1-fluoroethylene on a 3 m × 12.7 mm 20% $AgNO_3$ saturated diethylene glycol on Chromosorb P column at 25° gave *trans*-$CClF{=}CClH$ with 3.5% cis impurity. Gas samples (25 cc at 1 atm) of 1-chloro-2-fluoroethylene were resolved with the same $AgNO_3$ prep scale column, yielding *cis*-$CHCl{=}CHF$ with 0.25% trans impurity. Liquid 2,3-dichlorohexafluoro-2-butene separated well on a 2 m × 19 mm 20% UCW-98 prep column at 23° with the cis product containing 0.2% trans. Dichloroethylene was also purified with the UCW-98 column to give *cis*-$CHCl{=}CHCl$ with 0.15% trans. The very small sample of *cis*-1,2-difluoroethylene available was used as supplied and contained 7.1% trans impurity.

*Analysis.* A Hewlett-Packard Model 5750 chromatograph with flame detector was used. All components of the various shocked samples could be resolved using a 1.83 m × 6 mm 10% $AgNO_3$-DEG column alone or with 1.83 m × 3 mm or 3.66 m × 3 mm 10% UCW-98 columns in series, all at room temperature. Peak areas were measured by triangulation. With one set of runs, areas were also found by Xeroxing the chromatograms, then cutting and weighing the peaks. Values for the rate constants derived from these two sets of areas were nearly identical with no systematic differences. Equal sensitivities were observed for cis and trans isomers. Calibration samples containing $C_2H_4$, 1,3-butadiene, and *cis*-2-butene were used to find relative sensitivities for these species. The cyclohexene peaks were not quantitatively measured.

*Shock Experiments.* Mixtures of the reactants, dilute in argon, were prepared in 5-l. Pyrex bulbs. A cathetometer was used for the cyclohexene-*cis*-2-butene mixture to assure accurate knowledge of the initial composition, since the cyclohexene peak was not analyzed in the shocked samples. Details of the various mixtures are in Table I. The residence times (flat portion of the pressure trace) ranged from 150-220 μsec. The Mylar diaphragms burst at 6-7 atm.

*Calculations.* The cyclohexene rate constant was calculattted using the integrated form of a nonreversible first-order rate law. Use of the peaks representing either ethylene or butadiene products formed in the decomposition gave identical results, where both peaks could be easily measured. The ethylene peak was usually easier to determine quantitatively. The cis-trans rate constants were evaluated using the integrated form of a reversible first-order rate law, with $k$(cis → trans) found regardless of the starting isomer.

## Results

Relative rate plots for the various experiments are given in Figures 1-3, with numerical results deduced from the graphs included in Table I. The slope of a relative rate plot gives the ratio of activation energies for the two systems. while the intercept can be related to the preexponential factors. One standard deviation in the slope and intercept imply deviations of about ±1.3 kcal in activation energy and ±0.3 in log $A^{\infty}$. However, to these must be added the uncertainties in the "standard" reaction, which for cyclohexene are estimated[5] at ±0.3 kcal/mol and ±0.2 in log $A^{\infty}$.

Tsang's[5] rate constant for cyclohexene decomposition is $k^{\infty} = 10^{15.30}\exp(-66{,}900/RT)$ sec$^{-1}$, and thus Figure 1 implies that for 2-butene $k^{\infty}$ (cis → trans) = $10^{14.62}\exp(-66{,}200/RT)$ sec$^{-1}$. This value was used in the other relative rate studies to find the Arrhenius parameters listed in Table I. Table II contains the Arrhenius parameters found during this work along with revised values for dichloroethylene and perfluoro-2-butene, based on the previous relative rate results[2] and the new *cis*-2-butene rate constant.

Note that Table I indicates that 2,3-dichlorohexafluoro-2-butene isomerization was measured relative to both 2-butene and 1,2-dichloroethylene. In the former experiments. the halogenated 2-butene isomerization nearly reached equilibrium before the hydrocarbon 2-butene reaction proceeded to measurable extents. Use of dichloroethylene as the standard gave much more reasonable data. and represents the first time in this series of studies that 2-butene was found to be an unacceptable reference standard. Figure 3 shows the results with *cis*-1,2-dichloroethylene as reference for *cis*-2,3-dichlorohexafluoro-2-butene.

## Discussion

For the systems reported in parts I[1] and II,[2] the reactions were measured starting with both the cis and trans isomer. Results in each case were consistent with the relation $k_1/k_{-1} = K_{eq}$, but kinetics studies are obviously not the best way of finding equilibrium constants, so that the reactions studied in the present work were followed in only one direction. None of these systems has an equilibrium constant drastically different from 1.0 (±0.4) over the temperature range 1000-1300°K, and the calculation of the rate constants does not depend sensitively on $K_{eq}$ since the extents of conversion were small, generally less than 10%, and never approached equilibrium levels.

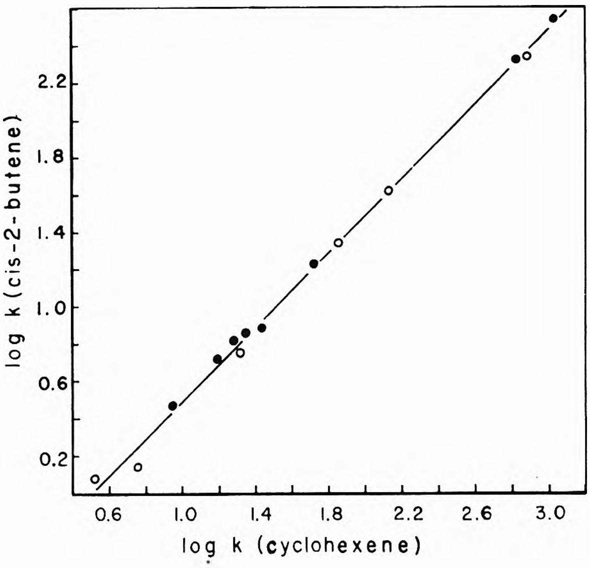

Figure 1. Relative rate graph of log $k^{\infty}$ (*cis*-2-butene → *trans*-2-butene) *vs.* log $k^{\infty}$ (cyclohexene → ethylene + 1,3-butadiene). Concentrations, slope, and intercept are listed in Table I. The filled circles represent the more dilute mixture.

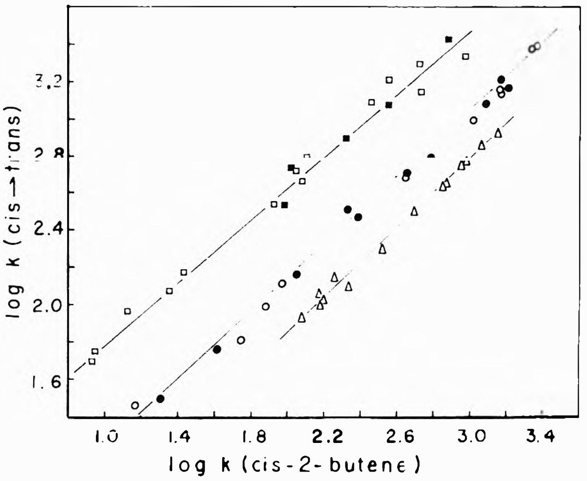

Figure 2. Relative rate graph of log $k^{\infty}$ (cis-halogenated ethylene → trans isomer) *vs.* log $k^{\infty}$ (*cis*-2-butene → *trans*-2-butene). Concentrations, slopes, and intercepts are listed in Table I. Filled symbols represent the more dilute mixture: triangles, 1,2-difluoroethylene; circles, 1-chloro-2-fluoroethylene; squares, 1,2-dichloro-1-fluoroethylene.

Nearly all reviews of cis-trans isomerization[6-9] are prefaced by remarks indicating the experimental difficulties caused by the sensitivity of the isomerization process to both free radical and heterogeneous catalysis. The latter problem is completely avoided with shock tube techniques since the heating is gas dynamic and the walls remain at room temperature. However, the problem of free radical catalysis deserves some attention. Small amounts of side products were observed during cyclopropane structural isomerization with either *cis*-2-butene or *tert*-butyl alcohol as reference standard,[10] and comments in that paper are relevant to this work as well. Essentially, although reference standards, concentrations, pressures, and residence times were varied over unusually wide ranges, no

**TABLE I:**

| Mixture[a] A | Mixture[a] B | % A | % B | No. of shocks | $P_1$, Torr | $T$, °K range | Slope | Intercept | Parameters for A: $E_a$, kcal | Parameters for A: Log $A^\infty$ |
|---|---|---|---|---|---|---|---|---|---|---|
| c-2-Butene | Cyclohexene | 4.31 | 3.69 | 6 | 80–140 | 993–1177 | 0.989 ± 0.017 | −0.497 ± 0.031 | 66.2 | 14.62 |
| c-2-Butene | Cyclohexene | 0.86 | 0.74 | 8 | 190–270 | 1020–1196 | 0.838 ± 0.025 | 0.95 ± 0.05 | 55.5 | 13.21 |
| t-CHCl=CFCl | c-2-Butene | 1.3 | 1.2 | 14 | 150–240 | 1057–1240 | | | | |
| t-CHCl=CFCl | c-2-Butene | 0.19 | 0.17 | 5 | 220–260 | 1142–1230 | 0.880 ± 0.02 | 0.37 ± 0.03 | 58.3 | 13.24 |
| c-CHCl=CHF | c-2-Butene | 0.40 | 0.46 | 12 | 160–280 | 1072–1283 | | | | |
| c-CHCl=CHF | c-2-Butene | 0.11 | 0.13 | 10 | 185–300 | 1083–1267 | | | | |
| c-CF$_3$CCl=CClCF$_3$ | c-2-Butene | 0.5 | 1.0 | 9 | 200–300 | 940–1150 | | | | |
| c-CF$_3$CCl=CClCF$_3$ | c-CHCl=CHCl | 0.85 | 0.85 | 11 | 220–320 | 1022–1198 | 0.989 ± 0.047 | 0.94 ± 0.10 | 56.3 | 14.17 |
| c-CHF=CHF | c-2-Butene | 1.1 | 1.5 | 14 | 150–210 | 1149–1261 | 0.917 ± 0.024 | 0.020 ± 0.062 | 60.7 | 13.42 |

[a] Cis = c; trans = t.

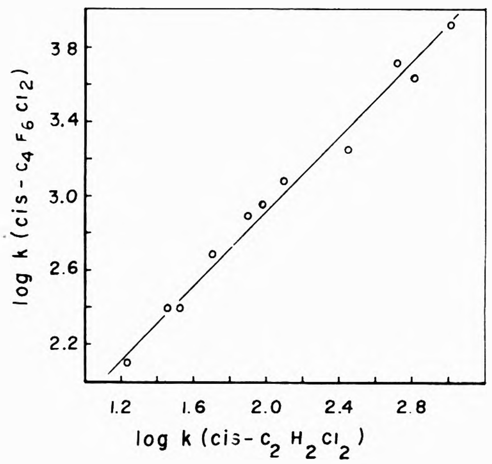

**Figure 3.** Relative rate graph of log $k^\infty$ (*cis*-2,3-dichlorohexafluoro-2-butene → trans) *vs.* log $k^\infty$ (*cis*-1,2-dichloroethylene → trans). Concentrations, slope, and intercept are listed in Table I.

**TABLE II:**

| System | Log $A^\infty$ | $E_a$ kcal/mol | $E_a$ kJ/mol | Log $k^\infty$ (cis → trans) at 1100 °K |
|---|---|---|---|---|
| *cis*-CH$_3$CH=CHCH$_3$ | 14.62 | 66.2 | 275 | 1.49 |
| *cis*-CF$_3$CF=CFCF$_3$ | 14.30 | 58.8 | 246 | 2.63 |
| *cis*-CF$_3$CCl=CClCF$_3$ | 14.17 | 56.3 | 236 | 2.98 |
| *cis*-CHF=CHF | 13.42 | 60.7 | 254 | 1.36 |
| *cis*-CHCl=CHF | 13.24 | 58.3 | 244 | 1.67 |
| *cis*-CHCl=CHCl | 13.39 | 56.9 | 238 | 2.09 |
| *cis*-CHCl=CFCl | 13.21 | 55.5 | 232 | 2.20 |

serious or systematic divergence of any of the results was observed. The implication is that the level of free radicals present during the experiments at these temperatures are ineffective as catalysts of the main reactions.

Recently concluded experiments on 2-butene pyrolysis in shock waves[11] provides even more direct evidence that the isomerization process is not free radical catalyzed under shock conditions. Quantitative calculations were made assuming equilibrium for the step $C_4H_8 \rightarrow \cdot CH_3 + \cdot C_3H_5$, and assuming a second-order isomerization rate constant at least as large as those reported for I atom[12] or $NO_2$[13] catalyzed 2-butene isomerization. The radical catalyzed reactions were studied at much lower temperatures, but Arrhenius parameters were reported. The assumption of equilibrium radical concentrations is probably a gross exaggeration, since even the main reaction of isomerization does not approach equilibrium during the residence times available. Still, the calculated catalyzed isomerization rate is smaller than the observed rate by a factor of 50 to 200. These considerations indicate that the shock tube relative rate technique does supply valid data on the homogeneous, unimolecular isomerization process.

The seven entries in Table II can be examined for trends in the Arrhenius parameters and dependence of these trends on structure. In addition, a related study[14] of 2-butene, 2-hexene, and 2-heptene isomerization gave identical rate parameters for the three olefins, so the butene entry really represents three different systems. The obvious correlation is between size and $A^\infty$. The $C_4$–$C_7$ systems all have log $A^\infty$ = 14.4 ± 0.2, while the ethylenes have log $A^\infty$ = 13.3 ± 0.1. The main factor effecting activation energy appears to be halogenation. All the halogenated species have $E_a$ = 58.5 ± 2.2 kcal, while

2-butene, 2-hexene, and 2-heptene are higher by nearly 8 kcal/mol. With the variations in both $\log A^\infty$ and $E_a$, the value of $\log k^\infty$ (cis → trans) (1100°K) appears rather randomly related to structural details, and no trends are apparent.

An earlier version of Table II provided the strongest suggestion that new measurements of 1,2-difluoroethylene isomerization might be worthwhile. Combining the relative rate data from part I with the new 2-butene parameters gave $\log k^\infty$ (cis-$C_2H_2F_2$) = 14.38 − 67,500/4.58$T$, which puts difluoroethylene way out of line with any trends. Figure 2 shows that the present data on $C_2H_2F_2$ has good precision and little scatter, but Figures 2 and 3 of part I also show high precision and in fact, cover a longer range. (The present study was limited in range by the 7.1% trans impurity in the sample. The *cis*-$C_2H_2F_2$ used in part I was 99.6% pure.) We have not yet discovered any reason for the difference between part I and this set of experiments, but we do plan to persue the matter. Meanwhile, our feeling is that the new results are more reliable. They certainly fit more neatly into Table II.

The preexponential factors of Table II are noticably larger than those previously reported by other investigators for the same or similar reactions (see tables in the reviews by Lin and Laidler,[7] Robinson and Holbrook,[8] or Benson[15]), with the exception of an "early" absolute shock tube study of *cis*-2-butene.[16] This observation suggests careful scrutiny of the rate constant accepted for 2-butene, since it is really the quantity which scales all the other relative rate isomerization results. In defense of the 2-butene rate constant used here we cite a number of successfully completed "loops" of reactions studied by the relative shock tube technique, and the high degree of consistency within these loops. Specifically, the cyclohexene → *tert*-butyl alcohol → *cis*-2-butene ← cyclohexene sequence (this study, part I, and ref 3) gave precisely the same value for 2-butene starting from either end, which means there was absolute internal consistency of the three separate studies involved. Another series includes cyclohexene → cyclopropane ← 2-butene ← cyclohexene (this study, ref 9 and 17) and ties the thoroughly investigated cyclopropane system directly in to the 2-butene isomerization, again with excellent internal correlation. Finally, the 2-chloropropane → cyclohexene → 2-butene ← *tert*-butyl alcohol ← cyclohexene ← ethylcyclobutane series (this work, part I, ref 3, 5, and 18) relates the isomerizations to the well studied alkyl halides and to the very clean decomposition reactions of the alkyl cyclobutanes, with excellent internal agreement. Thus, there appears to be strong experimental evidence supporting a value of $\log k^\infty$(*cis*-2-butene) = 14.62 − 66,200/4.58$T$.

Theoretical treatments of cis–trans isomerization have been given by Benson and coworkers in several forms[9,12,15] and in less quantitatively developed form by Lin and Laidler.[7] Agreement between theoretical predictions and the values reported in Table II are mixed. The dichloroethylene $A^\infty$ factor and activation energy agree almost exactly with estimates, but both the *cis*-2-butene and perfluoro-2-butene $A^\infty$ factors are nearly a factor of 10 larger than Benson's estimates. The previous paragraph lends experimental support to the apparently high $A^\infty$ value for 2-butene, and there is also some theoretical evidence available; Lin and Laidler[19] found much better agreement of RRKM calculations with experimental falloff data with $\log A^\infty$ = 14.55 (from ref 16) than when lower values for $A^\infty$ were used. Robinson and Holbrook[8] have clearly pointed out that RRKM calculations are rather insensitive to details of the transition state model, but do show a strong dependence on the values selected for $A^\infty$ and $E^\infty$.

In view of the trends which appear to be developing, additional cis–trans isomerization measurements on other partially halogenated $C_4$ and some $C_3$ olefins should be useful. The conjugation effects in molecules such as crotononitrile and 1,3-pentadiene should also be checked, and work in these areas is planned.

*Acknowledgments.* The author thanks the State University of New York Research Foundation for continuing support of this project.

## References and Notes

(1) P. M. Jeffers and W. Shaub, *J. Amer. Chem. Soc.*, **91**, 7706 (1969).

(2) P. M. Jeffers, *J. Phys. Chem.*, **76**, 2829 (1972).

(3) D. K. Lewis, *J. Phys. Chem.*, submitted for publication.

(4) W. Tsang, *J. Chem. Phys.*, **40**, 1498 (1964).

(5) W. Tsang, *Int. J. Chem. Kinet.*, **2**, 311 (1970).

(6) R. B. Cundall, *Progr. React. Kinet.*, **2**, 165 (1964).

(7) M. C. Lin and K. J. Laidler, *Can. J. Chem.*, **46**, 973 (1968).

(8) P. J. Robinson and K. A. Holbrook, "Unimolecular Reactions," Wiley, New York, N. Y., 1972.

(9) S. W. Benson and H. E. O'Neal, *Nat. Stand. Ref. Data Ser., Nat. Bur. Stand.*, No. **21**, 21 (1970).

(10) P. Jeffers, D. Lewis, and M. Saar, *J. Phys. Chem.*, **77**, 3037 (1973).

(11) P. Jeffers and S. H. Bauer, *Int. J. Chem. Kinet.*, in press.

(12) S. W. Benson, K. Egger, and D. Golden, *J. Amer. Chem. Soc.*, **87**, 468 (1965).

(13) J. L. Sprung, H. Akimoto, and J. N. Pitts, Jr., *J. Amer. Chem. Soc.*, **93**, 4358 (1971).

(14) S. H. Bauer, B. P. Yadava, and P. Jeffers, *J. Phys. Chem.*, **78**, 770 (1974).

(15) S. W. Benson, "Thermochemical Kinetics," Wiley, New York, N. Y., 1968.

(16) A. Lifshitz, S. H. Bauer, and E. L. Resler, *J. Chem. Phys.*, **38**, 2056 (1963).

(17) P. Jeffers, C. Dasch, and S. H. Bauer, *Int. J. Chem. Kinet.*, **5**, 545 (1973).

(18) W. Tsang, *J. Chem. Phys.*, **42**, 1805 (1965).

(19) M. C. Lin and K. J. Laidler, *Trans. Faraday Soc.*, **64**, 94 (1968).

# Low-Temperature Pulse Radiolysis. II. Time-Dependent Spectra of Anions of Aromatic Ketones

**Mikio Hoshino,* Shigeyoshi Arai, and Masashi Imamura**

*The Institute of Physical and Chemical Research, Wako-shi, Saitama 351, Japan*

*(Received February 5, 1974)*

*Publication costs assisted by The Institute of Physical and Chemical Research*

Using a pulse radiolysis technique the absorption spectra of anions of acetophenone, benzophenone, and their derivatives have been observed in ethanol at 100°K. The spectra obtained immediately after the 0.5-$\mu$sec pulse shift toward shorter wavelengths within about 200 $\mu$sec. The subsequent spectra are in good accord with those observed for the anions produced by steady $\gamma$ radiolysis at 77°K. These results indicate that reorientation of solvent molecules around the anion is responsible for the spectral shift in protic solvents. The spectra observed immediately after the pulse are due to the presolvated anions, and the subsequent spectra to the solvated ones. The temperature dependence of the decay of the presolvated benzophenone anion was also studied.

## Introduction

The solvent effect on the optical absorption spectrum is generally regarded as being due to the dielectric reorientation of solvent molecules around a solute molecule. Since the relaxation time of the dielectric reorientation is largely dependent on the solvent rigidity, one can expect to observe time-resolved emission or absorption spectra at low temperatures. Ware, *et al.*,[1] observed that the emission spectra of aminophthalimides in 1-propanol shift toward longer wavelengths with time at 203 and 173°K. This result suggests that the dielectric relaxation time is comparable with the fluorescence lifetime at the temperatures examined. For electrons produced in alcohols by pulse radiolysis at 77°K, Richards and Thomas[2] and Kevan[3] found time-resolved absorption spectra. Their results indicate that the electrons shallow trapped in alcohols become gradually deep trapped as the solvation proceeds. A similar observation for electrons in viscous liquid alcohols at low temperatures was reported by Baxendale and Wardman[4] and Gilles, *et al.*[5] These investigations provide valuable information on the nature and processes of solvation.

The present pulse radiolysis study at low temperatures was undertaken with the object of elucidating the solvation processes of anions of aromatic ketones. Transient absorption spectra obtained with ethanol solutions, in which solute anions are formed preferentially, were found to be time dependent. Comparing these spectra with those obtained by $\gamma$ radiolysis with different solvents at 77°K, we have concluded that the spectra observed immediately after pulses are ascribed to presolvated anions. This paper reports the first observation on the time-resolved spectra of anions of benzophenone, acetophenone, fluorenone, and their derivatives. The decay behavior of the presolvated anion at various temperatures was discussed in terms of the solvent reorientation.

## Experimental Section

Reagent grade ethanol supplied from Wako Pure Chemical Industries was used without further purification. 2-Methyltetrahydrofuran (MTHF, Wako Pure Chemical Industries) was stored on a sodium-potassium alloy after distillation on metallic sodium and transferred into a reaction cell before use. Benzophenone, fluorenone, and 2,2′-dihydroxybenzophenone of reagent grade from Aldrich Chemical Co. were used without further purification. Acetophenone, 4-hydroxybenzophenone, and 2-hydroxyacetophenone were obtained from Wako Pure Chemical Industries. 4-Hydroxybenzophenone was purified by recrystallization from an aqueous ethanol solution and the others were used without further purification. 4-Methylbenzophenone prepared by the Friedel-Crafts reaction of benzoyl chloride with toluene was recrystallized twice from an ethanol solution.

Pulsed electron beams of 2.7 and 2.8 MeV were generated from a Mitsubishi Van de Graaff accelerator. The pulse width of 0.5 or 1.0 $\mu$sec was used. The experimental procedures and apparatus were the same as described in a previous paper of this series.[5] Most of the experiments were done at a temperature of 100 ± 2°K. For the experiments on temperature dependence, optical measurements were carried out at several temperatures while decreasing the temperature of the sample placed on the cooled block. Temperatures were recorded by using a thermocouple inserted into solutions when the sample was pulsed.

## Results

*Benzophenone.* The transient absorption spectra of the benzophenone anion formed by pulse radiolysis at 100°K are shown in Figure 1. The spectrum observed immediately after the pulse has a peak at 780 nm, but after 170 $\mu$sec the peak shifts to 650 nm; no absorption remains at 780 nm after completion of the spectral shift (a few msec). As will be discussed later, this spectral shift has a close correlation with the solvent shift of the benzophenone anion observed in the steady $\gamma$ radiolysis at 77°K.

Characteristic features which accompany the spectral shift are (1) the optical absorption increases at short wavelengths (600–660 nm), while decreases at longer wavelengths (600–900 nm); (2) the peak absorbance observed immediately after the pulse is larger than that observed after 170 $\mu$sec; (3) there is an isosbestic point at 660 nm, where the absorbance is invariant during several seconds after the pulse; and (4) the relatively weak absorption band due to ketyl radical is observed at 550 nm.

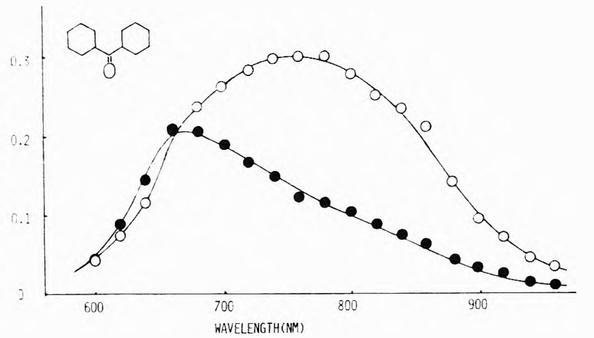

**Figure 1.** Absorption spectra of the benzophenone anion in ethanol at 100°K (0.16 *M* benzophenone): ○, immediately after the pulse; ●, at 170 μsec after the pulse.

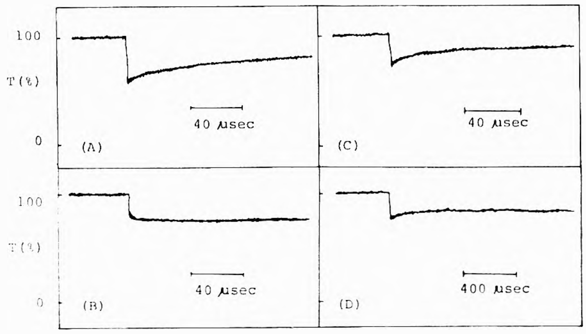

**Figure 2.** Oscilloscope traces for the decay of the benzophenone anion: A, at 760 nm in ethanol; B, at 620 nm in ethanol; C, at 760 nm in aqueous methanol (MeOH:$H_2O$ = 9:1 in volume); D, at 760 nm in 2-propanol.

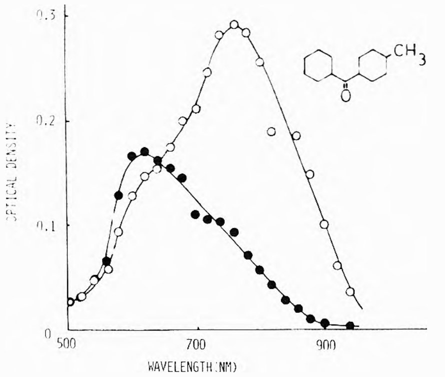

**Figure 3.** Absorption spectra of the 4-methylbenzophenone anion in ethanol at 100°K (0.15 *M* 4-methylbenzophenone): ○, immediately after the pulse; ●, at 8 msec after the pulse.

Figure 2 displays oscilloscope traces recorded at 760 and 620 nm at 100°K. The decay at 760 nm does not fit a first-order rate law. The initial decay is faster than the later. The results obtained for the methanol and 2-propanol solutions are essentially the same as those for the ethanol solution, although the decay rates are considerably different as shown in Figure 2.

Similar results were obtained for ethanolic solution of the 4-methylbenzophenone anion. The peak at 760 nm of the initial spectrum shifts to 620 nm at 8 msec after the pulse as shown in Figure 3.

*Acetophenone.* The absorption spectra of the acetophenone anion in ethanol solution are shown in Figure 4. The initial spectrum has an absorption peak at 480 nm and two shoulders on both sides. The peak wavelength changes to 460 nm after 170 μsec. The decay of the anion is as complex as that of the benzophenone anion.

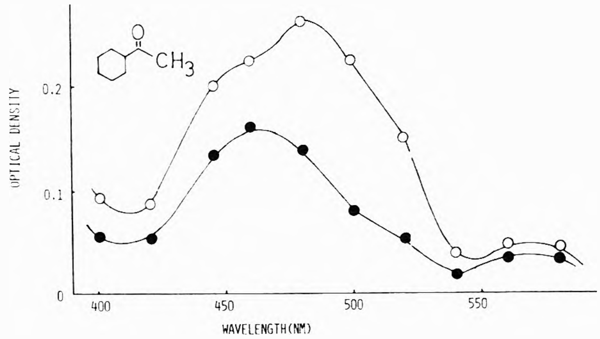

**Figure 4.** Absorption spectra of the acetophenone anion in ethanol at 100°K (0.2 *M* acetophenone): ○, immediately after the pulse; ●, at 170 sec after the pulse.

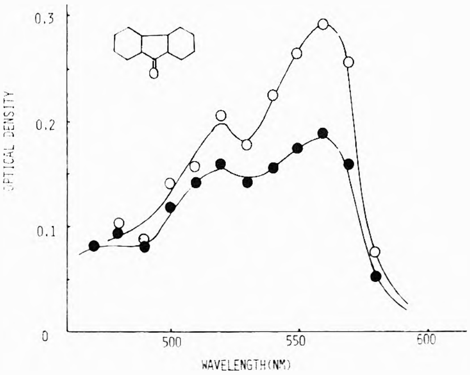

**Figure 5.** Absorption spectra of the fluorenone anion in ethanol at 100°K (0.16 *M* fluorenone): ○, immediately after the pulse; ●, at 170 μsec after the pulse.

The absorption spectrum of the acetophenone anion produced by γ radiolysis in organic solvents at 77°K is known to differ depending on the nature of the solvent. For example, the absorption peak locates at 440 nm in ethanol whereas at 475 nm in MTHF.[7]

*Fluorenone.* The initial absorption spectrum of the fluorenone anion in the ethanol solution at 100°K (Figure 5) has two peaks at 560 and 520 nm. The absorbance decreased with time over the entire wavelength region examined and the spectrum does not change appreciably in shape. This spectrum was identical with that obtained by γ radiolysis of an MTHF solution at 77°K. Hayon, *et al.*,[8] obtained the absorption spectrum with a peak at 450 nm by pulse radiolysis of alkaline aqueous ethanol solution of fluorenone at room temperature. This spectrum, however, is different from ours. We also obtained the absorption spectrum of the fluorenone anion by the pulse radiolysis of dimethylformamide solution at room temperature, which has an absorption peak at 550 nm as shown in Figure 6, in agreement with the result of the ethanol solution at 100°K.

*OH-Substituted Benzophenones and Acetophenone.* Figure 7 shows the absorption spectra of the 4-hydroxybenzophenone anion produced in ethanol solution by pulse radiolysis at 100°K. The initial peak of 710 nm shifts to 680 nm after 170 μsec. Included in Figure 7 for comparison is the absorption spectrum of this ion produced by γ radiolysis of an MTHF solution at 77°K.

It is known that 4-hydroxybenzophenone forms an intermolecular hydrogen bond with ether (1:1 complex) and al-

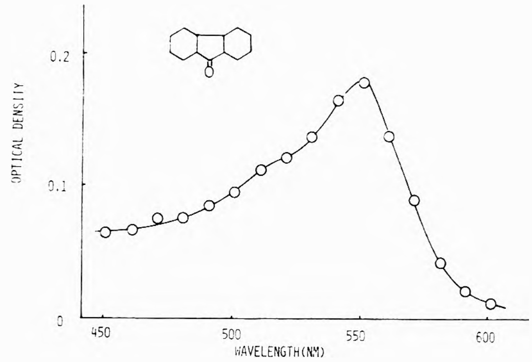

**Figure 6.** Absorption spectrum of the fluorenone anion in dimethylformamide obtained by pulse radiolysis at room temperature ($3.1 \times 10^{-1}$ *M* fluorenone).

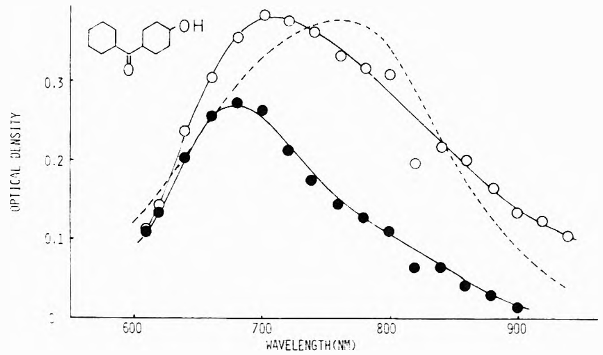

**Figure 7.** Absorption spectra of the 4-hydroxybenzophenone anion obtained by steady γ radiolysis in MTHF at 77°K (- - - -) and pulse radiolysis in ethanol at 100°K (0.2 *M* 4-hydroxybenzophenone): ○, immediately after the pulse; ●, at 170 μsec after the pulse.

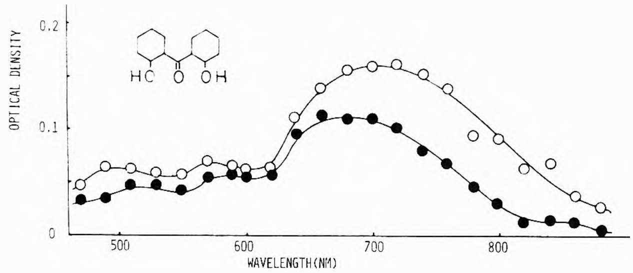

**Figure 8.** Absorption spectra of 2,2′-dihydroxybenzophenone anion in ethanol at 100°K (0.1 *M* 2,2′-dihydroxybenzophenone): ○, immediately after the pulse; ●, at 170 μsec after the pulse.

cohol (1:*n* complex),[9] but the spectral features of the anion are essentially the same as those of benzophenone anion.

Quite similar time-dependent spectra were observed for the 2,2′-dihydroxybenzophenone anion at 100°K as shown in Figure 8. In consequence of the faster decays at longer wavelengths, the absorption peak located initially at 720 nm shifts to shorter wavelengths as time proceeds.

The absorption spectra of the 2-hydroxyacetophenone anion in the ethanol solution are shown in Figure 9. The absorption peak at 480 nm of the initial spectrum shifts to 460 nm after 170 μsec. The shape and the shift with time are similar to those of the nonsubstituted acetophenone anion.

*Temperature Dependence of the Decay of the Benzophenone Anion.* Decay rates of benzophenone anions were determined at 760 nm as a function of temperature between 105 and 123°K. Figure 10 shows the plots of ln *D* *vs.* *t* at 118, 120, and 122°K, where *D* and *t* represent the optical density and time, respectively. We tentatively analyzed the decay curves as overlapping of the fast and slow components, as shown in Figure 10; both of them obey a first-order rate law. The rates of the slow decay were found from the original plots in Figure 10 and those of the fast decays, from the plots of ln $(D - D_1)$ *vs.* *t* in Figure 11, where $D_1$ is the optical density of the slow decay at time *t*. Figure 12 shows the Arrhenius plots for the two decays, from which the activation energies and entropies of activation were estimated to be 2.5 kcal mol$^{-1}$ and −10.6 cal deg$^{-1}$ mol$^{-1}$ for the fast decay and 5.4 kcal mol$^{-1}$ and +10.6 cal deg$^{-1}$ mol$^{-1}$ for the slow decay.

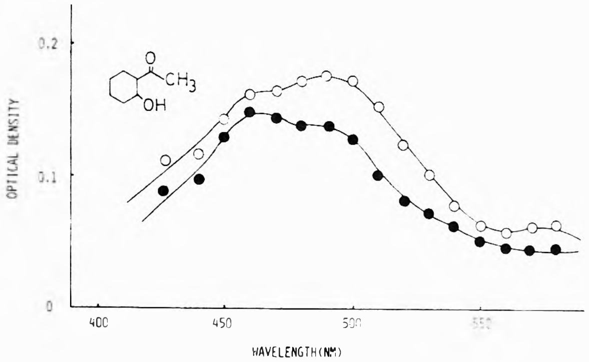

**Figure 9.** Absorption spectra of the 2-hydroxyacetophenone anion in ethanol at 100°K (0.18 *M* 2-hydroxyacetophenone): ○, immediately after the pulse; ●, at 170 μsec after the pulse.

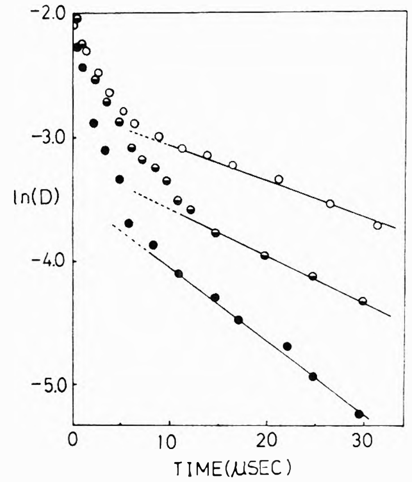

**Figure 10.** Kinetic plots for the decay of the benzophenone anion. Optical densities (*D*) determined at 760 nm and at temperatures of 118 (○), 120 (◐), and 122°K (●).

## Discussion

*Solvent Reorientation as a Cause of the Blue Shift.* A general scheme for the formation of the solute anion in ether or alcohol is described as

$$S \rightsquigarrow S^- + e_m \text{ (mobile)} \qquad (1)$$

$$e_m \longrightarrow e_t \text{ (trapped)} \qquad (2)$$

$$e_m + M \longrightarrow M^- \qquad (3)$$

where S and M represent a solvent and solute molecule, respectively. Reaction 2 is likely to be excluded in the presence of solute molecules in a concentration as high as in this study; in fact, the absorption spectrum of $e_t$ was

**TABLE I: Peak Wavelengths of Absorption of Benzophenone Anion in Various Solvents**

| Solvent | Water | Aqueous methanol[a] | Ethanol | DMSO[b] | DMF[b] | Acetone | MTHF |
|---|---|---|---|---|---|---|---|
| Dielectric constant | 78 | 36.8[c] | 24.3 | 48.9 | 36.7 | 20.7 | 4.6 |
| Presolvated anion, nm | | 730[d] | 780[d] | | | | 780[d] |
| Solvated anion, nm | 615[e] | 630[d] | 640[d] | 720[f,g] | 720[f] | 720[f,g] | 780[f,h] |

[a] Methanol:water = 9:1 in volume. [b] DMSO = dimethyl sulfoxide; DMF = dimethylformamide. [c] Reference 14. [d] Results obtained in the present study by pulse radiolysis at 100°K. [e] Reference 8. [f] Results obtained in the present study by pulse radiolysis at room temperature. [g] Triethylamine of 0.1 *M* was added as a cation scavenger. [h] Reference 11.

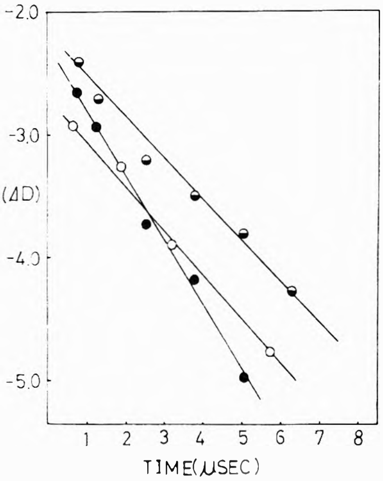

**Figure 11.** Kinetic plots for the earlier decay of the benzophenone anion. $\Delta D = D - D_1$, where $D_1$ is the optical density of the later decay at time *t*. Optical densities determined at 760 nm and at temperatures of 118 (○), 120 (◒), and 122°K (●).

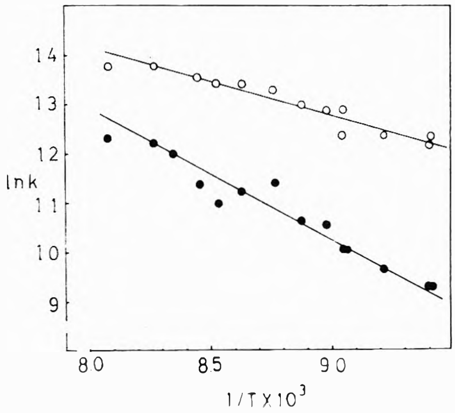

**Figure 12.** Arrhenius plots for the earlier decay (○) and later decay (●) of the benzophenone anion.

not observed even immediately after the pulse for all the solutions investigated.

Transient absorption spectrum of the benzophenone anion produced by flash photolysis or pulse radiolysis is known to show a large solvent shift; the absorption peak is located at 630 nm in aqueous 2-propanol[10] and at 780 nm in tetrahydrofuran (THF) solution.[11] The absorption spectra obtained with organic glasses by $\gamma$ radiolysis at 77°K are similar to those mentioned above. Shida and Hamill,[7] who observed absorption spectra of aromatic and aliphatic ketones at 77°K, reported the absorption peak of the benzophenone anion to be at 630 nm in an ethanol matrix and at 800 nm in a MTHF matrix.

The time-dependent spectral change of the anions observed in the present study may be interpreted by the gradual lowering of the ground-state energy caused by reorientation of the solvent molecules around the anion. Table I lists the peak wavelengths of the benzophenone anion in several solvents. The solvent shift of the absorption band does not appear to depend on the dielectric constant of solvent, but is particularly significant in hydroxylic solvents, suggesting that reorientation of the OH group may be essentially responsible for the shift. A similar argument was given by Schmidt and Allen[12] for the formation of the potential well of electrons in hydroxylic solvents. For the benzophenone anion it is suggested that the canonical structure described must be favored relative to the others on the basis of the valence bond framework.[13] It is probable, therefore, that the solvent reorientation takes place around the CO⁻ group, and OH groups occupy the position closer to the CO⁻ group of the benzophenone anion than do other solvent molecules.

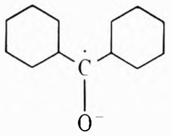

It has been suggested by Shida and Hamill[7] that the blue shift of the absorption band in alcohols is due to hydrogen bonding between the anion and alcohol molecules. However, this explanation is not appropriate for the following reasons. (1) Since benzophenone is known to form hydrogen bond with alcohol molecules,[15] the benzophenone anion produced initially must be hydrogen bonded. However, the spectrum is rather similar to that in MTHF which is not capable of forming hydrogen bonds. (2) The decay rate of the presolvated anion in alcohols observed at the longer wavelength decreases in the order of methanol, ethanol, and 2-propanol in the same way as observed for electrons.[3,4] These facts suggest that the time-dependent spectral change is due to the reorientation of alcohol molecules around the anion.

The initial spectra in ethanol solutions at 100°K are similar to those obtained in MTHF glasses at 77°K by $\gamma$ radiolysis and the subsequent spectra are in good accordance with those obtained in ethanol glasses at 77°K by $\gamma$ radiolysis. These results lead us to a conclusion that the initial absorption spectrum is due to a presolvated anion which relaxes to a solvated anion within about 200 μsec at 100°K.

Recently, Shida, *et al.*,[16] determined the extinction coefficient of the benzophenone anion to be $1.08 \times 10^4$ $cm^{-1}$ $M^{-1}$ at 800 nm in MTHF and $6.7 \times 10^3$ $cm^{-1}$ $M^{-1}$ at 630 nm in ethanol, the ratio being 1.62. The ratio of the maximum optical density of the presolvated benzophenone anion to that of the solvated one is 1.5, which is close to the above value of 1.62. This fact lends further support that the electronic structure of the presolvated anion resemble that of the anion in MTHF.

The acetophenone anion behaves quite similarly to the benzophenone anion. The presolvated anion is formed immediately after the pulse and reorientation of solvent molecules occurs within about 200 $\mu$sec at 100°K.

The absorption spectrum of the fluorenone anion observed after the pulse in the ethanol solution at 100°K does not change its shape with time. However, the initial spectrum is expected to be due to the presolvated anion and the spectrum observed after 170 $\mu$sec, to the solvated one, since the time of solvent reorientation is about 200 $\mu$sec as demonstrated in the experiments of benzophenone and acetophenone. It is probable that the energy of stabilization due to the solvent reorientation are not different between the ground and excited states of the fluorenone anion. This will result in no spectral shift of the absorption band with time.

The spectral behavior of anions of OH-substituted benzophenones and acetophenone are similar to those of the nonsubstituted ones. These facts indicate that, although the OH group forms hydrogen bonds with alcohol, the effect of the hydrogen bond is not so serious as to result in a large shift of the absorption band or a change of a relaxation time of a presolvated anion at the temperature examined. It is concluded that the anions of aromatic ketones exist as presolvated ones immediately after the pulse, and subsequently change into the solvated ones within the similar relaxation time.

*Temperature Dependence of the Decay Rate of the Presolvated Benzophenone Anion.* The decays observed at low temperatures represent the solvation process of the presolvated anions. As shown in Figure 2, the decay of the presolvated benzophenone anion in the initial stage is faster than that in the later stage. This phenomenon may be interpreted on the assumption that solvent reorientation becomes quite slow as solvation proceeds. In other words, the solvent sphere formed rapidly in the initial stage around an anion would shield the coulombic field to reduce the rate of the reorientation in the outer shell.

There seems to be an alternative interpretation in which a rigid solution of ethanol is assumed to consist of regions of different viscosities. The solvent reorientation may take place easily around an anion in the "soft" region, giving rise to the fast decay of the presolvated anion in the initial stage. In the later stage, the reorientation of solvent molecules occurs more slowly in the "hard" region, resulting in the slow decay. The environmental heterogenity of rigid solutions has also been proposed for the interpretation of a nonexponential decay of emission.[17,18]

A possible explanation for these two regions is as follows. One is a low viscosity region in which ethanol molecules orient randomly, and the other is a high viscosity region in which ethanol molecules are bound tightly by hydrogen bonding. In the former region, therefore, it is expected that the solvent reorientation occurs more easily and the activation energy is smaller than that in the latter region as determined experimentally. The significant difference in the entropy of activation between the fast and slow processes may also be interpreted on the same basis: the negative entropy of activation is realized in the former region where the randomly oriented ethanol molecules should be reoriented around anions and the positive one, in the latter region where the break down of hydrogen bonds occurs on solvation. It is noteworthy that the kinetic parameters of the electrons in 1-propanol obtained by Baxendale and Wardman[4] are 5.9 kcal mol$^{-1}$ and +12 cal deg$^{-1}$ mol$^{-1}$, which are close to the present values for the slow decay in spite of the different solvent and solute.

*Acknowledgment.* The authors express their thanks to Dr. Tadamasa Shida for his helpful discussions. Thanks are also due Mr. Seiichi Tagawa and Mr. Isamu Kinoshita for their assistance in the experimental work.

## References and Notes

(1) W. R. Ware, P. Chow, and S. K. Lee, *Chem. Phys. Lett.*, **2**, 356 (1968).
(2) J. T. Richards and J. K. Thomas, *J. Chem. Phys.*, **53**, 218 (1970).
(3) L. Kevan, *J. Chem. Phys.*, **56**, 838 (1972).
(4) J. H. Baxendale and P. Wardman, *J. Chem. Soc., Faraday Trans. 1*, **69**, 584 (1973).
(5) L. Gilles, J. E. Aldrich, and J. W. Hunt, *Nature (London), Phys. Sci.*, **243**, 72 (1973).
(6) S. Arai, S. Tagawa, and M. Imamura, *J. Phys. Chem.*, **78**, 519 (1974).
(7) T. Shida and W. H. Hamill, *J. Amer. Chem. Soc.*, **88**, 3683 (1966).
(8) H. Hayon, T. Ibata, N. N. Lichtin, and M. Simic, *J. Phys. Chem.*, **76**, 2072 (1972).
(9) M. Hoshino and M. Koizumi, *Bull. Chem. Soc. Jap.*, **45**, 2731 (1972).
(10) G. Porter and F. Wilkinson, *Trans. Faraday Soc.*, **57**, 1686 (1961).
(11) D. Beaumond and M. A. T. Rogers, *Trans. Faraday Soc.*, **6**, 2973 (1969).
(12) W. F. Schmidt and A. O. Allen, *J. Chem. Phys.*, **52**, 4790 (1970).
(13) N. Hirota in "Radical Ions," E. T. Kaiser and L. Kevan, Ed., Wiley, New York, N. Y., 1968, p 46.
(14) J. Timmerman in "Physico-Chemical Constants of Binary Systems," Vol. 4, Interscience, New York, N. Y., 1960, p 168.
(15) R. S. Becker, *J. Mol. Spectrosc.*, **3**, 1 (1959).
(16) T. Shida, S. Iwata, and M. Imamura, *J. Phys. Chem.*, **78**, 741 (1974).
(17) T. E. Martin and A. H. Kalantar, *J. Chem. Phys.*, **49**, 244 (1968).
(18) F. Castilli and L. S. Foster, *J. Amer. Chem. Soc.*, **95**, 7223 (1973).

# Enthalpies of Mixing in Liquid Alkaline Earth Fluoride–Alkali Fluoride Mixtures. II. Calcium Fluoride with Lithium, Sodium, and Potassium Fluorides

**O. J. Kleppa*** **and K. C. Hong**

*The James Franck Institute and Department of Chemistry, The University of Chicago, Chicago, Illinois 60637*

*(Received February 25, 1974)*

*Publication costs assisted by the National Science Foundation*

The enthalpies of mixing of the liquid mixtures of $CaF_2$ with LiF, NaF, and KF have been determined calorimetrically by solid–liquid mixing experiments at 1081°. The results cover concentrations up to about 50 mol % $CaF_2$ and indicate that for these three systems the interaction parameters, $\lambda^M = \Delta H^M / X_1X_2$, vary little with composition. Consistent with the conformal solution theories of Davis, $\lambda^M$ changes linearly with the size parameter $\delta_{12} = (d_1 - d_2)/d_1d_2$. The partial enthalpies of the alkali fluorides, derived from the new integral enthalpy data, are very comparable to the corresponding excess Gibbs energies derived from the phase diagrams.

## Introduction

Systematic investigations of the solution properties of simple charge-unsymmetrical fused salt mixtures of the type $AX_2$–BX have been underway in this laboratory for a number of years. This work has emphasized measurements of the enthalpies of mixing in relatively low melting systems, such as, *e.g.*, the alkaline earth nitrate–alkali nitrates,[1] the lead chloride–alkali chlorides,[2] the alkaline earth chlorides and bromides with the alkali salts,[3,4] as well as transition metal chloride–alkali chloride systems.[5-7] There has been only one study of the corresponding fluorides, that by Holm and Kleppa of the $BeF_2$–AlkF mixtures.[8] The present communication reports the first extension of this work to the higher melting alkaline earth fluoride–alkali fluoride systems. Other investigations are in progress and will be reported in future work.

Apart from $BeF_2$, which melts at 555°, the alkaline earth fluorides have quite high melting points: $MgF_2$, 1290°; $CaF_2$, 1418°; $SrF_2$, 1477°; $BaF_2$, 1368°. At or above these temperatures the vapor pressures of the alkali fluorides are too high to allow precise heat of mixing calorimetry. For this reason the present work is based on solid–liquid measurements. At 1081°, the temperature adopted in the present investigation, we were able to study solutions which contain up to about 50 mol % calcium fluoride.

## Experimental Section

*Apparatus.* All calorimetric experiments were performed in a new twin microcalorimeter designed for operation at temperatures up to 1400–1500°. This apparatus will be described elsewhere.[9] The calorimeter is largely constructed from sintered alumina components and is maintained in a cylindrical furnace heated by three Pt 40 Rh heating elements.

The apparatus has two essentially identical 25-mm diameter Calvet-type calorimeters, each with a 64 couple Pt–Pt 13 Rh thermopile constructed from 0.6-mm wire. The two thermopiles are connected in series, bucked against each other.

The output from the thermopile system is amplified by a Leeds and Northrup d.c. amplifier (9835-B) and displayed on a Leeds and Northrup Type H-Azar recorder. The emf *vs.* time curves are integrated by means of an Ott precision planimeter.

All experiments were carried out in platinum or graphite containers under an atmosphere of dry, purified argon. Two different experimental arrangements were adopted. These are shown schematically in Figure 1.

Inside the platinum protection tube of the calorimeter proper there is a fused silica "liner" which provides a complete envelope for the contents of the calorimeter. The liner is, in turn, protected against the aggressive fluoride vapors by means of a thin-walled (~0.2 mm) nickel "crucible," about 20 mm in diameter × 155 mm long. In spite of this precaution, the attack on the fused silica liner was considerable, and the lower part of the liner usually had to be rebuilt after three to five experiments.

The nickel crucible contains either the main graphite crucible (used for work involving LiF and NaF) or a platinum crucible (used for KF experiments). In order to prevent alloying between nickel and platinum they are separated by a thin-walled fused silica tube.

The graphite and platinum crucibles serve as containers for one of the two fluoride salts to be mixed. The other salt is kept either in a smaller platinum cup or in a two-shell graphite assembly, as indicated in the figure. These are in turn attached to 7 mm o.d. ceramic tubes which can be manipulated from outside the furnace insulation.

*Chemicals.* The chemicals used were (i) lithium fluoride, Fisher Certified Reagent; (ii) sodium fluoride, Baker Analyzed Reagent; (iii) potassium fluoride, Baker and Adamson (min 99.0% KF) Anhydrous, Granular Reagent; (iv) calcium fluoride, Mallinckrodt Chemical Works, Analytical Reagent. Before their use in the calorimeter, the alkali fluorides were mixed with ammonium fluoride (Fisher Certified Reagent) and melted in a graphite (LiF, NaF) or platinum (KF) crucible in an argon atmosphere. After solidification of the melt, clear crystals were selected from the sample. Before use, calcium fluoride was heated with ammonium fluoride at about 600° in an argon atmosphere.

The purity of the salts was checked by an ion-exchange method. LiF, NaF, and $CaF_2$ were of 99.8 to 99.9% purity, while KF was confirmed to be better than 99.0% KF.

*Procedures.* All the experiments reported in the present work were carried out at 1081 ± 1°, which is well below the melting temperature of calcium fluoride, Hence, all measurements were of the solid-liquid type. If the empirical equations of Pugh and Barrow[10] apply, the vapor pressures of LiF and NaF at this temperature are about $10^{-3}$ atm, that of KF about $10^{-2}$ atm.

Immediately before insertion into the calorimeter, the fused silica liner with its contents was preheated for a period of about 15 min to a temperature about 50° above the operating temperature of the calorimeter. In typical runs the total time elapsed prior to mixing was 45 to 60 min. Under these conditions the weight *loss* of the most volatile salt, KF, as determined in a blank experiment, was about 0.5%; the simultaneous weight *gain* of the calcium fluoride sample, presumably due to reaction with the KF vapor, was 0.02%. These errors are very small and have been neglected. Note that a major part of the experimental uncertainty in our determinations of the liquid-liquid enthalpies of mixing arises from the corresponding uncertainty in the enthalpy of fusion of calcium fluoride (see below).

Calibration of the calorimeter was by the platinum drop method, based on the heat content equation for pure platinum as given by Kelley.[11] Pieces of platinum wire of 2 mm diameter and weighing about 1 g were dropped from room temperature into the calorimeter. The calorimeter temperature was measured by means of a Pt-Pt—13Rh thermocouple which was checked against a Pt-Pt—10Rh couple which had been calibrated by the National Bureau of Standards. A correction of 5% was applied for the heat pickup of the platinum wire during its drop into the calorimeter.

## Results

In order to avoid incomplete solid-liquid mixing, all measurements were carried out on compositions leading to the formation of liquid mixtures with less than about 50 mol % calcium fluoride. Some of the data in the KF-$CaF_2$ systems (at $X_{CaF_2} > 0.2$) were obtained through experiments in which solid $CaF_2$ was added to a melt of lower calcium fluoride concentrations. These measurements are identified as such in Table I and Figure 2.

The results of the solid-liquid heat of mixing measurements, $\Delta H_{SL}{}^{M}$, are given in Table I. The enthalpies of liquid-liquid mixing, $\Delta H^{M}$, and the corresponding enthalpy interaction parameters, $\lambda^{M} = \Delta H^{M}/X_1X_2$, are related to $\Delta H_{SL}{}^{M}$ by the relation

$$\Delta H^{M} = \Delta H_{SL}{}^{M} - X_2\Delta H_f(t) \tag{1}$$

$$\lambda^{M} = \frac{\Delta H^{M}}{X_1X_2} = \frac{1}{X_1}\left(\frac{\Delta H_{SL}{}^{M}}{X_2} - \Delta H_f(t)\right) \tag{2}$$

In these expressions $X_2$ is the mole fraction of calcium fluoride while $\Delta H_f(t)$ is the heat of fusion of calcium fluoride at the temperature of the measurements (1081°). In the limiting case for $X_2 = 1$, the enthalpy of mixing, $\Delta H^{M}$, is zero. Therefore, we have

$$\Delta H_f(t) = \lim_{X_2 \to 1} \Delta H_{SL}{}^{M}/X_2 \tag{3}$$

In Figure 2 we have plotted the experimental quantities $\Delta H_{SL}{}^{M}/X_2$ against $X_2$ for the three calcium fluoride-alkali fluoride systems. The figure also shows $\Delta H_f(1081) = 9.84$ kcal/mol at $X_2 = 1.00$. This value has been calculated from the reported enthalpy of fusion of $CaF_2$ (7.1 ± 0.1 kcal/mol at 1418°)[12] plus the enthalpy change associated with the phase transformation in $CaF_2$ at 1151° (1.14 ± 0.1 kcal/mol)[12] while at the same time correcting for the heat capacity difference between liquid, undercooled $CaF_2$, and the solid salt, integrated over the temperature range 1081-1418° (~1.6 kcal/mol). Note that our own data for $\Delta H_{SL}{}^{M}/X_2$, if extrapolated linearly to $X_2 = 1$, are in excellent agreement with this value, which is believed to be correct to ±0.3 kcal/mol or better.

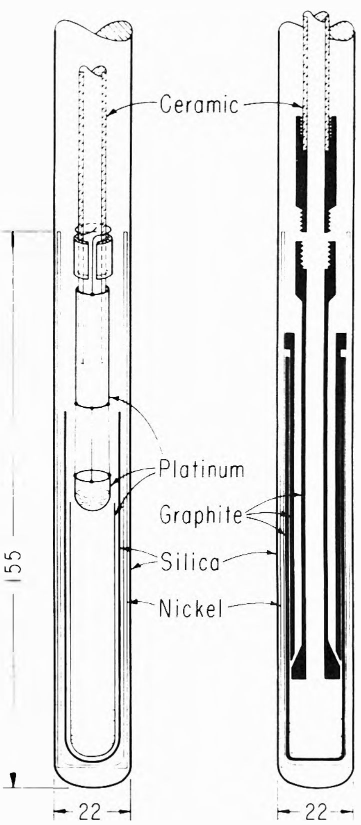

**Figure 1.** Schematic diagram of experimental arrangements used for calorimetric measurements.

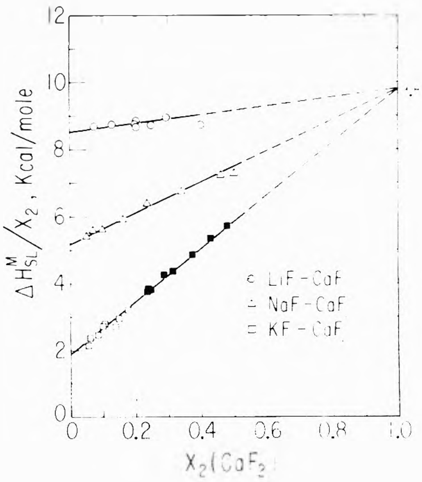

**Figure 2.** Plots of $\Delta H_{SL}{}^{M}/X_{CaF_2}$ *vs.* $X_{CaF_2}$. Enthalpy of fusion of $CaF_2$ at 1081° (9.84 kcal/mol), calculated from data given by JANAF.[12] Data for $CaF_2$-KF indicated by solid symbols based on multiple additions of solid $CaF_2$ to KF.

Adopting 9.84 kcal/mol for the enthalpy of fusion of calcium fluoride, we have calculated the (liquid-liquid) enthalpies of mixing and the interaction parameters, $\lambda^{M}$,

**TABLE I: Molar Enthalpies of Mixing of Solid Calcium Fluoride with Liquid Alkali Fluorides at 1081°[a]**

| System | $X_2$ | Total moles | $\Delta H_{SL}{}^M/X_2$, kcal/mol |
|---|---|---|---|
| $CaF_2$–LiF | 0.0759 | 0.1088 | 8.67 |
| | 0.1295 | 0.1167 | 8.73 |
| | 0.2005 | 0.0799 | 8.74 |
| | 0.2021 | 0.0758 | 8.88 |
| | 0.2035 | 0.1044 | 8.70 |
| | 0.2504 | 0.0570 | 8.73 |
| | 0.2959 | 0.1069 | 8.97 |
| | 0.3999 | 0.1234 | 8.72 |
| $CaF_2$–NaF | 0.0500 | 0.1199 | 5.43 |
| | 0.0690 | 0.1193 | 5.61 |
| | 0.1000 | 0.0678 | 5.62 |
| | 0.1629 | 0.0328 | 5.92 |
| | 0.2369 | 0.0392 | 6.40 |
| | 0.3392 | 0.0493 | 6.76 |
| | 0.4600 | 0.0656 | 7.24 |
| | 0.5000 | 0.0658 | 7.29 |
| $CaF_2$–KF | 0.0546 | 0.1208 | 2.16 |
| | 0.0617 | 0.1216 | 2.40 |
| | 0.0846 | 0.1046 | 2.49 |
| | 0.1017 | 0.0888 | 2.73 |
| | 0.1069 | 0.0884 | 2.83 |
| | 0.1396 | 0.0634 | 2.72 |
| | 0.1491 | 0.0675 | 2.94 |
| | 0.1771 | 0.0970 | 3.21 |
| | 0.2391 | 0.0755 | 3.77[b] |
| | 0.2421 | 0.0759 | 3.85[b] |
| | 0.2514 | 0.0767 | 3.81[b] |
| | 0.2873 | 0.0806 | 4.29[b] |
| | 0.3148 | 0.0839 | 4.39[b] |
| | 0.3742 | 0.0919 | 4.87[b] |
| | 0.4313 | 0.1011 | 5.34[b] |
| | 0.4809 | 0.1108 | 5.73[b] |

[a] $X_2$ = mole fraction of calcium fluoride. [b] Experiments based on multiple (two–four) additions of solid calcium fluoride.

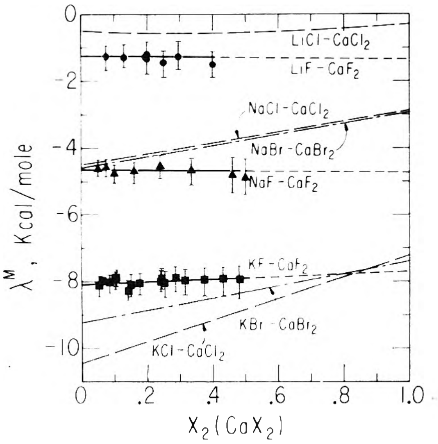

Figure 3. Plots of $\lambda^M = \Delta H^M/X_1X_2$ vs. $X_2$ for $CaX_2$–AlkX mixtures. Data for chloride and bromide systems for Oestvold.[4]

for the three calcium fluoride–alkali fluoride systems. The interaction parameters are plotted against $X_2$ in Figure 3, along with published data for the corresponding chloride and bromide mixtures.

If we assume that $\lambda^M$ depends linearly on $X_2$, *i.e.*

$$\lambda^M = a + bX_2 \qquad (4)$$

we obtain the values of $a$ and $b$ listed in Table II. Although our treatment of the data is very sensitive to uncertainty in the adopted value of the enthalpy of fusion of $CaF_2$, it is apparent that the asymmetry parameters are quite small. Thus, to a first approximation the three calcium fluoride–alkali fluoride systems may be described as energetically symmetrical, *i.e.*, to have interaction parameters which are independent of composition.

**TABLE II: Summary of Enthalpy of Mixing Data for Calcium Fluoride–Alkali Fluoride Mixtures at 1081°[a]**

| System | $a$ | $b$ | $4\Delta H_{0.5}{}^M$ |
|---|---|---|---|
| LiF–$CaF_2$ | −1.26 | −0.09 | −1.30 |
| NaF–$CaF_2$ | −4.64 | −0.09 | −4.68 |
| KF–$CaF_2$ | −8.09 | 0.43 | −7.88 |

[a] $\Delta H^M = X_1X_2(a + bX_2)$. $X_2$ = mole fraction of calcium fluoride; data in kcal/mol.

## Discussion

A more detailed discussion of the thermodynamic properties of the alkaline earth fluoride–alkali fluoride liquid mixtures will not be attempted until reliable calorimetric information is available for a wider range of binary fluoride systems. Even so, it is of considerable interest to present a brief comparison of our new data with the recent work of Oestvold on other alkaline earth halide–alkali halide systems.[4]

On the whole Oestvold's study supports the view that the main contributions to the enthalpies of mixing in these systems are (a) the reduction in Coulomb repulsion between second nearest neighbor cations, and (b) cation–anion polarization, principally due to the polarization of the common anion by its neighboring cations. However, since most of Oestvold's work dealt with the binary chlorides and bromides, and since he had no information on the corresponding fluorides, he was unable to draw firm conclusions regarding the relative importance of Coulomb and polarization terms.

(1) Oestvold found that, for a given alkaline earth halide, the enthalpy interaction parameter varies in an essentially linear manner with the parameter $\delta_{12} = (d_1 - d_2)/d_1d_2$. In this expression $d_1$ and $d_2$ are the characteristic cation–anion distances in the two salts; these are obtained from the sums of the ionic radii $d_1 = r_+ + r_-$; $d_2 = r_{++} + r_-$. Similar behavior is observed for many other charge-unsymmetrical systems. Although such a linear dependence is predicted by the conformal solution theories of Davis,[13,14] it offers by itself no basis for assessing the relative significance of Coulomb and polarization forces.

For the calcium fluoride–alkali fluorides we plot $\lambda^M$ against $\delta_{12}$ in Figure 4; this figure also gives an equivalent plot for the corresponding calcium chloride and bromide mixtures. Note that in the calcium chloride family the $CaCl_2$–LiCl system shows a pronounced deviation from the straight line defined by the larger alkali cations; this deviation is not found for $CaF_2$–LiF. Actually similar deviations for the lithium containing systems are observed in all previously investigated charge-unsymmetrical chloride, bromide, and iodide families. It is possible that these deviations may be attributed to the radius ratio effect, *i.e.*, to the fact that in liquid lithium chloride, bromide, and iodide the core repulsion between the anions increases the effective cation–anion distance, so that this is no longer well approximated by the sum of the cation and anion radii. In lithium fluoride, with a radius ratio $r_+/r_- = 0.425$, one would not expect that this effect should be significant; our new data for the calcium fluoride mixtures are consistent with this view.

(2) Oestvold found that while there is very little difference between the enthalpies of mixing in the calcium chloride and calcium bromide mixtures, there is a system-

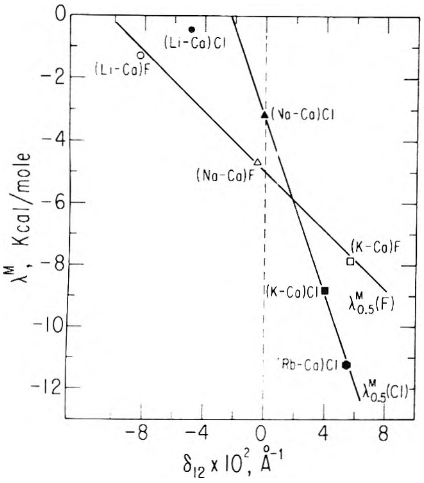

**Figure 4.** Plots of $\lambda_{0.5}^M$ *vs.* $\delta_{12}$ for $CaF_2$–AlkF and $CaCl_2$–AlkCl mixtures.

atic decrease in the enthalpy of mixing in the sequence $SrCl_2$–AlkCl > $SrBr_2$–AlkBr > $SrI_2$–AlkI. The more negative values found in the salts with the larger common anion were attributed to increasing importance of cation–anion polarization. If cation–anion polarization is significant also in the considered calcium halide systems, one would expect the fluorides to be less exothermic than the corresponding chloride and bromide mixtures. Actually, we find that $CaF_2$–LiF and $CaF_2$–NaF are *more* exothermic than the corresponding chlorides, while $CaF_2$–KF is slightly *less* exothermic.

(3) Oestvold noted that many of the alkaline earth halide–alkali halide mixtures show very pronounced energetic asymmetries, *i.e.*, a strong dependence of the interaction parameter on composition. In 28 of the 32 systems studied by him, he found that the interaction parameter in the pure alkaline earth halide is more positive than in the pure alkali halide. He suggested that the observed asymmetries might possibly be related to his choice of the "ionic fraction" rather than the "equivalent fraction" as his concentration variable. Actually, as noted by Oestvold, the theoretical justification for the use of equivalent fractions in binary, charge-unsymmetrical fused salt systems is less than convincing. In view of the very low energetic asymmetries found in the calcium fluoride mixtures, our new data provide no support for this practice.

(4) Oestvold found that for alkaline earth halide–alkali halide mixtures in which there is no "complex" formation, the entropies of mixing are well approximated by the Temkin model,[15] *i.e.*, on the basis of an assumed random mixing of the singly charged and doubly charged cations.[16]

For the calcium fluoride systems considered in the present work the equilibrium phase diagrams are available. In the calculations below we used the data of Deadmore and Machin[17] (LiF–$CaF_2$) and of Cantor[18] (NaF–$CaF_2$). For KF–$CaF_2$ we took the diagram from the compilation of Robertson.[19] If we are justified in assuming that solid solubility of $CaF_2$ in the alkali fluorides is negligible, the phase diagrams allow easy calculation of the partial excess Gibbs energies of the alkali fluorides along the liquidus curve

$$\bar{G}_{AF}^{E} = \Delta S_f(T - T_f) + T\Delta C_p(T_f/T - 1 - \ln (T_f/T)) - RT \ln X_{AF} \quad (5)$$

In this expression, $T_f$ and $\Delta S_f$ are the melting temperature and entropy of fusion of AF, respectively, while $\Delta C_p$ is the heat capacity difference between the liquid and solid alkali fluoride. This difference is assumed to be constant between $T_f$ and the liquidus temperature $T$. Figure 5 gives plots of the calculated value of $\bar{G}_{AF}^{E}$ against $X_{CaF_2}^2$ for the concentration range, $0 < X_{CaF_2} < 0.3$. In these calculations we have adopted the entropies of fusion reported by Kelley,[11] and have set $\Delta C_p$ = 0.83, 1.10, 1.67 cal/deg mol for LiF, NaF, and KF, respectively.[11] In the same figure we give plots of $\bar{H}_{AF}$ derived from our own calorimetric data. For LiF–$CaF_2$ and KF–$CaF_2$ there is little or no difference between $\bar{G}_{AF}^{E}$ and $\bar{H}_{AF}$, indicating excellent agreement with the Temkin model. For NaF–$CaF_2$ the values of $\bar{H}_{NaF}$ are systematically slightly more negative than the calculated values of $\bar{G}_{NaF}^{E}$. It is very probable that these slight apparent deviations from the Temkin model may be attributed to a small solid solubility (1–2%) of $CaF_2$ in NaF. In view of the similarity of the ionic radii of $Ca^{2+}$ and $Na^+$ (0.99 and 0.95 Å, respectively), among the three systems studied this clearly is the system most likely to exhibit solid solubility.

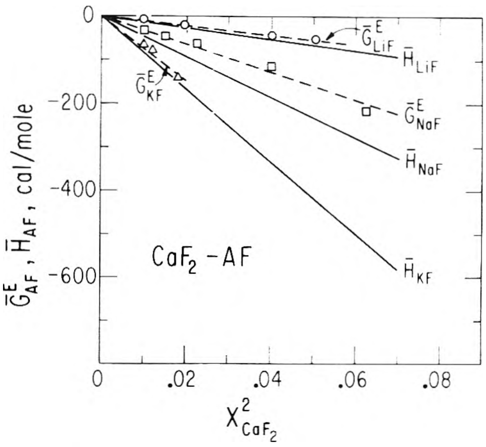

**Figure 5.** Plots of $\bar{H}_{AlkF}$ and $G_{AlkF}^{E}$ *vs.* $X_{CaF_2}^2$.

*Acknowledgments.* This work has been supported by the National Science Foundation. It has also benefited from the general support of Materials Science at The University of Chicago provided by NSF-MRL.

## References and Notes

(1) (a) O. J. Kleppa, *J. Phys. Chem.*, **66**, 1668 (1962); (b) O. J. Kleppa and L. S. Hersh, *Discuss. Faraday Soc.*, **32**, 99 (1961); (c) F. G. McCarty, L. S. Hersh, and O. J. Kleppa, *J. Chem. Phys.*, **41**, 1522 (1964).
(2) F. G. McCarty and O. J. Kleppa, *J. Phys. Chem.*, **68**, 3346 (1964).
(3) O. J. Kleppa and F. G. McCarty, *J. Phys. Chem.*, **70**, 1249 (1966).
(4) T. Oestvold, *J. Phys. Chem.*, **76**, 1616 (1972).
(5) G. N. Papatheodorou and O. J. Kleppa, *J. Inorg. Nucl. Chem.*, **32**, 889 (1970).
(6) G. N. Papatheodorou and O. J. Kleppa, *Inorg. Chem.*, **10**, 782 (1971).
(7) G. N. Papatheodorou and O. J. Kleppa, *J. Inorg. Nucl. Chem.*, **33**, 1249 (1971).
(8) J. L. Holm and O. J. Kleppa, *Inorg. Chem.*, **8**, 207 (1969).
(9) O. J. Kleppa and M. E. Melnichak, to be submitted for publication.
(10) A. Pugh and R. Barrow, *Trans. Faraday Soc.*, **54**, 671 (1958).
(11) K. K. Kelley, *U. S. Bur. Mines Bull.*, 584 (1960).
(12) "JANAF Thermochemical Tables," Clearinghouse for Federal Scientific and Technical Information, 1967.
(13) H. T. Davis, *J. Chem. Phys.*, **41**, 2761 (1964).
(14) H. T. Davis, *J. Phys. Chem.*, **76**, 1629 (1972).
(15) M. Temkin, *Acta Phys. Chem. USSR*, **20**, 411 (1945).
(16) T. Oestvold, *J. High Temp. Sci.*, **4**, 51 (1972).
(17) D. L. Deadmore and J. S. Machin, *J. Phys. Chem.*, **64**, 824 (1960).
(18) S. Cantor, *J. Phys. Chem.*, **65**, 2208 (1962).
(19) W. D. Robertson, "Binary Phase Diagrams of Halide Salts," Yale 2723-1, Clearinghouse for Federal Scientific and Technical Information, 1966.

# Studies in High-Pressure Mass Spectrometry. V. Thermodynamics of Solvation Reactions. $NH_4^+$–$NH_3$

**M. R. Arshadi and Jean H. Futrell***

*Department of Chemistry, University of Utah, Salt Lake City, Utah 84112*

*(Received December 3, 1973)*

*Publication costs assisted by the National Science Foundation*

The ammonia clustered ions $NH_4^+(NH_3)_n$ have been studied by means of a high-pressure mass spectrometer. The temperature and the pressure ranges covered were from 208 to 750°K and from 0.5 to 1.6 Torr, respectively. Thermodynamic data for reactions $NH_4^+(NH_3)_{n-1} + NH_3 \rightarrow NH_4^+(NH_3)_n$ have been determined. The free energy changes for $n = 1$ to 6 at 300°K are −15.5(0,1), −9.4(1,2), −6.0(2,3), −3.4(3,4), −0.4(4,5), and 0(5,6) kcal/mol. The corresponding enthalpy changes are −21.6(0,1), −16.4(1,2), −13.5(2,3), −11.7(3,4), −7.0(4,5), and −6.5(5,6) kcal/mol. These values are in good agreement with previous results obtained using high-pressure mass spectrometry and support the existence of two solvation shells for this system. Furthermore, the data indicate that differences in binding energy with increasing solvation of ligands in the outer shell are much less pronounced than those of the inner shell. The metastable ions due to loss of one ligand molecule from clusters have been observed and accounted for. Some minor peaks due to clusters of the kind $NH_4^+(NH_3)_{n-1}H_2O$ have also been observed. The ratios of intensities of these peaks to those of $NH_4^+(NH_3)$ are larger for $n = 5$ and 6 than $n = 1$ to 4. This has been attributed to the preferential addition of $H_2O$ in the second shell.

## Introduction

Although solvation of ions by neutral molecules in the gas phase has been known since the early days of mass spectrometry,[1] the vigorous study of this subject did not start until a few years ago when instruments capable of operating at high ion source pressure were first developed. Since then a number of investigations of the solvation of positive as well as negative ions have been carried out[2-6] and some interesting results have been obtained. These results have a variety of applications in upper atmosphere, radiation, and other related fields of chemistry and physics.

Consider an ion, $A^+$, produced as a result of collisions of electrons or some other ionizing media with neutral molecules, M, in the ion source of a mass spectrometer. If the source pressure is high enough, these ions can interact with other molecules of M or some other gas, B, and form ion clusters of the type $A^+M_i$ or $A^+B_n$, according to the following series of reactions

$$A^+ + B \xrightarrow{M} A^+B \qquad (1)$$

$$A^+B + B \xrightarrow{M} A^+B_2 \qquad (2)$$

$$A^+B_{n-1} + B \xrightarrow{M} A^+B_n \qquad (3)$$

These reactions are exothermic and require a third body (the major gas, M) to deactivate the clusters just formed. If equilibrium conditions prevail in the ion source, the equilibrium constant $K_{(n-1),n}$ is given by the following expression

$$K_{(n-1),n} = \frac{I_n}{I_{n-1}}\frac{1}{P_B} \qquad (I)$$

where $I_{n-1}$ and $I_n$ are the ion intensities of $AB_{n-1}^+$ and $AB_n^+$, respectively, recorded by the mass spectrometer and $P_B$ is the partial pressure of gas B in the ion source. From a study of these reactions as a function of ion source temperature and a plot of the equilibrium constants as a function of reciprocal temperatures, the enthalpy change of the individual reactions, $\Delta H°_{n-1,n}$, is obtained. The standard free energy change, $\Delta G°_{n-1,n}$, and the entropy change, $\Delta S°_{n-1,n}$, are calculated from the following equations

$$\Delta G°_{n-1,n} = -RT \ln K_{n-1,n} \qquad (II)$$

$$\Delta G°_{n-1,n} = \Delta H°_{n-1,n} - T\Delta S°_{n-1,n} \qquad (III)$$

where $R$ is the universal gas constant and $T$ is the temperature in °K.

Using the above technique, we have studied the reaction

$$NH_4^+(NH_3)_{n-1} + NH_3 \rightleftharpoons NH_4^+(NH_3)_n \qquad (4)$$

This system has been previously studied by Searles and Kebarle.[7] However, because of the importance of this system with regard to the formation of first and second solvation shells and formation of mixed clusters, it was decided to initiate a study of these reactions in this laboratory with the ammonia system and extend it to aliphatic and aromatic amines.

## Experimental Section

The basic apparatus used for this study was a Varian MAT CH7 mass spectrometer modified for high-pressure studies. The detailed description of this instrument will be given elsewhere[8] and only a brief description pertinent to the present work is given below.

The ion source is made of stainless steel and is provided with a resistance heater and a cooling coil. Thus its temperature can be varied from liquid nitrogen temperature up to about 850°K. The temperature is measured by means of a chromel–alumel thermocouple inserted in the wall of the ion source. To assure that the true gas temperature is registered, another thermocouple was inserted inside the ion source, from time to time during this study, and a series of calibrations of the ion source thermocouple was obtained.

The pressure inside the ion source is determined by an M.K.S. Baratron, connected directly to the ion source. A schematic diagram of the ion source is shown in Figure 1. This ion source is designed for gas tight operation at pressures as high as 20 Torr. The distance between the electron beam, travelling across the ion source, and ion exit slit is of the order of 15 mm. The ion exit slit is 0.025 × 3 mm. These conditions presumably result in a diffusion-controlled travel of the ions to the ion exit slit, as is required for attainment of thermodynamic equilibrium. The pulse mode operation which was carried out previous to this study[9] demonstrated that the ion residence time under typical operating conditions ranges from 1 to 10 msec. Thus it is believed that the clustered ions formed in the ion source have ample time to become collisionally deactivated at the ion source pressure range (0.4–1.6 Torr) used in this study.

In this study the repeller potential was purposely held at zero with respect to the ion source, although a repeller potential of less than 2 V did not seem to affect the clusters distribution. After leaving the ion source, the ions are magnetically mass analyzed. The ion source housing is evacuated by means of a 2400 l./sec diffusion pump and the analyzer tube is differentially pumped by a 400 l./sec diffusion pump. At an ion source pressure of 1 Torr, the ion source housing pressure is of the order of 1 × $10^{-5}$ and the analyzer tube pressure is less than $10^{-6}$ Torr. This low pressure attained in the system minimizes the chance of collisional stripping of the higher clusters outside the ion source.

The ammonia used in this study was obtained from Matheson Co. and its purity as indicated by the manufacturer was 99.5%. No further purification was attempted. The gas entered the ion source through the gas inlet system which was maintained at or close to the ion source temperature. The flow was controlled by a Nupro Model SS-4BMG needle valve. The variation of ion source pressure during each run was less than 5% as indicated by an M.K.S. Baratron differential pressure gauge. No reagent gas was used in these experiments; that is, all the runs were made with pure ammonia at various pressures. To assure the achievement of equilibrium conditions in the ion source, a series of runs with different pressures (from 0.4 to 1.6 Torr) was made at each temperature.

## Results and Discussion

The thermodynamic values for reaction 4 obtained in this work are summarized in Table I. The temperature range covered in this study was from 208 to 750°K and the pressure range was from 0.5 to 1.6 Torr. All runs were made with pure ammonia.

The results from equilibrium constant measurements at constant ion source temperature but variable gas pressure indicate that equilibrium was likely achieved in the range of 0.8 to 1.5 Torr. Figure 2 shows some typical results obtained for $K_{0,1}$. In general the change of equilibrium constant, $K_{n-1,n}$, with pressure was in the order of 15–20% at a particular temperature, which is certainly within the experimental accuracy expected for this type of study. Furthermore variation of $K_{n-1,n}$ in Figure 2 over this pressure range is random and does not signify any trend in the data. For the runs which were made at the ion source pressures of 0.6 Torr and below, there was a decrease in the value of the equilibrium constant. This may reflect the decrease in the ion residence time with decrease in the ion source pressure. We also noted a decrease in $K$ values at pressures higher than 1.5 Torr, which probably results from collisional-induced decomposition of higher clusters very near the ion exit slit or in the ion accelerating portion of the instrument. This type of decomposition should appear as a shoulder in the low mass side of the lower clusters. This indeed was observed in some of the runs made at high pressure. Moreover, the observance of metastable ions corresponding to loss of one ammonia molecule from clusters indicated that some dissociation of the clusters in the field free region of the instrument also occurs. Lack of a strong temperature dependence suggests that a substantial fraction of these processes is collision induced. In most instances the ratios of the intensities of metastable ions (presumably both collision-induced and unimolecular dissociation) to

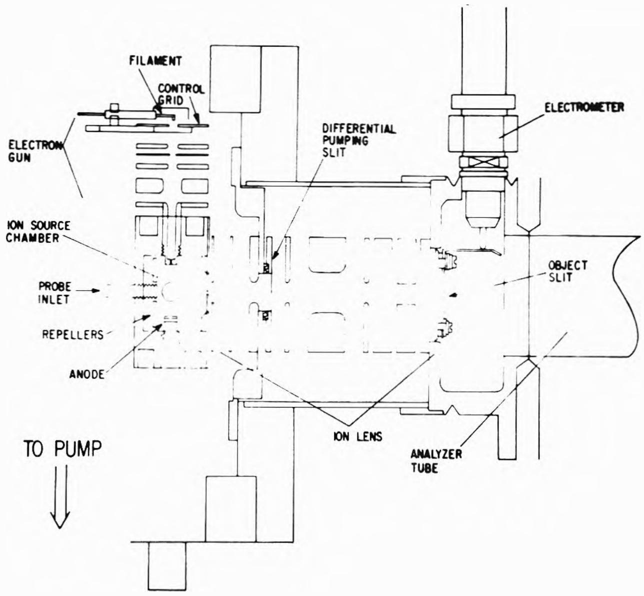

Figure 1. Schematic drawing of the ion source.

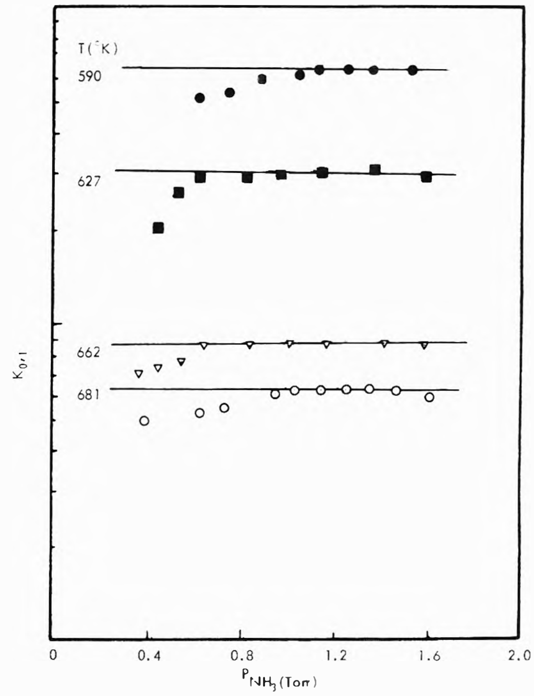

Figure 2. Plots of $K_{0,1}$ at constant temperature as a function of the ion source pressure.

TABLE I: Thermodynamic Values for Reaction 4

| | $-\Delta G°_{298}$, kcal/mol | | | $-\Delta H$, kcal/mol | | | $-\Delta S°$, eu | | | $-\Delta(\Delta H_{n-1,n})$ | | |
|---|---|---|---|---|---|---|---|---|---|---|---|---|
| $n-1, n$ | This work | SK[a] | PCK[b] | This work | SK[a] | PCK[b] | This work | SK[a] | PCK[b] | This work | SK[a] | PCK[b] |
| 0,1 | 15.5 | 17.5 | 17.1 | 21.5 | 27.0 | 24.8 | 20 | 32 | 26 | 5.3 | 10 | 7.3 |
| 1,2 | 9.4 | 9.0 | 8.9 | 16.2 | 17.0 | 17.5 | 23.7 | 26.8 | 23 | 2.7 | 0.5 | 3.7 |
| 2,3 | 6.0 | 6.4 | 6.1 | 13.5 | 16.5 | 13.8 | 25.2 | 34 | 26 | 1.8 | 2.0 | 1.3 |
| 3,4 | 3.4 | 3.8 | 3.7 | 11.7 | 14.5 | 12.5 | 27.9 | 36 | 30 | 4.7 | 7.0 | |
| 4,5 | 0.4 | 0.2 | | 7.0 | 7.5 | | 21.5 | 25 | | 0.5 | | |
| 5,6 | 0 | | | 6.5 | | | 21.9 | | | | | |

[a] Reference 7. [b] Reference 13.

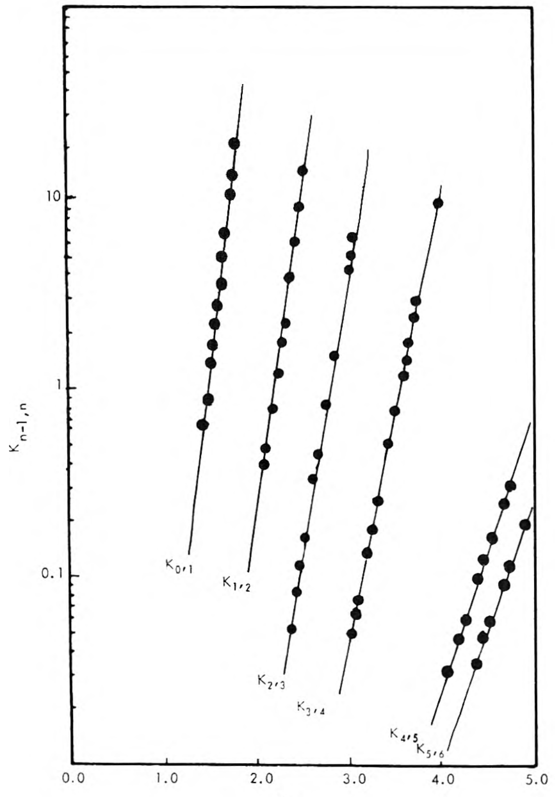

**Figure 3.** Plots of $K_{n-1,n}$ as a function of reciprocal temperature °K.

those of the parent ions were around 1–4%. For the transition

$$NH_4^+(NH_3)_5 \longrightarrow NH_4^+(NH_3)_4 + NH_3 \qquad (5)$$

this ratio was slightly higher, about 7%. Although this percentage given is only approximate, the increase in the ratio could be the result of lower stability of $NH_4^+(NH_3)_5$ with respect to clusters of lower mass to charge ratio. This is also indicated in our results, given in Table I, as a large difference in the values of $\Delta H_{4,5}$ and $\Delta H_{3,4}$. This point will be discussed briefly later.

The van't Hoff plots for the various equilibria studied are shown in Figure 3. Each point in this figure represents the average value of $K_{n-1,n}$ obtained at different $NH_3$ pressures and the respective temperatures. In addition to the data represented in Figure 3, we have observed some other points, on the low-temperature side of each van't Hoff line, which were too low to fit on the respective plot. This has also been observed in other studies carried out both in this laboratory[10] and elsewhere,[11] and has been attributed to the insufficient time and/or number of collisions for establishment of equilibrium for the reaction under consideration. Consequently, as these points are not representative of equilibrium conditions, they have been omitted from the plots of Figure 3. In Figure 4, we show this special condition for 0–1 equilibrium. It should be noted that this is the most severe case and much less "fall-off" behavior is observed for the higher (lower $\Delta H$) clusters.

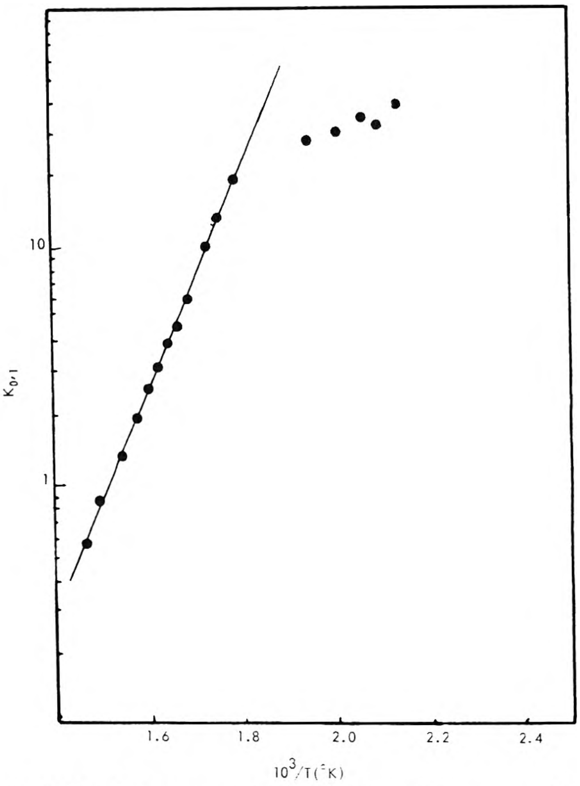

**Figure 4.** Plot of $K_{0,1}$ as a function of reciprocal temperature °K.

Column 5 of Table I shows a difference of −4.7 kcal/mol between $\Delta H_{3,4}$ and $\Delta H_{4,5}$. Comparison of this value with −1.8 kcal/mol for $(\Delta H_{2,3} - \Delta H_{3,4})$ and −0.5 kcal/mol for $(\Delta H_{4,5} - \Delta H_{5,6})$ establishes a discontinuity which can reasonably be interpreted as filling an inner shell around the ion $NH_4^+$ by adding the maximum number of four ligand molecules. This phenomenon has also been observed in Searles and Kebarle's study of the same system[7] and has been attributed to the tetrahedral structure of the ammonium ion $NH_4^+$. It is interesting, furthermore, to notice that the difference in $\Delta H_{4,5}$ and $\Delta H_{5,6}$ is only 0.5 kcal/mol. If this difference can be taken as a typical value for the second solvation shell around $NH_4^+$, it indicates that the ligands in the second shell are much less strongly bound by the central ion than those of the first shell. The shielding effect of the inner shell implied by this result is not unrea-

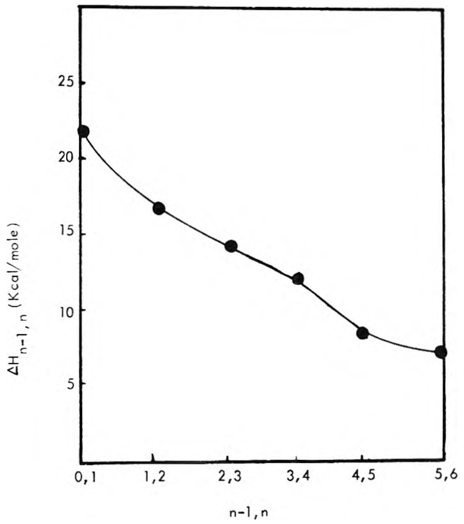

**Figure 5.** Plot of $\Delta H_{n-1,n}$ as a function of $(n-1),n$.

sonable. In Figure 5 we give a plot of $\Delta H_{n-1,n}$ as a function of $n - 1,n$. The drop-off between $\Delta H_{3,4}$ and $\Delta H_{4,5}$ is readily apparent.

Also included in Table I are values obtained by Searles and Kebarle.[7] As may be seen, the overall general agreement in these two studies is very good. Considering the inherent differences in the two instruments and the conditions under which these two studies were made the agreement in the $\Delta G°_{300}$ values is noteworthy. In the case of $\Delta H$, however, the agreement, although still acceptable, is not as striking. A maximum discrepancy of 25% is noted. We are of the opinion that errors involved in gas temperature measurements are the most likely remaining experimental difficulty.

Assuming this is true, it seems that this error was more serious in the high-temperature range, that is in the case of $n = 1$. In a recent study made by Kebarle and coworkers[12] on water cluster formation, the negative $\Delta H_{0,1}$ obtained was 4 kcal/mol less than the value reported previously by the same group.[2] Considering the fact that the high-temperature ($T > 400°K$) portion of the original $H^+(H_2O)_n$ study by Kebarle, *et al.*, was carried out with proton beam mass spectrometer,[2] the same instrument used in ammonia study, it may be reasonable to assume the $-\Delta H$ value obtained by Searles and Kebarle for the reaction

$$NH_4^+ + NH_3 \longrightarrow NH_7^+ + NH_3 \qquad (6)$$

is also too high by about 4–5 kcal/mol. Such a correction would bring the data from ref 7 into excellent agreement with the present work. It is interesting, furthermore, that the newer values obtained for $\Delta H_{0,1}$ and $\Delta H_{1,2}$ by Kebarle, *et al.*, for

$$H^+(H_2O)_{n-1} + H_2O \longrightarrow H^+(H_2O)_n \qquad (7)$$

are better in line with the results of the work carried out with the CH 7 mass spectrometer for the same system in this laboratory.[10]

Recently Payzant, Cunningham, and Kebarle (PCK) have reinvestigated equilibrium in the ammonia system[13] using the improved apparatus and techniques utilized in this recent work with protonated water equilibria.[12] It may be seen that the data columns headed PCK are in substantially better agreement with the present research than the earlier report from that laboratory. We take this to be a gratifying confirmation of the general analysis presented above. Not reported in the table but also relevant to the present discussion is a study by the flowing afterglow method of certain of these equilibria by Fehsenfeld and Ferguson.[14] Their measured value at 298°K is undoubtedly a more reliable datum than the extrapolated values obtained in the present research. They obtained a value of $\Delta G°_{298} \geq -9.7$ kcal/mol for the 1,2 equilibrum, −6.5 for 2,3, and −3.4 for the 3,4 equilibrium, in nearly exact agreement with our experimental results.

The excellent agreement with the more recent research lends considerable confidence in the thermodynamic data deduced for the ammonia system. The only equilibrium reaction for which the experimental results may not be entirely reliable is the 0,1 reaction. In this case the exothermicity of the reaction is sufficiently high that we cannot be certain that the excess energy in the adduct ion is completely removed by the ammonia bath gas molecules. It should be noted that for this system the theoretical estimate of $\Delta H(0,1)$ by Mulet, Peyerimhoff, and Buenker[15] is −36 kcal/mol, substantially greater than the experimental values of −21.5 kcal/mol in present research and −24.8 kcal/mol obtained by Payzant, Cunningham, and Kebarle.[13] It is possible therefore that equilibrium is not achieved in this lowest member of the series and the experimental values which we deduce are still somewhat low. It is also possible, of course, that the theoretically calculated result may be too large by a few kilocalories/mole. In any case, for higher members of the series reported here we feel that the data are relatively reliable and can be taken as a guide for related research and future calculations.

In a study of ion–molecule reactions, Wincel[16] reports −6.3 and −5.5 kcal/mol for $\Delta G°_{0,1}$ and $\Delta G°_{1,2}$, respectively, at 400°K. These values are not in agreement with either those reported by Payzant, Cunningham, and Kebarle or with the current study. Our values for $\Delta G°_{0,1}$ and $\Delta G°_{1,2}$ at 400°K are −13.5 and −7.1 kcal/mol, respectively, in good agreement with −14.4 and −8.3 kcal/mol, obtained by Kebarle, *et al.*[13] We are unable to rationalize these differences other than to suggest that equilibrium may not have been established in Wincel's apparatus.

In addition to the series of the peaks due to $NH_4^+(NH_3)_n$, a second, minor series of peaks one unit higher in mass was noted. The ratios of the intensities of peaks in this second series to those in the major one, after correction for isotopic contributions, were around 1% for $n$ smaller than 4 and around 5–8% for $n$ equal to 5 and 6. We think this minor series is due to $NH_4^+(NH_3)_{n-1}(H_2O)$. Although no quantitative conclusions can be drawn without a knowledge of the partial pressure of water in the ammonia stream, this increase of intensity ratios beyond $n = 4$ is qualitatively consistent with the principle that water molecules are taken up preferentially in the second shell.[7] We hope in a future study of the competitive solvation of the gaseous ions to compare these two processes energetically.

*Acknowledgments.* This research was supported by National Science Foundation Grant GP No. 24257. Partial support was provided by National Institutes of Health Career Development Award 5K04-GM42390-04GMK. Dr. Arshadi would like to thank Arya-Mehr University of Technology for the sabbatical leave and partial financial support.

## References and Notes

(1) J. J. Thompson and E. Rutherford, *Phil. Mag.*, **42,** 392 (1896).
(2) P. Kebarle, S. K. Searles, A. Zolla, J. Scarborough, and M. Arshadi, *J. Amer. Chem. Soc.*, **89,** 6393 (1967).
(3) F. H. Field, *J. Amer. Chem. Soc.*, **91,** 2827 (1969).
(4) M. Arshadi, R. Yamdagni, and P. Kebarle, *J. Phys. Chem.*, **74,** 1475 (1970).
(5) M. DePaz, J. J. Leventhal, and L. Friedman, *J. Chem. Phys.*, **51,** 3748 (1969).
(6) I. Dzidic and P. Kebarle, *J. Chem. Phys.*, **74,** 1466 (1970).
(7) S. K. Searles and P. Kebarle, *J. Phys. Chem.*, **72,** 742 (1968).
(8) M. L. Vestal and J. H. Futrell, to be submitted for publication.
(9) M. L. Vestal, 20th Annual Conference on Mass Spectrometry and Allied Topics, Dallas, Tex, June 1972.
(10) J. H. Futrell and M. L. Vestal, 20th Annual Conference on Mass Spectrometry and Allied Topics, Dallas, Tex, June 1972.
(11) D. P. Beggs and F. H. Field, *J. Amer. Chem. Soc.*, **93,** 1576 (1971).
(12) J. P. Briggs, R. Yamdagni, and P. Kebarle, *J. Amer. Chem. Soc.*, **94,** 5129 (1972).
(13) J. D. Payzant, A. J. Cunningham, and P. Kebarle, *Can. J. Chem.*, **51,** 3242 (1973).
(14) F. C. Fehsenfeld and E. E. Ferguson, *J. Chem. Phys.*, **59,** 6272 (1973).
(15) P. Mulet, S. D. Peyerimhoff, and R. J. Buenker, *J. Amer. Chem. Soc.*, **94,** 8301 (1972).
(16) H. Wincel, *Int. J. Mass. Spectrom. Ion Phys.*, **9,** 267 (1972).

# Thermodynamics of Polycarboxylate Aqueous Solutions. II. Dilatometry and Calorimetry of Nickel and Barium Binding

**F. Delben* and S. Paoletti**

*Laboratorio di Chimica delle Macromolecole, Istituto di Chimica, Università di Trieste, Trieste, Italy* *(Received November 19, 1973)*

Calorimetric and dilatometric data on the binding of $Ni^{2+}$ and $Ba^{2+}$ ions by three maleic acid copolymers in tetramethylammonium perchlorate aqueous solution at 25° and at different neutralization degrees of the polyacids are reported. The results show a marked dependence of the thermodynamic binding parameters on the nature of the metal ion bound. The present data, and those previously obtained for the binding reaction between $Cu^{2+}$ ions and the same copolymers, are compared.

## Introduction

In a recent paper from this laboratory the results obtained by means of calorimetric and dilatometric measurements on the protonation of, and $Cu^{2+}$ ions binding by, three maleic acid (MA) copolymers have been reported.[1]

We wish to report here similar data concerning $Ni^{2+}$ and $Ba^{2+}$ ions binding by the same copolymers (hydrolyzed maleic anhydride–ethylene, MAE; hydrolyzed maleic anhydride–propylene, MAP; and hydrolyzed maleic anhydride–isobutene, MAiB) in 0.05 $M$ $(CH_3)_4NClO_4$ and at 25°, and to discuss the observed differences in the set of thermodynamic binding parameters in a comparative way.

## Experimental Section

(*a*) *Materials.* Maleic acid–ethylene copolymer (MAE), maleic acid–propylene copolymer (MAP), and maleic acid–isobutene copolymer (MAiB) samples, all of the 1:1 alternating type[2,3] were received from the Monsanto Chemical Co. Their molecular weight was about $10^5$.[2] Stock solutions of the three polyacids were prepared as previously described.[2,4] In the preparation of the polyelectrolyte solutions for both calorimetric and dilatometric experiments standardized $(CH_3)_4NOH$ (a BDH product, employed without purification) solutions were used.

Nickel perchlorate was prepared by allowing carbonate (Erba RP) to react with warm aqueous $HClO_4$ (an Erba product, 70% w/w solution). The resultant solution was filtered and cooled. The metal perchlorate was collected and recrystallized twice from water; the titer of the nickel perchlorate solutions was determined using EDTA.[5] Barium perchlorate was prepared by allowing excess barium carbonate (Erba RP) to react with warm dilute $HClO_4$; the resultant solution was filtered and directly standardized using EDTA.[6] Pure $(CH_3)_4NClO_4$ was prepared as previously described.[1]

In all cases, freshly distilled water, obtained by a Heraeus quartz bidistillator, was used.

(*b*) *Methods.* The calorimetric experiments were carried out at 25° using an LKB 10700-1 flow microcalorimeter, following a procedure already described.[4] Also the treatment of the calorimetric data follows previously reported procedures.[1] (See paragraph at end of text regarding supplementary material.)

Linderstroem-Lang dilatometers were used to measure volume changes, as described previously.[7] The water insoluble liquid used was $n$-heptane, purified as previously described.[8]

All measurements were carried out at 25°, with a constancy of bath temperature much better than 0.001 deg/hr, following the dilatometric method successfully applied by Begala and Strauss.[7] Corrections for effects due to dilution on mixing were found to be almost always negligible.

All equilibrium dialysis experiments were carried out using cellulose tubings (Kalle AG, Wiesbaden), treated prior to use as previously described.[1]

The metal concentration in the polyelectrolyte-free "external" solutions was determined by atomic absorption spectrometry (Perkin-Elmer 290-B, with acetylene as fuel) for barium, and by atomic absorption spectrometry or by EDTA for nickel. The final uncertainty in the calculated fraction of bound metal ions should not exceed 2 and 5% for nickel and barium, respectively.

Potentiometric titrations were performed in a thermostated vessel at 25 ± 0.05° using a Radiometer PH M 4d pH meter equipped with Radiometer "combination" electrode, GK-2301 C.

## Results and Discussion

The microcalorimetric data, obtained following closely the experimental procedures[4] and the treatment[1] described elsewhere, are plotted in Figure 1.

$\Delta \bar{H}_T$ values ($\Delta \bar{H}_T$ is a differential enthalpy of binding, in kcal/mol of metal bound, taken as the slope of the $\Delta H_T$ *vs.* $R(M^{2+})$ curve at the limit of $R(M^{2+}) \rightarrow 0$, where $R(M^{2+})$ is the ratio of metal bound to monomeric units concentration) for $Ni^{2+}$ and $Ba^{2+}$ ions are reported in Table I, together with those of $Cu^{2+}$ ions for the same experimental conditions.[1]

It is clearly seen that the $\Delta \bar{H}_T$ values associated to the binding reactions, at least for our experimental conditions, are positive and markedly decreasing passing from $Cu^{2+}$ to $Ni^{2+}$ to $Ba^{2+}$, respectively. Two facts deserve attention here. First, our calorimetric $Ni^{2+}$–MAE binding data appear not to agree with those obtained by other authors ($\Delta H = -0.97$ kcal/mol).[9] This discrepancy depends, in our opinion, essentially on the different degree of neutralization, $\alpha$,[10] of the polymer chains, *i.e.*, $\alpha$ is 1.0 in our case and is 0.5 for Purdie, *et al.*[9]

This trend (increasing $\Delta \bar{H}$ values with increasing $\alpha$) has been also reported for the MAP–Cu and MAiB–Cu binding, even for other experimental conditions.[1]

Second, the $\Delta \bar{H}_T$ for binding reaction decreases, for each polyelectrolyte, passing from $Cu^{2+}$ to $Ni^{2+}$ to $Ba^{2+}$ ions, respectively. This can be related to the decreasing ability, from $Cu^{2+}$ to $Ba^{2+}$ ions, to bind carboxylic groups yielding true site binding. In the case of the interaction between $Cu^{2+}$ ions and partially neutralized polycarboxylic acids the existence of complexes has in fact been established;[9,11–14] on the contrary $Ba^{2+}$ ions are known to form almost pure electrostatic bonds with charged polyelectrolytes.[7]

Our experimental data support the hypothesis that the $Ni^{2+}$ ions can be bound by carboxylic groups to give a chelate intermediate between a site binding complex and an ion pair. Different binding depends on both the charge density to ionic volume ratio (and therefore on the hydration degree) and the electronic configuration of the different metal ions. Direct studies on the carboxylic group–metal ion bond length could eventually support this hypothesis. Also our dilatometric data can help us in this direction.

The dilatometric results are plotted in the Figures 2 and 3. The slope of the curves at $R = 0$, $\Delta \bar{V}_T$, is the volume increase (in ml/mol of "complex") when the first metal ion is bound by the polyelectrolyte chain. As can be seen from Table I, the $\Delta \bar{V}_T$ at $\alpha = 1.0$ is, for each polymer–metal complex, always lower than the corresponding value at $\alpha = 1.2$ or 1.5. This evidence has been already discussed in terms of the hydration of the bicarboxylic groups.[1] Further evidences indicates that it is very difficult to interpret the dilatometric data relating them directly to the nature of metal ion and/or of polyelectrolyte chain. We can observe, however, that, at least at $\alpha = 1.2$ and 1.5, there is an increase in the $\Delta \bar{V}_T$ values passing from MAE to MAP and to MAiB, respectively, for each metal bound. Furthermore, our present results indicate that the behavior of $Ni^{2+}$ is intermediate between those of $Cu^{2+}$ and $Ba^{2+}$, respectively, at the above-mentioned values of $\alpha$ (see Table I). The not well-understandable trend of $\Delta \bar{V}_T$ at $\alpha = 1.0$ is likely to be due to a superposition of various effects, some of which have been mentioned above. It is worth pointing out, however, that our data agree with those already published by other authors.[7]

In order to evaluate the variation in entropy associated with the binding process (which could contribute, together with the dilatometric results, to a better structural interpretation of the binding phenomenon) we tried to cal-

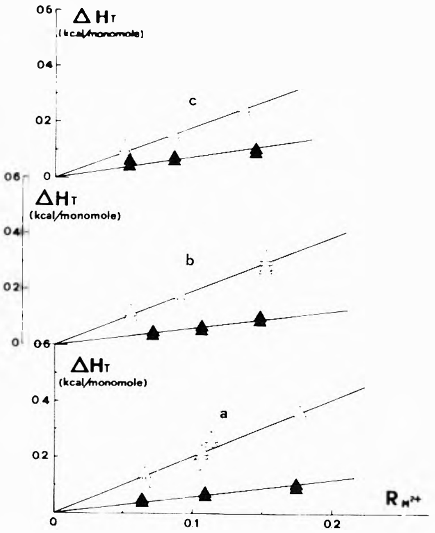

**Figure 1.** Enthalpy changes on the addition of $Ni(ClO_4)_2$ and $Ba(ClO_4)_2$ respectively to tetramethylammonium polycarboxylates at $\alpha = 1.0$ in 0.05 *M* $(CH_3)_4NClO_4$ at 25°. The abscissa, $R(M^{2+})$, denotes the moles of added $Ni^{2+}$ or $Ba^{2+}$ bound per monomole of total polyacid. The ordinate, $\Delta H_T$, gives the total enthalpy change in kcal per monomole of total polyacid: (a) MAE; (b) MAP; (c) MAiB; (△) $Ni^{2+}$; (▲) $Ba^{2+}$.

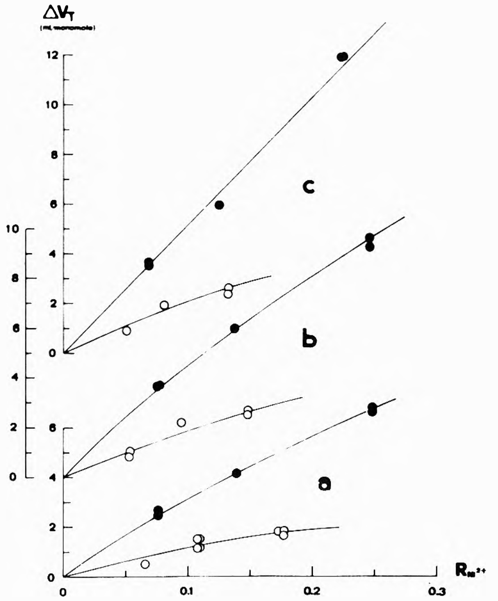

**Figure 2.** Volume changes on the addition of $Ni(ClO_4)_2$ to tetramethylammonium polycarboxylates at various degrees of neutralization, $\alpha$, in 0.05 *M* $(CH_3)_4NClO_4$ at 25°. The abscissa, $R(Ni^{2+})$, denotes the moles of added $Ni^{2+}$ bound per monomole of total polyacid. The ordinate, $\Delta V_T$, gives the total volume change in milliliters per monomole of total polyacid: (a) MAE; (b) MAP; (c) MAiB; (○) $\alpha = 1.00$; (●) $\alpha = 1.50$.

**TABLE I: Thermodynamics of $Cu^{2+}$, $Ni^{2+}$, and $Ba^{2+}$ Binding by Three Hydrolyzed Maleic Anhydride Copolymers**

| Polymer | Metal | $\alpha$ | $\Delta H_T$, kcal/mol of complex | $\Delta G_B{}^{\circ}$,[a] kcal/mol of complex | $\Delta S$ | $\Delta V_T$, ml/mol of complex |
|---|---|---|---|---|---|---|
| MAE | $Cu^{2+}$ | 1.00 | 4.4 | 7.6 | 40 | 32 |
| | | 1.20 | 4.4 | | | 41 |
| | | 1.50 | | | | 52 |
| | $Ni^{2+}$ | 1.00 | 2.0 | 6.4 | 28 | 13 |
| | | 1.50 | | | | 36 |
| | $Ba^{2+}$ | 1.00 | 0.6 | 5.9 | 22 | 24 |
| | | 1.50 | | | | 24 |
| MAP | $Cu^{2+}$ | 1.00 | 4.0 | 8.9 | 43 | 26 |
| | | 1.20 | 4.0 | | | 52 |
| | $Ni^{2+}$ | 1.00 | 2.0 | 6.4 | 28 | 20 |
| | | 1.50 | | | | 51 |
| | $Ba^{2+}$ | 1.00 | 0.6 | 6.1 | 22 | 25 |
| | | 1.50 | | | | 39 |
| MAiB | $Cu^{2+}$ | 1.00 | 4.0 | 10.1 | 47 | 31 |
| | | 1.20 | 4.0 | | | 85 |
| | | 1.50 | | | | 85 |
| | $Ni^{2+}$ | 1.00 | 1.8 | 8.1 | 33 | 23 |
| | | 1.50 | | | | 52 |
| | $Ba^{2+}$ | 1.00 | 0.7 | 7.2 | 27 | 13 |
| | | 1.50 | | | | 40 |

[a] $pK_1$ and $pK_2$ for $\Delta G_B$ evaluation are respectively MAE, 4.4, 7.1; MAP 4.1, 8.0; MAiB, 3.4, 9.4. $\Delta G_B{}^{\circ}$ are extrapolated to $R = 0$ $\Delta G_B$ values (see text).

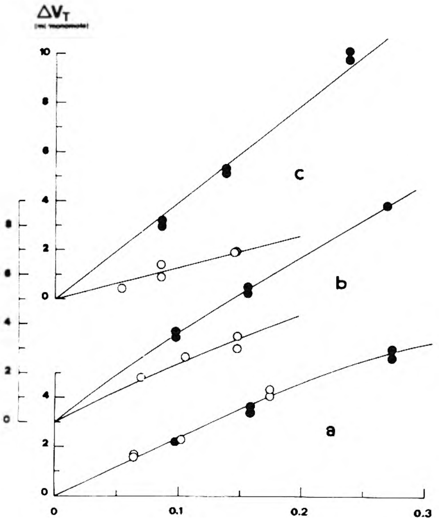

Figure 3. Volume changes on the addition of $Ba(ClO_4)_2$ to tetramethylammonium polycarboxylates at various degrees of neutralization, $\alpha$, in 0.05 $M$ $(CH_3)_4NClO_4$ at 25°. The abscissa, $R(Ba^{2+})$, denotes the moles of added $Ba^{2+}$ bound per monomole of total polyacid. The ordinate, $\Delta V_T$, gives the total volume change in milliliters per monomole of total polyacid: (a) MAE; (b) MAP; (c) MAiB; (○) $\alpha = 1.00$; (●) $\alpha = 1.50$.

culate the free-energy changes associated to the process. Our effort, although not fully successful, gives some interesting indications.

If $AH_2$, $AH^-$, and $A^{2-}$ stand for discharged, monodissociated, and bidissociated monomeric unit, respectively, $M^{2+}$ represents the divalent chelated counterion, and MA is a "monomole" of complex, we can picture the whole binding reaction, at $\alpha = 1.0$, as follows

$$AH^- \longrightarrow A^{2-} + H^+ \quad (1)$$

$$A^{2-} + M^{2+} \longrightarrow MA \quad (2)$$

$$H^+ + AH^- \longrightarrow AH_2 \quad (3)$$

From this scheme and if in a first approximation we do not take into account the possibility of the following reaction[9]

$$AH^- + M^{2+} \longrightarrow AHM^+ \quad (4)$$

or similar ones, the stoichiometric or apparent equilibrium constant of the "pure" binding reaction 2 is the following

$$K_{MA}{}^{app} = [MA]/[A^{2-}][M^{2+}]$$

$[M^{2+}]$ is known from dialysis equilibrium experiments, by analyzing the polyelectrolyte-free "external" solutions (see Experimental Section). [MA] is known from the total concentration of metal, $C_{tot}$, and $[M^{2+}]$; $[MA] = C_{tot} - [M^{2+}]$; finally, $[A^{2-}]$ can be evaluated from the titration curves of each single polyelectrolyte. The $K_{MA}{}^{app}$ values are of limited reliability for three principal reasons (besides the fact that the quantities in the expression are the stoichiometric concentrations, and not the activities): (1) the uncertainty in the dialysis equilibrium data (±2% for $Cu^{2+}$ and $Ni^{2+}$, and ±5% about for $Ba^{2+}$ ions concentrations values, respectively) do not permit an exact calculation of bound to total metal ratio, particularly at the highest ratio values; (2) $K_1{}^{app}$ and $K_2{}^{app}$, the first and second polyacid dissociation constants, respectively, which must obviously be known in order to calculate $[A^{2-}]$, are not necessarily the same in the absence and in the presence of divalent metal ions. Furthermore, one can easily verify that a nonexact choice of these values can lead to macroscopic errors in the evaluation of $A^{2-}$ groups concentration; (3) dialysis equilibrium measurements can in principle give the "exact" (see above) amount of metal ions that are surely not bound at all to the polyelectrolyte backbone; it is not possible however to know the exact fraction of the remaining ions really "site bound" to the polyelectrolyte and that quantity surrounding the polymeric backbone and interacting with it more weakly by long-range electrostatic forces.

Keeping these difficulties in mind, we have calculated the apparent equilibrium constants for the binding reaction at $\alpha = 1.0$; these were found in each case to depend on $R$. We cannot say if this trend has physical significance or if it is fictitious (due, for example, to the omission of the electrostatic potentials and/or activity coefficients). In Table I the corresponding roughly approximate free-energy variations $\Delta G_B°$ ($\Delta G_B°$ is the free-energy value extrapolated to $R = 0$) and the associated $\Delta S$ values are reported.

We are well aware of the fact that our treatment needs some criticisms. First of all, let us consider again the complete process of binding at $\alpha = 1.0$. It is immediately understood that our calorimetric data are comprehensive not only of the second stage (the "pure" binding reaction), but also of the other two stages (partial second dissociation and partial first proton association). A correction for the mentioned dissociation enthalpies should be performed; this is very difficult however for two principal reasons. First, the enthalpy of proton exchange is not a fixed value for each polymer chain, but depends on the dissociation degree of the chain itself; second, it does not seem reasonable to assume that such enthalpy can be insensitive to the presence of bound metal ions. We can say, however, according to enthalpy of protonation data collected in our laboratory,[1] that these corrections must not be able to change considerably the above mentioned $\Delta H_T$ and, of course, the associated $\Delta S$ values.

If we compare the $\Delta S$ with the $\Delta \bar{V}_T$ data (see Table I) we can immediately observe that there is a good (see above) correlation between the $\Delta S$ and $\Delta \bar{V}_T$ trends. If we attribute these variations to the hydration phenomena, it is possible to affirm that, independently of the particular polyacid considered, the number of water molecules lost in the binding reaction by each metal ion decreases in the order $Cu^{2+} > Ni^{2+} > Ba^{2+}$. This fact can be qualitatively related with the decreasing positive $\Delta H_T$ values we obtained passing from $Cu^{2+}$ to $Ni^{2+}$ to $Ba^{2+}$ ions, respectively.

All these considerations do not take into account that in the polymer chain an important role is played by the conformational and configurational situation of each monomeric unity.

In order to better evaluate the influence of local configuration on the thermodynamics of both dissociation and divalent metal ion binding for nearest neighbor carboxylic groups, we are beginning a study of some appropriate "model" monomeric compounds.

*Acknowledgments.* This work has been sponsored by the Italian Consiglio Nazionale delle Ricerche.

The authors are indebted to professor V. Crescenzi for many helpful discussions.

*Supplementary Material Available.* A complete list of dilatometric, calorimetric, and dialysis equilibrium experimental data will appear following these pages in the microfilm edition of this volume of the journal. Photocopies of the supplementary material from this paper only or microfiche (105 × 148 mm, 24× reduction, negatives) containing all of the supplementary material for the papers in this issue may be obtained from the Journals Department, American Chemical Society, 1155 16th St., N.W., Washington, D. C. 20036. Remit check or money order for $3.000 for photocopy or $2.00 for microfiche, referring to code number JPC-74-1486.

## References and Notes

(1) V. Crescenzi, F. Delben, S. Paoletti, and J. Škerjanc, *J. Phys. Chem.*, **78**, 607 (1974).
(2) E. Bianchi, A. Ciferri, R. Parodi, R. Rampone, and T. Tealdi, *J. Phys. Chem.*, **74**, 1050 (1970).
(3) P. L. Dubin and U. P. Strauss, *J. Phys. Chem.*, **74**, 2842 (1970).
(4) V. Crescenzi, F. Delben, F. Quadrifoglio, and D. Dolar, *J. Phys. Chem.*, **77**, 539 (1973).
(5) H. Flaschka, *Mikrochemie*, **39**, 38 (1952).
(6) G. Anderegg, H. Flaschka, R. Sallmann, and G. Schwarzenbach, *Helv. Chim. Acta*, **37**, 113 (1954).
(7) A. J. Begala and U. P. Strauss, *J. Phys. Chem.*, **76**, 254 (1972).
(8) S. Katz and T. G. Ferris, *Biochemistry*, **5**, 3246 (1966).
(9) B. J. Felber, E. M. Hodnett, and N. Purdie, *J. Phys. Chem.*, **72**, 2496 (1968).
(10) The value of $\alpha$ equal to 2 corresponds, in our notations, to complete neutralization of the polydicarboxylic acids.
(11) H. P. Gregor, L. B. Luttinger, and E. M. Loebl, *J. Phys. Chem.*, **59**, 366 (1955).
(12) A. M. Kotliar and H. Morawetz, *J. Amer. Chem. Soc.*, **77**, 3692 (1955).
(13) H. Morawetz, *J. Polym. Sci.*, **17**, 442 (1955).
(14) F. T. Wall and S. J. Gill, *J. Phys. Chem.*, **58**, 1128 (1954).

# Micellar Effects on the Ionization of Carboxylic Acids and Interactions between Quaternary Ammonium Ions and Aromatic Compounds[1]

**Clifford A. Bunton**[*2] **and M. J. Minch**[3]

*Departments of Chemistry, University of California, Santa Barbara, California 93106 and Tulane University, New Orleans, Louisiana 70118*

*(Received November 8, 1973; Revised Manuscript Received April 22, 1974)*

*Publication costs assisted by the U. S. Public Health Service*

The incorporation of carboxylic acids or phenol into cationic micelles of cetyltrimethylammonium bromide, CTABr, increases acidity but quantitative estimates of p$K_a$ changes are complicated because pH values, measured with a glass electrode, are not directly related to proton activity in surfactant solutions. This incorporation was studied by nmr spectroscopy. On a time average, aromatic carboxylate ions are near the micelle surface, with the aromatic ring between adjacent quaternary ammonium head groups, while the acids penetrate more deeply into the micelle. Similar interactions occur between a variety of aromatic compounds and nonmicellar *n*-butyltrimethylammonium ion. The association of aliphatic carboxylate ions with CTABr micelles increases with their chain length, indicating that both hydrophobic and electrostatic factors affect the acidity of incorporated acids.

Incorporation of acids into cationic micelles may increase their dissociation,[4-10] but to date all the oxygen acids examined in this matter have been large molecules (mostly pH indicators) with structures too complicated for any simple estimation of their orientation in micelles, and only limited generalizations have been made. Hartley[4] observed that if the indicator is neutral in one form then the equilibrium will be displaced to the acid side by anionic, and to the alkaline side by cationic, micelles, but that if both forms of the indicator are of opposite sign to the micelle, the direction of displacement depends on specific factors. In the few instances when micellar effects on indicator dissociations were quantitatively determined,[5,8,11] the results indicated that both hydrophobic and electrostatic forces are involved.

Acidities of simpler aromatic and aliphatic carboxylic acids are also increased by incorporation into cationic micelles of hexadecyltrimethylammonium bromide, CTABr, and we relate this increased acidity, by nmr spectral studies, to the time average orientations of the undissociated acid and anion and to their interactions with neighboring surfactant molecules. These results bear directly on recent cautionary comments[12] regarding the interpretation of kinetic results if buffers are used to control hydrogen ion concentration in surfactant solutions; they show that the relative concentration (and reactivity) of buffer species may differ between the micellar and bulk solvent phases, complicating the analysis of any kinetics involving buffer catalysis.

These results also point out the origin of the uncertainties inherent in using pH indicators in the presence of colloids[8,13] or in determining the p$K_a$ of functional groups buried in the interior of macromolecules.[14] They also suggest that considerable caution should be employed when interpreting pH dependent binding between small molecules and proteins.[15] In the earlier work on the effect of anionic micelles on pH[12] it was necessary to consider the distribution of hydrogen ions between water and the micelles, but this should not be a problem with cationic micelles.

We also report nmr spectral data for solutions of nonmicellar quaternary ammonium salts with added aromatic compounds, which support our earlier conclusions[16] about the interactions between ammonium cations and aromatic anions and molecules.

## Experimental Section

*Materials.* Solid carboxylic acids were recrystallized from hot water and dried (≤100°). Acetic and butanoic acid and all inorganic compounds were used without further purification. The purification of CTABr has been described.[16] *n*-Butyltrimethylammonium bromide was prepared from the alkyl bromide and trimethylamine in isopropyl alcohol followed by recrystallization from EtOH–petroleum ether. The nmr spectra were consistent with the assigned structures.

All sodium carboxylates were made from equivalent amounts of the carboxylic acid and carbonate free sodium hydroxide, and were recrystallized from dry ethanol and oven dried (≤100°).

*Nmr Spectra.* The nmr spectra of mixtures of CTABr with various carboxylic acids and their sodium salts in 90% (v/v) $D_2O$–$H_2O$ were determined on an HA-100 nmr spectrometer (probe temperature 31 ± 1°). The nmr spectra of *n*-alkylammonium bromide with various solutes were similarly determined. For some experiments a Varian 1024 channel computer of average transients was used. The HA-100 was locked on water (frequency sweep mode) and all chemical shifts (relative to water) for any one series of samples were recorded as close together in time as possible to avoid changes in the chemical shift of water resulting from temperature fluctuation; for the same reason, the lock was maintained continuously for any one series of samples. The reproducibility of chemical shifts was within 0.01 ppm.

*Acidity Measurements.* The effect of added CTABr on the pH meter readings for buffer solutions (or dilute HCl) was typically determined by dissolving 5.00 g (0.0137 mol) of CTABr in a portion of the buffer solution (50 ml final volume) and adding aliquots of this buffered surfactant solution to 500 ml of solution in a stoppered bottle equipped with a pH electrode under nitrogen. All solutions were made using charcoal filtered deionized water (pH 7 ± 0.5). A Beckman Zeromatic SS-3 pH meter and a

Curtin combination electrode (calomel reference) were used. The temperature was maintained at 25 ± 1°. The pH meter readings ($pH_{obsd}$) were taken about 3 min apart after each addition of CTABr solution, and the pH meter did not drift between additions if the buffer concentration was $10^{-3}$ *M*. With higher buffer concentrations there was no drift after prolonged stirring.

Most $pH_{obsd}$ *vs.* CTABr plots contained 20 points and duplicate plots were always parallel and never separated by greater than 0.1 pH unit. For monobasic buffer solutions with equimolar concentrations of the acid and base species, the $pH_{obsd}$ values before adding CTABr were within 10% (frequently better) of the literature $pK_a$ values for the buffer. The electrode was stored in pH 7 buffer (Curtin) and was washed with distilled water before each experiment. The meter was standardized with the appropriate buffer (pH 7 or 4) before and after each experiment; seldom had the machine drifted, and the drift was always smaller than the change in $pH_{obsd}$ caused by CTABr, and we were concerned only with changes in pH.

## Results and Discussion

*Acidity Measurements in Surfactant Solutions.* The glass electrode is specific for the hydrogen ion, and any change in acid dissociation with added surfactant should be observable with a pH meter. However, ΔpH cannot be interpreted solely in terms of increased buffer dissociation unless the liquid junction potential of the salt bridge remains constant when surfactant is added and surfactants could change the characteristics of the glass electrode itself. In principle[17,18] one can never unequivocally separate these effects, but our observations suggest that the ionization of hydrophobic organic buffer acids is increased by incorporation into cationic micelles and that this is largely responsible for any $pH_{obsd}$[19] change occurring at CTABr concentrations well above its critical micelle concentration, cmc.

The addition of CTABr to hydrophilic buffer solutions only changes pH if the buffers are very dilute and the CTABr concentration is below or near its cmc. Figure 1 indicates that the pH change is negligible if relatively high concentrations ($\geq 0.02$ *M*) of hydrophilic buffers are used; the pH of solutions containing formate, carbonate, phosphate, or acetate buffers remains constant, within experimental error, even in 0.03 *M* CTABr. But more dilute solutions of the same buffers are markedly affected. In these solutions, the addition of small amounts of CTABr increases $pH_{obsd}$ until the CTABr concentration exceeds the cmc (see Table I).

Dilute solutions of strong acids or bases are similarly affected by CTABr concentrations below the cmc (Figure 2); further CTABr causes little effect. This observation is particularly important because this increase in $pH_{obsd}$ must be due to an electrolyte effect on the electrode system. Increasing surfactant concentration below the cmc increases the interfacial concentration of surfactant molecules; above the cmc, all interfaces are effectively saturated and additional surfactant forms micelles.[20,21] For a cationic surfactant such as CTABr, this means that the glass electrode becomes coated with an ionic layer at the cmc and higher CTABr concentrations do little to change this layer. Therefore, if the ionic strength of a buffer solution is very low, addition of CTABr will change $pH_{obsd}$ (until the cmc is reached) because of an electrolyte effect. On the other hand, with high buffer concentration, $pH_{obsd}$ will be nearly constant because the electrode is surrounded by ions regardless of the CTABr concentration. If this explanation is valid, then CTABr should cause little change in $pH_{obsd}$, even with low buffer concentration, if the ionic strength is maintained high with NaCl. This is the case with acetate buffers; see column D, Table I.

All dilute buffers give similar slight increases in $pH_{obsd}$ when CTABr is brought to its cmc and, with strong acids or hydrophilic buffers, $pH_{obsd}$ remained unaltered by additional CTABr. With more hydrophobic buffers, there is a marked reduction in $pH_{obsd}$ at higher CTABr concentrations, and the more hydrophobic the buffer the more dramatic the decrease. Changes in $pH_{obsd}$ for aliphatic carboxylate buffers are given in Figure 3 and for aromatic carboxylate buffers in Figure 4. This $pH_{obsd}$ reduction

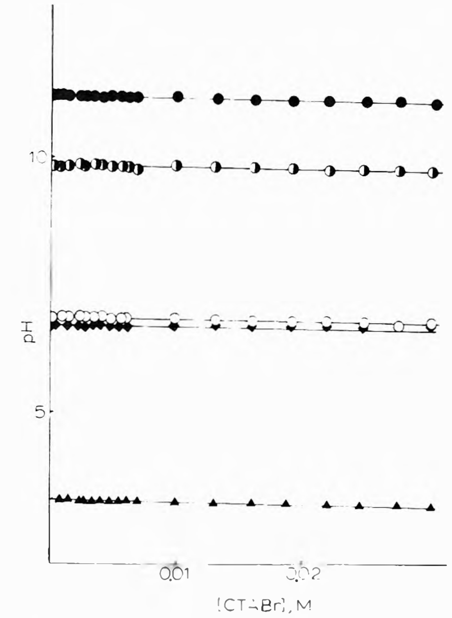

**Figure 1.** Effect of CTABr upon pH of 0.02 *M* hydrophilic buffer solutions: ●, $K_2HPO_4$–$K_3PO_4$; ◑, $NaHCO_3$–$Na_2CO_3$; ○, $KH_2PO_4$–$K_2HPO_4$; ◆ $NH_4OAc$; ▲, formic acid–sodium formate.

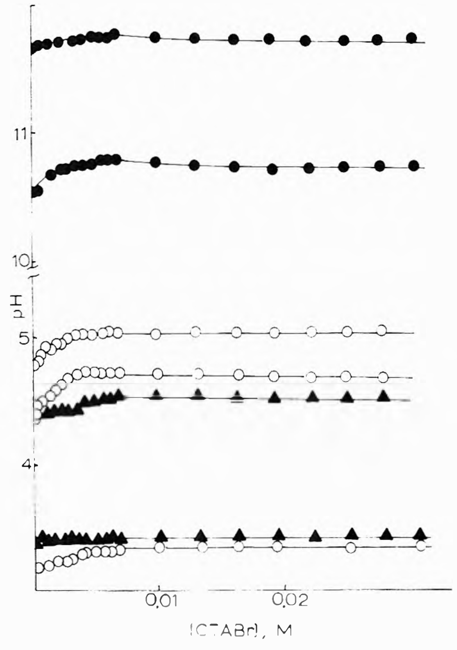

**Figure 2.** Effect of CTABr upon pH of dilute strong acids or bases: ●, $9 \times 10^{-3}$ and $9 \times 10^{-4}$ *M* NaOH; ○ $6.8 \times 10^{-4}$, $5 \times 10^{-5}$, and $10^{-6}$ *M* HCl; ▲, $3 \times 10^{-3}$ and $3 \times 10^{-4}$ *M* *p*-toluenesulfonic acid.

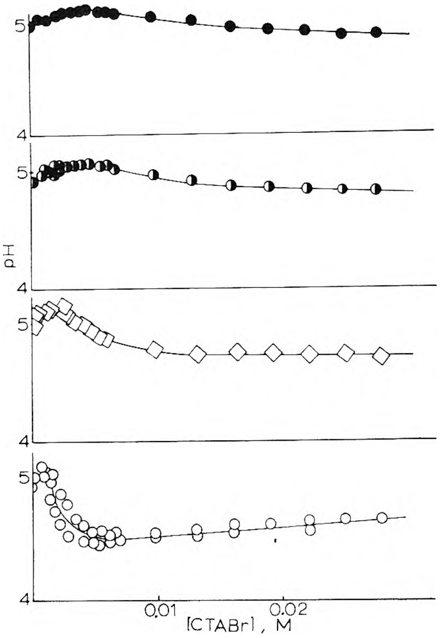

Figure 3. Effect of CTABr upon pH of equimolar aliphatic acid–sodium salt buffers ($10^{-3}$ *M*): ●, acetic; ◑, butanoic; ◇, hexanoic; ○ octanoic acid.

**TABLE I: Effect of CTABr upon the pH of Acetate Buffer Solutions**[a]

| $C_{\mathrm{CTABr}}$, *M* | A | B | C | D | E |
|---|---|---|---|---|---|
| | 4.76 | 4.59 | 4.55 | 4.48 | 6.48 |
| 0.0007 | 4.76 | 4.59 | 4.58 | 4.48 | 6.51 |
| 0.0014 | 4.76 | 4.59 | 4.60 | 4.48 | 6.57 |
| 0.0023 | 4.77 | 4.60 | 4.62 | 4.48 | 6.60 |
| 0.0027 | 4.77 | 4.60 | 4.64 | 4.48 | 6.61 |
| 0.0034 | 4.77 | 4.61 | 4.68 | 4.48 | 6.62 |
| 0.0040 | 4.77 | 4.61 | 4.69 | 4.48 | 6.63 |
| 0.0048 | 4.76 | 4.61 | 4.70 | 4.48 | 6.64 |
| 0.0055 | 4.76 | 4.61 | 4.70 | 4.48 | 6.64 |
| 0.0061 | 4.76 | | 4.70 | 4.49 | 6.64 |
| 0.0067 | 4.77 | 4.60 | 4.69 | 4.49 | 6.64 |
| 0.0099 | 4.76 | 4.58 | 4.65 | 4.49 | 6.60 |
| 0.0131 | 4.75 | 4.57 | 4.62 | 4.48 | 6.58 |
| 0.0162 | 4.75 | 4.54 | 4.61 | 4.48 | 6.53 |
| 0.0192 | 4.75 | 4.53 | 4.59 | 4.49 | 6.51 |
| 0.0221 | 4.76 | 4.52 | 4.58 | 4.48 | 6.50 |
| 0.0250 | 4.75 | 4.52 | 4.58 | 4.48 | 6.48 |
| 0.0278 | 4.75 | 4.51 | 4.56 | 4.49 | 6.48 |
| 0.0305 | 4.76 | 4.51 | 4.55 | 4.49 | 6.50 |

[a] Values of pH measured in the solutions: A, acetic acid, Na acetate (0.1 *M* each); B, acetic acid, Na acetate (0.01 *M* each); C, acetic acid, Na acetate (0.001 *M* each); D, acetic acid, Na acetate (0.001 *M* each), 0.2 *M* NaCl; E, 0.002 *M* ammonium acetate.

must be due to increased acid dissociation. An electrolyte effect is ruled out because there is no decrease in $\mathrm{pH_{obsd}}$ with the strong toluene-*p*-sulfonic acid (Figure 2) even though the hydrophobic tosylate anion is similar to the other aromatic anions in its ionic properties and ability to associate with CTABr.[16] The very low buffer concentration (0.001 *M*) relative to the maximum CTABr concentration (0.03 *M*) also rules out a salt effect on the glass electrode. We will discuss the details of the interaction between carboxylate anions and CTABr with our nmr spectral observations.

Varying the buffer ratio of monocarboxylic acid buffers affects only the pH range and not the relation between

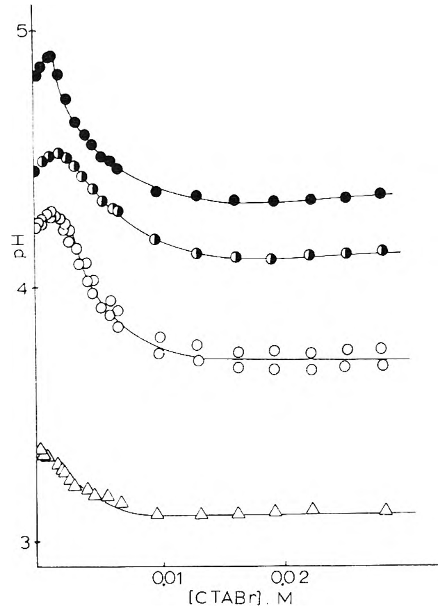

Figure 4. Effect of CTABr upon pH of aromatic acid buffers: ●, 2-phenylpropanoic acid–sodium salt ($10^{-3}$ *M* each); ◑, phenylacetic acid–sodium salt ($10^{-3}$ *M* each); ○, benzoic acid–sodium benzoate ($10^{-3}$ *M* each); △, $3 \times 10^{-3}$ *M* salicylic acid–$1 \times 10^{-3}$ *M* sodium salicylate.

$\mathrm{pH_{obsd}}$ and surfactant concentration, which again distinguishes specific medium effects from increased acid dissociation. The observed pH of a buffer solution containing a monobasic acid HA is given by

$$\mathrm{pH_{obsd}} = \mathrm{p}K_a{}^0 - \log \frac{[\mathrm{HA}]}{[\mathrm{A}^-]} + \log \frac{\gamma\mathrm{A}^-}{\gamma\mathrm{HA}} + E_j \quad (1)$$

where $\gamma\mathrm{A}^-$ and $\gamma\mathrm{HA}$ are molar activity coefficients and $E_j$ is a constant related to the electrode junction potential. For low ionic strength solutions, $E_j$ undoubtedly changes with added CTABr until slightly above the cmc and this change may be partly responsible for the increase in $\mathrm{pH_{obsd}}$ at low CTABr concentrations. If at all CTABr concentrations above the cmc $E_j$ is independent of surfactant concentration, then the change in observed pH is given by eq 2 which contains no direct reference to the buffer ratio.

$$\Delta\mathrm{pH_{obsd}} = \Delta\mathrm{p}K_a{}^0 + \Delta \log \frac{\gamma\mathrm{A}^-}{\gamma\mathrm{HA}} \quad (2)$$

Table II shows that $\mathrm{pH_{obsd}}$ decreases by about 0.5 pH unit when CTABr is added to benzoic acid–sodium benzoate buffer, regardless of the buffer ratio, suggesting that benzoic acid is a stronger acid when incorporated into CTABr micelles.

Table III shows that the first and second ionizations of hydrophilic aliphatic dicarboxylic acids (*e.g.*, adipic and sebacic acid) are similarly enhanced by CTABr micelles, but the second ionization of phthalic acid is decreased by CTABr (Figure 5) because the carboxy groups of phthalic acid are fixed and the second ionization must be accompanied by considerable reorientation of the whole ion if both anionic groups are to become equally exposed to the solvent, resulting in a loss of beneficial hydrophobic interaction between the aromatic group and surfactant. More flexible aliphatic diacids can adopt partial loop-like conformations with both anionic ends exposed to solvent while the methylene chain is submerged in the micelle. Alternatively these hydrophilic solutes may be stretched out along the micelle–water interface.

**TABLE II: Effect of CTABr upon the pH of Benzoate Buffer**[a]

| $C_{CTABr}$, M | Buffer A | Buffer B | Buffer C | Buffer D |
|---|---|---|---|---|
| | 3.47 | 4.21 | 4.67 | 7.10 |
| 0.0007 | 3.59 | 4.24 | 4.68 | 7.09 |
| 0.0014 | 3.61 | 4.26 | 4.69 | 7.11 |
| 0.0023 | 3.62 | 4.22 | 4.65 | 7.13 |
| 0.0027 | 3.59 | 4.18 | 4.60 | 7.13 |
| 0.0034 | 3.54 | 4.10 | 4.54 | 7.11 |
| 0.0040 | 3.51 | 4.02 | 4.49 | |
| 0.0048 | 3.48 | 3.98 | 4.44 | |
| 0.0055 | 3.45 | 3.92 | 4.39 | 7.07 |
| 0.0061 | 3.42 | 3.89 | 4.36 | |
| 0.0067 | 3.41 | 3.84 | 4.32 | 7.03 |
| 0.0099 | 3.35 | 3.74 | 4.20 | 6.91 |
| 0.0131 | 3.32 | 3.70 | 4.14 | 6.86 |
| 0.0162 | 3.31 | 3.68 | 4.11 | |
| 0.0192 | 3.30 | 3.67 | 4.10 | 6.78 |
| 0.0221 | 3.30 | 3.67 | 4.09 | |
| 0.0250 | 3.30 | 3.68 | 4.09 | |
| 0.0278 | 3.31 | 3.68 | 4.09 | |

[a] Values of pH measured in the solutions: A, 0.002 *M* benzoic acid; B, benzoic acid, Na benzoate (0.001 *M* each); C, 0.001 *M* benzoic acid, 0.002 *M* Na benzoate; D, 0.001 *M* Na benzoate.

**TABLE III: Effect of CTABr upon the pH of Dibasic Acid Buffer**[a]

| $C_{CTABr}$, M | Buffer A | Buffer B | Buffer C | Buffer D |
|---|---|---|---|---|
| | 4.48 | 5.57 | 4.51 | 5.63 |
| 0.0007 | 4.53 | 5.69 | 4.65 | 5.79 |
| 0.0014 | 4.57 | 5.71 | 4.53 | 5.88 |
| 0.0023 | 4.60 | 5.72 | 4.39 | 5.90 |
| 0.0027 | 4.60 | 5.69 | 4.25 | 5.90 |
| 0.0034 | 4.57 | 5.65 | 4.13 | 5.88 |
| 0.0040 | 4.53 | 5.61 | 4.08 | 5.85 |
| 0.0048 | 4.50 | 5.59 | 4.01 | 5.80 |
| 0.0055 | 4.49 | 5.55 | 3.98 | 5.74 |
| 0.0061 | 4.47 | 5.52 | 3.96 | 5.69 |
| 0.0067 | 4.46 | 5.50 | 3.94 | 5.64 |
| 0.0099 | 4.39 | 5.40 | 3.92 | 5.46 |
| 0.0131 | 4.35 | 5.35 | 3.94 | 5.38 |
| 0.0192 | 4.31 | 5.30 | 3.98 | 5.33 |
| 0.0221 | 4.31 | 5.30 | 4.00 | 5.32 |
| 0.0250 | 4.31 | 5.29 | 4.02 | 5.32 |
| 0.0278 | 4.32 | 5.29 | 4.04 | 5.35 |

[a] Values of pH measured in the solutions: A, 0.002 *M* adipic acid, 0.001 *M* NaOH; B, 0.002 *M* adipic acid, 0.003 *M* NaOH; C, 0.002 *M* sebacic acid, 0.001 *M* NaOH; D, 0.002 *M* sebacic acid, 0.003 *M* NaOH.

The results in Table IV show that $pH_{obsd}$ is decreased by addition of CTABr to phenoxide buffer. Additional evidence for strong interactions between the cationic head groups and the aromatic ring are shown by the effects of phenols and phenoxide ions upon CTABr-catalyzed decarboxylation.[16b]

In a related experiment the absorbance of *p*-nitrophenol at pH 7.24 (phosphate buffer) increased from 0.757 to 0.832 ($\lambda_{max}$ 396 nm) on the addition of 0.055 *M* CTABr. However CTABr slightly increases rather than decreases, the pH of pyridine-HCl buffers.

*Nmr Spectral Studies.* The interaction between CTABr and incorporated hydrophobic buffers increases when these buffers ionize, with very obvious alterations in the nmr spectra of aqueous mixtures of CTABr and carboxylic acids. The nmr spectrum of CTABr (0.02 *M* in 90% $D_2O$) has a sharp singlet ($\delta_{HOD}^{N\text{-}Me}$ = 1.51 ppm upfield from water) attributable to the nine *N*-methyl protons, a broad peak ($\delta_{HOD}^{C\text{-}CH_2}$ = 3.37-3.38 ppm) for the 14 carbon chain methylenes, a triplet ($\delta_{HOD}^{C\text{-}CH_3}$ = 3.78 ppm) for the carbon chain methyl, and a weak irregular triplet ($\delta_{HOD}^{N\text{-}CH_2}$ ≈ 1.4) for the *N*-methylene proton resonance.[23] These chemical shifts are only slightly dependent upon CTABr concentration and at the low concentrations used in many experiments (0.01-0.07 *M*), they are essentially constant.[16,25] But at higher CTABr concentrations, the *N*-methyl and *C*-methylene protons shift slightly downfield (Figure 6). Organic buffer acids change the shape and chemical shifts of some of the peaks in the nmr spectrum of CTABr, especially if the buffer is an aromatic carboxylic acid. For example, the addition of un-ionized benzoic or *p*-toluic acid causes small upfield shifts in the *N*-methyl proton signal and in part of the signal for the *C*-methylene

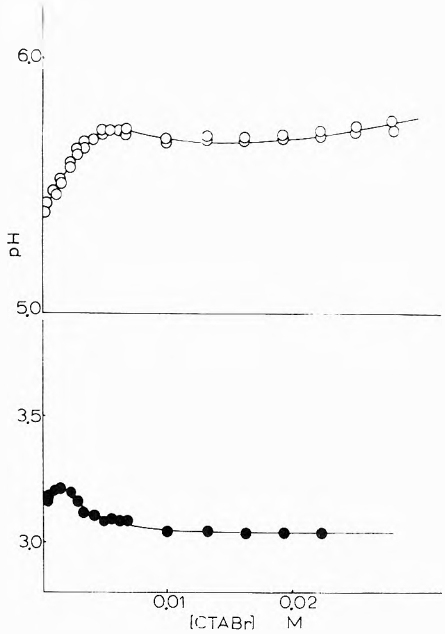

Figure 5. Effect of CTABr upon pH of 2 × $10^{-3}$ *M* phthalic acid with added NaOH: ○, 1.5 × $10^{-3}$ *M* NaOH; ●, 1.0 × $10^{-3}$ *M* NaOH.

**TABLE IV: Effect of CTABr upon the pH of Phenoxide Buffer**[a]

| $C_{CTABr}$, M | $pH_{obsd}$ A | $pH_{obsd}$ B |
|---|---|---|
| 0.0000 | 10.19 | 9.44 |
| 0.0003 | 10.18 | 9.46 |
| 0.0007 | 10.19 | 9.49 |
| 0.0014 | 10.20 | 9.50 |
| 0.0023 | 10.20 | 9.50 |
| 0.0027 | 10.20 | 9.50 |
| 0.0034 | 10.19 | 9.49 |
| 0.0040 | 10.18 | 9.47 |
| 0.0048 | 10.17 | 9.45 |
| 0.0055 | 10.14 | 9.42 |
| 0.0061 | 10.13 | 9.40 |
| 0.0067 | 10.11 | 9.38 |
| 0.0099 | 10.04 | 9.28 |
| 0.0131 | 9.98 | 9.21 |
| 0.0162 | 9.92 | 9.17 |
| 0.0192 | 9.90 | 9.14 |
| 0.0221 | 9.88 | 9.12 |
| 0.0250 | 9.87 | 9.10 |
| 0.0278 | 9.86 | 9.10 |
| 0.0305 | 9.84 | 9.10 |

[a] At 25.0°. A, 0.01 *M* phenol + 0.0075 *M* NaOH; B, 0.02 *M* phenol + 0.0072 *M* NaOH.

**TABLE V: Effect of Undissociated Acids on the Nmr Spectrum of CTABr**[a]

| Acid | $10^2C_{\text{acid}}$, $M$ | $\delta_{\text{HOD}}^{\text{N-Me}}$,[d] ppm | $\delta_{\text{HOD}}^{\text{C-CH}_2(1)}$,[e] ppm | $\delta_{\text{HOD}}^{\text{C-CH}_2}$, ppm | $\delta_{\text{HOD}}^{\text{C-CH}_2(2)}$,[f] ppm |
|---|---|---|---|---|---|
| Benzoic[b] | 0.0 | 1.51 | | 3.36[g] | |
| | 1.0 | 1.53 | | 3.37[g] | |
| | 2.0 | 1.55 | 3.36 | | 3.42 |
| | 3.1 | 1.58 | 3.38 | | 3.50 |
| | 5.2 | 1.62 | 3.37 | | 3.59 |
| | 6.2 | 1.64 | 3.37 | | 3.63 |
| | 7.3 | 1.65 | 3.36 | | 3.64 |
| | 8.3 | 1.66 | 3.38 | | 3.70 |
| Toluic[c] | 0.0 | 1.52 | | 3.36[g] | |
| | 0.1 | 1.52 | | 3.37[g] | |
| | 0.2 | 1.56 | | 3.40[g] | |
| | 0.4 | 1.58 | 3.40 | | 3.44 |
| | 0.6 | 1.59 | 3.38 | | 3.47 |
| | 0.8 | 1.58 | 3.40 | | 3.45 |

[a] Chemical shifts upfield from water resonance in 90% $D_2O$ (v/v). [b] With 0.031 $M$ CTABr. [c] With 0.017 $M$ CTABr. [d] Chemical shift of CTABr *N*-methyl protons. [e] Chemical shift of CTABr low-field *C*-methylene signal. [f] Chemical shift of upfield *C*-methylene signal. [g] Before C-methylene signal separates; when the concentration of benzoic acid exceeds that of CTABr the *C*-methyl signal is obscured by the *C*-methylene signal.

**TABLE VI: Effect of Benzoic Acid–Sodium Benzoate Buffers on the Nmr Spectrum of CTABr**[a]

| $10^2C$ benzoic acid, $M$ | $10^2C$ benzoate ion, $M$ | $C_{\text{ion}}/C_{\text{acid}}$ | $\delta_{\text{C-Me}}^{\text{N-Me}}$,[b] ppm | $\delta_{\text{C-CH}_3}^{\text{C-CH}_2(1)}$,[c] ppm | $\delta_{\text{C-CH}_3}^{\text{C-CH}_2(2)}$,[d] ppm |
|---|---|---|---|---|---|
| 4.57 | 0.00 | 0.00 | −2.20 | −0.38 | −0.25 |
| 4.11 | 0.45 | 0.11 | −2.20 | −0.38 | −0.23 |
| 3.66 | 0.90 | 0.25 | −2.18 | −0.38 | −0.22 |
| 3.20 | 1.35 | 0.42 | −2.18 | −0.38 | −0.20 |
| 2.74 | 1.80 | 0.66 | −2.15 | −0.39 | −0.20 |
| 2.29 | 2.25 | 0.98 | −2.13 | −0.38 | −0.19 |
| 1.37 | 3.14 | 2.29 | −2.11 | −0.39 | −0.16 |
| 0.91 | 3.59 | 3.95 | −2.10 | −0.39 | −0.17 |
| 0.46 | 4.04 | 8.78 | −2.09 | −0.40 | −0.17 |
| 0.00 | 4.49 | 8.78 | −2.08 | −0.40 | −0.18 |

[a] Chemical shifts downfield from *C*-methyl signal of CTABr in 90% $D_2O$ (v/v). [b] Chemical shift of CTABr *N*-methyl protons. [c] Chemical shift of low-field CTABr *C*-methylene protons. [d] For high-field *C*-methylene protons.

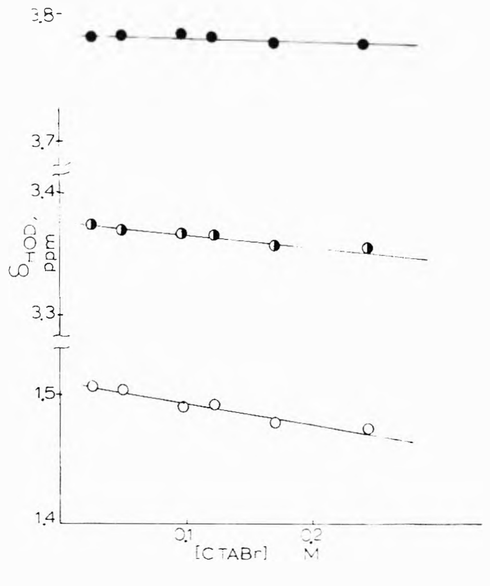

**Figure 6.** Concentration dependence of CTABr chemical shifts (upfield from water): ●, *C*-methyl; ◑, *C*-methylene; and ○, *N*-methyl protons.

protons. The changes in the nmr spectra of 0.031 $M$ CTABr with increasing benzoic acid and of 0.017 $M$ CTABr with toluic acid are given in Table V where the chemical shifts are reported as ppm upfield from the water peak.[23,26]

The changes in the nmr spectra of 0.065 $M$ CTABr with various ratios of sodium benzoate–benzoic acid are given in Table VI. The concentration of aromatic compound was constant (0.045 $M$) and was less than that of CTABr so that the surfactant *C*-methyl proton resonance was clearly measurable and all the chemical shifts could be reported relative to it, thereby avoiding uncertainties due to changes in the HOD reference frequency with added salt. The *N*-methyl protons are shifted further upfield by benzoate ion than by benzoic acid, indicating that association between the aromatic ring and the cationic head groups is facilitated by charge neutralization. The chemical shift changes become more pronounced upon ionization because repulsive electrostatic forces are replaced by attractive forces, decreasing the average distance between the aromatic molecule and the $CTA^+$ head groups, and strongly suggesting that the ionization of aromatic carboxylic acids is enhanced by a cationic micelle because it stabilizes the whole micelle–buffer aggregate.

Both aromatic and aliphatic carboxylate ions cause an upfield shift of the CTABr *N*-methyl proton signals (Figure 7), and it is similar (~0.1 ppm) for all the aliphatic ions, and nearly four times as large for all the aromatic ions.[27] The shift changes caused by the aliphatic ions are due to the electrostatic field of the carboxylate group and to exclusion of solvent. The larger upfield shift induced by the aromatic ions is due to the anisotropy of the aromatic ring. This ring current effect has quite precise geometrical requirements,[28] and only those surfactant protons situated in the field of the ring are substantially shifted. Because only the signals for the *N*-methyl and some of the methylene protons are shifted upfield, the buffer molecules must have a time-average location close to the micelle surface.

probably with the aromatic moiety moving freely in and out of the Stern layer but with an average location between the cationic head groups of adjacent surfactant ions, as proposed for the incorporation of sodium arene sulfonates into CTABr micelles.[16] Ericksson and Gillberg[25] have shown by nmr that polar aromatic compounds such as nitrobenzene are solubilized in the Stern layer of CTABr micelles. Figure 7 also shows that all the aromatic carboxylate ions give about the same upfield shift when the aromatic ion concentration is less than or similar to that of CTABr, *i.e.*, when only a few aromatic ions are incorporated into any micelle. We take this to imply that despite their different structures, all these aromatic ions have very similar average locations in the micelle. Because sodium benzoate, phenylacetate and 2-phenylpropionate all give similar *N*-methyl proton shifts, their aromatic rings must be similarly located despite differences in charge neutralization between the $-N^+(CH_3)_3$ and $-CO_2^-$ groups, and in the van der Waals interactions. Possible arrangements are I and II.

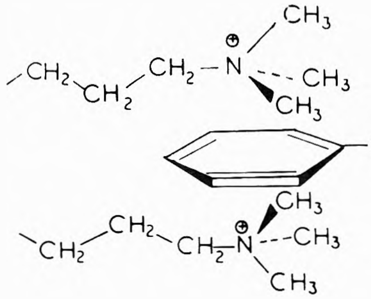

I

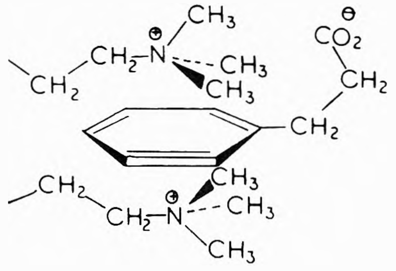

II

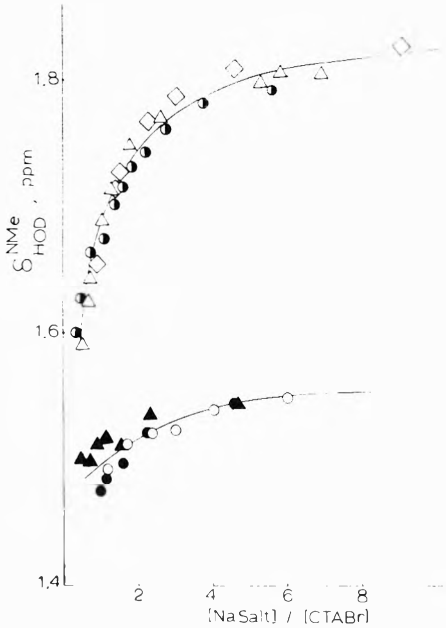

**Figure 7.** Concentration dependence of the CTABr *N*-methyl proton chemical shift (upfield from water) with 0.2 *M* sodium salts: ◑, phenylacetate; △, benzoate; ◇, 2-phenylpropanoate; ▲ butanoate; ●, acetate; ○, pivalate.

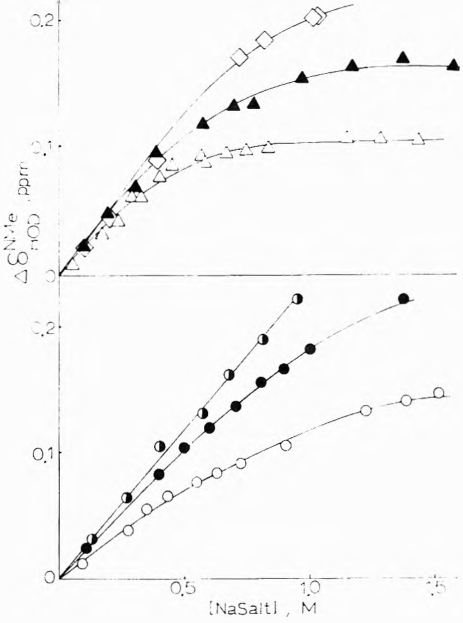

**Figure 8.** Upfield shift of the *N*-methyl proton signals of *n*-butyltrimethylammonium bromide (relative to the *C*-methyl proton signal) with sodium salts: ◇, *p*-methylphenoxide; ▲, toluate; △, tosylate; ◑, phenoxide; ●, benzoate; ○ benzenesulfonate.

Similar associations between quaternary ammonium ions and aromatic compounds have been established for both micellar[16,29] and nonmicellar[30-33] systems and are probably very common; for example, nonmicellized quaternary ammonium cations associate with aromatic anions in aqueous solution. Various aromatic anions shift the *N*-methyl proton signal of *n*-butyltrimethylammonium bromide (0.145 *M* in 90% v/v $D_2O$) upfield, relative to the *C*-methyl proton signal (Figure 8), and these relative chemical shift changes, $\Delta\delta_{C\text{-Me}}^{N\text{-Me}}$, give linear plots of $1/\Delta\delta_{C\text{-Me}}^{N\text{-Me}}$ *vs.* $1/C_{\text{Na salt}}$ consistent with the association equilibrium constants given in Table VII. These association constants are small and not of high precision (for both theoretical and experimental reasons[34]) but the data indicate association between the aromatic ring and the $-^+N(CH_3)_3$ group. Similar observations were made of changes in the proton chemical shift of $(CH_3)_4NBr$ relative to the HOD frequency, an addition of benzene and various undissociated phenols (Figure 9). $[(CH_3)_3N_4Br]$ = 0.14 *M* except for the experiments with resorcinol where 0.24 *M* $(CH_3)_4NBr$ was used. Electron-releasing substituents increase the relative shifts, suggesting that the association also increases although possible effects upon the HOD frequency complicate any analysis; however, saturation of the solution with benzene has no effect. These observations are consistent with those made on the association of the relatively hydrophobic tri-*p*-anisylmethyl carbocation with phenols.[35] Although these associations may be induced in part by the structure of water,[36] the geometries of these association complexes suggest that dispersion effects are involved; for example, the relative

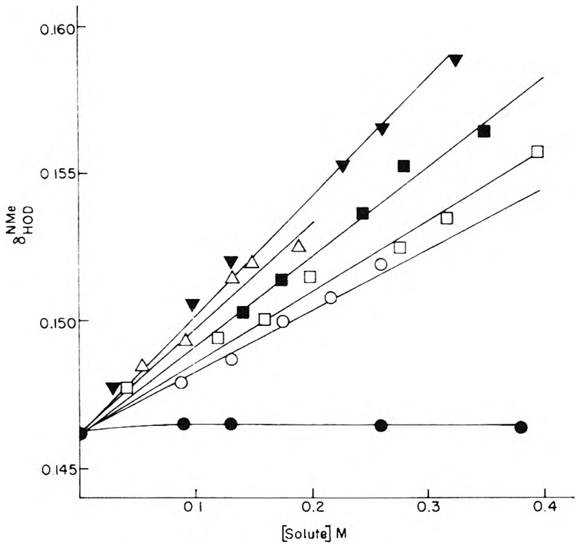

Figure 9. Effect of aromatic compounds on the proton chemical shift of $(CH_3)_4NBr$ relative to HOD: ●, benzene (saturated); □, phenol; ▼, pyrogallol; △, catechol; ■, resorcinol; ○, phloroglucinol.

**TABLE VII: Equilibrium Constants for the Association between *n*-Butyltrimethylammonium Bromide and Aromatic Anions**[a]

| Compound | $K_{assoc}$, $M^{-1}$ | $\Delta_{max}$,[b] ppm |
|---|---|---|
| Sodium tosylate | 2.5 | 0.146 |
| Sodium *p*-toluate | 1.3 | 0.275 |
| Sodium benzenesulfonate | 0.61 | 0.302 |
| Sodium benzoate | 0.27 | 0.870 |
| Sodium *p*-methylphenoxide | 0.24 | 1.000 |
| Sodium phenylacetate | 0.16 | 1.639 |

[a] For 0.145 *M* *n*-butyltrimethylammonium bromide with 0.0 to 1.0 *M* Na salts at 31°. [b] Maximum change in the chemical shift of the *N*-methyl proton signal (relative to *C*-methyl) predicted by the intercepts of double reciprocal plots.

chemical shifts of *N*-methyl protons (Figure 9) increase with substitution of hydrophilic, but electron-releasing hydroxyl groups. (Phloroglucinol appears to be an exception to this generalization, but we had solubility problems with this compound, and these data are less reliable than the others.)

It also seems that ion pairing in water does not require that direct contact charge neutralization be all important. Indeed the suggested structures permit effective solvation of the anionic or polar oxygens, and the nmr results show the partially positive *N*-methyl protons interacting with the aromatic π system. Because some of the virtual electronic oscillators of the aromatic ring have relatively low excitation energies, this type of interaction should be stronger than interactions between quaternary ammonium ions and saturated carboxylate ions of similar volumes. For this reason aromatic compounds interact with CTABr micelles more strongly than do aliphatic compounds of similar volume;[16,25] similarly acid dissociations of aromatic acids are more enhanced by cationic micelles.

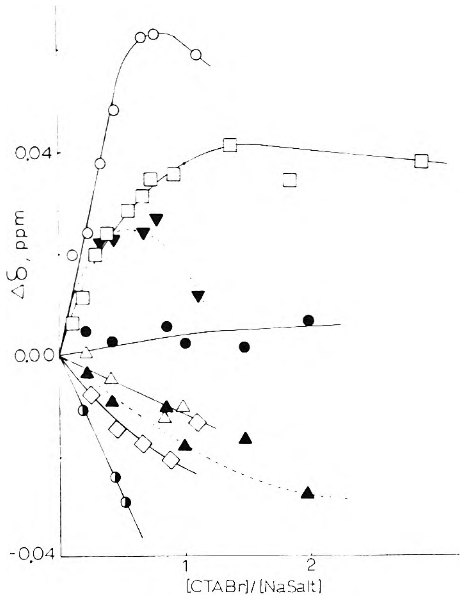

Figure 10. Effect of CTABr on the chemical shift of the aliphatic protons of sodium salts: ○ and ▼ for α and β protons (respectively) of 2-phenylpropanoate; □, phenylacetate; ●, △ and ▲ for α, β, and γ protons of *n*-butanoate; ◇, acetate; ◑, pivalate. Lines drawn arbitrarily.

**TABLE VIII: Salt Effects on the Nmr Spectrum of CTABr**[a]

| Salt | $C_{salt}$, *M* | $W_{1/2}^{N\text{-}Me}$,[b] Hz | $\delta_{C\text{-}Me}^{N\text{-}Me}$,[c] ppm |
|---|---|---|---|
| | | 2.5 | −2.28 |
| $NaNO_3$ | 0.13 | 5 | −2.26 |
| | 0.32 | 6 | −2.25 |
| | 0.59 | 6 | −2.24 |
| | 0.88 | 9 | −2.24 |
| NaOAc | 0.11 | 2 | −2.28 |
| | 0.54 | 3 | −2.28 |
| | 0.99 | 4 | −2.27 |
| | 1.37 | 3 | −2.27 |
| $Na_2SO_4$ | 0.07 | 5 | −2.28 |
| | 0.16 | 2 | −2.28 |
| | 0.21 | 4 | −2.28 |
| | 0.39 | 4 | −2.29 |
| | 0.56 | 3 | −2.26 |
| | 0.73 | 3 | −2.26 |
| | 0.94 | 3 | −2.30 |
| | 1.30 | 3 | −2.27 |
| NaBr | 0.32 | 3 | −2.32 |
| | 0.38 | 5 | −2.33 |
| | 0.59 | 4 | −2.35 |
| | 0.63 | 5 | −2.33 |
| | 0.76 | 4 | −2.35 |
| | 1.22 | 7 | −2.39 |

[a] In 90% $D_2O$ (v/v). [b] Width at half-height of *N*-methyl proton signal. [c] Chemical shift of *N*-methyl signal, downfield from *C*-methyl signal.

In micellar systems, added compounds cause large nmr spectral changes only when they are hydrophobic enough to be taken into the micelle, and hydrophilic inorganic electrolytes cause only small changes in the nmr spectrum of 0.04 *M* CTABr in 90% $D_2O$; both the *N*-methyl and *C*-methylene peaks are broadened and the former is moved either up or down field (relative to the *C*-methyl signal) depending on the nature of the added ion. Some salt effects on the chemical shift and width at half-height ($W_{1/2}$) of the *N*-methyl peak are given in Table VIII. High concentrations of salts change the size and shape of cationic micelles specifically,[37,38] and could give the small nmr spectral changes in Table VIII, which are produced only by high salt concentrations.

The large nmr changes caused by low concentrations of hydrophobic buffers are due to specific association between buffer and surfactant molecules and, for this reason, the nmr spectra of the hydrophobic buffers are sensitive to the buffer–CTABr concentration ratio. The changes in the methyl and methylene proton signals of several sodium carboxylates in various concentrations of CTABr are shown in Figure 10. The chemical shift changes are reported as $\Delta\delta$ (the difference in chemical shift of the *N*-methyl protons relative to water measured with and without CTABr). These values were not corrected for any change in the water resonance frequency, but this problem was minimized by using the same concentration of sodium carboxylate for any one series. A positive $\Delta\delta$ value corresponds to an upfield shift. Although, at first glance, Figure 10 seems to represent a medley of specific effects, some generalizations can be made. The methylene and methyl proton signals of aromatic compounds are shifted well upfield, with a maximum shift when the salt and surfactant concentrations are similar. The methyl protons of acetate and pivalate are shifted downfield as are the $\beta$ and $\gamma$ protons of sodium butanoate. For the latter compound, the $\alpha$ hydrogens are shifted slightly upfield. Because even the nmr spectrum of a hydrophilic ion such as acetate changes with CTABr concentration, it seems that all carboxylate ions interact with CTABr micelles.

In an earlier study of the interactions between sodium arenesulfonates and CTABr, we reported that the signal of the aromatic protons is shifted upfield, with the maximum shift occurring when arenesulfonate and CTABr are in equal concentration.[16] The ortho and meta proton signals of sodium benzoate are shifted upfield and, as for sodium tosylate,[16] the meta proton signal is maximally shifted when the benzoate and $CTA^+$ ions have one-to-one stoichiometry. These chemical shifts, relative to the resonance frequency of water, are given in Figure 11, with the chemical shifts of the aromatic protons of the corresponding undissociated acids. The chemical shifts of the acid are downfield of the corresponding shifts of the anion because the neutral aromatic molecule is on the average more deeply buried in the micelle because hydration is less important with the acid.

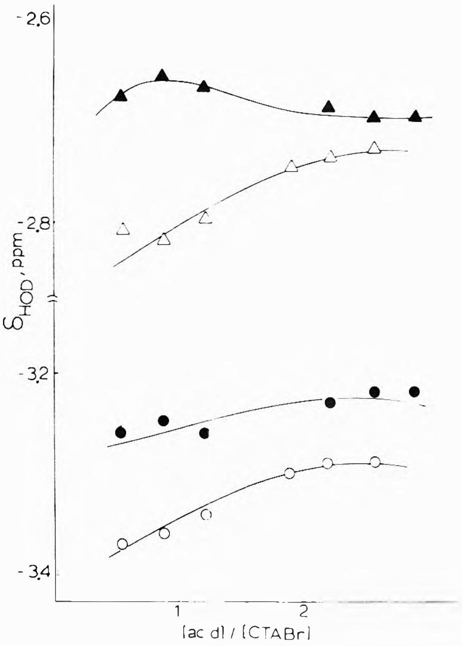

**Figure 11.** Effect of CTABr on the chemical shift of the meta–para (triangles), and ortho protons (circles) of $3 \times 10^{-2}$ *M* benzoic acid, as the un-ionized acid and with fivefold excess NaOH (open and filled symbols, respectively). Chemical shifts measured downfield from water.

Taken altogether, the nmr results show that the average sites of incorporation of aromatic acids and their anions differ, with the anion apparently more exposed to water than the neutral molecule, but the "average location" suggested by nmr spectroscopy cannot be unambiguously described in terms of an average penetration depth. Observed nmr shifts are related to penetration depth only if the chemical shifts corresponding to the "fully in" and "fully out" states and the time spent in each state are known. By itself, the large upfield shift of the *N*-methyl protons of CTABr is no certain indicator of penetration depth because close association between the cationic head group and an aromatic anion would give a large spectral change without deep penetration, while a more deeply penetrating neutral molecule may cause little spectral change if its association with surfactant is weaker.

## Conclusions

The addition of micellized CTABr increases the acid dissociation of carboxylic acids, especially hydrophobic ones. A precise determination of this increase is difficult because surfactant alters the response of the glass electrode, but a reasonable estimate (based on the shape of pH *vs.* CTABr concentration plots at several ionic strengths) is that the p$K_a$ of a very hydrophobic acid is decreased by 0.5 p$K$ unit. Less hydrophobic acids are less affected. This increased acidity is not merely due to charge neutralization; it stems from a stabilization of the whole micelle which accompanies acid ionization. There are several lines of evidence to support this viewpoint.

(1) Only hydrophobic acids are appreciably affected, but if charge neutralization was the only factor, all carboxylic acids would be equally affected by CTABr concentrations high enough to ensure interaction (the nmr data in Figure 10 suggest that this condition is met even for acetate ion).

(2) The second ionization of phthalic acid is inhibited by CTABr micelles. This cannot be explained solely on the basis of charge neutralization but is consistent with the loss of hydrophobic interactions that must accompany the formation of phthalate dianion, which must reside very near the micellar surface.

(3) Hydrophobic acid anions interact with $CTA^+$ ions more strongly than do undissociated acids. Increased line broadening upon ionization indicates that ionization leads to increased van der Waals' association between surfactant molecules.

This study was focused on the effect of cationic micelles on the dissociation of carboxylic acids but certain conclusions can be drawn for other systems. For example, acid dissociations may be affected by hydrophobic interactions with polyelectrolytes, liquid crystals, or proteins with consequences for the pH dependence of macromolecular conformations and reactivity. Considerable caution must be exercised in using so-called "intrinsic p$K_a$'s" when interpreting such phenomena. In addition interactions between aromatic molecules and ions and nonmicellized quaternary ammonium ions are important and appear to involve interactions between the cation and the aromatic $\pi$ cloud.

*Acknowledgments.* We acknowledge helpful discussions with Dr. John M. Brown.

## References and Notes

(1) Support of this work by the National Science Foundation, the Arthritis and Metabolic Diseases Institute of the USPHS, the Research Corporation, and Tulane University is gratefully acknowledged.

(2) Address correspondence to University of California.

(3) USPHS Postdoctoral Fellow.

(4) G. S. Hartley, *Trans. Faraday Soc.*, **30**, 444 (1934).

(5) E. J. Fendler and J. H. Fendler, *Advan. Phys. Org. Chem.*, **8**, 271 (1970).

(6) G. S. Hartley and J. W. Roe, *Trans. Faraday Soc.*, **36**, 101 (1949).

(7) T. Krishnappa, K. S. Doss, and B. S. Rao, *Proc. Indian Acad. Sci.*, **23**, 47 (1946).

(8) C. F. Hiskey and T. A. Downey, *J. Phys. Chem.*, **58**, 835 (1954).

(9) M. T. A. Behme and E. H. Cordes, *J. Amer. Chem. Soc.*, **87**, 260 (1965).

(10) E. L. Colichman, *J. Amer. Chem. Soc.*, **73**, 3385 (1951).

(11) L. K. J. Tong and M. C. Glesmann, *J. Amer. Chem. Soc.*, **79**, 4305 (1957).

(12) C. A. Bunton and B. Wolfe, *J. Amer. Chem. Soc.*, **95**, 3742 (1973).

(13) S. P. L. Sorensen, *Biochem. Z.*, **21**, 215 (1929).

(14) C. Tanford, *Advan. Protein Chem.*, **17**, 70 (1962).

(15) For example, see U. Kragh-Hansen and J. V. Moller, *Biochim. Biophys. Acta*, **295**, 438, 447 (1973).

(16) (a) C. A. Bunton, M. Minch, J. Hidalgo, and L. Sepulveda, *J. Amer. Chem. Soc.*, **95**, 3262 (1973); (b) C. A. Bunton in "Reaction Kinetics in Micelles," E. H. Cordes, Ed., Plenum Press, New York, N. Y., 1973.

(17) R. G. Bates, "Determination of pH. Theory and Practice," Wiley, New York, N. Y., 1964.

(18) G. Eisenmann, Ed., "Glass Electrodes for Hydrogen and Other Cations," Marcel Dekker, New York, N. Y., 1967.

(19) By $pH_{obsd}$ we mean the phenomenological pH;[17] *i.e.*, the conventional pH meter reading of a stable machine standardized with NBS standard buffer solutions.

(20) K. Shinoda, T. Nakagawa, B.-I. Tamamushi, and T. Isemura, "Colloidal Surfactants," Academic Press, New York, N. Y., 1963.

(21) The cmc of CTABr is $7.8 \times 10^{-4}$ *M*; *cf.* ref 22.

(22) E. W. Anacker, R. M. Ruch, and J. S. Johnson, *J. Phys. Chem.*, **68** 81 (1964).

(23) The differences in signal shape and integrated area make this assignment unambiguous and, except for the *N*-methylene signal, all the peaks are clearly separated so that any substantial change in their chemical shift can be unambiguously measured. The *N*-methylene proton signal is very broad because of spin–spin coupling by adjacent protons and (possibly) quadrupole coupling by the nitrogen. In some solutions it is also partially covered by the *N*-methyl signal (or its spinning sideband) so its chemical shift changes were not measurable in these experiments.

Internal reference compounds, *e.g.*, NaDDS, may perturb micellar structure, and therefore were not used. All chemical shifts were measured relative to the HOD signal which could be slightly sensitive to temperature and large changes in electrolyte concentration, and they are reported relative to this signal. However we confine our discussion to the relative chemical shift changes of different protons in the same molecule or to cases where the chemical shift changes are very much larger than any expected shifts in the HOD peak.[24] In addition the surfactant concentrations used in most of our experiments were much lower than the concentrations for which shifts in the HOD frequency have been observed.

(24) J. N. Shoolery and B. Alder, *J. Chem. Phys.*, **23**, 805 (1955); J. C. Hindman, *ibid.*, **36**, 1000 (1962); V. H. G. Hertz and W. Spalthoff, *Z. Elektrochem.*, **63**, 1096 (1959).

(25) J. C. Eriksson and G. Gillberg, *Acta Chem. Scand.*, **20**, 2019 (1966).

(26) There is no change in the HOD frequency, relative to that of 0.028 *M* sodium 3-(trimethylsilyl)-1-propanesulfonate, upon the addition of benzoic acid to 90% (v/v) $D_2O$–$H_2O$ up to saturation in the absence of CTABr. This internal reference may not be satisfactory in the presence of CTABr because this sulfonate ion could interact strongly with the cationic micelle.[23] However the addition of 0.07 *M* benzoic acid and 0.095 *M* CTABr to HOD changes its chemical shift relative to the reference by <0.1 ppm, which is a small effect relative to those which we discuss, and is almost certainly caused by a change in the chemical shift of the reference in the presence of CTABr.[16a] The fact that the low field portion of the C-methylene signal ($\delta_{HOD}{}^{C-CH_2(1)}$) of CTABr does not change with added benzoic acid suggests that the HOD is constant under these conditions. This conclusion is consistent with the insensitivity of the HOD frequency to low concentrations of nonmicellizing electrolytes[16,24] and with our observation that 0.12 *M* CTABr causes a negligible shift (<0.05 ppm) in the HOD frequency using 10% $H_2O$, measured relative to external TMS at 100 mHz.

(27) The changes in chemical shift in Figure 7 are relative to water. Errors due to changes in the reference frequency were minimized by holding the sodium carboxylate concentration constant (0.2 *M*) and varying the CTABr concentration. CTABr produces only small changes (<0.04 ppm) in the HOD resonance frequency.

(28) C. E. Johnson and F. A. Bovey, *J. Chem. Phys.*, **29**, 1012 (1958).

(29) L. S. C. Wan, *J. Pharm. Sci.*, **57**, 1903 (1968); H. Takruri and B. Ecanow, *ibid.*, **55**, 979 (1966); G. R. Walter and W. S. Gump, *ibid.*, **51**, 770 (1962).

(30) E. M. Arnett, M. Ho, and L. L. Schaleger, *J. Amer. Chem. Soc.*, **92**, 7039 (1970); S. J. Rehfield, *ibid.* **95**, 4489 (1973).

(31) J. E. Desnoyers, G. E. Pelletier, and C. Jolicoer, *Can. J. Chem.*, **43**, 3232 (1965).

(32) E. F. J. Duynstee and E. Grunwald, *Tetrahedron*, **21**, 2401 (1965).

(33) J. Gordon, J. C. Robertson, and R. L. Thorne, *J. Phys. Chem.*, **74**, 957 (1970); J. Gordon and R. L. Thorne, *ibid.*, **73**, 3643, 3652 (1969).

(34) J. Homer, C. J. Jackson, P. M. Whitney, and E. M. Everdell, *Chem. Commun.*, 956 (1971); I. D. Kuntz and M. D. Johnson, *J. Amer. Chem. Soc.*, **89**, 6008 (1967); M. W. Hanna and A. L. Ashbaugh, *J. Phys. Chem.*, **68**, 811 (1964), and references therein.

(35) C. A. Bunton and S. K. Huang, *J. Amer. Chem. Soc.*, **95**, 2701 (1973).

(36) R. M. Diamond, *J. Phys. Chem.*, **67**, 2513 (1963).

(37) E. W. Anacker and H. M. Ghose, *J. Phys. Chem.*, **67**, 1713 (1963); *J. Amer. Chem. Soc.*, **90**, 3161 (1968).

(38) T. Cohen and T. Vassiliades, *J. Phys. Chem.*, **65**, 1774 (1961).

# Raman Spectra of Molten Mixtures Containing Aluminum Fluoride. I. The LiF–Li$_3$AlF$_6$ Eutectic Mixture

**Signe Kjelstrup Ratkje**

*The University of Trondheim, Norwegian Institute of Technology, Division of Physical Chemistry, N-7034 Trondheim-NTH, Norway*

**and Erling Rytter***

*The University of Trondheim, Norwegian Institute of Technology, Division of Inorganic Chemistry, N-7034 Trondheim-NTH, Norway*

*(Received January 10, 1974)*

*Publication costs assisted by Elkem-Spigerverket A/S, Norway*

A diamond-windowed cell and a furnace for Raman spectroscopy of molten salts have been constructed. The apparatus can be used for fluorides up to 1100°. Two bands, one moderately strong at 556 cm$^{-1}$ and one weak at 347 cm$^{-1}$, were observed for the molten LiF–Li$_3$AlF$_6$ eutectic mixture at 730°. The former frequency was assigned to $\nu_1(A_{1g})$ and the latter to $\nu_5(F_{2g})$ of the AlF$_6{}^{3-}$ ion. The half-width of the 556-cm$^{-1}$ band, 140 cm$^{-1}$, suggests that the AlF$_6{}^{3-}$ octahedra are highly distorted. No dissociation into AlF$_4{}^-$, AlF$_3$, or other species was detected.

## Introduction

Structural entities in molten mixtures containing aluminum fluoride have been of great interest for a long time, mainly in connection with the electrolyte in technical aluminum production. Till now, however, the main methods of investigating these systems have been calorimetry, density and viscosity measurements, and phase diagram investigations (see Holm[1] for further references).

Spectroscopy on the molten AlkF–AlF$_3$ systems would be a valuable supplement to these physicochemical measurements because the information given by spectroscopy is more closely related to the structure of the melt. Attempts to do this have only been made by Solomons, *et al.*[2] However, their dissociation degree of the AlF$_6{}^{3-}$ ion is far higher than those obtained by other methods. The present work can be regarded as an attempt to clarify the structural problems of AlkF–AlF$_3$ melts, starting with investigations of the lower melting systems.

## Experimental Section

Apparatus for Raman spectroscopy on molten fluorides has previously been described in the literature.[2-4] This kind of apparatus should in general be designed to meet the following requirements. (i) It should be possible to heat the cell and furnace to a high temperature (1100° for alkali-aluminum fluorides). (ii) The corrosion problem should be taken into account. (iii) Evaporation of the melt should be kept to a minimum to prevent composition change of the sample and corrosion. (iv) The cell material should possess wetting properties which are suitable for molten fluorides. (v) The collection of the Raman light should be adequate. (vi) It should be easy to fill and empty the cell chamber. (vii) It should be easy to change samples.

Formerly two windowless cells have been constructed for Raman spectroscopy.[2,3] For absorption spectroscopy a cell with diamond windows has been reported.[5] The windowless Raman cells seem to cause great corrosion problems.[6] Solomons, *et al.*,[2] report that the sample, Na$_3$AlF$_6$(l), could be contained in the cell for approximately 30 min only, due to evaporation from the melt. Moreover, the wetting properties of a windowless cell are critical,[6] and the collection of the Raman light probably would not be as efficient as with a cell with diamond windows. Therefore, in spite of the high diamond costs, we decided to use a closed cell. Diamond may become somewhat opaque at 1100° because of intrinsic semiconductor properties.[7] However, the meniscus of molten cryolite could be observed visually at 1050° through the diamond window. With regard to the furnace, fulfilment of the above requirements is mainly a matter of choosing suitable materials. The apparatus described here has been tested with molten cryolite up to 1100°. The limiting temperature depends upon the lower annealing temperature of the quartz used in the furnace tube, which is about 1150°.[8]

*Raman Cell.* A graphite cell equipped with diamond windows and surrounded by a boron nitride sleeve was chosen to fulfil conditions i–vii. The cell is shown in Figure 1.

The cell body (D) was machined from a dense graphite, Graphitite-G (Carborundum Co.). In contrast to other graphite qualities this type is not wetted by the molten mixtures of LiF or NaF with AlF$_3$. Graphitite-G does not contain impurities corresponding to more than 0.04 wt % ashes. The cylindric sleeve (A) was made from boron nitride, Grade A (Carborundum Co.), in order to prevent corrosion of the quartz furnace tube. Experience showed that graphite in contact with the quartz increased the crystal growth in the glass, which then turned opaque.

A graphite ring (B) and a disk (F) together with the cylindric sleeve kept the windows (E) of diameter 6.35 mm, thickness 1.00 mm, in the correct positions. The side window rested against an edge in the cylindric hole while the bottom window rested on the graphite disk. Diamonds, Type IIA (D. Drukker & Zn., Amsterdam), were used as windows. However, it should be noted that Type I diamonds, which are less expensive, are also transparent in the visible region.

Excess vapor from the cell chamber escaped through a hole of diameter 0.8 mm in the upper part of the cell body

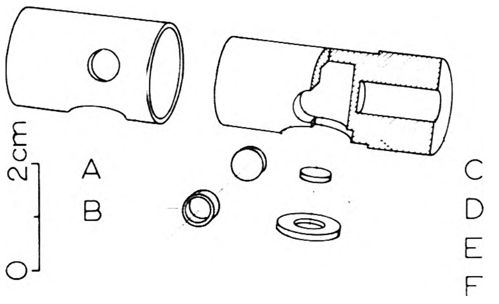

**Figure 1.** The Raman cell for molten fluorides: (A) boron nitride cyclindric sleeve, (B) graphite ring, (C) hole for thermocouple, (D) graphite cell body, (E) diamond windows, (F) graphite disk.

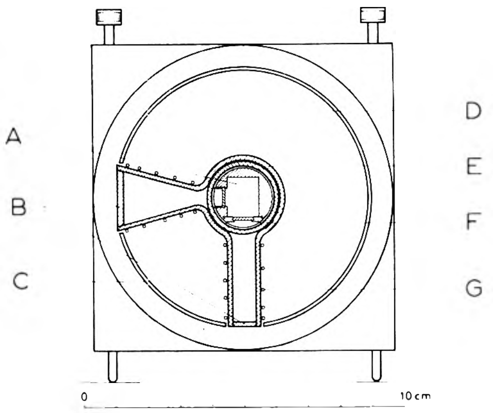

**Figure 2.** Cross-section diagram of the furnace and the cell: (A) cell chamber, (B) side tubes for beam passage, (C) copper furnace wall, (D) Kaowool insulation, (E) quartz furnace tube, (F) inner quartz tube, (G) Kanthal heating wire.

(not shown on Figure 1). This hole was necessary to allow thermal expansion of the gas in the cell.

In order to measure the temperature, a hole (C) was drilled in the graphite block as close to the cell chamber as the strength of the graphite would allow. The protecting tube of the thermocouple fitted tightly into this hole and had, at the same time, a supporting function for the cell, making it possible to regulate the cell position.

*Furnace.* The furnace was based on a Kanthal furnace described by Motzfeldt.[9] The model was reduced to a length of 20 cm and a width of 10 cm to fit the cell chamber of a Cary 82 spectrometer, and materials were chosen to suit our special purpose. Thus quartz was chosen as the furnace tube material instead of alundum because of its transparency. A cross-section diagram of the furnace is given in Figure 2.

The heating wire (G), Kanthal A, thickness 0.60 mm, was wound on the furnace tube (E) and on the side tubes (B). The side tubes were first covered with asbestos bands to reduce thermal radiation from the heating wire. The electrical circuits were adjusted with variable resistors which were connected to the furnace. In this way a temperature gradient less than 10°/cm was maintained in the cell region at 1000°.

The side tubes permitted a 90° beam alignment. The laser beam was incident on the bottom of the cell. The intensity loss of the escaping Raman light was reduced by the conical form of the horizontal side tube. To protect the furnace from accidental corrosion, an inner quartz tube (F) could be used. This tube was examined after the experiment and changed if necessary. It has the disadvantage of reducing the intensity of the scattered beam by 20%.

Kaowool was used as insulating material (D) because of its ease of handling. The furnace was cooled by water circulated through copper tubes on the outside of the wall (C). To reduce the oxidation of graphite, inert gas (Ar or $N_2$) was passed through the furnace tube. Oxidation of the diamond windows is prevented by the presence of graphite.

*Chemicals.* The chemicals used were LiF, pro analysi (Merck, Darmstadt), and $AlF_3$, pure (Riedel de Haën A.G., Seelze-Hannover). LiF was dried, melted under vacuum, and purified by crystallization. $AlF_3$ was sublimated twice in a vacuum furnace at 910°. In each case clear crystals were used.

*Procedure.* Appropriate amounts of LiF and $AlF_3$ were weighed and transferred to the cell chamber in a drybox. The windows, graphite ring and disk, and the boron nitride sleeve were mounted. The closed cell was transferred to the furnace and the sample premelted to ensure adequate mixing.

The spectra were recorded with a Cary 82 spectrometer equipped with a Coherent Radiation Model 52 B argon ion laser using the excitation at 4880 Å. All the standard lenses of the spectrometer could be used, and the only critical adjustment necessary was the position of the furnace. As aluminum fluoride is a weak Raman scatterer, there were problems with intensity. These can be overcome by using a third diamond window in order to allow multiple passes of the laser beam.[10] Recording spectra at temperatures higher than 800° require, in addition, a chopper system to remove the thermal background radiation. In contrast to the $AlkCl-AlCl_3$ systems,[11] noise due to microparticles in the melt was not severe.

## Results

The Raman spectrum of the molten $LiF-Li_3AlF_6$ eutectic mixture at 730° is presented in Figure 3. Apart from the 1332-$cm^{-1}$ diamond band,[12] the spectrum reveals two broad Raman bands, one moderately strong and one weak. From the two spectra of highest quality the background was subtracted and the following frequencies were found: 556 ± 5 and 347 ± 10 $cm^{-1}$. The band at 556 $cm^{-1}$ is approximately symmetric, with a half-width as high as 140 $cm^{-1}$.

The temperature is estimated to be accurate to ±10°, the main error being the temperature gradient in the furnace. Because of the sharply rising background, which strongly increased with temperature, we did not test for any possible temperature dependence of the spectrum. The eutectic mixture of the $LiF-Li_3AlF_6$ system, 85.5 mol % LiF + 14.5 mol % $AlF_3$,[1] was investigated because it represents one of the lowest melting binary fluoride systems containing aluminum. The uncertainty of composition is estimated to be ±0.3 mol %. Error due to evaporation of $LiAlF_4$ is less than 0.1 mol %.

## Discussion

It is reasonable to assume that the Raman spectrum of the $LiF-Li_3AlF_6$ eutectic mixture can be interpreted in terms of more or less well-defined Al-F complexes.

The corresponding sodium system has been investigated by many authors (see Holm[1] for further references) and according to these, the most probable entities occurring in the cryolite melts are $AlF_3$, $AlF_4^-$, and $AlF_6^{3-}$. Before

**TABLE I: $AlF_4^-$ ($T_d$) Totally Symmetric Stretching Frequency**

| Substance or method of calculation | $\nu_1(A_1)$, cm$^{-1}$ | Ref |
|---|---|---|
| $Na_3AlF_6$(l), 1030° | 633 | 2 |
| Force constants transferred from $NaAlF_4$[a] | 696 | |
| Force constants transferred from $LiAlF_4$ | 631 | |
| Compliants transferred from $LiAlF_4$ | 612 | |
| Isoelectronic series of $MF_4$[b] | $\leq$665 | 2 |

[a] The force field of $NaAlF_4$ is less reliable than for $LiAlF_4$ (ref 18). [b] The less than or equal sign is introduced due to the anomalous behavior of $AlCl_4^-$ compared to other tetrachlorides.

**TABLE II: $AlF_6^{3-}$ ($O_h$) Raman Frequencies $\nu_1$ and $\nu_5$**

| Substance or method of calculation | $\nu_1(A_{1g})$, cm$^{-1}$ | $\nu_5(F_{2g})$, cm$^{-1}$ | Ref |
|---|---|---|---|
| $Na_3AlF_6$(s) | 554 | 335 | 2[a] |
| $(NH_4)_3AlF_6$(s) | 544 | 318 | [b] |
| $Na_3AlF_6$(l), 1030° | 575 | | 2 |
| LiF–$Li_3AlF_6$ eutectic (l), 730° | 556 | 347 | |
| Isoelectronic series of $MF_6$ | ~540 | | 2 |

[a] The 335-cm$^{-1}$ band has not been assigned by the authors. [b] K. Wieghardt and H. H. Eysel, *Z. Naturforsch. B*, **25**, 105 (1969).

going into details in the interpretation, it is therefore necessary to estimate the positions of the Raman active modes of these species. The positions of the totally symmetric stretching frequencies are especially important. They should follow the general rule that an increase in coordination number leads to a decrease in the stretching frequency.[13]

*Estimation of $AlF_n$ Frequencies.* For $AlF_3$ a planar $D_{3h}$ model with three Raman active frequencies, $\nu_1$, $\nu_3$, and $\nu_4$ is assumed. The $\nu_2$, $\nu_3$, and $\nu_4$ modes have been observed by ir spectroscopy of the gas at 950–1250°[14,15] and by matrix isolation.[16] Average values for the antisymmetric stretch $\nu_3$ and the bend $\nu_4$ are 950 and 265 cm$^{-1}$, respectively. Büchler, *et al.*,[15] calculate a value of 800 cm$^{-1}$ for $\nu_1$. However, this is far higher than the observed totally symmetric Al–F frequencies for $AlF_4^-$ and $AlF_6^{3-}$ (Tables I and II). The value *650 cm$^{-1}$* as estimated in the JANAF tables[17] is much more reasonable.

Solomons, *et al.*,[2] report the totally symmetric stretching frequency $\nu_1$ of a tetrahedral $AlF_4^-$ in molten cryolite. A tetrahedral configuration is also found in matrix isolated $LiAlF_4$ and $NaAlF_4$ gas molecules.[18] The published force fields of the latter molecules make possible a calculation of $\nu_1$ for $AlF_4^-$ ($T_d$) by transferring force constants. Transference of the more physically meaningful concept of compliants has also been performed. Cyvin[18,19] should be consulted for notations. The terminal stretching valence compliants of $LiAlF_4$ are given by

$$n_d = \frac{1}{2}(F_{33}^{-1}(A_1) + F_{11}^{-1}(B_1))$$

$$n_{dd} = \frac{1}{2}(F_{33}^{-1}(A_1) - F_{11}^{-1}(B_1))$$

which yield

$$F^{-1}(A_1) = n_d + 3n_{dd} = 2F_{33}^{-1}(A_1) - F_{11}^{-1}(B_1)$$

when $F^{-1}(A_1)$ refers to $AlF_4^-$. Literature data as well as the results of the calculations are summarized in Table I. From the table it is reasonable to assume a value of *630 ± 20* cm$^{-1}$ for $\nu_1$.

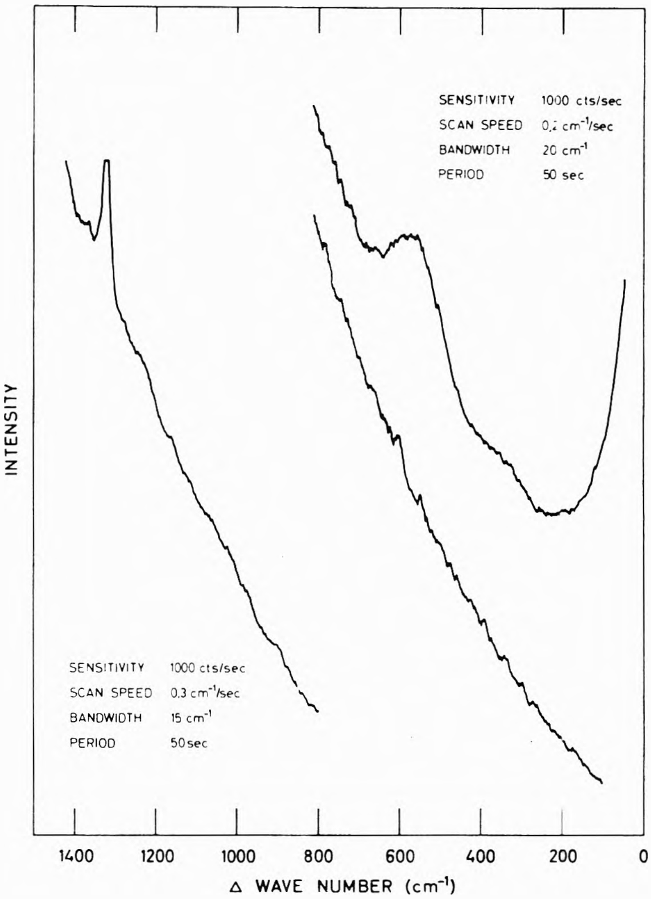

**Figure 3.** The Raman spectrum of the molten LiF–$Li_3AlF_6$ eutectic mixture at 730°. The lower right-hand curve shows the thermal background recorded at a speed of 0.6 cm$^{-1}$/sec and with a pen period of 20 sec.

The situation is easier for the octahedral $AlF_6^{3-}$ since this ion exists as a discrete entity in the solid state. Table II gives the measured solid state Raman data, the previously assigned melt frequency[2] and the present data for the totally symmetric $\nu_1$ mode and the bending mode $\nu_5$. No value for the antisymmetric stretching vibration $\nu_2$ has been reported.

*Molten LiF–$Li_3AlF_6$ Eutectic Mixture.* Although polarization data are not available there is little doubt that the observed frequency at 556 cm$^{-1}$ belongs to a totally symmetric Al–F stretching vibration. In Table II it should be noted that we assign this band to $\nu_1$ of $AlF_6^{3-}$. The correspondence with the frequency found for this ion in molten cryolite[2] is reasonably good, although it is a little surprising that this frequency, 575 cm$^{-1}$, is higher than the present one. This is contrary to the general rule for counterion effects.[20] However, the 575-cm$^{-1}$ band is reported "not to be really isolatable with any certainty from the intense and noisy background pattern." The occurrence of a weak band at 347 cm$^{-1}$ supports the interpretation of the LiF–$Li_3AlF_6$ eutectic mixture spectrum (Table II).

The very large half-width of the 556-cm$^{-1}$ band deserves a comment. A contribution from $AlF_4^-$ to the high-frequency side, and from the antisymmetric stretching mode $\nu_2(E_g)$ and hot bands to the low-frequency side, cannot be rejected. However, due to the approximately symmetric shape of the band and no sign of shoulders, these contributions probably do not present the full explanation. Furthermore, it is not likely that broadening from collisions resulting in short correlation times is essential. We may refer to the half-width of the totally symmetric stretching frequency of $BF_4^-$ at 606° which was found[6] to be approximately 20 $cm^{-1}$. The $\nu_1$ mode of an octahedral $AlF_6^{3-}$ should be sensitive to environmental effects, but this could hardly give a broadening of the magnitude observed. It is more likely that the structure of the $AlF_6^{3-}$ ions themselves is distorted, thus giving rise to a set of frequencies from differently perturbed octahedral species. Holm[21] proposed that some of the octahedra in the cryolite mixtures with mole fraction of $AlF_3 < 0.25$ should be distorted to a structure having an $AlF_3$ core and three additional fluorine ions at larger distances from aluminum. Such a complex would probably give a main symmetric stretching vibration at a higher frequency than the observed one. It should be mentioned that no conclusion regarding a quasilattice structure, ion-pair formation, or local charge fluctuations can be drawn at this stage.

From the two observed frequencies, the following symmetry and valence force constants may be calculated (see Cyvin[19] for notations)

$$F(A_{1g}) = f_r + 4f_{rr} + f_{rr}' = 3.46 \text{ mdyn/Å}$$

$$F(F_{2g}) = f_\alpha - 2f_{\alpha\alpha}' + f_{\alpha\alpha}''' = 0.34 \text{ mdyn/Å}$$

In accord with predictions, due to the greater number of ligands, the stretching force constant is somewhat lower than found in $LiAlF_4$.[18] The bending constant is in the same range as for the latter molecule. These statements are only qualitative since the influence of the interaction force constants is uncertain.

*Dissociation Equilibria.* The dissociation schemes

$$AlF_6^{3-} = AlF_3 + 3F^- \quad (1)$$

$$AlF_6^{3-} = AlF_4 + 2F^- \quad (2)$$

seem by now to be the most popular ones for the molten cryolite mixtures.[21] Vrebenska and Malinovsky[22] used the last equation and found by cryoscopic measurements a degree of dissociation $\alpha$ in pure lithium cryolite at 782° equal to 0.4. However, when the amount of $AlF_3$ in the system is decreased from 25.0 (at 782°) to 14.5 mol % (at 730°), the equilibrium will shift to the left and lower the value of $\alpha$ to approximately 0.2. This calculation is based on the assumption that the dissociation constant is independent of the temperature in the interval 730–782°, and that the activity coefficient term varies very little in the composition range 14.5–25.0 mol % $AlF_3$. The assumptions are justified by Holm[21] for the sodium system. Our investigation gives no sign of the species $AlF_4^-$ (or $AlF_3$), but the thermodynamic value of $\alpha \sim 0.2$ cannot be rejected without further investigations.

For sodium cryolite Solomons, *et al.*, report, from the Raman spectrum, a degree of dissociation $\alpha$ as high as 0.8 for reaction scheme 2 at 1030°. With the same assumptions as above, this value will be reduced to 0.65 for a change in composition to 14.5 mol % $AlF_3$. When this result is compared to the present one, the difference in the temperature of the melts should be taken into consideration. A lower temperature should reduce the $\alpha$ value. On the other hand, the substitution of $Na^+$ with $Li^+$ should give a higher degree of dissociation. The counterion effect is found to be large for other molten salt equilibria.[11,23] The thermodynamic value $\alpha = 0.3$ (1030°) found for sodium cryolite[1] is in agreement with this effect when compared to $\alpha = 0.4$ (782°) for lithium cryolite.[22] The results found by Solomons, *et al.*, therefore seem to be at variance with ours. We hope to examine this problem further in the near future, using a Raman instrument fitted with a chopper to remove thermal radiation from the sample.

*Acknowledgment.* The authors are indebted to N. Waeraas for advice regarding the design of the cell and the furnace. In addition we wish to thank Dr. P. Klaeboe for allowing tests of the apparatus on his Cary 81 Raman spectrometer and Dr. K. Larsson for the use of a Cary 82 Raman spectrometer to record the spectra. We gratefully acknowledge the financial support and interest in the project of Elkem-Spigerverket A/S. We also thank Royal Norwegian Council for Scientific and Industrial Research and The Norwegian Research Council for Science and the Humanities for their support.

## References and Notes

(1) J. L. Holm, Ph.D. Thesis, Institute of Inorganic Chemistry, The University of Trondheim, NTH, Norway, 1971.
(2) C. Solomons, J. H. R. Clarke, and J. O'M. Bockris, *J. Chem. Phys.*, **49**, 445 (1968).
(3) A. S. Quist, *Appl. Spectrosc.*, **25**, 80 (1971).
(4) A. S. Quist, *Appl. Spectrosc.*, **25**, 82 (1971).
(5) L. M. Toth, J. P. Young, and G. P. Smith, *Anal. Chem.*, **41**, 683 (1969).
(6) A. S. Quist, J. B. Bates, and G. E. Boyd, *J. Chem. Phys.*, **54**, 4896 (1971).
(7) This was pointed out to us by one of the reviewers.
(8) G. W. Morey, "The Properties of Glass," 2nd ed, Reinhold, London, 1954.
(9) K. Motzfeldt in "Physiochemical Measurements at High Temperatures," J. O'M. Bockris, Ed., Butterworths, London, 1960.
(10) H. A. Oye, E. Rytter, P. Klaeboe, and S. J. Cyvin, *Acta Chem. Scand.*, **25**, 559 (1971).
(11) E. Rytter, H. A. Oye, S. J. Cyvin, B. N. Cyvin, and P. Klaeboe, *J. Inorg. Nucl. Chem.*, **35**, 1185 (1973).
(12) F. Stenman, *J. Appl. Phys.*, **40**, 4164 (1969).
(13) D. M. Adams, "Metal-Ligand and Related Vibrations," Arnold, London, 1967.
(14) L. D. McCory, R. C. Paule, and J. L. Margrave, *J. Phys. Chem.*, **67**, 1086 (1963).
(15) A. Buchler, E. P. Marram, and J. K. Stauffer, *J. Phys. Chem.*, **71**, 4139 (1967).
(16) A. Snelson, *J. Phys. Chem.*, **71**, 3202 (1967).
(17) "JANAF Thermochemical Data," The Dow Chemical Company, Thermal Laboratory, Midland, Mich., 1971.
(18) S. J. Cyvin, B. N. Cyvin, and A. Snelson, *J. Phys. Chem.*, **75**, 2609 (1971).
(19) S. J. Cyvin, "Molecular Vibrations and Mean Square Amplitudes," American Elsevier, New York, N. Y., 1968.
(20) E. Rytter and H. A. Oye, *J. Inorg. Nucl. Chem.*, **35**, 4311 (1973).
(21) J. L. Holm, *Inorg. Chem.*, **12**, 2062 (1973).
(22) J. Vrebenska and M. Malinovsky, *Collect. Czech. Chem. Commun.*, **38**, 659 (1973).
(23) J. L. Holm and O. J. Kleppa, *Inorg. Chem.*, **8**, 207 (1969).

# Spectra and Structure of Boron–Nitrogen Compounds. II. Infrared and Raman Spectra of Trimethylamine–Borane[1]

**J. D. Odom, J. A. Barnes,[2] B. A. Hudgens,[3] and J. R. Durig***

*Department of Chemistry, University of South Carolina, Columbia, South Carolina 29208*

*(Received January 23, 1974)*

*Publication costs assisted by the National Science Foundation*

The infrared (33–4000 cm$^{-1}$) and Raman (0–3500 cm$^{-1}$) spectra of $(CH_3)NBH_3$, $(CH_3)_3NBD_3$, $(CD_3)_3NBH_3$, and $(CD_3)_3NBD_3$ have been recorded for the solid state at low temperatures. The spectra have been interpreted in detail on the basis of $C_{3v}$ molecular symmetry. The valence force field model has been utilized in calculating the frequencies and potential energy distribution. The calculated potential constants for the adduct are compared to those previously reported for the Lewis base moiety. The N–B stretch was found to be extensively mixed with the N–C symmetric stretch. Nevertheless, the Raman bands at 680, 660, 641, and 610 cm$^{-1}$ for the $(CH_3)_3NBH_3$, $(CH_3)_3NBD_3$, $(CD_3)_3NBH_3$, and $(CD_3)_3NBD_3$ molecules, respectively, have been shown to be approximately 65% or more N–B stretching motion. The N–B force constant was found to have a value of 2.59 mdyn/Å which seems consistent with adduct stability. CNDO/2 calculations were carried out to calculate the barrier to internal rotation of the $BH_3$ group, the dipole moment, and the N–C force constant.

## Introduction

Although there have been numerous studies on the relative stabilities of the group IIIA Lewis acids with the group VA Lewis bases, there is still conflict concerning the assignment of the boron–nitrogen stretching mode for this dative bond. In the initial vibrational study of trimethylamine–borane, Rice, *et al.*,[4] assigned this normal vibration to a band at 1255 cm$^{-1}$ whereas the nitrogen–carbon stretching modes were assigned to bands at 1005 and 667 cm$^{-1}$. However, this assignment was not supported by the shift factors which resulted from the deuteration of the borane moiety and Taylor[5] reassigned the 667-cm$^{-1}$ band to the B–N stretching mode. This latter assignment was found to lead to a force constant near 2.59 mdyn/Å which is consistent with the expected boron–nitrogen bond strength.

In a recent study of the electronic spectrum of trimethylamine–borane, Raymonda[6] retained the earlier assignment of Rice, *et al.*,[4] of the B–N stretching mode at 1255 cm$^{-1}$ with the lower frequencies for the N–C stretching modes. Therefore, there still appears to be some confusion concerning the assignment of the normal modes for this molecule. In addition, we have been interested in the barriers to internal rotation around C–N bonds[7] and recently reported both the $A_2$ and E torsional frequencies of trimethylamine. Thus, we felt an investigation of the low-frequency spectrum of trimethylamine–borane might provide information on the change in barrier heights around the C–N bond with coordination of the borane moiety as well as the barrier around the B–N bond. No vibrational studies have been reported for the $(CD_3)_3NBH_3$ and $(CD_3)_3NBD_3$ isotopic species of trimethylamine–borane and no frequencies have been reported for any of the isotopic species in the solid state. Thus, we are reporting the results of an infrared and Raman study of $(CH_3)_3NBH_3$, $(CH_3)_3NBD_3$, $(CD_3)NBH_3$, and $(CD_3)_3NBD_3$ in the solid state.

## Experimental Section

All manipulations were carried out in a conventional high vacuum system equipped with greaseless stopcocks. Diborane-6 was produced by the addition of commercial potassium borohydride or sodium borohydride-$d_4$ to hot polyphosphoric acid.[8] Purification was achieved by trap-to-trap distillation through a trap held at −160° (isopentane slush) into a trap at −196°. Purity was confirmed by vapor pressure measurements at −112°.[9] Trimethylamine (Matheson) was purified on a low-temperature vacuum fractionation column[10] until it produced a vapor pressure of 680 Torr at 0°.[9] Trimethylamine-$d_9$ was obtained from Merck Sharp and Dohme and used without further purification. Trimethylamine and diborane-6 in a 2:1 ratio were condensed together at −196° and allowed to react as they warmed to room temperature.[11] After completion of the reaction, the $(CH_3)_3NBH_3$ was purified by passing the reaction mixture through a trap at −20°. Traces of $B_2H_6$ or $(CH_3)_3N$ were collected in a trap held at −196°. The other isotopic species were prepared in a similar manner. Samples were transferred to the various sampling cells without contact with the atmosphere or other external contamination.

The Raman spectra were measured from 0 to 3500 cm$^{-1}$ at room temperature with a Cary Model 82 Raman spectrophotometer[12] which had been calibrated with neon emission lines. The samples were deposited in glass capillaries and sealed with a torch.

The far-infrared spectra of trimethylamine–borane-$d_0$ (TMNB), -$d_3$, -$d_9$, and -$d_{12}$ were recorded between 33 and 350 cm$^{-1}$ with a Beckman IR-11 double-beam grating spectrophotometer which was purged with dry nitrogen. The instrument was calibrated with water vapor frequencies.[13] The low-temperature cell used has been described elsewhere.[14] The sample was allowed to sublime slowly onto a silicon substrate which was in thermal contact with a brass heat sink cooled by boiling liquid nitrogen.

The mid-infrared spectra were recorded from 4000 to 250 cm$^{-1}$ with a Perkin-Elmer 621 grating spectrophotometer which was purged with dry nitrogen and calibrated in the usual manner.[15] The spectra were recorded with a cell held at −78° and equipped with CsI windows.

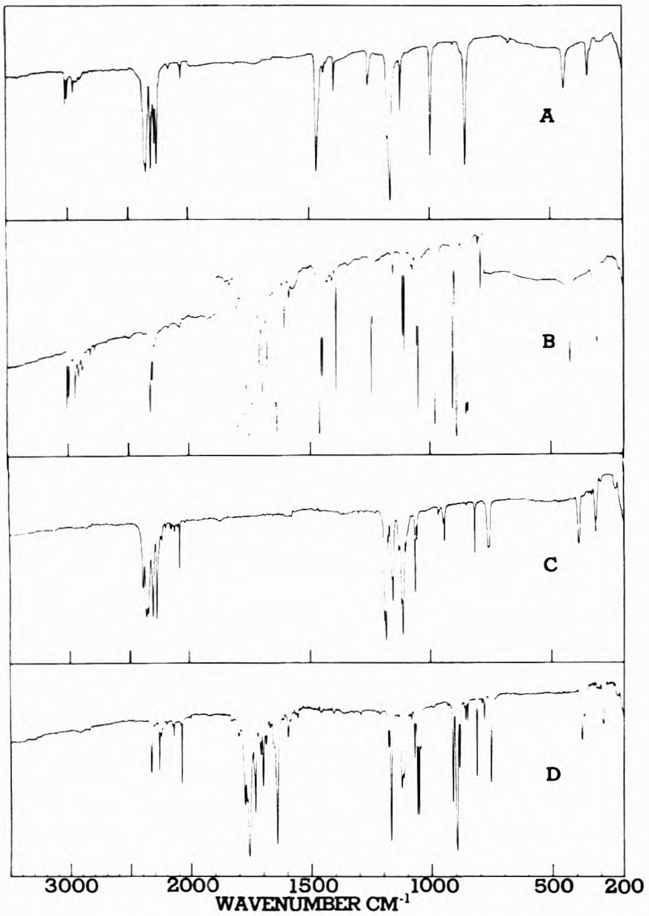

**Figure 1.** A, B, C, and D, show infrared spectra of solid $(CH_3)_3NBH_3$, $(CH_3)_3NBD_3$, $(CD_3)_3NBH_3$, and $(CD_3)_3NBD_3$, respectively. The ordinate is in arbitrary units of absorption.

The spectra which are shown in Figures 1-3 indicate that the $-BD_3$ species also contained some hydrogen which is not unexpected due to the technique used to prepare the diborane-6 as well as the slight hydrogen contamination in the $NaBD_4$.

## Results

Clearly the most important vibrational frequency is the B-N stretching mode since this vibration is expected to reflect to some degree the strength of the B-N dative bond. As pointed out in the Introduction, the 1255-cm$^{-1}$ band has been previously assigned[4,6] to this mode. However, it is quite clear from the Raman spectra of the solids that the B-N stretch falls at 680, 660, 641, and 610 cm$^{-1}$ for the $(CH_3)_3NBH_3$, $(CH_3)_3NBD_3$, $(CD_3)_3NBH_3$, and $(CD_3)_3NBD_3$ molecules, respectively. This assignment is in accord with that of Taylor[5] and results in a reasonable value of the force constant for this normal mode. It should be pointed out that the normal coordinate calculations show some mixing of the B-N stretch with the symmetric $NC_3$ stretch and the symmetric $NC_3$ deformation and the potential energy diagram PED for this band is 90, 75, 55, and 58% B-N stretch for the trimethylamine-borane-$d_0$, -$d_3$, -$d_9$, and -$d_{12}$, respectively. The mixing is supported by the frequency shifts with isotopic substitution. Also, it should be mentioned that the B-N stretching mode is not found in the infrared spectrum except for the $(CH_3)_3NBH_3$ molecule; the extremely low intensity of this normal mode in the infrared spectrum could have led to some of the earlier confusion associated with the assignment of this vibration.

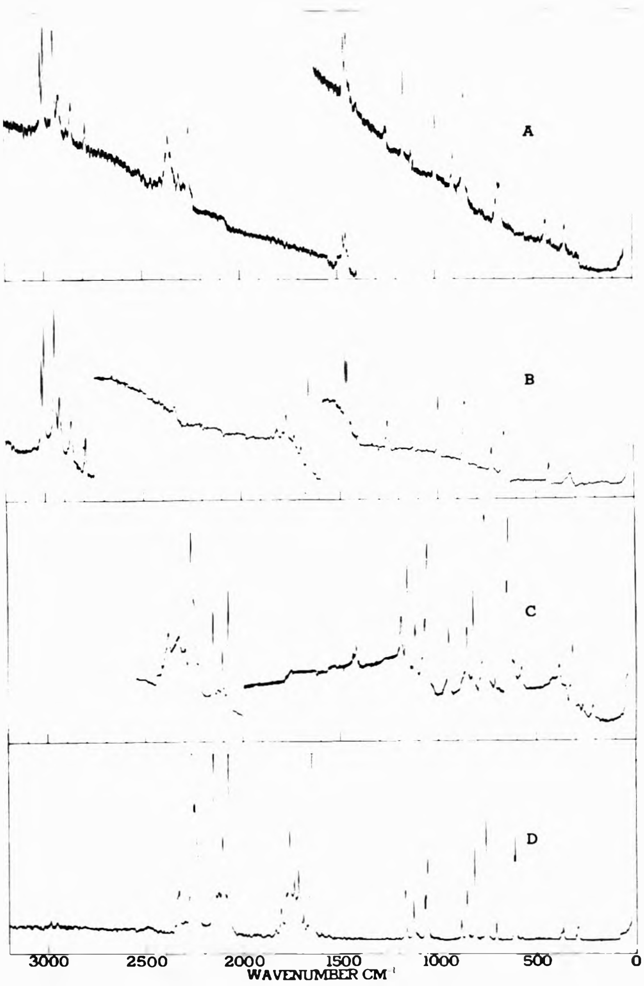

**Figure 2.** A, B, C, and D, show Raman spectra of solid $(CH_3)_3NBH_3$, $(CH_3)_3NBD_3$, $(CD_3)_3NBH_3$, and $(CD_3)_3NBD_3$, respectively. The ordinate is in arbitrary units of intensity.

The Raman band near 859 cm$^{-1}$ for the $(CH_3)_3NBH_3$ and $(CH_3)_3NBD_3$ molecules which is found to shift to 759 cm$^{-1}$ with deuteration of the methyl groups can be assigned predominantly to the $NC_3$ symmetric stretching mode. The assignment of the other skeletal stretching mode, the $NC_3$ antisymmetric stretch, is complicated considerably by the difference in the mixing of this normal mode for the molecules with the $(CH_3)_3N$ and $(CD_3)_3N$ moieties. For the molecules containing the $CH_3$ groups, the $NC_3$ antisymmetric stretch falls near 1000 cm$^{-1}$ but for the molecules with $CD_3$ groups, this motion can best be assigned to bands around 1180 cm$^{-1}$. This assignment is consistent with that given for the corresponding mode in trimethylamine.[16]

The intensity of the skeletal deformations of the Lewis base moiety decreases relative to the C-V-B bend (V = N, P, As) as the group is descended.[17,18] As in trimethylphosphine-borane,[17] the frequencies of both skeletal deformations are higher in the adduct than in the Lewis base. Both deformations are sensitive to the deuteration of the borane group and the methyl group. The antisymmetric $NC_3$ deformation, which shifts from 446 to 386 cm$^{-1}$ on deuteration of the methyl groups, shows shifts of twelve and six wave numbers for the -$d_0$ and -$d_9$ species, respectively, on deuteration of the borane group. The symmetric

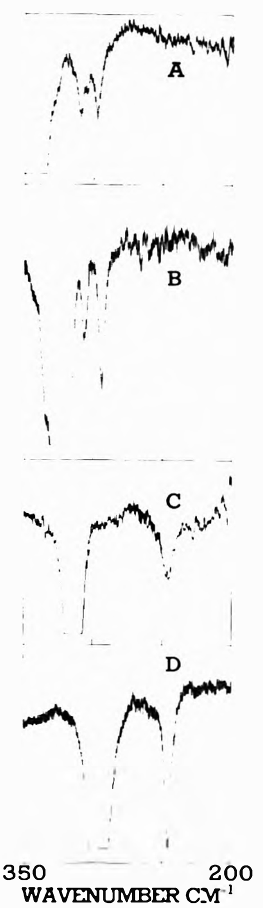

**Figure 3.** A, B, C, and D, show far-infrared spectra of solid $(CH_3)_3NBH_3$, $(CH_3)_3NBD_3$, $(CD_3)_3NBH_3$, and $(CD_3)_3NBD_3$, respectively. The ordinate is in arbitrary units of absorption.

$NC_3$ deformation does not shift as much as the antisymmetric mode with deuteration of the borane and methyl groups. The symmetric mode shows a much greater sensitivity to the borane group than does the antisymmetric motion. The symmetric $NC_3$ deformation is observed at 351, 326, 316, and 297 $cm^{-1}$ for trimethylamine–borane-$d_0$, -$d_3$, -$d_9$, and -$d_{12}$, respectively.

The ∠CNB bending mode is observed as a shoulder on the low-frequency side of the symmetric $NC_3$ deformation. The amount of separation of the ∠CNB bend from the symmetric $NC_3$ deformation decreases with the increase in number of deuteriums in the molecule until the two modes are unresolvable in trimethylamine–borane-$d_{12}$.

Assuming $C_{3v}$ symmetry, one obtains from group theory that the nine methyl stretches span the representations $\Gamma(CH_3) = 2A_1 + A_2 + 3E$. The $A_2$ methyl stretch is unobserved. In trimethylamine–borane-$d_0$ and -$d_3$ the four bands at 3081, 3002, 2954, and 2930 $cm^{-1}$ are attributed to the five observable fundamentals. The antisymmetric methyl stretches of E symmetry are assigned to bands at 3018 and 3002 $cm^{-1}$ which are observed to shift to 2155 and 2145 $cm^{-1}$ on deuteration of the methyl groups. The symmetric (E) methyl stretch is observed at 2930 $cm^{-1}$ and this mode shifts to 2077 $cm^{-1}$ on methyl deuteration.

The isotopic shifts for the $A_1$ methyl stretches are smaller than the shifts observed for the E methyl stretches. The shifts in the N–B stretch and the symmetric $NC_3$ deformation are so large that the two $A_1$ methyl stretches must be assigned to the bands at 2265 and 2145 $cm^{-1}$, if the product rule is to be satisfied. Thus, the adduct differs greatly from the Lewis base in the assignment of the $CD_3$ stretching modes. The antisymmetric $CD_3$ stretch and the symmetric $CD_3$ stretch are assigned to the 2265- and 2145-$cm^{-1}$ bands, respectively.

In trimethylamine all five of the methyl deformations are resolved. In trimethylamine–borane-$d_0$ and -$d_3$ only three bands are observed. Antisymmetric methyl deformations of $A_1$ and E symmetry are assigned to the band at 1475 $cm^{-1}$ in trimethylamine–borane-$d_0$ and -$d_3$. On deuteration, the antisymmetric methyl deformations assigned to the 1475-$cm^{-1}$ band shift to 1076 ($A_1$) and 1063 $cm^{-1}$ (E). The other antisymmetric deformation of E symmetry is assigned to a band at 1461 $cm^{-1}$ in the trimethylamine–borane-$d_0$ and -$d_3$ and shifts to 1057 $cm^{-1}$ in the -$d_9$ and -$d_{12}$ molecules. Both the $A_1$ and the E symmetric methyl deformations are assigned to the 1407 $cm^{-1}$ band in trimethylamine–borane-$d_0$ and -$d_3$. On deuteration, the symmetric methyl deformations shift to 1131 ($A_1$) and 1118 $cm^{-1}$ (E).

Of the three methyl rocks, two are easily assigned and are calculated to be relatively pure modes in the normal coordinate analysis. These two modes are the $A_1$ rock and one of the rocks of E symmetry. The methyl rock of $A_1$ symmetry is observed at 1127 $cm^{-1}$ and shifts to 898 $cm^{-1}$ on deuteration. The E methyl rock occurs at 1122 $cm^{-1}$ and on deuteration shifts to 853 $cm^{-1}$. The third methyl rock is of E symmetry and is strongly mixed with the $NC_3$ antisymmetric stretch. In trimethylamine–borane-$d_0$ and -$d_3$ this methyl rock is best assigned to a band at 1259 $cm^{-1}$; however, in trimethylamine–borane-$d_9$ and -$d_{12}$ this mode best fits the PED description of a band at 818 $cm^{-1}$.

The amount of separation between the $BH_3$ symmetric and antisymmetric stretches is much greater than was observed in either trimethylphosphine–borane[17] or trimethylarsine–borane.[18] In trimethylamine–borane, the antisymmetric $BH_3$ stretch is observed at 2368 $cm^{-1}$ and shifts to 1762 $cm^{-1}$ on deuteration. The symmetric $BH_3$ stretch is assigned to a band at 2264 $cm^{-1}$ and is observed to shift to 1646 $cm^{-1}$ with deuteration.

The $BH_3$ deformations in trimethylamine–borane occur at higher frequency than the corresponding modes in trimethylphosphine–borane[17] and trimethylarsine–borane.[18] The antisymmetric $BH_3$ deformation is mixed with the methyl rocks. Since the ∠NCH force constant is larger than the ∠HBH force constant, this mixing causes the antisymmetric deformation to occur at the higher frequency of 1168 $cm^{-1}$. This deformation shifts on deuteration to 865 $cm^{-1}$. The separation of the antisymmetric deformation from the symmetric deformation in the -$d_0$ and -$d_9$ compounds is only four wave numbers. The separation in the trimethylphosphine–borane[17] and trimethylarsine–borane[18] is approximately 55 $cm^{-1}$. The frequency of the symmetric $BH_3$ deformation is dependent on both the ∠HBH and the ∠NBH force constants and since the NBH force constant is much larger than the ∠PBH or ∠AsBH force constant while the HBH remains the same as was calculated for the phosphorus and arsenic analogs, the separation would be expected to be less. The symmetric $BH_3$ deformation which is more strongly coupled with the $CH_3$ rocking mode than the antisymmetric $BH_3$ deformation is observed at 1164 $cm^{-1}$. The symmetric $BD_3$ deformation as in the phosphorus and arsenic analogs shows $^{10}B$–$^{11}B$ splitting which is observed at 920 and 904 $cm^{-1}$ for the $^{10}B$ and the $^{11}B$ species, respectively.

The $BH_3$ rocking frequency in trimethylamine–borane is significantly coupled with other modes in each of the four isotopic species studied. In trimethylamine-borane-$d_0$ the $BH_3$ rock is observed at 915 $cm^{-1}$. The rock in this isotopic species is strongly coupled with the antisymmetric $NC_3$ stretch. The $BD_3$ rock in trimethylamine-borane-$d_3$ is coupled to a lesser degree with both the antisymmetric $NC_3$ stretch and the methyl rocks. In both the -$d_9$ and -$d_{12}$ species the borane rock is coupled with the methyl rocks.

The only torsion clearly identified is the $CD_3$ torison of E symmetry observed at 245 $cm^{-1}$. From the normal coordinate analysis the $CH_3$ (E) torsion in trimethylamine–borane-$d_0$ falls between the symmetric $NC_3$ deformation at 351 $cm^{-1}$ and the $NC_3$ rock at 340 $cm^{-1}$. The latter is a shoulder on the 351 $cm^{-1}$ band and is observed only in the infrared spectrum. In the -$d_3$ species the $CH_3$ (E) torsion is observed by a broad band at 326 $cm^{-1}$. The methyl and $BH_3$ torsions of the "silent" $A_2$ symmetry are not observed.

## Normal Coordinate Analysis

The normal coordinates were calculated to aid in the assignment of the vibrational modes. The analysis was performed using the Wilson *GF*-matrix method[19] and computer programs written by Schachtschneider.[20] The *G* matrix was calculated using structural parameters determined by Odom, *et al.*[1] The initial value of the N–B force constant was taken from previously published work on this compound by Taylor.[5] The initial force constants for the $BH_3$ moiety were taken from the valence force field (VFF) calculation on trimethylphosphine-borane.[17] The initial values for the force constants for trimethylamine were taken from the VFF calculation by Dellepiane and Zerbi.[16] An initial force field of 24 force constants was selected to fit 98 frequencies. This force field was later expanded to 36 force constants is an effort to improve the fit. In the least-squares refinement, the observed frequencies were weighted by $(1/\lambda)$ and the behavior of the $J'WJ$ matrix was constantly tested as described elsewhere.[17] The calculated frequencies are listed for the four isotopic species in Tables I–IV[21] and have average errors of 0.6, 0.9, 1.1, and 0.9%, respectively. In the calculation of the final force field, all interaction force constants with magnitudes less than 0.04 mdyn/Å were omitted. The remaining 23 force constants are reported in Table V. The following interaction force constants were initially included in the calculation, but were found not to greatly improve the fit: $F_{\alpha}$, $F_{\epsilon}$, $F_{R\epsilon}$, $F_{\alpha\phi}$, $F_{\beta\phi}$, $F_{\beta\epsilon}$, $F_{R\alpha}$, $F_{R\phi}$, $F_{QR}$, $F_{Q\epsilon}$, and $F_{\sigma}$ During the latter stages of refinement, the principal force constants with the exception of the N–B stretching force constant remained invariant to changes in the interaction force constants. The N–B force constant was quite sensitive to the force field employed and, from the PED, it is clear that the N–B stretch participated to a small degree in most of the skeletal modes in the $A_1$ symmetry block.

## CNDO/2 Calculations

In trimethylamine Dellepiane and Zerbi found the N–C force constant to be 4.971 mdyn/Å.[16] In the present study the value of the N–C force constant is calculated to be 4.92 mdyn/Å. From the microwave studies of both the Lewis base and the adduct, the N–C bond length is found to increase from 1.451[22] to 1.495 Å[1] on adduct formation. Since one would expect the N–C force constant to decrease more than 0.05 mdyn/Å for an increase of 0.04 Å in bond length, the CNDO/2 calculations were carried out to investigate this anomaly.

The initial structures were taken[1,2] from the appropriate microwave studies. The structures of the methyl and borane groups were fixed. The skeletal parameters [trimethylamine: $\angle$CNC and $r$(NC), and trimethylamine-borane: $\angle$BNC, $r$(NB), and $r$(NC)] were varied to minimize the total energy. The total energy was then evaluated for at least 10 values of the N–C bond distances. The bond distances were selected such that the potential curve was determined up to the first excited state of the $CN_3$ symmetric stretch. The points were fitted by least squares to the equation $y = ax^2 + bx + c$; thus, the force constant is equal to $2a$.

The force constants calculated from the curve fit of the CNDO/2 data were more than an order of magnitude larger than the values obtained from the normal coordinate analyses of both the adducts and the Lewis base. From the CNDO/2 calculations, the N–C force constant for the adduct is found to be less than 2% smaller than the N–C force constant for the Lewis base. This is consistent with the results obtained from the normal coordinate analysis.

The equilibrium CNDO/2 N–C bond distances in both trimethylamine and the trimethylamine–borane were much shorter than the experimentally determined bond lengths [$(CH_3)_3N$ exptl., 1.451 Å; CNDO/2, 1.418 Å; and $(CH_3)_3NBH_3$ exptl., 1.495 Å; CNDO/2, 1.427 Å]. Thus, empirically, the CNDO/2 structure correctly reflected the increase of the N–C bond length upon adduct formation but not the magnitude of the increase. The CNDO/2 equilibrium $\angle$CNB of 95° was found to be much smaller than the experimentally determined angle of 110.9°. The dipole moment for the adduct calculated from the equilibrium CNDO/2 structure, 4.45 D, agreed very well with the observed dipole moment[1] of 4.59 D; however, the dipole moment calculated from the microwave structure yielded a value of 6.31 D. The dipole moment calculated for the Lewis base from the equilibrium CNDO/2 structure of 1.65 D was much larger than the measured value of 0.67 D.

Using the microwave structure[1] the barrier to internal rotation of the $-BH_3$ group was calculated by CNDO/2 to be 2.9 kcal/mol. A barrier of 3.4 kcal/mol was suggested in the microwave work which was compared to the barrier of $NH_3BH_3$. The barrier for the latter molecule of 2.9 kcal/mol was the result[23] of an *ab initio* calculation. For comparison, the barrier of $NH_3BH_3$ was recalculated using the CNDO/2 program which yielded a value of 2.4 kcal/mol for the barrier. Thus, the barriers calculated by CNDO/2 appear to be too small by approximately 0.5 kcal/mol.

## Discussion

Except in the methyl stretching region, the fundamental vibrations seem to be well predicted by the normal vibrations of trimethylamine plus the "group frequencies" of the $BH_3$ moiety. The lengthening of the N–C bond on formation of the adduct is attributed to transfer of electron density from the N–C bond to the N–B bond, not to any rehybridization effects. Even though the N–C bond lengthened significantly from 1.451 Å in trimethylamine to 1.495 Å in trimethylamine–borane, the N–C force constant did not decrease as much as would be expected.

This trend was predicted qualitatively by the CNDO/2 calculation.

Trimethylamine–borane satisfies Timmermanns' criteria[24] for being a globular molecule which frequently leads to the formation of a plastic crystal. Since none of the $A_2$ modes are observed and since none of the E modes show site or factor group splitting, one may conclude that the operative symmetry is the molecular symmetry, $C_{3v}$. The

Table I. Fundamental Frequencies (cm$^{-1}$) and Assignments for $(CH_3)_3NBH_3$.[a]

| $(CH_3)_3NBH_3$ | | $(CH_3)_3N$[b] | | $(CH_3)_3NBH_3$ | |
|---|---|---|---|---|---|
| Infrared ν(cm$^{-1}$) | Raman Δν(cm$^{-1}$) | Infrared ν(cm$^{-1}$) | Raman Δν(cm$^{-1}$) | Calculated (cm$^{-1}$) | Assignment and Approximate Description |
| 3018 mw | 3019 s | 2970 | | 3009 | $\nu_{16}$ (E)(100%) |
| 3002 mw | 3004 vs | 2944 | | 3000 | $\nu_1$ ($A_1$) $CH_3$ antisymmetric stretch (100%) |
| 3002 mw | 3004 vs | 2818 | | 2982 | $\nu_{17}$ (E) (100%) |
| 2954 w | 2953 vs | 2878 | | 2945 | $\nu_3$ ($A_1$) $CH_3$ symmetric stretch (100%) |
| 2922 vw | 2930 m | 2768 | | 2944 | $\nu_{18}$ (E) (100%) |
| 2360 s | 2373 m | | | 2359 | $\nu_{19}$ (E) $BH_3$ antisymmetric stretch (100%) |
| 2264 s | 2266 m | | | 2279 | $\nu_3$ ($A_1$) $BH_3$ symmetric stretch (100%) |
| 1473 s | 1475 mw | 1482 | | 1485 | $\nu_{20}$ (E) $CH_3$ antisymmetric deformation (75%), $CH_3$ rock (25%) |
| 1473 s | 1475 mw | 1461 | 1485 | 1478 | $\nu_4$ ($A_1$) $CH_3$ antisymmetric deformation (100%) |
| 1467 sh m | 1461 mw | 1461 | 1448 | 1475 | $\nu_{21}$ (E) $CH_3$ antisymmetric deformation (80%), $CH_3$ rock (20%) |
| 1400 mw | 1407 vw | 1446 | 1433 | 1414 | $\nu_{22}$ (E) $CH_3$ symmetric deformation (91%), $CH_3$ stretch (5%) |
| 1400 mw | 1407 vw | 1405 | | 1404 | $\nu_5$ ($A_1$) $CH_3$ symmetric deformation (100%) |
| 1259 mw | 1258 w | 1272 | 1283 | 1259 | $\nu_{23}$ (E) $CH_3$ rock (45%), $NC_3$ antisymmetric stretch (30%), $CH_3$ antisymmetric deformation (15%), $NC_3$ antisymmetric deformation (10%) |
| 1168 sh m | 1168 s | | | 1174 | $\nu_{24}$ (E) $BH_3$ antisymmetric deformation (90%) |
| 1164 vs | | | | 1154 | $\nu_6$ ($A_1$) $BH_3$ symmetric deformation (85%), $CH_3$ rock (15%) |
| 1127 m | 1125 w | 1183 | 1183 | 1125 | $\nu_7$ ($A_1$) $CH_3$ rock (75%), $BH_3$ symmetric deformation (10%), $CH_3$ antisymmetric deformation (10%) |
| 1122 sh m | | 1108 | 1100[c] | 1114 | $\nu_{25}$ (E) $CH_3$ rock (80%), $CH_3$ antisymmetric deformation (15%) |
| 1002 s | 1004 s | 1043 | 1048 | 1014 | $\nu_{26}$ (E) $NC_3$ antisymmetric stretch (55%), $CH_3$ rock (35%), $BH_3$ rock (10%) |
| 910 vw | 915 m | | | 916 | $\nu_{27}$ (E) $BH_3$ rock (68%), $NC_3$ antisymmetric stretch (32%) |
| 859 s | 860 vs | 825 | 826 | 859 | $\nu_8$ ($A_1$) $NC_3$ symmetric stretch (70%), N-B stretch (30%) |
| 680 vw | 680 m | | | 682 | $\nu_9$ ($A_1$) N-B stretch (75%), $NC_3$ symmetric stretch (25%) |
| 448 m | 446 w | 425 | 422 | 448 | $\nu_{28}$ (E) $NC_3$ antisymmetric deformation (98%) |
| 351 m | 350 w | 366 | 364 | 339 | $\nu_{10}$ ($A_1$) $NC_3$ symmetric deformation (72%), $CH_3$ antisymmetric stretch (13%), $CH_3$ rock (10%) |
| 340 sh w | | | | 338 | $\nu_{30}$ (E) $NC_3$ rock (60%), $CH_3$ torsion (19%), $CH_3$ rock (13%) |

[a] Abbreviations used: v, very; w, weak; m, medium; s, strong; sh, shoulder.

[b] The infrared and Raman gas frequencies are taken from Reference 28 and Reference 29, respectively.

[c] This mode was not observed in the gas so the liquid frequency is listed from the same reference.

Table II. Fundamental Frequencies (cm$^{-1}$) and Assignments for $(CH_3)_3NBD_3$.[a]

| $(CH_3)_3NBD_3$ | | $(CH_3)_3N$[b] | | $(CH_3)_3NBD_3$ | |
|---|---|---|---|---|---|
| Infrared ν(cm$^{-1}$) | Raman Δν(cm$^{-1}$) | Infrared ν(cm$^{-1}$) | Raman Δν(cm$^{-1}$) | Calculated (cm$^{-1}$) | Assignment and Approximate Description |
| 3017 mw | 3019 s | 2970 | | 3009 | $\nu_{10}$ (E) (100%) |
| 3002 mw | 3004 vs | 2944 | | 3000 | $\nu_1$($A_1$) $CH_3$ antisymmetric stretch (100%) |
| 3002 mw | 3004 vs | 2818 | | 2982 | $\nu_{17}$ (E) (100%) |
| 2951 mw | 2952 vs | 2878 | | 2945 | $\nu_2$ ($A_1$) $CH_3$ symmetric stretch (100%) |
| 2924 w | 2925 m | 2768 | | 2944 | $\nu_{18}$ (E) (100%) |
| 1763 vs | 1767 w | | | 1782 | $\nu_{19}$ (E) $BD_3$ antisymmetric stretch (100%) |
| 1646 vs | 1650 s | | | 1633 | $\nu_3$ ($A_1$) $BD_3$ symmetric stretch (100%) |
| 1470 vs | 1471 m | 1482 | | 1484 | $\nu_{20}$ (E) $CH_3$ antisymmetric deformation (75%), $CH_3$ rock (20%) |
| 1470 vs | 1471 m | 1461 | 1485 | 1478 | $\nu_4$ ($A_1$) $CH_3$ antisymmetric deformation (80%), $CH_3$ rock (20%) |
| 1458 m | 1461 m | 1461 | 1448 | 1474 | $\nu_{21}$ (E) $CH_3$ antisymmetric deformation (80%), $CH_3$ rock (20%) |
| 1401 s | 1406 vw | 1446 | 1433 | 1411 | $\nu_{22}$ (E) $CH_3$ symmetric deformation (95%) |
| 1401 s | 1406 vw | 1405 | | 1404 | $\nu_5$ ($A_1$) $CH_3$ symmetric deformation (85%), $NC_3$ symmetric stretch (8%), $CH_3$ symmetric stretch(7%) |
| 1254 s | 1256 m | 1272 | 1283 | 1253 | $\nu_{23}$(E) $CH_3$ rock (41%), $NC_3$ antisymmetric stretch (23%), $CH_3$ antisymmetric deformation (16%), $NC_3$ antisymmetric deformation (9%) |
| 1126 m | 1124 vw | 1183 | 1183 | 1129 | $\nu_7$ ($A_1$) $CH_3$ rock (77%), $CH_3$ antisymmetric deformation (14%), $CH_3$ antisymmetric stretch (8%) |
| 1120 m | | 1108 | 1100[c] | 1111 | $\nu_{25}$ (E) $CH_3$ rock (83%), $CH_3$ antisymmetric deformation (17%) |
| 992 s | 996 s | 1043 | 1048 | 1004 | $\nu_{26}$ (E) $NC_3$ antisymmetric stretch (69%), $CH_3$ rock (23%) |
| 920 s | | | | | $\nu_6$ ($A_1$) $^{10}BD_3$ symmetric deformation (77%), N-B stretch (23%) |
| 904 vs | | | | 898 | $\nu_6$ ($A_1$) $^{11}BD_3$ symmetric deformation (77%), N-B stretch (23%) |
| 865 s | | | | 844 | $\nu_{24}$ (E) $BD_3$ antisymmetric deformation (95%) |
| | 863 s | | | | |
| 858 s | | 825 | 826 | 856 | $\nu_8$ ($A_1$) $NC_3$ symmetric stretch (72%), N-B stretch (19%) |
| | 722 mw | | | 723 | $\nu_{27}$ (E) $BD_3$ rock (82%) |
| | 660 m | | | 646 | $\nu_9$ ($A_1$) N-B stretch (69%), $NC_3$ symmetric stretch (18%), $NC_3$ symmetric deformation (13%) |
| 434 m | 432 w | 425 | 422 | 445 | $\nu_{28}$ (E) $NC_3$ antisymmetric deformation (98%) |
| 326 m | 326 w | 366 | 364 | 328 | $\nu_{10}$ ($A_1$) $NC_3$ symmetric deformation (75%), $CH_3$ antisymmetric stretch (13%), $CH_3$ rock (11%) |
| 321 m | | | | 312 | $\nu_{30}$ (E) $NC_3$ rock (66%), $CH_3$ rock (14%), $CH_3$ symmetric deformation (10%) |

[a] Abbreviations used: see Table I.

[b] The infrared and Raman gas frequencies are taken from Reference 28 and Reference 29, respectively.

[c] This mode was not observed in the gas so the liquid frequency is listed from the same reference.

Table III. Fundamental Frequencies (cm$^{-1}$) and Assignments for $(CD_3)_3NBH_3$.[a]

| $(CD_3)_3NBH_3$ | | $(CD_3)_3N$[b] | | $(CD_3)_3NBH_3$ | |
|---|---|---|---|---|---|
| Infrared ν(cm$^{-1}$) | Raman Δν(cm$^{-1}$) | Infrared ν(cm$^{-1}$) | Raman Δν(cm$^{-1}$) | Calculated (cm$^{-1}$) | Assignment and Approximate Description |
| 2354 s | 2350 m | | | 2359 | $\nu_{19}$ (E) $BH_3$ antisymmetric stretch (100%) |
| 2265 s | 2266 vs | | | 2279 | $\nu_3$ ($A_1$) $BH_3$ symmetric stretch (100%) |
| 2265 s | 2266 vs | 2186 | | 2201 | $\nu_1$ ($A_1$) (100%) |
| 2155 vw | 2156 s | 2234 | | 2213 | $\nu_{16}$ (E) $CD_3$ antisymmetric stretch (100%) |
| 2145 vw | | 2182 | | 2178 | $\nu_{17}$ (E) (100%) |
| 2145 vw | | 2032 | | 2129 | $\nu_2$ ($A_1$) $CD_3$ symmetric stretch (100%) |
| 2077 m | 2077 s | | | 2128 | $\nu_{18}$ (E) (100%) |
| 1181 vs | 1190 m | 1223 | 1229 | 1196 | $\nu_{23}$ (E) $CD_3$ rock (11%), $BH_3$ antisymmetric deformation (43%), $NC_3$ antisymmetric stretch (28%), $BH_3$ rock (17%) |
| 1154 sh m | 1159 s | | | 1152 | $\nu_{24}$ (E) $BH_3$ antisymmetric deformation (34%), $CD_3$ rock (21%), $NC_3$ antisymmetric stretch (19%), $NC_3$ antisymmetric deformation (8%) |
| 1154 s | | | | 1158 | $\nu_6$ ($A_1$) $BH_3$ symmetric deformation (78%), $CD_3$ symmetric deformation (13%), $NC_3$ symmetric stretch (9%) |
| 1131 mw | | 1002 | 1008 | 1122 | $\nu_5$ ($A_1$) $CD_3$ symmetric deformation (48%), $NC_3$ symmetric stretch (22%), $BH_3$ deformation (7%) |
| 1118 vs | 1117 m | 1071 | | 1118 | $\nu_{22}$ (E) $CD_3$ symmetric deformation (59%), $NC_3$ antisymmetric stretch (24%), $CD_3$ symmetric stretch (6%), $BH_3$ antisymmetric deformation (6%) |
| 1076 w | 1073 sh m | | | 1057 | $\nu_4$ ($A_1$) $CD_3$ antisymmetric deformation (85%), $CD_3$ rock (14%) |
| 1062 s | | 1063 | 1068 | 1053 | $\nu_{20}$ (E) $CD_3$ antisymmetric deformation (85%), $CD_3$ rock (8%) |
| 1054 sh mw | 1057 vs | | | 1046 | $\nu_{21}$ (E) $CD_3$ antisymmetric deformation (87%) |
| 941 m | 944 m | | | 934 | $\nu_{27}$ (E) $BH_3$ rock (60%), $CD_3$ rock (28%) |
| 898 vw | | | 1147 | 905 | $\nu_7$ ($A_1$) $CD_3$ rock (53%), N-B stretch (13%), $CD_3$ antisymmetric stretch (11%) |
| 851 vw | 853 m | 873 | 881 | 839 | $\nu_{25}$ (E) $CD_3$ rock (68%), $NC_3$ antisymmetric stretch (19%) |
| 816 m | 818 s | 807 | | 830 | $\nu_{26}$ (E) $CD_3$ rock (51%), $NC_3$ antisymmetric stretch (19%), $BH_3$ rock (13%), $CD_3$ symmetric deformation (10%) |
| 759 m | 761 vs | 739 | 748 | 761 | $\nu_8$ ($A_1$) $NC_3$ symmetric stretch (33%), N-B stretch (38%), $CD_3$ rock (20%), $CD_3$ symmetric deformation (10%) |
| | | 641 vs | | 640 | $\nu_9$ ($A_1$) N-B stretch (55%), $NC_3$ symmetric stretch (40%) |
| 386 m | 384 w | 370 | 357 | 380 | $\nu_{28}$ (E) $NC_3$ antisymmetric deformation (90%) |
| 316 m | 314 m | 310 | 318 | 314 | $\nu_{10}$ ($A_1$) $NC_3$ symmetric deformation (77%), $CD_3$ antisymmetric stretch (12%), $CD_3$ rock (8%) |
| 314 sh m | 314 m | | | 322 | $\nu_{30}$ (E) $NC_3$ rock (68%), $CD_3$ rock (8%), $CD_3$ symmetric deformation (8%) |
| 246 w | | 193 | 202 | 246 | $\nu_{29}$ (E) $CD_3$ torsion (100%) |

[a] Abbreviations used: see Table I.

[b] The infrared gas and Raman liquid frequencies are taken from Reference 28 and Reference 29, respectively.

Table IV. Fundamental Frequencies (cm$^{-1}$) and Assignments for $(CD_3)_3NBD_3$.[a]

| $(CD_3)_3NBD_3$ | | $(CD_3)_3N$[b] | | $(CD_3)_3NBD_3$ | |
|---|---|---|---|---|---|
| Infrared ν(cm$^{-1}$) | Raman Δν(cm$^{-1}$) | Infrared ν(cm$^{-1}$) | Raman Δν(cm$^{-1}$) | Calculated (cm$^{-1}$) | Assignment and Approximate Description |
| 2264 | 2265 | 2186 | | 2201 | $\nu_1$ ($A_1$) (100%) |
| 2153 | 2153 | 2234 | | 2214 | $\nu_{16}$ (E) $CD_3$ antisymmetric stretch (100%) |
| 2143 | | 2182 | | 2178 | $\nu_{17}$ (E) (100%) |
| 2143 | | 2032 | | 2129 | $\nu_2$ ($A_1$) $CD_3$ symmetric stretch (100%) |
| 2077 | 2077 | | | 2128 | $\nu_{18}$ (E) (100%) |
| 1761 | 1763 | | | 1780 | $\nu_{19}$ (E) $BD_3$ antisymmetric stretch (100%) |
| 1644 | 1646 | | | 1633 | $\nu_3$ ($A_1$) $BD_3$ symmetric stretch (100%) |
| 1172 | 1172 | 1223 | 1229 | 1155 | $\nu_{23}$ (E) $NC_3$ antisymmetric stretch (50%), $CD_3$ rock (24%), $NC_3$ antisymmetric deformation (10%) |
| 1127 | 1129 | 1002 | 1008 | 1129 | $\nu_5$ ($A_1$) $CD_3$ symmetric deformation (56%), $NC_3$ antisymmetric stretch (28%) |
| 1119 | 1110 | 1071 | | 1115 | $\nu_{22}$ (E) $CD_3$ symmetric deformation (74%) |
| 1074 | 1071 | | | 1057 | $\nu_4$ ($A_1$) $CD_3$ antisymmetric deformation (85%), $CD_3$ rock (13%) |
| 1063 | | 1063 | 1068 | 1054 | $\nu_{20}$ (E) $CD_3$ antisymmetric deformation (84%) |
| 1055 | 1056 | | | 1045 | $\nu_{21}$ (E) $CD_3$ antisymmetric deformation (88%) |
| 916 | | | | | $\nu_6$ ($A_1$) $^{10}BD_3$ symmetric deformation |
| 900 | | | | 893 | $\nu_6$ ($A_1$) $^{11}BD_3$ symmetric deformation (53%), $CD_3$ rock (29%) |
| 888 | 887 | | 1147 | 907 | $\nu_7$ ($A_1$) $CD_3$ rock (35%), N-B stretch (22%), $BD_3$ symmetric deformation (17%), $NC_3$ symmetric deformation (8%) |
| 863 | | | | 865 | $\nu_{24}$ (E) $BD_3$ antisymmetric deformation (35%), $CD_3$ rock (50%) |
| 855 | 857 | 873 | 881 | 855 | $\nu_{25}$ (E) $CD_3$ rock (42%), $NC_3$ antisymmetric stretch (21%), $BD_3$ antisymmetric deformation (18%) |
| 817 | 818 | 807 | | 823 | $\nu_{26}$ (E) $CD_3$ rock (49%), $BD_3$ antisymmetric deformation (31%) $NC_3$ antisymmetric stretch (8%) |
| 759 | 759 | 739 | 748 | 751 | $\nu_8$ ($A_1$) $NC_3$ symmetric stretch (42%), N-B stretch (23%), $CD_3$ rock (15%), $CD_3$ symmetric deformation (13%) |
| | 708 | | | 703 | $\nu_{27}$ (E) $BD_3$ rock (73%) |
| | 610 | | | 610 | $\nu_9$ ($A_1$) N-B stretch (58%), $NC_3$ symmetric stretch (31%) |
| 382 | 380 | 370 | 357 | 378 | $\nu_{28}$ (E) $NC_3$ antisymmetric deformation(95%) |
| 297 | 297 | 310 | 318 | 305 | $\nu_{10}$ ($A_1$) $NC_3$ symmetric deformation (76%), $CD_3$ antisymmetric stretch (12%), $CD_3$ rock (8%) |
| 297 | 297 | | | 296 | $\nu_{30}$ (E) $NC_3$ rock (65%), $CD_3$ rock (12%), $CD_3$ symmetric deformation (11%) |
| 245 | | 193 | 202 | 244 | $\nu_{29}$ (E) $CD_3$ torsion (100%) |

[a] Abbreviations used: see Table I.

[b] The infrared gas and Raman liquid frequencies are taken from Reference 28 and Reference 29, respectively.

Table V. Internal Force Constants for Trimethylamineborane-$d_0$, -$d_3$, -$d_9$, and -$d_{12}$.[a]

| Force Constant | Group | Mdyn/Å | Force Constant | Group | Mdyn/Å |
|---|---|---|---|---|---|
| $K_R$ | N-B stretch | 2.59±.09 | $F_{R\delta}$ | N-B stretch/∢NBH bend | 0.24±.03 |
| $K_Q$ | N-C stretch | 4.91±.10 | $F_{Qq}$ | N-C stretch/C-H stretch | 0.45±.06 |
| $K_r$ | B-H stretch | 2.94±.02 | $F_{Q\alpha}$ | N-C stretch/∢CNC bend | 0.63±.08 |
| $K_q$ | C-H stretch | 4.90±.02 | $F_{Q\beta}$ | N-C stretch/∢CNB bend | 0.74±.08 |
| $H_\alpha$ | ∢CNC bend | 1.51±.05 | $F_{Q\phi}$ | N-C stretch/∢NCH bend | 0.26±.03 |
| $H_\beta$ | ∢CNB bend | 0.94±.04 | $F_r$ | B-H stretch/B-H stretch | 0.04±.01 |
| $H_\gamma$ | ∢HBH bend | 0.40±.01 | $F_{q\alpha}$ | C-H stretch/∢CNC bend | 0.60±.09 |
| $H_\delta$ | ∢NBH bend | 0.71±.02 | $F_{q\beta}$ | C-H stretch/∢CNB bend | 0.58±.12 |
| $H_\sigma$ | ∢HCH bend | 0.53±.01 | $F_{q\phi}$ | C-H stretch/∢NCH bend | 0.55±.05 |
| $H_\phi$ | ∢NCH bend | 0.89±.01 | $F_\beta$ | ∢CNB bend/∢CNB bend | -0.40±.03 |
| $\tau$ | $CH_3$ torsion | 0.024±.002 | $F_{\beta\phi}$ | ∢CNB bend/∢NCH bend | -0.59±.03 |
| $F_{RQ}$ | N-B stretch/N-C stretch | 0.20±.04 | $F_{\phi'}$ | ∢NCH bend/∢NCH bend | -0.10±.01 |
| $F_{R\alpha}$ | N-B stretch/∢CNC bend | -0.20±.05 | | | |

[a] All bending force constants were divided by 1Å.

corresponding trimethylphosphine molecule has definitely been shown[25] to be a plastic crystal and there is no reason to believe that this molecule would not also crystallize in a plastic phase; thus, the effective symmetry is consistent with the predicted symmetry. Further studies to determine the nature of this crystal seem to be warranted.

It appears that the Raman effect is the best method to observe the N–B stretching mode. Several studies on phosphorus–boron adducts have shown[17,26,27] the Raman technique to be more sensitive to the P–B stretching mode than the infrared technique. Evidence from the nitrogen–boron adducts that have been studied to date indicates the N–B stretch should occur between 600 and 800 cm$^{-1}$.

The two force constants determined by the borane group, the B–H stretch and the ∠HBH bend, do not vary greatly from one borane adduct to another. The B–H stretching force constant in several nitrogen,[5] phosphorus,[17] and arsenic[18] adducts has a value of 3.0 ± 0.1 mdyn/Å. In the same collection of compounds, the ∠HBH bending force constant has the value 0.38 ± 0.03 mdyn/Å.

The external top angle bending force constant is the only borane moiety force constant that reflects the identity of the atom to which the borane group is bonded. Since this force constant participates in both the $BH_3$ rock and the symmetric deformation, the frequencies of both of these modes vary depending on the donor element. The external top bending force constant decreases in value as one descends group Va in the periodic table. The following examples of the external top bending force constant are taken from the trimethyl adducts: ∠NBH, 0.71 mdyn/Å; ∠PBH, 0.62 mdyn/Å; and ∠AsBH, 0.58 mdyn/Å. As would be expected from the trend of decreasing magnitudes of the external top bending force constants and the relative invariance of the ∠HBH bending force constant, the amount of separation between the antisymmetric deformation and symmetric deformation increases and the frequency of both the symmetric deformation and the rock decreases as one descends the series.

The CNDO/2 calculation in the present study points out some of the limitations of this method. This method gave very poor results for the force constants but it appears that it can be used to compare differences in force constants among a series of molecules. From this method, one calculates the dipole moment very well for the CNDO/2 equilibrium structure, but one calculates a very high value for the dipole if the structure as determined from microwave data is used.

As an aid in checking the assignments, the Teller–Redlich product rule was calculated for the $A_1$ and E symmetry species of the four isotopic molecules. The average error for the $A_1$ symmetry species is 1.1% for each of the three isotopically substituted molecules. The error for the -$d_9$ and -$d_{12}$ species of E symmetry is less than 0.8%; however, the error in $(CH_3)_3NBD_3$ is 3.8%. Thus, the error in the E symmetry species of the -$d_3$ compound is rather large, but on reexamination of the assignment, there can be little doubt that it is correct. Only three modes in the E symmetry block enter into the calculation of the theoretical isotopic shift for the -$d_3$ molecule. The antisymmetric $BH_3$ stretch shows a shift of 1.345 on deuteration. The band assigned to this mode at 2360 cm$^{-1}$ is the most intense band in the $BH_3$ stretching region in the infrared spectrum and the band at 1762 cm$^{-1}$ to which the antisymmetric $BD_3$ stretch is assigned is again the most intense infrared band in this region. No other band above 1670 cm$^{-1}$, the theoretical lower limit for the antisymmetric stretch, is sufficiently intense to be assigned to this mode. The antisymmetric $BH_3$ deformation, which is assigned to a shoulder on the intense band at 1164 cm$^{-1}$ is assigned to a band at 865 cm$^{-1}$ in the -$d_3$ molecule and gives a shift factor of 1.35. In the infrared spectrum, the band at 865 cm$^{-1}$ is very intense and in the Raman spectrum it is a weak shoulder on the 853-cm$^{-1}$ band which is assigned to the $A_1$ $NC_3$ symmetric stretch. Again, there is not another band above the theoretical minimum of 828 cm$^{-1}$ to which the antisymmetric $BD_3$ deformation can be assigned. The $BH_3$ rock is assigned to a Raman band at 915 cm$^{-1}$ in the -$d_0$ and to a Raman band at 722 cm$^{-1}$ in the -$d_3$ molecule. The next band below the 722-cm$^{-1}$ band is the 660-cm$^{-1}$ band assigned to the N–B stretch. If the rock were assigned to this band, the Teller–Redlich rule would be violated. In conclusion, bands for all three of these modes were assigned close to the same frequency in the -$d_{12}$ compound where the error in the product rule is only 0.6%; thus, it is concluded that the assignment for these modes is correct.

*Acknowledgment.* The authors gratefully acknowledge the financial support of this work by the National Science Foundation by Grant No. GP-33780. One of us (J. A. B.) wishes to thank the National Cancer Institute for a postdoctoral fellowship (No. 1-F02-CA-51378-01).

*Miniprint Material Available.* Full-sized photocopies of the miniprinted material (Tables I–V) from this paper only or microfiche (105 × 148 mm, 24× reduction, negatives) containing all of the miniprinted and supplementary material for the papers in this issue may be obtained from the Journals Department, American Chemical Society, 1155 16th St., N.W., Washington, D. C. 20036. Remit check or money order for $3.00 for photocopy or $2.00 for microfiche, referring to code number JPC-74-1503.

## References and Notes

(1) Part I: J. D. Odom, Y. S. Li, and J. R. Durig, *J. Mol. Struct.*, **16**, 443 (1973).

(2) NIH Postdoctoral Fellow, 1972–1972.

(3) Taken in part from the thesis of B. A. Hudgens to be submitted to the Department of Chemistry in partial fulfillment of the Ph.D. Degree.

(4) B. Rice, R. J. Galiano, and W. J. Lehmann, *J. Phys. Chem.*, **61**, 1222 (1957).

(5) R. C. Taylor, *Advan. Chem. Ser.*, **No. 42**, 59 (1964).

(6) J. W. Raymonda, *Chem. Phys. Lett.*, **11**, 491 (1971).

(7) J. R. Durig, S. M. Craven, and J. W. Bragin, *J. Chem. Phys.*, **53**, 38 (1970).

(8) A. D. Norman and W. L. Jolly, *Inorg. Syn.*, **11**, 15 (1968).

(9) D. F. Shriver, "The Manipulation of Air-Sensitive Compounds," McGraw-Hill, New York, N. Y., 1969.

(10) J. Dobson and R. Schaeffer, *Inorg. Chem.*, **9**, 2183 (1970).

(11) A. B. Burg and H. I. Schlesinger, *J. Amer. Chem. Soc.*, **59**, 780 (1937).

(12) The Raman spectrophotometer was purchased with funds from a National Science Foundation Grant, No. GP-28068.

(13) R. T. Hall and J. M. Dowling, *J. Chem. Phys.*, **47**, 2454 (1967); **52**, 1161 (1970).

(14) F. G. Baglin, S. F. Bush, and J. R. Durig, *J. Chem. Phys.*, **47**, 2104 (1967).

(15) IUPAC, "Tables of Wavenumbers for the Calibration of Infrared Spectrometers," Butterworths, Washington, D. C., 1961.

(16) G. Dellepiane and G. Zerbi, *J. Chem. Phys.*, **48**, 3573 (1968).

(17) J. D. Odom, B. A. Hudgens, and J. R. Durig, *J. Phys. Chem.*, **77**, 1972 (1973).

(18) J. R. Durig, B. A. Hudgens, Y. S. Li, and J. D. Odom, to be submitted for publication.

(19) E. B. Wilson, J. C. Decius, and C. Cross, "Molecular Vibrations. The Theory of Infrared and Raman Vibrational Spectra," McGraw-Hill, New York, N. Y., 1955.

(20) J. H. Schachtschneider, Technical Report No. 231-64 and 57-65, Shell Development Company.

(21) See paragraph at end of paper regarding miniprinted material.
(22) D. R. Lide, Jr., and D. E. Mann, *J. Chem. Phys.*, **28**, 572 (1958).
(23) W. E. Palke, *J. Chem. Phys.*, 56, 5308 (1972).
(24) J. Timmermans, *J. Phys. Chem. Solids*, **18**, 1 (1961).
(25) R. Thomas, *Diss. Abstr.*, **26**, 3069 (1965).
(26) R. C. Taylor and T. C. Bissot, *J. Chem. Phys.*, **25**, 780 (1956).
(27) J. D. Odom, S. Riethmiller, J. D. Witt, and J. R. Durig, *Inorg. Chem.*, **12**, 1123 (1973).
(28) J. N. Gayles, *Spectrochim. Acta, Sect. A*, **23**, 1521 (1967).
(29) P. H. Clippard and R. C. Taylor, *J. Chem. Phys.*, **50**, 1472 (1969).

# Transition State Enthalpies of Transfer in Aqueous Dimethyl Sulfoxide Solutions. The Alkaline Hydrolysis of Ethyl Acetate

**Richard Fuchs,*[1] C. Patrick Hagan, and Randolph F. Rodewald**

*Department of Chemistry, University of Houston, Houston, Texas 77004* *(Received October 31, 1973; Revised Manuscript Received April 29, 1974)*

Enthalpies of solution of ethyl acetate in water, DMSO, and nine aqueous DMSO mixtures, and of tetraphenylphosphonium bromide, sodium tetraphenylborate, sodium bromide, and sodium hydroxide in two aqueous DMSO mixtures have been measured. Using the extrathermodynamic assumption $\Delta\Delta H_s(\mathrm{Ph_4P^+})$ = $\Delta\Delta H_s(\mathrm{Ph_4B^-})$ enthalpies of transfer of hydroxide ion from water to aqueous DMSO mixtures have been calculated. $\Delta\Delta H_s$ values for ethyl acetate have also been obtained. Transition state enthalpies of transfer for the alkaline hydrolysis reaction have been derived from the $\Delta\Delta H_s$ values and experimental enthalpies of activation. Above 15 mol % DMSO $\Delta\Delta H_s$ (transition state) is more positive than $\Delta\Delta H_s$ (reactants). Thus, the increasing reaction rates observed with increasing DMSO concentration do not result from the large enthalpy of desolvation of hydroxide ion which is compensated by desolvation of the transition state, but, rather, by an entropy effect.

## Introduction

A remarkable increase in the nucleophilicity and basicity of anions is observed upon transfer from protonic solvents to dipolar aprotic solvents.[2] The effect is particularly large for anions having negative charge localized on a small atom.[2,3] Frequently, ionic compounds containing small anions ($\mathrm{F^-}$, $\mathrm{HO^-}$, $\mathrm{CH_3O^-}$) have low solubility in aprotic solvents, and it is fortunate that the high reactivity of these anions is retained to a considerable degree in mixtures of protonic and aprotic solvents in which the appropriate salts are soluble.[2,4]

Haberfield[4] has compared the alkaline ester hydrolysis reaction in two aqueous ethanol and two aqueous dimethyl sulfoxide (DMSO) mixtures. Using the relationship[5] $\Delta\Delta H^t = \Delta\Delta H_s + \Delta\Delta H^*$, where $\Delta\Delta H_s$ is the enthalpy of transfer of the reactants from one solvent to another, and $\Delta\Delta H^*$ is the difference in the activation enthalpies of the reaction in the two solvents, the enthalpy of transfer of the transition state ($\Delta\Delta H^t$) was determined. Haberfield made the reasonable assumption that the enthalpy of activation for the reaction is essentially equal to that of the first step, the addition of hydroxide ion to the carbonyl carbon atom giving a tetrahedral intermediate. The very large desolvation of hydroxide ion on transfer from aqueous ethanol to aqueous DMSO is only partially reflected in the enthalpy of activation. The transition states, like hydroxide ion, were demonstrated to undergo substantial desolvation upon solvent transfer. Although such discussions of ion and transition state solvation are based only on the enthalpy contribution to solvation, and ignore the entropy contribution, it was nevertheless surprising that hydroxide was reported[4] to be 3.5 kcal/mol *less* solvated upon transfer from a less to a more highly aqueous DMSO mixture (mole fraction 0.70 → 0.60).

We have recently examined single ion enthalpies of transfer among DMSO–water mixtures to 50 mol % DMSO.[6] Hydroxide ion is increasingly desolvated as DMSO is increased beyond 10 mol %. Rates of alkaline hydrolysis of ethyl acetate have been measured and the activation enthalpies reported[7,8] for mixtures of DMSO and water up to 60 mol % DMSO. If we assume that the molar heat of vaporization is an approximate indication of the hole energy of a solvent, then it appears that large ions[6] and neutral molecules[9] of low polarizability have a tendency to be desolvated with increasing hole energy. Since water and DMSO mix highly exothermally, it is likely that the total of all solvent–solvent forces is greater in the mixture than in either pure solvent, and that the hole energy of the mixture is also greater. There is, however, no general agreement on which experimental property of a solvent, if any, can be taken as an accurate measure of the hole energy. The enthalpy of transfer of a solute from one solvent to another depends on changes in hole energy, the strength of individual solvent–solute interactions, and the number of these interactions, as well as other factors. From the enthalpy of transfer one sees the change in the sum of these effects. Our surmises concerning hole energies thus represent only one possible model.

The transition state for the alkaline hydrolysis of ethyl acetate (which presumably resembles the tetrahedral intermediate) is an anion of considerable size and rather low

**TABLE I: Enthalpies of Solution[a] in Aqueous DMSO at 25°**

| % DMSO[b] | Mol %[c] | $Ph_4PBr$[d] | $NaBPh_4$[d] | NaBr | NaOH | EtOAc[e] |
|---|---|---|---|---|---|---|
| $H_2O$[f] | 0 | 1.9 ± 0.1[g] | −4.5 ± 0.1 | −0.12 ± 0.01 | −10.5 ± 0.2 | −2.3 ± 0.1 |
| 15[f] | 5 | 4.0 ± 0.1 | −1.3 ± 0.1 | −0.51 ± 0.03 | −10.5 ± 0.1 | −1.1 ± 0.1 |
| 30[f] | 11 | 4.6 ± 0.1 | −0.46 ± 0.03 | −0.74 ± 0.01 | −10.4 ± 0.3 | 0.19 ± 0.06 |
| 50[f] | 20 | 5.2 ± 0.1 | −1.3 ± 0.1 | −1.1 ± 0.1 | −7.3 ± 0.1 | 1.6 ± 0.1 |
| 60[f] | 27 | 4.7 ± 0.1 | −4.2 ± 0.1 | −1.6 ± 0.1 | −6.4 ± 0.1 | 1.9 ± 0.1 |
| 65[f] | 32 | 3.7 ± 0.1 | −6.0 ± 0.1 | −1.9 ± 0.1 | −5.7 ± 0.1 | 2.0 ± 0.1 |
| 70[f] | 37 | 3.8 ± 0.1 | −7.5 ± 0.1 | −2.6 ± 0.1 | −4.1 ± 0.1 | 1.8 ± 0.1 |
| 80[f] | 50 | 2.5 ± 0.1 | −10.8 ± 0.2 | −3.7 ± 0.1 | −3.4 ± 0.1 | 1.5 ± 0.1 |
| 85 | 59 | 2.0 ± 0.1 | −12.3 ± 0.1 | −4.3 ± 0.1 | −2.8 ± 0.1 | 1.2 ± 0.1 |
| 90 | 70 | 1.6 ± 0.1 | −13.0 ± 0.4 | −4.9 ± 0.1 | −2.1 ± 0.1 | 0.93 ± 0.1 |
| DMSO[f] | 100 | 0.34 ± 0.07 | −14.3 ± 0.1 | −6.2 ± 0.1 | 0.0 | 0.62 ± 0.04 |

[a] Values of $\Delta H_s$ in kcal/mole are averages of 3–12 determinations on samples at $10^{-4}$ to $10^{-3}$ $M$. [b] Per cent by volume. $X$% DMSO is made from $X$ volumes of DMSO + (100 − $X$) volumes of water. [c] Mole per cent DMSO. [d] Ph = phenyl. [e] Ethyl acetate. [f] Values other than EtOAc in these solvents from ref 6. [g] Average deviation.

polarizability. It would therefore be of considerable interest to examine the transition state solvation in the various aqueous DMSO solutions.

## Results

Some newly measured enthalpies of solution ($\Delta H_s$) are listed in Table I. These, together with previously measured values,[6] were used to calculate the enthalpies of transfer in Table II. Single ion $\Delta\Delta H_s$ values were calculated using the assumption[6] $\Delta\Delta H_s[(C_6H_5)_4P^+] = \Delta\Delta H_s[(C_6H_5)_4B^-]$. The enthalpies of transfer for the reactants, hydroxide ion, and ethyl acetate, together with enthalpy of activation data were used to calculate the transition state enthalpies of transfer in Table III. From the enthalpies of transfer and previously published free energies of transfer,[10] entropies of transfer of ethyl acetate from water to aqueous DMSO mixtures have been calculated, and are presented in Table IV.

**TABLE II: Enthalpies of Transfer[a] from Water to Aqueous DMSO at 25°**

| % DMSO[b] | $\Delta\Delta H_s$: $Ph_4P^+$ [c] | $Na^+$ | $Br^-$ | $OH^-$ | EtOAc |
|---|---|---|---|---|---|
| 15 | 2.8 | 0.4 | −0.7 | −0.4 | 1.2 |
| 30 | 4.1 | 0.9 | −1.4 | −0.8 | 2.5 |
| 50 | 3.7 | −0.5 | −0.5 | 3.7 | 3.9 |
| 60 | 2.3 | −2.0 | 0.5 | 6.1 | 4.2 |
| 65 | 1.0 | −2.5 | 0.8 | 7.3 | 4.3 |
| 70 | 0.7 | −3.7 | 1.2 | 10.1 | 4.1 |
| 80 | −1.0 | −5.3 | 1.6 | 12.4 | 3.8 |
| 85 | −1.7 | −6.1 | 1.8(1.2)[d] | 13.8 | 3.5 |
| 90 | −2.0 | −6.5 | 1.7(1.3)[d] | 14.9 | 3.2 |
| DMSO | −2.6 | −7.2 | 1.0 | 17.7 | 2.9 |

[a] Values of $\Delta\Delta H_s$ in kcal/mole. Estimated error 0.2–0.3 kcal/mol. [b] Per cent by volume. [c] $\Delta\Delta H_s(Ph_4B^-) = \Delta\Delta H_s(Ph_4P^+)$. [d] Values in parentheses from ref 16.

**TABLE III: Transition State Enthalpies of Transfer[a,b] in the Base-Catalyzed Hydrolysis of Ethyl Acetate at 25°**

| % DMSO[c] | Mol %[d] | $E_a$[b,e] | $\Delta\Delta H^*$[b] | $\Delta\Delta H_s$-($OH^-$)[b] | $\Delta\Delta H_s$-(EtOAc)[b] | $\Delta\Delta H^{\ddagger}$ |
|---|---|---|---|---|---|---|
| $H_2O$ | 0 | 11.4 | | | | |
| 10 | 3 | 11.2 | −0.2 | −0.3 | 0.9 | 0.4 |
| 20 | 6 | 11.0 | −0.4 | −0.8 | 1.7 | 0.5 |
| 40 | 15 | 11.2 | −0.2 | 1.0 | 3.3 | 4.1 |
| 60 | 28 | 11.7 | 0.3 | 6.0 | 4.2 | 10.5 |
| 80 | 51 | 12.3 | 0.9 | 12.2 | 3.8 | 16.9 |
| 84.5 | 58 | 12.5 | 1.1 | 13.4 | 3.6 | 18.1 |

[a] Reference solvent: water. [b] Kcal/mole. [c] Solvent is 100 − (% DMSO) ml water per 100 ml total volume. [d] Mole per cent DMSO. [e] Energy of activation from ref 7.

## Discussion

*The Tetraphenylphosphonium Tetraphenylborate Assumption.* This assumption for estimating single ion enthalpies of transfer has previously[6] been discussed and recommended. In transfers from water to DMSO the $Ph_4PBPh_4$ assumption gives single ion values[6] in better agreement with Arnett's values[11] based on the $Ph_4AsBPh_4$ assumption than does another set of values[12] also based on the $Ph_4AsBPh_4$ assumption. In transfers[12] from methanol to DMF, methanol to DMSO, propylene carbonate to DMF, and propylene carbonate to methanol, single ion values for $Ph_4As^+$ and $Ph_4P^+$ differ by 0.2 kcal/mol or less, which is less than the combined experimental error limits in measurement. There appears to be no reason to believe that the two assumptions do not give equivalent results.

If the two assumptions were not exactly equivalent, or if $\Delta H_s(Ph_4PBr)$ or $\Delta H_s(NaBPh_4)$ were somewhat in error, the calculated values of $\Delta\Delta H_s$ of all the anions would be incorrect by the same amount.[6] Our conclusions in the next section regarding the *relative* (enthalpy of) solvation of hydroxide ion and an anionic transition state would, therefore, be unaffected.

*Transition State Enthalpies of Transfer.* Over the solvent composition range examined in Table III (0–58 mol % DMSO) the rate of alkaline ethyl acetate hydrolysis[7] increases with increasing DMSO concentration, by a factor of about 6. The free energy of activation meanwhile decreases by about 1 kcal/mol. The enthalpy of activation (or $E_a$), on the other hand, *increases* by 1.1 kcal/mol, and $T\Delta S^*$ (at 25°) increases by 2.1 kcal/mol. The minimum in the plot of $\Delta H^*$ *vs.* solvent composition occurs at about 10 mol % DMSO. Tommila[7] discussed the form of the curve in terms of changes in solvation of the reactants and transition state, and attributed the $\Delta H^*$ minimum to a minimum in transition state solvation.[13] The present results (Table III) indicate that the principal enthalpy factor operative at this composition is desolvation of ethyl acetate by 1.7 kcal/mol, relative to the solvent water. Hydroxide ion reaches a solvation maximum at this point (in terms of enthalpy). The transition state $\Delta\Delta H_s$ becomes increasingly positive with DMSO addition throughout the entire solvent composition range, but this becomes more pronounced at DMSO concentrations greater than about 10 mol %. It has been recognized that the free energies of transfer of neutral molecules[11] and of ions[14] from water to organic solvents are determined by the $T\Delta\Delta S$ term as much as or more than by $\Delta\Delta H_s$. Unfortunately, comparable $\Delta\Delta G$ values for hydroxide ion are not presently avail-

**TABLE IV: Free Energy, Enthalpy, and Entropy of Transfer of Ethyl Acetate from Water to Aqueous DMSO at 25°**

| % DMSO[a] | Mol %[b] | Log $^{w}\gamma^{sc}$ | $\Delta\Delta G^{d,e}$ | $\Delta\Delta H_s{}^{d}$ | $T\Delta\Delta S^{d,f}$ |
|---|---|---|---|---|---|
| 30.5 | 11 | 0.088 | 0.12 | 2.5[g] | 2.4 |
| 50 | 20 | 0.105 | 0.14 | 3.9 | 3.8 |
| 63 | 30 | 0.024 | 0.03 | 4.2[g] | 4.2 |
| 72.5 | 40 | −0.134 | −0.18 | 4.0[g] | 4.2 |
| 80 | 50 | −0.270 | −0.37 | 3.8 | 4.2 |
| 85 | 59 | −0.421 | −0.57 | 3.5 | 4.1 |
| 89 | 67 | −0.567 | −0.77 | 3.3[g] | 4.1 |
| 94 | 80 | −0.675 | −0.92 | 3.1[g] | 4.0 |
| 97.5 | 91 | −0.755 | −1.0 | 3.0[g] | 4.0 |

[a] Per cent by volume. [b] Mole per cent DMSO. [c] Solvent activity coefficients of EtOAc from ref 10. [d] Kcal/mole. [e] $\Delta\Delta G = 2.303RT \log {}^{w}\gamma^{s}$. [f] $T\Delta\Delta S = \Delta\Delta H_s - \Delta\Delta G$. [g] Values estimated graphically.

able.[15] Whereas $\Delta\Delta H_s$ values for ethyl acetate suggest desolvation in all aqueous DMSO mixtures relative to water, the more appropriate criterion of solvation, $\Delta\Delta G$, indicates slight desolvation at low DMSO concentrations, and then increased solvation with increasing DMSO. Both $\Delta\Delta H_s$ and $T\Delta\Delta S$ reach maxima at about the concentration of maximum solvent structure, DMSO·2H$_2$O (33 mol %). However, $T\Delta\Delta S$ varies only slightly above 20 mol % DMSO, whereas $\Delta\Delta H_s$ decreases continuously, resulting in the observed decrease in $\Delta\Delta G$.

The fact that $\Delta G^*$ decreases by about 1 kcal/mol over the range of 0–58% DMSO, while $\Delta H^*$ increases by 1.1 kcal/mol,[7] indicates that the principal effect of solvent change in this system is a nonenthalpy (entropy) one. In view of the large positive $\Delta\Delta H_s$ values for OH$^-$ and EtOAc on transfer from water to the mixed solvents (Table II), it is surprising that $\Delta H^*$ does not diminish. However, at greater than 15 mol % DMSO $\Delta\Delta H^t$ (for the transition state) is more positive that those of the reactants combined (Table III). Assuming that the transition state rather closely resembles the tetrahedral intermediate

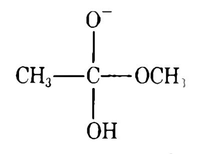

$$CH_3-\overset{\overset{\large O^-}{|}}{\underset{\underset{\large OH}{|}}{C}}-OCH_3$$

one would expect substantial desolvation with increasing DMSO concentration, first, on the basis of the inability of DMSO to strongly solvate a negatively charged oxygen atom (as with HO$^-$), and, second, because of the large "hole" energy which must be expended to accommodate this large ion within the highly structured mixed solvents, which is greater than that required to make the "small hole" for the hydroxide ion. It is not immediately obvious whether $\Delta\Delta H^t$ should be smaller than $\Delta\Delta H_s$ (reactants), of equal size, or slightly larger, as is observed.

A previous report[4] that hydroxide ion has a positive enthalpy of transfer from 70 to 60 mol % aqueous DMSO is in disagreement with the present results (Table II), which show a value of −1.1 kcal/mol (90 → 85 vol %; 70 → 59 mol %). Haberfield[4] derived $\Delta\Delta H_s$(OH$^-$) from the $\Delta\Delta H_s$ value for aqueous tetrabutylammonium hydroxide, and $\Delta\Delta H_s$(Bu$_4$N$^+$). Since the latter value is in agreement with a previous transfer value for tetrabutylammonium ion,[16] it is probable that an erroneous value of $\Delta\Delta H_s$(OH$^-$) resulted from the procedure of working with small differences between very large values of $\Delta H_s$(Bu$_4$NOH·130.9H$_2$O) and $\Delta H_s$(130.9H$_2$O). Values of $\Delta\Delta H_s$(OH$^-$) in Table III are based on direct $\Delta H_s$ measurements using anhydrous sodium hydroxide. Corrections for large amounts of water were, therefore, unnecessary.

## Experimental Section

Ethyl acetate (Baker Analyzed reagent grade) samples were introduced into the calorimeter using a 10-μl syringe. The purification of solvents and other reagents and the calorimetric procedure have been previously described.[6] Sample concentrations were $10^{-4}$ to $10^{-3}$ $M$. No dependence of $\Delta H_s$ on concentration was noted in this range.

## References and Notes

(1) Support of this research by the Robert A. Welch Foundation (Grant No. E-136) is gratefully acknowledged. The authors also wish to thank Professor A. J. Parker for helpful discussions.
(2) A. J. Parker, *Chem. Rev.*, **69**, 1 (1969).
(3) R. Fuchs and L. L. Cole, *J. Amer. Chem. Soc.*, **95**, 3194 (1973).
(4) P. Haberfield, J. Friedman, and M. F. Pinkston, *J. Amer. Chem. Soc.*, **94**, 71 (1972).
(5) E. M. Arnett, W. G. Bentrude, J. J. Burke, and P. M. Duggleby, *J. Amer. Chem. Soc.*, **87**, 1541 (1965).
(6) R. Fuchs and C. P. Hagan, *J. Phys. Chem.*, **77**, 1797 (1973).
(7) E. Tommila and M. L. Murto, *Acta Chem. Scand.*, **20**, 923 (1966).
(8) D. D. Roberts, *J. Org. Chem.*, **30**, 3516 (1965).
(9) R. Fuchs and R. F. Rodewald, *J. Amer. Chem. Soc.*, **95**, 5897 (1973).
(10) B. G. Cox and P. T. McTigue, *Aust. J. Chem.*, **20**, 1815 (1967).
(11) E. M. Arnett and D. R. McKelvey, *J. Amer. Chem. Soc.*, **88**, 2598 (1966).
(12) C. V. Krishnan and H. L. Friedman, *J. Phys. Chem.*, **73**, 3934 (1969); **75**, 3606 (1971).
(13) It should be recognized that Professor Tommila wrote this discussion more than a decade ago, when no experimental values of $\Delta\Delta H_s$ or $\Delta\Delta G$ were available for the reactants or transition state. In spite of this the major points of his discussion are remarkably correct.
(14) B. G. Cox and A. J. Parker, *J. Amer. Chem. Soc.*, **95**, 402 (1973).
(15) Values of $\Delta\Delta G$ for hydroxide ion from water to aqueous DMSO mixtures have been reported [A. K. Das and K. K. Kundu, *J. Chem. Soc., Faraday Trans. 1*, **69**, 730 (1973)]. These are based on an extrathermodynamic assumption [D. Feakins and P. Watson, *J. Chem. Soc.*, 4734 (1963)], which, for the halide ions [K. H. Khoo, *J. Chem. Soc. A*, 2932 (1972)] gives values surprisingly similar to one another, and for chloride ion gives a value far larger than that based on the Ph$_4$MBPh$_4$ type of assumption.[2] We velieve that the use of these $\Delta\Delta G$(OH$^-$) values with the present $\Delta\Delta H_s$ values would not provide meaningful conclusions.
(16) R. Fuchs, D. S. Plumbee, J., and R. F. Rodewald, *Thermochim. Acta*, **2**, 515 (1971).

# A Spectroscopic Study of Carbazole by Photoselection[1]

G. E. Johnson

*Webster Research Center, Xerox Corporation, Webster, New York 14580*

*(Received September 13, 1973)*

*Publication costs assisted by the Xerox Corporation*

Carbazole and four of its nitrogen-substituted derivatives have been investigated using photoselection techniques. The polarization of the lowest energy transition in absorption as well as both fluorescence and phosphorescence emissions is found to be wavelength dependent in all cases. This indicates the presence of forbidden character in these transitions. Transitions to higher lying states are seen to be uniformly polarized. Introduction of an unsaturated vinyl or phenyl group on the nitrogen atom gives new spectral features at wavelengths underlying and to the blue of the second excited electronic state of carbazole and its *N*-alkyl derivatives. Assignments of the first four excited singlet states and the lowest triplet state of these carbazoles are made on the basis of these results.

## I. Introduction

Carbazole and carbazole related systems have in recent years attracted much attention. Poly(*N*-vinylcarbazole) (PVK) in particular has been the subject of numerous studies, many of which were undoubtedly stimulated by the finding that PVK is one of the most sensitive photoconductive organic polymers.[2a] Included among these efforts are investigations of the formation and emission of excimer states in PVK films[2b] and in solution,[3] and how these states relate to the process of energy transfer in solid films.[4] Interest in the generation of charge carriers[5] and their transport[6] in PVK films has been high. The investigation concerning the transfer of electronic excitation was extended to include doped crystals of *N*-isopropylcarbazole. Another carbazole derivative, 1,3-bis(*N*-carbazolyl)propane, which serves as a useful model for PVK, has been investigated with regard to the formation of intramolecular excimer states.[7,8] These investigations are representative of the types of photophysical processes which have been of concern in the carbazole system and by no means include all the efforts applied in this direction.

A necessary starting point in any attempt to understand the excited state interactions which strongly influence photophysical processes such as excimer formation and emission, energy transfer, and charge carrier generation in the solid state is knowledge concerning the nature of the electronic states of the monomeric chromophore units themselves. In this regard two significant spectroscopic studies of carbazole have been made. The first vapor-phase spectrum of carbazole was measured by Pinkham and Wait[9] and assignments of the two lowest lying electronic transitions made on the basis of molecular orbital calculations. These results were in agreement with earlier theoretical predictions of Mataga, *et al.*[10] Bree and Zwarich[11] in a very detailed study of carbazole combined polarized infrared and Raman spectra of carbazole single crystals with polarized absorption and fluorescence spectra of carbazole dissolved in a fluorene crystal to assign fundamental vibrational modes and the lowest lying electronic state. Another polarized absorption study on neat crystals of carbazole extended the polarization results to include the second electronic transition.[12] The (0,0) transitions to the first and second excited singlet states were found to be polarized along the short in-plane ($Z$) and long in-plane ($Y$) molecular axes respectively (see Figure 1). These results are in agreement with the calculations and thus assignment of these two states as $^1A_1$ and $^1B_2$ in $C_{2v}$ symmetry appears firmly established.

It is the purpose of this paper to report the results of an investigation concerning the spectroscopic behavior of the lower lying states of carbazole and four of its nitrogen-substituted derivatives using the technique of photoselection.[13] The polarization of transitions in absorption is measured relative to both fluorescence and phosphorescence transition moments. Whereas the spectroscopic studies on neat or mixed carbazole crystals are limited to the two lowest lying transitions due to difficulties in achieving sufficiently thin crystals or the overlapping of guest and host absorptions it is possible in rigid glass solutions to extend measurements to higher lying states. The relative orientation of absorbing and emitting transiton moments obtained from photoselection when combined with the results of the crystal studies enables all transitions to be assigned on an absolute basis. The polarization throughout the lowest absorption band is found to be mixed and the results interpreted in terms of the presence of a significant amount of so-called forbidden character in this electronically allowed transition. Details concerning the vibronic coupling mechanism operative in fluorescence and phosphorescence emission are similarly probed and assignment of the lowest triplet state made.

## II. Experimental Section

*A. Materials. 1. Solutes. N-Isopropylcarbazole* (NIPC) (supplied by Dr. H. Hoegl of the Battelle Memorial Institute, Geneva, Switzerland) was obtained in the form of large, optically clear, single crystals grown from the melt following repeated zone refining of the original vacuum-sublimed starting material. A number of experiments were repeated using NICP (Eastman Kodak White Label) purified by multiple recrystallization from isopropyl alcohol (IPA). The experimental results obtained for both materials were in strict agreement.

*N-Ethylcarbazole* (Southern Dyestuff Company, Charlotte, N. C.) was purified by multiple recrystallization from IPA.

*N-Phenylcarbazole* (Aldrich Chemical Company, Inc., Milwaukee, Wisc., Research Grade) was purified by multiple recrystallization from IPA.

*N-Vinylcarbazole* (Badische Aniline and Soda Fabrik AG, distributed by Wunder and Wolff and Co., New York, N. Y.) was purified by multiple recrystallization from methanol in amber glassware to yield thin colorless platelets. Vacuum sublimed NVK yielded identical experimental results.

*Carbazole* (James Hinton) was zone refined material used as received.

2. *Solvents. 3-Methylpentane (3MP)* (Phillips Petroleum Co., Bartlesville, Okla., Pure Grade) was purified by chromatography on an activated alumina column. The resulting material had 90% transmittance at 2200 Å with zero absorbance at 2500 Å, the shortest wavelength at which it was possible to obtain polarization data.

*Isopentane (isoP)* (Hartman-Leddon Co., Philadelphia, Pa., Fluorometric Grade) was used as received.

*EPA* (diethyl ether, isoP, ethyl alcohol, in a volume ratio of 5:5:2, obtained from American Instrument Co.) was used as received.

*B. Polarization of Absorption and Emission at 77°K.* The photoselection measurements were made using well-established, and by now familiar, techniques[14,15] and need not be described in detail here. Monochromatic exciting light was provided by a 1-kW General Electric A-H6 high-pressure mercury arc dispersed through a Bausch and Lomb 500-mm focal length monochromator with a reciprocal linear dispersion of 3.3 nm/mm. Linearly polarized exciting light was provided by an ultraviolet transmitting dichroic film deposited on a fused quartz substrate (Polacoat Inc., Blue Ash, Ohio, formula 105uv film). The rigid solutions were immersed in bubble-free liquid nitrogen maintained in a fused quartz, optical dewar.

The polarized emission emanating from the sample was analyzed by a detection system placed at right angles to the exciting light beam. The emission is collected with the aid of a fused quartz lens and passed through a second polarizer (Polacoat, Inc.) mounted on the entrance slit of a viewing monochromator. The viewing monochromator consisted of two Jarrell-Ash, 0.25-m Ebert monochromators ($f/3.5$, reciprocal linear dispersion of 3.2 nm/mm) mounted in tandem in a double monochromator configuration. Emission is detected with either an EMI 9558 or a RCA IP 28 photomultiplier tube placed at the exit slit side of the second Jarrell-Ash monochromator. The output current from the photomultiplier tubes is read out using a Keithley Model 610A electrometer.

*C. Absorption and Emission Spectra.* All absorption spectra were recorded on a Cary Model 14 spectrophotometer. The emission spectra were recorded using the same experimental arrangement used to measure polarization of emission and emission excitation spectra. The phosphorescence lifetimes were determined by following the output of the Keithley 610A on an Esterline-Angus Model E1101-S recorder. Fluorescence lifetimes were measured using the time correlated single photon counting technique. The nanosecond fluorometer was assembled with ORTEC electronics.

## III. Results and Discussion

Presentation and discussion of the results will proceed in the following manner. First a general, qualitative description of the absorption and emission spectra of the different carbazoles is given. Next the polarization of transitions in absorption as determined by polarized emission excitation spectra are discussed. Assignments of the first four electronic states are made. It will be seen that the polarization of the lowest lying absorption band is mixed, signifying the presence of a significant amount of so-called "forbidden" character[16] in the symmetry allowed electronic transition. Next the polarized fluorescence spectra as determined by exciting the (0,0) transitions of the two lowest lying states are discussed. It will be shown how these results complement the polarization of the $^1L_b \leftarrow {}^1A$ band system and in particular show the lack of any significant out-of-plane polarized intensity. Finally polarization of phosphorescence and polarization of phosphorescence excitation spectra are discussed. These results lead to an unequivocal assignment of the lowest triplet state of these carbazoles, and give insight into the higher order mechanisms leading to dipole allowed character in this transition.

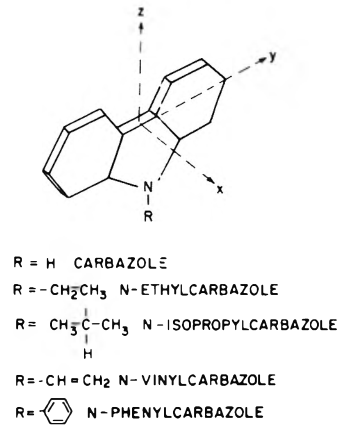
z
y
x
N
R
R = H CARBAZOLE
R = -CH₂-CH₃ N-ETHYLCARBAZOLE
R = CH₃-C-CH₃ N-ISOPROPYLCARBAZOLE
H
R = -CH=CH₂ N-VINYLCARBAZOLE
R = N-PHENYLCARBAZOLE

**Figure 1.** Structure and coordinate system for carbazole.

*A. Absorption and Emission Spectra.* Absorption spectra of carbazole, *N*-isopropylcarbazole (NIPC), *N*-ethylcarbazole (NEC), *N*-phenylcarbazole (NPK), and *N*-vinylcarbazole (NVK) were each measured in nonpolar 7:3 3MP:isoP and polar EPA solvents at room temperature and 77°K. The spectra of carbazole, NEC, and NIPC are, as expected, nearly identical. Those carbazoles containing an unsaturated group on the nitrogen are themselves similar but distinctly different from carbazole and its *N*-alkyl derivatives. The absorption spectrum of NIPC in 7:3 3MP:isoP mixture at 77°K is shown in Figure 2. Four distinct bands are noted with the respective (0,0) transitions located at 345, 295, 264 and 246 nm, respectively. The spectrum of NPK under the same experimental conditions is shown in Figure 3.

The first two bands, which henceforth will be designated $^1L_b \leftarrow {}^1A$ and $^1L_a \leftarrow {}^1A$, respectively, in the Platt notation,[17] show considerable vibrational structure. Both bands are characterized by a rather sharp (0,0) which is the most intense transition in the band and the lack of a significant progression in any vibrational mode. This is characteristic of electronically allowed transitions where there is no appreciable change in the equilibrium nuclear configuration between ground and excited states. These two transitions are essentially unchanged irrespective of whether an unsaturated group or a saturated alkyl group is on the nitrogen. Distinct differences between the two classes of carbazoles do exist however at wavelengths to the blue of and underlying the $^1L_a \leftarrow {}^1A$ band. The band

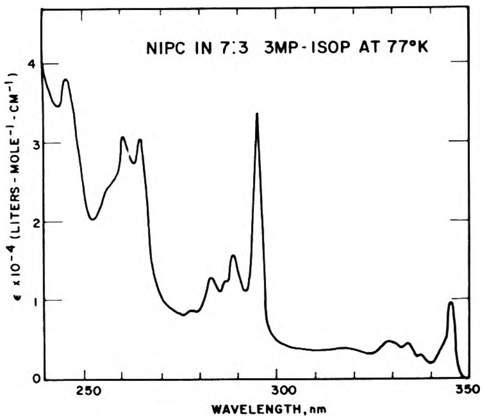

Figure 2. Absorption spectrum of NIPC in 7:3 3MP:isoP at 77°K.

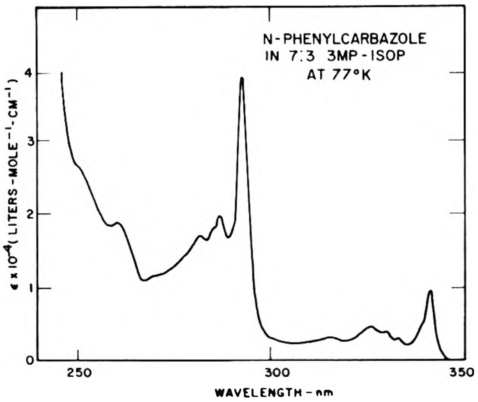

Figure 3. Absorption spectrum of NPK in 7:3 3MP:isoP at 77°K.

in the region of 264 nm which is clearly evident in the spectrum of carbazole, NEC, and NIPC no longer appears in the spectrum of NPK or NVK. Discussion of these differences will be deferred until the polarization of absorption results are presented.

The spectroscopic behavior of all the carbazole derivatives was, with the exception of frequency shifts, the same in both the nonpolar hydrocarbon and polar EPA solvents. Due to its limited solubility in 7:3 3MP:isoP it was not possible to study carbazole in this solvent at 77°K. Cooling to 77°K apparently led to the formation of microcrystallites since the rigid solutions had a slightly turbid appearance. Consistent with microcrystal formation was the depolarized nature of fluorescence, and the lack of phosphorescence from these samples as well as agreement of the position of the (0,0) transition of the $^1L_b \leftarrow {}^1A$ band with that reported for the single crystal.[12]

Emission spectra of each compound were also measured in both solvent mixtures at 77°K. In low temperature glasses the frequency of the (0,0) transition of the $^1L_b \rightarrow {}^1A$ fluorescence coincides with that of the corresponding absorption when solutions of approximately $2 \times 10^{-5}$ *M* or less were studied. At concentrations higher than this the effects of reabsorption of emission were particularly severe. The fluorescence spectrum of a dilute solution of NIPC in rigid 7:3 3MP:isoP at 77°K is shown in Figure 4. The fluorescence spectra of the other derivatives were nearly identical as indeed the similarity of the $^1L_b \leftarrow {}^1A$ absorption band in all compounds would suggest. Rather good mirror image symmetry between the fluorescence band and the lowest energy absorption band is evident.

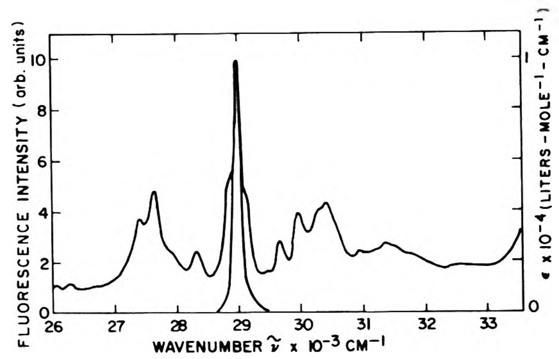

Figure 4. Absorption and fluorescence spectra of NIPC in 7:3 3MP:isoP at 77°K.

The phosphorescence spectra of NIPC in rigid 7:3 3MP:isoP and EPA solvents at 77°K are shown in Figure 9. This again is typical of the other derivatives with the following exceptions: phosphorescence from carbazole in the nonpolar hydrocarbon matrix was not observed, as mentioned earlier, due to the formation of microcrystals. NVK did not phosphoresce in either the mixed hydrocarbon or EPA solvent at 77°K, the result apparently of efficient, nonradiative deactivation of the lowest triplet state. The position of the (0,0) transitions in absorption and phosphorescence along with fluorescence and phosphorescence lifetimes are tabulated in Tables I and II. The spectroscopic behavior of these carbazoles when going from nonpolar to polar solvents is typical of what is generally observed for transitions to singlet ($\pi,\pi^*$) states. It is interesting to note, however, that the phosphorescence (0,0) blue shifts slightly in polar solvent as opposed to the general red shift noted for transitions to singlet ($\pi,\pi^*$) states; this rather atypical solvent shift noted for the phosphorescence emission is consistent with other results (*vide infra*) concerning the lowest triplet state.

*B. Polarization of Absorption.* The relative polarizations of transitions in absorption are determined by measuring a polarized emission excitation spectrum. The low temperature sample of rigidly held, randomly oriented solute molecules is excited at various wavelengths throughout the different absorption bands while emission at a fixed wavelength is detected at right angles to the exciting light. With the available intensities it was possible to use 1- and 3.2-nm bandwidth light in excitation and emission, respectively. The emission intensity at each excitation frequency is measured using the four possible orientations of the polarizers in the excitation and emission light paths. From these four intensity values the polarization ratio *N* is calculated where $N = (I_{\parallel}/I_{\perp})_V(I_{\parallel}/I_{\perp})_H$, $(I_{\parallel}/I_{\perp})_V$ is the ratio of the intensities of vertically to horizontally polarized emission when excited with vertically polarized light and $(I_{\parallel}/I_{\perp})_H$, the ratio of the intensities of parallel and perpendicularly polarized emission with horizontally polarized excitation. The polarization ratio, *N*, is related to the relative orientation of transition moments in absorption and emission. The theoretical value of $N = 3$ indicates absorption polarized along a single molecular axis followed by emission polarized along the same axis. The value of $N = 0.5$ indicates single axis absorption followed by emission along a perpendicular molecular axis.[13] Experimentally these theoretical limits are never achieved even for those cases where the molecular symmetry demands that intrinsic molecular transition moments are parallel or perpendicular to one another. It has been cus-

**TABLE I: Results of Absorption and Emission Measurements in Nonpolar 7:3 3MP:isoP Solvent**

| | Carbazole | NEC | NIPC | NVK | NPK |
|---|---|---|---|---|---|
| Room Temperature | | | | | |
| $^1L_b(0,0)$, cm$^{-1}$ | 30,260 | 29,110 | 29,130 | 29,520 | 29,500 |
| $^1L_a(0,0)$, cm$^{-1}$ | 34,420 | 34,080 | 34,070 | 34,310 | 34,260 |
| $^1B_a(0,0)$, cm$^{-1}$ | 39,250 | 38,020 | 37,990 | | |
| 77°K | | | | | |
| $^1L_b(0,0)$, cm$^{-1}$ | 29,390 | 28,950 | 29,000 | 29,360 | 29,350 |
| $^1L_a(0,0)$, cm$^{-1}$ | 34,050 | 33,950 | 33,920 | 34,270 | 34,190 |
| $^1B_a(0,0)$, cm$^{-1}$ | | 37,820 | 37,900 | | |
| $^3L_a(0,0)$, cm$^{-1}$ | | 24,260 | 24,320 | | 24,410 |
| $\tau_{\rm phos}$, sec | | 6.6 | 7.1 | | 6.0 |

**TABLE II: Results of Absorption and Emission Measurements in Polar EPA Solvent**

| | Carbazole | NEC | NIPC | NVK | NPK |
|---|---|---|---|---|---|
| Room Temperature | | | | | |
| $^1L_b(0,0)$, cm$^{-1}$ | 29,720 | 29,050 | 29,090 | 29 540 | 29,500 |
| $^1L_a(0,0)$, cm$^{-1}$ | 34,130 | 34,040 | 34,040 | 34 330 | 34,250 |
| $^1B_a(0,0)$, cm$^{-1}$ | 39,020 | 38,100 | 37,950 | | |
| $\tau_{\rm fl}$, nsec | 15.7 | | 16.4 | 10.1 | 11.1 |
| 77°K | | | | | |
| $^1L_b(0,0)$, cm$^{-1}$ | 29,520 | 28,800 | 28,900 | 29 260 | 29,300 |
| $^1L_a(0,0)$, cm$^{-1}$ | 34,020 | 33,900 | 33,920 | 34 300 | 34,220 |
| $^1B_a(0,0)$, cm$^{-1}$ | 38,760 | 37,900 | 37,900 | | |
| $^3L_a(0,0)$, cm$^{-1}$ | 24,600 | 24,370 | 24,380 | | 24,570 |
| $\tau_{\rm phos}$, sec | 7.7 | 8.1 | 8.2 | | 7.1 |
| $\tau_{\rm fl}$, nsec | 15.0 | | 16.2 | 11.7 | 11.3 |

tomary, at least in those cases where photoselection has been used in a more quantitative way, in an attempt to detail the nature of the wavefunctions of the combining electronic states, to introduce a "randomization factor" to correct for these departures from ideal behavior.[14] This is not deemed necessary here in this more qualitative study.

The polarization of emission excitation spectrum of NIPC in 7:3 3MP:isoP at 77°K is shown in Figure 5. Excitation at the (0,0) component of the $^1L_b \leftarrow {}^1A$ band yielded a value of $N = 2.3$ when viewing the (0,0) − 700-cm$^{-1}$ vibronic band in fluorescence. Ideally of course one wishes to view the (0,0) transition in fluorescence but this is not possible due to interference from scattered exciting light. The value $N = 2.3$ is a considerably greater departure from the theoretical limit of $N = 3$ than might reasonably be expected for the case of parallel transition moments. In this regard many molecules of the same or lower symmetry and with the lowest energy transitions of significantly greater intensity were found to yield values as great as $N = 2.80$ on this experimental system when viewing fluoresescence and exciting at wavelengths within the lowest energy absorption bands. The value of $N = 2.80$ is thus about the maximum that can be achieved experimentally with this set-up. The value of $N = 2.3$ achieved with NIPC when exciting into the (0,0) of the $^1L_b \leftarrow {}^1A$ band results from the fact that the (0,0) − 700 cm$^{-1}$ vibronic band in fluorescence is already mixed polarized.

As excitation proceeds toward higher frequencies within the $^1L_b \leftarrow {}^1A$ absorption band the polarization ratio is observed to decrease with alternations occurring at particularly intense vibronic bands. A minimum value of $N$ approaching the theoretical limit of 0.5 is reached at the (0,0) transition of the $^1L_a \leftarrow {}^1A$ band indicating that this transition is along a molecular axis very nearly perpendicular to the emitting axis. The polarization ratio remains constant throughout the $^1L_a \leftarrow {}^1A$ absorption band. The polarization ratio starts to increase as excitation proceeds to higher lying vibrational levels of the $^1B_a$ state and most likely represents the overlap of an oppositely polarized electronic transition at still higher energy. Exactly the same behavior was observed for carbazole and NIPC in EPA solvent at 77°K and for NEC in both rigid hydrocarbon and EPA solvent at 77°K. These results are in accordance with an earlier photoselection study of carbazole in ethanol.[18]

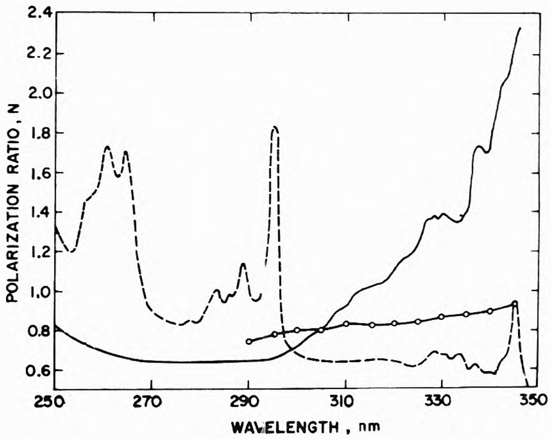

Figure 5. Polarization of emission excitation spectrum of NIPC in 7:3 3MP:isoP at 77°K: (——) polarization ratio viewing the 700-cm$^{-1}$ vibronic transition in fluorescence; (-O-O-) polarization ratio viewing the (0,0) transition in phosphorescence; (- - - -) absorption spectrum, arbitrary units.

As mentioned in the Introduction the polarization of the pure electronic transition moment linking the ground and $^1L_b$ states has been shown to be along the short, in-plane ($Z$) molecular axis.[11,12] This knowledge alone, combined with the fact that these transitions are unquestionably of a $\pi^* \leftarrow \pi$ nature and thus necessarily polarized in the molecular plane, fixes the direction of the transition to the second and third excited states of carbazole, NEC, and NIPC as along the long in-plane ($Y$) molecular axis. The transition to the fourth electronic state is apparently polarized along the $Z$ axis. However, because of low light intensity in this wavelength region the experimental results are only suggestive. This ordering of states agrees with the theoretical assignments of Mataga, *et al.*[10]

The most distinctive feature of the polarization of fluorescence excitation spectrum is of course the changing polarization ratio as excitation proceeds from the origin to higher lying vibronic levels of the $^1L_b \leftarrow {}^1A$ band. The polarization ratio is a maximum at the origin but decreases sharply at excitation frequencies slightly to the blue. It was noted that for every derivative investigated a distinct shoulder exists immediately to the blue of the (0,0) of the $^1L_b \leftarrow {}^1A$ band; the same shoulder is also present in the fluorescence and phosphorescence emission bands at energies slightly lower than their respective origins. This shoulder is apparently due to a vibronic transition at approximately 200 cm$^{-1}$ to high frequency of the electronic origin. The polarization ratio continues to show an overall decrease as excitation progresses to higher vibronic levels with oscillations present at the more intense vibronic peaks. This behavior clearly signals the presence of vibronic coupling leading to a significant amount of "forbidden" character within this band. The oscillator strength of the lowest electronic transition, as obtained by integration of the $^1L_b \leftarrow {}^1A$ band, is 0.056 ± 0.002 for all these carbazoles. By separating this band into allowed and "forbidden" components, in the manner of Kalantar and Albrecht,[19] one finds approximately 40% of the total intensity is "forbidden."

A vibrational analysis of the $^1L_b \leftarrow {}^1A$ and $^1L_a \leftarrow {}^1A$ bands based on the photoselection results is presented in Table III. The basis of this analysis is the fact that vibronic theory to first order predicts that the "forbidden" intensity in an allowed electronic transition should appear as separate components each based on a different normal mode. Each "forbidden" component has the same Franck-Condon envelope as the allowed part only separated from the true origin by the frequency of the vibronically active normal mode.[19] Local minima in the value of $N$ are observed particularly clearly at (0,0) + ~200 cm$^{-1}$, (0,0) + ~450 cm$^{-1}$, and (0,0) + ~1000 cm$^{-1}$. These vibrational modes are considered to be $b_2$ vibronic origins; this is confirmed by polarization of fluorescence measurements.

Figures 6 and 7 present the polarization of fluorescence excitation spectra of NPK and NVK in 7:3 3MP:isoP at 77°K. The spectra are unchanged in polar EPA solvent. The polarization of the $^1L_b \leftarrow {}^1A$ and $^1L_a \leftarrow {}^1A$ bands, including the vibronic details, is the same as for carbazole and its $N$-alkyl derivatives. Essential differences exist, however, at wavelengths to the blue of the $^1L_a \leftarrow {}^1A$ band and particularly for NPK, at wavelengths underlying this transition. The distinct long-axis in-plane polarized transition to a $^1B_2(^1B_a)$ state which existed for carbazole, NEC, and NIPC is not observed for NPK and NVK. Instead an oppositely polarized transition occurs, which in the case of NPK strongly overlaps the $^1L_a \leftarrow {}^1A$ band. Consideration of the absorption spectrum of NPK in the light of the photoselection results indicates this band to be rather broad, unstructured, and of low maximum extinction coefficient. The situation for NVK is similar although it is clear the overlap of the predominantly $Z$ polarized band with the $^1L_a \leftarrow {}^1A$ band is less severe and the intensity of the "new" band is apparently greater than for NPK. The polarization ratio for both NPK and NVK again decreases at still higher energies indicating the presence of a $Z$ axis polarized transition. The electronic state symmetries of the first four excited states of NPK and NVK are $A_1$, $B_2$, $A_1$, and $B_2$, respectively, while those of carbazole, NEC, and NIPC are $A_1$, $B_2$, $B_2$, and $A_1$.

**TABLE III: Vibrational Structure of the $^1L_b \leftarrow {}^1A$ and $^1L_a \leftarrow {}^1A$ Bands of NIPC**

| $\bar{\nu}$, cm$^{-1}$ | $\Delta\bar{\nu}$, cm$^{-1}$ | Polarization | Analysis |
|---|---|---|---|
| | | $^1L_b$ | |
| 29,000 | 0 | $z$ | (0,0) $A_1$ |
| ~29,200 | ~200 | $y$ | 0,200 ($b_2$?) |
| 29,450 | 450 | $y$ | 0,450 ($b_2$) |
| 29,700 | 700 | $z$ | 0,700 ($a_1$) |
| 30,000 | 1000 | $y$ | 0,1000 ($b_2$) |
| 30,280 | 1280 | $z$ | 0,1280 ($a_1$) |
| 30,450 | 1450 | $z$ | 0,1450 ($a_1$) |
| 30,680 | 1680 | $y$ | 0,200 ($b_2$) + 1450 ($a_1$)<br>0,450 ($b_2$) + 1280 ($a_1$)<br>0,1000 ($b_2$) + 700 ($a_1$) |
| 31,000 | 2000 | $z$ | 0,700 ($a_1$) + 1280 ($a_1$) |
| 31,250 | 2250 | $y$ | 0,1000 ($b_2$) + 1280 ($a_1$) |
| 31,450 | 2450 | $y$ | 0,1000 ($b_2$) + 1450 ($a_1$) |
| 31,900 | 2900 | $z$ | 0,2 × 1450 ($a_1$) |
| | | $^1L_a$ | |
| 33,920 | 0 | $y$ | (0,0) $B_2$ |
| 34,630 | 710 | $y$ | 0,710 ($a_1$) |
| 34,900 | 980 | $y$ | 0,980 ($a_1$) |
| 35,310 | 1390 | $y$ | 0,1390 ($a_1$) |
| 35,590 | 1670 | $y$ | 0,710 + 980 |
| 35,980 | 2060 | $y$ | 0,710 + 1390 |
| 36,700 | 2780 | $y$ | 0,2 × 1390 |
| 36,970 | 3050 | $y$ | 0,710 + 980 + 1390 |

The similarity of the spectroscopy of carbazole, NEC, and NIPC is not surprising since alkyl groups are in general spectrally inert. Still there are rather significant spectral shifts with $N$-alkylation and these have been nicely interpreted by Mataga, *et al.*,[10] in their theoretical description of the electronic structure of carbazole. There an independent systems approach was used to arrive at the electronic wave functions of carbazole. The electronic wave functions are linear combinations of those of planar biphenyl with those involving the transfer of an electron from >N-H to a vacant orbital on biphenyl. The first ($^1L_b$) and third ($^1B_a$) electronic states of carbazole were shown to be mixed with a considerable amount of CT character while the second ($^1L_a$) state was almost totally that of locally excited states of biphenyl. Replacement of the hydrogen by alkyl groups should lead to a lowering of the energy of the CT configurations and thus to lowering of the $^1L_b$ and $^1B_a$ states of carbazole to an extent greater than the $^1L_a$ state. The experimental results are in accordance with this prediction. The $^1L_b$ and $^1B_a$ states of carbazoles are red shifted considerably more than the $^1L_a$ state upon $N$-alkylation. (See Tables I and II.)

Replacement of the hydrogen by unsaturated groups such as vinyl or phenyl has been seen to lead to significant spectroscopic differences from those of carbazole and its $N$-alkyl derivatives. Most notable is the appearance of a new $Z$ axis polarized transition in both NVK and NPK in the 270-nm region. In spite of this similarity which emerges from the photoselection results the absorption spectra of these two compounds are quite different. At wavelengths corresponding to the distinct $^1B_a \leftarrow {}^1A$ band observed in carbazole, NEC, and NIPC, NPK displays rather weak, unstructured absorption while in NVK there is considerable absorption but the transitions are apparently strongly overlapped. The origin of these spectral differences can be rationalized in a qualitative but general manner in terms

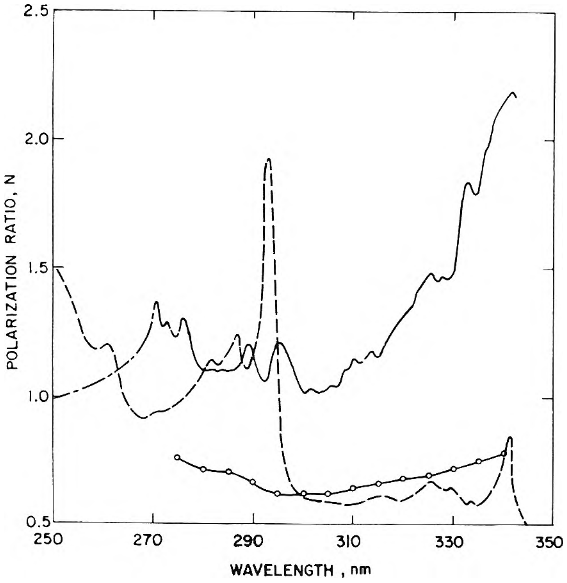

**Figure 6.** Polarization of emission excitation spectrum of NPK in 7:3 3MP:isoP at 77°K: (——) polarization ratio viewing the ~700-cm$^{-1}$ vibronic band in fluorescence; (-O-O-) polarization ratio viewing the (0,0) band in phosphorescence; (- - - - - -) absorption spectrum, arbitrary units.

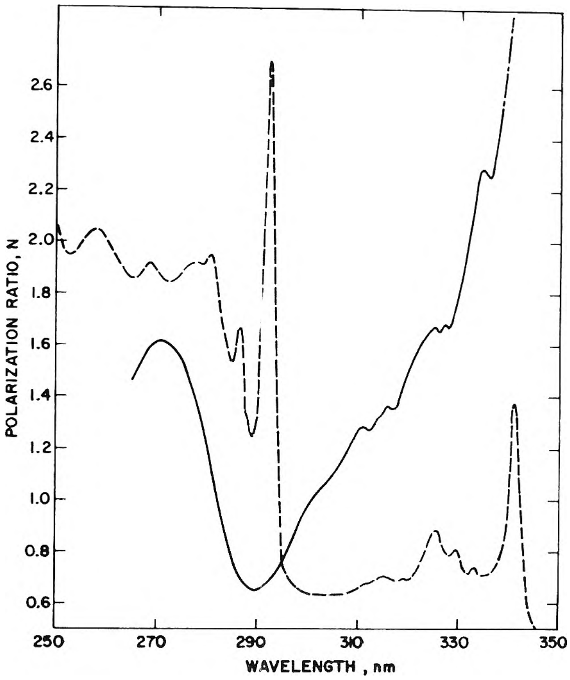

**Figure 7.** Polarization of fluorescence excitation spectrum of NVK in 7:3 3MP:isoP at 77°K: (——) polarization ratio viewing the (0,0) band in fluorescence; (- - - - - -) absorption spectrum, arbitrary units.

of the interaction of transition dipoles localized on the carbazole and substituent groups.

In the case of both phenyl and vinyl derivatives the orientation of the substituent with respect to the carbazole plane is necessarily such that $\pi \leftarrow \pi$ transitions localized on the substituent have a sizeable component along the carbazole fixed $Z$ molecular axis. In the case of the phenyl group for example transitions corresponding to the $^1B_{1u} \leftarrow {}^1A_g$ transition of benzene would lie almost totally along the $Z$ direction. The photoselection results along with the absorption spectrum indicate the presence of a $Z$ axis polarized transition of high intensity at wavelengths beyond 250 nm for carbazole. A splitting due to the interaction of these two $Z$ polarized transition dipoles leads to two states; the one of lower energy results from the in-phase or head-to-tail arrangement of the transition moments.[20] The transition to this state is allowed while the transition to the higher lying state, resulting from the out-of-phase arrangement of transition dipoles, is forbidden. On this basis the existence of a $Z$ polarized transition at wavelengths overlapping with $^1L_a \leftarrow {}^1A$ and $^1B_a \leftarrow {}^1A$ bands of carbazole appears reasonable. A similar origin for the $Z$ polarized transition in NVK appears likely. Here the most probable orientation of the vinyl group with respect to carbazole would be such as to give a sizeable component of a perturbed ethylene transition dipole along the $Z$ direction. A dipole–dipole interaction of the high lying $Z$ polarized carbazole transition with this component of the only accessible ethylene transition also leads to an allowed $Z$ axis polarized transition at lower energy than that of either group alone.

In both NPK and NVK the polarization ratio is observed to decrease at still higher energy indicative of a $Y$ or long-axis in-plane polarized transition. In the case of NVK this is probably due to a $^1B_b \leftarrow {}^1A$ transition like that observed in carbazole, NEC, and NIPC. This transition should remain relatively unperturbed in NVK since there can be very little interaction between the carbazole $^1B_a \leftarrow {}^1A$ transition dipole and that due to the ethylene localized transition. Energetically these transitions are rather far apart and sterically it would seem that the component of the ethylene $\pi^* \leftarrow \pi$ transition which lies in the $XY$ plane would be predominantly perpendicular to the $Y$ polarized carbazole transition. Furthermore even if energetically and geometrically some interaction were possible, the state to which a transition is allowed would be higher in energy than either of the two interacting states.[20] The absorption spectrum of NVK (see Figure 7) is crowded in this region perhaps reflecting the presence of this relatively unperturbed $^1B_a \leftarrow {}^1A$ carbazole localized transition. The absorption spectrum of NPK (see Figure 6) reflects considerable perturbation of the $^1B_a \leftarrow {}^1A$ carbazole transition; the transition apparently being blue shifted into a region of overlapping bands. Perhaps this reflects on an interaction between the $^1B_a \leftarrow {}^1A$ carbazole localized transition dipole and a perturbed benzene transition of $^1B_{2u} \leftarrow {}^1A_g$ parentage which is present at this energy. The allowed transition to the two states arising from this interaction would lie at higher energy than either transition alone. If this interaction is the origin for the rather distinct spectral changes in NPK, it further implies that the phenyl ring undergoes rather free rotation about the nitrogen–carbon bond. For steric reasons alone it would seem that the most probable orientation of the phenyl group would be perpendicular to the plane of the carbazole moiety. However, perpendicular orientation of the phenyl and carbazole planes would give no interaction between $Y$ axis polarized carbazole transition dipoles and transitions to $^1B_{2u}$ like states of a phenyl ring. In this case the $^1B_a \leftarrow {}^1A$ transition of carbazole should remain relatively unperturbed. Maximum interaction will occur for those molecules in which the planes of the phenyl and carbazoyl groups are parallel. In the rigid glass at 77°K a distribution of orientations is undoubtedly frozen in. This would result in an apparent loss in intensity of the carbazole $^1B_a \leftarrow {}^1A$ transition due to transfer of intensity to the allowed

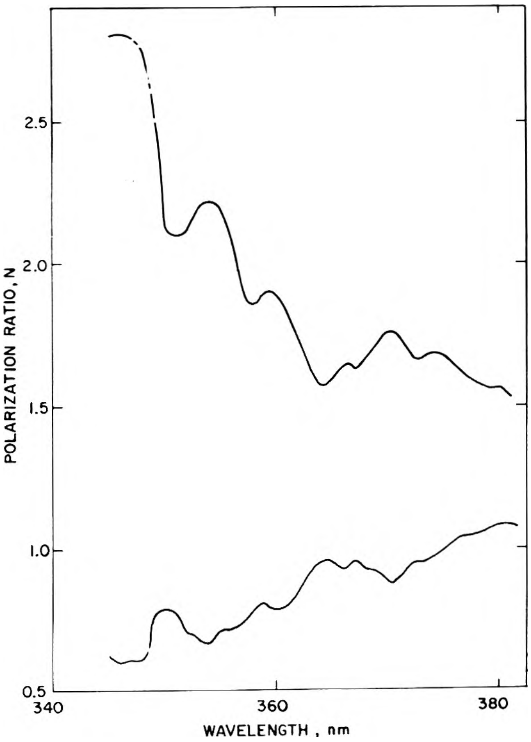

**Figure 8**. Polarization of fluorescence spectrum of NIPC in 7:3 3MP:isoP at 77°K: upper curve, excited at the (0,0) of the ${}^1L_b \leftarrow {}^1A$ band; lower curve, excited at the (0,0) of the ${}^1L_a \leftarrow {}^1A$ band.

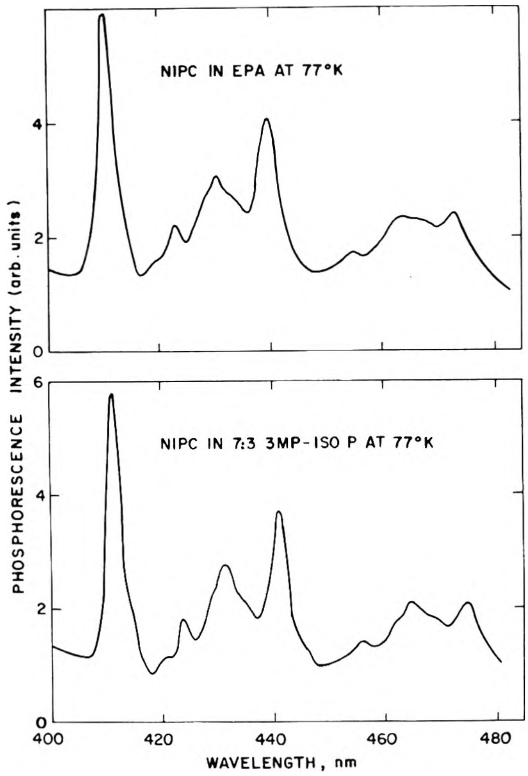

**Figure 9**. Phosphorescence spectra of NIPC in 7:3 3MP:isoP and EPA at 77°K.

component of the two states arising from the interaction. The absorption spectrum of NPK is in qualitative accord with this interpretation.

*C. Polarization of Fluorescence*. Polarized emission spectra are measured the same way as described earlier for polarization of emission excitation spectra except of course the excitation frequency is fixed while the viewing frequency is varied.

Polarization of fluorescence data for NIPC in 7:3 3MP:isoP at 77°K are shown in Figure 8. The excitation band width of 6.6 nm was rather broad while the fluorescence band width was 0.32 nm. The upper curve in Figure 8 corresponds to excitation at the (0,0) of the ${}^1L_b \leftarrow {}^1A$ band. When the fluorescence is viewed in the region of its (0,0) the polarization ratio $N$ approaches the value of 3, characteristic of single axis absorption followed by emission along the same molecular axis. This, of course, is what is expected. The polarization ratio changes throughout the fluorescence band just as was observed for the lowest energy absorption band. The changing polarization ratio observed here is also indicative of a significant amount of "forbidden" character in this allowed transition.

The lower curve of Figure 8 shows the polarization of fluorescence results with excitation into the (0,0) of the ${}^1L_a \leftarrow {}^1A$ band. Here the polarization ratio when viewing the (0,0) of the fluorescence band approaches the value of 0.5, a result of course, expected in the light of the measurements of the polarization of absorption. Again the polarization ratio is seen to be wavelength dependent with this dependence being complementary to the changes observed with excitation to the origin of the ${}^1L_b \leftarrow {}^1A$ band.

The mirror-like symmetry which exists between the polarization of fluorescence data under excitation in the (0,0) of the ${}^1L_b \leftarrow {}^1A$ and ${}^1L_a \leftarrow {}^1A$ bands is a key observation. As noted earlier, the results obtained from polarization of emission excitation spectra are not able to distinguish between vibronically active $b_1$ or $b_2$ modes. The polarization of fluorescence results do make this distinction. It is seen that for those vibronic transitions in fluorescence where the polarization ratio achieves a minimum with ${}^1L_b \leftarrow {}^1A$ excitation the ratio is a local maximum with ${}^1L_a \leftarrow {}^1A$ excitation. These results exclude the presence of any significant out-of-plane polarized intensity in fluorescence. The results described for NIPC in the nonpolar hydrocarbon glass are equivalent for the other derivatives investigated.

*D. Polarization of Phosphorescence and Phosphorescence Excitation Spectra*. The phosphorescence spectra of NIPC in 7:3 3MP:isoP and EPA solvents at 77°K are shown in Figure 9. Again this is typical of the other carbazoles investigated here with the exception of NVK which does not phosphoresce. The spectra are characterized by the appearance of a strong (0,0) followed by considerable vibrational structure which is somewhat better resolved in the nonpolar hydrocarbon glasses. Energies and lifetimes of the lowest triplet state of each compound can be found in Tables I and II.

The appearance of the strong (0,0) transition in phosphorescence indicates that the predominant mechanism whereby the spin forbidden transition linking the lowest triplet and ground states acquires some allowed character is by direct spin orbit coupling of the triplet state to some singlet state(s) having a dipole allowed transition to the ground state. The lowest triplet state, simply by virtue of its long lifetime alone, can be identified as a $(\pi,\pi^*)$ state[21] and thus must belong to either the $A_1$ and $B_2$ irreducible representation of the $C_{2v}$ point group. Simple group theoretical considerations, knowing that the orbital part of the spin orbit coupling operator transforms as a

**TABLE IV: Mechanisms for Bringing Dipole Allowed Singlet Character into the Lowest Triplet State**

I. Direct spin orbit coupling
Lowest triplet
Spin orbit coupling operator
Singlet character, ${}^1\Theta_m$, in the lowest triplet state and polarization of ${}^1\Theta_m \leftarrow {}^1\Theta_0$

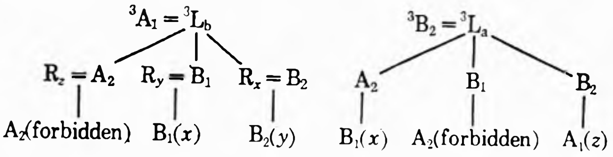

II. Spin orbit coupling to an intermediate singlet with vibronic coupling in the singlet manifold
Lowest triplet
Spin orbit operator
Intermediate singlet
Active vibrations
Singlet state

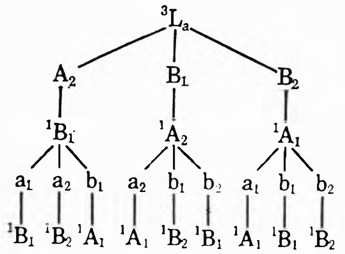
${}^3L_a$
$A_2$
$B_1$
$B_2$
${}^1B_1$
${}^1A_2$
${}^1A_1$
$a_1$ $a_2$ $b_1$ $a_2$ $b_1$ $b_2$ $a_1$ $b_1$ $b_2$
${}^1B_1$ ${}^1B_2$ ${}^1A_1$ ${}^1A_1$ ${}^1B_2$ ${}^1B_1$ ${}^1A_1$ ${}^1B_1$ ${}^1B_2$

III. Vibronic coupling in the triplet manifold followed by spin orbit coupling
Lowest triplet
Active vibrations
Intermediate triplet
Spin orbit operator
Singlet state

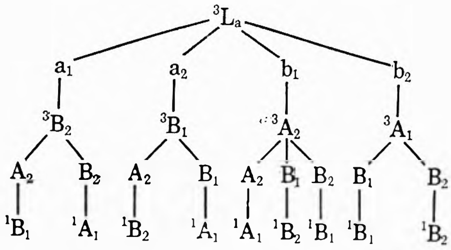
${}^3L_a$
$a_1$ $a_2$ $b_1$ $b_2$
${}^3B_2$ ${}^3B_1$ ${}^3A_2$ ${}^3A_1$
$A_2$ $B_2$ $A_2$ $B_1$ $A_2$ $B_1$ $B_2$ $B_1$ $B_2$
${}^1B_1$ ${}^1A_1$ ${}^1B_2$ ${}^1A_1$ ${}^1A_1$ ${}^1B_2$ ${}^1B_1$ ${}^1B_1$ ${}^1B_2$

rotation,[21] predict that phosphorescence will be polarized $X$ and $Y$ if the lowest triplet is ${}^3A_1({}^3L_b)$ and $X$ and $Z$ if it is ${}^3B_2({}^3L_a)$. (See Table IV.) These possibilities are examined by measuring the polarization of the emission excitation spectrum while viewing the electronic origin of the phosphorescence.

The results of these emission excitation measurements are displayed in Figures 5 and 6. It has been shown that the transition moment between the ground state and the origin of the ${}^1L_b \leftarrow {}^1A$ and ${}^1L_a \leftarrow {}^1A$ bands is polarized short- and long-axis in-plane, respectively. The phosphorescence emission appears to be polarized perpendicular to both in-plane axes, since the polarization ratio $N$ approaches 0.5 under both excitations. However, it will be noted that the theoretical limit of 0.5 is approached more closely as excitation proceeds toward the purely $Y$ or long-axis in-plane polarized ${}^1L_a \leftarrow {}^1A$ transition. This indicates that the phosphorescence emission contains a small amount of $Z$ axis polarized intensity in addition to the predominant out-of-plane polarized intensity. The lowest triplet state of these carbazoles can be assigned unequivocally on this basis as ${}^3L_a$.

The polarization of phosphorescence spectrum of NIPC in EPA at 77°K is shown in Figure 10. The upper curve corresponds to excitation at the origin of the ${}^1L_b \leftarrow {}^1A$ band while the lower curve was obtained with excitation to the origin of the ${}^1L_a \leftarrow {}^1A$ band. Of course at the origin of the phosphorescence emission band this is simply a confirmation of the polarization of phosphorescence excitation results. The changing polarization of phosphorescence, just as in absorption and fluorescence, indicates the presence of vibronic activity. In addition to the first-order, direct spin orbit coupling one or more of the nuclear coordinate dependent mechanisms for mixing dipole allowed character into the lowest triplet state are active. These vibronic mechanisms were first discussed by Albrecht in a study of the benzene problem.[22] Second-order perturbation theory revealed a very weak first-order term due to the nuclear coordinate dependence of the spin orbit coupling operator and two second-order terms: (1) spin orbit coupling to an intermediate singlet followed by vibronic coupling in the singlet manifold and (2) vibronic coupling in the triplet manifold followed by spin orbit coupling of this intermediate triplet to a singlet state.

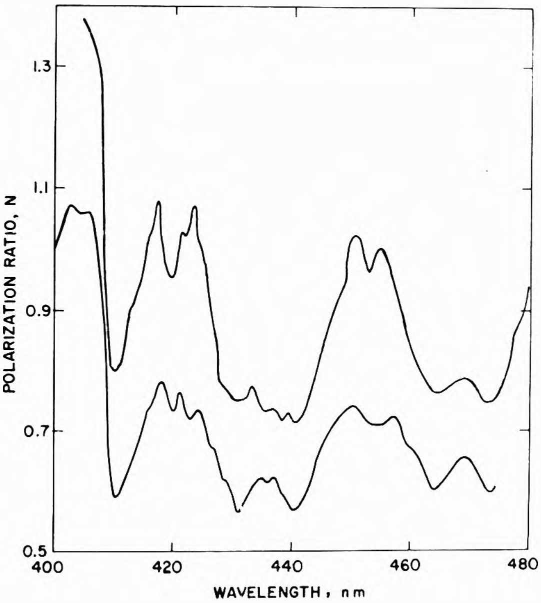

**Figure 10.** Polarization of phosphorescence spectra of NIPC in EPA at 77°K: upper curve, excited at the (0,0) of the ${}^1L_b \leftarrow {}^1A$ band; lower curve, excited at the (0,0) of the ${}^1L_a \leftarrow {}^1A$ band.

The majority of the phosphorescence intensity is due to the direct spin orbit coupling of the lowest triplet state with high lying singlet $(\sigma,\pi^*)$, $(\pi,\sigma^*)$ or Rydberg states since it is these states which are dipole coupled to the ground state with out-of-plane polarized transition moments. A smaller but discernible amount of $Z$ axis polarized intensity is also present due to direct spin orbit coupling the most likely candidate being the $^1L_b$ state since it lies closest in energy. The polarization ratio observed at the electronic origin of the phosphorescence emission should be observed at all vibronic transitions involving excitation of totally symmetric $a_1$ vibrations. This is clearly the case at 1140, 1640, 2800 (1140 + 1640 cm$^{-1}$), and 3225 cm$^{-1}$ (2 × 1640 cm$^{-1}$) to low frequency of the origin. The vibronic transitions at (0,0) − 570 cm$^{-1}$ and (0,0) − 2200 cm$^{-1}$ also appear to be polarized similarly although the ratio is not identical with that of the (0,0). These transitions are weak, however, and obviously are strongly overlapped.

The polarization ratio is observed to increase rather sharply at wavelengths immediately to the red of the origin and between particularly strong $a_1$ vibrational modes independent of whether excitation is to the (0,0) of the $^1L_b \leftarrow {}^1A$ or $^1L_a \leftarrow {}^1A$ transitions. This signifies the presence of intensity polarized parallel to both $Z$ and $Y$ molecular axes. Because of the weakness of these vibrations and the considerable overlap which exists no clear cut distinction can be made between those vibronic transitions which are $Z$ or $Y$ polarized. One mode in particular, however, appears to contain more $Z$ axis character than does the (0,0) or any vibronic transition involving excitation of $a_1$ modes. At about (0,0) − 720 cm$^{-1}$ there appears to be more intensity due to coupling with the $Z$ axis polarized $(\pi,\pi^*)$ $^1A_1$ state than occurs *via* direct spin orbit coupling. The 720-cm$^{-1}$ mode thus appears to be a vibronic origin in the phosphorescence spectrum and symmetry arguments (see Table IV) tell us that $a_1$, $a_2$, or $b_1$ modes can all be active in mixing the $^3L_a$ state with $^1A_1$ character. Both nontotally symmetric $a_2$ or $b_1$ modes of about the right frequency exist.[11] However, in both absorption and fluorescence an $a_1$ mode with a frequency of about 700 cm$^{-1}$ was observed and it is of some interest to at least speculate on the possibility of this $a_1$ mode being vibronically active.

The existence of vibronically active, totally symmetric modes clearly appears in the Herzberg–Teller formalism. However, photoselection, at least in the singlet manifold, cannot identify such activity since both allowed and forbidden parts of the band are polarized alike. High-resolution, single crystal spectroscopy can make this distinction and indeed vibronically active $a_1$ modes have been identified in this manner for phenanthrene.[23] If the only source of intensity in the phosphorescence emission was direct spin orbit coupling, then simultaneous excitation of totally symmetric modes should not alter the ratio of $X$ to $Z$ polarized intensity observed at the origin. In first-order spin vibronic or either of the second-order mechanisms the vibronic activity of an $a_1$ mode would appear as a change in the $X$ to $Z$ intensity ratio. This increased amount of $Z$ polarized intensity is perhaps a manifestation of this.

The long-axis in-plane ($Y$) polarized intensity in phosphorescence can only be mixed in by nontotally symmetric vibrations. (See Table IV.) Here the most accessible route would appear to be spin orbit coupling of the $^3L_a$ state to the $^1L_b$ state which in turn is vibronically coupled to the $^1L_a$ state. Spin orbit coupling of the $^3L_a$ state with the $^1L_b$ state undoubtedly exists since $Z$ polarized intensity appears at the origin. The results of the polarized fluorescence and fluorescence excitation measurements have shown the $^1L_b$ state to be strongly vibronically coupled to the $^1L_a$ state. The vibronic transition which appears as a weak shoulder to the red of the phosphorescence origin evidently plays a key role here just as in absorption and fluorescence. In this regard it should be stated that all of the photoselection results would be consistent with interpretation of this distinct shoulder as a vibronic transition involving excitation of a nontotally symmetric $b_2$ mode at ~200 cm$^{-1}$. Other experimental evidence for such a mode, however, does not exist. Bree and Zwarich assigned a strong transition at 220 cm$^{-1}$ as being due to an $a_1$ vibration, the lowest frequency $b_2$ mode being 505 cm$^{-1}$.[11] In view of their results, it would appear that the photoselection data must reflect something other than a vibronically active $b_2$ mode with a frequency of about 200 cm$^{-1}$. Perhaps it is not unreasonable to think in terms of excitation from the ground state in which one quantum of an $a_1$ mode with a frequency of 220 cm$^{-1}$ is excited to an upper state in which one quantum of a $b_2$ mode of the appropriate frequency is excited. This point remains unresolved.

Previous discussion has stressed the point that the results are independent of the surrounding solvent. Because of the extreme forbiddenness of the $^3L_a \rightarrow {}^1A$ transition the possibility that the results might reflect on the perturbing influence of the solvent must be considered and was in fact the primary reason for using both nonpolar hydrocarbon and polar EPA solvent. The wavelength dependence of the polarization ratio observed throughout the phosphorescence spectrum is the same in both solvents and thus the vibronic activity reflects on true molecular parameters. The polarization of phosphorescence excitation spectra, however, revealed a greater amount of short-axis in-plane ($Z$) intensity in the nonpolar solvent. This observation does not reflect a certain amount of rotational depolarization of the long-lived phosphorescence in the less viscous 7:3 3MP:isoP matrix since excitation into the $^1L_a \leftarrow {}^1A$ band gave the same value for $N$ in both solvents.

The increased amount of $Z$-polarized phosphorescence in nonpolar matrices signifies stronger direct spin orbit coupling to $(\pi,\pi^*)$ singlet states. This result is consistent with the shorter phosphorescence lifetime observed in nonpolar glasses. The greater amount of dipole allowed $(\pi,\pi^*)$ singlet character in the lowest triplet in addition to the still predominant $(\sigma,\pi^*)$ or $(\pi,\sigma^*)$ singlet character shortens the phosphorescence lifetime due to the greater intensity of the $\pi^* \leftarrow \pi$ transitions.

## IV. Summary and Conclusions

The lower lying electronic states of carbazole and four of its nitrogen-substituted derivatives have been investigated using photoselection techniques. The relative polarizations of transitions linking the ground and first four excited electronic states were determined. These relative polarizations are then placed on an absolute basis knowing the absolute direction of a single transition available from mixed crystal studies. Assignment of these transitions based on electronic state symmetries is then made.

The polarization of transitions throughout the lowest energy absorption band is seen to be wavelength dependent. Wavelength dependent polarization ratios are also observed throughout the fluorescence and phosphorescence emission bands. The existence of mixed polarization in both fluorescence and the lowest lying absorption band signals the presence of a significant amount of "forbidden" character in the lowest electronic state. Polarization of phosphorescence excitation spectra enables the lowest triplet state to be assigned as $^3L_a$. The observation of wavelength dependent polarization of phosphorescence spectra indicates that in addition to direct spin orbit coupling the lowest triplet state acquires allowed singlet character by certain, higher order, nuclear coordinate dependent mechanisms. Plausible routes have been suggested on the basis of the photoselection results.

The spectral features mentioned above are characteristic of all the carbazoles investigated here. Replacement of a hydrogen or alkyl group by an unsaturated vinyl or phenyl group leads to new spectral features at higher energies. These changes have been interpreted in terms of an interaction between transition dipoles localized on carbazole and the unsaturated substituent.

*Acknowledgment.* The author is indebted to Dr. J. H. Sharp for a number of useful discussions and for his interest throughout the course of this investigation. The efforts of both referees are gratefully acknowledged. Their careful reading of the original manuscript lead to many critical comments which were indeed valuable.

## References and Notes

(1) Presented in part at The Twenty-eighth Symposium on Molecular Structure and Spectroscopy, The Ohio State University, Columbus, Ohio, June 1973.
(2) (a) H. Hoegl, *J. Phys. Chem.*, **69**, 755 (1965); (b) W. Klopffer, *Ber. Bunsenges. Phys. Chem.*, **73**, 865 (1969).
(3) C. David, M. Piens, and G. Geuskens, *Eur. Polym. J.*, **8**, 1291 (1972).
(4) W. Klopffer, *J. Chem. Phys.*, **50**, 2337 (1969).
(5) H. Bauser and W. Klopffer, *Chem. Phys. Lett.*, **7**, 137 (1970).
(6) D. M. Pai, *J. Chem. Phys.*, **52**, 2285 (1970).
(7) W. Klopffer, *Chem. Phys. Lett.*, **4**, 193 (1969).
(8) W. Klopffer and W. Liptay, *Z. Naturforsch. A*, **25**, 1091 (1970).
(9) C. A. Pinkham and S. C. Wait, Jr., *J. Mol. Spectrosc.*, **27**, 325 (1968).
(10) N. Mataga, Y. Torihashi, and K. Ezumi, *Theor. Chim. Acta*, **2**, 153 (1964).
(11) A. Bree and R. Zwarich, *J. Chem. Phys.*, **49**, 3344, 3355 (1968).
(12) S. C. Chakravorty and S. C. Ganguly, *J. Chem. Phys.*, **52**, 2760 (1970).
(13) A. C. Albrecht, *J. Mol. Spectrosc.*, **6**, 84 (1961); *Progr. Reac. Kinet.*, **5**, 301 (1970).
(14) A. M. Kalantar and A. C. Albrecht, *Ber. Bunsenges. Phys. Chem.*, **68**, 361 (1964).
(15) T. Azumi and S. P. McGlynn, *J. Chem. Phys.*, **37**, 2413 (1962).
(16) A. C. Albrecht, *J. Chem. Phys.*, **33**, 156 (1960).
(17) J. R. Platt, *J. Chem. Phys.*, **17**, 484 (1949); see also N. S. Ham and K. Ruedenberg, *J. Chem. Phys.*, **25**, 13 (1956).
(18) H. Schutt and M. Zimmermann, *Ber. Bunsenges. Phys. Chem.*, **67**, 54 (1963).
(19) A. H. Kalantar and A. C. Albrecht, *Ber. Bunsenges. Phys. Chem.*, **68**, 361, 377 (1964).
(20) See, for example, E. G. McRae and M. Kasha, "Physical Processes in Radiation Biology," Academic Press, New York, N. Y., 1964.
(21) See, for example, S. K. Lower and M. A. El-Sayed, *Chem. Rev.*, **66**, 199 (1966).
(22) A. C. Albrecht, *J. Chem. Phys.*, **38**, 354 (1963).
(23) D. P. Craig and R. D. Gordon, *Proc. Roy. Soc., Ser. A*, **288**, 69 (1965).

---

# Electron Spin Resonance Spectra of Some Hydroxycyclohexadienyl Radicals Derived from Aromatic Carboxylic Acid Anions

**Gordon Filby* and Kirsten Gunther**

*Institut für Radiochemie, Kernforschungszentrum, Karlsruhe, West Germany*

*(Received October 1, 1973; Revised Manuscript Received February 27, 1974)*

*Publication costs assisted by Kernforschungszentrum*

The addition of hydroxyl radicals to a series of aromatic carboxylic acid anions has been studied by mixing titanous chloride, hydrogen peroxide, and the acid in an aqueous continuous flow system. In the majority of cases (exceptions were phthalic and isophthalic acids) spectra could be interpreted in terms of radicals arising from attack at all possible free ring positions with little or no specificity. Investigation of the influence of pH on the spectra of the tetra- and pentacarboxylic acids indicates that the acid-base properties of the adduct hydroxycyclohexadienyl radicals are not essentially different from those of the parent substance. The geometry and hyperfine splitting constants are briefly discussed.

The electron spin resonance spectra of a large number of short-lived organic radicals in aqueous solution have been observed by rapid-flow mixing of inorganic ions (generally Ti(III) or Fe(II)) and hydrogen peroxide in the presence of an organic compound shortly before their passage through the cavity of an esr spectrometer.[1] The radical producing reactions may be represented by the simplified scheme

$$\mathrm{Ti(III)} + \mathrm{H_2O_2} \longrightarrow \mathrm{Ti(IV)} - \mathrm{OH^-} + \mathrm{OH}\cdot \qquad (1)$$

$$\mathrm{OH} + \mathrm{RH} \longrightarrow \mathrm{R}\cdot + \mathrm{H_2O} \qquad (2)$$

$$\mathrm{OH} + \mathrm{RH} \longrightarrow \mathrm{RH(OH)}\cdot \qquad (3)$$

Numerous investigations have been concerned with the analysis of intermediates,[2] reaction kinetics,[3] and comparisons of radicals generated by the Fenton (Fe(III)), titanous chloride,[4] or photolytic systems.[5] In most cases the identities of the radicals formed from a particular substrate are independent of the mode of initiation though the ratios of the radical concentrations (when it is possible to form more than one) often show significant variations. Such variations can however arise from a single substrate and oxidizing system and result simply from differing kinetics of formation and/or decay of the various resulting radicals.[6] Earlier cases[2] reporting differences in the nature of the radicals generated from Fentons and the titanous chloride reagent have recently been explained by proposing the additional decay mode of R·[7-9]

$$R\cdot + Fe^{3+} \longrightarrow Fe^{2+} + R \qquad (4)$$

It is now well established that, in its reactions with organic compounds, the hydroxyl radical displays electrophilic character. This has been demonstrated with both aliphatic and aromatic substrates when the radical is generated either by pulse radiolysis[10] or by chemical methods.[11,12] Moreover a quantitative study of a large number of aromatic compounds has shown that the reactivities of these compounds can be correlated by the Hammett equation with a negative $\rho$ value.[10,13] In its reactions the hydroxyl radical generally shows the characteristics of hydrogen abstraction from C–H bonds and addition to the double bond of organic substrates containing not only carbon, hydrogen, and oxygen[14] but also nitrogen,[15] phosphorus,[16] fluorine,[17] and chlorine[18] atoms. Addition of a hydroxyl radical to an aromatic system, the process corresponding to (3) above

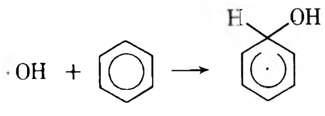

results in the formation of a hydroxycyclohexadienyl radical which may be observed by esr. This result complements other evidence that the free-radical hydroxylation of benzene occurs *via* addition of a hydroxy radical followed by oxidation of the resulting adduct.

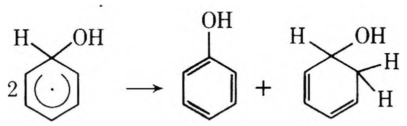

An interesting feature of the cyclohexadienyl radicals produced is the surprisingly large splittings caused by interaction with $\beta$ protons (*e.g.*, for R = H,[19] $a_H$ = 47.71 G, while for R = OH,[20] $a_H$ = 36.0 G). The origin of these splittings has been a matter of some speculation, having been accounted for by the valence-bond,[21] spin-polarization, and hyperconjugation models.[22] More recently Corvaja and Giacometti[23] suggested a monohomocyclopentadienyl structure to account for the spin distribution.

The hydroxylation of aromatic carboxylic acids has not been studied in detail and most of the information stems from radiation chemical studies. Thus Downes[24] showed that for dilute benzoic acid solutions at pH 4 or 9 all three isomeric hydroxy acids were formed with $G$ values of 0.74, 0.42, and 0.33 for the ortho, meta, and para derivatives, respectively. The acid was also decarboxylated to an extent of $G$ = 0.73. In a later study Loeff and Swallow[25] observed the formation of a dialdehyde ($G \sim 0.5$). Sakamoto and Tsuchihashi[26] reported the presence of dimeric products in aerated solutions. Radiolytic decarboxylation has also been discussed by Anbar, *et al.*,[27] who consider that the enhanced reactivity of certain carboxylate anions toward OH radicals may be due to the additional pathway provided by electron transfer

$$RCOO^- + \dot{O}H \longrightarrow OH^- + RCOO^{\cdot -} \longrightarrow$$
$$OH^- + R\cdot + CO_2$$

As an extension to our work on the hydroxylation of carboxyl substituted aromatics[28] we present here a study of the reactions of hydroxyl radicals with some of the homologous aromatic polycarboxylic acids. The hydroxyl radicals were produced chemically (Ti(III)-$H_2O_2$), for the most part in alkaline solution.

## Experimental Section

*Materials.* Titanous chloride and hydrogen peroxide were (a) 15% aqueous and (b) 30% aqueous solutions, respectively, supplied by Merck, Darmstadt. EDTA was obtained from EGA Chemie of Steinheim, West Germany. The polycarboxylic acids were tested by gas chromatography (as methyl esters) and insofar as they showed a purity of not less than 95% were used without further purification. Others, particularly the tricarboxylic acid isomers, were converted to their sodium salts, recrystallized from hot water, and reconverted to the free acid.

*Electron Spin Resonance.* The esr spectrometer is described elsewhere.[29] The reaction cell was generally a home-made one similar to that supplied by Varian though in some cases we used a specially designed cell with a continuously variable mixing-measurement distance.[30] Thus equipped we were able to maximize our signals for flow rate and reaction time. The microwave frequency was determined using a Hewlett-Packard 5246 L frequency counter. The magnetic field was measured directly by means of an AEG nuclear magnetic resonance field meter. Splitting constants and $g$ factors were determined by comparison with an aqueous solution of Fremy salt (13.0 G). pH adjustments were performed on a Knick pH meter using Merck standard buffer solution for calibration.

For experiments above pH 2, the titanous containing solution contained disodium ethylenediaminetetraacetate (2.8 g/l.) and a quantity of sodium hydroxide sufficient to give the required pH. The pH values quoted are these observed before mixing the solutions. The following reaction conditions were employed: total flow rate 2-7 ml/sec (optimized for signal maximum), reaction temperature 25 ± 2°; $TiCl_3$ concentration ($5 \times 10^{-3}$ $M$), hydrogen peroxide concentration ($2 \times 10^{-1}$ $M$), carboxylic acid concentration (0.05–0.1 $M$). Generally the substrate was only included in the oxidizing stream though in certain cases, *e.g.*, phthalic acid, it was necessary to double the concentration and divide it equally between the two streams. This modification sometimes allowed higher stationary concentrations to be achieved. All experiments were conducted with gravity flow.

## Results and Discussion

We assume that the p$K$ values of the resulting radicals do not differ greatly from those of the starting materials and hence designate the species formed in alkaline solutions as carboxylate substituted hydroxycyclohexadienyl radicals.[31] We find ample support for this proposal in our observation that decreasing the pH only gradually led to supplementary splittings (seen as line broadening) at about the p$K$ values corresponding to the last ionization of the polycarboxylic acid. Such splittings have recently been employed by Fessenden[32] to determine the acid-base properties of polycarboxylic acid electron adducts. Changes in p$K$ of four units were characteristically observed. Presumably in these cases the additional electron alters the acid-base properties of the substrate much more drastically than in the case of the neutral hydroxycyclohexadienyl radical. This is apparently connected with the increased charge delocalization in the electron adducts in contrast to our less delocalized systems.

*Esr Spectra and Their Assignments.* Of the radicals which we wish to discuss, esr parameters for benzoic acid and trimesic acid (1,3,5-benzenetricarboxylic acid) have been reported previously. The remainder are reported here for the first time. The starting materials, hydroxycyclohexadienyl radicals derived therefrom, and hyperfine splitting constants are all shown in Table I. We discuss the results in homologous series.

(*a*) *Benzoic Acid.* In common with Norman and Dixon[20] and Shiga, *et al.*,[33] the spectra observed for this substrate proved too complicated for a complete analysis. Whereas experiments run at acid concentrations of 0.1–0.2 *M* and pH 9.0–9.5 yielded weak uninterpretable spectra reduction of the pH to 7 allowed registration of a stronger, though still complicated spectrum consisting of some 90–100 lines. Taking characteristic splitting constants (see Table I for such values) for the various possibilities

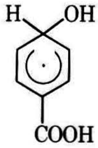
A

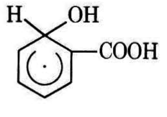
B

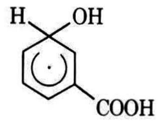
C

and assuming that, in common with all other cases quoted here, hydroxycyclohexadienyl radicals are observed, we can calculate the number of lines expected from each species together with the total spectral width. Neglecting the small hydroxylic proton which in any case is probably not resolved here we arrive at 18 (50–57 G), 24 (~59 G), and 24 lines (~59 G) for A, B, and C, respectively. Our total spectral width is approximately 80 G. Thus we may conclude that indeed all three possible cyclohexadienyl adducts are involved. Additionally the absence of irregular line patterns (deviations from the Pascal triangle intensities) in the spectrum suggests that if any positional preference for OH attack exists it must be small.

(*b*) *Dicarboxylic Acids.* Here we investigated all three isomers. Phthalic acid (1,2-benzenedicarboxylic acid, total concentration $10^{-1}$ *M*) revealed only a weak, though easily assignable, spectrum consisting of 12 lines due to 1H–2H–1H couplings. Owing to the high instrument modulation necessary to achieve registration the hydroxylic proton doublet of the resulting hydroxycyclohexadienyl radical was not resolved. The presence of the triplet of 8.52 G (two ortho positions free) supports the assignment (Table I). We were not able to observe the radical possible *via* hydroxyl attack at position 3 (stereochemically equivalent to position 6). This may be due to a lower stationary state concentration resulting from a positional preference for attack of hydroxyl or an enhanced decay rate for this particular radical.

In the case of isophthalic acid we were gain forced to employ extreme instrument conditions in order to achieve even moderate spectra. This rendered resolution of the hydroxyl proton impossible. The recorded spectra were however easily assigned to radicals derived *via* attack at positions 4 and 5. No trace of the hydroxycyclohexadienyl derived from reaction at C3 could be detected under a wide variety of experimental conditions. This may be due to the reduced electron density resulting from the two ortho placed carboxyl groups causing a diminution in affinity to electrophilic attack. With terephthalic acid (1,4-benzenedicarboxylic acid) only one hydroxycyclohexadienyl is expected and good spectra of it could be easily recorded. The spectrum consists of 32 lines arising from a 1H–1H–1H–1H–1H set of interactions. Thus the characteristic pattern leads unambiguously to assignment of the radical as shown (Table I).

(*c*) *Tricarboxylic Acids.* In most cases for these and the following tetra- and pentacarboxylic acids very intense spectra could be recorded as a result of the low number of spectral lines and the high steady-state concentration caused by the diminished bimolecular radical–radical decay rate constants for the multiply charged species. The radical observed from trimesic acid (1,3,5-benzenetricarboxylic acid) by reaction with hydroxyl radicals in acid solution has been reported by Norman and Dixon[20] who observed a spectrum consisting of a widely split doublet ($a$ = 24.4 G) each line of which was split into a triplet ($a_1$ = 2.6 G). The lower doublet splitting observed by them is probably connected with the fact that the hydroxylic and probably also the carboxylic protons make a contribution to the line width at low pH thus rendering accurate measurement of the methylene coupling parameters difficult. Our spectrum consisted of lines arising from 1H–1H–2H interactions with line widths of 0.23–0.25 G. Examination of the molecular symmetry indicates that it will only be possible to observe one specific hydroxycyclohexadienyl radical. The situation is however different with the remaining tricarboxylic acids investigated. For example, with hemimellitic acid, hydroxycyclohexadienyl radicals resulting from attack on the 4 and 5 positions (see Table I for numbering) could result and signals corresponding to these are indeed observed (Figure 1). Similarly trimellitic acid, for which three radicals are possible, yields them all in high concentration (Figure 2). In this particular compound the total number of lines per radical is identical in each case, *i.e.*, the esr spectral pattern in all three radicals results from a 1H–1H–1H–1H set of interactions so that peak intensities of corresponding lines indicate semiquantitatively the relative concentrations of the various radicals formed. Thus the radical resulting from attack as C5 is present in the highest concentration (approximately twice that of the others) with those from C3 and C6 attack observable in approximately the same concentration.

(*d*) *Tetracarboxylic Acids.* Here only prehnitic (1,2,3,4-benzenetetracarboxylic acid) and pyromellitic acid (2,3,5,6-benzenetetracarboxylic acid) were available for investigation. In each case only one hydroxycyclohexadienyl radical is possible. Eight-line spectra resulting from 1H–1H–1H interactions were easily identified. In his recent pulse radiolytic–esr study of aromatic carboxylate anions Fessenden[32] observed the formation of two OH adducts (I and II) in comparable concentrations from pyromellitic acid at pH 12.2. I has splitting constants and *g* factors identical, within experimental error, with those observed by us. We were however only able to observe any second species under special conditions, namely, using very long reaction times in the variable reaction cell[30] (pH 8). Under these conditions we observed a second radical ($a_1$ = 12.96 G, $a_2$ = 3.26 G, $a_3$ = 1.16 G) to which we

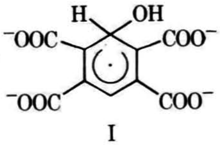
I

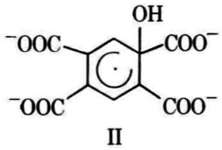
II

**TABLE I: Esr Parameters for Hydroxycyclohexadienyl Radicals in the Aromatic Carboxylic Acid Series**[a]

| Starting material[b] | Observed radicals | *g* factor | Assigned position | Hyperfine constants, G[c] |
|---|---|---|---|---|
| 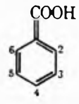 Benzoic acid | 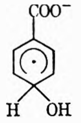 | | | 34.71[d]<br>8.35 (1),[e] 2.59 (1),<br>2.79 (1), 12.53 (1) |
| 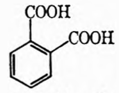 Phthalic acid | 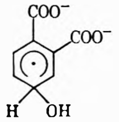 | | 4<br>3 and 5<br>6 | 34.3[d]<br>8.5 (2)<br>3.0 (1) |
| 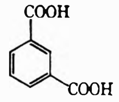 Isophthalic acid | 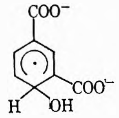 | | 4<br>5<br>2 and 6 | 28.0[d]<br>7.8 (1)<br>2.6 (2) |
| | 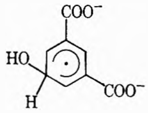 | | 5<br>2<br>4 and 6 | 35.3[d]<br>10.5 (1)<br>8.25 (2 |
| 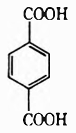 Terephthalic acid | 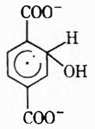 | 2.0023 | 2<br>3<br>5<br>6 | 30.65, 0.56<br>8.18 (1)<br>12.55 (1)<br>2.80 (1) |
| 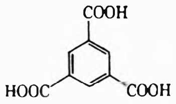 Trimesic acid | 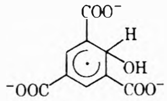 | 2.0024 | 2<br>4 and 6 | 26.11, 0.51<br>2.61 (2) |
| 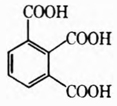 Hemimellitic acid | 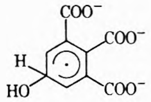 | 2.0026 | 5<br>4 and 6 | 33.9, 0.63<br>8.43 (2) |
| | 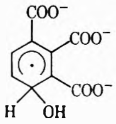 | 2.0029 | 4<br>5<br>6 | 32.91, 0.56<br>8.91 (1)<br>2.52 (1) |
| 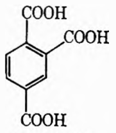 Trimellitic acid | 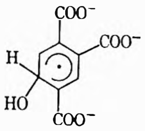 | 2.0027 | 5<br>6<br>3 | 30.45, 0.55<br>7.41 (1)<br>2.77 (1) |
| | 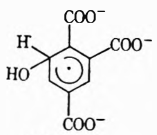 | 2.0025 | 6<br>3<br>5 | 32.45, 0.61<br>12.51 (1)<br>8.35 (1) |
| | 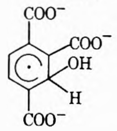 | 2.0028 | 3<br>6<br>5 | 27.72, 0.54<br>12.25 (1)<br>2.77 (1) |
| 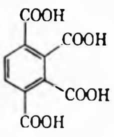 Prehnitic acid | 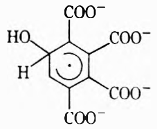 | 2.0025 | 6<br>5 | 31.93, 0.69<br>7.69 (1) |

**TABLE I** *(Continued)*

| Starting material[b] | Observed radicals | $g$ factor | Assigned position | Hyperfine constants, G[c] |
|---|---|---|---|---|
| 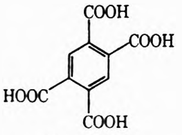 Pyromellitic acid | 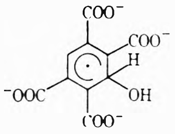 | 2.0026 | 3<br>6 | 29.76, 0.58<br>12.24 (1) |
| 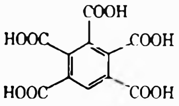 Pentacarboxylic acid | 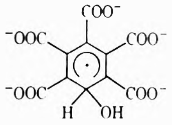 | 2.0028 | 4 | 27.83, 0.68 |

[a] Temperature 25–27°, pH 8. [b] The numbering shown for benzoic acid is maintained throughout the table. [c] The number of equivalent protons showing the given splitting constant is shown in parentheses. For positions given pairs of hyperfine constants the second always refers to the hydroxylic proton. [d] The high instrument modulation required to observe a signal rendered it impossible to resolve the hydroxylic proton. [e] The nonequivalent meta protons, data taken from ref 40.

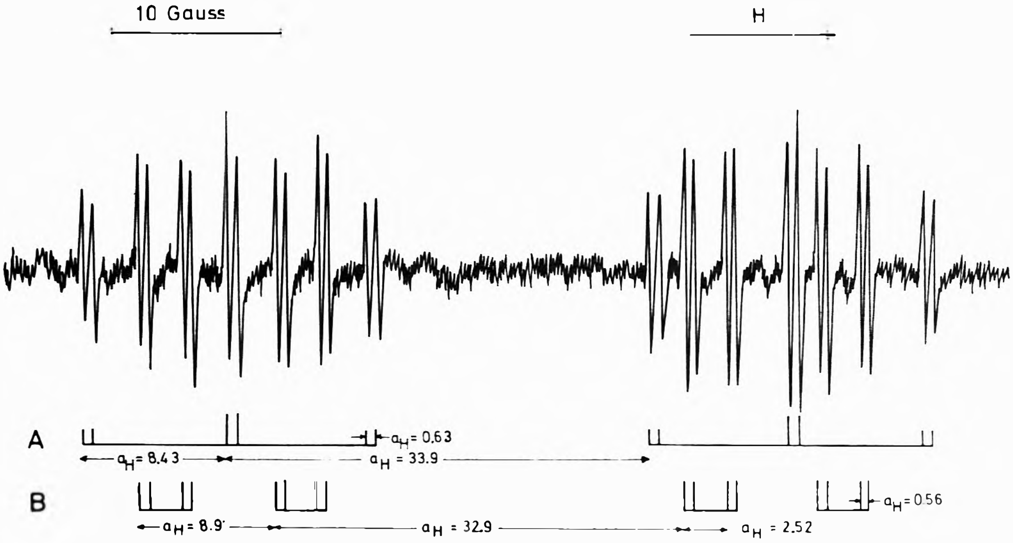

**Figure 1.** Esr spectra of hemimellitate radicals at pH 8: modulation 100 kHz, 0.5 G, time constant 1.0 sec. The magnetic field direction increases from left to right. The stick diagram demonstrates the analysis for radicals by attack at positions 5 (A) and 4 (B).

ascribe structure II, presumably an intermediate involved in decarboxylation and possibly ring opening reactions. The esr parameters are however somewhat different than those observed by Fessenden ($a_1$ = 11.79, $a_2$ = 0.68 G, $a_3$ = 0.26 G). The reason for this is not clear though it may be connected with (a) the different pH's used in the two studies or (b) possible complexation of the radical with titanium ions in our case. Another notable feature is the differing radical concentrations observed; we were never able to observe II (i) at short reaction times or (ii) in concentrations higher than approximately $\frac{1}{20}$ that of the normal hydroxycyclohexadienyl (I). Additionally, work with the variable cell showed that II decayed only slightly slower than I ($k_{\rm I}/k_{\rm II}$ ~ 0.8–0.9). Clearly then although formation of II is not especially favored, once formed it leads to products with about the same ease as I.

The former fact is probably connected with the extremely reduced ring electron density which must be caused by the adjacent ortho and para carboxyl groups.

(e) *Penta- and Hexacarboxylic Acids.* Only one pentacarboxylic acid is possible and with it only one hydroxycyclohexadienyl radical. Weak lines, symmetrically placed around those of the proton spectrum, were attributed to $^{13}$C satellites. With mellitic acid (benzenehexacarboxylic acid) we were unable to observe any esr signal under varying conditions of flow and pH. No supplementary lines due to addition to a carboxyl bearing ring carbon were observed despite the apparently favored conditions for their observation (five and six negative charges, respectively). Apparently the opposing effects, *i.e.*, diminished nucleophilicity and large steric effect dominate in these cases.

*Effect of pH on the Esr Spectra.* Reducing the pH from 8 to 4 while employing identical flow conditions resulted in all cases except pyromellitic, prehnitic, and benzenepentacarboxylic acids in a complete disappearance of the esr spectrum, which could not be retrieved by altering the flow rates. All the acids employed have p$K$ values in the range 2–6. Hence it appears that the protonated species decay at such rates that the minimum detectable stationary concentration cannot be achieved. Similarly in the case of the higher carboxylated acids a drastic lowering of the stationary state concentration occurred while simultaneously line broadening due to the appearance of extra small splittings arising from the protonated carboxyl groups appears (Figure 3). From the onset of broadening (pH 4–5) we are able to propose that acid–base properties

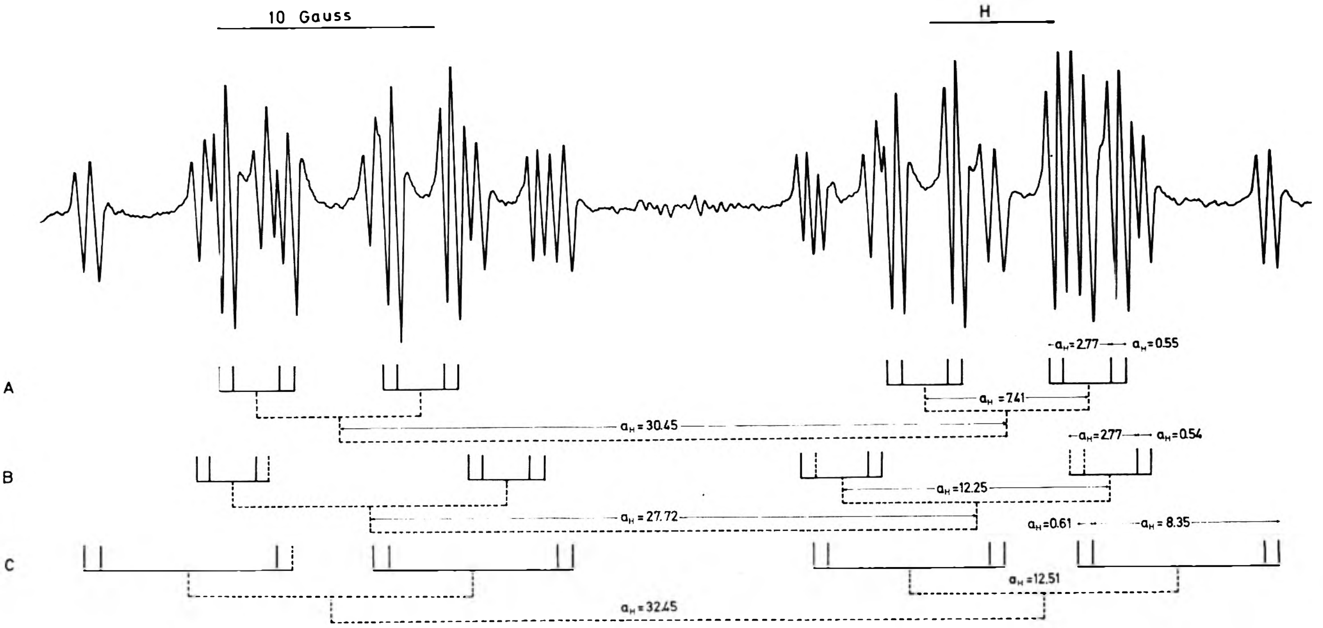

**Figure 2.** Esr spectra of trimellitate radicals at pH 8. The conditions are the same as in Figure 1. The stick diagrams demonstrate the analysis for radicals formed by attack at positions 5 (A), 3 (B), and 6 (C).

of the hydroxycyclohexadienyl radicals derived from pyromellitic acid are not essentially different from the parent substance itself (p$K_1$ = 1.9; p$K_2$ = 2.9; p$K_3$ = 4.5; p$K_4$ = 5.6). Judging from the extent of broadening the splitting constant for the "protonating" protons must be ~1 G in line with those usually observed. The proton exchange rate must be of the order of $10^8$–$10^9$ $M^{-1}$ sec$^{-1}$.

*Position of Attack of Hydroxyl Radicals.* Shiga and Isomoto[34] have recently demonstrated that in the case of furan derivatives hydroxyl radicals generated *via* Fenton's reagent attack the position of maximal free valence (FV) and minimal localization energy to radical attack ($L_r$). Accepting such a correlation as established in our case we may work backward and conclude that, since in all cases but one (isophthalic acid) we observed all possible isomeric radicals, the corresponding quantities show differences too small to be detected by the esr method.[35]

*Steric Configuration of the Hydroxycyclohexadienyl Radicals.* The geometry of neither cyclohexadienyl nor hydroxycyclohexadienyl radicals is known with certainty though the former was recently postulated to be planar. Clearly a knowledge of the $^{13}C$ hyperfine coupling constants would be of interest in answering this problem. The attending difficulties, *i.e.*, preparation of sufficient enriched aromatic for such an experiment or achieving a sufficiently high stationary state concentration to observe $^{13}C$ lines in natural abundance, render such experiments with unsubstituted aromatics hopeless. We have recently taken advantage of the diminished bimolecular decay rates of polycarboxylate to measure the $^{13}C$ couplings in natural abundance.[36] The smallness of the splitting constants in pyromellitate and benzenepentacarboxylate (all ~20 G) support the proposition of a planar ring at least in these cases. It would appear difficult to argue that such bulky charged groups favor a planar conformation (more likely the opposite) and hence it seems likely that in the simple case the ring remains essentially planar, possibly interconverting between half chair forms.

*Trends in the Coupling Constants.* It is of interest to compare the coupling constants of these radicals internally and with their cyclohexadienyl and hydroxycyclohexadienyl analogs. Immediately apparent are the large effects on the methylene coupling constants caused by introduction of ortho and para carboxylate groups to hydroxycyclohexadienyls. For example, substitution of one ortho and one para group (isophthalic acid) results in a reduction of the methylene coupling constant by 8 G. Introduction of a second ortho $CO_2^-$ group (trimesic acid) results in a further reduction of ~2 G thus demonstrating the lowest observed methylene hfsc (26.11 G) in this series. In strong contrast are the marginal effects observed on substituting meta $CO_2^-$ groups, the methylene hfsc scarcely differing from that of a simple hydroxycyclohexadienyl radical. For example, introduction of two meta $CO_2^-$ groups (isophthalic acid) results in a methylene splitting actually slightly greater than for the free hydroxycyclohexadienyl. The above observations are somewhat striking in view of the established low polarity of the $CO_2^-$ group ($\sigma^m$ = $0.10\sigma^p$ = 0.13). Furthermore the effects of meta and para substitution are not additive[37] as might have been expected from a simple Hammett treatment.[38] Since this, however, is only strictly applicable to well-behaved aromatic systems, a breakdown is not unexpected. Perhaps a new set of Hammett constants could achieve a fit though we have not attempted this owing to the paucity of our experimental data. The reason for the strong influence of ortho and para substitution is presumably connected with the ability of this group to remove spin from the ring by a conjugative mechanism, *i.e.*, the structures below play an essential role in stabilizing the radicals

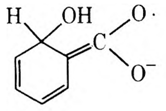

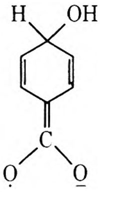

Support is found for this suggestion in the comparison of the radicals derived from isophthalic (two meta positions

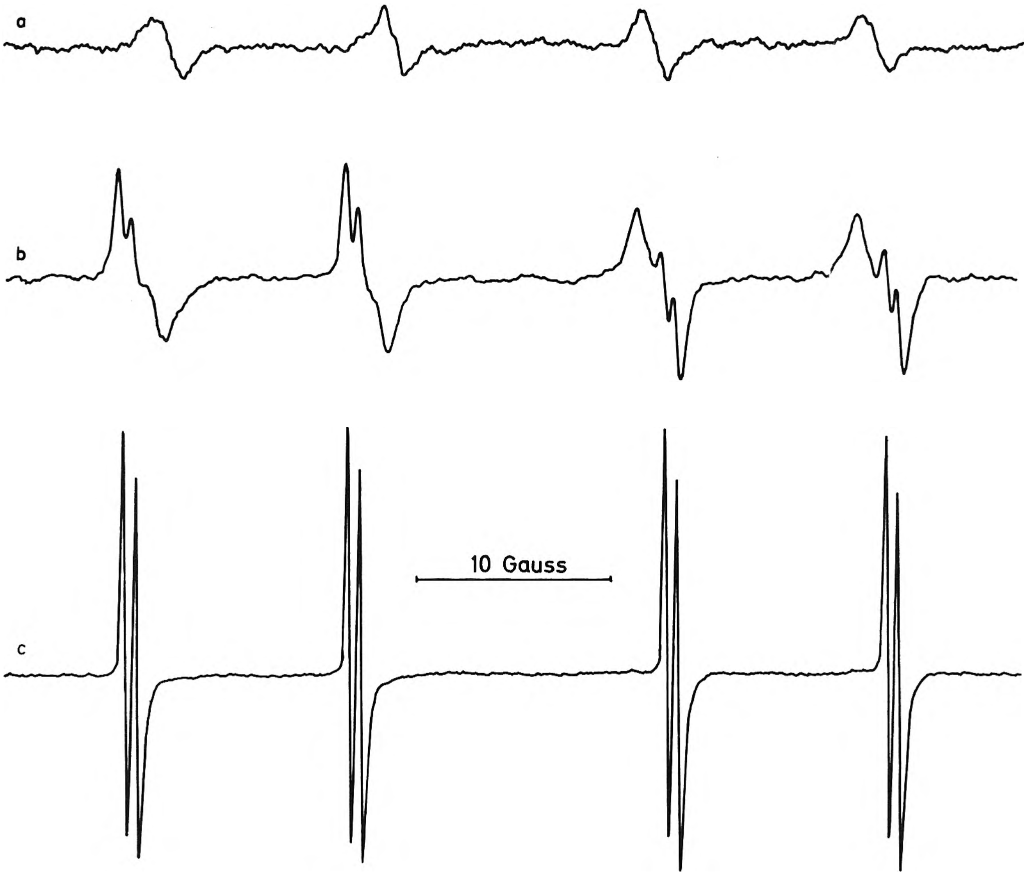

**Figure 3.** Effect of pH on the esr spectra of pyromellitate radicals. The conditions are the same as in Figures 1 and 2: (a) pH 4, (b) pH 5, (c) pH 8.

occupied $a_H$ = 35.3 G) and phthalic acids (one meta and one para $a_H$ = 34.3 G) where similar hfsc's should be expected. The lower splitting observed for the para-substituted compound thus exemplifies the role of the conjugative mechanism.

Finally we wish to point out that the technique used by Whiffen[39] to correlate the methylene coupling constants in cyclohexadienyl fails to reproduce them in the case of unsubstituted hydroxycyclohexadienyl and the appropriate carboxylate substituted species described here. In all cases the results achieved are about 30% higher than those observed. Clearly in the unsubstituted case delocalization of spin onto the hydroxyl oxygen renders untenable the basic assumption, *i.e.*, that the admixing coefficient of the hydrogen orbitals is proportional to the coefficient of the $\pi$ orbital at each of the ortho carbon atoms.

## References and Notes

(1) For leading references see "Annual Reports of the Chemical Society," Part B, particularly the years 1968-1970.
(2) T. Shiga, A. Boukhors, and P. Douzo, *J. Phys. Chem.*, **71**, 4264 (1967); **71**, 3559 (1967).
(3) R. E. James and F. Sicilio, *J. Phys. Chem.*, **75**, 1326 (1971).
(4) W. T. Dixon and R. O. C. Norman, *J. Chem. Soc.*, 3119 (1963).
(5) H. Livingston and H. Zeldes, *J. Chem. Phys.*, **44**, 1245 (1966).
(6) W. G. Filby and K. Gunther, unpublished results.
(7) R. O. C. Norman and P. R. West, *J. Chem. Soc. B*, 389 (1969).
(8) G. Czapski, *J. Phys. Chem.*, **75**, 2957 (1971).
(9) W. A. Armstrong, *Can. J. Chem.*, **47**, 3747 (1969).
(10) M. Anbar, D. Meyerstein, and P. Neta, *J. Phys. Chem.*, **70**, 2660 (1966).
(11) W. T. Dixon, R. O. C. Norman, and A. L. Buley, *J. Chem. Soc.*, 3625 (1964).
(12) R. O. C. Norman and R. J. Pritchett, *J. Chem. Soc. B*, 926 (1967).
(13) G. O. Phillips, W. G. Filby, J. S. Moore, and J. V. Davies, *Carbohyd. Res.*, **16**, 89 (1971).
(14) R. O. C. Norman and B. C. Gilbert, *Advan. Phys. Org. Chem.*, **5**, 53 (1967), and references therein.
(15) H. Taniguchi, *J. Phys. Chem.*, **74**, 3143 (1970).
(16) E. A. C. Lucken, *J. Chem. Soc. A*, 1354 (1966).
(17) C. R. E. Jephcoate and R. O. C. Norman, *J. Chem. Soc. B*, 48 (1968).
(18) W. E. Griffiths, G. F. Longster, J. Myatt, and P. F. Todd, *J. Chem. Soc. B*, 530 (1967).
(19) R. W. Fessenden and R. H. Schuler, *J. Chem. Phys.*, **38**, 773 (1963).
(20) W. T. Dixon and R. O. C. Norman, *J. Chem. Soc.*, 4857 (1964).
(21) H. Fischer, *J. Chem. Phys.*, **37**, 1094 (1962).
(22) J. P. Colpa and E. DeBoer, *Mol. Phys.*, **7**, 333 (1964).
(23) C. Corvaja and G. Giacometti, *Theor. Chim. Acta*, **14**, 352 (1969).
(24) A. M. Downes, *Aust. J. Chem.*, **11**, 154 (1958).
(25) T. Loeff and A. J. Swallow, *J. Phys. Chem.*, **68**, 2470 (1964).
(26) A. Sakamoto and G. Tsuchihashi, *Bull. Chem. Soc. Jap.*, **34**, 660 (1961).
(27) M. Anbar, D. Meyerstein, and P. Neta, *J. Chem. Soc. B*, 742 (1966).
(28) K. Gunther, W. G. Filby, and A. K. Eiben, *Tetrahedron Lett.*, 3, 251 (1971).
(29) W. G. Filby and K. Günther, *Z. Naturforsch. B*, **27**, 1289 (1972).
(30) W. G. Filby and K. Günther, *Lab. Pract.*, **22**, 283 (1973).
(31) L. M. Dorfman, I. A. Taub, and R. E. Buhler, *J. Chem. Phys.*, **36**, 3051 (1962); according to these authors the $pK_a$ of the hydroxyl group in the benzoic acid cyclohexadienyl is apparently greater than 14. Hence our assumption seems reasonable.
(32) P. Neta and R. W. Fessenden, *J. Phys. Chem.*, **77**, 620 (1973).
(33) T. Shiga, T. Kishimoto, and E. Tomita, *J. Phys. Chem.*, **77**, 330 (1973).
(34) T. Shiga and A. Isomoto, *J. Phys. Chem.*, **73**, 1139 (1969).
(35) A word of criticism. Such correlations of MO quantities and structure can only be valid (a) when the molecule is unperturbed by oncoming reagents and (b) in the absence of an overtly large contribution from a, at time zero or very shortly thereafter, *i.e.*, before the differing decay rate constants of the separate isomers begin to make a contribution to the observed radical concentration. Neither condition a nor b can be claimed to be fulfilled in such experiments. It would thus appear that little is to be gained from such attempted correlations of structure and reactivity.
(36) W. G. Filby and K. Gunther, *J. Chem. Phys.*, in press.

(37) O. Exner in "Advances in Linear Free Energy Relationships," N. B. Chapman and J. Shorter, Ed., Plenum Press, New York, N. Y., 1972.

(38) For a recent discussion of substituent effects of the esr parameters of aromatic radicals see E. G. Janzen, *Accounts Chem. Res.*, **2**, 279 (1969).

(39) D. H. Whiffen, *Mol. Phys.*, **6**, 223 (1963). This author proposed that the $CH_2$ hyperfine splitting constant (hfs) will be of the form $Q(c_0 + c_0')^2$ where $c_0$ and $c_0'$ are the Huckel coefficients of the singly occupied $\pi$ orbital at each of the ortho carbon atoms and $Q$ has its usual significance. The $Q$ values of Fessenden and Schuler[19] (38 G) and Fischer[21] (35 G) were both employed; those of $c_0$ and $c_0'$ were calculated from the observed ortho spin density. This method predicted a value for the $CH_2$ hfs of 47.7 G in good agreement with that observed (48.8 G).

(40) K. Eiben and R. W. Fessenden, *J. Phys. Chem.*, **75**, 1186 (1971).

# Effect of Urea on Magnetic Relaxation in Aqueous Solutions of Poly(ethylene oxide)[1]

**A. A. Jones and W. H. Stockmayer***

*Department of Chemistry, Dartmouth College, Hanover, New Hampshire 03755*

*(Received February 11, 1974)*

*Publication costs assisted by the National Science Foundation*

The nmr relaxation times $T_1$ and $T_2$ and the chemical shift of poly(ethylene oxide) in heavy water were measured as a function of urea concentration. Only a gradual change in these properties was observed from 0 to 10 $m$ urea with no indication of a sharp transition in the conformation of the polymer.

## Introduction

Hammes and Lewis[2a] measured ultrasonic absorption in aqueous solutions of poly(ethylene oxide), PEO, and latter Hammes and Schimmel[2b] investigated the effect of urea on these solutions. Their results were interpreted in terms of a cooperative polymer–solvent interaction which underwent a transition between 2 and 4 $m$ urea, as indicated by a 50% decrease in the relaxation time (of the order of several nanoseconds).[2,3] Similar behavior was also reported for PEO in aqueous solutions of guanidinium hydrochloride.[4] The dependence of the phenomenon on chain length led to the conclusion that a fairly large region of polymer plus solvent, involving perhaps 100 monomer residues, was involved in the cooperative process.

Later Kessler, O'Brien, and Dunn[5] remeasured the ultrasonic absorption of PEO in water over a wider range of frequencies and found that more than one relaxation time was needed to fit their data. A considerable part, but by no means all, of their measured absorption appears to agree with the frequency dependence of the shear viscosity of the polymer solution, as given by the well-known Rouse-Zimm theory.[6,7] A difference of opinion[8,9] remains with respect to the interpretation of the ultrasonic behavior of this system, and it appears to be a difficult matter to identify unique absorption mechanisms. A somewhat analogous situation is encountered[10] in polystyrene solutions in organic solvents; the reported ultrasonic relaxation times[11,12] cannot be completely and quantitatively reconciled with other dynamical measurements, including viscoelasticity, dielectric and nmr relaxation, and fluorescence depolarization.

The ambiguity in interpreting the ultrasonic data in the PEO–water case may also extend to the PEO–urea–water system, and to the ostensible transition in the ultrasonic absorption centered at 2.5 $m$ urea. The role of the polymer in the transition is of special interest, since Hammes and Schimmel[2b] report only a steady change in the intrinsic viscosity (which is a sensitive measure of the equilibrium polymer conformation) as the urea concentration is increased. Furthermore, the reported transition and its interpretation in terms of an abrupt change in the polymer–solvent interaction has been compared with the denaturation of proteins.[2b-4] The possible significance of such a transition in a synthetic polymer, as well as the uncertainty in the interpretation of the ultrasonic absorption, has led us to investigate the PEO–urea–water system by nmr.

Liu and Ullman[13] have reported nmr measurements on solutions of PEO in water, aqueous HCl, and pentachloroethane. The relaxation times $T_1$ and $T_2$ were interpreted in terms of local motion of the polymer chain and the effects of the different solvents on the conformation of the polymer. Further study of aqueous PEO solutions with nmr thus appeared to be useful for examining the alleged transition between 2 and 4 $m$ urea, although a cooperative polymer–solvent binding rate would not be directly observed in the nmr properties of the polymer. The most effective relaxation mechanism for the polymer at high molecular weight is intramolecular dipole–dipole relaxation[13] and therefore is not a function of the water exchange time. The exchange might be observable in the solvent relaxation time, although the exchange of water protons with urea would be the dominant relaxation mechanism.[14] On the other hand, one would expect a transition in the local solvent structure to cause a conformational change in the polymer and a change in the effective solvent viscosity experienced by the local motion,[10] both of which would be reflected in the nmr relaxation times. Lastly, the chemical shift is a sensitive measure of solvent interaction, particularly hydrogen bonding,[15] and could be expected to reflct a change in solvent character.

## Experimental Section

A sample of poly(ethylene oxide) of molecular weight

20,000 was obtained from the Dow Chemical Co. Heavy water of 99.7% isotopic purity was purchased from Aldrich Chemical Co., Inc. One lot of deuterated urea was prepared by repeated recrystallizations from $D_2O$ and one lot of 98% isotopic purity was purchased from Wilmad Glass Co., Inc. Samples prepared from either source gave similar results.

Solutions of PEO, heavy water, and deuterated urea were prepared by weight and then transferred to heavy-wall 5-mm precision nmr tubes. The samples were subjected to five freeze-pump-thaw cycles to remove dissolved oxygen.

The relaxation times were measured by pulse experiments employing a modified Varian HA-60-IL spectrometer. The longitudinal relaxation time $T_1$ was measured with a 180-90° pulse sequence and the transverse relaxation time $T_2$ with a 90-180° pulse sequence. The $T_2$ measurement was unaffected by diffusion because of the large diffusion coefficient[16] of PEO at this molecular weight and the relatively homogeneous field used. The chemical shift difference between PEO and HOD was measured by locking on the PEO signal and measuring the frequency shift of the HOD signal. Temperature was maintained within 1° by a Varian variable temperature controller.

## Results

Results of the $T_1$ experiments on solutions of PEO in heavy water as a function of deuterated urea concentration are given in Figure 1. The polymer concentration was $9 \pm 2$ wt % and was varied (as by Hammes and Schimmel[2b]) to produce a constant mole fraction of ethylene oxide monomer of about 0.04. The analogous results for $T_2$ on the same samples are given in Figure 2. Neither the $T_1$ nor $T_2$ results are dependent upon the exact polymer concentration for the solutions studied.[13] The uncertainty in the $T_1$ values is ±5% and uncertainty in $T_2$ is ±15%. The larger uncertainty in $T_2$ reflects the possibility of a systematic error, but the precision in this measurement is ±5%. The latter is the more important quantity since a comparison among $T_2$ values at various urea concentrations is desired.

The results for $T_1$ and $T_2$ in pure heavy water can be compared with those of Liu and Ullman.[13] Their results for PEO of molecular weight 20,000 in $H_2O$ at 25° were $T_1 = 0.42$ sec and $T_2 = 0.27$ sec. At molecular weight 20,000, they observed no change from $H_2O$ to $D_2O$. They determined $T_1$ from a saturation recovery experiment and $T_2$ from the line width. Their value for $T_1$ agrees quite well with ours, but the value of $T_2$ does not. The latter discrepancy may be attributed to systematic errors frequently encountered in determining $T_2$ from either line width[17] or pulse experiments.[18]

The chemical shift difference between PEO and HOD is given in Figure 3 as a function of urea concentration.

## Discussion

There is no indication of a sharp transition in any of the measured nmr properties as a function of urea concentration. The relaxation times $T_1$ and $T_2$ are nearly inversely proportional to the known[2b] solvent viscosity as the urea concentration is changed. This behavior is easy to interpret if the effective local viscosity in the vicinity of the moving chain segment is proportional to the observed solvent viscosity; in the extreme-narrowing limit[15] the orientational correlation time is then just proportional to solvent viscosity and gradually increases with increasing urea concentration. According to the detailed analysis attempted by Liu and Ullman[13] in terms of local chain motions for PEO, this correlation time is of the order of 0.1 nsec. In contrast, the reported ultrasonic relaxation times (at 10°) are about 6 nsec in water and low urea concentrations but *decrease* (despite the increase in solvent viscosity) to about 3 nsec between 2 and 4 *m* urea.

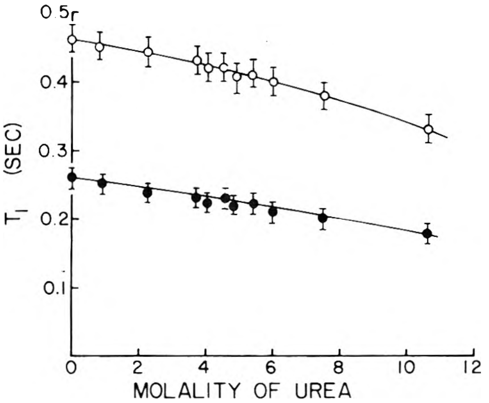

**Figure 1.** Spin-lattice relaxation time $T_1$ of the protons in PEO as a function of urea concentration: filled circles, 10°; open circles, 25°.

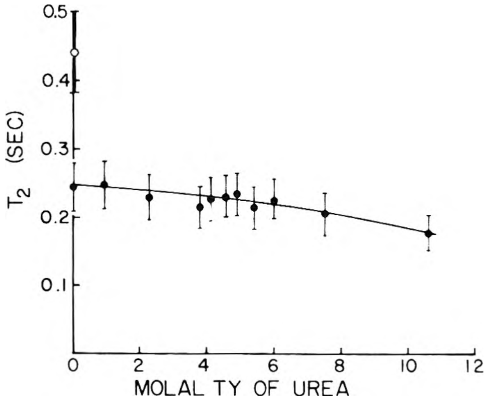

**Figure 2.** Spin-spin relxation time $T_2$ of the protons in PEO as a function of urea concentration: filled circles, 10°; open circles, 25°.

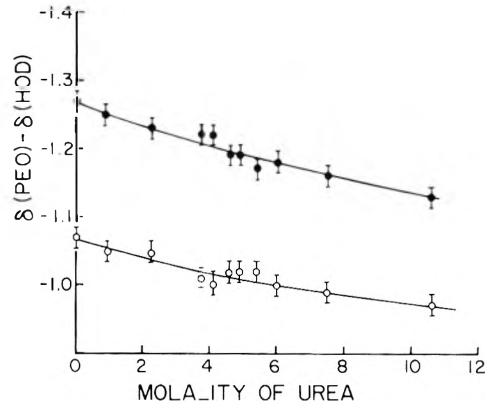

**Figure 3.** Chemical shift difference between the protons of PEO and those of HOD *vs.* urea concentration: filled circles, 10°; open circles, 25°.

As seen from Figure 3, the chemical shift appears to change smoothly with urea concentration. Vold, Daniel, and Chan[14] found the chemical shift of water in neutral urea solutions to be independent of the urea concentration, but observed a shift of the signal under acidic or basic conditions. This shift was attributed to chemical exchange of protons between water and urea. The small trend in our results can be ascribed to this exchange, for although the solutions were prepared to be close to neutral they were unbuffered, and the direction of the observed shift and the observed broadening of the HOD signal are in agreement with this explanation. In any event, this is a small effect which cannot obscure the conclusion that there is no significant change in the shielding of the PEO protons due to changes in their solvent environment.

The lack of a visible transition in the nmr spectra of the polymer is somewhat surprising if a truly cooperative polymer–solvent interaction is altered by addition of urea. Since the obsrved ultrasonic relaxation process is much slower than those which govern the observed dielectric[19] and nmr relaxation[13] phenomena, it might be argued that the present experiments are simply irrelevant to the question. However, as Hammes and Schimmel[2b] themselves remark, "Undoubtedly some changes in the configuration of the polymer occur concurrently with the changes in the local water structure"; yet neither the intrinsic viscosity nor the proton chemical shift of the polymer give any hint of other than very gradual changes in equilibrium polymer conformation. More specifically, when the urea concentration is changed from 2 to 4 *m* the rate of the acoustically observed relaxation process is apparently doubled, but over this range the proton chemical shift changes by less than 0.1 ppm and the intrinsic viscosity increases by about 5%. The transition in the *rate* of the acoustical process is thus remarkable in that no visible attendant transition (to within our 5% precision) is visible in either local or large-scale conformational or solvation *equilibria.* A way out of this dilemma might be to suppose that the polymer conformations involved in the acoustical cooperative process are selectively rather compact ones which do not contribute greatly to the over-all chain dimensions and thus produce no visible transition in the intrinsic viscosity. It seems a bit harder to explain the absence of transitions in the effective local viscosity as seen by nmr or in the chemical shift.

The ultrasonic observations thus still stand alone as indicators of the transition in solvation structure. In the absence of other evidence, it seems wise to adopt a skeptical stance[20] with respect to any particular mechanism offered to explain the observations. Clearly, extension of the ultrasonic experiments over a broader frequency range would be highly desirable.

*Acknowledgment.* We thank Drs. Michael J. Gerace, Gordon G. Hammes, Paul R. Schimmel, and Robert D. White for helpful discussions.

## References and Notes

(1) Supported by the National Science Foundation.
(2) (a) G. G. Hammes and T. B. Lewis, *J. Phys. Chem.*, **70**, 1610 (1966); (b) G. G. Hammes and P. R. Schimmel, *J. Amer. Chem. Soc.*, **89**, 442 (1967).
(3) G. G. Hammes and P. B. Roberts, *J. Amer. Chem. Soc.*, **90**, 7119 (1968).
(4) G. G. Hammes and J. C. Swann, *Biochemistry*, **6**, 1591 (1967).
(5) L. W. Kessler, W. D. O'Brien, and F. Dunn, *J. Phys. Chem.*, **74**, 4096 (1970).
(6) B. H. Zimm, *J. Chem. Phys.*, **24**, 269 (1956).
(7) P. E. Rouse, *J. Chem. Phys.*, **21**, 1272 (1953).
(8) S. A. Hawley and F. Dunn, *J. Chem. Phys.*, **50** 3523 (1969).
(9) G. G. Hammes and P. B. Roberts, *J. Chem. Phys.*, **52**, 5496 (1970).
(10) W. H. Stockmayer, *Pure Appl. Chem. Suppl., Macromolecules*, **8**, 379 (1973).
(11) H. J. Bauer, H. Hässler, and M. Immendörfer, *Discuss. Faraday Soc.*, **49**, 238 (1970).
(12) W. Ludlow, E. Wyn-Jones, and J. Rassing, *Chem. Phys. Lett.*, **13**, 477 (1972).
(13) R. J. Liu and R. Ullman, *J. Chem. Phys.*, **48**, 1758 (1967).
(14) R. L. Vold, E. S. Daniel, and S. O. Chan, *J. Amer. Chem. Soc.*, **92**, 6771 (1970).
(15) J. A. Pople, W. G. Schneider, and H. J. Bernstein, "High Resolution Nuclear Magnetic Resonance," McGraw-Hill, New York, N. Y., 1959.
(16) P. Rempp, *J. Chim. Phys.*, **54**, 432 (1957).
(17) F. A. Bovey, "High Resolution NMR of Macromolecules," Academic Press, New York, N. Y., 1972.
(18) T. C. Farrar and E. D. Becker, "Pulse and Fourier Transform NMR," Academic Press, New York, N. Y., 1971.
(19) M. Davies, G. Williams, and G. D. Loveluck, *Z. Elektrochem.*, **64**, 575 (1960).
(20) A. Holtzer and M. F. Emerson, *J. Phys. Chem.*, **73**, 26 (1969).

# Structure of Liquid Water. II. Improved Statistical Thermodynamic Treatment and Implications of a Cluster Model[1]

**Barry R. Lentz,[2a] Arnold T. Hagler, and Harold A. Scheraga*[2b]**

*Department of Chemistry, Cornell University, Ithaca, New York 14850 and Weizmann Institute of Science, Rehovoth, Israel*

*(Received December 11, 1973)*

An earlier statistical thermodynamic treatment of a cluster model of liquid water is extended, and many of the approximations of the earlier treatment are improved. The results of recent *ab initio* LCAO–MO calculations are used to include an estimate of the effects of cooperativity on the internal partition function of a cluster, and these effects unexpectedly make large-size clusters unfavorable. Also, on the basis of recent *ab initio* LCAO–MO calculations, hydrogen-bonded ring structures are included in the model. The intermolecular normal mode frequency spectrum of a cluster is calculated explicitly by making use of a recently proposed "effective pair potential" for water molecule interactions. These and other improvements over the earlier treatment are incorporated into a partition function, and the thermodynamic properties of liquid water are calculated over the range of 0 to 100°, using only two adjustable parameters. The distribution of cluster species resulting from these calculations contains only very small clusters (of size $<10$), and the mole fraction of hydrogen bonds decreases from 0.47 at 0° to 0.43 at 100°. The intermolecular vibrational spectrum of liquid water (and its temperature dependence) is calculated from the distribution of cluster species and the normal mode frequencies of these cluster species. The approximations made in the theory are analyzed in terms of their effect on the results and in terms of their implications for the structure of liquid water. As in the earlier treatment, the results of the calculation have much in common with the continuum point of view. At the same time, they provide a tentative explanation for the apparent "two-state" properties of water, and yield new insight into the possible nature of this liquid.

## I. Introduction

In a previous paper, Hagler, Scheraga, and Nemethy[3] (hereafter referred to as HSN) provided a statistical thermodynamic treatment of a "cluster" model of liquid water and evaluated its advantages and shortcomings. In the present paper, we attempt to eliminate some of the approximations and to improve the treatment of HSN. In particular, we use the results of recent *ab initio* LCAO–MO studies of water molecule interactions[4-6] to incorporate the effects of nonadditive (cooperative) hydrogen bonding in the internal partition function of a cluster, and to take account of the relative stabilities of hydrogen-bonded rings and noncyclic structures. An immediate consequence of this revised treatment of the internal potential energy of a cluster is an estimate of part of the internal entropy of a cluster, previously[3] included in a parameter but which is now calculable (thereby allowing us to remove one adjustable parameter from the theory). In addition, account is taken of the dependence of the intermolecular normal mode vibrational frequencies on cluster size and geometry, and an improved treatment is given for the rotational degrees of freedom of a cluster and for the dependence of the hard-sphere diameter on cluster size (in the translational partition function). Reference should be made to the earlier paper of HSN[3] in conjunction with the present paper.

The theory has been developed in two stages. In the preliminary calculations (reported elsewhere[7]), all possible cluster sizes up to 100 water molecules[8] were included in the partition function. Because of the large range of cluster sizes treated, certain approximations were required in order to carry out the computations in a reasonable amount of computer time. In particular, these approximations included (1) the use of a $\gamma$ distribution to represent the distribution of cluster sizes (a procedure also followed by HSN[3]) and (2) a simplified treatment of the effects of cluster size and connectivity (shape or geometry) on the frequencies of the intermolecular normal modes of a cluster. The results of these preliminary calculations indicated that there is a negligible number of clusters containing ten or more water molecules. Using these results,[7] we are able to reformulate the problem here by restricting the partition function to a distribution of *small* clusters. In this reformulation (with which this paper is concerned), the assumed $\gamma$ distribution is abandoned, and the normal mode frequencies of the small clusters are calculated explicitly using the approximate pair potential of Ben-Naim and Stillinger[9] (henceforth, the BNS potential). The results of this theoretical treatment then provide a basis for evaluating a cluster model for liquid water, for reconciling the discrete-species and continuum models, and for suggesting further improvements in the model.

## II. Brief Review of Other Theories

Several models of liquid water are available, all of which are moderately successful in matching one or more of its properties. Unfortunately, many of the earlier theories suffer either from underdefinition of the model or from overparameterization in the treatment of the model.[10] Several of these theories have been considered in two recent review articles,[10,11] as well as in two recently compiled volumes on the nature of water.[12,13] However, several new theoretical treatments[14-21] have appeared which were not discussed in these reviews. One of the most extensive is that of Rahman and Stillinger[14,15] who applied the molecular dynamics technique to water using the BNS[9] "effective pair potential." Two important limitations of this treatment should be kept in mind in interpreting the results of this work. First, as pointed out previously by Weres and Rice,[17] the purely classical molecular dynamics technique cannot properly treat the orientational modes of a water molecule since these modes have energy level spacings which are considerably larger than $kT$ throughout the liquid range of temperatures. Second, the two-body potential function[9] used in the calculations does not include the nonadditive (cooperative) terms shown to be important in recent *ab initio* LCAO–MO calculations[4-6] of water molecule interactions. Also, recent calculations[17,22] have shown that this potential is too stiff, as far as the rotational motion of a tetrahedrally coordinated water molecule is concerned. Despite these limitations, two important qualitative insights are obtained from this work. First of all, Stillinger and Rahman[15] found that there is a bimodal distribution of the pair-interaction energies, and their results suggest the existence of a temperature-invariant point in these distributions reminiscent of the isosbestic point observed[23] in Raman spectroscopy which is interpreted as indicating the existence of two states of hydrogen bonding in water.[23-25] (It is interesting to note that the distributions of cluster species resulting from our calculations are also bimodal (see section VIII).) Secondly, they obtained a very large configurational heat capacity (in fact, about twice[15] the value estimated[26] from experiment) from their "continuum" treatment of water.

Two other recent treatments[16,17] of water consider the structure of the liquid from the point of view of a cell or "lattice-gas" theory in which the body-centered cubic lattice of ice VII (which can be regarded as two interpenetrating ice Ic lattices[27]) is assumed.[28] Bell[16] chose as his basic cell the simplest structure from the body-centered cubic lattice that will allow for both open hydrogen-bonded local order and for dense local structures as exist in ice VII. Introducing a parameter for the interaction energy of each of three possible near-neighbor configurations (hydrogen bonded, favorably oriented but nonhydrogen bonded, dense packed), Bell was able to qualitatively reproduce the maximum in the density and the minimum in the isothermal compressibility of liquid water in terms of a breakdown of open hydrogen-bonded local structure into dense local structure as the temperature increases; the thermal properties of liquid water were not specifically calculated. In their theory, Weres and Rice[17] avoided the introduction of energy parameters by using the BNS[9] potential to evaluate roughly the statistical weights for each basic cell configuration. Weres and Rice also used a much larger and more complicated basic cell than that assumed by Bell. Unfortunately, this not only makes their treatment more involved, but also prevents a rigorous treatment of the configurational entropy of their lattice-gas model (*e.g.*, they obtained −1.4 eu instead of zero for the configurational entropy of ice). However, one of the most serious defects of their theory is its treatment of non-hydrogen-bonded first neighbors. For example, the possibility of two types of non-hydrogen-bonded first neighbors (*i.e.*, favorably oriented but nonhydrogen bonded, and densely packed, as considered by Bell[16]) was not taken into account in developing the configurational partition function. Also, in obtaining the statistical weights to be applied to different basic cell configurations, these authors employed an approximate perturbation treatment for non-hydrogen-bonded first neighbors that cannot properly account for the different effects to be expected of densely packed (repulsive) and favorably interacting non-hydrogen-bonded first neighbors. The inadequate treatment of non-hydrogen-bonded first neighbors is especially serious because of the large number of such non-hydrogen-bonded first neighbors predicted by their results (2, as compared to 2.7 hydrogen-bonded first neighbors). The importance of such non-hydrogen-bonded first neighbors is further revealed by consideration of the most likely basic cell configurations predicted by this theory (see Figure 7 of ref 17). Some of these basic cell configurations appear to be very unlikely (specifically the configuration of their[17] Figure 7 that occurs with a frequency of 24.3% and has no first or second neighbors in one hemisphere about the central water molecule). Finally, it is surprising that Weres and Rice find essentially no structural change in water over the temperature range from 0 to 100°, despite the fact that Bell[16] does. We suspect that this might be related to anomalies in the approximate treatment of the configurational entropy by Weres and Rice. Without introducing any adjustable parameters, Weres and Rice were able to fit the enthalpy and entropy of water between 0 and 100° only to within 1130 to 720 cal/mol (42 to 16%) and 0.8 to 2.6 eu (5.3 to 12.5%), respectively, where the deviations are based on the experimental values and references reported in our present paper (rather than in that of Weres and Rice) so as to be directly comparable to the deviations obtained in our paper (see Table IV).

The recent treatment of Angell[21] is basically a simple two-state theory.[30] The unique feature of this treatment is the assumption of a glass-like "totally connected random tetrahedral network structure" as the basic structure in water. The two "states" are envisioned as "broken" or "made" hydrogen bonds in this network. With two adjustable parameters, Angell fits Eisenberg and Kauzmann's[26] estimate of the configurational part of $C_v$ of liquid water from 0 to 100°, and empirically rationalizes the temperature dependence of the viscosity. Aside from the possibility of overparameterization (only one experimental property, relaxational $C_v$, is fit with the use of two parameters), this theory suffers most from the ambiguous definition of the glass-like structure. Estimation from the parameters used by the author of the enthalpy and entropy for the conversion of ice to this substance at 0° yields values that are ~70 to 80% of the experimental enthalpy and entropy of fusion. Thus, from its thermodynamic properties, this glass-like structure should be essentially liquid water, and the remaining 20–30% comes from the breakdown of the glass-like structure. Before this model can be useful in providing insight into the structure of liquid water, the assumed glass-like structure must be defined better and shown to be able to account for the thermodynamic properties of liquid water.

Of the various models that have been proposed for liquid water,[10-13] the cluster model treated in this paper allows a degree of structural definition that makes possible a fairly detailed statistical thermodynamic treatment. It also has the advantage of being at least qualitatively consistent with most of the properties of liquid water[10-13] (including the results from small angle X-ray scattering,[32] since the earlier treatment[3] indicated that most clusters are small, containing less than 11 water molecules, and that very few clusters contained as many as 60 or 70 water molecules; and the present theory predicts even smaller cluster sizes, most clusters containing less than five water molecules). The degree of success or failure of this fairly well-defined version of the cluster model for water should provide some insight into the nature of this complex liquid.

## III. Model and Form of the Partition Function

The model used here has been described in detail by HSN.[3] We reiterate the principal features here for the sake of clarity. We assume that liquid water consists of a distribution of clusters of sizes from 1 to 9,[33] and that these clusters are as compact as possible, consistent with a maximum degree of hydrogen bonding. Specific interactions between clusters are not considered and, for the purpose of treating their translational degrees of freedom, they are treated as hard spheres in a constant background potential (this assumption is discussed further in ref 3). Because the clusters are assumed to be independent (except for the existence of the uniform background potential), the canonical partition function for this model, $Z(N, V, T)$, may be separated into partition functions for the external and internal degrees of freedom of clusters, $Q_{\text{ext}}$ and $Q_{\text{int}}$, respectively (see eq 1 of ref 3). Then, by the standard maximum term arguments of statistical mechanics,[34] we may obtain the thermodynamic functions of the model in terms of the equilibrium distribution of clusters (see eq 2 of ref 3). The specific translation of the cluster model into an internal and an external partition function[33] is considered in sections IV and V.

## IV. Internal Partition Function

In formulating the contribution to the total partition function from the internal degrees of freedom of clusters, we write the total internal partition function at given $V$ and $T$ as a product over the individual internal partition functions of clusters of different sizes

$$Q_{\text{int}}(N_0, V, T; \{N_j\}) = \prod_{j=1}^{9}\left[\sum_n (e^{-\beta E_{nj}} Q_{\text{vib},nj})\right]^{N_j} \qquad (1)$$

where $N_0$ is Avogadro's number, $N_j$ is the number of clusters containing $j$ water molecules, $\{N_j\}$ is a vector (representing a distribution function of cluster sizes) whose $j$th component is $N_j$, with the constraint that $\Sigma_j jN_j = N_0$, $\beta = 1/kT$, and $E_{nj}$ is the energy and $Q_{\text{vib},nj}$ the vibrational partition function of the $n$th configuration of a $j$-sized cluster. In order to make the evaluation of this partition function tractable, we further assume that only clusters with the maximum degree of hydrogen bondedness and compactness consistent with their size will make significant contributions to this partition function.[35] With this in mind, we assume that the vibrational partition functions of the most important configurations of a $j$-sized cluster will be roughly equivalent and thus $Q_{\text{vib},nj}$ may be removed from the sum over "$n$" in eq 1. The evaluation of this vibrational partition function for different cluster species will be considered in section IVB. First, however, we will treat the remainder of the sum over cluster configurations, which we shall call the "internal configurational" partition function ($Q_{\text{IC},j}$; this corresponds to $Q_{\text{HB},j}Q_{\text{entropy},j}$ of ref 3).

*A. "Internal Configurational" Partition Function.* As pointed out by HSN,[3] there are basically two ways of obtaining different configurations of a $j$-size cluster. First, one may change the positions of the oxygen atoms of the water molecules while still managing to form hydrogen bonds between molecules. Thus, a hexamer might be pictured as a "boat" ring, a "chair" ring, a planar ring, a five-membered ring with one molecule hydrogen bonded to it, a four-membered ring with two attached water molecules (each of these structures having six hydrogen bonds), etc. Since the first four of these structures have energies within about 2 kcal/mol of the minimum-energy planar ring (according to our hydrogen-bonding energy formalism developed in this section and in the Appendix), we should expect at least these four (including the planar ring) to contribute to some extent to $Q_{\text{IC},6}$. Since the preliminary calculations,[7] in which the degeneracy arising from many possible arrangements of oxygen atoms in a $j$-sized cluster was treated in terms of a parameter, indicated that the partition function was insensitive to this degeneracy parameter, we have chosen to consider only one oxygen arrangement for each cluster size.

The second way of obtaining different configurations of a $j$-size cluster is to change the relative orientations of the molecules within the clusters (keeping the positions of their oxygens fixed). This amounts to changing the positions of the hydrogen atoms within the cluster and will thus be called hydrogen randomness (this is the same phenomenon that gives rise to the residual entropy of ice I, as discussed by Pauling[36]). The form of the IC partition function now becomes

$$Q_{\text{IC},j} = \sum_n e^{-\beta E_{nj}} \qquad (2)$$

where the sum is now taken only over all possible hydrogen arrangements ($n$) of a $j$-sized cluster ($E_{nj}$ being the energy of the $n$th arrangement).

*Hydrogen Entropy and Bond Energy.* In order to evaluate $\Sigma_n e^{-\beta E_{nj}}$ of eq 2, it must be recognized that many physically distinct arrangements of hydrogen atoms in a $j$-sized cluster will have the same energy. Thus, we designate the $k$th energy state of $j$-sized cluster by the symbol $\epsilon_{kj}$, and the number of hydrogen arrangements having energy $\epsilon_{kj}$ is then given by $\eta(\epsilon_{kj})$. Then, the IC partition function of a $j$-sized cluster becomes

$$Q_{\text{IC},j} = \sum_k \eta(\epsilon_{kj})e^{-\beta\epsilon_{kj}} \qquad (3)$$

The dependence of $\eta(\epsilon_{kj})$ on cluster size should incorporate two features. First, if $\epsilon'_{kj}$ is defined as the average energy per hydrogen bond in a $j$mer in the $k$th energy state (*i.e.*, if $\epsilon'_{kj}$ is $\epsilon_{kj}$ divided by the number of hydrogen bonds in a $j$mer), then the spread in $\epsilon'_{kj}$ for different clusters of size $j$ must narrow as we go from small to large clusters [*i.e.*, the distribution functions, $\eta(\epsilon'_{kj})$, must narrow]. For example, in a dimer the spread in potential energy between the trans and cis arrangements is 1.43 kcal/mol of bond;[6] on the other hand, in ice (where all hydrogen configurations have the same energy[36]) $\eta(\epsilon'_{kj})$ becomes a $\delta$ function. The energy $\epsilon'_{kj}$ may be separated into two contributions, that from hydrogen-bonded neighbors (the near-neighbor contributions, $\epsilon_{kj}^{(2)}$) and that from all other interactions in the cluster. The dependence of the extremes of the near-neighbor contribution to $\epsilon'_{kj}$ on $j$ (the evaluation of which is discussed in the Appendix) is shown in Figure 1, which illustrates how the spread in the energies of different hydrogen configurations of a cluster decreases with increasing $j$. Second, the total number of possible hydrogen arrangements per water molecule [*i.e.*, $(\eta_{\text{T},j})^{1/j}$, where $\eta_{\text{T},j} = \Sigma_k\eta(\epsilon_{kj})$] should decrease with in-

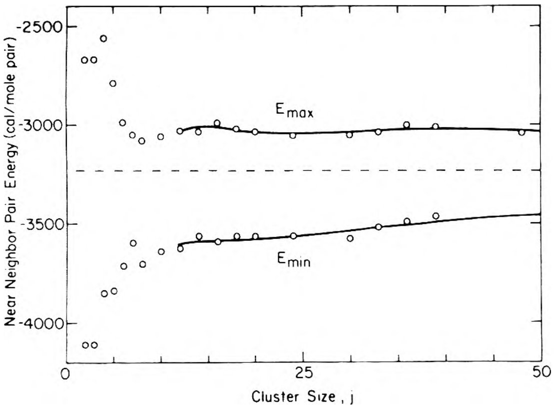

**Figure 1.** Maximum ($E_{\max}$) and minimum ($E_{\min}$) values of the nearest-neighbor interaction energy in a $j$-size cluster. The circles represent energies computed for the hydrogen bonding arrangements in molecular models of clusters built so as to maximize or minimize the number of most favorable near-neighbor interactions. The solid curves for $j > 12$ were obtained by fitting the data to polynomials in $1/j$. Both curves asymptotically approach the dashed curve (the limit for ice I).

creasing cluster size (and hence with increasing degree of hydrogen bonding). For example, there are approximately 2.04 possible hydrogen configurations per molecule in a "boat" hexamer [where $2.04 = 72^{1/6}$, with $\eta_{T,6} = 72$ being obtained by model building (see the Appendix)], but only approximately 3/2 per molecule in ice I.[36] These two aspects of the dependence of $\eta(\epsilon_{kj})$ on cluster size are utilized in the Appendix (see Evaluation of $Q_j^{(2)}$) to develop approximate distribution functions for different sized clusters.

In the evaluation of the internal configurational partition function of a $j$mer, $Q_{\mathrm{IC},j}$, it is desirable to include the contribution from nonadditivity (*i.e.*, cooperativity), obtained from recent molecular orbital calculations,[4-6] in the estimation of $\epsilon_{kj}$. For a quantitative treatment of the effect of cooperativity as well as that of hydrogen randomness [expressed in terms of $\eta(\epsilon_{kj})$] on the relative stability of different size clusters, we make the assumption that $\epsilon_{kj}$ is separable into two additive terms: one [$\epsilon_{kj}^{(2)}$] which, as mentioned above, depends on the relative configuration of nearest neighbors and another ($\epsilon_j$) which is independent of hydrogen configuration but includes second-neighbor interactions, three-body non-additive potentials, and dispersion interactions. Thus

$$\epsilon_{kj} = \epsilon_{kj}^{(2)} + \epsilon_j \tag{4}$$

The same assumption was used[6] to compute the lattice energy of ice. In fact, we employ arguments similar to those used earlier[6] (and the same potentials[6]) to evaluate $\epsilon_{kj}^{(2)}$ and $\epsilon_j$, as discussed in the Appendix.

The details of the evaluation of $\sum_k \eta(\epsilon_{kj}) e^{-\beta\epsilon_{kj}}$ are presented in the Appendix for clusters of size 1 to 100,[37] but we comment here on some of the assumptions made in this calculation. First, it is necessary to assume a given geometry (*i.e.*, a given oxygen arrangement) for each size cluster. This was done in a manner that is consistent with the previously mentioned requirement (see discussion following eq 1 above) that the number of hydrogen bonds in a cluster of given size be maximized. This approximation amounts to the consideration of only a few of the many possible oxygen arrangements of the small clusters found[7] to dominate in our theory,[35] and is one of the limitations of our treatment (see section X below). For $j$ = 8 and 9, we use the same cluster geometries assumed by HSN[3] in order to obtain the number of $i$-bonded molecules in a cluster of size $j$. Following HSN,[3] we ignore one-bonded molecules for clusters larger than $j$ = 7. For $j \leq 7$, we select different geometries than those used by HSN,[3] on the basis of recent conclusions of Lentz and Scheraga.[6] Specifically, we select ring structures for $j$ = 4, 5, and 7 (keeping the cyclic 6-mer of HSN), since rings contain one more hydrogen bond than the corresponding noncyclic structure, and involve very little ring strain, even in the case of a tetramer. The selected values of the fraction of $i$-bonded molecules in a cluster of size $j$, $y_{ij}$, are given in Table I together with $y_{Bj}$, the fraction of broken hydrogen bonds,[38] where

**TABLE I: Cluster Connectivity and Size**

| Cluster size $j$ | Mole fraction, $y_{ij}$<br>One-bonded | Two-bonded | Three-bonded | Four-bonded | $y_{Bj}$[a] |
|---|---|---|---|---|---|
| 2 | 1.00 | 0 | 0 | 0 | 0.75 |
| 3 | 0.67 | 0.33 | 0 | 0 | 0.67 |
| 4[b] | 0 | 1.00 | 0 | 0 | 0.50 |
| 5[b] | 0 | 1.00 | 0 | 0 | 0.50 |
| 6 | 0 | 1.00 | 0 | 0 | 0.50 |
| 7[b] | 0 | 1.00 | 0 | 0 | 0.50 |
| 8 | 0 | 0.75 | 0.25 | 0 | 0.44 |
| 9 | 0 | 0.77 | 0.23 | 0 | 0.44 |

[a] $y_{Bj}$ is the fraction of bonds broken in a $j$-size cluster relative to the total possible number of bonds that the cluster could have if all molecules were tetracoordinated as in ice, *i.e.*, $y_{Bj} = N_{Bj}/2j$, where $N_{Bj}$ [$= (j/2)(4 - \sum_i i y_{ij})$] is the number of broken bonds in a $j$-size cluster (as in ref 3). [b] These values differ from those in ref 3.

$$y_{B_j} = 1 - (1/4)\sum_{i=1}^{4} i y_{ij} \tag{5}$$

The values of $y_{ij}$ are used in the evaluation of $\sum_k \eta(\epsilon_{kj}) e^{-\beta\epsilon_{kj}}$ in the Appendix.

Second, we consider the assumption in which $\epsilon_j$ is considered to be independent of hydrogen configuration in a $j$-sized cluster. The contribution to $\epsilon_j$ that is most likely to depend on the hydrogen configuration of a cluster is the second-neighbor two-body interaction.[6] In the calculation of the lattice energy of ice,[6] the use of an *average* second-neighbor energy for "sequential" and "nonsequential" trimer arrangements (see Appendix; Evaluation of $\epsilon_j$) is not unreasonable because the geometrical constraints of the lattice make all hydrogen configurations equally probable;[6,36] however, in treating *small* clusters, where additional freedom exists for more energetically favored hydrogen configurations to be adopted, the magnitude of the error in such a treatment is greater. Nevertheless, this assumption should not introduce much error (even for small clusters) because the major contribution from hydrogen randomness should arise from the near-neighbor interactions; *i.e.*, the maximum spread in the energies for different first-neighbor configurations [1.43 kcal/mol of bond,[6] which appears in $\epsilon_{kj}^{(2)}$] is much larger than the maximum spread in the energies for different second-neighbor configurations [0.25 kcal/mol, estimated from MO calculations,[5,6] or about 0.5 kcal/mol computed here with the empirical BNS[9] potential; this would appear in $\epsilon_j$]. Thus, by taking $\epsilon_j$ independent of hydrogen configuration in a $j$-size cluster, we are neglecting at most 0.25–0.5 kcal/mol spread in the second-neighbor interaction energies, which is smaller than the 1.43 kcal/mol spread in the near-neighbor interaction energy which we have taken into ac-

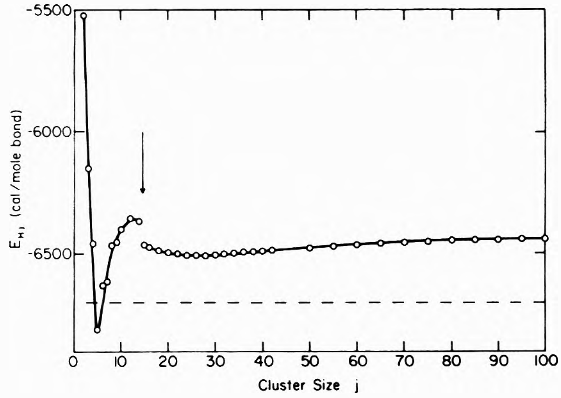

**Figure 2.** Dependence of average hydrogen bond energy on cluster size at 0°. The curve at large $j$ (*i.e.*, $\gg$ 100) approaches the dashed curve (the limit for ice I) asymptotically. The dashed curve was assumed by HSN[3] to hold for all values of $j$.

count. At any rate, if we were to take this spread into account, we would expect the distribution functions, $\eta(\epsilon_{kj})$, to be altered somewhat, but without any significant qualitative change in their variation with cluster size.

The error that may be introduced by considering only a few of the many possible oxygen arrangements of a cluster is considered in section X. The absolute error introduced by failure to account properly for the spread in the terms included in $\epsilon_j$ (three-body, second-neighbor, and dispersion energies) has been estimated[6] to be less than 20%. Aside from this error, it must be remembered that there are also uncertainties[6] in the interaction potentials, even though they were obtained[6] from extensive-basis *ab initio* LCAO–MO calculations. If we assign an error limit of 10% to these potentials, then we might expect our treatment of the internal partition function of a cluster to be in error by no more than about 30%. Since the errors involved in the treatment of different clusters should be similar, the error in the *relative* stabilities of different size clusters should be less than the absolute error. In summary, then, we have a reasonable quantitative treatment of the effects of hydrogen randomness and hydrogen-bond cooperativity on the *relative* stabilities of different size clusters.

After $\Sigma_k \eta(\epsilon_{kj}) e^{-\beta\epsilon_{kj}}$ is evaluated (see Appendix), and $Q_{\mathrm{IC},j}$ thus computed, we may obtain the average energy per bond in a $j$-size cluster, $E_{\mathrm{H}j}$, as

$$E_{\mathrm{H}_j} = -[1/(2j - N_{Bj})]\partial \ln Q_{\mathrm{IC},j}/\partial\beta \qquad (6)$$

where $(2j - N_{BJ})$ is the number of unbroken hydrogen bonds in a $j$-size cluster. This quantity is referred to zero for separated water molecules *at rest* in the gas phase (since this is the zero for the potentials obtained from MO calculations[5,6] which form the basis for the calculation of $\epsilon_{kj}^{(2)}$ and $\epsilon_j$), and is comparable to $-E_H'$ of HSN.[3] $E_{\mathrm{H}j}$ is plotted[37] against $j$, at 0°, in Figure 2. The shape of this curve results from both the effects of hydrogen randomness (contained in the first neighbor term, $\epsilon_{kj}^{(2)}$) and the effect of second neighbor and cooperative interactions (contained in $\epsilon_j$). This contrasts with the curves of Figure 1 which reflect only the possible spread in near-neighbor interaction energies due to our approximate treatment of hydrogen randomness (*i.e.*, possible spread in $\epsilon_{kj}^{(2)}$). Since at 0°, the *average* near-neighbor energy of a cluster is close to the near-neighbor energy of the most stable hydrogen arrangement (*i.e.*, $E_{\min}$ of Figure 1), we can see the effects of the second neighbor and cooperative interaction energies by contrasting $E_{\mathrm{H}j}$ of Figure 2 with $E_{\min}$ of Figure 1. This comparison reveals that the relative unfavorability of very small clusters ($j$ = 2 and 3), compared to a hexamer for example, arises from the $\epsilon_j$ term (containing the cooperative, second neighbor and dispersion effects); the same is partly true in the region between $j$ = 7 and 12. Thus, a 12-mer (consisting of two six-membered rings) has less energy per bond than a hexamer because of the less favorable contributions of the cooperative and second-neighbor terms to the energy to be associated with three-bonded water molecules (these first appear in clusters of size $j$ = 8). Similarly, the less favorable contributions of these terms to the energy to be associated with one-bonded water molecules destabilizes clusters of size 2 and 3. These effects are illustrated in Table II, where the contributions of cooperative, second-neighbor, and dispersion effects to $E_{\mathrm{H}j}$ are listed for $j$ = 2 to 12. The destabilization of one-bonded and three-bonded water molecules in our treatment relative to the noncooperative treatment of HSN[3] is further illustrated in Figure 3, where we diagram the energy levels associated with $i$-bonded water molecules in both our treatment and that of HSN[3] (the derivation of Figure 3 is explained in the Appendix). A further comment on the behavior of $E_{\mathrm{H}j}$ (in Figure 2) should be made about the slight jump of less than 2% between $j$ = 14 and 15, which arises from the slight discontinuity in the connectivity relations (direct counting for $j$ < 14 and the empirical Némethy–Scheraga equations[38] for $j$ > 14). Since the results of our preliminary calculations[7] indicated essentially no clusters of size larger than ~10 [a result corroborated by the very small number of clusters of size 7, 8, or 9 found in this study (see section VIII)], the behavior of this part of the curve is immaterial. Finally, at infinite $j$, $E_{\mathrm{H}j}$ approaches the dashed line in Figure 2, which represents the energy per bond in ice[39] ($-E_{\mathrm{H}}'$ = −6700 = −13,400/2, which was used for all values of $j$ by HSN[3]).

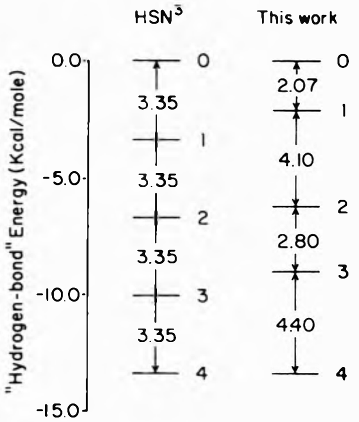

**Figure 3.** Cooperative and second-neighbor effects in hydrogen-bonded water molecules, expressed in terms of energy levels to be associated with $i$-bonded water molecules. First column illustrates assumption of HSN[3] who ignored cooperativity. Second column illustrates effects of treatment of cooperative and second-neighbor interactions given here. The numbers 4, 3, 2, 1, 0 refer to the number of bonds of a bonded species.

We may also obtain the hydrogen entropy per mole of water in a $j$-sized cluster, $S_{\mathrm{H}j}$, from $Q_{\mathrm{IC},j}$ as

$$S_{\mathrm{H}_j} = (1/j)[k \ln Q_{\mathrm{IC},j} - (1/T)\partial \ln Q_{\mathrm{IC},j}/\partial\beta] \qquad (7)$$

This is related to the residual entropy of ice,[36] and is plotted[37] in Figure 4 for $T$ = 0°. As $j$ approaches infinity, $S_{\mathrm{H}j}$ approaches the value for ice (dashed line in Figure 4).

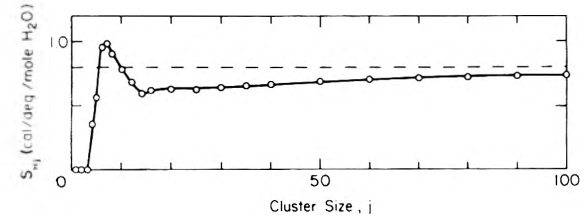

**Figure 4.** Internal entropy per mole of water in a $j$-size cluster at 0°, due to hydrogen randomness. The dashed line represents the asymptotic limit (the residual entropy of ice).

*Effect of Surrounding Liquid and Shift in Intramolecular Zero-Point Energies.* At this point we have a treatment of the internal potential energy (exclusive of vibrational contributions) of a gas-phase cluster relative to separated molecules at rest (if expressed in units of calories/mole of bond, this is $E_{Hj}$ of Figure 2). We now change the zero of energy to that of ice at 0°K in its ground intermolecular and intramolecular vibrational levels, so that the final free energy and energy to be calculated will be expressed with respect to the same standard state used in ref 3. To accomplish this, we simply add to $\epsilon_{kj}$ in eq 3, the energy of transferring $j$ moles of water from ice in its intermolecular ground state at 0°K to separated molecules at rest ($9900j = 13{,}400j - 3500j$, where 13,400 cal/mol is the lattice energy of ice,[39] and 3500 cal/mol is Whalley's estimate of the intermolecular ground state energy of ice[39,40]). It should be noted that we have so far taken no account of any shifts in intramolecular zero-point energy. We must now include the shift in intramolecular zero-point energy on breaking $N_{Bj}$ ($= 2jy_{Bj}$) moles of bonds in ice to form 1 mol of $j$mers in the gas phase. As discussed by HSN,[3] this is $[2jy_{Bj}(1400/2)]$, where 1400 cal/mol is the shift in intramolecular zero-point energy given by Whalley[39,40] for transfer of 1 mol of water from ice to the gas phase. Thus, $Q_{IC,j}$ becomes, relative to ice at 0°K in its intra- and intermolecular ground states

$$Q_{IC,j} = \sum_k \eta(\epsilon_{k_j}) \exp\{-\beta[\epsilon_{k_j}^{(2)} + \epsilon_j + jy_{Bj}(1400) + 9900j]\} \quad (8)$$

We must now transfer these clusters from the gas phase into the liquid. As discussed in ref 3, this adds the energy of interaction arising from the constant liquid background potential (see section III), which is expressed as $-N_{Bj}(c/V)$ per mole of $j$-size cluster (section IVB of ref 3). Finally we include the shift in intramolecular zero-point energy on transfer to the liquid [$-N_{Bj}(b'/V)$; section IVC of ref 3]. Combining these two terms [$(c/V) + (b'/V) = (a/V)$], we write $Q_{IC,j}$ for a cluster in the liquid with its energy relative to ice at 0°, in its inter- and intramolecular ground states. The constant $a$ is unknown, and will be treated as an adjustable parameter.

$$Q_{IC,j} = Q_j^{(2)} \exp\{-\beta[\epsilon_j - jy_{Bj}(2a/V - 1400) + 9900j]\} \quad (9)$$

where we have used $Q_j^{(2)}$ as defined in the Appendix.

*B. Vibrational Partition Function.* In the first paper of this series HSN[3] concluded that a major shortcoming of their treatment was the assumption that the intermolecular vibrational frequencies of a cluster were taken to be independent of cluster size and connectivity (or shape). They concluded from their results that small clusters had been overly unfavored because of the assignment of unreasonably large frequencies to the intermolecular normal modes of small clusters. Ideally, the treatment of the normal modes of a cluster would start with a knowledge of the interaction potential experienced by each molecule in the cluster. This interaction potential would be expected to vary considerably with the number of hydrogen-bonded neighbors of a given water molecule. Given such an interaction potential, the solution of the equations of motion for each cluster will yield a frequency spectrum for that cluster. Such a treatment involves prohibitively expensive calculations for the case of large clusters. Taking advantage of the results of our preliminary calculations,[7] however, we have limited our attention to a small number of small clusters and have calculated the normal modes of each cluster starting with an approximate description of the interaction potential of water molecules within the cluster.

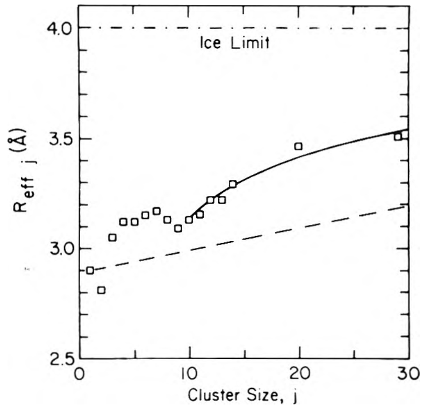

**Figure 5.** Effective diameter of a water molecule in a $j$-size cluster. The results of model building (□) are compared to the linear interpolation of HSN[3] (dashed line). The solid line arises from a fit of the results of model building (and the ice limit) to the empirical equation $R_{eff,j} = 4.0 - 3.36/j^{0.586}$.

The potential chosen here for these calculations is the BNS[9] "effective pair potential." The details of these normal mode calculations (using the BNS potential) are described elsewhere.[22] Unfortunately, although this potential is based on a qualitatively reasonable picture of the charge distribution in a water molecule it has been shown to predict somewhat large frequencies for the librational modes of tetracoordinated water molecules.[17,22] In order to correct for this limitation of the BNS potential, we have rescaled the librational frequencies resulting from these calculations by multiplying them by a factor (*viz.*, 0.67) which makes the average librational frequency of a tetrahedrally coordinated molecule[22] fall within the range of values obtained in various neutron scattering experiments for the librational maximum in ice[43] (*i.e.*, 600–700 cm$^{-1}$; see Table IX, Appendix B of ref 7 or Table II of ref 22 for a summary of the experimental data). A similar procedure (with essentially the same scaling factor) was followed by Weres and Rice[17] in their correction of this potential. The frequencies of translational normal modes were taken as computed, with no rescaling. A summary of the rescaled normal-mode frequencies of the cluster species is given in Table III.[44] The Cartesian coordinates of the water molecules in each of these clusters are given in ref 22.

Using the rescaled frequencies of Table III for a $j$-size cluster (for $j$ = 2 to 8, with a 9-mer treated as described in footnote *e* of Table III), the intermolecular vibrational partition function becomes

**TABLE II: Cooperative, Second-Neighbor, and Dispersion Contributions to $E_{H_j}$**

| Cluster size $j$ | Cooperative energy[a] | Second-neighbor energy[a] | First and second neighbor dispersion energy[a] |
|---|---|---|---|
| 2 | 0 | 0 | −900 |
| 3 | −490 | −520 | −920 |
| 4 | −990 | −520 | −920 |
| 5 | −990 | −1040 | −940 |
| 5*[b] | −560 | −520 | −970 |
| 6 | −990 | −1040 | −940 |
| 7 | −990 | −1040 | −940 |
| 8 | −910 | −930 | −960 |
| 9 | −920 | −940 | −960 |
| 10 | −870 | −870 | −970 |
| 11 | −860 | −850 | −970 |
| 12 | −850 | −840 | −970 |

[a] Units: calories per mole of bond. [b] This is a star pentamer.[35]

**TABLE III: Cluster Normal Mode Frequency Distributions**

| Cluster size $j$ | Frequencies of librational modes,[a] cm$^{-1}$ | | | Frequencies of low-frequency lattice modes,[b] cm$^{-1}$ | | |
|---|---|---|---|---|---|---|
| 2 | | 571 | 220 | 180 | 113 | |
| | | 506 | 207 | | | |
| 3 | 680 | 460 | 220 | 193 | 77 | |
| | 582 | 402 | 198 | 174 | 36 | |
| | | 293 | | 111 | | |
| 4 | 734 | 430 | 231 | 181 | 121 | |
| | 645 | 430 | 206 | 179 | 50 | |
| | 616 | 419 | 206 | 176 | | |
| | 616 | 293 | 192 | 176 | | |
| 5 | 810 | 518 | 259 | 219 | 108 | |
| | 744 | 459 | 245 | 216 | 102 | |
| | 696 | 447 | 218 | 182 | 36 | |
| | 685 | 388 | 207 | 180 | 21 | |
| | 629 | 361 | 196 | 156 | | |
| 5*[c] | 943 | 541 | 288 | 214 | 125 | 47 |
| | 700 | 474 | 272 | 207 | 96 | 39 |
| | 649 | 434 | 261 | 205 | 79 | 29 |
| | | 409 | | 157 | 51 | |
| | | 342 | | 132 | 50 | |
| 6 | 767 | 463 | 255 | 230 | 129 | |
| | 695 | 463 | 228 | 222 | 73 | |
| | 695 | 436 | 228 | 222 | 73 | |
| | 693 | 411 | 188 | 165 | 50[d] | |
| | 693 | 411 | 187 | 165 | 30 | |
| | 661 | 319 | 173 | 159 | 21[d] | |
| 7 | 888 | 532 | 325 | 224 | 148 | 21 |
| | 815 | 506 | 278 | 220 | 129 | |
| | 777 | 475 | 268 | 201 | 101 | |
| | 734 | 466 | 254 | 194 | 99 | |
| | 669 | 442 | 230 | 183 | 54 | |
| | 620 | 399 | 210 | 181 | 45 | |
| | 585 | 387 | 204 | 167 | 31 | |
| 8[e] | 933 | 570 | 344 | 233 | 156 | 34 |
| | 855 | 535 | 304 | 222 | 136 | 29 |
| | 749 | 474 | 289 | 217 | 94 | |
| | 747 | 454 | 278 | 211 | 88 | |
| | 731 | 447 | 255 | 206 | 84 | |
| | 700 | 432 | 210 | 182 | 49 | |
| | 667 | 408 | 206 | 173 | 46 | |
| | 638 | 367 | 202 | 166 | 40 | |

[a] These have been rescaled as described in the text. [b] Detailed analysis of the nature of the normal mode motions has been made only for $j$ = 5*.[22] On the basis of this analysis the low-frequency modes might be described *roughly* as hindered translational modes ($\nu_T$); torsional motions about the O–H···O hydrogen bond ($\nu_{torsion}$), and highly coupled O···O···O deformation modes ($\nu_b$). [c] Normal mode frequencies of the tetracoordinated star pentamer.[35] [d] Because of computational difficulties, these two frequencies had to be estimated by interpolating between the results for the cyclic pentamer and the cyclic heptamer. [e] It should be noted that limitation of available computer time made it difficult to obtain a set of normal mode frequencies for a cluster of size 9 (thus no entry for this size cluster is given in this table). We have obtained approximate vibrational thermodynamic functions (*i.e.*, *F*, *U*, *S*) for a nonamer by extrapolating the vibrational thermodynamic properties of a heptamer and octamer.

$$Q_{\text{vib},j} = \prod_{l=1}^{6j-6} [\exp(-h\nu_{jl}/2kT)][1 - \exp(-h\nu_{jl}/kT)]^{-1} \quad (10)$$

where $\nu_{jl}$ is the frequency of the $l$th normal mode of a $j$-size cluster.

## V. External Partition Function

As in ref 3, the external partition function is expressed as the product of partition functions over the translational and rotational degrees of freedom of clusters (eq 13 of ref 3).

*A. Translational Partition Function.* We have adopted completely the treatment of the configurational (translational) partition function given by HSN.[3] As mentioned in section III, this treatment requires the assumption that the clusters may be considered to behave (at least as far as their translational degrees of freedom are concerned) as a system of hard spheres whose attractive interactions may be treated by a uniform background potential (see section IVA of this paper, and section VA of ref 3). The thermodynamic properties of such a system have been derived by Lebowitz and Rowlinson[45] from Lebowitz's solution[46] of the generalized Percus-Yevick equation (eq 17–20 of ref 3 summarize these results).

In order to use these results, we need specify only the hard-sphere diameter of each cluster, $R_j$. If we accept HSN's estimate of the effective hard-sphere diameter[47] for a monomer (2.9 Å), then this quantity must increase in larger clusters until it reaches 4.0 Å for ice I.[3] Because the dependence of $R_{\text{eff},j}$[47] on $j$ between these limits is unknown, we have resorted to model building in order to estimate the dependence of the effective diameter per water molecule on cluster size. By measuring the displaced volume of foil-wrapped space-filling models (*i.e.*, by immersion of the models in water), the data in Figure 5 were obtained.[48] In Figure 5, our estimate of $R_{\text{eff},j}$ is compared to the linear interpolation of HSN. It is worth noting that our model building results predict that clusters in the range of $j$ = 15 to 30 should be considerably bulkier than the simple linear interpolation of HSN indicates. This added bulkiness will mediate against the existence of clusters in this size range even more than did the diameters used by HSN, since the configurational entropy of a system of hard spheres must decrease as the spheres become larger.

*B. Rotational Partition Function.* In the first paper of this series, HSN used the rotational partition function of a freely rotating rigid body to treat the rotational degrees of freedom of a cluster. They found it necessary, however, to include an adjustable parameter that effectively reduced the amount of orientational configuration space available to a cluster. In analogy to the linear motion of a particle in a one-dimensional potential, we might think of this as having the effect of treating the rotational degrees of freedom of a cluster by the partition function of a rigid body rotating in a "square" potential well. Although the exact nature of the orientational potential between clusters is uncertain, it does seem likely that such an orientational "square well" must overestimate the steepness of this potential to some extent, and therefore underestimate the contribution of the rotational degrees of freedom of a cluster to the internal energy and heat capacity.

Instead, we have approximated the orientational potential experienced by a cluster in the field of its neighbors with a harmonic potential function. Thus, the three normal rotational motions of a cluster are thought of as taking place under the influence of a harmonic potential (the same harmonic potential will be used for each of the three rotational degrees of freedom of a given cluster) and are therefore hindered rotations. This procedure not only approximates the orientational potential experienced by a cluster with a "softer" potential than that used by HSN, but also allows us to interpret the necessary rotational parameter as a measure of the frequencies of the librational modes of clusters of water molecules. The rotational partition function is thus taken as

$$Q_{\mathrm{rot}} = \prod_{j=1}^{9}([\exp(-hf_j/2kT)][1 - \exp(-hf_j/kT)]^{-1})^3 \qquad (11)$$

where $f_j$ is a mean librational frequency of a $j$-sized cluster

$$f_j = (1/2\pi)(K_j/I_j)^{1/2} \qquad (12)$$

$$I_j = [(I_A I_B I_C)_j]^{1/3} \qquad (13)$$

where $(I_A I_B I_C)_j$ and $K_j$ are the product of the moments of inertia and the rotational force constant, respectively, of a $j$-sized cluster. The moments of inertia are those used by HSN,[3] except for $j$ = 4, 5, and 7, for which our assumed cluster geometries differ from those of HSN (see section IVA).

Since we have no way of estimating *a priori* the values of the rotational force constants, $K_j$, these must be adjusted. In order not to introduce an unreasonable number of parameters, we shall adjust only the force constant of the monomer and obtain the other $K_j$'s from $K_1$ and a suitable model for the variation of $K_j$ with $j$; $K_j$ is chosen such that a point on the surface of a cluster moves through a characteristic distance (during a hindered rotation) independent of the size of the cluster. Thus we take

$$K_j = K_1(R_j/R_1)^2 \qquad (14)$$

where the rotational force constant for a monomer is given by

$$K_1 = d/V \qquad (15)$$

and $d$ is an adjustable parameter as in ref 3. The volume dependence is such that $K_1$ approaches zero (free rotation) in the limit of infinite volume. The assumption that a characteristic distance is independent of cluster size may be compared with the assumption of HSN that their $\sigma'$ is independent of cluster size; the assumption of HSN, unlike this one, implies that a point on the surface of a cluster moves through larger and larger distances as the size of the cluster increases.

## VI. Summary of the Partition Function

As noted in section III, the partition function of liquid water is expressed as the product of the external and internal partition functions of a system of clusters. The internal partition function of a cluster is composed of (A) an "internal configurational" partition function which contains (1) the internal potential energy of a cluster (including cooperative and second neighbor terms), (2) the hydrogen randomness of a cluster, (3) the shift in intramolecular zero-point energy accompanying the breaking of a hydrogen bond, and (4) the interaction of the cluster with the "background" liquid; and (B) a vibrational partition function which incorporates the normal mode frequencies of a cluster calculated within the harmonic approximation, using the approximate water molecule interaction potential of BNS.[9] The external partition function consists of a term which leads to the configurational entropy of the system of hard-sphere clusters, and a hindered rotational partition function which assumes a harmonic orientational potential between clusters. It should be noted that the "background" interaction term, which formally should be included as part of the external partition function,[3] for the sake of convenience has been included in the "internal configurational" partition function. Collecting all the terms derived in sections IV and V, we obtain an expression for the complete partition function

$$Z(N_0, V, T; \{N_j\}) = \prod_j \Bigg\{ [Q_j^{(2)} \exp\{-\beta(\epsilon_j - jy_{Bj}[2a/V - 1400] + 9900j)\}]^{N_j/N_0} \times \left[\prod_{l=1}^{6j-6} (\exp\{-h\nu_{jl}/2kT\})(1 - \exp\{-h\nu_{jl}/kT\})^{-1}\right]^{N_j} \times [([\exp\{-hf_j/2kT\}][1 - \exp\{-hf_j/kT\}]^{-1})^3]^{N_j} \Bigg\} \times Q_{\mathrm{trans}}(N_0, V, T; \{N_j\}) \qquad (16)$$

where $Q_{\mathrm{trans}}$ is given by eq 20 of ref 3. The two parameters of the partition function are $a$ (in eq 9) and $d$ (in $f_j$ of eq 12–15). We note that the distribution vector, $\{N_j\}$, is the one that maximizes the partition function (see section III above or section III of HSN[3]), and that the "product over $j$" ($\Pi_j$) represents the product over all cluster species considered in this work.

## VII. Distribution of Cluster Sizes and Computational Procedures

As pointed out in sections III and VI, the partition function for any given set of parameters, $a$ and $d$, must be a maximum (*i.e.*, the free energy must be a minimum) with respect to the distribution vector $\{N_j\}$. In the calculations, we have allowed all the $N_j$'s for $j$ = 1 to 9 to vary independently, subject to the normalization condition that

$$\sum_{j=1}^{9} jN_j/N_0 = \sum_{j=1}^{9} X_j = 1 \qquad (17)$$

where $X_j$ is the mole fraction of water molecules in $j$-size clusters.

Actually, the minimization of the free energy at each temperature is carried out with respect to only eight variables because of the normalization condition of eq 17. These variables are taken as $\zeta_j$ for $j$ = 1 to 8, where

$$X_j = \exp \zeta_j/s \qquad j = 1 \text{ to } 8$$
$$X_9 = 1/s \qquad (18)$$
$$s = 1 + \sum_{j=1}^{8} \exp \zeta_j$$

The nested minimization by which we adjust $a$ and $d$ to obtain a fit to experiment is carried out by (a) choosing initial values for $a$ and $d$, (b) using these values to calculate the free energy, $F$, and energy, $U$, and their per cent

**TABLE IV: Comparison of Calculated and Experimental Thermodynamic Properties of Water**

| | Free energy[a] | | | Internal energy[a] | | | Entropy[b] | | | Heat capacity[b] | | |
|---|---|---|---|---|---|---|---|---|---|---|---|---|
| Temp, °C | Calcd | Obsd[d] | Error[c] | Calcd | Obsd[d] | Error[c] | Calcd | Obsd[d] | Error[c] | Calcd | Obsd[d] | Error[c] |
| 0 | −1459.7 | −1435 | −1.72 | 2913.9 | 2708 | 7.60 | 16.020 | 15.17 | 5.61 | 11.60 | 18.16 | −36.1 |
| 10 | −1621.5 | −1589 | −2.05 | 3032.9 | 2889 | 4.98 | 16.447 | 15.82 | 3.96 | 12.33 | 18.05 | −31.7 |
| 20 | −1783.2 | −1750 | −1.90 | 3159.7 | 3070 | 2.92 | 16.870 | 16.44 | 2.62 | 12.97 | 18.01 | −28.0 |
| 30 | −1946.0 | −1917 | −1.51 | 3292.2 | 3251 | 1.27 | 17.288 | 17.05 | 1.39 | 13.52 | 17.99 | −24.9 |
| 40 | −2109.8 | −2091 | −0.90 | 3430.3 | 3431 | −0.02 | 17.700 | 17.63 | 0.40 | 13.99 | 17.99 | −22.2 |
| 50 | −2275.5 | −2270 | −0.24 | 3572.3 | 3611 | −1.07 | 18.105 | 18.20 | −0.52 | 14.40 | 18.00 | −20.0 |
| 60 | −2443.3 | −2455 | 0.48 | 3718.0 | 3791 | −1.93 | 18.502 | 18.75 | −1.32 | 14.76 | 18.02 | −18.1 |
| 70 | −2631.4 | −2645 | 1.20 | 3866.8 | 3971 | −2.62 | 18.893 | 19.28 | −2.01 | 15.06 | 18.04 | −16.5 |
| 80 | −2785.7 | −2840 | 1.91 | 4018.6 | 4153 | −3.24 | 19.276 | 19.80 | −2.65 | 15.34 | 18.07 | −15.1 |
| 90 | −2960.1 | −3041 | 2.66 | 4173.5 | 4333 | −3.68 | 19.652 | 20.31 | −3.24 | 15.58 | 18.11 | −14.0 |
| 100 | −3137.1 | −3246 | 3.36 | 4330.7 | 4515 | −4.08 | 20.021 | 20.80 | −3.75 | 15.81 | 18.15 | −12.9 |

[a] Units calories per mole $H_2O$. [b] Units calories per mole $H_2O$ per degree. [c] Error in fit reported as per cent error = (calculated − observed)100/observed. [d] Reference 55.

deviations from experiment at each of 11 temperatures from 0 to 100°, (c) summing the squares of these deviations over the eleven temperatures to obtain the goodness of fit parameter,[49] $\chi^2$, *i.e.*,

$$\chi^2 = \sum_T \{[(F_{\text{calcd},T} - F_{\text{obsd},T})100/F_{\text{obsd},T}]^2 + [(U_{\text{calcd},T} - U_{\text{obsd},T})100/U_{\text{obsd},T}]^2\} \qquad (19)$$

(d) varying $a$ and $d$ and then repeating b and c to minimize the sum of squares of the deviations ($\chi^2$). An algorithm suggested by Powell[50] is used for this minimization. It should be noted that carrying out step b involves the minimization of the free energy with respect to the $N_j$'s at each of the 11 temperatures considered; this is necessary in order to fulfill the "maximum term" condition mentioned in section III. The minimization of the free energy with respect to the set of $N_j$ should not be interpreted as introducing any new adjustable parameters into the theory, since, for every $N_j$ varied, there exists the added constraint that $\partial F/\partial N_j = 0$ (*i.e.*, the condition of thermodynamic equilibrium between the clusters). A conjugate gradient algorithm proposed by Fletcher[51] is used for the minimization of the free energy with respect to the $N_j$'s (in practice, with respect to the more convenient variables $\zeta_j$, as mentioned above). When this minimization has been properly carried out (for given values of $a$ and $d$), then the free energies per mole of water in all the cluster species are equal (indicating equilibrium between the clusters). This provides us with a check on the minimization.

## VIII. Results and Comparison with Experiment

Initially, the computations were carried out with only one oxygen arrangement per $j$-mer (*i.e.*, one that maximizes the degree of hydrogen bonding, as discussed in section IV), and the results of this treatment are referred to briefly in section A. Then, in order to examine the effect of inclusion of more than one oxygen arrangement per $j$-mer (specifically, arrangements resulting in less than the maximum possible degree of hydrogen bonding), the computations reported more fully in section B were carried out, in which two oxygen arrangements were included for clusters with $j = 5$.

*A. One Oxygen Arrangement per j-mer.* With one oxygen arrangement per $j$-mer, and $j = 1$ to 9, minimization of the quantity $\chi^2$ described in section VII led to the following values of the two adjustable parameters: $a$ = 91,100 cal cm$^3$/mol of bond, and ln $d = -24.1$ (where the units of $d$ are dyn cm$^4$/radian$^2$ molecule; or, in thermochemical units, $d$ = 492,000 cal cm$^3$/radian$^2$ mol). With these values of the adjustable parameters, the fit of the experimental free energy and internal energy by the corresponding theoretical values of these quantities (between 0 and 100°) is characterized by a reduced $\chi^2$ parameter[52] of 1.59. The computed distributions of cluster sizes consist almost exclusively of clusters with $j \leq 6$, and the mole fraction of water molecules in clusters of size 9, *i.e.*, $X_9$, is less than 0.0002 at all temperatures. These distributions are bimodal, with most of the water molecules being in rings with $j = 5$ and 6 at all temperatures (the remainder being mostly species with $j = 2$ and 3). With increasing temperature, the concentrations of these species decrease while the concentrations of species with $j = 2$ and 3 increase. Thus, the physical picture that emerges from these results is one in which fairly rigid hydrogen-bonded rings break down with increasing temperature into smaller, less completely hydrogen-bonded structures.

*B. Effect of More than One Oxygen Arrangement per j-mer.* In section A, we considered only one oxygen arrangement per $j$-mer, *viz.*, that which maximized the degree of hydrogen bonding in each cluster. In order to examine the effect of including more than one oxygen arrangement, we have arbitrarily included an additional (less completely hydrogen bonded) species for $j = 5$, specifically the "star" pentamer (*i.e.*, a central water molecule hydrogen bonded to four others, this being the pentamer assumed by HSN[3]) along with the ring pentamer which appeared in the calculations of section VIIIA.[53] When, the star pentamer was included, the nonamer was omitted in the computations. With this change, reminimization of $\chi^2$ leads to the following essentially unaltered values of the adjustable parameters: $a$ = 91,500 cal cm$^3$/mol of bond and ln $d = -23.9$ (or $d$ = 601,000 cal cm$^3$/radian$^2$ mol). The resulting fit to the experimental free energy and internal energy is characterized by a reduced $\chi^2$ parameter[52] of 1.47, which is better than that (1.59) obtained in section A; the improvement of the fit with a negligible change in $a$ and $d$ indicates that the improvement is due to the inclusion of the star pentamer. The computed free energy, internal energy, and entropy are compared to the experimental values[55] in Figures 6–8, and tabulated in Table IV. The fit to the free energy is quite reasonable over the entire temperature range, but the fit to the internal energy and entropy is somewhat worse (the largest deviation being that of the internal energy at 0°). The principal reason for our failure to fit the internal en-

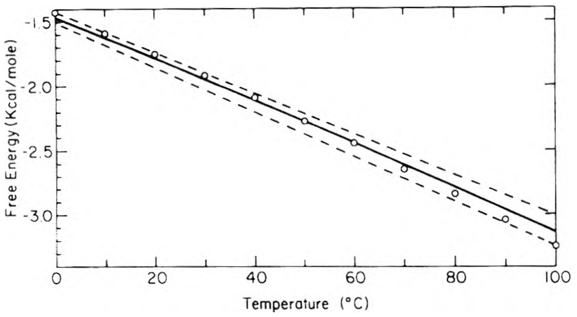

**Figure 6.** Comparison of the calculated and experimental values of the Helmholtz free energy, $F$ (the experimental values being essentially the same as the Gibbs free energy, $G$), as a function of temperature. The points are experimental values,[55] the solid curve is calculated with the "best fit" parameters, and the two dashed curves are generated with parameters that cause the theory to match the data perfectly at 0 and 100°, respectively (see text).

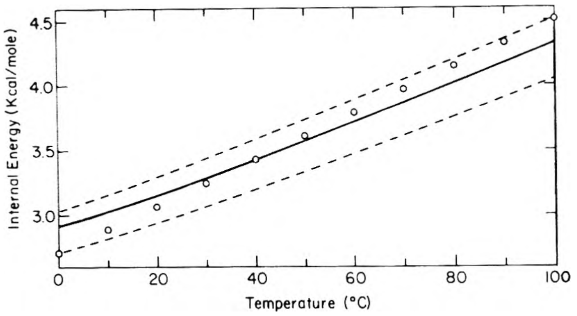

**Figure 7.** Comparison of the calculated and experimental values of the internal energy, $U$ (the experimental values being essentially the same as the enthalpy, $H$), as a function of temperature. The points are experimental values,[55] and the curves are as in Figure 6.

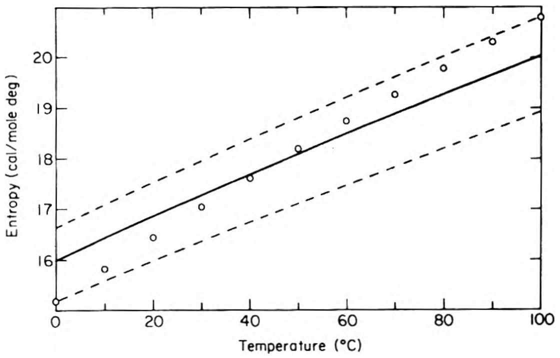

**Figure 8.** Comparison of the calculated and experimental values of the entropy, $S$, as a function of temperature. The points are experimental values,[55] and the curves are as in Figure 6.

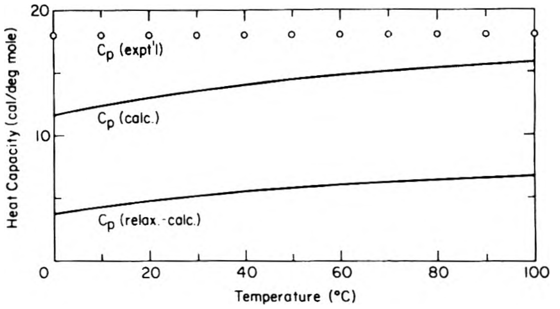

**Figure 9.** Relaxational heat capacity, and comparison of the calculated and experimental values of the heat capacity as a function of temperature. The points are experimental values of $C_p$;[55] the curves are theoretical ones.

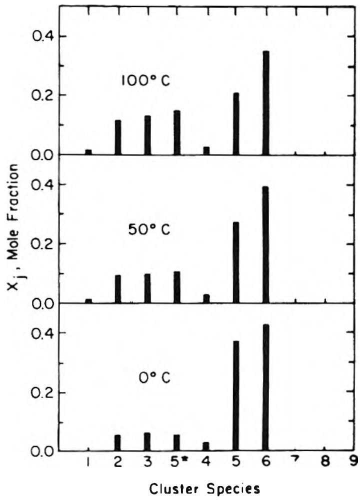

**Figure 10.** Calculated distributions of the mole fraction of water molecules in various cluster species at three temperatures. The star pentamer is represented by 5* and is presented beside the dimer and trimer because it, like them, is a "nonrigid" cluster species (see section X of text).

ergy and entropy better is the inability of our theory to account for the rapid increase of these quantities with temperature. This is reflected in our poor fit to the experimental heat capacity (see Table IV and Figure 9). Such poor fits to the heat capacity are not uncommon,[3,38,58] since the second derivative in the free energy is involved in calculating the heat capacity.

The distributions that minimize the calculated free energy are shown in Figure 10 for three values of the temperature. It may be noted that, in agreement with the results of HSN,[3] our results indicate the existence of very few monomers at any temperature (~0.7% at 0° and ~1.6% at 100°). The temperature dependence of the quantity $X_{5^*}$ (*i.e.*, the mole fraction of water present in star pentamers) is also of interest. This quantity increases with temperature (as do $X_2$ and $X_3$) until, at 100°, it is almost as large as $X_5$ (the mole fraction of water in *cyclic* pentamers).

The contributions from various terms of the partition function to the free energy, internal energy, and entropy are presented in Tables V-VII. It should be noted that 3500 cal/mol (the intermolecular zero-point energy of ice at 0°K[39,40,42]) has been added to $F_{\text{IC}}$ and $U_{\text{IIB}}$, as calculated from the "internal configurational" term in the partition function summarized in eq 16, so as to make these quantities comparable with those in Tables II and III of HSN.[3] Although the distributions differ, so that a direct comparison with the results of HSN is impossible, some observations can be made. The contributions of the translational degrees of freedom in our calculation ($F_{\text{trans}}$ and $U_{\text{trans}}$) are of the same order as calculated by HSN.[3] However, $F_{\text{vib}}$ and $U_{\text{vib}}$ are considerably smaller than reported by HSN[3] because of our assignment of lower frequencies than those of HSN to the normal modes of small clusters. Although our $F_{\text{rot}}$ is comparable to $F_{\text{rot}}$ of HSN,[3] $U_{\text{rot}}$ is larger than theirs, principally because we have used a harmonic oscillator rather than a free-rotor partition function for the rotational degrees of freedom of

**TABLE V: Contributions to the Total Free Energy**[a]

| $t$, °C | $F_{\text{trans}}$ | $F_{\text{rot}}$ | $F_{\text{vib}}$ | $F_{\text{IC}}$ | $F_{\text{total}}$[b] |
|---|---|---|---|---|---|
| 0 | −959 | −317 | 948 | 2369 | −1460 |
| 10 | −1028 | −339 | 842 | 2404 | −1621 |
| 20 | −1102 | −362 | 735 | 2446 | −1783 |
| 30 | −1178 | −387 | 627 | 2492 | −1946 |
| 40 | −1257 | −412 | 517 | 2543 | −2110 |
| 50 | −1339 | −439 | 406 | 2597 | −2275 |
| 60 | −1424 | −466 | 294 | 2653 | −2443 |
| 70 | −1511 | −495 | 180 | 2712 | −2613 |
| 80 | −1600 | −525 | 66 | 2773 | −2786 |
| 90 | −1691 | −556 | −49 | 2836 | −2960 |
| 100 | −1785 | −588 | −165 | 2900 | −3137 |

[a] All units are calories per mole. [b] As in ref 3, 3500 cal[39] has been subtracted from the sum of the free energies to obtain $F_{\text{total}}$.

**TABLE VI: Contributions to the Total Internal Energy**[a]

| $t$, °C | $U_{\text{trans}}$ | $U_{\text{rot}}$ | $U_{\text{vib}}$ | $U_{\text{HB}}$ | $U_{\text{total}}$[b] |
|---|---|---|---|---|---|
| 0 | 176 | 366 | 3331 | 2541 | 2914 |
| 10 | 186 | 387 | 3380 | 2580 | 3033 |
| 20 | 197 | 408 | 3430 | 2624 | 3160 |
| 30 | 207 | 430 | 3481 | 2674 | 3292 |
| 40 | 218 | 452 | 3533 | 2727 | 3430 |
| 50 | 228 | 474 | 3586 | 2783 | 3572 |
| 60 | 239 | 496 | 3640 | 2842 | 3718 |
| 70 | 250 | 518 | 3695 | 2903 | 3867 |
| 80 | 261 | 541 | 3752 | 2965 | 4019 |
| 90 | 272 | 563 | 3809 | 3030 | 4173 |
| 100 | 283 | 585 | 3866 | 3096 | 4331 |

[a] All units are calories per mole. [b] As in ref 3, 3500 cal[39] has been subtracted from the sum of the internal energies to obtain $U_{\text{total}}$.

**TABLE VII: Contributions to the Total Entropy**[a]

| $t$, °C | $S_{\text{trans}}$ | $S_{\text{rot}}$ | $S_{\text{vib}}$ | $S_{\text{H}}$ | $S_{\text{total}}$ |
|---|---|---|---|---|---|
| 0 | 4.16 | 2.50 | 8.73 | 0.63 | 16.02 |
| 10 | 4.29 | 2.57 | 8.97 | 0.62 | 16.45 |
| 20 | 4.43 | 2.63 | 9.20 | 0.61 | 16.87 |
| 30 | 4.57 | 2.70 | 9.42 | 0.60 | 16.29 |
| 40 | 4.71 | 2.76 | 9.64 | 0.59 | 17.70 |
| 50 | 4.85 | 2.83 | 9.85 | 0.58 | 18.10 |
| 60 | 4.99 | 2.89 | 10.05 | 0.57 | 18.50 |
| 70 | 5.13 | 2.95 | 10.25 | 0.56 | 18.89 |
| 80 | 5.27 | 3.02 | 10.44 | 0.55 | 19.28 |
| 90 | 5.41 | 3.08 | 10.63 | 0.54 | 19.65 |
| 100 | 5.54 | 3.14 | 10.81 | 0.53 | 20.02 |

[a] All units are calories per degree per mole. Obtained from the quantities in Tables V and VI.

**TABLE VIII: Structural Parameters of Liquid Water**

| $t$, °C | $V$ (exptl), cm$^3$/mol | $C_{\text{p, relax}}$, cal/mol deg | $X_{\text{HB}}$[a] | $(E_{\text{I}})_{\text{aq}}$, cal/mol of bond | $(E_{\text{U}})_{\text{aq}}$, cal/mol of bond |
|---|---|---|---|---|---|
| 0 | 18.018 | 3.63 | 0.468 | 2387 | 2250 |
| 10 | 18.021 | 4.22 | 0.463 | 2402 | 2233 |
| 20 | 18.048 | 4.71 | 0.458 | 2422 | 2224 |
| 30 | 18.093 | 5.13 | 0.454 | 2447 | 2220 |
| 40 | 18.157 | 5.47 | 0.449 | 2476 | 2221 |
| 50 | 18.234 | 5.76 | 0.445 | 2508 | 2227 |
| 60 | 18.324 | 6.00 | 0.441 | 2543 | 2237 |
| 70 | 18.425 | 6.19 | 0.437 | 2579 | 2250 |
| 80 | 18.538 | 6.36 | 0.434 | 2618 | 2266 |
| 90 | 18.663 | 6.51 | 0.430 | 2659 | 2286 |
| 100 | 18.798 | 6.64 | 0.427 | 2701 | 2309 |

[a] The median of the distribution is 5.0 at all temperatures. This constancy does not imply that the distribution is not dependent on temperature. As seen from the behavior of $X_{\text{HB}}$ and from Figure 10, the number of dimers, trimers, and star pentamers increases, and the number of pentamers and hexamers decreases, with increasing temperature.

a cluster. Finally, our values of $S_{\text{H}}$ [hydrogen entropy; given by $(U_{\text{HB}} - F_{\text{IC}})/T$] are less than half the values of $S_{\text{int}}$ of HSN. Some of this difference can be attributed to our neglect of the oxygen entropy,[54] while some of it may be due to the difference in the distributions, as noted above (*i.e.*, large clusters, of size 20 or 30, have quite large internal entropies in the formulation of HSN).

In Table VIII we have compiled various quantities that describe the temperature-induced structural changes computed for liquid water. The constant pressure relaxational heat capacity, $C_{\text{p,relax}}$, is taken to be the derivative of $U_{\text{HB}}$ with respect to temperature. This is also plotted in Figure 9. A reasonable, experimentally based estimate of this quantity (analogous to the estimate of $C_{\text{v,relax}}$ given by Eisenberg and Kauzmann[26]) was made here and yielded a value of about 8 to 9 cal/mol deg over the temperature range of liquid water. The fact that the calculated $C_{\text{p,relax}}$ is too small, especially at low temperatures, is probably the reason for our underprediction of the total heat capacity.

The mole fraction of unbroken hydrogen bonds, $X_{\text{HB}}$, also appears in Table VIII. Since the energy associated with a hydrogen bond depends on cluster size and geometry in our theory, we cannot calculate a quantity that is the same as $(E_{\text{H}})_{\text{aq}}$ of HSN[3] ("the energy necessary to break a hydrogen bond in the liquid, including the difference in intramolecular zero-point energies in the bonded and unbonded states"[3]). However, we present in Table VIII two quantities that are related to $(E_{\text{H}})_{\text{aq}}$. The first, $(E_{\text{I}})_{\text{aq}}$, is the average energy per mole of bond required to break $(1 - X_{\text{HB}})$ of the bonds in ice to obtain the equilibrium distribution of water clusters at a given temperature [as for $(E_{\text{H}})_{\text{aq}}$, this quantity contains the shift in intramolecular zero-point energy on breaking a hydrogen bond], *i.e.*

$$(E_{\text{I}})_{\text{aq}} = (1/2)U_{\text{HB}}/(1 - X_{\text{HB}}) \qquad (20)$$

where the quantity (½) appears since there are two hydrogen bonds per water molecule in ice. The second quantity, $(E_{\text{U}})_{\text{aq}}$, is the average energy per bond needed to break all the bonds in the equilibrium distribution of water clusters at a given temperature and produce all unbonded water molecules in the liquid (again, this includes the shifts in the intramolecular zero-point energies). This is calculated by first summing over $j$ the product of the energy to break all the bonds of a $j$-mer in the liquid $[-2(1 - y_{Bj})E_{Hj} - (1 - y_{Bj})(2a/V - 1400)]$ times the fraction of water present in $j$-mers $(X_j)$, to obtain the energy (per mole of water) to break all the bonds existing in water at a given temperature and volume. This quantity is then divided by the average number of bonds per water molecule $(2X_{\text{HB}})$ at that temperature and volume to yield

$$(E_{\text{U}})_{\text{aq}} = \{1/(2X_{\text{HB}})\}\sum_j X_j[-2(1 - y_{Bj})E_{Hj} - (1 - y_{Bj})(2a/V - 1400)] \qquad (21)$$

If the energies of all the hydrogen bonds in all the clusters present in water were the same as the energy of a hydrogen bond in ice (as assumed by HSN[3]), then $(E_{\text{I}})_{\text{aq}}$ and $(E_{\text{U}})_{\text{aq}}$ would be equal and, in fact, equal to $(E_{\text{H}})_{\text{aq}}$ (assuming that the same value for the parameter of background potential, $a$, were used to derive each quantity).

**TABLE IX: Summary of Experimental Data of Intermolecular Motions in Liquid Water**

| Method | Ref | Description of results[a] | |
|---|---|---|---|
| | | Hindered translations ($\nu_T$ and $\nu_b$) | Librations ($\nu_L$) |
| Ir | 65 | Weak band peaked at ~193 cm$^{-1}$, overlapping with the librational band; very weak unassigned maximum at ~280 cm$^{-1}$; no 60-cm$^{-1}$ band observed. | Broad, intense band; broadens and red shifts with increasing temperature (maximum ~700 cm$^{-1}$ at 5°, ~650 cm$^{-1}$ at 75°). |
| Raman | 23, 64, 66 | Bands approximately assigned to 166 and 60 cm$^{-1}$; marked decrease in intensity with increase in temperature. | Broad band resolved into two major Gaussian components at 450 and 722 cm$^{-1}$, and a minor component at 550 cm$^{-1}$ (25°); marked decrease in intensity and slight red shift with increasing temperature. |
| INS[b] | 67 | Indications of peaks at 52, 77, 95, 155, 275 cm$^{-1}$ (273.3°K). | Broad band[69] with maximum at ~580 cm$^{-1}$. |
| INS[b] | 68 | Difficult to resolve because of overlap with $\nu_R$; low-frequency band (~60 cm$^{-1}$) broadened and perhaps split relative to ice. | Broad band;[69] red shifts and broadens with increasing temperature; maximum ~650–600 cm$^{-1}$; possible high-frequency band[69] at ~900–1000 cm$^{-1}$. |

[a] $\nu_b$, O···O···O coupled deformation mode; $\nu_T$, translational mode; $\nu_L$, librational mode. Red shift refers to shift of band toward lower frequencies; *i.e.*, to the left in Figure 11. [b] Inelastic neutron scattering.

The fact that these quantities are not equal is a direct result of the inclusion of cooperative effects, second-neighbor interactions, and hydrogen randomness in our development of the internal energies of clusters (resulting in hydrogen-bond energies which depend on cluster size and geometry). A number of recent spectral studies of $H_2O$, $D_2O$, and HOD have been interpreted as providing evidence for the existence of at least two states of hydrogen bonding in liquid water (*e.g.*, see ref 24, 25, and 59–61), but this interpretation is by no means universally accepted.[62] On the basis of this interpretation, however, Walrafen[24] has derived, from the temperature dependence of the ratio of the intensities of what are assumed[24] to be the hydrogen-bonded and non-hydrogen-bonded components of the O–D stretching band, an estimate of 2500 ± 600 cal/mol as the energy to break a hydrogen bond in water. Both $(E_{\mathrm{I}})_{\mathrm{aq}}$ and $(E_{\mathrm{U}})_{\mathrm{aq}}$ are within the range of this estimate. For another comparison with experiment, it may be noted that, on the basis of infrared studies, Luck has concluded[59,60] that only about 10–20% of the possible hydrogen bonds in water are broken over the temperature range 0–100° (a conclusion that disagrees with our computed values of the fraction of unbroken bonds, $X_{\mathrm{HB}}$, in Table VIII). Luck's estimate of $1 - X_{\mathrm{HB}}$, however, requires the identification of the spectroscopic properties of OH groups in water vapor near its critical point (*i.e.*, at $t$ = 387° and density = 0.239 g/cc[60]) with those of unbonded OH groups.[60] With this assumption, Luck obtained his estimate of 10–20%. Since only a fraction of the "unbonded" OH groups in liquid water at atmospheric pressure could be identified with a molecule in the near-critical vapor (by Luck's own analysis[59]), Luck's results must be considered to form a lower bound to the quantity $1 - X_{\mathrm{HB}}$. Thus, it is not surprising that our estimate of the number of broken hydrogen bonds in liquid water is greater than Luck's estimate.

Two properties of our partition function deserve comment here. First, we have investigated the sensitivity of our results to the frequencies assigned to the normal modes of the clusters. This was accomplished by incorporating the approximate frequency assignments of Table IX of ref 7 (assigned on the basis of a simple 4,3,2-bonded model, ignoring intermolecular coupling effects) into our calculations with $j$ = 1 to 9 and then reminimizing $\chi^2$. The resulting fit (with $a$ = 90,600, ln $d$ = −24.3) was not as good (reduced $\chi^2$ = 2.02) as found (section VIIIA above) with the cluster normal-mode frequencies calculated using the BNS[9] potential. The resulting distributions are quantitatively different from those presented in Figure 11, but their qualitative behavior with temperature remains the same as found above for the normal-mode frequencies derived from the BNS[9] potential: (a) at no temperature was there a significant fraction of water in clusters of size 8 or 9; (b) the fraction of water in the hydrogen-bonded rings decreased with increasing temperature with a corresponding increase in smaller, less completely hydrogen-bonded structures. These results suggest that, although quantitative refinement might result from an improved treatment of the cluster normal mode frequencies, it is not likely that the qualitative nature of our results would change.

Second, it should be pointed out that a perfect fit to the thermodynamic properties of water could have been obtained, had the parameters, $a$ and $d$, been allowed to vary with temperature (*i.e.*, at each temperature a value of $a$ and $d$ can be found that will cause the calculated free energy, internal energy, and heat capacity to match the experimental values perfectly). The thermodynamic properties obtained with the values of $a$ and ln $d$ giving perfect fits at 0° (94,400 cal cm$^3$/mol and −22.7) and 100° (90,400 cal cm$^3$/mol and −24.5), respectively, are plotted in Figures 6–8 (along with those of Table IV resulting from the "best fit" values of $a$ and $d$) in order to give some idea of the sensitivity of our results to the values assigned to the parameters. Reference to Figures 7 and 8 makes it clear that a principal failing of our partition function is its inability to predict the proper temperature dependence of the internal energy and entropy (and thus to predict the heat capacity). It may be noted that both $a$ and $d$ decrease with increasing temperature (in fact, most rapidly so at low temperatures). The formal introduction of such temperature dependence would allow us to reproduce the temperature dependence of the internal energy and entropy, but would add *at least* two more adjustable parameters to our theory, and the theory would then be so heavily parameterized that an improved fit would have little meaning. We mention these results here, however, because of their possible importance in ultimately understanding the physical origin of this temperature dependence, and in evaluating our model in order to deduce implications about the structure of water (see section X below).

## IX. Qualitative Results. Comparison with Experiment

We now consider in a qualitative way the compatibility of our theory with several of the characteristic properties of water, *viz.*, the distribution of the intermolecular normal-mode frequencies, pressure–volume properties (in particular the relaxational isothermal compressibility), and the radial distribution function.

A frequency spectrum may be derived from our results since we know the concentrations of all of the cluster species present at equilibrium (at each temperature) and the normal-mode frequency spectrum for each cluster (see section IVB and Table III). We have constructed histograms of the distributions of frequencies, $g(\nu_l)$, characteristic of our model at each temperature, according to

$$g(\nu_l) = \sum_j N_j \Gamma_j(\nu_l - \Delta; \nu_l + \Delta) \qquad (22)$$

where $\Gamma_j$ is the number of normal modes of a $j$-mer with frequencies in the range $\nu_l - \Delta$ to $\nu_l + \Delta$. Histograms obtained in this way are presented in Figure 11 for 0 and 100° (for $\Delta = 10\ \text{cm}^{-1}$), along with a qualitative[63] representation of the Raman spectra obtained by Walrafen.[64] Also, the principal features of the experimental frequency spectra obtained by infrared[65] and Raman[23,66] spectroscopy and by inelastic neutron scattering[67,68] are compiled in Table IX, and may be compared in a qualitative fashion[63] with the features of our calculated frequency distributions of Figure 11. The agreement of our calculated $g(\nu_l)$ with experiment (see Figure 11 and Table IX) is quite good, considering the approximations that we have had to make in treating our model. Our calculated $g(\nu_l)$ indicates the existence of two major bands in the librational region (frequency maxima at ~450 and 700 cm$^{-1}$), whose positions correspond well with the positions of the two main peaks resolved by Walrafen[23] from his Raman data (~450 and 722 cm$^{-1}$; an additional very weak peak is claimed[23] to be centered at 550 cm$^{-1}$). It should be noted that our choice of a scaling factor for the librational frequencies calculated with the BNS potential (see section IVB) was based on the motion of a four-bonded water molecule in a star pentamer. Since our distributions are not dominated by this species, our scaling procedure cannot be expected *a priori* to lead to this level of agreement. In addition the predicted range of frequencies of the librational modes is very broad (extending from within the translational band, $\nu_T$, to about 940 cm$^{-1}$), in good qualitative agreement with the experimental results (see Table IX and Figure 11). Also, our predicted frequency distribution shows a shift toward lower frequency [as demonstrated by the sums of $g(\nu_l)$ over the bracketed regions in Figure 11] at 100° relative to 0°, which is in qualitative agreement with the temperature-induced red shift evident in the infrared[65] and neutron scattering data.[68] Our calculations also correctly predict the existence of two bands in the low-frequency region of the spectrum (corresponding to hydrogen bond stretching and coupled O···O···O deformations; $\nu_T$ and $\nu_b$, respectively).

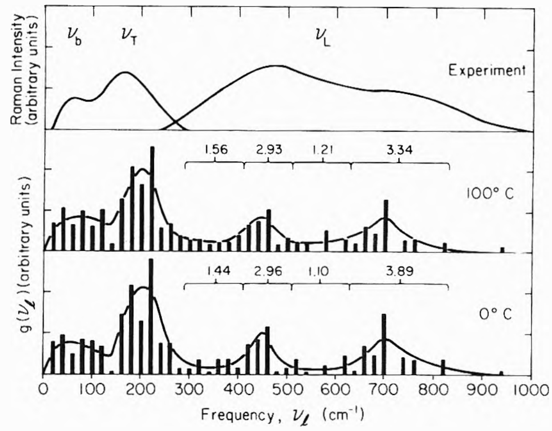

**Figure 11.** Calculated histograms of the frequency distributions, $g(\nu_l)$, at two temperatures. The units of $g(\nu_l)$ are arbitrary and the histograms have been normalized to the same value at both temperatures. The smooth curves drawn through the histograms represent a roughly averaged $g(\nu_l)$. The numbers over the bracketed regions are the sum of $g(\nu_l)$ over those regions. The top curve is a qualitative representation of the experimental Raman spectrum taken from Figures 4 and 5 of ref 64. The units of Raman scattering intensity are arbitrary and are not related between the two regions of the spectrum, $\nu_b + \nu_T$ and $\nu_L$.

Despite the overall good agreement of our calculated $g(\nu_l)$ with the qualitative features of the experimental frequency spectra, there are areas of some disagreement. Most obvious is our calculated resolution of two distinct librational bands, as compared to the experimental observation of a single, poorly defined, broad band, or two broad, overlapping bands (*e.g.*, see the Raman spectrum[64] qualitatively represented in Figure 11). This discrepancy may be the result of two of the approximations made in our treatment, *viz.*, inclusion of only a small fraction of the many possible small-cluster species and the failure to account for specific intercluster interactions. Correction for these two approximations would greatly increase the range of possible local environments of a water molecule, and thus could be expected to broaden both of the predicted bands in the librational region, perhaps to the point that only one very broad band would be observed. A less-obvious disagreement with experiment is our calculation of the maximum in the translational band ($\nu_T$; maximum ~210 cm$^{-1}$) at a somewhat higher frequency than is observed (155[66] to 193[64] cm$^{-1}$). This result may be partly related to the approximation made in rescaling the librational frequencies calculated using the Ben-Naim and Stillinger potential (see section IVB). Reference to Table III indicates that there are quite a few coupled librational normal modes with frequencies in the range 180 to 240 cm$^{-1}$. It is quite possible that the rescaling approximation would cause the frequencies assigned to these coupled librational modes to be too low (see section IVB) and thus overpredict the density of normal modes in this frequency range. Finally, it should be noted that the sum of $g(\nu_l)$ decreases only slightly with temperature (by about 5% from 0 to 100° due to the decrease in the number of vibrational degrees of freedom as clusters break down), in contrast to the marked decrease in integrated Raman intensity observed by Walrafen[23] (a decrease by a factor of 3 or 4). Assuming that only the intermolecular normal modes of completely hydrogen bonded water molecules could contribute to the Raman intensity, Walrafen interpreted[64] this decrease in integrated intensity in terms of the disappearance of four-bonded water molecules with increasing temperature. However, if Walrafen's observed decrease in intensity is due to a specific Raman selection rule (as he suggests[64]), then this decrease cannot be compared[63] to any decrease in our calculated sum of $g(\nu_l)$. Indeed, such a drastic reduction in intensity with increasing temperature is not observed in infrared[65] or neutron scattering studies.[68] In regard to Walrafen's interpretation of his Raman spectra,[64] it might be noted that our results predict rather closely the major maxima of the librational peaks (~450 and 722 $\text{cm}^{-1}$) that Walrafen resolved from his data,[23] although our calculations do not involve only the motions of four-bonded water molecules, but rather the coupled motions of incompletely hydrogen-bonded water molecules in small clusters. Thus, one need not invoke the existence of tetrahedrally bonded water molecules to explain either the large librational frequencies or the breadth of the librational band in liquid water.

The limitations imposed by the form of the configurational (*i.e.*, translational) partition function used (*i.e.*, one derived from the Percus–Yevick equation for a mixture of hard spheres) make it impossible to predict the P-V-T properties of water quantitatively (see section X). The inapplicability of the theory at high pressure was discussed by HSN[3] and attributed to the use of a hard-sphere repulsion for the interaction of clusters. Even at low pressure, however, the approximate nature of the results obtained from the Percus–Yevick equation make it futile to expect an accurate prediction of the pressure or compressibility (the reason for this is discussed in section X). Thus, for example, the pressure calculated from our partition function ($P = kT\,\partial \ln Z/\partial V$) is approximately −1400 atm at 0° and −400 atm at 100°. Despite these limitations on the quantitative predictions of $P$–$V$–$T$ properties, we can test whether it is possible to rationalize such properties qualitatively in terms of the species present in our model. Such properties are often rationalized in terms of a breakdown of a "bulky" species into a "close-packed" species (*e.g.*, see section IX of HSN[3] for a discussion of the temperature dependence of the volume). An example is the isothermal compressibility, $\kappa_T = -(1/V)(\partial V/\partial P)_T$. The relaxational portion of this quantity (*i.e.*, that part due to the breakdown of structure in the liquid) can be accounted for by simple two-state models in terms of a difference in molar volume, $\Delta V$, between the bulky and compact states.[31] Davis and Jarzynski[31] have compiled these values of $\Delta V$ for a number of two-state models, and have shown that those models that predict a value of the relaxational compressibility close to the experimentally estimated value[71] all have values of $\Delta V$ in the range of about 7 to 9 $\text{cm}^3$/mol. If we calculate the difference in the molar volume of water in our hexamers and in our dimers (taken as spheres of diameter $R_6$ and $R_2$, respectively), and then divide this difference by the packing factor for our clusters in the liquid [the packing factor (*i.e.*, the value of $\xi$ of the Percus–Yevick theory; see eq 17–19 of HSN[3]) is about 0.5 at all temperatures], we find $\Delta V \sim 6$ $\text{cm}^3$/mol, which is slightly smaller than the value of $\Delta V$ suggested by the two-state analysis of Davis and Jarzynski.[31] Thus, this analysis would seem to indicate that the differences in density among the various species in our model account qualitatively for the relaxational isothermal compressibility of liquid water, although (from what is expected by calculation with a two-state model) they are quantitatively slightly small.

The main features of the radial distribution function of water are generally interpreted as reflecting a local tetrahedral order (sharp peak at about 2.9 Å, corresponding to approximately 4.4 nearest neighbors) which extends to some extent even to second and third neighbors (broader maxima at 4.5 and 7 Å).[72] Interpretation of the *shape* of the 2.9-Å peak implies the presence of "at least two types of near-neighbor configurations" in the liquid.[72] In general, unless the predicted cluster sizes are very large (as in ref 38), a cluster model is not sufficiently well defined (in particular, with respect to the relative positions and orientations of molecules in *neighboring* clusters) to allow for a quantitative prediction of the radial distribution function. Normally, however, a cluster theory can be rationalized as being at least qualitatively consistent with the existence of tetrahedral order implied by the radial distribution function[72] because of the fairly large number of 3- or 4-bonded water molecules present in moderate-to-large clusters.[3] Since the distributions resulting from our work predict the existence of very few clusters containing more than eight or nine water molecules, we have no way of even qualitatively predicting such local tetrahedral structure implied by the radial distribution function. Thus, without more specific information about cluster packing and intercluster structure, we cannot say, even qualitatively, whether or not our theory is consistent with the radial distribution function.

## X. Interpretations of Results and Criticism of Theory

In this work, we have attempted to extend the treatment of the cluster model presented by HSN[3] by removing a number of the approximations made by these authors. Unfortunately, there still remain some serious approximations which limit our ability to interpret the model in terms of the structure of real water. However, the nature of the results and the shortcomings of the model suggest possible implications about the structure of real water (discussed here, and summarized in section XI), and provide insight into the meaning of a "cluster model" as applied to water.

Our most serious approximations are related to the evaluation of the configurational partition function of a system of clusters. First, in order to separate $Q_{\text{ext}}$ and $Q_{\text{int}}$, we have ignored specific interactions between clusters, and treated these as "average" interactions described in terms of two adjustable parameters, $a$ and $d$. Second, for the purpose of evaluating the configurational partition function, the clusters have been treated as hard spheres with temperature-independent diameters, $R_j$. Particularly in the case of the small clusters that dominate in our calculated distributions, the assumption of spherical shape must be considered a crude approximation. Also, the assumed temperature independence of these diameters ignores the effects of possible thermal expansion of the clusters. Third, the thermodynamic properties of a system of hard spheres, derived[45] from the solution of the Percus–Yevick equation and the compressibility equation of state, must be realized to be only approximate. In fact, this approximation is known to be in error[45] in the range of high densities considered here (cluster packing density, $\xi \sim 0.5$). As pointed out by Egelstaff,[73] the failure of this approximation is most seriously reflected in the calculation of the pressure, since this involves the cancellation of two large, approximate quantities in order to obtain a small one. In our case, $P_{\text{HS}}$ [the hard-sphere pressure (see eq 18 of HSN;[3] ~5000 atm)] plus $P_{\text{rot}}$ ($kT\,\partial \ln Q_{\text{rot}}/\partial V$; ~ 400 to 600 atm) must cancel with the internal cohesive pressure ($-a/V^2$; ~ −6000 atm) to yield the experimental pressure of 1 atm. Thus, our theory completely fails in attempts to predict the pressure[74] or pressure-volume properties (*e.g.*, see section IX for the calculated pressure). It should be noted that the errors involved in such quantities as the calculated internal energy and free energy are not nearly so large as in the calculated pressure, since these quantities are directly related to the individual large quantities mentioned above and not to their difference. However, our failure to correctly predict the pressure does point out the approximate nature of our treatment of the configurational partition function.

The importance of interactions between clusters (which, as noted above, have been ignored) is suggested by the magnitudes of the parameters $a$ and $d$. The value of $a$ corresponds to a background interaction of about 5080 cal/mol of bond (which is large compared to an estimated[39] energy of 6700 cal/mol of bond in ice);[75] the value of $d$ corresponds to a monomer librational frequency of about 580 $\mathrm{cm}^{-1}$ (as compared to a mean librational frequency of about 650 $\mathrm{cm}^{-1}$ in ice[42,43]), and indicates an intercluster potential that varies rapidly with respect to cluster rotational motion. To the extent that these large values of the parameters do not compensate for approximations in other terms of the partition function [*e.g.*, the rescaling of the calculated librational frequencies (see section IVB, or the errors in the configurational partition function discussed above)], they imply fairly strong interactions between clusters. Indeed the large value of $d$ implies that these interactions are strongly orientationally dependent. Such interactions might reasonably be pictured as involving distorted (*i.e.*, nonlinear, or "bent") hydrogen bonds. Such a picture of intercluster structure would allow us to rationalize the approximately tetrahedral coordination predicted by the radial distribution function determined by X-ray diffraction. Also, the observed tendency of $a$ and $d$ to decrease with temperature (see section VIIIB) could be interpreted (again assuming that this behavior is not occurring as a compensation for an error in another term of the partition function) in terms of the disruption, on average, of the intercluster interactions with increasing temperature, which is not represented by the volume dependence of eq 9 and 15, respectively. Such an interpretation might well account for part of our underprediction of the heat capacity of liquid water in that our model may not adequately represent the nature (and, therefore, the temperature dependence) of intercluster interactions.

There are other inadequacies in the formulation of the theory which are not as serious as the treatment of the interactions between clusters and the treatment of the configurational partition function. One of these is the consideration of only a few of the many possible small-cluster oxygen arrangements that might exist in water. Inclusion of additional loosely hydrogen-bonded (*i.e.*, linear or branched-chain) clusters of each size should cause both the energy and entropy to increase more rapidly with increasing temperature, since these loosely hydrogen-bonded species are entropically favored, but energetically unfavored. Indeed, the addition of the star pentamer as a possible cluster species did improve the fit to experiment as discussed in section VIIIB. Another approximation that might be affecting our results is the scaling of the cluster normal-mode librational frequencies obtained by use of the BNS potential[9] (see sections IVB and IX). A significant improvement on this approximation should be possible by deriving an improved potential for the interaction of water molecules which reproduces the properties of water including its intermolecular vibrational frequencies.[76] It should also be noted that the cluster normal-mode calculations take no account of the orientational dependence of the intercluster interactions implied by the large values of our parameter $d$. Indeed, as noted in section IX, the use of this approximate procedure might be part of the cause of the discrepancies noted in our calculated frequency distributions. Also in this regard, we note an inconsistency of our theory in that we use the noncooperative BNS potential to derive the normal-mode frequencies of clusters, and yet calculate the internal potential energy of a cluster using two- and three-body potentials estimated from *ab initio* LCAO-MO calculations. This was necessary in order to include the effects of cooperativity.

Despite these failings of our treatment, it is possible to interpret our results as confirming and extending the conclusions of HSN regarding the small numbers of large clusters present in water.[77] The failure of HSN to consider the effects of cooperativity might have mediated against this conclusion in their case, since cooperativity was thought to favor the formation of large clusters in the original Frank-Wen model.[78] In fact, our treatment of cooperative and second-neighbor effects results in increased favorability of some small clusters (especially cyclic ones) over intermediate and large cluster (relative to the noncooperative treatment of HSN). This results from the preponderance, in intermediate and large-size clusters, of three-bonded water molecules, which are disfavored because they contain unfavorable "nonsequential" three-body and second-neighbor interactions (see Appendix A and Figure 3). The stability of small clusters in our treatment is further enhanced relative to the treatment of HSN by our frequency assignments (a possibility suggested by HSN), and by our consideration of ring structures for small clusters as suggested by *ab initio* LCAO-MO calculations.[6] Of these three effects (cooperative and second-neighbor interactions, frequencies, rings), however, the inclusion of cooperative and second-neighbor interaction energies (which appear in $\epsilon_j$) contributed *the least* to the added stability of small clusters (relative to clusters of size greater than about 15) in this treatment (*e.g.*, see Appendix B, section iii of ref 7).

Aside from the predicted importance of only small clusters, another interesting feature of the cluster distributions resulting from our theory is their bimodal character (see Figure 10). It should be noted that the bimodal *appearance* of the distributions in Figure 10 depends considerably on the properties of a cluster of size four. However, it is not simply this bimodal appearance that is significant, but rather the fact that the distributions reflect the breakdown with increasing temperature of fairly rigid (*i.e.*, having large normal-mode frequencies) hydrogen-bonded rings, containing one hydrogen bond per water molecule (*e.g.*, the cyclic pentamer or hexamer), into less rigid, open, hydrogen-bonded structures possessing less than one hydrogen bond per water molecule (*e.g.*, the star pentamer, trimer, etc.). The bimodal character could not have been described by the smooth, singly-peaked $\gamma$ distribution used by HSN.

In view of our prediction of the predominance of primarily small clusters in water, and of the unexpected effect of cooperativity in stabilizing *small* clusters relative to large ones, we must reinterpret what is meant by a "cluster" model for liquid water. It should be stressed that our results do *not* imply the *usual*[3,38,78] cluster-model concept of *large* hydrogen-bonded regions breaking down with increasing temperature into smaller regions or monomers. In fact, *all* the clusters occurring in our theory are small. Although our results do show the breakdown of some of the larger small clusters into even smaller ones with increasing temperature, these results also show the importance of the conversion from rigid to less rigid structures. Thus, the picture that must evolve, if our results are to be interpreted in terms of the actual structure of water, is one of small regions of local order. The nature of the distributions predicted by our results suggests that these local structures might be classified into two general categories: (1) rigid, energetically favored local structures (*e.g.*, the cyclic pentamer), and (2) less-rigid, entropically favored local structures (*e.g.*, the star pentamer). Interconversion between these two classes of local structures involves the disruption of hydrogen bonds (*e.g.*, converting the cyclic to the star pentamer). Our results suggest that the disappearance of the more rigid, energetically favored local structures with increasing temperature can, at least partially, account for the large relaxational heat capacity of water (see Table VIII of section IVB). Another possible source of relaxational heat capacity involves the continual disruption with increasing temperature of the fairly strong intercluster interactions [not explicitly taken into account in our treatment, but implied by the observed (see section VIIIB) tendency of $a$ and $d$ to decrease with increasing temperature]. It may also be noted that the differences in molar volumes between local structures in these classes can lead to large values of the relaxational compressibility (section IX, $P$-$V$-$T$ properties), as observed in liquid water. It should be noted that this hypothetical picture, quite naturally implied by the results of our "cluster" model treatment, has much in common with a continuum point of view (since our model allows water molecules to exist in a wide range of possible states) even though it is based on a model which postulates the existence of discrete cluster species. Thus, our results are clearly inconsistent with an interpretation of the properties of liquid water in terms of only two states. One obvious example of this is the calculated frequency spectrum of liquid water presented in section IX, which, because of the many possible states of water molecules in our model, can account for a continuous spectrum. Such a result could not have been predicted by a simple two-state model. Our results do allow, however, for a tentative interpretation of the "two-state" behavior of many of the properties of liquid water,[30,31] where the two "states" that these results suggest are not single states, but rather correspond to the two general categories of local order mentioned above (each of which may contain a broad range of geometrically different local structures).

## XI. Summary and Conclusions

The purpose of this paper has been to extend and improve the treatment of a "cluster" model for liquid water given by HSN, in order to obtain further insight into the structure of this liquid. To this end, we have used the results of recent *ab initio* LCAO-MO calculations to incorporate the effects of cooperative hydrogen bonding and to obtain an estimate of the hydrogen internal entropy of a cluster (allowing us, to a first approximation, to remove the cluster internal entropy parameter of HSN). Since preliminary calcuations[7] indicated a predominance of small clusters, we are able finally to limit our attention to only nine cluster species and to calculate explicitly their normal-mode frequency distributions using the approximate BNS pair potential.[9] Consideration of only a few cluster species also has allowed us to remove the approximation[3,7] of the smooth, singly peaked $\gamma$ distribution, which we have shown[7] to be inadequate in that this approximation results in "anomalous second minima," such as obtained by HSN.[3] We have also investigated the effect of allowing a given size cluster (specifically a pentamer) to exist in more than one geometrical arrangement of its oxygens, which improved the fit of our theory to experiment. Along with these improvements in the internal partition function of our clusters and in the description of the distribution of clusters present in water, we have made some minor improvements in the external partition function (in comparison with the treatment of HSN). These include (1) treatment of the rotational degrees of freedom of a cluster in terms of a harmonic oscillator partition function, and (2) a better estimate of the variation of the hard-sphere diameters, $R_j$, of clusters with cluster size.

With these improvements, the free energy, internal energy, and entropy of water were fit reasonably well over the entire liquid temperature range (0 to 100°) with the use of only *two* adjustable parameters (as compared to a fit obtained with *three* parameters by HSN over the temperature range 0 to 60°, or the many more adjustable parameters used in most other theories[10]). As was the case with HSN, the heat capacity was considerably underpredicted over this temperature range. The frequency spectrum of the intermolecular normal modes in liquid water has been very reasonably reproduced, considering the small number of cluster species taken into account and the approximations made.

The distributions of clusters resulting from our calculations were shown to contain only very small cluster species (principally, containing less than seven water molecules), confirming and extending the earlier conclusions of HSN[3] regarding the small number of large clusters likely to be present in liquid water. In this regard, it was found that the effect of our treatment of cooperativity was to disfavor large-size clusters relative to the noncooperative model for hydrogen bonding used by HSN.[3] The nature of these distributions of small clusters was tentatively taken to reflect an equilibrium between two general categories of local structures. The differences in the properties of the local structures in these two categories were seen to be related to their degree of hydrogen bonding and to their "rigidity," as reflected in their intermolecular normal-mode frequencies. This further emphasizes the importance of the intermolecular vibrational frequencies in obtaining a quantitative understanding of the thermodynamic properties of water (as pointed out by HSN[3]). It was noted that our results reflect a "cluster model" insofar as this term applies that small hydrogen-bonded clusters break up into still smaller, less rigid ones, with fewer hydrogen bonds, rather than the traditional view of a breakdown of large clusters into small ones with increasing temperature.

Since our principal aim is to gain some insight into the structure of liquid water, we have examined the discrepancies in our results in terms of the major approximations made in the treatment of the cluster model. One of the most important areas of uncertainty in our theory was shown to be the treatment of intercluster interactions and the related configurational (*i.e.*, cluster translational) partition function. It was suggested that the use of the approximate Percus-Yevick treatment for a mixture of hard spheres made it impossible to properly predict the pressure of our system. Interpretation of the behavior of our intercluster parameters, $a$ and $d$, has suggested a tentative picture of intercluster structure. The failure of our model to adequately represent the nature of intercluster interactions has been taken as one possible reason for our underprediction of the heat capacity of liquid water. Another important approximation was shown to be the consideration of only a very few of the many possible geometrically different small cluster species. It was noted that consideration of a broad range of species could improve both the fit of our theory to the experimental internal energy and entropy as well as the prediction of the intermolecular normal mode frequency spectrum.

Finally, the picture of water extracted from this analysis of our results was noted to have much in common with a continuum point of view at the same time that it provides an explanation for the apparent discrete nature of many of the experimental properties of water. It should also be noted that our results cannot support a simple "two-state" interpretation of the properties of water. On the contrary, as pointed out by HSN,[3] a simple two-state model is not capable of allowing for the many possible states of a water molecule implied by our model (a fact which allows us to predict the intermolecular frequency distribution of liquid water approximately while a simple two-state model could not).

The results of this investigation have led us to attempt further improvements in our theory. Certainly, a principal goal of future efforts in this direction must involve a consideration of additional cluster species. Another area of possible improvement would be in the treatment of the configurational partition function. The development of an improved potential function for water molecule interactions should be of high priority, since this would make possible a better treatment of the normal modes of clusters, and could possibly be used to investigate the nature of the background potential. It might be possible, for example, to use such an improved potential to develop estimates for the parameters for specific cluster-cluster interactions and to incorporate these into a composition-dependent background potential in a manner analogous to that suggested by Snider and Herrington[79] for binary liquid mixtures. Also, such a potential function might be used to study the packing of water clusters around simple polar and nonpolar molecules, and thus lead to a treatment of the solvation of such molecules.

## Appendix

*Evaluation of* $\Sigma_k\eta(\epsilon_{kj})e^{-\beta\epsilon_{kj}}$. Having assumed that we can separate $\epsilon_{kj}$ into hydrogen-configuration-dependent and -independent terms (eq 4), $Q_{\mathrm{IC},j}$ of eq 3 becomes

$$Q_{\mathrm{IC},j} = e^{-\beta\epsilon_j}\sum_k \eta[\epsilon_{kj}^{(2)}]e^{-\beta\epsilon_{kj}^{(2)}} \tag{A-1}$$

We designate $\Sigma_k\eta[\epsilon_{kj}^{(2)}]e^{-\beta\epsilon_{kj}^{(2)}}$ as $Q_j^{(2)}$.

*Evaluation of* $Q_j^{(2)}$. The actual distributions $\eta[\epsilon_{kj}^{(2)}]$ were obtained by building many clusters of a given $j$ (for $j$ = 6, 12, 20, and 39) from molecular models, evaluating $\epsilon_{kj}^{(2)}$ from first-neighbor, quantum-mechanical results of two-body interactions at oxygen-oxygen distances of 2.76 Å[80] from Table III of ref 6, and counting the number of times a particular range of values of $\epsilon_{kj}^{(2)}$ appeared. These distributions were approximated reasonably well by a Gaussian shape for large clusters ($j$ = 20 and 39), but became more skewed for smaller $j$ ($j$ = 12), and were not at all Gaussian like at $j$ = 6. Again, by model building, we determined the extremes of the average first-neighbor interaction energies, $\epsilon_{kj}^{(2)}$, for various values of $j$ from 4 to 48. These extremes ($E_{\mathrm{min}}$ and $E_{\mathrm{max}}$) are plotted in Figure 1 (in units of calories per mole of first-neighbor interaction, *i.e.*, as $\epsilon'_{kj}{}^{(2)}$) together with empirical curves (polynomials in $1/j$) used to fit the data (from $j$ = 12 to $\infty$). For each size cluster from $j$ = 12 to 100, a Gaussian distribution was defined by[82]

$$\eta[\epsilon_{kj}^{(2)}] = [\eta_{\mathrm{T}_j}/\sigma(2\pi)^{1/2}]\exp\{-(1/2)[(\epsilon_{kj}^{(2)} - \mu)/\sigma]^2\} \tag{A-2}$$

where $\epsilon_{kj}^{(2)}$ is now a continuous variable

$$\mu = 2j(1 - y_{Bj})(E_{\mathrm{max}} + E_{\mathrm{min}})/2 \text{ for each } j \tag{A-3}$$

$$\sigma = 2j(1 - y_{Bj})(E_{\mathrm{max}} - E_{\mathrm{min}})/6 \text{ for each } j \tag{A-4}$$

and $\eta_{\mathrm{T}_j}$ is a normalizing factor, being the total number of hydrogen configurations for a $j$-size cluster, given approximately by

$$\ln(\eta_{\mathrm{T}_j}) = jy_{2j}\ln 2 + (jy_{3j} + jy_{4j})\ln(3/2) \tag{A-5}$$

where $jy_{ij}$ is the number of $i$-bonded species in a $j$-mer, $k$ ln (3/2) is the entropy per four-bonded species in ice (assumed here also for a three-bonded water molecule), and $k$ ln 2 is the entropy per two-bonded species (obtained by assuming that the free hydrogen of a "sequential" two-bonded water molecule can occupy either of two sites, independent of the hydrogen configuration of the rest of the cluster). It should be noted that the assumption of two hydrogen configurations per two-bonded species causes $(\eta_{\mathrm{T}_j})^{1/j}$ to increase with decreasing $j$, an aspect of $\eta_{\mathrm{T}_j}$ which was anticipated in the text (section IVA. Hydrogen Entropy and Bond Energy). Even though eq A-5 is approximate, it must be recalled that the hydrogen entropy in ice is only ~0.8 eu; therefore, a reasonable error in this quantity can be tolerated.

Using the continuous distribution function of eq A-2, the sum in eq A-1 was evaluated (by summation between $\mu - 3\sigma$ and $\mu + 3\sigma$), for $j \geq 12$. For clusters of size $j \leq 6$, where the Gaussian assumption breaks down, distribution functions obtained from model building (without the assumption of a Gaussian shape, and with $\eta_{\mathrm{T}_j}$ determined by model building and not by eq A-5) were used to evaluate this sum. For the region $j$ = 7 to 11, it was found that the thermodynamic properties of clusters obtained by extrapolating the Gaussian approximation to these smaller clusters joined reasonably smoothly with the results for $j \leq 6$ (except for $j$ = 7; the properties of this cluster were thus adjusted to fit this smooth extrapolation).

*Evaluation of* $\epsilon_j$. Once we have assumed that $\epsilon_j$ is independent of the hydrogen configuration of a $j$-sized cluster, we can evaluate it in a manner completely analogous to the treatment of second-neighbor, dispersion, and three-body, nonadditive interactions in ref 6 (the reader should refer to the Appendix of this reference in order to better understand what follows). We recognize that, while a water molecule in ice I participates as the central molecule in six linear trimer arrangements, a three-bonded water in a cluster (which, of course, is not ice) participates in only three such arrangements and a two-bonded water in only one. Examination of cluster models quickly reveals that two of the trimers in which a three-bonded water participates must be "sequential" (both accepting and donating one hydrogen in forming hydrogen bonds), while one trimer must be "nonsequential" (accepts or donates two hydrogens). A two-bonded water molecule is free to participate in either sequential or nonsequential trimers but, since sequential arrangements are considerably favored over nonsequential ones,[4,5] we consider only those clusters whose two-bonded waters participate in sequential trimers. We may now use the formalism employed in ref 6 to obtain energies characteristic of $i$-bonded molecules and write

$$\epsilon_j = \sum_{i=1}^{4} j y_{ij} e_i \tag{A-6}$$

where $jy_{ij}$ is the number of $i$-bonded molecules in a $j$-mer, $e_4$ is the three-body, second-neighbor, and dispersion energy contribution to the lattice energy of ice calculated in ref 6 (including a correction term, $e_{\mathrm{corr}}$), and the other $e_i$'s are

$$e_1 = (1/2)V_{\mathrm{AB}}^{\mathrm{D}} = -0.45 \text{ kcal/mol of one-bonded water}$$

$$e_2 = 2[V_{\mathrm{ABC}}^{(3)} + V_{\mathrm{AC}}^{(2)}]_{\mathrm{av\ seq}} + V_{\mathrm{AB}}^{\mathrm{D}} + V_{\mathrm{AC}}^{\mathrm{D}} = -2.97 \text{ kcal/mol of two-bonded water}$$

$$e_3 = 2[V_{\mathrm{ABC}}^{(3)} + V_{\mathrm{AC}}^{(2)}]_{\mathrm{av\ seq}} + [V_{\mathrm{ABC}}^{(3)} + V_{\mathrm{AC}}^{(2)}]_{\mathrm{av\ nonseq}} + (3/2)V_{\mathrm{AB}}^{\mathrm{D}} + 3V_{\mathrm{AC}}^{\mathrm{D}} + e_{\mathrm{corr}} = -4.16 \text{ kcal/mol of three-bonded water} \tag{A-7}$$

where the bracketed quantities are the average values of the three-body ($V_{\mathrm{ABC}}^{(3)}$) and second-neighbor ($V_{\mathrm{AC}}^{(2)}$) interaction potentials used in ref 6 for "sequential" and "nonsequential" trimers, and where the $V^{\mathrm{D}}$'s are dispersion interaction energies (see ref 6). All of the values pertain to an O$\cdots$O separation of 2.76 Å.[80] The $e_{\mathrm{corr}}$ term has been included here in $e_3$ and $e_4$ to account for third- and higher-neighbor interactions which we have so far ignored in the calculation of $\epsilon_j$, but which probably are of some importance in larger clusters.[84] $e_{\mathrm{corr}}$ is chosen arbitrarily as $-0.5$ kcal/mol so as to make the energy per mole of water in an infinite cluster match the experimentally estimated lattice energy of ice ($-13.4$ kcal/mol);[39] *i.e.*, $-0.5$ is added to the computed[6] latice energy ($-12.9$) at 2.76 Å to obtain $-13.4$ kcal/mol. It should be noted that we have also ignored four-body and higher cooperative terms in the calculation of $\epsilon_j$. The evidence now available seems to indicate that these terms should be small [$V^{(4)}$ is small for the cyclic tetramer[6]] and that the three-body effect should be the principal nonadditive contribution.[85]

In order to illustrate the cooperative nature of our treatment of sequential and nonsequential trimer effects, we have diagrammed the energies associated with 4-, 3-, 2-, and 1-bonded water molecules in Figure 3. In calculating the energy level associated with an $i$-bonded water molecule (shown in Figure 3), we have treated the near-neighbor interactions of this molecule as having the average value of $\epsilon_{kj}^{(2)}$ in ice ($\epsilon_{\mathrm{ice}}^{(2)} = -3.23$ kcal/mol;[6] *i.e.*, the dashed line of Figure 1). Then the energy level associated with an $i$-bonded molecule is given by

$$E_i = (i/2)\epsilon_{\mathrm{ice}}^{(2)} + e_i \tag{A-8}$$

These energy levels are compared in Figure 3 to those assumed by HSN.[3] It should be noted that the calculated value of $\epsilon_j$ includes the second-neighbor two-body interactions and the linear-trimer three-body interactions between all the water molecules in a $j$-sized cluster. These interactions have been partitioned among the $i$-bonded molecules by assigning an energy ($e_i$) to each molecule. It must be stressed that $e_i$ is not simply the interaction energy of an $i$-bonded molecule with its second neighbor molecules, but is rather an energy assigned to an $i$-bonded water molecule so that, when the sum in eq A-6 is evaluated, all three-body and second-neighbor two-body interactions in a $j$-sized cluster will be properly counted.

## Addendum

After this paper was completed, a preprint of a paper[86] came to our attention, in which Rahman and Stillinger have determined the distribution of hydrogen-bonded polygons in configurations generated by their molecular dynamics simulation for liquid water. The shape of the distribution of hydrogen-bonded polygons depends on the cut-off pair interaction energy ($V_{\mathrm{HB}}$[86]) used to define a "made" hydrogen bond. The distribution obtained with $V_{\mathrm{HB}} = -3.939$ kcal/mol (a value of $V_{\mathrm{HB}}$ which results in a temperature-invariant point in the pair interaction energy distribution function,[86] and therefore a value that the authors[86] feel is a reasonable choice for $V_{\mathrm{HB}}$) peaks at polygons of size 5 and 6 but includes nontrivial contributions from polygons of size 8, 9, and 10. The authors attribute the nonmonotonic behavior of this polygon distribution function in the neighborhood of 9- and 10-mers to the particular choice of $V_{\mathrm{HB}}$. They suggest that a slightly less negative value of $V_{\mathrm{HB}}$ would result in some 10-mers being counted as two 6-mers. Thus, aside from some uncertainty as to the importance of larger polygons (*i.e.*, of size 8, 9, and 10), these results seem to be in *qualitative* agreement with the results presented here in that they suggest the importance of small cyclic hydrogen-bonded structures in liquid water. It is interesting to note that these two theoretical studies, which start from entirely different sets of assumptions, lead to qualitatively similar predictions.

## References and Notes

(1) This work was supported by research grants from the National Science Foundation (GB-28469X3) and from the National Institute of General Medical Sciences of the National Institutes of Health, U. S. Public Health Service (GM-14312).

(2) (a) NIH predoctoral trainee; (b) Cornell University.

(3) A. T. Hagler, H. A. Scheraga, and G. Némethy, *J. Phys. Chem.*, **76**, 3229 (1972).

(4) J. Del Bene and J. A. Pople, *J. Chem. Phys.*, **52**, 4858 (1970).

(5) D. Hankins, J. W. Moskowitz, and F. H. Stillinger, *J. Chem. Phys.*, **53**, 4544 (1970).

(6) B. R. Lentz and H. A. Scheraga, *J. Chem. Phys.*, **58**, 5296 (1973).

(7) B. R. Lentz, Ph.D. Thesis, Cornell University, Aug. 1973.

(8) It was shown previously[3] that this is a generous upper limit, there being a negligible number of clusters of such large size.

(9) A. Ben-Naim and F. H. Stillinger, Jr., in "Water and Aqueous Solutions," R. A. Horne, Ed., Wiley-Interscience, New York, N. Y., 1972, Chapter 8.

(10) A. T. Hagler, H. A. Scheraga, and G. Némethy, *Ann. N. Y. Acad. Sci.*, **204**, 51 (1973).

(11) P. Krindel and I. Eliezer, *Coord. Chem. Rev.*, **6**, 217 (1971).

(12) R. A. Horne, Ed., "Water and Aqueous Solutions," Wiley-Interscience, New York, 1972.

(13) F. Franks, Ed., "Water, a Comprehensive Treatise," Vol. 1, Plenum Press, New York, N. Y., 1972.

(14) A. Rahman and F. H. Stillinger, *J. Chem. Phys.*, **55**, 3336 (1971).

(15) F. H. Stillinger and A. Rahman, *J. Chem. Phys.*, **57**, 1281 (1972).

(16) G. M. Bell, *J. Phys. C*, **5**, 889 (1972).

(17) O. Weres and S. A. Rice, *J. Amer. Chem. Soc.*, **94**, 8983 (1972).

(18) Actually, the application of cell theory to liquid water, as in ref 16 and 17, is not new. To our knowledge, two earlier treatments[19,20] of this type have been published.

(19) M. Weissmann and L. Blum, *Trans. Faraday Soc.*, **64**, 2605 (1968).

(20) K. Arakawa and K. Sasaki, *Bull. Chem. Soc. Jap.*, **43**, 3048 (1970).

(21) C. A. Angell, *J. Phys. Chem.*, **75**, 3698 (1971).

(22) B. R. Lentz, A. T. Hagler, and H. A. Scheraga, *J. Phys. Chem.*, in press.

(23) G. E. Walrafen, *J. Chem. Phys.*, **47**, 114 (1967).

(24) G. E. Walrafen, *J. Chem. Phys.*, **48**, 244 (1968).

(25) A recent review of spectral investigations of water interpreted from the point of view of a "consecutive hydrogen-bond disruption model" is given by G. E. Walrafen in Chapter 5 of ref 13.

(26) D. Eisenberg and W. Kauzmann, "The Structure and Properties of Water," Oxford University Press, New York, N. Y. 1969, p 174.

(27) B. Kamb, *J. Chem. Phys.*, **43**, 3917 (1965).

(28) Actually, Weres and Rice[17] claim to use a unit of the ice VIII lattice as their model. The detailed structure of this form of ice is not known, but it is thought to involve a distortion of the ice VII structure, but with the protons ordered.[29]

(29) B. Kamb in "Structural Chemistry and Molecular Biology," A. Rich and N. Davidson, Ed., W. H. Freeman and Co., San Francisco, Calif., 1968, pp 507–542.

(30) In ref 3, arguments are given against two-state theories basically because they neglect the fact that in real water there must exist a whole range of possible states of a water molecule. While this is true, it is an important fact that many of the observed properties of water can be interpreted to a reasonable first approximation in terms of a simple two-state picture.[31]

(31) C. M. Davis and J. Jarzynski in Chapter 10 of ref 12.

(32) A. H. Narten and H. A. Levy, *Science*, **165**, 447 (1969).

(33) Initially, the partition function was formulated by allowing for the existence of all possible clusters of size from 1 to 100. In that formulation, allowance was made for the various possible arrangements of the oxygens in a cluster of given size, a crude method was used to estimate the normal-mode frequencies of a cluster of given size, and a continuous, singly-peaked $\gamma$ distribution was used to describe the distribution of cluster sizes (as in ref 3). Calculations with this preliminary formulation of the partition function (reported elsewhere[7]) indicated that there is a negligible number of clusters containing ten or more water molecules. Therefore, the final formulation of the partition function, reported in this paper, is based on the earlier conclusion[7] that clusters containing only from one to nine water molecules need be considered. This is substantiated by our final results which show that even the mole fraction of 9-mers is small.

(34) T. L. Hill, "An Introduction to Statistical Thermodynamics," Addison-Wesley, Reading, Mass., 1960.

(35) In the results (presented in section VIII), we test to some extent the effects of this assumption by allowing for the simultaneous existence of two cluster species of size 5; *viz.*, a cyclic one with five hydrogen bonds (the maximum number possible for this size cluster) and one with four hydrogen bonds (specifically a "star" pentamer having a central water molecule tetrahedrally hydrogen bonded to four others, this being the pentamer considered by HSN[3]). Since these two pentamers have completely different hydrogen-bonded geometries, they will naturally have different vibrational partition functions, as well as a different number of hydrogen bonds.

(36) L. Pauling, *J. Amer. Chem. Soc.*, **57**, 2680 (1935).

(37) Even though the present treatment considers only clusters of size 1 to 9, we present the development of the IC partition function for all clusters of size 1 to 100 as in the preliminary calculations.[7] This is necessary since the treatment of clusters of size 7, 8, and 9 depends on the results of the treatment of larger clusters (specifically $j \geq 12$; see Appendix).

(38) G. Némethy and H. A. Scheraga, *J. Chem. Phys.*, **36**, 3382 (1962).

(39) The quantity 13,400 cal/mol is the lattice energy of ice at 0°K as calculated on p 139 of ref 26. This calculation involves use of estimates of the intermolecular zero-point energy in ice (3500 cal/mol) and the shift in intramolecular zero-point energy on going from ice to vapor (1400 cal/mol) made by Whalley.[40] While we were in the process of writing this paper, a new (as yet unpublished) estimate of these quantities was brought to our attention.[41] We have chosen to continue to use the old estimates because (a) we feel they involve no more uncertainty than the new estimates (in particular, the new estimate of the intermolecular zero-point energy is inconsistent with an independent estimate derived from heat capacity data,[42] which agrees with Whalley's old estimate[40]), (b) inclusion of these new estimates[41] in our results (see section VIII) would cause the parameter *a* to decrease by $\sim$2.5% (certainly a trivial uncertainty given the approximations made in our theory).

(40) E. Whalley, *Trans. Faraday Soc.*, **53**, 1578 (1957).

(41) E. Whalley in "Physics and Chemistry of Ice," E. Whalley, S. Jones, and J. W. Gold, Ed., Royal Society of Canada, in press.

(42) A. J. Leadbetter, *Proc. Roy. Soc., Ser. A*, **287**, 403 (1965).

(43) H. Prask, H. Boutin, and S. Yip, *J. Chem. Phys.*, **48**, 3367 (1968).

(44) It should be noted that this scaling procedure might introduce an error into the treatment since some highly coupled librational modes should probably not be scaled to the same extent as are the essentially uncoupled motions of a tetrahedrally bonded molecule. This might make the frequencies of some modes lower than they would have been had a better potential been available, enabling us to avoid the approximation of rescaling.

(45) J. L. Lebowitz and J. S. Rowlinson, *J. Chem. Phys.*, **41**, 133 (1964).

(46) J. L. Lebowitz, *Phys. Rev.*, **133**, A895 (1964).

(47) As in ref 3, the effective diameter per molecule in a *j*-size cluster, $R_{\mathrm{eff},j}$, is defined by $V_j/j = (\pi/6)(R_{\mathrm{eff},j})^3 = (\pi/6)R_j^3/j$.

(48) Actually, the hard-sphere volume of a *j*-mer is related to the measured displaced volume by a conversion factor that relates the measured displaced volume of a monomer to $V_1 = (\pi/6)(2.90\ \text{Å})^3$.

(49) P. R. Bevington, "Data Reduction and Error Analysis for the Physical Sciences," McGraw-Hill, New York, N. Y., 1969, Chapters 10 and 11.

(50) M. J. D. Powell, *Computer J.*, **7**, 155 (1964).

(51) R. Fletcher, *Computer J.*, 13, 317 (1970). See also R. Fletcher in report No. HL71/3566 of the U.K.A.E.A. Research Group, Atomic Energy Research Establishment, Harwell, Didcot, Berkshire, England.

(52) The reduced $\chi^2$, as described by Bevington,[49] is a measure of the goodness of fit after the variance of the experimental data has been taken into account. Since the error in the experimental data was estimated by HSN to be 2–3%, we have taken 2.5% as the variance in all experimental data. A value of the reduced $\chi^2$ less than about 1.5 would indicate that the fitting function is probably a reasonable description of the experimental data.[49]

(53) Actually, clusters of all sizes should be allowed to exist with all possible oxygen arrangements; this would account explicitly for the oxygen-randomness entropy discussed in section IV.[54] Such an expensive calculation cannot be done at this time, although a test calculation to determine the importance of this effect certainly does seem worthwhile. We have chosen the "star" pentamer for this test calculation, principally for convenience (*viz.*, its normal-mode frequencies have already been calculated[22]), and because the cyclic pentamer was one of the most populous species present in our original results (*i.e.*, those briefly discussed in section VIIIA).

(54) Inclusion of the "star" pentamer as an additional cluster species in eq 1 of section IV (see also footnote 35) results in an added entropy of mixing which appears as part of $F_{\mathrm{trans}}$ in the results of section VIIIB. This can be identified as part of the oxygen-randomness entropy discussed in section IV. Unlike the crude treatment given by HSN[3] and by us (in our preliminary calculations[7]), this method of including the oxygen entropy allows for the expected temperature dependence of this quantity.

(55) The experimental values of the free energy, internal energy, and entropy are those used by HSN[3] and were taken from ref 56a and 56b. The experimental heat capacity is calculated from eq 12 given in ref 57.

(56) (a) W. E. Sharp, Report of the Lawrence Radiation Laboratory, University of California UCRL 7118 (1962); (b) N. E. Dorsey, "Properties of Ordinary Water Substance," ACS Monograph No. 81, Reinhold, New York, N. Y., 1940.

(57) G. S. Kell in ref 13, Chapter 10.

(58) M. S. Jhon, J. Grosh, T. Ree, and H. Eyring, *J. Chem. Phys.*, **44**, 1465 (1966).

(59) W. A. P. Luck, *Discuss. Faraday Soc.*, **43**, 132 (1967).

(60) W. A. P. Luck in "Physico-Chemical Processes in Mixed Aqueous Solvents," F. Franks, Ed., Heinemann, London, 1967, p 11.

(61) W. A. Senior and R. E. Verrall, *J. Phys. Chem.*, **73**, 4242 (1969).

(62) H. R. Wyss and M. Falk, *Can. J. Chem.*, **48**, 607 (1970).

(63) Only qualitative comparison is possible because of the uncertainties about selection rules and individual band intensities in the infrared and Raman experiments. A similar uncertainty occurs in the effective spectral densities derived from neutron scattering measurements, and enhances the librational portion of the spectrum considerably relative to the translational portion.[43]

(64) G. E. Walrafen in "Hydrogen-Bonded Solvent Systems," A. K. Covington and P. Jones, Ed., Taylor and Francis, London, 1968, pp 9–29.

(65) D. A. Draegert, N. W. B. Stone, B. Curnutte, and D. Williams, *J. Opt. Soc. Amer.*, **56**, 64 (1966).

(66) G. E. Walrafen, *J. Chem. Phys.*, **40**, 3249 (1964).

(67) J. O. Burgman, J. Sciesinski, and K. Skold, *Phys. Rev.*, **170**, 808 (1968).

(68) P. von Blanckenhagen, *Ber. Bunsenges. Phys. Chem.*, **76**, 891 (1972).

(69) Large uncertainties in the neutron scattering data prevent detailed interpretation of band shapes and peak positions in the frequency spectra obtained by this technique in the region of librational normal modes. Specifically, the question of a high-frequency component (at about 900–1000 cm$^{-1}$) in these spectra would seem to be unresolved.[43,67,68,70]

(70) S. Yip, private communication.

(71) W. M. Slie, A. R. Donfor, Jr., and T. A. Litovitz, *J. Chem. Phys.*, **44**, 3712 (1966).

(72) A. H. Narten and H. A. Levy in ref 13, Chapter 8.

(73) P. A. Egelstaff, "An Introduction to the Liquid State," Academic Press, New York, N. Y., 1967, Chapter 7, especially section 7.6.

(74) Egelstaff notes, in fact, that approximations such as those used here are inadequate even for a simple fluid such as argon, near its triple point.

(75) We note that the parameter a contains not only the background interaction, but also the shift in intramolecular zero-point energy on transferring an O–H group from the gas into the liquid ($-b'/V$; see section IVA). Thus, the actual intermolecular background interaction is somewhat smaller than 5080 cal/mol of bond.

(76) L. L. Shipman and H. A. Scheraga, *J. Phys. Chem.*, **78**, 909 (1974).

(77) Use of the configurational partition function obtained from the Percus–Yevick equation should, in fact, underpredict the unfavorability of large, bulky clusters. This results because the hard-sphere pressure derived from the Percus–Yevick equation is expected to be an underestimate of the correct value at large packing densities, $\xi$ ($P_{HS} \rightarrow \infty$ as $\xi \rightarrow 1$, instead of at the value of $\xi$ characteristic of close-packed spheres, *viz.*, 0.74);[45] and the work of placing a large sphere into the liquid is approximately $P_{HS} \times$ volume of the sphere.[45]

(78) (a) H. S. Frank and W. Y. Wen, *Discuss. Faraday Soc.*, **24**, 133 (1957); (b) H. S. Frank, *Proc. Roy. Soc., Sec. A*, **247**, 481 (1958).

(79) N. S. Snider and T. M. Herrington, *J. Chem. Phys.*, **47**, 2248 (1967).

(80) Actually, the oxygen–oxygen distances used for a given cluster (there can be a range of distances for each cluster corresponding to different oxygen–oxygen pairs within the cluster) should be those that will minimize the total internal potential energy of the cluster. With the crude set of potentials used here, it would be impossible to carry out such a minimization procedure. Thus we have chosen to use the oxygen–oxygen distance observed for ice I[81] for all clusters.

(81) Reference 26, p 71.

(82) The definitions of $\mu$ and $\sigma$ are based on the assumption that almost all hydrogen configurations of a cluster should have average near-neighbor energies that fall between $E_{min}$ and $E_{max}$; *i.e.*, these limits are those for which 99.7% fall within $\pm 3\sigma$ of the average energy.[83]

(83) Reference 49, p 308.

(84) Third and fourth neighbor contributions to the lattice energy of ice are estimated[6] to be about −0.7 kcal/mol.

(85) It is possible to reproduce almost exactly the energy of a tetrahedral pentamer of water, calculated by Del Bene and Pople,[4] using the two- and three-body potentials which Del Bene and Pople derived from their study of a linear trimer of water.[4] This implies that, for such a tetrahedral structure, the four-body and five-body terms that Del Bene and Pople's *ab initio* calculations[4] would predict are either very small or they fortuitously cancel.

(86) A. Rahman and F. H. Stillinger, *J. Amer. Chem. Soc.*, **95**, 7943 (1973), preprint provided by F. H. Stillinger.

---

# Crystal Structure of a Dealuminated Y-Type Zeolite

**P. Gallezot,*[1] R. Beaumont, and D. Barthomeuf**

*Institut de Recherches sur la Catalyse CNRS, 69100 Villeurbanne, France and Université Claude Bernard, Lyon I, France*

*(Received March 4, 1974)*

*Publication costs assisted by the Centre National de la Recherche Scientifique*

The occupancy factor of Al and Si atoms in a 53% dealuminated Y zeolite has been determined and compared with that of the nondealuminated Y sample. The value is close to 1 in both cases. This indicates that aluminum extraction does not leave holes in the structure. It is likely that a silica migration causes a local recrystallization of the framework. The result is supported by a lack of any lattice defects and also by a decrease in unit cell constant.

## Introduction

The general methods for preparing the dealuminated zeolites derived from Y type zeolite and the various concepts on the nature of these materials have been recently reviewed by Kerr.[2a] The thermal treatments of $NH_4Y$ or HY zeolites in presence of water vapor or the chemical treatments with EDTA produce a migration or a removal of aluminum atoms from the zeolite framework. However there is still controversy about the new local arrangement of the framework at the site where an aluminum atom has been removed. Early Kerr[2b] proposed that each missing aluminum site is occupied by four hydrogen bonding to the oxygen atoms of the vacated tetrahedron. On heating, these OH groups would be expected to condense and new Si–O–Si bonds would be formed in the framework. The X-ray work of Maher, *et al.*,[3] has shown that after a specific treatment (sample IV) the occupancy factor of T (Si,Al) framework sites reaches unity and this was interpreted as being due to a migration of silicon atoms into the sites left vacant by aluminum removal. The same interpretation was given by Scherzer and Bass[4] on the basis of infrared results indicating an increase in the "degree of ordering" of the dealuminated zeolite. Peri[5] considering the shift to higher frequencies of the framework ir vibrations proposed that the Si atoms replace the lost Al atoms through a recrystallization of the framework. Vedrine, *et al.*,[6] have concluded from epr study of a deep-bed calcinated zeolite that vacancies of framework atoms are very unlikely to occur.

However these studies concern the ultrastable zeolites prepared at high temperature under hydrothermal conditions which according to Wyart and Sabatier[7] facilitate the transport of silica. The present work is devoted to an aluminum deficient zeolite (Na,H) [5.7]Y obtained by chemical extraction.[8] Crystal structures of the dealuminated sample and of a reference sample (Na,H) [2.5]Y were determined in order to observe modifications occuring in the zeolite framework during the dealumination process.

## Experimental Section

*Materials.* Commercial Union Carbide NaY has been used as a starting material and studied in its protonic form. The aluminum atoms have been removed by an aqueous solution of ethylenediaminetetraacetic acid (EDTA) according to the process described by Kerr.[2] No loss of silica has been detected in the extraction solution. The material obtained and the starting zeolite have the composition given in Table I.

*X-Ray Procedures.* The X-ray powder diffraction patterns were obtained by using a Guinier-type camera with the Cu K$\alpha$ radiation monochromatized with a curved

**TABLE I**

| Zeolite | Al/uc[a] | Si/Al | Na/uc |
|---|---|---|---|
| (NaH) [2.5]Y | 56 | 2.5 | 8.7 |
| (NaH) [5.7]Y | 26.5 | 5.7 | 4.2 |

[a] uc = unit cell.

quartz crystal. The camera has high temperature and controlled atmosphere attachments. The sample is mounted on a platinum grid which can be heated by a stabilized low voltage electric current. The temperature is estimated from a calibration curve giving the temperature as a function of the intensity of the heating current and also from the thermal expansion of the unit cell constant of the grid platinum. Cubic unit cell constant were obtained by averaging the values derived from ten diffraction lines at high Bragg angles the camera being properly calibrated. Multiple film technique was used to collect diffraction lines which were photometered and planimetered. Line intensities were corrected for absorption by the sample, for sample to film distances, and for the Lorentz polarization and multiplicity factors. The correction mentioned above are included in the ORFLS refinement program which has been also modified to derive structure factors from line intensities.[9] To represent the partially covalent character of the atoms present, scattering factors for $O^-$ were used and (Si,Al) sites weighted 2:4:3 for $Si^0$, $Si^{3+}$, and $Al^{2+}$. Atomic parameters were refined with 232 structure factors corresponding to all reflections with $h^2 + k^2 + l^2 \leq 395$ except the 111 line. Each structure factor was weighted at unity. It must be stressed that the structures were refined on the basis of structure factors derived from line intensities; this unavoidably lead to underestimated $R$ indexes and standard errors.

*Zeolites Treatment.* The reference and dealuminated sample were heated to 400° on the platinum grid of the camera in a current of dry oxygen. Then they were kept at 400° under a nitrogen atmosphere during the X-ray exposure (48 hr).

## Results and Discussion

It must be remembered that aluminum and silicon atoms cannot be distinguished from each other because of their nearly equal scattering factors; they will be mentioned as T atoms. If the dealumination process leaves vacancies in the framework, the occupancy factor (OF) of the T sites would be lower than unity; in the present case the OF are expected to decrease from 1 to 162/192 = 0.84 since ~30 Al atoms have been extracted. However meaningless variation or constancy of the OF may occur during a least-squares refinement because there is a close correlation between OF, temperature factors, and even scale factor. In order to detect physically meaningless OF variations the crystal structure of the reference sample (Na,H) [2.5]Y was also determined and the OF of its framework atoms were allowed to vary. Moreover several refinements were computed to test the reliability of the framework atoms population. The corresponding atomic parameters are listed in Table II. Interatomic distances and angles computed from the atomic coordinates issued from refinement IV are given in Table III. A structure factors listing corresponding to refinement IV are available in the microfilm edition of the journal.[10] During refinement I the OF of the framework atoms were fixed at 1 and the scale factor, coordinates, and temperature factors were refined. The resulting new parameters were then fixed on refinement II whereas the OF were allowed to vary. In refinement III only the parameters of T atoms were refined. Table III shows that the OF have not deviated appreciably from unity during refinement II and III. Finally all the parameters except the scale factor were refined simultaneously (refinement IV). After five least-squares iterations the OF have not diverged too much from their initial values. Moreover the deviations from unity are greater for the reference sample than for the dealuminated sample. Other trials have been performed, for example, refining the OF while the temperature factors were fixed at low values. In any case the OF have about the same magnitude for both samples and never approach the 0.84 value expected for a 53% dealuminated sample having permanent vacancies.

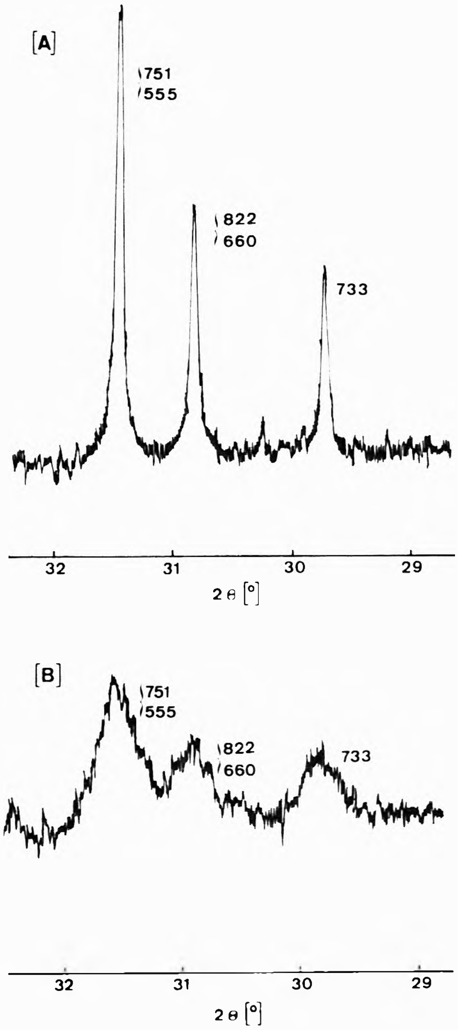

Figure 1. Effect of the dehydroxylation of the HY zeolite on line profile and background level of its X-ray pattern: (A) HY zeolite heated for 15 hr in flowing $O_2$ at 400°; (B) same conditions but 550°. (Microphotometer recording of Guinier photograph taken with Cu K$\alpha_1$ radiation).

These results clearly show that the dealumination treatment does not induce significant change of the OF of framework atoms. Two interpretations may account for those data: (i) the removal of aluminum atoms destroys completely a part of the zeolite but the dealumination treatment leaves the other part unchanged; (ii) the aluminum atoms are homogeneously removed from the framework and the vacancies are refilled through a local recrys-

**TABLE II: Atomic Coordinates, Temperature Factors, and Occupancy Factors**

| | | Reference sample ($a$ = 24.67 Å) | | | | Dealuminated sample ($a$ = 24.53 Å) | | | |
|---|---|---|---|---|---|---|---|---|---|
| | | Ref I[a] | Ref II | Ref III | Ref IV | Ref I | Ref II | Ref III | Ref IV |
| T | X | 0.1259(1) | 0.1259 | 0.1258(1) | 0.1258(1) | 0.1262(2) | 0.1262 | 0.1264(2) | 0.1265(2) |
| (Si,Al) | Y | −0.0537(1) | −0.0537 | −0.0537(1) | −0.0537(1) | −0.0537(2) | −0.0537 | −0.0536(2) | −0.0536(2) |
| | Z | 0.0363(1) | 0.0363 | 0.0363(1) | 0.0362(1) | 0.0369(2) | 0.0369 | 0.0371(2) | 0.0370(2) |
| | B | 2.4(1) | 2.4 | 2.3(1) | 2.1(2) | 1.7(2) | 1.7 | 1.6(2) | 1.5(2) |
| | OF[b] | 1 | 0.998(5) | 0.990(10) | 0.972(10) | 1 | 0.999(8) | 0.996(15) | 0.988(17) |
| | P[c] | 192 | 191.6(1.0) | 190(2) | 187(2) | 192 | 191.9(1.5) | 191.2(3.0) | 189.7(3.2) |
| | X = −Y | 0.1059(2) | 0.1059 | 0.1059 | 0.1063(2) | 0.1059(4) | 0.1059 | 0.1059 | 0.1059 |
| O1 | Z | 0.0 | 0.0 | 0.0 | 0.0 | 0.0 | 0.0 | 0.0 | 0.0 |
| | B | 4.1(3) | 4.1 | 4.1 | 4.5(4) | 2.4(3) | 2.4 | 2.4 | 2.0(5) |
| | OF | 1 | 0.99(2) | 1 | 1.01(2) | 1 | 1.01(2) | 1 | 0.99(3) |
| | P | 96 | 95(2) | 96 | 97(2) | 96 | 97(2) | 96 | 95(3) |
| | X = Y | −0.0019(3) | −0.0019 | −0.0019 | −0.0020(3) | −0.0021(4) | −0.0021 | −0.0021 | −0.0023(4) |
| O2 | Z | 0.1419(4) | 0.1419 | 0.1419 | 0.1419(3) | 0.1414(5) | 0.1414 | 0.1414 | 0.1410(5) |
| | B | 3.9(3) | 3.9 | 3.9 | 4.2(4) | 2.4(3) | 2.4 | 2.4 | 2.6(6) |
| | OF | 1 | 1.00(2) | 1 | 1.04(4) | 1 | 0.99(2) | 1 | 0.99(4) |
| | P | 96 | 96(2) | 96 | 100(4) | 96 | 95(2) | 96 | 95(4) |
| | X = Y | 0.1760(3) | 0.1760 | 0.1760 | 0.1757(3) | 0.1748(4) | 0.1748 | 0.1749 | 0.1746(4) |
| O3 | Z | −0.0369(4) | −0.0369 | −0.0369 | −0.0362 | −0.0378(6) | −0.0378 | −0.0378 | −0.0378(6) |
| | B | 4.3(3) | 4.3 | 4.3 | 6.1(5) | 4.0(4) | 4.0 | 4.0 | 5.2(7) |
| | OF | 1 | 1.02(2) | 1 | 1.12(3) | 1 | 1.00(2) | 1 | 1.07(5) |
| | P | 96 | 98(2) | 96 | 107(3) | 96 | 96(2) | 96 | 103(5) |
| | X = Y | 0.1771(3) | 0.1771 | 0.1771 | 0.1772(3) | 0.1783(4) | 0.1783 | 0.1783 | 0.1785(4) |
| O4 | Z | 0.3225(4) | 0.3225 | 0.3225 | 0.3220(4) | 0.3222(6) | 0.3222 | 0.3222 | 0.3222(6) |
| | B | 4.2(3) | 4.2 | 4.2 | 5.2(4) | 4.1(4) | 4.1 | 4.1 | 4.7(7) |
| | OF | 1 | 1.00(2) | 1 | 1.06(3) | 1 | 1.00(2) | 1 | 1.04(4) |
| | P | 96 | 96(2) | 96 | 102(3) | 96 | 96(2) | 96 | 100(4) |
| X = Y = | Z | 0.0 | 0.0 | 0.0 | 0.0 | 0.0 | 0.0 | 0.0 | 0.0 |
| NaI | B | 2.5 | 2.5 | 2.5 | 2.5 | 2.5 | 2.5 | 2.5 | 2.5 |
| | OF | 0.20(3) | 0.20 | 0.20 | 0.20(3) | 0.19(4) | 0.19 | 0.19 | 0.20(4) |
| | P | 3.2(5) | 3.2 | 3.2 | 3.2(5) | 3.0(6) | 3.0 | 3.0 | 3.2(6) |
| X = Y = | Z | 0.055(2) | 0.055 | 0.055 | 0.057(2) | 0.062(3) | 0.062 | 0.062 | 0.061(2) |
| NaI′ | B | 2.5 | 2.5 | 2.5 | 2.5 | 2.5 | 2.5 | 2.5 | 2.5 |
| | OF | 0.10(2) | 0.10 | 0.10 | 0.10(2) | 0.15(3) | 0.15 | 0.15 | 0.16(3) |
| | P | 3.2(6) | 3.2 | 3.2 | 3.2(6) | 4.8(1.0) | 4.8 | 4.8 | 5.1(1.0) |
| X = Y = | Z | 0.233(2) | 0.233 | 0.233 | 0.233(2) | 0.235(4) | 0.235 | 0.235 | 0.233(5) |
| NaII | B | 2.5 | 2.5 | 2.5 | 2.5 | 2.5 | 2.5 | 2.5 | 2.5 |
| | OF | 0.12(2) | 0.12 | 0.12 | 0.13(3) | 0.07(3) | 0.07 | 0.07 | 0.07(3) |
| | P | 3.9(6) | 3.9 | 3.9 | 4(1) | 2.2(1.0) | 2.2 | 2.2 | 2(1) |

[a] Ref = refinement. [b] OF = occupancy factor. [c] P = population.

tallization process. The first interpretation can be readily discarded. The complete destruction of a part of the structure is not likely since, first of all, no silica has been found in the extraction solution and, secondly, some properties of the zeolite have been modified. The unit cell parameter of dealuminated zeolite (24.53 Å) has undergone a strong decrease with respect to the reference sample (24.67 Å). Infrared studies also indicate changes in vibration frequencies of T-O bonds.[11] Moreover the dealuminated material exhibits specific properties such as improved thermal stability and marked changes in acid, adsorptive, and catalytic properties[8,12-14] which can be related only to change in the framework composition.

The second interpretation implies a local recrystallization in the framework because no significant amount of atom vacancies has been detected in the dealuminated zeolite. Moreover the X-ray pattern of the dealuminated zeolite does not exhibit any broadening of diffraction lines or anomalous fall of line intensities (particularly notable at high Bragg angles). These features can be observed whenever structure defects are present, for example, the diffraction pattern of a dehydroxylated HY zeolites gives tangible evidence of faults corresponding to atom vacancies and atom shifts in the tetrahedra altered by the dehydroxylation (Figure 1). There would be far more severe framework defects if there were no recrystallization in the dealuminated zeolite. Indeed there are 30 missing Al atoms per unit cell so that 30 tetrahedra would be permanently damaged and 120 tetrahedra (sharing corners with the 30) would be expected to suffer some distorsion. Such defects would be undoubtably revealed by the X-ray powder pattern. They would also give some modifications of the infrared spectra of framework vibrations; in fact the only changes noted for dealuminated samples concern the dependence of the vibration frequencies of T-O bonds on Si/Al ratio[11] as was previously obtained in a series of non-aluminum deficient zeolites.[15]

The most probable scheme of recrystallization supposes that the tetrahedron touched by aluminum extraction must be rebuilt around a silicon atom. This raises two questions: where do the silicon atoms originate and how are they transported? There are two possible sources of silicon atoms in the materials, siliceous impurities often present in synthetic zeolites and the silicon atoms of the zeolite framework. If silica comes from impurities this involves a dissolution and transport of silica in the liquid phase. Moreover the amount of such impurities should be, at least, nearly 10% of the zeolite weight. Because of this rather high value and the lack of silica in the solution (which pH would not facilitate the silica dissolution), this source of silicon atoms is unlikely. If the silicon atoms originate from the framework (more probably in the form of

**TABLE III: Interatomic Distances (Å) and Bond Angles (Deg) (after Refinement IV)**

| | Reference sample | Dealuminated sample |
|---|---|---|
| T–O(1) | 1.648(4) | 1.651(6) |
| T–O(2) | 1.635(4) | 1.624(5) |
| T–O(3) | 1.637(4) | 1.615(6) |
| T–O(4) | 1.622(4) | 1.598(7) |
| M | 1.635 | 1.622 |
| O(1)–O(2) | 2.72(1) | 2.68(1) |
| O(1)–O(3) | 2.64(1) | 2.60(1) |
| O(1)–O(4) | 2.65(1) | 2.63(1) |
| O(2)–O(3) | 2.65(1) | 2.64(1) |
| O(2)–O(4) | 2.67(1) | 2.66(1) |
| O(3)–O(4) | 2.69(1) | 2.67(1) |
| M | 2.67 | 2.65 |
| O(1)–T–O(2) | 110.8(3) | 109.2(5) |
| O(1)–T–O(3) | 106.5(4) | 105.2(6) |
| O(1)–T–O(4) | 107.4(4) | 107.6(6) |
| O(2)–T–O(3) | 107.8(4) | 108.6(6) |
| O(2)–T–O(4) | 109.5(4) | 110.2(6) |
| O(3)–T–O(4) | 110.3(4) | 111.3(6) |
| M | 108.7 | 108.7 |
| T–O(1)–T | 139.0(5) | 141.1(5) |
| T–O(2)–T | 147.0(5) | 150.6(5) |
| T–O(3)–T | 145.1(5) | 148.0(5) |
| T–O(4)–T | 142.5(5) | 139.6(5) |
| M | 143.4 | 144.8 |

silica such as $Si(OH)_4$), they have to move in the bulk of a particle to replace Al atoms. Peri suggested that in his samples, obtained without a liquid phase, there is a jump of silica from hole to hole to rebuild the aluminosilicate structure. So the surface of the particle should become richer in alumina. In the present dealumination process occuring in aqueous media, it is possible to imagine two limiting processes. One, deduced from that of Peri in which each aluminum atom removed is replaced by another atom such as in a vessell full of balls, a ball destroyed would be replaced by another ball by settling with respect to structural requirements. The process may consist of a permanent, rather low, homogeneous, local recrystallization with no need to invoke an enrichment of the surface in aluminum atoms. The second process also involves a local recrystallization of the framework, new $SiO_4$ tetrahedra being formed in the place of the $AlO_4^-$ removed. The silica needed for this process would originate from a destroyed part of each crystallite *via* diffusion along the porous network. Thus the crystal structure of external surface layers may well be destroyed during the leaching treatment with EDTA which simultaneously removes the Al atoms from the bulk (a rounding off of crystallites due to the destruction of surface layers may even occur during current ion-exchange process as shown by Penchev, *et al.*[16]). These destroyed layers would act as a silica source for the inside of the crystallites and the aluminum atoms contained in this part would react with EDTA so that no amorphous material would be left.

In both processes, about 19% of the volume of each crystallite is enough to yield a sufficient amount of silicon for the recrystallization and the particle size would be decreased in the same manner by Al removal. A calculation made on a theoretical spheric crystal, of which the radius is 1000 Å, indicated that only a 68-Å thick spheric shell (less than three unit cells) has to be removed for the dealuminated sample studied here. The two schemes proposed are not in disagreement with the proposed mechanisms for zeolite crystallization. In fact, the dealumination is performed during several hours, in aqueous media, and at about 100°. To obtain a well-crystallized dealuminated sample requires several hours. (The fast introduction of large amounts of extracting agent EDTA involves lattice defects.) Therefore the silica transport could be explained by the concept of surface diffusion at the liquid-solid interfaces.[17]

## Conclusion

The assumption that dealumination is followed by a local recrystallization in the framework is in agreement with the structural results obtained in this work. Indeed the process involving the formation of new $SiO_4$ tetrahedra in the framework positions damaged by alumina removal accounts for the invariability of the framework atoms occupancy factors, the absence of lattice defects, and the decrease of unit cell constant due to the greater proportion of Si–O bonds in the framework.

Moreover this hypothesis fully explains other particular properties such as increase of thermal stability, regular changes with alumina content in vibration frequencies of T–O bonds, and, in acid, adsorption and catalytic properties.

*Supplementary Materials Available.* A listing of structure factors will appear following these pages in the microfilm edition of this volume of the journal. Photocopies of the supplementary material from this paper only or microfiche (105 × 148 mm, 24× reduction, negatives) containing all of the supplementary material for the papers in this issue may be obtained from the Journals Department, American Chemical Society, 1155 16th St., N.W., Washington, D. C. 20036. Remit check or money order for $3.00 for photocopy or $2.00 for microfiche, referring to code number JPC-74-1550.

## References and Notes

(1) Address correspondence to Institut de Recherches sur la Catalyse CNRS.
(2) (a) G. T. Kerr, *Advan. Chem. Ser.*, **No. 121**, 219 (1973); (b) *J. Phys. Chem.*, **72**, 2594 (1968).
(3) P. K. Maher, F. D. Hunter, and J. Scherzer, *Advan. Chem. Ser.*, **No. 101**, 266 (1971).
(4) J. Scherzer and J. L. Bass, *J. Catal.*, **28**, 101 (1973).
(5) J. B. Peri, *Proc. Int. Congr. Catal., 5th*, **1**, 329 (1972).
(6) J. C. Vedrine, A. Abou-Kais, J. Massardier, and G. Dalmai-Imelik, *J. Catal.*, **29**, 120 (1973).
(7) J. Wyart and G. Sabatier, *C. R. Acad. Sci., Paris*, **238**, 702 (1954).
(8) R. Beaumont and D. Barthomeuf, *J. Catal.*, **26**, 218 (1972).
(9) P. Gallezot, Y. Ben Taarit, and B. Imelik, *J. Catal.*, **26**, 295 (1972).
(10) See paragraph at the end of paper regarding supplementary material.
(11) P. Pichat, R. Beaumont, and D. Barthomeuf, *C. R. Acad. Sci., Paris*, **272**, 612 (1971).
(12) R. Beaumont and D. Barthomeuf, *J. Catal.*, **27**, 45, (1972); **30**, 288 (1973).
(13) R. Beaumont, P. Pichat, D. Barthomeuf, and Y. Trambouze, *Catalysis*, **1**, 343 (1973).
(14) D. Barthomeuf and B. H. Ha, *J. Chem. Soc., Faraday Trans. 1*, **69**, 2158 (1973).
(15) E. M. Flaningen, H. Khatami, and H. A. Szymanski, *Advan. Chem. Ser.*, **No. 101**, 201 (1971).
(16) I. Tsolouski, H. Minchev, and V. Penchev, *C. R. Acad. Sci. Bulg.*, **23**, 811 (1970).
(17) E. M. Flaningen, *Advan. Chem. Ser.*, **No. 121**, 119 (1973).

# Sequence and Shape of the Molecular Orbitals of the Disulfide HSSH[1]

**Donald B. Boyd**

*The Lilly Research Laboratories, Eli Lilly and Company, Indianapolis, Indiana 46206* *(Received November 8, 1973)*

*Publication costs assisted by Eli Lilly and Company*

The variations in molecular orbital eigenvalues and shapes as a function of internal rotation in $H_2S_2$ computed in the CNDO/2 (complete-neglect-of-differential-overlap) approximation substantiate the correlation of the occupied MO's predicted earlier by EH (extended Hückel) calculations. By examining previously unpublished *ab initio* results, the qualitative validity of the CNDO/2 and EH descriptions is verified, and the incongruity of some other models of disulfide electronic structure is analyzed. Electron density maps of the individual CNDO/2 MO's, appropriately deorthogonalized to a Slater-type basis set, reveal precisely their shapes and demonstrate important differences between the CNDO/2 and EH wave functions. Predicted $\lambda_{max}$ and intensities of the first electronic transition vary as a function of dihedral angle in a manner consistent with uv and CD spectra, and a new assignment of the higher excited states of disulfides is presented. Oscillator strengths computed in the dipole length formalism and with the virtual orbital approximation are qualitatively similar to those obtained in the dipole velocity formalism and with configuration interaction wave functions. Predicted ionization potentials, barriers to internal rotation, net atomic charges, bond strengths, and dipole moments are correlated with recently available experimental and quantum mechanical data on various disulfides.

## Introduction

The molecular orbitals (MO's) of disulfides have been the subject of a wealth of papers in the recent literature.[2-17] The quantum chemical findings have aided in the interpretation of the interesting ultraviolet absorption, optical activity, ionization potential, and conformational properties arising from the disulfide linkage -S-S- occurring in diverse molecules, especially those of biological significance. Most commonly, the MO calculations have been performed on simple model compounds, hydrogen persulfide, $H_2S_2$, or dimethyl disulfide, $(CH_3)_2S_2$, with dihedral angles between the substituents measured around the S-S axis selected at values observed in more complex disulfides. By and large, many of the salient features of the electronic structure of the disulfide moiety seem to be fairly well understood. For instance, our earlier[2,3] calculations dealing with the above compounds by the EH (extended Hückel) method[18,19] yielded wave functions which successfully explained the red shift and decrease in oscillator strength of the lowest energy transition due to twisting either molecule from its normal dihedral angle of about 90° to larger or smaller values. Energy levels, charges, and overlap populations varied in a reasonable manner as a function of internal rotation about the S-S bond. However, serious questions have recently arisen in regard to the exact ordering and shapes of the occupied MO's of disulfides. Discrepancies between some of the more recent treatments of the disulfide MO's need to be examined in order to show where improvements in the approximate theories would be helpful and in order to construct a more unified picture of the electron structure of the -S-S- moiety. Also, because no eigenvalues or wave functions were published from the *ab initio* treatments of $H_2S_2$,[7-9] it has not been possible to determine the reliability of some predictions from the numerous approximate MO studies. In order to ascertain further information on these matters, we will present here the results of our CNDO/2 (complete-neglect-of-differential-overlap) calculations on $H_2S_2$ and key results from two of the *ab initio* calculations on $H_2S_2$. The availability of new experimental data on various disulfides from uv, circular dichroism (CD), photoelectron, and Raman spectroscopy also makes this study of the MO results worthwhile.

For purposes of example, CNDO/2 MO's of the simplest disulfide $H_2S_2$ are computed with dihedral angles between the two S-S-H planes ranging from 0 (cis) to 180° (trans), assuming fixed bond lengths and angles as before.[2,3] Standard CNDO/2 parameters are employed.[20,21] As in our EH calculations,[2,3] the 3d atomic orbitals (AO's) of sulfur are included in the basis set of valence AO's. In CNDO/2 the exponent of the 3d AO's is taken to be the same as the Slater value of the S3s and S3p AO's (spd basis set[20]).

In the next section, we begin by describing the CNDO/2 MO's of $H_2S_2$. Then these are compared to those previously computed by approximate and *ab initio* MO methods. The interconnection between the numerous quantum mechanical treatments is shown and certain differences are elucidated. The precise shape of the individual CNDO/2 MO's of $H_2S_2$ are displayed with the aid of electron density maps yielding for the first time definitive answers as to the character of the semiempirical MO's and also showing some significant contrasts between EH and CNDO/2 electron distributions. By comparing uv absorptions predicted in the virtual orbital approximation with those from more rigorous CNDO-CI (configuration interaction) calculations, we are able to refine and elaborate uv and CD spectral assignments and to pinpoint some of the theoretical treatments which are not completely compatible with experimental electronic spectra. Trends in the ionization potentials of dialkyl disulfides are rationalized on the basis of lone-pair interactions and induction. In the last section, population analyses are used to show the effect of internal rotation on the charge distribution of $H_2S_2$ and to explain the origin of the cis and trans rotational barriers. Further characterizations of

TABLE I: Corresponding Labels of the MO's in Disulfides at 0° Dihedral Angle from Various MO Calculations[a]

| Present work and ref 2 | Bergson[b] | Linderberg and Michl[c] | Yamabe, *et al.*[d] | Woody[e] | Richardson, *et al.*[f] |
|---|---|---|---|---|---|
| 4b, S–S $\sigma^*$ | $\sigma_-$ | $\psi_8$, $\sigma^*$S–S, b | LVMO, b | $\sigma^*$, $b_1$ | LUMO2($\sigma_{SS}^*$), b |
| 4a, n(p type) | $\pi_{-2}$ | $\psi_7$, a | n(p type), a | $n_1$($\pi$ type), $a_2$ | HOMO1(n'), a |
| 3b, n($sp^2$ type) | $\pi_{-1}$ | $\psi_6$, b | n($sp^2$ type), b | $n_2$($\sigma$ type), $b_1$ | HOMO2($\sigma_{SH}'$), b |
| 3a, S–S $\sigma$ | $\sigma_+$ | | n($sp^2$ type), a | | HOMO3($\sigma_{SS}$), a |
| 2b, $\pi$(p type) | $\pi_{+1}$ | | n(p type), b | $n_4$($\pi$ type), $b_2$ | HOMO4(n), b |
| 2a, $\pi$($sp^2$ type) | $\pi_{+2}$ | | $sp^2$ type, a | $n_3$($\sigma$ type), $a_1$ | HOMO5($\sigma_{SH}$), a |

[a] The references should be consulted for further details of the other authors' notation. In columns 2 and 5 the ordering of the levels as listed is different from the original ordering by energy because the energies had been estimated on crude assumptions. In some cases, the labels are supplemented with symmetry labels based on unpublished data. LV and LU abbreviate lowest vacant and lowest unoccupied. In column 1 we use the designations n for the MO's consisting mainly of the nonbonding, out-of-phase combinations of the 3p AO's on each sulfur and $\pi$ for the MO's with the in-phase combinations. Each n or $\pi$ MO in column 1 is distinguished by whether the S3p AO out of the S–S–H plane is involved (p type) or the in-plane S3p AO's are involved ($sp^2$ type). The latter $sp^2$-type MO's also have considerable S–H $\sigma$ character, so that they can be equally well labeled S–H $\sigma$ as in column 6. [b] Reference 5. [c] Reference 10. [d] Reference 11 [e] Reference 15. [f] Reference 16.

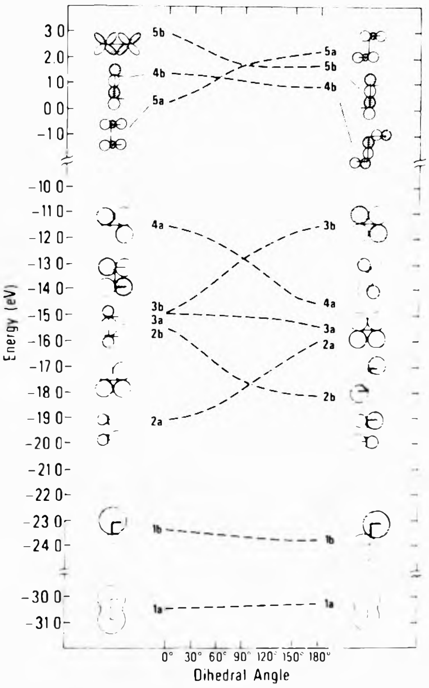

Figure 1. Correlation diagram for the variations of the CNDO/2 eigenvalues ($\epsilon$) in $H_2S_2$. Eigenvalues were computed at dihedral angles from 0 (cis) to 180° (trans) in 10° intervals, so that any tendency of two levels to approach each other would be detected. The shapes of the MO's are depicted schematically based on the sign and phase of the AO's with large LCAO-MO coefficients for the 0 and 180° conformers on the left and right, respectively. The levels are labeled according to $C_2$ symmetry throughout; the molecule possesses $C_{2v}$ symmetry at 0° and $C_{2h}$ symmetry at 180°. In the ground state each MO is doubly occupied with the valence electrons, except the virtual orbitals, 4b, 5a, and 5b.

deorthogonalized CNDO/2 wave functions in terms of population analyses and dipole moments are described.

## Sequence of the MO's in $H_2S_2$

Plotted in Figure 1 is the variation of the CNDO/2 eigenvalues ($\epsilon$) as a function of dihedral angle. The shapes of the MO's are sketched for the 0 and 180° conformers; the character of the MO's at 90° is shown in greater detail in the next section using electron density plots. Considering first the filled MO's, the correlation diagram of Figure 1 is strikingly similar to the corresponding EH correlation diagram,[2] although quantitatively, of course, the CNDO/2 and EH methods yield slightly different $\epsilon$ and linear combinations of the AO's (LCAO) in the MO's. Important to our discussion we note that both the pattern of variation of the filled MO's and the general shapes of these MO's are the same as we have described earlier in the EH study. As we[2] and others[11,16] have found, the conformational dependence of the high-lying doubly occupied MO's of $H_2S_2$ is very similar to that of $(CH_3)_2S_2$, so that the correlation of the filled MO's in Figure 1 may be regarded as fairly representative of what would be obtained by CNDO/2 for other $R_2S_2$ compounds, provided that the R groups do not contain functionalities which extensively interact with the disulfide moiety. Apparent in Figure 1 are the avoided crossings and interchanges of character of 2b and 3b near 0° and 3a and 4a near 180°.

The pattern of variation of the low-lying *empty* MO's in Figure 1 is somewhat different from that obtained by EH theory.[2] A feature of most previous quantum mechanical treatments of $H_2S_2$ is that the lowest empty MO (LEMO) has S–S $\sigma^*$ character, and its energy is nearly independent of dihedral angle. CNDO/2 fails to yield this description: the S–S $\sigma^*$ character is in 4b, the next lowest empty MO at small dihedral angles, but near 90°, 4b does become the LEMO and retains its antibonding character between the sulfurs. At large dihedral angles, both 4b and 5b possess S–S $\sigma^*$ character. The CNDO/2 method is somehow parameterized so as to place an S–H $\sigma^*$ level as low as or lower than the S–S $\sigma^*$ level. As others have noted[16] the empty CNDO/2 MO's have a large admixture of S3d AO's, although our sketches in Figure 1 do not adequately represent this. EH calculations[2,4,19] previously indicated the importance of the 3d orbitals in the excited states of sulfur compounds.

## Comparison to Other Calculations

MO calculations on $H_2S_2$ have been so numerous[2,5,7-11,14-16] that one would think some standardization of the MO labels would have taken place. Unfortunately, just about every author has chosen his own notation based either on symmetry, character, or order. This obscures the similarity among many of the calculational results. In some cases, the literature description of the MO's has not been sufficient to determine the degree of similarity of one author's MO's with another's. It therefore seems worthwhile to present a comparison of orbital labels along with a comparison of the MO's themselves. This has been made possible by helpful correspondence from the authors mentioned in the acknowledgments.

Equivalent labels of disulfide MO's are shown in Table I. The correspondences relate MO's with the same sym-

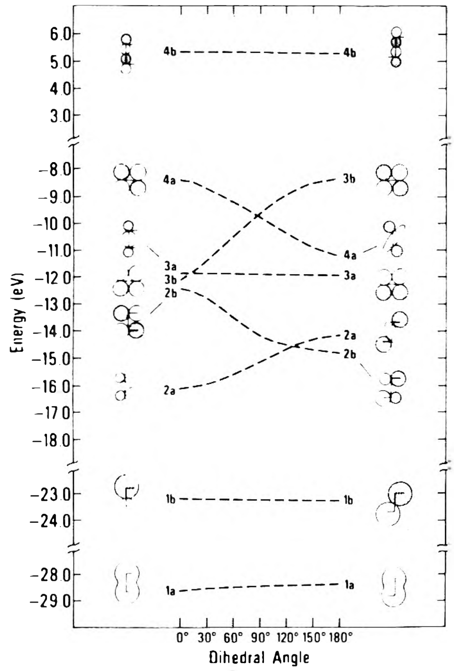

**Figure 2.** Correlation diagram of Schwartz's (ref 7) SCF $\epsilon$ of $H_2S_2$. Eigenvalues were available at dihedral angles of 0, 90, 135, and 180°. The shapes of the MO's are depicted schematically as in Figure 1.

metry and shape and the same variation in energy as the dihedral angle begins to open up from 0°, except for Woody's orbitals[15] as noted below. It should be pointed out that only a label based on symmetry in the $C_2$ point group will apply at all dihedral angles because the sequence of levels changes as the orbitals of different symmetry cross and the character of some levels mix together and change drastically as the dihedral angle is varied (Figure 1). Also, by labeling the MO's by symmetry one avoids the pitfalls of constructing a model where two MO's of the same symmetry are forced to cross.

The most important conclusion to be drawn from a comparison of the various other semiempirical MO calculations[5,10,11,13,16] on disulfides is that the MO's are basically like what we obtain by EH[2] and CNDO/2 calculations. Different parameters, molecular geometries, and levels of approximation have some effect on the $\epsilon$ and LCAO-MO coefficients, but most methods show the filled MO's to correlate as described in the previous section.

One approximate model of the electronic structure of the disulfide moiety, which has recently been proposed by Woody,[15] is somewhat different from the rest. It employs a model similar to Bergson's[5] wherein two of the four $sp^3$ hybrids on each sulfur are combined into four so-called nonbonding MO's, $n_1$, $n_2$, $n_3$, $n_4$, which are presumed to be occupied by the four lone pairs. The other sulfur electrons are allocated to the remaining hybrids which form the $\sigma$ bonds; these electrons are not included explicitly. The LEMO is assumed to be a conformationally independent S-S $\sigma^*$ orbital. The spacing of the n levels is set by admittedly unrealistic[15] overlap arguments and by imitating the apparent ordering of Yamabe, *et al.*[11] But as we have done in Table I, the relative energies of Woody's $n_3$ and $n_4$ at 0° dihedral angle are to be reversed; $n_3$ cannot correspond to Yamabe's third highest MO (which is the S-S $\sigma$ level not included by Woody), but rather $n_3$ would correspond to Yamabe's fifth highest occupied MO at 0°.

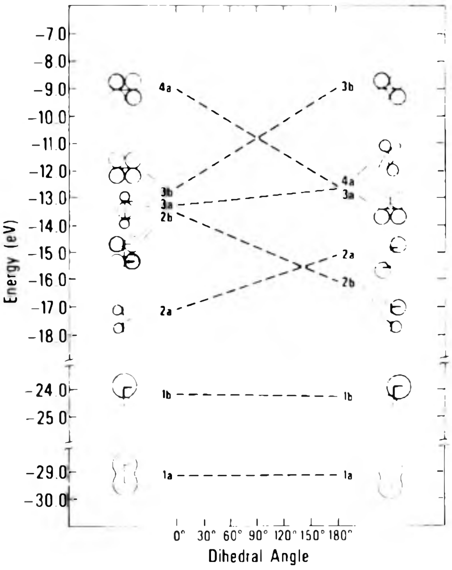

**Figure 3.** Correlation diagram of Veillard and Demuynck's (ref 8) SCF $\epsilon$ of $H_2S_2$. Eigenvalues were available only at 0 and 180°; corresponding levels are connected by straight lines. The shapes of the MO's are diagrammatic since information on only the largest AO character of each MO was available.

This fifth highest occupied MO (2a in our notation) is $sp^2$ type like the third highest MO as noted in Table I. Thus, the approximations Woody employed in arriving at the relative energies of the n orbitals, such as the neglect of the energy difference between S3s and S3p AO's, give an unreasonable result. In addition, fixing the n MO's as linear combinations of $sp^3$ hybrids leads to violation of the noncrossing rule because the only way to have an in-phase p-type orbital as the fourth highest MO at 0° and as the degenerate HOMO at 90° was to force $n_4$ to cross another MO of the same symmetry ($n_2$). The semiempirical MO methods achieve this sequencing *a priori*, and the *ab initio* calculations, discussed next, simply give the p-type character to the two high-lying MO's 4a and 3b in the 0-90° dihedral range. Thus, by having $n_4$ with its in-phase p-type character as the second highest MO from 0 to 90°, the violation could have been avoided and would also have mimicked *ab initio* results more closely.

Consider now the comparison of MO levels from CNDO/2 (Figure 1) and EH[2] calculations with those from *ab initio* self-consistent-field (SCF) calculations on $H_2S_2$.[7,8] The *ab initio* $\epsilon$ and LCAO-MO coefficients have not previously been described in the literature. Because of the computer times involved in obtaining the wave functions, they are not available for as many dihedral angles as are the semiempirical MO's. Nevertheless, the general pattern of variation in $\epsilon$ can be traced in Figures 2 and 3. Schwartz's SCF Gaussian-type-function calculations[7] yielded a relatively high total energy (−792.66 au at 90°), whereas with a larger Gaussian basis set, Veillard and Demuynck[8] obtained the lowest energy to date (−796.18 au). Both *ab initio* treatments produce correlation diagrams in striking similarity with each other and to the semiempirical ones. There are three MO levels relatively insensitive to dihedral angle (1a, 1b, and 3a) and two pairs of MO's which become degenerate in a gauche conformation (2a and 2b, and 3b and 4a). The main points of discrepancy between Figures 1, 2, 3, and Figure 1 of ref 2 are that Schwartz's 3b MO at small dihedral angles drops very slightly below 3a, and the character of 3b and 2b, which are relatively closely spaced at 0° and of the same symmetry with respect to twofold rotation, are interchanged at small dihedral angles in the semiempirical and *ab initio* correlation diagrams. However all the available data consistently predict the highest occupied MO at every dihedral angle and the two HOMO's near 90° to be of lone-pair character formed principally by the out-of-plane 3p AO on each sulfur, *i.e.*, n(p type). The most well-defined experimental data on uv absorption and ionization potentials of disulfides pertain to these HOMO's. In Schwartz's calculations (Figure 2), computer output for the LEMO shows that it is nearly independent of dihedral angle and has S-S $\sigma^*$ character. The LEMO in Veillard and Demuynck's calculation possibly has more S-H $\sigma^*$ character. Virtual orbitals from an *ab initio* calculation are known to have less significance than do the occupied MO's, but, nevertheless, to see most of the essential features of disulfide electronic structure as predicted by the semiempirical methods to be substantiated by more rigorous ones is gratifying.

## Shape of the CNDO/2D MO's of $H_2S_2$

Previously, we have examined only the total valence electron densities from EH wave functions in regard to molecular formation, bonding, and the effect of internal rotation on the charge distribution.[3] Here we consider the density in the individual CNDO/2 MO's. In order to compute and view these densities, the important first step is to deorthogonalize the CNDO/2 LCAO-MO coefficients with a Löwdin transformation, $\mathbf{C}' = \mathbf{S}^{-1/2}\mathbf{C}$, where $\mathbf{S}$ is the overlap matrix between AO's, $\mathbf{C}$ is the coefficient matrix output by CNINDO, and $\mathbf{C}'$ is the CNDO/2D (deorthogonalized) coefficient matrix.[21-24] By renormalizing the MO's in this manner it is possible to include both the one-center and two-center orbital products, $\chi_p(\mathbf{r})\chi_q(\mathbf{r})$, in the evaluation of the density. Without deorthogonalization, density contributions from the two-center terms (AO's $\chi_p(\mathbf{r})$ and $\chi_q(\mathbf{r})$ on different atoms) would have to be left out. It has been properly pointed out that leaving out all off-diagonal terms ($\chi_p(\mathbf{r})\chi_q(\mathbf{r})$, $p \neq q$) is clearly inadequate.[25] For these reasons deorthogonalization of neglect-of-differential-overlap wave functions seems to be the preferable approach to computing these electron densities.[22,26]

The electron density in an MO, $\psi_m$, is evaluated[27,28] from $D(\mathbf{r}) = 2\psi_m{}^*(\mathbf{r})\psi_m(\mathbf{r}) = 2\Sigma_{p,q}C_{pm}{}'C_{qm}{}'\chi_p(\mathbf{r})\chi_q(\mathbf{r})$, where $C_{pm}{}'$ are the CNDO/2D LCAO-MO coefficients and $\chi_p(\mathbf{r})$ are the Slater-type basis functions (AO's). The density is computed at each point $\mathbf{r}$ in a plane through the molecule, and contours are constructed through points of equal density. Figures 4-15 show electron density maps taken directly from computer printout.[3] The letters conveniently label the contours according to the magnitude of the densities as given in the figure captions. Since the density, $2\psi_m{}^*(\mathbf{r})\psi_m(\mathbf{r})$, rather than the MO itself, $\psi_m(\mathbf{r})$, is being plotted, the phase of each region of the MO is not shown in the figures. However, nodal surfaces separate the lobes drawn with closed contours, and the phase of the lobes change as one crosses a node. In the captions are given the expectation values of position of each CNDO/2D MO, $\langle\psi_m|\mathbf{r}|_m\rangle$, measured out from the S-S axis along the $C_2$ axis. These values are indicative of the gross charge distributions, whereas the contour diagrams show the details of how the electrons are distributed.

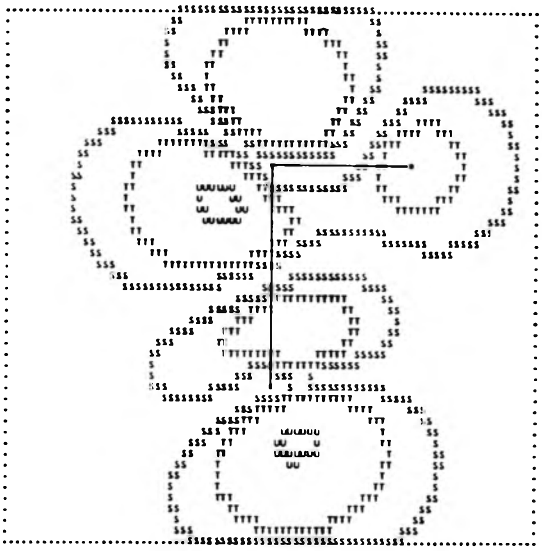

**Figure 4.** Electron density in MO 4b. This is the LEMO at 90° Expectation value of position is 0.02 Å toward the side of the molecule with the hydrogens. The apparent fusion of the lower two lobes near $S_1$ is an artifact of the limited resolution of the printer. Magnification of this region confirms the existence of a node between the lobes (which have opposite signs in the MO). Some contours may appear to be discontinuous, but this is also an artifact of the limited resolution. In this and subsequent figures, $H_2S_2$ is in an orthogonal conformation (90° dihedral angle). The plane of this map coincides with the $S_1$-$S_2$-$H_3$ plane. Internuclear axes are drawn between bonded atoms; $H_4$ lies below the plane being plotted and is bonded to $S_1$ in the lower half of the figure. The maps in all figures cover 5 × 5 Å and use contour letters corresponding to the following densities: S for 0.0008, T for 0.008, and U for 0.08 e/bohr$^3$; 1 bohr = 0.52917 Å. An occupation number of two is assumed for purposes of computing the density in the virtual MO's.

The three lowest empty MO's and the seven MO's filled by the valence electrons are plotted in Figures 4-9, 12-15 for $H_2S_2$ with a 90° dihedral angle. The empty MO's 5b and 5a are rather complex with considerable S3d and S-H $\sigma^*$ character and are given in the supplementary material mentioned at the end of this article. The lowest empty MO (4b) in Figure 4 obviously possesses S-S $\sigma^*$ character as indicated by the nodal surface intersecting the middle of the S-S axis. The two highest occupied MO's (4a and 3b) in Figures 5 and 6 are each disected by two nodal surfaces and are the nonbonded or lone-pair MO's. The tipping of the dumbbell-shaped lobes on each sulfur with respect to the S-S-H planes reveals that some S-H $\sigma$ bonding character is also present in 4a and 3b. This shape contrasts with the simpler LCAO-MO descriptions[5,15] of the n MO's which describe these as combinations of only out-of-plane sulfur hybrid AO's. The third highest occupied MO (3a, Figure 7) has distinct S-S $\sigma$ bonding character and is broken by two nodal surfaces passing through each sulfur. At still lower energy we have MO's 2b and 2a, which some have called S-S $\pi$ bonding and others have labeled S-H $\sigma$ bonding. Actually, as seen in Figures 8 and 9, both characterizations are valid; each MO has one nodal surface intersecting the plane of the figures roughly along the S-S axis, but there is no node separating the $3p_\pi$ regions near each sulfur and no node disecting perpendicularly the S-H internuclear region. The principal AO combinations making up the two lowest energy MO's filled with valence electrons are simply $S_13s - S_23s$ (1b) and $S_13s + S_23s$ (1a) and plots of these are given in the supplementary material mentioned at the end of this article. The shapes

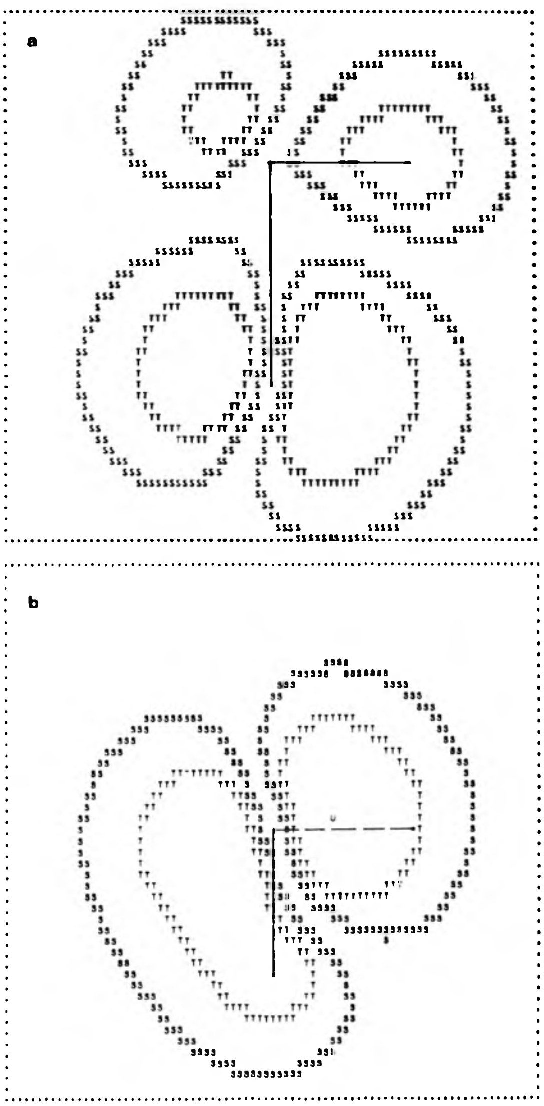

**Figure 5.** Electron density in MO 4a in the $S_1$–$S_2$–$H_3$ (a) plane and in the (b) plane passing through $S_1$ perpendicularly to the S–S axis. Expectation value of position is 0.18 Å toward the hydrogens. The dashed line in b is the projection of the $S_2$–$H_3$ axis onto the plane being computed.

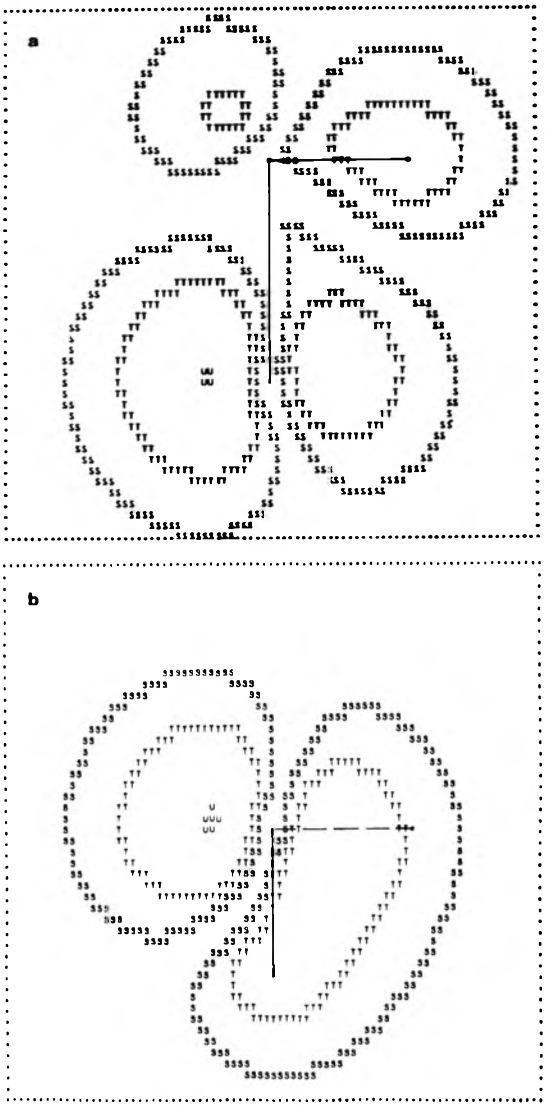

**Figure 6.** Electron density in MO 3b in the S–S–H (a) plane and in the (b) plane as in Figure 5. Expectation value of position is essentially at the S–S axis.

of the above seven filled MO's and the LEMO at 90° by CNDO/2D are completely harmonious with the unpublished LCAO-MO coefficients of Schwartz[7] and Yamabe, *et al.*[11]

The total valence electron density is plotted in Figure 10 and is the sum of the densities of the seven filled MO's. Note the depression in density near each sulfur nucleus because the dense aggregation of sulfur 1s, 2s, and 2p electrons are, of course, not included. By subtracting the spherically symmetric, valence-electron, atomic densities,[3,22,29-31] one obtains the difference density map in Figure 11. Whereas the nodes in the MO maps above correspond to zero density, nodal surfaces in the difference map correspond to points where the density in the molecule and in the sum of the constituent atoms are equal. These are denoted by the dotted contours. The interesting features of the difference map are the peaks of density gain and the valleys of density loss brought about by formation of the molecule from the atoms. Ordinarily, gains occur in $\sigma$-bonding, $\pi$-bonding, and lone-pair regions.

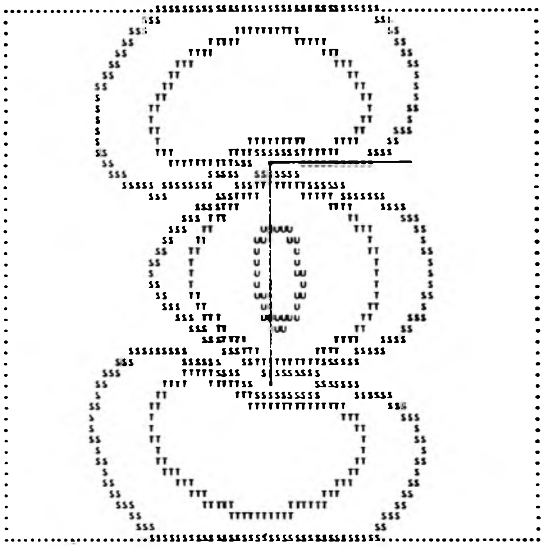

**Figure 7.** Electron density in MO 3a. Expectation value of position is 0.05 Å away from the hydrogens.

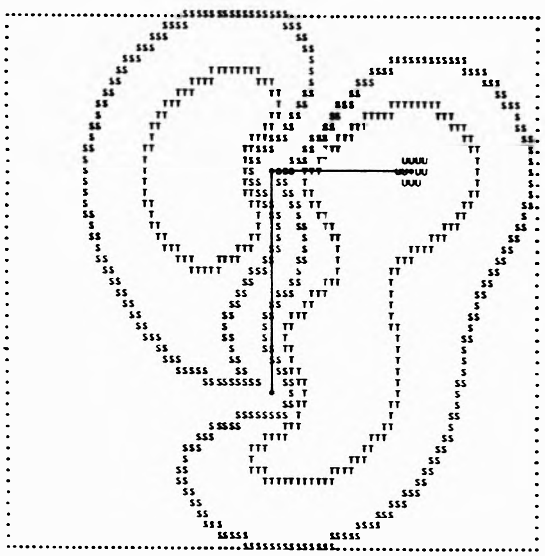

**Figure 8.** Electron density in MO 2b. Expectation value of position is 0.27 Å toward the hydrogens.

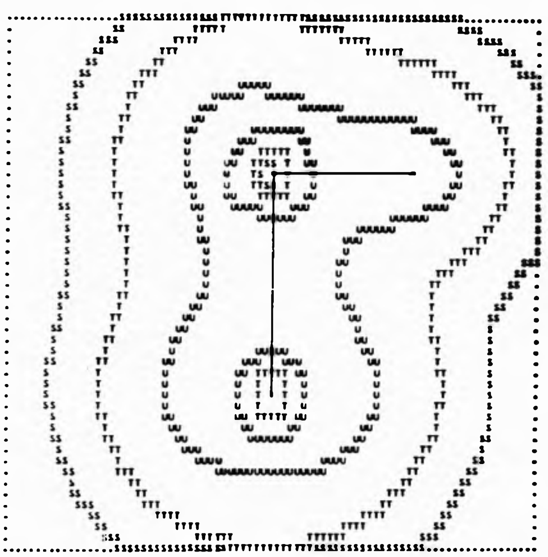

**Figure 10.** Total CNDO/2D density due to the fourteen valence electrons in $H_2S_2$ at a dihedral angle of 90°.

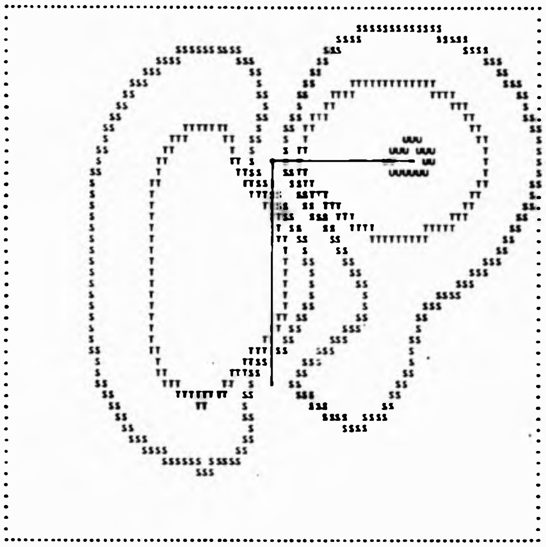

**Figure 9.** Electron density in MO 2a. Expectation value of position is 0.25 Å toward the hydrogens.

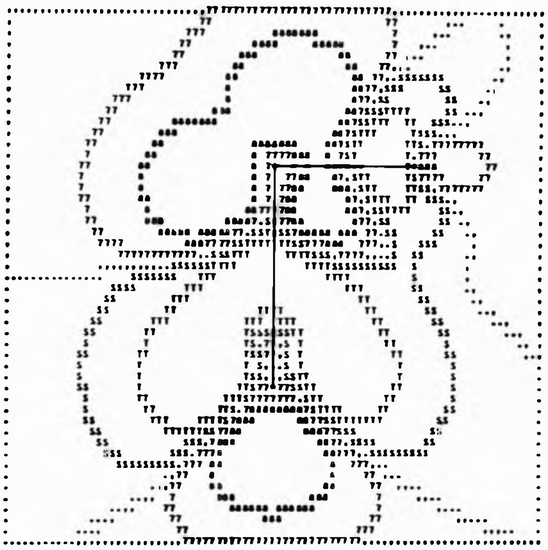

**Figure 11.** Difference density in $H_2S_2$ obtained by subtracting the constituent atomic densities centered at the locations of the atoms in the molecule from the total CNDO/2D density. Contour labels are as in Figure 4, with 7 denoting −0.0008, 8 denoting −0.008, and 9 denoting −0.08 e/bohr$^3$. Positive contours correspond to regions where the electrons are more dense than in the sum of the densities of the two sulfurs and two hydrogens, negative contours correspond to regions where the electrons are deficient with respect to the atomic densities, and dotted contours correspond to points where the density in the molecule and the atomic densities are equal.

As expected, the CNDO/2D difference map in Figure 11 gives a smoother charge distribution (lower peaks and shallower valleys) relative to the EH difference map[3] because of the iterative SCF procedure and explicit account of interelectron repulsions in arriving at the wave function in CNDO/2 theory. However, unlike the EH difference map for the 90° conformer of $H_2S_2$, Figure 11 fails to reveal any buildup of lone-pair density on the sulfurs in the S–S–H plane. This means that the density *gain* with respect to the atoms is clearly not as quasispherical[3,32] according to CNDO/2D as one obtains by EH theory, although both the CNDO/2D and EH *total* densities around each sulfur have the appearance of being roughly spherical in the regions away from the hydrogens. The EH difference map[3] of $H_2S_2$ showed that the regions of space with lone-pair electron density buildup were approximately what would be expected from one electron pair being in an sp$^2$ hybrid AO and the other being in the leftover p-type AO on each sulfur.[33] On the other hand, Figure 11 resembles more closely the situation where the two lone pairs are in regions shaped like sp$^3$ hybrids. The question of whether the CNDO/2D or EH picture is closer to reality cannot be fully resolved until basis set independent *ab initio* density maps are obtained, but a limited basis set *ab initio* density map of $H_2S$ did show a net gain in density in the plane of the molecule with respect to the atoms.[30] Other features of Figure 11 to be noted are that CNDO/2D gives density buildups in the $\sigma$-bonding regions along the S-S and S-H internuclear axes and in the cylindrical $\pi$-bonding region around the S-S axis. The presence of these features is quite reasonable, although EH theory failed to show a $\sigma$-bonding density peak between the sul-

**TABLE II: Comparison of Virtual Orbital and CI Calculations on the First n → $\sigma^*$ Transition in $H_2S_2$**

| Dihedral angle, deg | EH[a] | | CNDO/2D[b] | | CNDO/2D-CI[c] | |
|---|---|---|---|---|---|---|
| | $\lambda_{max}$, nm | $f$ | $\lambda_{max}$, nm | $f$ | $\lambda_{max}$, nm | $f$ |
| 0 | 305 | 0.014 | 317 | 0.008 | 457 | 0.001 |
| 30 | 297 | 0.026 | 307 | 0.022 | 404 | 0.007 |
| 60 | 276 | 0.063 | 284 | 0.067 | 353 | 0.102 |
| 90 | 251 | 0.137 | 258 | 0.166 | 310 | 0.130 |
| 120 | 278 | 0.015 | 304 | 0.003 | 353 | 0.073 |
| 150 | 304 | 0.009 | 349 | 0.000 | | |
| 180 | 315 | 0.007 | 366 | 0.000 | 429 | 0.101 |

[a] Computed by the procedure of ref 2. [b] Present work: $\lambda_{max} = 1239.8/(\epsilon_{L} - \epsilon_{HOMO} - 9.06\ eV)$ and $f = 0.0245(\epsilon_{L} - \epsilon_{HOMO} - 9.06\ eV)|\mathbf{R}^{L,HOMO}\ (au)|^2$ where **R** is the transition moment integral between the CNDO/2D MO's. [c] Data from ref 16. The authors of this paper adopt an S–S–H bond angle about 0.5° different from what we use; insignificant differences of less than 0.002 au in eigenvalues and 0.005 au in total energies result from this geometrical change.

furs. Also the EH map showed that its S-H bonding peak was polarized off the S–H axis as if[34] EH theory would predict the S-S-H bond angle to be too large similar to its erroneous prediction of linear water.[35]

### Ultraviolet Spectral Properties of Disulfides

Spectral uv and CD data on various disulfide-containing molecules have shown that, in general, the further the dihedral angle is from 90°, the more red shifted is the lowest energy transition.[2] Thus, disulfides with a dihedral angle of about 90°, such as $(CH_3)_2S_2$, exhibit absorptions around 250-255 nm. Twisting the CSSC dihedral angle open or closed 30° results in a bathochromic shift of 20-40 nm. Further closing of the dihedral angle can shift the first transition all the way to 370 nm.[2] Also, it is known that the extinction coefficient of the first transition is at a maximum when the disulfide dihedral angle is near 90° and diminishes as the dihedral angle is opened or closed. These facts can be readily understood on the basis of the conformational dependence of the MO's as obtained at several levels of approximation.[2,5,10,11,16] In the virtual orbital approximation,[2,4,19] the first transition is regarded as an excitation from the HOMO (4a or 3b depending on dihedral angle) to the LEMO. In EH theory,[2] the LEMO is 4b, and since its energy and shape are nearly independent of conformation, the shifts in $\lambda_{max}$ and oscillator strength are mainly due to the change in energy and character of 4a and 3b. The same situation is obtained from CNDO/2 theory, although here the picture is complicated by the crossing of 4b and 5a and the mixing of S–H $\sigma^*$ character into the LEMO (Figure 1).

Ideally, complete CI wave functions should be employed in computing spectral properties of disulfides. This has been done in two instances, for at least the valence electrons. Linderberg and Michl[10] obtained CNDO-CI wave functions expanded with 3s and 3p AO's on sulfur and predicted the first transition of $H_2S_2$ with a 90° dihedral angle to be at 502 nm with Sichel–Whitehead parameters[36] and at 248 nm with Santry–Segal parameters.[20] Richardson,[16] *et al.*, included S3d AO's in their basis set and used Santry–Segal parameters to predict the first transition at 310 nm for the 90° conformer. Both of these CNDO-CI studies successfully showed the first transition to red shift and lose intensity as the molecule was twisted away from the orthogonal conformation.

In view of the fact that Richardson,[16] *et al.*, computed oscillator strengths from dipole velocity integrals and we have employed dipole length integrals, this is an opportune situation for comparison of the two approaches. Their calculations used CNDO-CI wave functions, whereas our calculations are based on the virtual orbital approximation, but both involve treating all one- and two-center transition moments after deorthogonalizing the LCAO-MO coefficients and both employ Santry–Segal parameters.[20] Since we are mainly interested in the lowest energy disulfide n → $\sigma^*$ transition, we take the excited state configuration as . . . $3a^23b^24a4b$ or . . . $3a^24a^23b4b$, depending on the dihedral angle. The energy gap between the filled and virtual orbitals is too big to be able to use the CNDO/2 $\epsilon$ directly in the virtual orbital approximation, but they may be scaled as in Table II. Also in Table II are the $\lambda_{max}$ and oscillator strengths ($f$ values) predicted by EH[2] and the CNDO/2D-CI[16] calculations. All methods show the proper conformational dependence of the first transition, and, significantly, they give similar magnitudes to the $f$ values, except EH and CNDO/2D $f$ values are very small at dihedral angles where 3b is the HOMO.

The higher energy transitions should be better predicted by a CI description of the excited states than with the virtual orbital approximation. All the various studies using this approximation predict a monotonic blue shift for the second longest wavelength transition due to forcing the disulfide moiety to assume dihedral angles larger or smaller than 90°. On the other hand, CNDO-CI calculations[16] show the second transition to undergo a minute hypsochromic shift from 308 nm at 90° to 307 nm near 80°, but below 80° the shift is back toward the red. CD studies of disulfides with differing conformation indicate that the CI description is qualitatively more satisfactory: at 90° the second transition is believed[2,10,15,16] to be nearly degenerate with the first at about 250 nm; at 60° it blue shifts to about 240 nm; and in going to still smaller dihedral angles the shift is bathochromic.[2,37-40] The CNDO-CI,[16] EH,[2] and Bergson[5,15] studies are in agreement in predicting a short wavelength, overlapping pair of transitions in disulfides with a 90° dihedral angle, similar to the degenerate pair of S–S n → $\sigma^*$ transitions responsible for the long wavelength band near 250 nm. There is no consensus as to what orbitals are involved in these short wavelength transitions: n(p type) → S–R $\sigma^*$,[16] n(p type) → 3d,[2] or n(sp² type) → S–S $\sigma^*$.[5,15] These transitions, most likely of the first type with a significant[16,19] percentage of 3d character mixed in, would be associated with the uv absorption observed in the vicinity 205–210 nm in 90° disulfides.[40] At still shorter wavelength in 90° disulfides would come the intense S–S $\sigma$ → S–S $\sigma^*$ transition at about 196 nm.[6]

A problem with the Bergson model of disulfide orbitals was revealed in Woody's quantitative calculations on oscillator strength and rotatory strength performed using transition moment integrals evaluated from the dipole velocity (gradient) operator, but with the virtual orbital approximation and the crude representation of the four n MO's.[15] The uv and CD spectral data were interpreted[15] in terms of the four disulfide n → $\sigma^*$ transitions, without explicit calculation of the important S–S $\sigma$ → S–S $\sigma^*$ or n → S–R $\sigma^*$ excitations. The first and second transitions in the dihedral angle range 60–90° were assigned by Woody as $n_1$ → $\sigma^*$ and $n_4$ → $\sigma^*$ and the predicted oscillator strengths of these transitions were only slightly smaller than experiment. However, the lowest energy transition was incorrectly predicted with the Bergson orbitals to gain intensity, rather than lose it, as the disulfide is twisted away from the 90° conformation toward 0 or 180°.[15] Thus, the Bergson model does not allow for the proper reorganization of orbital shapes resulting from internal rotation.

There have been two attempts to use the Bergson model[5] to understand the CD spectra of disulfides.[10,15] Linderberg and Michl[10] successfully explained the low inherent optical activity in disulfides with a 90° dihedral angle and correctly predicted the sign of the Cotton effect for two cyclic polypeptides possessing a disulfide bridge with a dihedral angle apparently greater than 90°.[41,42] Woody's application of the Bergson model confirmed the variations in the Cotton effects on a quantitative basis.[15] However, a possibly misleading facet of the Bergson model is that it predicts the rotatory strength of the two lowest energy transitions at 90° to be *exactly* equal and of opposite sign.[10,15] The reason for this is that the degenerate pair of HOMO's are equivalent combinations of $3p_\pi$ or hybrid AO's in the Bergson approximation, except that one is even with respect to $C_2$ rotation, and the other is odd. A diminution of inherent optical activity in the 250-nm region is, indeed, supported by CD data.[10,43] We hasten to point out that exact cancellation of rotatory strengths from the two S–S n → $\sigma^*$ transitions and hence complete lack of optical activity near 250 nm may be fortuitous. The very important CNDO[10] and CNDO–CI[10,16] calculations demonstrate that cancellation is possible to some degree depending quite heavily on the geometrical parameters, *e.g.*, bond angles, involved. In other words, the simple picture predicted by the Bergson model[10,15] is not always maintained when better wave functions are employed.

## Ionization Potentials of Disulfides

The pattern of variation of the MO energy levels of $H_2S_2$ in Figures 1–3 has a direct bearing on the ionization potentials (IP) expected for various dialkyl disulfides $R_2S_2$. There are at least two effects of the R groups which must be taken into account when interpreting the first two IP's. One is a conformational effect having to do with the interaction of the sulfur lone pairs with each other, and the other is an electronic effect due to interaction of the lone-pair orbitals with the R groups.

The conformational effect has to do with whether the R groups are bulky as in $(t\text{-Bu})_2S_2$, which would tend to open the C–S–S–C dihedral angle above the normal value near 90°,[44] or whether the R group bridges the sulfurs in a five- or six-membered ring, which would reduce the dihedral angle considerably below 90°.[2] Such conformational differences would determine (within the framework of Koopmans' theorem[45]) which regions of a correlation diagram (Figures 1–3) are applicable to a given molecule. For instance, in molecules with dihedral angles close to 90°, the first and second IP's should be and are very close due to the near degeneracy of 4a and 3b. As the conformation approaches either the cis, or hypothetical trans, planar forms, then there should be a larger split between the first and second IP's corresponding to the larger energy difference in 4a and 3b. The uv data[37] and IP data[13] are very consistent in indicating a split of 0.85–0.95 eV between the two highest occupied MO's at 60° dihedral angle. The third highest IP is from the S–S $\sigma$ MO (3a in $H_2S_2$) by most theoretical treatments and hence should be relatively less dependent on dihedral angle. This is, indeed, found to be the case experimentally.[13]

The second effect of an alkyl group R on the first few IP's of the disulfides has to do with how well the R group can destabilize the high-lying MO's localized on the disulfide moiety and/or stabilize the cation formed by ionization. Either or both of these mechanisms may be operative. An experimental fact[13] is that for a series of $R_2S_2$ compounds all with nearly the same C–S–S–C dihedral angle of about 90°, the larger the R group is, the lower are the first several IP's. In other words, increasing the chain length or degree of branching in R makes it easier to ionize electrons from the disulfide moiety. EH calculations on $H_2S_2$ and $(CH_3)_2S_2$ show that the methyl groups raise the energies of the lone-pair MO's $n_a$ and $n_b$ (4a and 3b in $H_2S_2$) and the S–S $\sigma$ MO (3a in $H_2S_2$).[2,46] Thus, *via* Koopmans' theorem the IP's from these levels should be lower in $(CH_3)_2S_2$ than in $H_2S_2$. This expectation is consistent with the observed first and second IP's of 8.8–9.0 and 9.1–9.2 eV in $(CH_3)_2S_2$[13,54] compared to 10.0–10.2 and 10.3–10.5 in $H_2S_2$.[13,55] The other electronic mechanism for lowering the IP's of $R_2S_2$ compounds is the stabilization of the cation and concurrent narrowing of the energy gap between $R_2S_2$ and $R_2S_2^+$. The stabilization is completely consistent with the inductive ability of the alkyl groups.[56] The larger R groups can more effectively delocalize the ionic charge over the periphery of the molecule. This phenomenon is analogous to that found in a CNDO/2 study of the gas-phase acidies of some alcohols where the negative charge in the alkoxyl anions was found to be stabilized by spreading out over the peripheral hydrogens; the larger alkyl groups with their greater surface area formed the more acidic alcohols.[50]

We should not conclude this section without noting that the *ab initio* calculations[7,8] are superior to the semiempirical ones in regard to the accuracy of the predicted first and second IP's of $H_2S_2$. The experimental values are mentioned above. Our EH calculations[2] on the 90° rotamer of $H_2S_2$ gave values which were too high, 12.50 and 12.61 eV (using Koopmans' theorem). Predictions from the present CNDO/2 calculations likewise are too high: 12.78 and 12.85 eV. Linderberg and Michl's CNDO calculation[10] with Sichel-Whitehead parameters[36] gave 11.1 and 11.2 eV. Schwartz's *ab initio* calculations[7] predicted the first and second IP's at 9.67 and 9.72 eV *via* Koopmans' theorem. Veillard and Demuynck's calculations,[8] while not directly giving eigenvalues at 90°, still gave the two highest occupied MO's crossing in the range 10.5–11.0 eV at this dihedral angle.

## Conformational Preference and Charge Distribution of $H_2S_2$

An important property of the –S–S– linkage in proteins and other molecules is its preferred skew conformation. For instance, the X-ray determined structures of insulin[57] and other proteins[12] possess disulfide linkages of P or M chirality with C–S–S–C dihedral angles averaging around 90°. Unless restricted by a ring structure or external forces,[2] the optimum dihedral angle at the S–S bond of all disulfides is about 90°. As with almost[11] all previous MO treatments[3] of disulfides, the present CNDO/2 calculations yield a minimum in the total energy at about 90°. The barriers to internal rotation of 10.9 (cis) and 3.6 kcal/mol (trans) are higher than predicted by EH theory[2] and agree better with *ab initio* results.[3,7–9] Our CNDO/2 barrier heights are also higher than others have obtained from earlier CNDO calculations because in one case the 3d AO's of sulfur were apparently not included[9] and in the other case Sichel-Whitehead,[36] rather than Santry-Segal,[20] parameters were employed.[10]

Reasons for the 90° conformational preference have been established in earlier calculations,[2,3] and the present CNDO/2 calculations only serve to confirm these. The Mulliken[58] overlap population between the sulfurs of $H_2S_2$ peaks at 90° as the dihedral angle is varied from 0 to 180° as seen in Table III in the supplementary material mentioned at the end of this article. This trend in both the EH and CNDO/2D data implies the possibility of some variation is S–S stretching frequencies as a function of dihedral angle recently sought in the Raman spectra of disulfides.[59] Also apparent in Table III is the fact that the EH overlap populations for the S–S bond tend to be larger than the *ab initio*[7,8] and CNDO/2D values, mainly because the $\sigma$ component to the overlap population is over four times larger from the EH wave function than from CNDO/2D. The overlap populations for the S–H bond do not vary greatly with H–S–S–H dihedral angle and reach a minimum of 0.408 at 90° by CNDO/2D.

The net atomic charges and dipole moments computed at the equilibrium geometry of $H_2S_2$ are most relevant to experiment. Nevertheless, these quantities from CNDO/2, CNDO/2D, and EH[2] wave functions, which are given in Table IV available as supplementary material, display an interesting dependence on dihedral angle. The CNDO/2 and CNDO/2D net atomic charges are expectedly smaller in magnitude than the EH values. Deorthogonalization brings the CNDO/2 charges into closer agreement with the EH values, just as in the case of adenine.[22] Significantly, the CNDO/2 and CNDO/2D charges show the same dihedral angle dependence as do the EH charges: the charge on sulfur is least negative at about 90°. This corresponds to the enhancement of hyperconjugation or back donation which transfers electron density away from the sulfurs as the dihedral angle approaches 90°.[3] The lowering of charge density on the sulfurs in the gauche conformations as measured by the net charges (Table IV) and by electron density maps[3] suggests that the steric size of the regions occupied by the lone-pair electrons is actually greater in the unfavorable planar conformations than in the gauche ones. The total occupation of the five S3d AO's is small, but nonnegligible, varying from 0.240 at 0° dihedral angle to 0.281 at 90° and 0.249 at 180° by CNDO/2D. Deorthogonalization decreases the apparent occupancy of the 3d AO's and increases that of the 3s AO's.

The three sets of point charge dipole moments in Table IV are mostly smaller than the corresponding values predicted with the one- and two-center terms included. The point charges do not adequately account for the lone-pair contributions which make the side of the molecule with the hydrogens the positive end of the dipole. Even with the one- and two-center terms included, the apparent polarity of the molecule seems rather low according to CNDO/2 and CNDO/2D. The CNDO/2D $\mu_{\rm tot}$ value at 90° of 0.29 D is only 0.03 D closer to the experimental value of 1.18 D[60] than in the CNDO/2 $\mu$ value. In most other molecules also, deorthogonalization does not improve predicted dipole moments very much.[22,23,36] Making the hydrogens less electronegative[46] in CNDO/2 theory would improve the predicted dipole moment.

## Epilog

A fairly unified picture of the electronic structure of the disulfide moiety has emerged from our comparison of the *ab initio* and semiempirical MO studies. The main qualitative difference between the approximate and rigorous MO calculations, namely, the interchange of character between closely spaced MO levels of the same symmetry, cannot be used to judge the relative accuracy of the calculations with presently available experimental data. The few semiempirical studies which predict alternate views of the disulfide MO's have been delineated with the purpose of showing where improved parameterizations or other refinements in the approximate theories may be necessary. The unified description of the electronic structure of the disulfide moiety has extended the basis for understanding and predicting numerous observables, such as uv absorption, optical activity, ionization potentials, conformation, structure, and dipole moments, of not only small model compounds, but also of complex proteins, enzymes, antibiotics, and other biomolecules with the disulfide linkage.

*Acknowledgments.* The author expresses his appreciation to J. Demuynck, R. B. Hermann, R. Hoffmann, M. M. Marsh, L. A. Neubert, F. S. Richardson, M. E. Schwartz, A. Veillard, R. W. Woody, and H. Yamabe for stimulating discussions and/or correspondence. Drs. Schwartz, Veillard, and Demuynck generously made available unpublished data from their calculations, and Drs. Neubert, Richardson, and Woody kindly provided preprints. The present study was facilitated by the expertise of J. S. Lipscomb in computer programming and D. W. Smith in implementing CNINDO on our IBM 370/155 computer.

*Supplementary Material Available.* Tables III and IV and Figures 12–15 will appear following these pages in the microfilm edition of this volume of the journal. Photocopies of the supplementary material from this paper only or microfiche (105 × 148 mm, 24× reduction, negatives) containing all of the supplementary material for the papers in this issue may be obtained from the Journals Department, American Chemical Society, 1155 16th St., N.W., Washington, D. C. 20036. Remit check or money order for \$3.00 for photocopies or \$2.00 for microfiche, referring to code number JPC-74-1554.

## References and Notes

(1) Paper XI of the series "Mapping Electron Density in Molecules." See ref 3 for paper X.
(2) D. B. Boyd, *J. Amer. Chem. Soc.*, **94**, 8799 (1972), and references therein.
(3) D. B. Boyd, *Theor. Chim. Acta*, **30**, 137 (1973), Paper X.
(4) D. B. Boyd, *J. Med. Chem.*, **16**, 1195 (1973).
(5) G. Bergson, *Ark. Kemi*, **12**, 233 (1958); **18**, 409 (1962).
(6) S. D. Thompson, D. G. Carroll, F. Watson, M. O'Donnell, and S. P. McGlynn, *J. Chem. Phys.*, **45**, 1367 (1966). See, also, ref 2.
(7) M. E. Schwartz, *J. Chem. Phys.*, **51**, 4182 (1969).
(8) A. Veillard and J. Demuynck, *Chem. Phys. Lett.*, **4**, **476** (1970).
(9) I. H. Hillier, V. R. Saunders, and J. F. Wyatt, *Trans. Faraday Soc.*, **66**, 2665 (1970).
(10) J. Linderberg and J. Michl, *J. Amer. Chem. Soc.*, **92**, 2619 (1970).
(11) H. Yamabe, H. Kato, and T. Yonezawa, *Bull. Chem. Soc. Jap.*, **44**, 22, 604 (1971). The conformational dependence of the MO eigenvalues of $H_2S_2$ were satisfactorily predicted by these calculations, even though the calculations failed to reveal a trans barrier as is found to be nonnegligible by most other calculations (see ref 3).
(12) D. Perahia and B. Pullman, *Biochem. Biophys. Res. Commun.*, **43**, 65 (1971).
(13) G. Wagner, Doctoral Dissertation, Johann Wolfgang Goethe University, Frankfurt am Main, Federal Republic of Germany, 1971; H. Bock and G. Wagner, *Angew. Chem., Int. Ed. Engl.*, **11**, 150 (1972); G. Wagner and H. Bock, *Chem. Ber.*, **107**, 68 (1974).

(14) B. Meyer and K. Spitzer, *J. Phys. Chem.*, **76**, 2274 (1972). In doing iterative EH calculations on sulfanes, $H_2S_n$, these authors ignored the skewed conformation of these compounds; see, *e.g.*, H. Wieser, P. J. Krueger, E. Muller, and J. B. Hyne, *Can. J. Chem.*, **47**, 1633 (1969). For reasons not apparent, the IEH energy level diagrams of $H_2S_2$ at 0 and 180° dihedral angles bear little resemblance to other semiempirical results on this molecule.

(15) R. W. Woody, *Tetrahedron*, **29**, 1273 (1973).

(16) J. Webb, R. W. Strickland, and F. S. Richardson, *J. Amer. Chem. Soc.*, **95**, 4775 (1973).

(17) W. M. Moreau and K. Weiss, *J. Amer. Chem. Soc.*, **88**, 204 (1966); L. N. Kramer and M. P. Klein, *Chem. Phys. Lett.*, **8**, 183 (1971); R. F. Hudson and F. Filippini, *J. Chem. Soc., Chem. Commun.*, 726 (1972).

(18) D. B. Boyd and W. N. Lipscomb, *J. Theor. Biol.*, **25**, 403 (1969); R. Hoffmann, D. B. Boyd, and S. Z. Goldberg, *J. Amer. Chem. Soc.*, **92**, 3929 (1970), Paper IV; D. B. Boyd and R. Hoffmann, *ibid.*, **93**, 1064 (1971), Paper VI.

(19) D. B. Boyd, *J. Amer. Chem. Soc.*, **94**, 6513 (1972).

(20) D. P. Santry and G. A. Segal, *J. Chem. Phys.*, **47**, 158 (1967).

(21) J. A. Pople and D. L. Beveridge, "Approximate Molecular Orbital Theory," McGraw-Hill, New York, N. Y., 1970; P. A. Dobosh, CNINDO, Program 141, Quantum Chemistry Program Exchange, Department of Chemistry, Indiana University, Bloomington, Ind. 47401.

(22) D. B. Boyd, *J. Amer. Chem. Soc.*, **94**, 64 (1972), Paper IX, and references therein.

(23) D. B. Boyd in "The Purines: Theory and Experiment," E. D. Bergmann and B. Pullman, Ed., The Israel Academy of Sciences and Humanities, Jerusalem, 1972, p 48.

(24) P.-O. Löwdin, *J. Chem. Phys.*, **18**, 365 (1950).

(25) H. L. Hase, H. Meyer, and A. Schweig, *Theor. Chim. Acta*, **28**, 99 (1972); D. B. Boyd, *ibid.*, **23**, 383 (1971), Paper VIII.

(26) J. W. McIver, Jr., P. Coppens, and D. Nowak, *Chem. Phys. Lett.*, **11**, 82 (1972). Other authors have not made explicit the procedure used to plot neglect-of-differential-overlap wave functions, see, *e.g.*, S. Ishimaru, H. Kato, T. Yamabe, and K. Fukui, *J. Phys. Chem.*, **77**, 1450 (1973). W. L. Jorgensen and L. Salem, "Organic Chemist's Book of Orbitals," Academic Press, New York, N. Y., 1973, use the transformation $\mathbf{C}[\mathbf{C}^{+}\mathbf{SC}]^{-1/2}$.

(27) D. B. Boyd, *J. Amer. Chem. Soc.*, **91**, 1200 (1969), Paper II.

(28) Unlike the total density in a molecule, the electron density in an MO is not directly observable; see, *e.g.*, E. Steiner, *Annu. Rep. Progr. Chem., Sect. A*, **67**, 5 (1972). But the density in an MO is real in the sense that electron ionizations and excitations are indicative of MO levels. Also, the relative phase of the lobes in an MO may be deduced from reaction mechanisms, if the rules of R. Hoffmann and R. B. Woodward, *Accounts Chem. Res.*, **1**, 17 (1968), can be applied to this direction.

(29) D. B. Boyd, *Theor. Chim. Acta*, **18**, 184 (1970), Paper V.

(30) D. B. Boyd, *J. Chem. Phys.*, **52**, 4846 (1970), Paper III; D. B. Boyd and W. N. Lipscomb, *ibid.*, **46**, 910 (1967), Paper I.

(31) D. B. Boyd, *Theor. Chim. Acta*, **20**, 273 (1971), Paper VII.

(32) S. Wolfe, L. M. Tel, W. J. Haines, M. A. Robb, and I. G. Csizmadia, *J. Amer. Chem. Soc.*, **95**, 4863 (1973).

(33) Although the lone-pair regions of a difference map should not be identified with the MO's from which ionizations occur, it is known that ionization potential data and MO calculations are consistent with distinct first and second ionizations from n(p type) and n($sp^2$ type) MO's localized near a divalent sulfur. See, *e.g.*, D. A. Sweigart and D. W. Turner, *J. Amer. Chem. Soc.*, **94**, 5599 (1972); J. C. Dunzli, D. C. Frost, and L. Weiler, *ibid.*, **95**, 7880 (1973); G. L. Bendazzoli, G. Gottarelli, and P. Palmieri, *ibid.*, **96**, 11 (1974); and ref 13.

(34) H. Nakatsuji, *J. Amer. Chem. Soc.*, **96**, 30 (1974).

(35) R. Hoffmann, *J. Chem. Phys.*, **40**, 2745 (1964).

(36) J. M. Sichel and M. A. Whitehead, *Theor. Chim. Acta*, **7**, 32 (1967); **11**, 220, 239, 254, 263 (1968).

(37) L. A. Neubert, Ph.D. Thesis, Indiana University, Bloomington, Ind., 1969; M. Carmack and L. A. Neubert, *J. Amer. Chem. Soc.*, **89**, 7134 (1967).

(38) G. Bergson, G. Claeson, and L. Schotte, *Acta Chem. Scand.*, **16**, 1159 (1962), report the second uv band at about 280 nm for $1\alpha,5\alpha$-epidithioandrostane-$3\alpha,17\beta$-diol, which is thought to have a nearly cis planar disulfide linkage. The existence of this disulfide band is confirmed in the CD (ref 39). No such band was assumed to exist in the study of epidithiapiperazinediones by R. Nagarajan and R. W. Woody, *J. Amer. Chem. Soc.*, **95**, 7212 (1973).

(39) L. A. Neubert and M. Carmack, *J. Amer. Chem. Soc.*, **96**, 943 (1974), advance a novel supposition that the five or six highest disulfide bands all undergo red shifts as the dihedral angle is closed from 90 to 0°. The CD bands observed at 220 and 240 nm in 60° disulfides are extrapolated to about 210 and 225 nm for 90° disulfides, which would place them between the two observable uv bands around 205–210 and 250 nm. Definitive CD evidence of such intermediate bands is yet to be established. The signs and $\lambda_{max}$ of the Cotton effects claimed for disulfides with dihedral angles greater than 90° (ref 41 and 42) are consistent with the energy levels involved in the long wavelength excitations crossing in the correlation diagram as theory predicts (ref 2, 10, 15, and 16). Furthermore, the lack of a positive Cotton effect degenerate with a negative Cotton effect at 250 nm would leave unexplained the low inherent optical activity of 90° disulfides at this wavelength (ref 10 and 43).

(40) D. B. Boyd. Presented at the International Symposium on Quantum Biology and Quantum Pharmacology, Sanibel Island, Fla., Jan 17, 1974.

(41) U. Ludescher and R. Schwyzer, *Helv. Chim. Acta*, **54**, 1637 (1971), report nmr and CD data for [2,7-cystine]gramicidin S. Their conformational assignment of P chirality and 120° dihedral angle at the disulfide linkage would have the sulfurs cocked so that each is proximal to an amide nitrogen, whereas in cyclocystine (ref 43) and epidithiapiperazinediones (ref 2) they prefer to be closer to the carbonyl carbons of the attached peptides. Proximity of the positive carbonyl carbon center (ref 2) and the sulfur lone-pair electrons would be preferred not only by electrostatic attraction, but also by repulsion between the sulfur and nitrogen lone pairs. The sulfur lone-pair density seen in the electron density maps of the present paper and ref 3 would be better accommodated above a carbonyl carbon.

(42) M. Ptak, *Biopolymers*, **12**, 1575 (1973), gives evidence for preferring a 130–140° C–S–S–C dihedral angle in malformin A, rather than the 70–80° proposed by J. P. Casey and R. B. Martin, *J. Amer. Chem. Soc.*, **94**, 6141 (1972).

(43) B. Donzel, B. Kamber, K. Wüthrich, and R. Schwyzer, *Helv. Chim. Acta*, **55**, 947 (1972), report uv, CD, and nmr data on cyclo-L-cystine. The nmr data and a shoulder in the uv at about 250 nm ($\epsilon$ 474) are consistent with a 90° dihedral angle at the disulfide linkage. The tail of a negative Cotton effect at 228 nm extends through the 250-nm region, so that the rotatory strength of any transitions in this region must be too low to be detectable.

(44) H. Bock and B. G. Ramsey, *Angew. Chem., Int. Ed. Engl.*, **12**, 734 (1973), assume a C–S–S–C dihedral angle of 70° for $(t\text{-Bu})_2S_2$, whereas earlier work (ref 13) proposed a more reasonable value of about 110°.

(45) T. Koopmans, *Physica*, **1**, 104 (1933).

(46) The reason for the destabilization of these MO's is that the occupied $\sigma$ orbitals of the methyl group perturbatively interact (ref 47) with the disulfide orbitals, thereby lowering the energy of the former orbitals and raising the energy of the latter. The destabilization is not explainable in terms of charge migrations due to the R group because the EH calculations (ref 2) show that negative net atomic charge on the sulfurs is lower in $(CH_3)_2S_2$ than in $H_2S_2$, from which one could naively guess that the electrons on the disulfide moiety would be electrostatically stabilized due to methylation. The predicted direction of charge migration due to replacement of hydrogens by alkyl groups is not clear cut: EH (ref 2), CNDO/2 (ref 21 and 48), and *ab initio* (ref 49) calculations indicate charge density moves away from an atom with lone pairs due to a methyl group, but in going to still larger alkyl groups, CNDO/2 calculations (ref 50) indicate that charge density generally moves *onto* the electron-rich center. Investigations in which the relative net atomic charges on hydrogens and carbons are critical may not be definitively studied by CNDO/2 or INDO (ref 21) because of the serious and often overlooked problem of these methods making the hydrogens too negative with respect to comparable *ab initio* charges (ref 49) and those deduced from experiment (ref 51). The most commonly used CNDO/2 and INDO parameters (ref 21) need to be revised to make the hydrogens less electronegative with respect to carbon, and the various alternate parameterizations (ref 36, 50, 52, and 53) need to be pursued in this regard. In calculations to be published, we have found that deorthogonalization of CNDO/2 and INDO MO's prior to the population analysis does not entirely rectify this situation, although it does help lower the apparent charge density on the hydrogens.

(47) See, *e.g.*, R. Hoffmann, *Accounts Chem. Res.*, **4**, 1 (1971).

(48) J. A. Pople and M. Gordon, *J. Amer. Chem. Soc.*, **89**, 4253 (1967).

(49) W. J. Hehre and J. A. Pople, *J. Amer. Chem. Soc.*, **92**, 2191 (1970).

(50) R. B. Hermann, *J. Amer. Chem. Soc.*, **92**, 5298 (1970).

(51) H. Boaz, *Tetrahedron Lett.*, 55 (1973).

(52) R. B. Hermann, H. W. Culp, R. E. McMahon, and M. M. Marsh, *J. Med. Chem.*, **12**, 749 (1969).

(53) H. Fischer and H. Kollmar, *Theor. Chim. Acta*, **13**, 213 (1969), and references therein. The parameters of Fischer and Kollmar do lower the hydrogen charge densities in the right direction.

(54) H. W. Kroto and R. J. Suffolk, *Chem. Phys. Lett.*, **15**, 545 (1972).

(55) R. W. Kiser, "Introduction to Mass Spectroscopy and Its Applications," Prentice-Hall, Englewood Cliffs, N. J., 1965; R. W. Kiser and B. G. Hobrock, *J. Phys. Chem.*, **66**, 1214 (1962); I. Omura, K. Higasi, and H. Baba, *Bull. Chem. Soc. Jap.*, **29**, 501 (1956).

(56) L. S. Levitt and B. W. Levitt, *Chem. Ind. (London)*, 132 (1973).

(57) T. Blundell, G. Dodson, D. Hodgkin, and D. Mercola in "Advances in Protein Chemistry," C. B. Anfinsen, Jr., J. T. Edsall, and F. M. Richards, Ed., Vol. 26, Academic Press, New York, N. Y., 1972, p 279.

(58) R. S. Mulliken, *J. Chem. Phys.*, **23**, 1833 (1955).

(59) H. E. Van Wart, A. Lewis, H. A. Scheraga, and F. D. Saeva, *Proc. Nat. Acad. Sci. U. S.*, **70**, 2619 (1973); E. J. Bastian, Jr., and R. B. Martin, *J. Phys. Chem.*, **77**, 1129 (1973); R. B. Martin, *ibid.*, **78**, 855 (1974).

(60) C. P. Smyth, A. J. Grossman, and F. B. Jennings, *J. Amer. Chem. Soc.*, **62**, 1219 (1940).

# Diffusion and Thermal Diffusion in Binary Dense Gas Mixtures of Loaded Spheres and Rough Spheres

**Marc O. Baleiko and H. Ted Davis***

*Departments of Chemical Engineering and Chemistry, University of Minnesota, Minneapolis, Minnesota 55455* *(Received January 23, 1973; Revised Manuscript Received November 13, 1973)*

The results of fairly extensive numerical calculations of the diffusion and thermal diffusion coefficients obtained from Enskog's theory are presented for binary dense gas mixtures of loaded spheres and of rough spheres. The common result of both model theories in the limit of vanishing polyatomic parameters is the smooth hard-sphere value of the transport coefficients. The second-order Chapman–Enskog binary diffusion coefficients for rough spheres mixtures and for loaded sphere mixtures are well approximated over the entire density range by the first-order Chapman–Enskog formulas. Effects due to differences in masses and differences in eccentricity parameters in loaded sphere molecules are of equal importance in determining the sign and order of magnitude of the thermal diffusion coefficient. The effect due to different molecular diameters is nearly an order of magnitude smaller. In the rough sphere model, the effects of different masses and molecular sizes generally outweigh the effects due to different moments of inertia and usually determine the sign and order of magnitude of the thermal diffusion coefficient. Calculations for the dense gas $D_2$–HT system for both polyatomic models show strong composition and density dependence of the thermal diffusion factor. The form of the trial function has a significant effect upon the value of the thermal diffusion factor for rough spheres and the effect of spin anistropy, in particular, becomes very important as the density increases. The orientational anisotropy has a negligible effect upon the thermal diffusion factor for loaded spheres, whereas the spin anisotropy accounts for about 10% of the thermal diffusion factor for this model.

## I. Introduction

The formal results of the Enskog transport theory of dense gas mixtures of loaded spheres[1] and of rough spheres[2] (some mistakes in ref 2 have been corrected in ref 1) are used herein to obtain numerical estimates of the diffusion and thermal diffusion coefficients for these model fluids. Since the details and results of the formal theory are exceedingly lengthy, we present here only the barest outline of the theory and concentrate instead on assessing by numerical computation the role of rotational motions in diffusive processes. The formulas used in the computations are available in ref 1 and 2 and on microfilm.[3] It is hoped that the many tables and figures given in the following sections will be helpful in predicting qualitative trends for real fluids at high temperatures (where the attractive interactions are not important).

The loaded sphere molecules are characterized by loaded sphere parameters or eccentricity parameters, which are reduced moments of inertia defined as $a_\nu = m_{\nu\mu}\xi_\nu^2/\Gamma_\nu$ and $a_\mu = m_{\nu\mu}\xi_\mu^2/\Gamma_\mu$, where $m_{\nu\mu}$ $[\equiv m_\nu m_\mu/(m_\nu + m_\mu)]$ is the reduced mass for the species $\nu$ and $\mu$, $\xi$ is the eccentricity or displacement of mass center from geometric center, and $\Gamma_\nu$ is the principal moment of inertia for a molecule of species $\nu$. For real molecules that we hope to be adequately described as loaded spheres, the eccentricity $\xi$ is quite small. The eccentricity parameter having a value of zero corresponds to the case of a degenerate loaded sphere (actually a smooth hard sphere where the centers of mass and geometry coincide). Perhaps the largest physically realistic value of the eccentricity parameter is 0.167 for the HT molecule in the $D_2$–HT binary system.

The rough sphere molecules are characterized by rough sphere parameters, which are reduced moments of inertia defined as $\kappa_\lambda = 4I_\lambda/m_\lambda\sigma_\lambda^2$ for $\lambda = \nu,\mu$. $I_\lambda$ is the moment of inertia, $m_\lambda$ is the mass, and $\sigma_\lambda$ is the diameter of a molecule of species $\lambda$. The value of $\kappa_\lambda$ may vary from a value of zero when all the mass is concentrated at the center of the sphere to a value of ⅔ when all the mass is evenly distributed on the surface of the sphere. The limit $\kappa_\nu = \kappa_\mu \to 0$ corresponds to the smooth hard-sphere limit.

The general theory of the dense gas loaded sphere (LS) mixture has been applied to a binary mixture. Likewise, the general theory of the rough sphere (RS) dense gas mixture has been applied to the case of a binary system. For these two models the expression for the relative diffusion velocity in a two-component system of species $\nu$ and $\mu$ has the form

$$\mathbf{V}_\nu - \mathbf{V}_\mu = -\frac{n^2}{n_\nu n_\mu}[\mathfrak{D}_{\nu\mu}\mathbf{d}_{\nu\mu} + D_\mathrm{T}\nabla \ln T] \tag{1.1}$$

where $\mathfrak{D}_{\nu\mu}$ is the binary diffusion coefficient and $D_\mathrm{T}$ is the thermal diffusion coefficient. $\mathbf{d}_{\nu\mu}$ is a generalized diffusion force which for loaded spheres is given by

$$\mathbf{d}_{\nu\mu}^{(\mathrm{LS})} = (\rho nkT)^{-1}(\rho_\mu\nabla P_\nu - \rho_\nu\nabla P_\mu) - \frac{\rho_\nu\rho_\mu}{\rho nkT}(m_\nu^{-1}\chi_\nu - m_\mu^{-1}\chi_\mu) + n^{-1}b_{\nu\mu}g_{\nu\mu}(n_\nu\nabla n_\mu - n_\mu\nabla n_\nu) + n^{-1}b_{\nu\mu}\frac{\sigma_\nu - \sigma_\mu}{2\sigma_{\nu\mu}}n_\nu n_\mu\nabla g_{\nu\mu} \tag{1.2}$$

For rough spheres we have

$$\mathbf{d}_{\nu\mu}^{(\mathrm{RS})} = (\rho nkT)^{-1}(\rho_\mu\nabla P_\nu - \rho_\nu\nabla P_\mu) - \frac{\rho_\nu\rho_\mu}{\rho nkT}(m_\nu^{-1}\chi_\nu - m_\mu^{-1}\chi_\mu) + n^{-1}b_{\nu\mu}g_{\nu\mu}(n_\nu\nabla n_\mu - n_\mu\nabla n_\nu) \tag{1.3}$$

In these expressions $n_\nu$ is the number density of species $\nu$, $n$ is the total number density, $\rho_\nu$ is the mass density of species $\nu$, $\rho$ is the total mass density, $\chi_\nu$ is the external force on a particle of species $\nu$, $P_\nu$ is the hydrostatic pressure due to species $\nu$, $\sigma_\nu$ is the diameter of a particle of species $\nu$, $\sigma_{\nu\mu} = (\sigma_\nu + \sigma_\mu)/2$, $b_{\nu\mu} = (2/3)\pi\sigma_{\nu\mu}{}^3$ and $g_{\nu\mu}$ is the contact value of the equilibrium pair correlation function for a pair of particles of species $\nu$ and $\mu$.

The generalized diffusion force for loaded spheres has the additional term proportional to $\nabla g_{\nu\mu}$. This term arises from a particular evaluation of the pair correlation function in the molecular chaos assumption used to close the hierarchy of equations for the singlet distribution function. In the development of the kinetic equations in the formal theory it is assumed that the doublet distribution function for a pair of particles, say molecule 1 of species $\nu$ with center of mass located at position $\mathbf{r}$ characterized by the dynamical variables $\tau$, and molecule 2 of species $\mu$ with center of mass located at $\mathbf{r} + \boldsymbol{\delta}_{\nu1} - \boldsymbol{\delta}_{\mu2}$ characterized by dynamical variables $\tau_2$, may be written as the product of a correlation function which is independent of momenta, and two singlet distribution functions. This assumption has the form

$$f_{\nu\mu}(\mathbf{r}, \tau_1, \mathbf{r} + \boldsymbol{\delta}_{\nu1} - \boldsymbol{\delta}_{\mu2}, \tau_2; t) = g_{\nu\mu}(\mathbf{r} + \boldsymbol{\delta}_{\nu1}) f_\nu(\mathbf{r}, \tau_1; t) f_\mu(\mathbf{r} + \boldsymbol{\delta}_{\nu1} - \boldsymbol{\delta}_{\mu2}, \tau_2; t) \quad (1.4)$$

For loaded spheres

$$\boldsymbol{\delta}_{\nu1} = \xi_\nu \mathbf{e}_1 - {}^1\!/_2\sigma_\nu \mathbf{k}$$

$$\boldsymbol{\delta}_{\mu2} = \xi_\mu \mathbf{e}_2 + {}^1\!/_2\sigma_\mu \mathbf{k}$$

where $\mathbf{k}$ is the unit vector in the direction from the geometric center of molecule 2 to the geometric center of molecule 1 at the moment of impact, and $\mathbf{e}$ is the unit vector in the direction from the center of mass to the center of geometry with $\xi$ the distance the center of mass is displaced from the center of geometry. For rough spheres whose centers of mass and geometry coincide, $\xi_\nu = \xi_\mu = 0$, so that

$$\boldsymbol{\delta}_{\nu1} = - {}^1\!/_2\sigma_\nu \mathbf{k}$$

$$\boldsymbol{\delta}_{\mu2} = {}^1\!/_2\sigma_\mu \mathbf{k}$$

In writing the molecular chaos assumption it seems consistent to evaluate $g_{\nu\mu}$ at the point of contact of the two molecules, *i.e.*, $g_{\nu\mu}(\mathbf{r} + \boldsymbol{\delta}_{\nu1})$. If the pair correlation function for species of different molecular size is evaluated somewhat arbitrarily at the midpoint of the line joining the centers of mass or geometry, *i.e.*, $g_{\nu\mu} = g_{\nu\mu}(\mathbf{r} + {}^1\!/_2[\boldsymbol{\delta}_{\nu1} - \boldsymbol{\delta}_{\mu2}])$ the results are somewhat more symmetric forms for the subsequent kinetic equations and the $\nabla g_{\nu\mu}$ term does not appear in the generalized diffusion force. This was done in the rough sphere theory. In the loaded sphere theory $g_{\nu\mu}$ was evaluated at the point of contact of the two molecules and the additional term, which is a result of the effect of different molecular radii, appears in $\mathbf{d}_{\nu\mu}$. Both expressions for $\mathbf{d}_{\nu\mu}$ reduce in the low density limit to the proper dilute gas expression.[4]

It should be pointed out that the choice of where to evaluate $g_{\nu\mu}$ in the molecular chaos assumption does not affect the formulas for either $\mathfrak{D}_{\nu\mu}$ or $D_T$ for either model. The only result is the inclusion of the $\nabla g_{\nu\mu}$ term in the generalized diffusion force. For the loaded and rough sphere fluids, $g_{\nu\mu}$ is a function of $n_\nu$, $n_\mu$ only, so this term is a density gradient term.

Difference in concentration of the species, a pressure gradient in the system, different external forces on the species, and a temperature gradient can all give rise to a mass flux. The theoretical values of the transport coefficients are associated with the particular forms of the driving forces given here. For comparison of theory and experiment some care must be exercised so that the mass flux is expressed in terms of the same driving forces. The theoretical and experimental values of the transport coefficients may then be properly compared as coefficients of the same driving forces.

The formulas for the binary diffusion coefficient and the thermal diffusion coefficient in terms of the scalar coefficients arising in the Chapman–Enskog solution technique to the order of approximations made are for the loaded sphere model

$$\mathfrak{D}_{\nu\mu}{}^{(\mathrm{LS})} = {}^1\!/_2\frac{n_\nu n_\mu}{n}(2kT)^{1/2}\Big[m_\nu{}^{-1/2}({}^{\mathrm{LS}}C_{\nu1}{}^{00} + \frac{1}{3}{}^{\mathrm{LS}}C_{\nu2}{}^{00} + \frac{1}{3}{}^{\mathrm{LS}}C_{\nu3}{}^{00}) - m_\mu{}^{-1/2}({}^{\mathrm{LS}}C_{\mu1}{}^{00} + \frac{1}{3}{}^{\mathrm{LS}}C_{\mu2}{}^{00} + \frac{1}{3}{}^{\mathrm{LS}}C_{\mu3}{}^{00})\Big] \quad (1.5)$$

$$D_{\mathrm{T}}{}^{(\mathrm{LS})} = \frac{n_\nu n_\mu}{n^2}kT\Big[m_\nu{}^{-1/2}({}^{\mathrm{LS}}A_{\nu1}{}^{00} + \frac{1}{3}{}^{\mathrm{LS}}A_{\nu2}{}^{00} + \frac{1}{3}{}^{\mathrm{LS}}A_{\nu3}{}^{00}) - m_\mu{}^{-1/2}({}^{\mathrm{LS}}A_{\mu1}{}^{00} + \frac{1}{3}{}^{\mathrm{LS}}A_{\mu2}{}^{00} + \frac{1}{3}{}^{\mathrm{LS}}A_{\mu3}{}^{00})\Big] \quad (1.6)$$

and for the rough sphere model

$$\mathfrak{D}_{\nu\mu}{}^{(\mathrm{RS})} = {}^1\!/_2\frac{n_\nu n_\mu}{n}(2kT)^{1/2}[m_\nu{}^{-1/2}({}^{\mathrm{RS}}C_{\nu1}{}^{00} + {}^1\!/_2{}^{\mathrm{RS}}C_{\nu2}{}^{00}) - m_\mu{}^{-1/2}({}^{\mathrm{RS}}C_{\mu1}{}^{00} + {}^1\!/_2{}^{\mathrm{RS}}C_{\mu2}{}^{00})] \quad (1.7)$$

$$D_{\mathrm{T}}{}^{(\mathrm{RS})} = \frac{n_\nu n_\mu}{n^2}kT[m_\nu{}^{-1/2}({}^{\mathrm{RS}}A_{\nu1}{}^{00} + {}^1\!/_2{}^{\mathrm{RS}}A_{\nu2}{}^{00}) - m_\mu{}^{-1/2}({}^{\mathrm{RS}}A_{\mu1}{}^{00} + {}^1\!/_2{}^{\mathrm{RS}}A_{\mu2}{}^{00})] \quad (1.8)$$

The scalar coefficients, $C_{\nu1}{}^{00}, \ldots, A_{\mu2}{}^{00}$, appearing in these formulas are solutions to sets of linear algebraic equations of the form

$$x^\alpha = \Delta \cdot Y^\alpha \quad (1.9)$$

Here $Y^\alpha$ is a column vector composed of the scalar coefficients corresponding to the $\alpha$th transport coefficient, for example, for mutual diffusion, to the approximation considered here for loaded spheres

$$\text{transpose } Y^\alpha \equiv (C_{\nu1}{}^{00}, C_{\nu1}{}^{10}, C_{\nu1}{}^{01}, C_{\nu2}{}^{00}, C_{\nu3}{}^{00}, C_{\mu1}{}^{00}, C_{\mu1}{}^{10}, C_{\mu1}{}^{01}, C_{\mu2}{}^{00}, C_{\mu3}{}^{00}) \quad (1.10)$$

The appropriate $Y^\alpha$ for thermal diffusion is obtained by substituting $A$ for $C$ in eq 1.10. The elements of the column vector $x^\alpha$ and of $\Delta$ are given in ref 1 and 2 and in ref 3 for the models considered here. Equation 1.9 must be solved subject to a constraint of the form $\Sigma\beta_i{}^\alpha Y_i{}^\alpha = 0$, where the $\beta_i{}^\alpha$ are constants depending on molecular mass and composition. Since the final forms of the solutions to eq 1.9 for mutual and thermal diffusion are rather unwieldy we shall not reproduce them here. Instead we shall give in section II much simpler but equally accurate formulas for the mutual diffusion coefficient and we shall present in section III numerical computations aimed at illustrating the qualitative and quantitative dependence of the thermal diffusion coefficients on density, molecular masses, radii, and rotational parameters for the models considered. In section IV we examine the predicted thermal diffusion factor for model parameters pertinent to a $D_2$–HT mixture.

In the case of smooth, rough and loaded spheres, the elements of the matrix $\Delta$ involve the contact value of the equilibrium pair correlation function $g_{\nu\mu}$. This function has the properties that $g_{\nu\mu} \to 1$ in the limit of zero density and $g_{\nu\mu} \to \infty$ in the limit of the density increasing to a state where molecular motion is impossible. We also have the symmetry property $g_{\nu\mu} = g_{\mu\nu}$. The pair correlation functions for loaded and rough spheres are the same as the corresponding smooth hard-sphere correlation functions. For our purposes we will use the forms given by Lebowitz and Rowlinson,[5] which are Percus–Yevick formulas for these functions for a mixture of hard-sphere molecules. For a two-component system of hard spherical molecules of radii $\sigma_\nu$ and $\sigma_\mu$, we have

$$g_{\nu\nu} = \left[1 + \frac{1}{8}b_{\nu\nu}n_\nu + \frac{1}{8\sigma_\mu}(3\sigma_\nu - 2\sigma_\mu)b_{\mu\mu}n_\mu\right] \times \left[1 - \tfrac{1}{4}(b_{\nu\nu}n_\nu + b_{\mu\mu}n_\mu)\right]^{-2} \tag{1.11}$$

$$g_{\mu\mu} = \left[1 + \frac{1}{8}b_{\mu\mu}n_\mu + \frac{1}{8\sigma_\nu}(3\sigma_\mu - 2\sigma_\nu)b_{\nu\nu}n_\nu\right] \times \left[1 - \tfrac{1}{4}(b_{\nu\nu}n_\nu + b_{\mu\mu}n_\mu)\right]^{-2} \tag{1.12}$$

and

$$g_{\nu\mu} = g_{\mu\nu} = (\sigma_\mu g_{\nu\nu} + \sigma_\nu g_{\mu\mu})/2\sigma_{\nu\mu} \tag{1.13}$$

## II. Binary Diffusion Coefficients

The values of the scalar coefficients in eq 1.5–1.8 depend on the trial function for the distortion $\phi$ of the singlet distribution function $f(\mathbf{r}, \tau, t)$ from its local equilibrium form $f_{1e}$. The equation

$$f = f_{1e}(1 + \phi) \tag{2.1}$$

defines $\phi$. For our computations, the "second-order" trial function for a fixed binary mixture was chosen to be of the form[6]

$$\phi_\nu = \left\{\left[C_{\nu1}^{00} + C_{\nu1}^{10}\left(\frac{5}{2} - W_\nu^2\right) + C_{\nu1}^{01}(1 + \gamma - \Omega_\nu^2)\right]\mathbf{1} + C_{\nu2}^{00}\boldsymbol{\Omega}_\nu\boldsymbol{\Omega}_\nu + 2C_{\nu3}^{00}(\tfrac{1}{2} - \gamma)\mathbf{e}_\nu\mathbf{e}_\nu\right\}:\mathbf{W}_\nu\mathbf{d}_{\nu\mu} + \left\{\left[A_{\nu1}^{00} + A_{\nu1}^{10}\left(\frac{5}{2} - W_\nu^2\right) + A_{\nu1}^{01}(1 + \gamma - \Omega_\nu^2)\right]\mathbf{1} + A_{\nu2}^{00}\boldsymbol{\Omega}_\nu\boldsymbol{\Omega}_\nu + 2A_{\nu3}^{00}(\tfrac{1}{2} - \gamma)\mathbf{e}_\nu\mathbf{e}_\nu\right\}:\mathbf{W}_\nu\nabla \ln T \tag{2.2}$$

where 1 denotes the unit tensor, $\mathbf{W}_\nu$ the reduced linear velocity

$$\mathbf{W}_\nu \equiv \sqrt{(m_\nu/2kT)}\,\mathbf{c}_\nu \tag{2.3}$$

and $\Omega$ the reduced angular velocity

$$\boldsymbol{\Omega}_\nu = \sqrt{(\Gamma_\nu/2kT)}\,\mathbf{w}_\nu \tag{2.4}$$

$\mathbf{c}$ is the velocity of the center of mass of molecule $\nu$, $\Gamma$ the principal (nontrivial) moment of inertia of species $\nu$, and $\omega_\nu$ the angular momentum of molecule $\nu$ about its center of mass. For smooth spheres $C_{\nu1}^{01} = C_{\nu2}^{00} = C_{\nu3}^{00} = A_{\nu1}^{01} = A_{\nu2}^{00} = A_{\nu3}^{00} = 0$. For rough spheres $\gamma = \frac{1}{2}$ and for loaded spheres $\gamma = 0$.

The coefficients $C_{\nu1}^{00}, \ldots, A_{\nu3}^{00}$ are of course determined by the theory. They are obtained as the components of the column vectors denoted as $Y^\alpha$ in eq 1.9. For a trial function of the form given by eq 2.2, the $A$'s and the $C$'s are determined by inverting nine by nine matrices. The trial function obtained by setting $C_{\nu1}^{10} = C_{\nu1}^{01} = C_{\nu2}^{00} = C_{\nu3}^{00} = 0$ yields the so-called first-order Chapman-Enskog approximation to the diffusion coefficient. For the three models considered here, the first-order results are

$$\mathfrak{D}_{\nu\mu} = \frac{3}{8}\left(\frac{kT}{2\pi m_{\nu\mu}}\right)^{1/2}(n\sigma_{\nu\mu}^2 g_{\nu\mu})^{-1}h \tag{2.5}$$

where for smooth hard spheres $h = 1$, for loaded spheres

$$h = 4/U_{\nu\mu}^{11(1)} \tag{2.6}$$

and for rough spheres

$$h = \frac{1 + \kappa_{\nu\mu}}{1 + 2\kappa_{\nu\mu}} \tag{2.7}$$

The quantity $U_{\nu\mu}^{11(1)}$, a symmetrical function of $a_\nu$ and $a_\mu$ defined by the expression

$$U_{\nu\mu}^{11(1)} = \int_{-1}^{1}\int_{-1}^{1}(1 + a_\nu x^2 + a_\mu y^2)^{-1/2}\,\mathrm{d}x\,\mathrm{d}y \tag{2.8}$$

is tabulated in Table I (microfilm, see ref 3). The quantity $\kappa_{\nu\mu}$ is defined by the expression

$$\kappa_{\nu\mu}^{-1} = m_{\nu\mu}[(m_\nu\kappa_\nu)^{-1} + (m_\mu\kappa_\mu)^{-1}] \tag{2.9}$$

We have compared for equimolar systems the diffusion coefficients predicted from the second-order theory (by solving the 9 × 9 matrix equation) with the first-order results obtained from eq 2.5. The cases studied involved ranging the mass ratios, $m_\nu/m_\mu$, and radius (or diameter) ratios, $\sigma_\nu/\sigma_\mu$, from $\frac{1}{2}$ to 2, the density from gas-like to liquid-like values, and the polyatomic parameters $\kappa_\nu$ and $a_\nu$ over the physically realistical values 0 to $\frac{2}{3}$ and 0 to 0.167, respectively. In all our computations, we found less than 1% deviation of the first-order predictions (eq 2.5) from the second-order predictions. Thus, we conclude that eq 2.5 is accurate to the second-order Chapman-Enskog approximation. This conclusion is well known[6] for smooth hard spheres and, therefore, is not surprising, although it is a happy conclusion in view of the simplicity of eq 2.5–2.9.

The diffusion coefficient of rough spheres is smaller than that of corresponding smooth spheres (the factor $h$ given by eq 2.7 runs from 1 to about 0.71 as the pair $\kappa_\nu, \kappa_\mu$ ranges from 0,0 to $\frac{2}{3}, \frac{2}{3}$). Thus, in the extreme case the rotational motion of rough spheres reduces the diffusion coefficient by about 29%.

Loaded sphere behavior provides an interesting contrast to rough sphere behavior. The diffusion coefficient of loaded spheres is actually greater than that of corresponding smooth spheres. The function $U_{\nu\mu}^{11(1)}$ decreases with increasing $a_\nu$ or $a_\mu$ and ranges from 4 to about 3.12 as the pair $a_\nu, a_\mu$ ranges from 0,0 to $\frac{1}{2}, \frac{1}{2}$. For the largest realistic values, $a_\nu = a_\mu = 0.167$, $h$ has a value of about 1.12, an increase of 12% over the corresponding smooth sphere value.

The self-diffusion limit (molecular parameters of species $\nu \equiv$ those of species $\mu$) of eq 2.5 was obtained earlier by Brown and Davis[7] using an exponential approximation to the autocorrelation function.

## III. Thermal Diffusion Coefficients

Unlike the case of mutual diffusion, the setting of $A_{\nu1}^{10} = A_{\nu1}^{01} = A_{\nu2}^{00} = A_{\nu3}^{00} = 0$ does not lead to a meaningful approximation to the thermal diffusion coefficient. First of all, eliminating these coefficients ignores thermal conduction by diffusive motion. Secondly, the trends obtained for the thermal diffusion coefficient to this low order of approximation disagree even qualitatively with the results of the full second-order approximation obtained from eq 2.2. Consequently, we must solve the

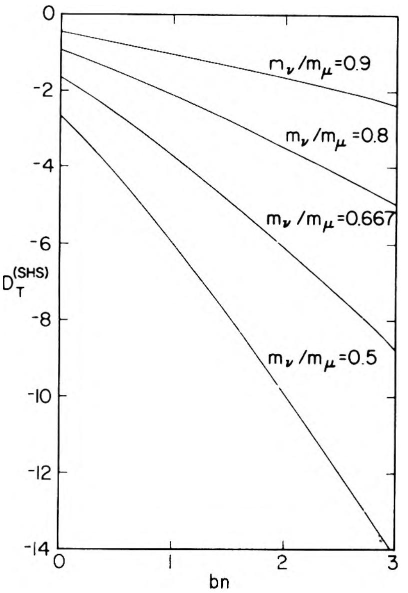

**Figure 1.** $D_T^{(SHS)}$ in units of $(kT/2\pi m_{\nu\mu})^{1/2} n^{-1}(2\sigma)^{-2}\ 10^{-2}$ vs. reduced density *bn*: $\sigma_\nu = \sigma_\mu = \sigma$, $x_\nu = x_\mu = 0.5$.

full set of equations represented by eq 1.9. Since this leads to rather complicated formulas we shall present here a few graphs illustrative of the numerical results, analytical details, and formulas being available elsewhere.[1-3] All the thermal diffusion computations presented in this section are for the special case of equimolar mixtures.

The thermal diffusion coefficient was calculated from the loaded sphere formalism in the limit $a_\nu = a_\mu = 0$ and from the rough sphere formalism in the limit $\kappa_\nu = \kappa_\mu = 0$. The common limit of these two polyatomic model theories is the smooth hard-sphere thermal diffusion coefficient $D^{(SHS)}$ which again provided a useful reducing quantity with which to measure the effects of the polyatomic character of the two models on thermal diffusion in subsequent calculations. These smooth hard-sphere results agree exactly with those predicted by McLaughlin and Davis,[8] who studied thermal diffusion in a mixture of smooth hard-sphere and square-well molecules.

Thermal diffusion coefficients were calculated for the two cases: (i) equal radii, $m_\nu/m_\mu$ = 0.5, 0.667, 0.8, 0.9, 1.0; and (ii) equal masses, $\sigma_\nu/\sigma_\mu$ = 0.5, 0.667, 0.8, 0.9, 1.0; for equal mole fractions.

Figure 1 depicts $D_T^{(SHS)}$ *vs.* reduced density *bn* for case i. $D_T^{(SHS)}$ is negative for all mass ratios less than unity. The magnitudes of the thermal diffusion coefficient increase with increasing *bn* for a fixed value of the mass ratio. The thermal diffusion effect decreases to zero as the mass ratio approaches unity and the mass difference driving force vanishes.

Figure 2 is a plot of $D_T^{(SHS)}$ *vs.* reduced density $b_{\nu\mu}n$ for case ii. This figure displays the different transport modes in dense systems. At low densities transport is pig-a-back, and $D_T^{(SHS)}$ is negative with the effect enhanced as $\sigma_\nu/\sigma_\mu$ decreases. At high densities $D_T^{(SHS)}$ is positive and increases as the species exhibit greater dissimilarity. At high densities the collisional mode of transport predominates. There is a value of the reduced density (approximately $b_{\nu\mu}n$ = 1.4) where the competing effects of the two modes of transport just balance and $D_T^{(SHS)}$ vanishes. The effect of different radii on thermal diffusion is generally an order of magnitude smaller than the effect due to differences in masses. Computations, presented elsewhere,[1] for the case $\sigma_\nu/\sigma_\mu = m_\nu/m_\mu = \alpha$ for varying $\alpha$ show that the mass is the controlling factor in establishing the magnitude and sign of the thermal diffusion coefficient in smooth hard-sphere molecules.

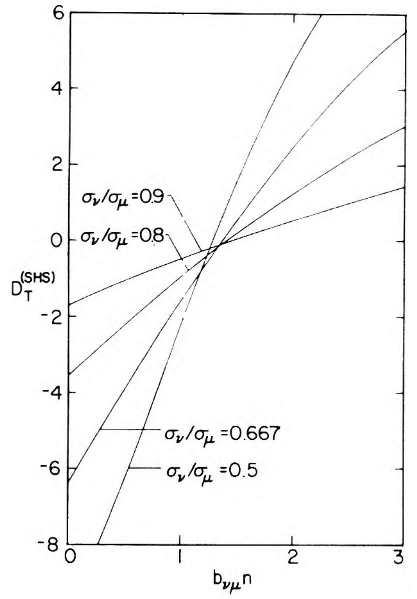

**Figure 2.** $D_T^{(SHS)}$ in units of $(kT/\pi m)^{1/2} n^{-1}\sigma_{\nu\mu}^{-2}\ 10^{-3}$ vs. reduced density $b_{\nu\mu}n$: $m_\nu = m_\mu = m$, $x_\nu = x_\mu = 0.5$

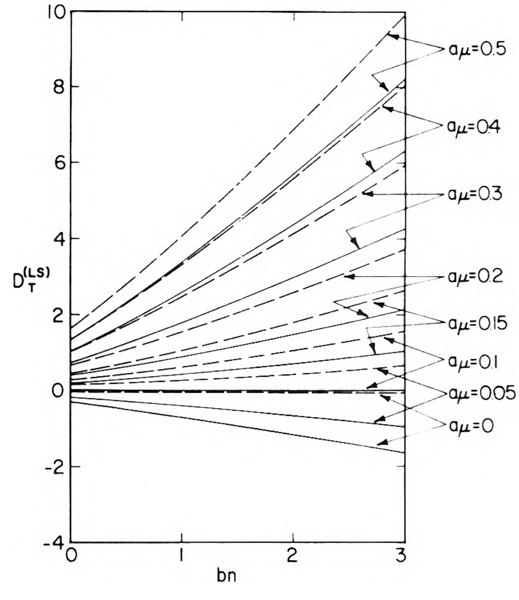

**Figure 3.** $D_T^{(LS)}$ in units of $(kT/\pi m)^{1/2} n^{-1}(2\sigma)^{-2}\ 10^{-2}$ vs. reduced density *bn*: $a_\nu = 0$, $m_\nu/m_\mu = \sigma_\nu/\sigma_\mu = 1$, $x_\nu = x_\mu = 0.5$ (dashed curves); $a_\nu = 0.10$, $m_\nu = m_\mu = \sigma_\nu/\sigma_\mu = 1$, $x_\nu = x_\mu = 0.5$ (solid curves).

The effect of different eccentricity parameters in the loaded sphere model is demonstrated in Figure 3. These are plots of $D_T^{(LS)}$ *vs.* *bn* for combinations of $a_\nu$ and $a_\mu$ for species of equal masses and equal radii. For fixed values of $a_\nu$, $D_T^{(LS)}$ is negative and increases in magnitude with *bn* for $a_\nu > a_\mu$, is identically zero for $a_\nu = a_\mu$, and is positive and increases with *bn* for $a_\nu < a_\mu$. The magnitude of the thermal diffusion coefficient for the case of different eccentricity parameters is nearly the same as that for different masses. The effect is greatest when the molecules exhibit the greatest dissimilarity, *i.e.*, when $|a_\nu - a_\mu|$ is maximal.

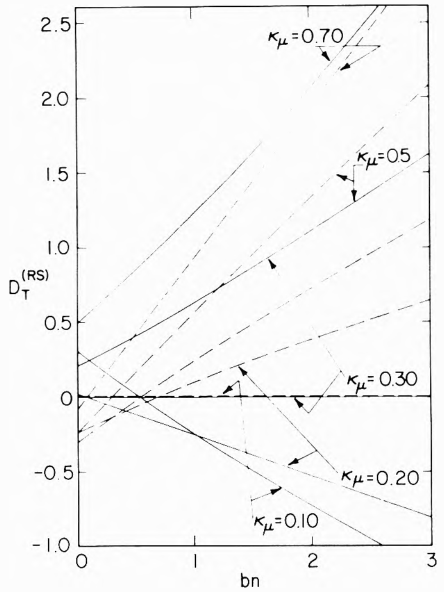

**Figure 4.** $D_T^{(RS)}$ in units of $(kT/\pi m)^{1/2}n^{-1}(2\sigma)^{-2}$ $10^{-3}$ *vs.* reduced density $bn$: $\kappa_\nu$ = 0.1, $m_\nu/m_\mu = \sigma_\nu/\sigma_\mu = 1$, $x_\nu = x_\mu$ = 0.5 (dashed curves); $\kappa_\nu$ = 0.3, $m_\nu/m_\mu = \sigma_\nu/\sigma_\mu = 1$, $x_\nu = x_\mu$ = 0.5 (solid curves).

The rough sphere thermal diffusion coefficient was calculated for different values of the reduced moments of inertia $\kappa_\nu$ and $\kappa_\mu$. For species of equal mass and molecular radius, dissimilar but symmetric mass distributions in the spheres give rise to different moments of inertia, and hence, provide a driving force that creates a thermal diffusion effect in such systems. Figure 4 shows plots of $D_T^{(RS)}$ *vs.* reduced density $bn$ for combinations of $\kappa_\nu$ and $\kappa_\mu$ for equal masses and equal radii. First we note that the effect of thermal diffusion due to differences in moments of inertia in the rough sphere model is generally one or two orders of magnitude smaller than the effect due to different eccentricity parameters in the loaded sphere model. At higher densities for moderately large values of $\kappa_\nu$ and $\kappa_\mu$, the qualitative behavior of $D_T^{(LS)}$ is the same as $D_T^{(LS)}$. That is, for reduced densities greater than approximately one, for a fixed value of $\kappa_\nu$, $D_T^{(RS)}$ is negative for $\kappa_\mu < \kappa_\nu$ and increases in a positive sense with increasing $\kappa_\mu$, is identically zero for $\kappa_\mu = \kappa_\nu$ (for all densities), and is positive for $\kappa_\mu > \kappa_\nu$ and increases with $\kappa_\mu$. At low densities the qualitative behavior of $D_T^{(RS)}$ does not appear the same. Figure 5 is a plot of $D_T^{(RS)}$ *vs.* $\kappa_\mu$ for the dilute gas limit $bn$ = 0. It is not true that a maximum thermal diffusion effect corresponds to the greatest dissimilarity in the species. Qualitatively speaking, our results are in agreement with the results of Trübenbacher[9] who studied the dilute gas rough sphere binary mixture. It was not possible to compare our numerical values with his since he studied thermal diffusion in the limit that the concentration of one species vanishes and for small differences in $\kappa_\nu$ and $\kappa_\mu$.

At this point we wish to examine the effect that loads and roughness have on the thermal diffusion effect when the species present have different masses or radii. For this purpose we define the reduced thermal diffusion coefficients

$$D_T^{(RS)*} = \frac{D_T^{(RS)}(\kappa_\nu, \kappa_\mu, b_{\nu\mu}n, m_\nu/m_\mu, \sigma_\nu/\sigma_\mu, n_\nu, n_\mu)}{D_T^{(SHS)}(b_{\nu\mu}n, m_\nu/m_\mu, \sigma_\nu/\sigma_\mu, n_\nu, n_\mu)} \tag{3.1}$$

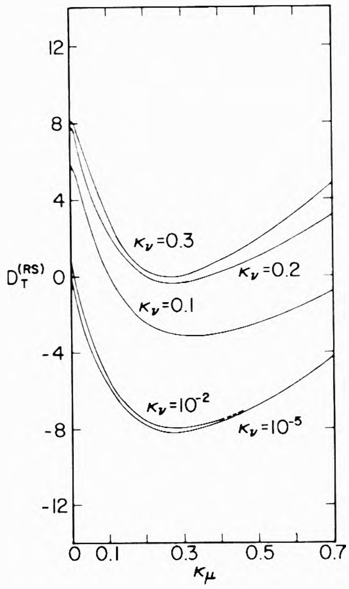

**Figure 5.** $D_T^{(RS)}$ in units of $(kT/\pi m)^{1/2}n^{-1}(2\sigma)^{-2}$ $10^{-3}$ *vs.* $\kappa_\mu$: $bn$ = 0, $m_\nu/m_\mu = \sigma_\nu/\sigma_\mu = 1$, $x_\nu = x_\mu$ = 0.5.

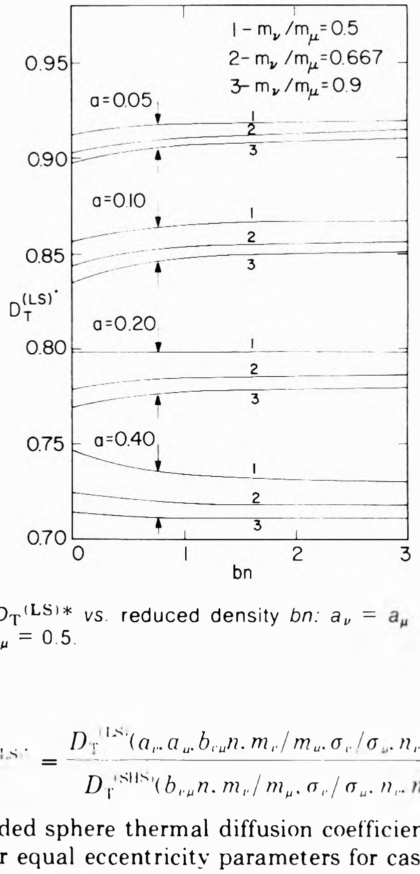

**Figure 6.** $D_T^{(LS)*}$ *vs.* reduced density $bn$: $a_\nu = a_\mu$ = a, $\sigma_\nu/\sigma_\mu$ = 1, $x_\nu = x_\mu$ = 0.5.

and

$$D_T^{(LS)*} = \frac{D_T^{(LS)}(a_\nu, a_\mu, b_{\nu\mu}n, m_\nu/m_\mu, \sigma_\nu/\sigma_\mu, n_\nu, n_\mu)}{D_T^{(SHS)}(b_{\nu\mu}n, m_\nu/m_\mu, \sigma_\nu/\sigma_\mu, n_\nu, n_\mu)} \tag{3.2}$$

The loaded sphere thermal diffusion coefficient was calculated for equal eccentricity parameters for case i. Figure 6 is a plot of $D_T^{(LS)*}$ *vs.* $bn$ for case i. The addition of equal loads to molecules of different masses results in reducing the thermal diffusion effect. Very little density dependence is exhibited. For a fixed value of $a$, $D_T^{(LS)*}$ decreases as $m_\nu/m_\mu$ tends toward unity. For a fixed value of $m_\nu/m_\mu$, the addition of equal loads to the molecules decreases $D_T^{(LS)*}$ as $a$ increases. The thermal diffusion coefficient for a particular mass ratio may be decreased only as much as 15-20% if the molecules have the maximum physically realistic load parameters.

Rough sphere thermal diffusion coefficients were calcu-

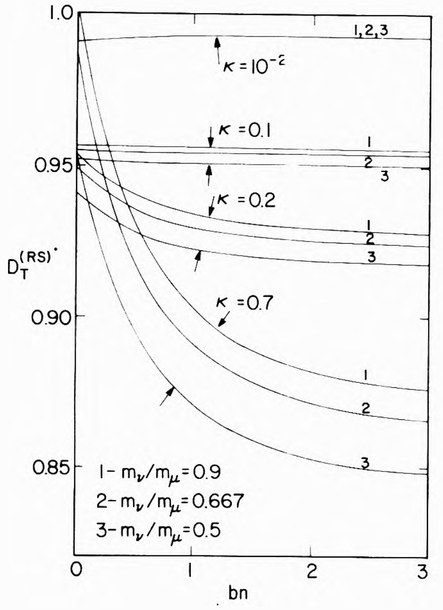

**Figure 7.** $D_T^{(RS)*}$ *vs.* reduced density *bn*: $\kappa_\nu = \kappa_\mu = \kappa$, $\sigma_\nu/\sigma_\mu = 1$, $x_\nu = x_\mu = 0.5$.

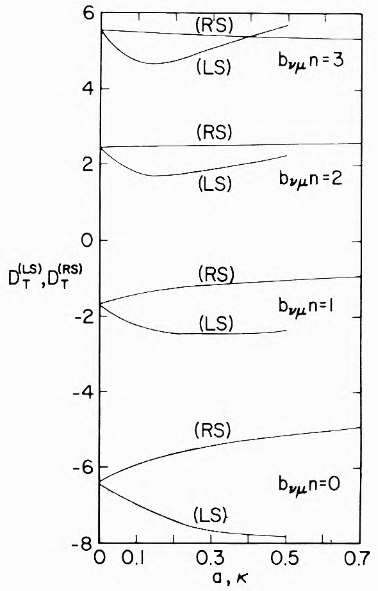

**Figure 8.** $D_T^{(LS)}$ *vs. a*, $D_T^{(RS)}$ *vs.* $\kappa$, in units of $(kT/\pi m)^{1/2} n^{-1} \sigma_{\nu\mu}^{-2}\ 10^{-3}$ for $\sigma_\nu/\sigma_\mu = 0.667$: $a_\nu = a_\mu = a$, $\kappa_\nu = \kappa_\mu = \kappa$, $m_\nu = m_\mu = m$, $x_\nu = x_\mu = 0.5$.

lated for the case $\kappa_\nu = \kappa_\mu = \kappa$ for systems in which the species have different masses. Figure 7 is a plot of $D_T^{(RS)*}$ *vs. bn* for case i. The curves exhibit a definite ordering at high densities where the collisional mode of transport dominates. At low densities $D_T^{(RS)*}$ does not vary monotonically with $\kappa$ for a fixed mass ratio, but exhibits a minimum with respect to $\kappa$ (a trait that seems to characterize the low density pig-a-back transport with rough sphere molecules). Generally speaking, $D_T^{(RS)}$ is reduced when roughness is added to molecules of different masses. The effect varies in magnitude but is only as much as 15% in a dense system with $m_\nu/m_\mu = 0.5$ and $\kappa$ at its largest physically realistic value.

Claypool[10] gives an expression for the thermal diffusion coefficient, derived from the Longuet-Higgins and Pople[11] scheme, for an isotopic mixture of rough spheres. He considered species of equal molecular size but different masses and moments of inertia. The theory gives the following result for the thermal diffusion coefficient

$$D_T = \frac{3n_1n_2(m_1 - m_2)}{8n\sigma_1^2T(n_1m_1 + n_2m_2)}\left(\frac{m_{\nu\mu}kT}{2\pi}\right)^{1/2} \times \left(\frac{P}{nkT} - 1\right)\left[\left(\frac{2\kappa_{\nu\mu} + 1}{\kappa_{\nu\mu} + 1}\right)g(\sigma_1)\right]^{-1} \quad (3.3)$$

This expression predicts that thermal diffusion vanishes when the masses are identical even though the species have different moments of inertia. It also predicts that the reduced thermal diffusion coefficient is independent of density and is given by $(\kappa_{\nu\mu} + 1)/(2\kappa_{\nu\mu} + 1)$. This behavior is in disagreement with what we have predicted above with Enskog's theory.

The thermal diffusion coefficients for loaded spheres with $a_\nu = a_\mu = a$ and for rough spheres with $\kappa_\nu = \kappa_\mu = \kappa$ were calculated for the case of unequal radii, *i.e.*, case ii. In Figure 8, which is a typical plot for one value of $\sigma_\nu/\sigma_\mu$ in case ii, the thermal diffusion coefficients pass from negative to positive values as density increases as did $D_T^{(SHS)}$. This is because the difference in molecular radii is still the only driving force for thermal diffusion. The presence of equal eccentricity parameters in loaded spheres that have different radii tends to decrease the value of $D_T^{(LS)}$ in a negative sense for all physically realistic values of the eccentricity parameters. The presence of roughness and equal rough sphere parameters in molecules that have different radii tends to increase $D_T^{(RS)}$ in the positive sense for all but the highest densities. The polyatomic effects are most important at values of $\sigma_\nu/\sigma_\mu$ near unity since the thermal diffusion coefficient is small and the polyatomic effects represent a large per cent deviation from the SHS results. The polyatomic effects are also of most importance for reduced densities in the range $1.0 < b_{\nu\mu}n < 1.5$, where the thermal diffusion coefficient vanishes due to competing transport modes.

To determine whether the effects of different masses and different loaded sphere parameters are of equal importance, $D_T^{(LS)*}$ was plotted *vs.* $a_\mu$ in Figure 9. The plot displays two different mass ratios for high and low densities for the case $a_\nu = 0$, which will provide the greatest loaded sphere effect. The plot demonstrates a qualitative additivity of the effects of different masses and loaded sphere parameters. In a system where the masses are quite different, e.g., $m_\nu/m_\mu = 0.5$, the polyatomic effect of dissimilar loaded spheres can reduce the thermal diffusion effect by 40–50%. In a system where the mass difference is small, e.g., $m_\nu/m_\mu = 0.9$, the effect of dissimilar loaded sphere parameters dominates, and the sign of the thermal diffusion coefficient can be reversed. This is not surprising, as earlier we saw that the effects of dissimilar loaded spheres was of the same order of magnitude as the effects due to dissimilar masses.

Though not explicitly depicted in a figure, the effect of introducing loaded sphere character to molecules that have different radii is substantial. The effects of different loaded sphere parameters are dominating in determining the sign and order of magnitude of the thermal diffusion effect in situations where the species exhibit a size difference. This again is not surprising in light of the fact that differences in loaded sphere parameters were found to produce a thermal diffusion effect on order of magnitude greater than simple differences in molecular size.

To determine the importance of considering both mass

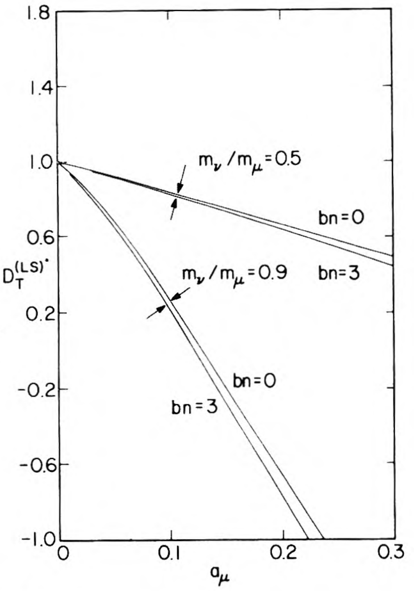

Figure 9. $D_T^{(LS)*}$ vs. $a_\mu$ for $a_\nu = 0$: $\sigma_\nu = \sigma_\mu = \sigma$, $x_\nu = x_\mu = 0.5$.

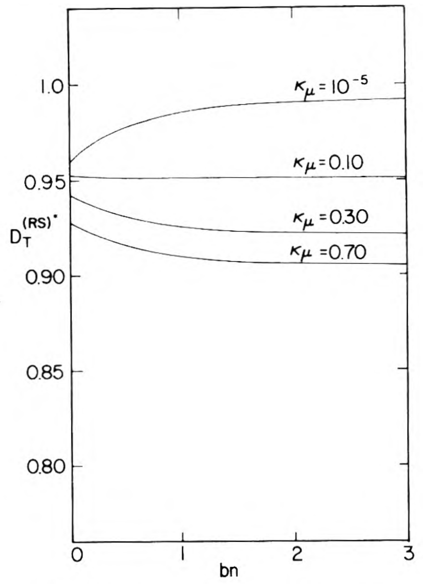

Figure 10. $D_T^{(RS)*}$ vs. reduced density $bn$: $\kappa_\nu = 0.1$, $m_\nu/m_\mu = 0.5$, $\sigma_\nu = \sigma_\mu = \sigma$, $x_\nu = x_\mu = 0.5$.

differences and the polyatomic effect of rough spheres differing in moments of inertia, $D_T^{(RS)}$ was calculated for case i for different values of $\kappa_\nu$, $\kappa_\mu$. Figure 10 depicts $D_T^{(RS)*}$ vs. $bn$ for $m_\nu/m_\mu = 0.5$ for $\kappa_\nu = 0.1$ and various values of $\kappa_\mu$. Differences in rough sphere parameters do not have a large effect on the thermal diffusion coefficient for this large a mass difference. In fact, even for small differences in masses we have found (but not reported here) that the maximum effect of different moments of inertia is a decrease in the thermal diffusion coefficient by 25%.

The thermal diffusion coefficient was also calculated for rough spheres with different rough sphere parameters for case ii. Our calculations show that the effects of different radii and different rough sphere parameters are not strongly coupled. Different molecular radii were found to produce a thermal diffusion effect of an order of magnitude greater than the effect of different moments of inertia. Except in the region of moderate densities where the thermal diffusion effect from unequal radii may vanish due to competing pig-a-back and collisional transfer modes, or for small values of the radius ratio, the sign and order of magnitude of the thermal diffusion effect is determined by the value of the radius ratio.

## IV. Dense Gas Mixtures of $D_2$ and HT

At this point we have made no attempt to model an actual binary system by either the rough sphere or loaded sphere model. Here we examine a dense gas mixture of $D_2$ and HT for both models. The gaseous system exhibits a thermal diffusion effect, and both the dilute gas rough sphere model and the dilute gas loaded sphere model have been employed in attempts to satisfactorily predict the phenomenon.

Trübenbacher[9] considered the molecules to be rough spheres with different moments of inertia and calculated the thermal diffusion factor $\alpha = D_T/x_\nu x_\mu \mathfrak{D}_{\nu\mu}$ for the binary mixture. With $\nu$ designating the species $D_2$ and $\mu$ designating the species HT, he postulated and molecules to be of equal mass and equal molecular size with $\kappa_\nu = 0.090$ and $\kappa_\mu = 0.068$. His prediction of $\alpha_T = 1.9 \times 10^{-3}$ is smaller than the experimental value[12] of 0.028 by a factor of about 15.

Sandler and Dahler,[13] realizing the system lends itself to description by the loaded sphere model, postulated the $D_2$ molecule as a smooth hard sphere and the HT molecule as a loaded sphere. Masses and molecular radii were assumed equal. Using a calculated value of the eccentricity parameter for HT of $a_\mu = 0.167$, they calculated a thermal diffusion factor approximately twice the experimentally observed value. When they used $a_\mu$ as an adjustable parameter to predict a proper rotational relaxation time for HT, a "semiempirical" value of $a_\mu$ was determined to be $a_\mu = 0.092$. This produces a value of $\alpha_T = 0.026$, which is in excellent agreement with experiment.

Our purpose in examining the dense gas rough sphere mixture model and the dense gas loaded sphere mixture model for the $D_2$-HT system is not to determine the success or failure of the models in predicting the dilute gas experimental value of the thermal diffusion factor; this question was answered quite well by Trübenbacher and Sandler and Dahler. We performed the calculations to give a concrete basis on which to compare the results of the dense gas theories, and also as a further check on our calculations in the dilute gas limit. We were unable to compare our calculations for the dense $D_2$-HT system to any experimental data.

The molecules $D_2$ and HT have a very small mass differences ($m_{D_2} - m_{HT} = 4.0294 - 4.0250 = 0.0044$ au) which by itself is incapable of adequately explaining the thermal diffusion effect. We calculated the diffusion coefficient and thermal diffusion factor for the dense gas $D_2$-HT system for the models: (i) $D_2$ and HT are smooth hard spheres with $\sigma_\nu/\sigma_\mu = 1$, $m_\nu/m_\mu = 4.0294/4.0250$. (ii) $D_2$ and HT are rough spheres with $\kappa_\nu = 0.090$, $\kappa_\mu = 0.068$, and $m_\nu/m_\mu = \sigma_\nu/\sigma_\mu = 1$. (iii) $D_2$ and HT are rough spheres with $\kappa_\nu = 0.090$, $\kappa_\mu = 0.068$, $m_\nu/m_\mu = 4.0294/4.0250$, and $\sigma_\nu/\sigma_\mu = 1$. (iv) $D_2$ and HT are loaded spheres with $a_\nu = 0$, $a_\mu = 0.167$, $m_\nu/m_\mu = \sigma_\nu/\sigma_\mu = 1$. (v) $D_2$ and HT are loaded spheres with $a_\nu = 0$, $a_\mu = 0.092$, $m_\nu/m_\mu = \sigma_\nu/\sigma_\mu = 1$.

The thermal diffusion factor is given in Table II (microfilm, see ref 3) for cases i-v for reduced densities in the range $0 < bn < 3$ for various compositions. For case i $\alpha_T$ varies only with density, that is, it is composition independent. The thermal diffusion factor for this case is positive and increases quite rapidly with density. At very low densities $\alpha_T$ for cases ii and iii has little dependence upon the composition, varying only about 7% for $bn = 0$, but is a strong function of composition at higher densities. In case ii for rough spheres of equal mass, $\alpha_T$ decreases from small positive values at low densities to large negative values at high densities. This density dependence may very well be the effect of the different transport modes characterizing the low and high density ranges. Case iii includes the effect of the small mass difference on the rough spheres. We see that for this case of a very small mass difference and small value of $\kappa_\nu$ and $\kappa_\mu$ the individual effects due to the mass difference and different moments of inertia superimpose qualitatively and add in a nearly quantitative manner to produce a net thermal diffusion effect. Previously we saw that this was not the case for large values of $\kappa_\nu$ and $\kappa_\mu$, where a coupling of the mass difference and different moments of inertia produced a net thermal diffusion effect quite different than would be expected if the two effects were independent. At high densities the very small mass difference determines the sign of the thermal diffusion factor.

For cases iv and v, $\alpha_T$ varies only about 10% over the entire range of compositions at low densities and less than 5% at high densities. $\alpha_T$ is positive and increases quite rapidly with density for all compositions. The agreement of our calculations at zero density and the results of Sandler and Dahler[13] is excellent.

All our reported rough sphere calculations were performed in the spin anisotropic approximation which includes the vector $\mathbf{W}\cdot\Omega\Omega$ in the expansion of **A** and **C** in the Chapman-Enskog scheme. A lower order approximation does not include this term, but only retains terms of the form $\mathbf{a}\cdot\mathbf{W}$, $\mathrm{b}\cdot\mathbf{W}(5/2 - W^2)$, and $\mathrm{h}\cdot\mathbf{W}(3/2 - \Omega^2)$ in the expansions of **A** and **C**. These two approximations are referred to, respectively, as the Kagan-Afanas'ev and Pidduck approximations.[14] For cases ii and iii the binary diffusion coefficient and thermal diffusion factor were calculated for equal mole fractions in the Pidduck approximation so we could compare the results without Kagan-Afanas'ev (KA) calculation and determine the sensitivity of the transport coefficients to the choice of the trial functions. As reported in section II, we found the value of the binary diffusion coefficient was virtually the same in both approximations. The thermal diffusion factor was quite sensitive to the effect of spin anisotropy. In cases ii and iii, $\alpha_T$ calculated in the KA approximation was decreased in the negative sense from the values given by the Pidduck approximation. At zero density in case ii the Pidduck approximation gave a value of $\alpha_T = 1.54 \times 10^{-3}$. Our calculation in the KA approximation is $1.25 \times 10^{-3}$, about 19% smaller. For case iii at zero density the Pidduck approximation gave a value of $\alpha_T = 2.03 \times 10^{-3}$. Our calculation in the KA approximation is $\alpha_T = 1.75 \times 10^{-3}$, nearly 14% smaller. At higher densities the effect of spin anisotropy is much larger. For case ii at $bn = 3$, the Pidduck approximation gave a value of $\kappa_T = -11.54 \times 10^{-3}$ while our KA calculation is $\kappa_T = -31.78 \times 10^{-3}$. For case (iii) at $bn = 3$ the values of $\alpha_T$ were found to be $45.29 \times 10^{-3}$ and $25.88 \times 10^{-3}$ for the Pidduck and KA approximations, respectively. These results illustrate the fact that the effects of spin anisotropy are very important in the dense rough sphere fluid, and perhaps warrant an extension of these calculations to test the effect of still higher approximations on the thermal diffusion coefficient. The fact that our result for case ii at zero density is somewhat lower than the result given by Trübenbacker[9] is not surprising in view of the fact that he used a lower approximation than the Pidduck, namely, $\mathbf{a}\cdot\mathbf{W} + \mathbf{b}\cdot\mathbf{W}(5/2 - W^2)$.

All our reported loaded sphere calculations include the effects of both an orientational anisotropy term $\mathbf{W}\cdot\mathbf{ee}$, and a spin anisotropy term $\mathbf{W}\cdot\Omega\Omega$ as expansion vectors for the functions **A** and **C** determining the diffusion and thermal diffusion coefficients. When orientational anisotropy is neglected the expansions for **A** and **C** have the KA form. When both orientational and spin anisotropy are neglected we have the Pidduck approximation. We performed the calculations for case iv and v for equal mole fractions in both the spin isotropic or Pidduck approximation and the orientation isotropic or KA approximation. The expansion vector $\mathbf{W}\cdot\mathbf{ee}$ was not included in the dilute gas theory of Sandler and Dahler[13] as previous evidence indicated it contributes a small amount to the value of transport coefficients. This was substantiated by our calculations in the dilute gas limit. Inclusion of the term leaves the binary diffusion coefficient essentially unchanged and lowers the thermal diffusion factor by less than 1% over the entire density range. The effect of spin anisotropy in the loaded sphere diffusion coefficient is also negligible. The effect on the thermal diffusion factor is greater in case iv than in case v, indicating that the effect increases with eccentricity parameter. The effect of spin anisotropy decreases with increasing density. For case iv at zero density the Pidduck approximation gives a value of $\alpha_T = 0.0474$ and the KA approximation a value of 0.0556, some 17% higher. For the case $bn = 0$, the Pidduck value of $\alpha_T$ is 6.32 whereas the KA value is 6.81, an increase of less than 8%. The differences between the Pidduck and KA approximations for case v are somewhat smaller, being 12.2% at zero density and only 5% at $bn = 3$.

We observe the thermal diffusion factor to increase rapidly with increasing density which suggests that at densities characteristic of the liquid phase we may expect the establishment of a concentration gradient one or two orders of magnitude larger than in very dilute gas systems. The tendency to establish a larger concentration gradient in the liquid system could then be employed to perhaps effect better separations while enjoying the advantage of the small volume in the liquid state.

*Acknowledgments.* The authors express their gratitude for financial support of this research furnished them by the National Science Foundation and the U. S. Army Research Office—Durham.

*Supplementary Material Available.* Listings of vector and matrix elements from which are obtained the scalar coefficients determining the mutual and thermal diffusion coefficients will appear following these pages in the microfilm edition of this volume of the journal. Photocopies of the supplementary material from this paper only or microfiche (105 × 148 mm, 24× reduction, negatives) containing all of the supplementary material for the papers in this issue may be obtained from the Journals Department, American Chemical Society, 1155 16th St., N.W., Washington, D. C. 20036. Remit check or money order for $3.00 for photocopy or $2.00 for microfiche, referring to code number JPC-74-1564.

## References and Notes

(1) M. Baleiko, Ph.D. Thesis, University of Minnesota, 1971.

(2) R. A. Stenzel, M. S. Thesis, University of Minnesota, 1967.
(3) See paragraph at end of paper regarding supplementary material.
(4) J. O. Hirschfelder, C. F. Curtiss, and R. B. Bird, "The Molecular Theory of Gases and Liquids," Wiley, New York, N. Y., 1954.
(5) J. L. Lebowitz and J. S. Rowlinson, *J. Chem. Phys.*, **41**, 133 (1964).
(6) S. Chapman and T. G. Cowling, "The Mathematical Theory of Nonuniform Gases," Cambridge University Press, New York, N. Y., 1953.
(7) R. Brown and H. T. Davis, *J. Phys. Chem.*, **75**, 1970 (1971).
(8) I. L. McLaughlin and H. T. Davis, *J. Chem. Phys.*, **45**, 2020 (1966).
(9) E. Trübenbacher, *Z. Naturforsch. A*, **17**, 539 (1962).
(10) J. L. Claypool, M.S. Thesis, University of Minnesota, 1968.
(11) H. C. Longuet-Higgins and J. A. Pople, *J. Chem. Phys.*, **25**, 884 (1956).
(12) J. Schirdewahn, A. Klemm, and L. Waldmann, *Z. Naturforsch. A*, **16**, 133 (1961).
(13) S. I. Sandler and J. S. Dahler, *J. Chem. Phys.*, **47**, 2621 (1967).
(14) For references to the work of F. B. Pidduck and of Yu. Kagan and A. M. Afanas'ev see D. W. Condiff, W. K. Lu, and J. S. Dahler, *J. Chem. Phys.*, **42**, 3445 (1965) and B. J. McCoy, S. I. Sandler, and J. S. Dahler, *ibid.*, **45**, 3485 (1966).

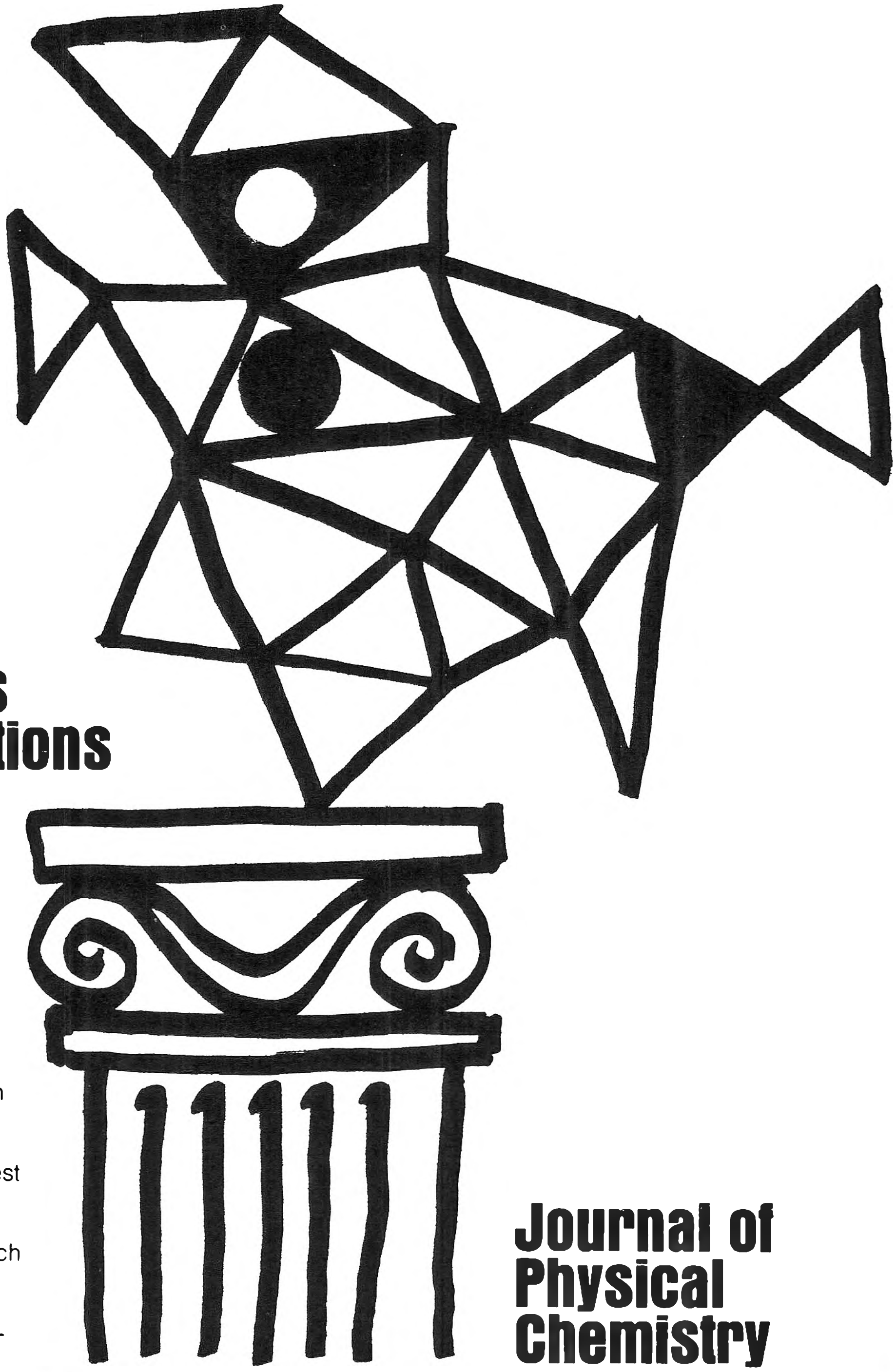

**New concepts**
**new techniques**
**new interpretations**

**. . . together**
**with valuable reports**
**on classical areas**

They are all waiting for you between the covers of our well-balanced JOURNAL OF PHYSICAL CHEMISTRY. Whatever your particular interest in physical chemistry, you'll find the JOURNAL's broad range of experimental and theoretical research reports are relevant and beneficial to your work. Each biweekly issue brings you an average of 30 authoritative, comprehensive reports on fundamental aspects of atomic and molecular phenomena, as well as timely notes, communications and reports plus the proceedings of selected symposia.

Join your fellow physical chemists who rely on JPC as an excellent biweekly source of data in both new and classical areas. Just complete and return the form to start your own subscription.

. . . *another ACS service*

**Journal of**
**Physical**
**Chemistry**

**The Journal of Physical Chemistry** **1974**
**American Chemical Society**
1155 Sixteenth Street, N.W.
Washington, D.C. 20036

Yes, I would like to receive the JOURNAL OF PHYSICAL CHEMISTRY at the one-year rate checked below:

| | *U.S.* | *Canada*** | *Latin America*** | *Other Nations*** |
|---|---|---|---|---|
| ACS Member One-Year Rate* | ☐ $20.00 | ☐ $25.00 | ☐ $25.00 | ☐ $26.00 |
| Nonmember | ☐ $60.00 | ☐ $65.00 | ☐ $65.00 | ☐ $66.00 |

Bill me ☐ Bill company ☐ Payment enclosed ☐

*Air freight rates available on request.*

Name ______________________

Street ______________________ Home ☐ Business ☐

City ______________ State ______ Zip ______

*NOTE: Subscriptions at ACS member rates are for personal use only. **Payment must be made in U.S. currency, by international money order, UNESCO coupons, U.S. bank draft, or order through your book dealer.

# Sulfur Research Trends

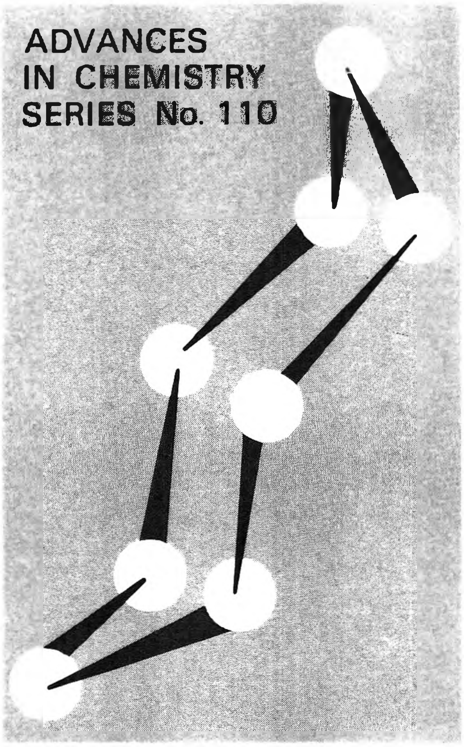

*A symposium sponsored by the Louisiana section of the American Chemical Society, chaired by David J. Miller and T. K. Wieuiorowski.*

Here is the most challenging and up-to-date roundup of the current findings and progress being made in the field of sulfur research today. These studies report all the latest trends in this rapidly developing area, from theoretical calculations on synthesis, bonding, and structure to new practical and applied uses.

**Sixteen papers probe varied aspects of sulfur research:**

**THEORETICAL**: *molecular orbital calculations, electron behavior, organosulfur structure*

**INORGANIC**: *spectrum of sulfur and its allotropes, transition metal complexes of donor ligands, sulfur nitrogen compounds, physical properties*

**ORGANIC**: *reactions with mercaptans, sulfur atoms and olefins, reactions with hydrogen*

**APPLIED**: *chalcogenide alloys, electrical conductivity, fluorinated polymers, elemental alteration, potential applications*

This timely review has lasting reference value for those involved in all areas of sulfur research. Put this volume to work for you.

231 pages with index Cloth (1971) $11.00
Postpaid in U.S. and Canada; plus 40 cents elsewhere.
Set of L.C. cards with library orders upon request.

## Other books in the ADVANCES IN CHEMISTRY SERIES on inorganic chemistry include:

**No. 102 Molecular Sieve Zeolites—II**
Thirty-six papers from the Second International Conference on Molecular Sieve Zeolites covering sessions on sorption and catalysis.
459 pages with index Cloth (1971) $16.00

**No. 101 Molecular Sieve Zeolites—I**
Forty-one papers from the Second International Conference on Molecular Sieve Zeolites covering sessions on synthesis, structure, mineralogy, and modification and general properties.
526 pages with index Cloth (1971) $16.00

**Nos. 101 and 102 ordered together** $30.00

**No. 98 Platinum Group Metals and Compounds**
Eleven articles on the synthesis, structure, determination, and industrial aspects of platinum group compounds; their magnetic, thermodynamic, and spectroscopic properties, and the recent chemistry of sigma- and pi-bonded complexes.
165 pages with index Cloth (1971) $9.00

**No. 89 Isotope Effects in Chemical Processes**
Methods of separating isotopes and labeled molecules—chemical exchange, electromigration, photochemical processes, and distillation—are examined, along with factors that suit a process to isotope separation—single stage fractionation, exchange rate, and reflux.
278 pages with index Cloth (1969) $13.00

**No. 82 Radiation Chemistry—II**
Thirty-six papers and 17 abstracts on radiation chemistry in gases, solids, and organic liquids. Includes three plenary lectures.
558 pages with index Cloth (1968) $16.00

**No. 81 Radiation Chemistry—I**
Forty-one papers and 17 abstracts on radiation chemistry in aqueous media, biology, and dosimetry. From the international conference at Argonne National Laboratory.
616 pages with index Cloth (1968) $16.00

**No. 81 and No. 82 ordered together** $30.00

**No. 80 Chemical Reactions in Electrical Discharges**
A wide range of topics is covered in 37 papers by chemists, physicists, and engineers—treatments of decomposition and dissociation reactions, ion-molecule reactions, chemical syntheses, and chemical engineering aspects and physics of reactions in electrical discharges.
514 pages with index Cloth (1969) $15.00

**No. 73 Trace Inorganics in Water**
Research reports; analytical developments including atomic absorption, flame emission, and neutron activation; and broad reviews, such as effects of trace inorganics on the ice-water system and the role of hydrous manganese and iron oxides on fixing metals in soils and sediments.
396 pages with index Cloth (1968) $12.50

**No. 72 Mass Spectrometry in Inorganic Chemistry**
A basic tool for chemical manipulations, the mass spectrometer, is a conventional monitor for any stage in a research problem to help establish what is going on. 21 research reports.
329 pages Cloth (1968) $12.00

**No. 71 Lanthanide-Actinide Chemistry**
The two series share similarities in chemical properties, magnetism, and radiant energy absorption and emission characteristic of *f*-electron species. But important differences exist—oxidation states, bonding, and complex ion formation. Lanthanides—13 papers; actinides—12.
359 pages Cloth (1967) $11.00

Order from **Special Issues Sales**
**American Chemical Society, 1155 Sixteenth Street, N.W., Washington, D.C. 20036**

24 08. 2517